GROWTH AND CHARACTERISATION OF TEXTURED SUPERCONDUCTING TAPES

By

Shadi Mohammad Abdel Kareem Al Khateeb

UNIVERSITY OF BIRMINGHAM

A thesis submitted to The University of Birmingham
for the degree of
DOCTOR OF PHILOSOPHY

Department of Metallurgy and Materials
The University of Birmingham
November 2009

Abstract

MgO thin films were deposited on Si (100) single crystals, NiW tapes, 310-austenitic stainless steel and Hastelloy C276 by the ultrasonic Spray Pyrolysis technique, using magnesium nitrate and magnesium acetate as precursors at many different conditions. Thermogravimetrical analysis (TGA) of the decomposition of the precursors was used as a guideline temperature for the thin film deposition. Biaxially textured and epitaxial MgO films were deposited on Si substrates using magnesium nitrate precursors. An amorphous MgO thin film was deposited on NiW tapes, NiO buffered NiW, 310-stainless steel and Hastelloy C276 when using low concentration of the magnesium nitrate precursor. Higher concentrations were needed to obtain (200) oriented MgO films on C276. However, NiW tapes and 310-stainless steel were found to be a non suitable substrate for MgO thin film deposition due to surface instability. A (200) oriented MgO thin film was grown on Hastelloy C276 using a magnesium acetate precursor at a much lower concentration compared to the nitrate precursor. The ISD deposition by spray pyrolysis (irrespective of the used precursor and the used substrate) produced MgO films that grew with the (200) normal to substrate surface as distinct to MgO films grown by thermal evaporation which grew with the (200) tilted to the substrate normal. Pulsed laser deposition (PLD) was used to deposit YBCO on MgO-buffered substrates. The characterization of the thin films was done using SEM, EBSD, XPS, AFM, X-ray diffraction 2θ-scans, rocking curve (ω-scans), phi (ϕ) scans, X-ray pole-figure measurements, and AC susceptibility. YBCO deposition by PLD on Si substrates buffered with MgO was not successful due to the thermal stresses developed in the MgO buffer. An EDX line scan performed on MgO films deposited on Hastelloy C276 from the acetate precursors confirmed the effectiveness of such layer as a diffusion barrier. It was found that c-axis oriented YBCO films were grown on c-axis oriented MgO films deposited on C276 from the nitrate and acetate precursors; however, MgO and YBCO films have a very weak in-plane texture. The AC susceptibility measurements show that the YBCO films have a broad superconducting transition temperature irrespective of the precursor used. To improve the superconducting transition temperatures, different annealing treatments were performed on the MgO buffer deposited on Hastelloy C276, however, it was found that the as deposited MgO buffer films and subsequent deposition of YBCO films gave the best superconducting transition temperatures. In an attempt to improve the in-plane texture of YBCO, CeO_2 was deposited by PLD on the spray pyrolysed MgO.

To my parents, my wife and my children

Acknowledgements

A great acknowledgment goes to my supervisors Prof. J.S. Abell and Prof. T.W. Button for their invaluable advices, sincere teaching and their kindness during the preparation of this thesis.

Thanks to Dr. Elizabeth Blackburn, from the Physics dept. for her help and giving access to the D5000 diffractometer for doing the rocking curve and phi scans measurements. Thanks to Dr. Tim Jackson from the electronic, electrical and computing engineering dept. for his help and giving the access to the laser laboratory.

I would like also to thank Dr. Yau Yau Tse, Dr. Chris Cooper, Dr. Seyed Koohpayeh, and Dr. Santiago Corujeira Gallo for their help in performing some of the needed experiments.

Thanks to Mr. Andy Bradshaw for his technical support. Thanks to my colleagues who supported me through the friendly chats and especially to Joe Tanner who helped me doing some laser depositions.

I would like to thank the Overseas Research Scholarship Award Scheme (ORSAS) and the Department of Metallurgy and Materials who covered jointly my tuition fees.

Finally, I would like to thank my parents, my wife and my brothers and sisters who stood behind my step by step until I finished my PhD.

Publications

1. Pavlopoulos D, Shadi Al-Khatiab, Button TW, Abell JS. Effort to produce textured CeO_2 and MgO films by the spray pyrolysis technique as buffer layers for coated conductors. Journal of Physics: Conference Series. 2008;97:012098.

2. Shadi Al Khateeb, T.W. Button, J.S. Abell. Spray pyrolysis of MgO templates on Hastelloy C276 and 310-austenitic stainless steel substrates for $YBa_2Cu_3O_7$ (YBCO) deposition by PLD. To be published.

3. D. Pavlopoulos, Shadi Al-Khateeb, T. W. Button, Abell JS. Spray Pyrolysis of Ceria (CeO_2) Thin Films and the Effect of Deposition Parameters on the Textural and Structural Properties. To be published.

4. D. Pavlopoulos, Shadi Al-Khateeb, T. W. Button, J. S. Abell. Spray Pyrolysis of MgO Thin Films on Si Single Crystals and the Effect of Deposition Time and Inclination Angle on the Texture and Morphology of the Films. To be published.

It should be mentioned that the first, third and fourth publications are not part of the experimental results presented in this thesis. However, these articles are used as references, within this thesis.

Table of contents

List of Figures

Figure 7.72: XRD patterns for the Hastelloy substrates deposited with MgO from 0.468M solution at 650°C for 48 minutes then annealed under 0.25 bar purified Ar at 1000°C for three hours.

Figure 7.73: SEM image for the Hastelloy substrate deposited with MgO from 0.468M solution at 650°C for 48 minutes then annealed under 0.25 bar purified Ar at 1000C for three hours.

Figure 7.74: A 5x5μm^2 AFM image for the Hastelloy substrate deposited with MgO from 0.468M solution at 650°C for 48 minutes then annealed under 0.25 bar purified Ar at 1000C for three hours.

Figure 7.75: XRD patterns for YBCO films deposited by PLD on the MgO films spray pyrolysed at different conditions.

Figure 7.76: SEM image for YBCO film deposited on MgO film spray pyrolysed on Hastelloy C276 using 0.468M of $Mg(NO_3)_2.6H_2O$ at 650°C for 64 minutes.

Figure 7.77: SEM image for YBCO film deposited on MgO film spray pyrolysed on Hastelloy C276 using 0.468M of $Mg(NO_3)_2.6H_2O$ at 650°C for 96 minutes.

Figure 7.78: SEM image for YBCO film deposited on MgO film spray pyrolysed on Hastelloy C276 using 0.78M of $Mg(NO_3)_2.6H_2O$ at 650°C for 48 minutes.

Figure 7.79: SEM image for YBCO film deposited on MgO film spray pyrolysed on Hastelloy C276 using 0.468M of $Mg(NO_3)_2.6H_2O$ at 700°C for 48 minutes.

Figure 7.80: A 5x5μm^2 AFM image for YBCO film deposited on MgO film spray pyrolysed on Hastelloy C276 using 0.468M of $Mg(NO_3)_2.6H_2O$ at 650°C for 64 minutes.

Figure 7.81: A 5x5μm^2 AFM image for YBCO film deposited on MgO film spray pyrolysed on Hastelloy C276 using 0.468M of $Mg(NO_3)_2.6H_2O$ at 650°C for 96 minutes.

Figure 7.82: A 5x5μm^2 AFM image for YBCO film deposited on MgO film spray pyrolysed on Hastelloy C276 using 0.78M of $Mg(NO_3)_2.6H_2O$ at 650°C for 48 minutes.

Figure 7.83: A 5x5μm^2 AFM image for YBCO film deposited on MgO film spray pyrolysed on Hastelloy C276 using 0.468M of $Mg(NO_3)_2.6H_2O$ at 700°C for 48 minutes.

Figure 7.84: XRD patterns for YBCO films deposited by PLD on the MgO films deposited by spray pyrolysis at 650°C from 0.468M solution for different deposition times.

Figure 7.85: SEM image for YBCO film deposited on MgO film spray pyrolysed on Hastelloy C276 using 0.468M of $Mg(NO_3)_2.6H_2O$ at 650°C for 32 minutes.

Figure 7.86: SEM image for YBCO film deposited on MgO film spray pyrolysed on Hastelloy C276 using 0.468M of $Mg(NO_3)_2.6H_2O$ at 650°C for 48 minutes.

Figure 8.49: XRD patterns for the Hastelloy substrate deposited with MgO from 0.093M at 600°C for 32 minutes after vacuum anneal at different temperatures and times.

Figure 8.50: XRD patterns with a narrow scan for the Hastelloy substrate deposited with MgO from 0.093M at 600°C for 32 minutes after vacuum anneal at different temperatures and times.

Figure 8.51: SEM image for the Hastelloy substrate deposited with MgO at 600°C for 32 minutes from 0.093M solution then annealed at 1000°C under vacuum for three hours.

Figure 8.52: EDX spectrum, using an accelerating voltage of 4KV, for MgO film deposited on Hastelloy C276 using 0.093M at 600°C with a deposition time of 32 minutes after being annealed at 1000°C for 3 hours.

Figure 8.53: A 5x5μm^2 AFM image for the Hastelloy substrate deposited with MgO at 600°C for 32 minutes from 0.093M solution then annealed at 1000°C under vacuum for three hours.

Figure 8.54: XRD patterns for the Hastelloy substrate deposited with MgO from 0.093M solution at 600°C for 32 minutes then annealed under 0.25 bar purified Ar at 1000°C for three hours.

Figure 8.55: SEM image for the Hastelloy substrate deposited with MgO from 0.093M solution at 600°C for 32 minutes then annealed under 0.25 bar purified Ar at 1000C for three hours.

Figure 8.56: XRD patterns for YBCO films deposited by PLD on the MgO films spray pyrolysed at different conditions.

Figure 8.57: SEM image for YBCO film deposited on MgO film spray pyrolysed on Hastelloy C276 using 0.093M $Mg(CH3COO)_2.4H_2O$ at 550°C for 64 minutes.

Figure 8.58: SEM image for YBCO film deposited on MgO film spray pyrolysed on Hastelloy C276 using 0.093M $Mg(CH3COO)_2.4H_2O$ at 600°C for 64 minutes.

Figure 8.59: SEM image for YBCO film deposited on MgO film spray pyrolysed on Hastelloy C276 using 0.093M $Mg(CH3COO)_2.4H_2O$ at 650°C for 32 minutes.

Figure 8.60: SEM image for YBCO film deposited on MgO film spray pyrolysed on Hastelloy C276 using 0.279M $Mg(CH3COO)_2.4H_2O$ at 600°C for 32 minutes.

Figure 8.61: A 5x5μm^2 AFM image for YBCO film deposited on MgO film spray pyrolysed on Hastelloy C276 using 0.093M $Mg(CH3COO)_2.4H_2O$ at 550°C for 64 minutes.

Figure 8.62: A 5x5μm^2 AFM image for YBCO film deposited on MgO film spray pyrolysed on Hastelloy C276 using 0.093M $Mg(CH3COO)_2.4H_2O$ at 600°C for 64 minutes.

Figure 8.63: A 5x5μm^2 AFM image for YBCO film deposited on MgO film spray pyrolysed on Hastelloy C276 using 0.093M $Mg(CH3COO)_2.4H_2O$ at 650°C for 32 minutes.

Figure 8.78: X-ray diffraction ϕ–scan for YBCO film deposited on MgO film spray pyrolysed at 600°C from 0.093M solution showing YBCO (013) with a FWHM of about 40^{o}.

Figure 8.79: EBSD histogram showing grain misorientation angles for YBCO film deposited on MgO film spray pyrolysed on Hastelloy C276 using 0.093M $Mg(CH3COO)_2.4H_2O$ at 550°C for 32 minutes.

Figure 8.80: EBSD histogram showing grain misorientation angles for YBCO film deposited on MgO film spray pyrolysed on Hastelloy C276 using 0.093M $Mg(CH3COO)_2.4H_2O$ at 600°C for 32 minutes.

Figure 8.81: Cross sectional SEM image of YBCO film deposited on MgO film spray pyrolysed on Hastelloy C276 using 0.093M $Mg(CH3COO)_2.4H_2O$ at 600°C for 32 minutes.

Figure 8.82: EDX line scan using 20KV of YBCO film deposited on MgO film spray pyrolysed on Hastelloy C276 using 0.093M $Mg(CH3COO)_2.4H_2O$ at 600°C for 32 minutes.

Figure 8.83: AC susceptibility measurement for YBCO deposited at 780^{o}C on the MgO buffer layer spray pyrolysed at different conditions.

Figure 8.84: XPS spectrum for the MgO thin film deposited on Hastelloy C276 substrate using 0.093M $Mg(CH3COO)_2.4H_2O$ at 600^{o}C for 32 min. showing the C 1s.

Figure 8.85: XRD patterns for CeO_2 films deposited by PLD at different conditions on the MgO films spray pyrolysed at 600°C from 0.093M for 32 minutes.

Figure 8.86: SEM image for CeO_2 film deposited by PLD at 710°C using $2x10^{-4}$ mbar O_2 on the MgO film deposited by spray pyrolysis at 600°C from 0.093M for 32 minutes.

Figure 8.87: SEM image for CeO_2 film deposited by PLD at 780°C using 0.6 mbar O_2 on the MgO film deposited by spray pyrolysis at 600°C from 0.093M for 32 minutes.

Figure 8.88: A $5x5\mu m^2$ AFM image for CeO_2 film deposited by PLD at 710°C using $2x10^{-4}$ mbar O_2 on the MgO film deposited by spray pyrolysis at 600°C from 0.093M for 32 minutes.

Figure 8.89: A $5x5\mu m^2$ AFM image for CeO_2 film deposited by PLD at 780°C using 0.6 mbar O_2 on the MgO film deposited by spray pyrolysis at 600°C from 0.093M for 32 minutes.

Figure 8.90: XRD patterns for YBCO and CeO_2 films deposited by PLD at different conditions on the MgO films deposited by spray pyrolysis at 600°C from 0.093M for 32 minutes.

Figure 8.91: SEM image for YBCO on CeO_2 film deposited by PLD at 710°C using $2x10^{-4}$ mbar O_2 on the MgO film deposited by spray pyrolysis at 600°C from 0.093M for 32 minutes.

Figure 8.92: SEM image for YBCO on CeO_2 film deposited by PLD at 780°C using 0.6 mbar O_2 on the MgO film deposited by spray pyrolysis at 600°C from 0.093M for 32 minutes.

Figure 8.93: A 5x5μm^2 AFM image for YBCO on CeO_2 film deposited by PLD at 710°C using 2x10^{-4} mbar O_2 on the MgO film deposited by spray pyrolysis at 600°C from 0.093M for 32 minutes.

Figure 8.94: A 5x5μm^2 AFM image for YBCO on CeO_2 film deposited by PLD at 780°C using 0.6 mbar O_2 on the MgO film deposited by spray pyrolysis at 600°C from 0.093M for 32 minutes.

Figure 8.95: AC susceptibility measurement for YBCO deposited on CeO_2 film deposited by PLD at 780°C using 0.6 mbar O_2 on the MgO film deposited by spray pyrolysis at 600°C from 0.093M for 32 minutes.

List of Tables

Nomenclature

A	Area (cm^2)
AACVD	Aerosol assisted chemical vapour deposition
AFM	Atomic force microscope
Al	Aluminium
AISI	American Iron and Steel Institute
Al_2O_3	Aluminium oxide or alumina
ASM	American Society for Metals
ArF	Argon fluorine
ASTM	American Society for Testing and Materials
BaO	Barium oxide
BaY_2O_4	Yttrium rich composition
BCC	Body centred cubic
Bi	Bismuth
Bi_2O_3	Bismuth oxide
BSCCO	Bi-Sr-Ca-Cu-O
BSI	British Standard Institute
CaO	Calcium oxide
CdO	Cadmium oxide
CDs	Memory discs
$Ce(CH_3COCHCOCH_3)_3$	Cerium acetylacetonate
$CeCl_3.7H_2O$	Cerium chloride heptahydrate
$Ce(NO_3)_3.6H_2O$	Cerium nitrate hexahydrate
CeO_2	Cerium oxide
CH_3CH_2OH	Ethanol
CH_3COCH_3	Acetone
Cr	Chromium
Cr_2N	Chromium nitride
CuO	Copper oxide
CuO_2	Copper dioxide
CVD	Chemical vapour deposition
$\overline{C}$	The average of the velocities of all the gas molecules (cm / sec)

D	The diffusivity of the gas or vapour (diffusion coefficient) (cm^2/sec)
d	The interplanar spacing (nm)
d_p	Particle or droplet diameter (cm)
d_{po}	The initial particle diameter (cm)
E_B	The electron binding energy (Joules)
EBSD	Electron backscattered diffraction
EDS	Energy dispersive spectroscopy
E_K	The kinetic energy of the ejected photo-electron (Joules)
ESAVD	Electrostatic spray-assisted vapour deposition
F_1	Correction factor
F_2	Correction factor
FCC	Face centred cubic
$Fe_2(SO_4)_3.9H_2O$	iron (III) sulfate nonahydrate
FWHM	Full width half maximum
f_t	Transducer frequency (Hz)
H	The magnetic field strength (Amp./m), differentiated from Henry's constant from context
H	Henry's constant which relates the concentration in the liquid to the partial pressure in the gas (L.atm/mole)
h	Plank's constant (6.626×10^{-34} Joule.second)
$H_2C_2O_4$	Oxalic acid
HBE	Higher binding energy
H_c	Critical magnetic field (Tesla)
H_{c1}	Lower critical field (Tesla)
H_{c2}	Upper critical field (Tesla)
He	Helium
HF	Hydrofluoric acid
Hg	Mercury
HTS	high temperature superconductor
HTSCs	high temperature superconductors
hυ	The incident photon energy (Joules)
In_2O_3	Indium oxide

IBAD	Ion beam assisted deposition
$InC1_3$	Indium chloride
IGC	Intergranular corrosion
ISD	Inclined substrate deposition
ISO	International organisation for standardisation
J_c	Critical current density (MA/cm^2)
K	Constant and its value depends on the corrosion rate unit, ex. $3.45x10^{-6}$ if the corrosion rate is in mm/yr
k	Spring constant (N/m)
k_B	Boltzmann's constant (erg/molecule. K)
Kn	Knudsen number, dimensionless
k_s	The surface reaction rate constant (cm/sec)
k_v	Reaction rate constant
$LaAlO_3$	Lanthanum aluminium oxide
LaB_6	Lanthanum boride
LAO	$LaAlO_3$
LBCO	La-Ba-Cu-O
M	Molecular weight (g/mole) or molarity (mole/l) or the magnetization of the material (the magnetic dipole moment per unit volume) (Amp/m) depending on context.
m_1	The mass of transported molecule or atom in the particle (g)
MCA	Multichannel analyzer
Me_3PO	Trimethylphosphine oxide
$Mg(CH_3COCHCOCH_3)_3$	Magnesium acetylacetonate
$Mg(CH_3COO)_2.4H_2O$	Magnesium acetate tetrahydrate
$Mg(NO)_3.6H_2O$	Magnesium nitrate hexahydrate
MgB_2	Magnesium diboride
$MgCO_3$	Magnesium carbonate
MgO	Magnesium oxide
$Mg(OH)_2$	Magnesium hydroxide
N	The number of points within a given area.
n	Order of diffraction

N_A	Avogadro's number (6.023×10^{23} molecules/mole)
NaCl	Sodium chloride
Nb	Niobium
Nb_3Ge	Niobium-germanium intermetallic compound
Ni	Nickel
NMR	Nuclear magnetic resonance
NiW	Nickel-tungsten intermetallic compound
N_∞	Droplet concentration per unit volume (number/cm^3)
p_1	Partial pressure of the vapour for species 1 far from the particle (dyne/cm^2)
p_{1s}	The reactant partial pressure at the particle surface (dyne/cm^2)
p_d	Partial pressure at the particle surface (dyne/cm^2)
p_e	The vapour pressure over a flat surface (dyne/cm^2)
PLD	Pulsed laser deposition
PVD	Physical vapour deposition
RABiTS	Rolling assisted biaxially textured substrates
RMS	Root mean square
r_v	The rate of reaction per unit volume (moles/cm^3 sec)
$SbCl_5$	Antimony pentachloride
SEM	Scanning electron microscopy
Si	Silicon
SiO_2	Silicon oxide
$SnCl_2$	Tin chloride (stannous chloride)
SND	substrate-nozzle distance
SnO_2	Tin oxide
SPM	Scanning probe microscopy
$SrCO_3$	Strontium carbonate
$SrTiO_3$	Strontium titanate
STM	scanning tunnelling microscopy
STO	$SrTiO_3$
T	Temperature (K or °C)
t	Time (second or hours)

T_c	Transition or critical temperature (K or °C)
TEM	Transmission electron microscopy
TGA	Thermogravimetrical analysis
TiN	Titanium nitride
Tl	Thallium
WDS	Wavelength dispersive spectroscopy
WEDM	Wire electric discharge machine
WQ	Water quench
x	Oxygen deficiency or cantilever deflection (m) depending on context.
XPS	X-ray photoelectron spectroscopy
XRD	X-ray diffraction
$\chi^{/}$	Real susceptibility (dimensionless)
$\chi^{//}$	Imaginary susceptibility (dimensionless)
Y	Yttrium
Y_2O_3	Yttria (yttrium oxide)
YBCO	Y-BA-Cu-O
YBCO-123	$YBa_2Cu_3O_{7-x}$
YSZ	Yttria stabilised zirconia
Z	Vertical position of the scanner
Z_{ave}	The average Z value within the given area
Z_i	The current Z value
$Zn(CH_3CO_2)_2.2H_2O$	Zinc acetate dihydrate
ZnO	Zinc oxide

Greek

α_s	Sticking coefficient (dimensionless)
θ	The Bragg angle, the angle between the incident X-ray beam and the particular crystal plane under consideration
λ	Wavelength of an incident monochromatic X-ray beam (nm) or mean free path of a gas (cm) depending on the context

μ	Viscosity (g/cm sec)
ν	Particle volume (cm^3)
ν_1	Volume of transported molecule or atom in the particle or volume of the reaction products (cm^3) depending on the context
υ	Frequency (Hz)
ρ	Density (g/cm^3)
ρ_1	Density of the material in the particle in the solid or liquid state (g/cm^3)
ρ_p	Particle density (g/cm^3)
σ	Surface tension (erg/cm^2)
τ_{GC}	Characteristic time for particle growth in continuum regime (second)
τ_{GF}	Characteristic time for particle condensation or evaporation in free molecular regime (second)
τ_{GSR}	The characteristic time for particle growth by surface reaction (second)
τ_{sat}	The time required to saturate the gas with the evaporating droplets (second)
Δm	Mass loss (g)

1 Introduction

The use of low temperature superconductors (LTS) has many limitations especially the low temperature refrigeration. Therefore, high temperature superconductors (HTS), which can be operated in a relatively inexpensive liquid nitrogen cryostat, have been produced and developed. The first generation of HTS wires were based on Bi-Sr-Ca-Cu-O (BSCCO) filaments embedded in an Ag alloy. The superconducting properties of the BSCCO family, however, are limited because of their intrinsically weak pinning properties in high magnetic fields. Therefore, $YBa_2Cu_3O_{7-x}$ (YBCO), the superconducting constituent of the second generation of HTS tapes, also referred to as coated conductors, is currently of great interest with regard to producing HTS wires based on flexible coated conductors, consisting of a layer of YBCO deposited on a thin metallic substrate. The interest in YBCO is because of its excellent transport properties in high magnetic field, and good mechanical flexibility. It can be produced with high degree of biaxial texture, has no high angle grain boundaries, and is easy to prepare single phase $YBa_2Cu_3O_{7-x}$ under normal temperature and pressure conditions. Therefore, it is a cost-effective way to manufacture flexible and high current density wires.

At present the coated conductors are produced by the relatively expensive ion beam assisted deposition (IBAD), inclined substrate deposition (ISD) and rolling assisted biaxially textured substrates (RABiTS). The challenge in these is to copy the texture of the substrate to YBCO through buffer layers.

Spray pyrolysis which is also called droplet deposition involves the deposition of evaporating droplets containing reactants onto surfaces, followed by further solvent evaporation and chemical reaction on the surface. It is used for the preparation of thin metals of noble metals, metal oxides, spinel oxides and superconducting compounds; because it is a simple, inexpensive, non-vacuum technique and has a high deposition rate. However, there are not many reports in literature referring to the deposition of buffer layers, and more specifically no reports for MgO on metallic substrates, by spray pyrolysis. Besides that, MgO is considered as compatible substrate onto which HTS (YBCO) can be deposited without a buffer layer and this will be confirmed in section 4.5.1. Therefore, MgO thin film may exhibit the same property and needs to be investigated.

The aim of this work is to use spray pyrolysis as the deposition technique for MgO as a single buffer layer; to reduce the usual multi-layer buffer architecture, on different substrates using magnesium acetates and magnesium nitrates as precursors.

Si single crystals were first used to optimise the deposition parameters. The deposition was then performed on NiW RABiTS substrates and on oxidised NiW i.e. on (200) textured NiO grown on NiW. For the purpose of making the process more cost effective, MgO was also deposited on polycrystalline metallic substrates (310-austenitic stainless steel and Hastelloy C276). The effects of different deposition conditions and different annealing treatments on the deposited MgO films on Hastelloy C276 were investigated. To evaluate the performance of MgO as a buffer layer, YBCO was subsequently deposited by PLD. This is a well established route to high quality films, although spray pyrolysis of the YBCO layer should also be a possibility in the future. In an attempt to control the in-plane texture of YBCO, CeO_2 was also deposited by PLD on top of the spray pyrolysed MgO on Hastelloy C276.

The characterization of the deposited thin films (MgO, CeO_2 and YBCO) was done using all or some of the following: SEM, EBSD, XPS, AFM, X-ray diffraction 2θ-scans, rocking curve (ω-scans), phi (ϕ) scans, and X-ray pole-figure measurements. The superconducting transition temperatures were measured using AC susceptibility.

In this work MgO was deposited epitaxially on Si substrates by spray pyrolysis. However, YBCO deposition by PLD on top of the spray pyrolysed MgO films resulted in broad superconducting transition temperatures due to the thermal strains in the deposited MgO films. MgO deposition by spray pyrolysis on 310-austenitic stainless steel, NiW RABiTS and on textured NiO grown on NiW RABiTS was not successful because of the substrate and/or NiO oxide layer instabilities under the spray pyrolysis deposition conditions. MgO deposition on Hastelloy C276 by spray pyrolysis (see chapter 8 and 9 where most of the work is presented) resulted in weak MgO (200) peaks when using the nitrate precursor and strong MgO (200) peaks when using the acetate precursors. Subsequent YBCO deposition by PLD resulted in broad superconducting transition temperatures due to the weakly textured MgO film when using the nitrate precursor and due to carbon contamination when using the acetate precursor. It was also found that MgO film (deposited from the nitrate and acetate precursors) smoothness on Hastelloy C276 is critical for subsequent YBCO deposition by PLD. The MgO films deposited by spray pyrolysis on Hastelloy C276 were best when as deposited without subsequent annealing treatment (under O_2, under vacuum or under Ar atmospheres) or subsequent CeO_2 deposition by PLD; which affected the MgO film smoothness and hence the subsequent YBCO deposition by

PLD. ISD deposition of MgO by spray pyrolysis resulted in untilted MgO (200) peaks, irrespective of the used precursor or the used substrate, as distinct to MgO films grown by thermal evaporation which grow with the (200) tilted to the substrate normal.

2 Theory and literature review

2.1 Superconductivity

2.1.1 History

Superconductivity was discovered in 1911 by a Dutch physicist, Kamerlingh Onnes [1], after his success in liquefying helium gas in 1908 [2, 3]. He found that mercury, when cooled below 4.2K (-269°C), will lose all its electrical resistance (Figure 2.1); the temperature at which this phenomenon occurs is called the transition or critical temperature T_c [1, 2]. Later, Kamerlingh Onnes and his collaborators at Leiden University found that superconductivity is exhibited by tin and lead at various low temperatures [1, 4]. Among the elements, Nb has the highest T_c of about 9.3K (-263.9°C) and, before the discovery of the so-called high-temperature superconductors, a highest T_c of about 23.2K (-250°C) was achieved in the intermetallic compound Nb_3Ge [4]. The new superconductors discovered subsequently are ceramics which are brittle and the superconducting properties are highly anisotropic [5]. In 1986 a new class of these superconductors, called the high temperature superconductors (HTS), was discovered by Bednorz and Muller [6] (Figure 2.2). They discovered the first high temperature superconductivity in Ba-La-Cu-O (LBCO) with a T_c of 30K [7]. Later in the same year Wu and co-workers discovered the Y-Ba-Cu-O system with a T_c of 93K for the $YBa_2Cu_3O_{7-x}$ (YBCO) composition [8]. The Bi, Tl and Hg cuprates with even higher transition temperatures were synthesised a little later. However, most research has centred on YBCO and Bi-Sr-Ca-Cu-O (BSCCO).

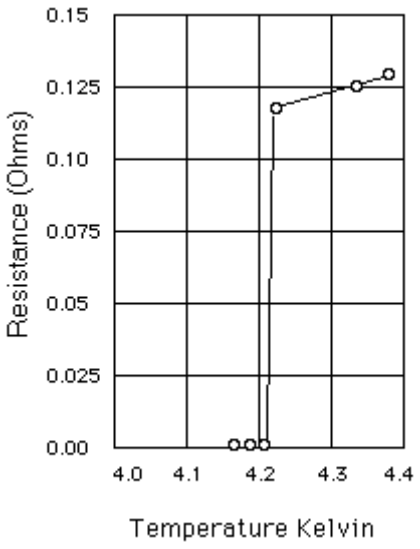

Figure 2.1: Vanishing of resistance below T_c [9].

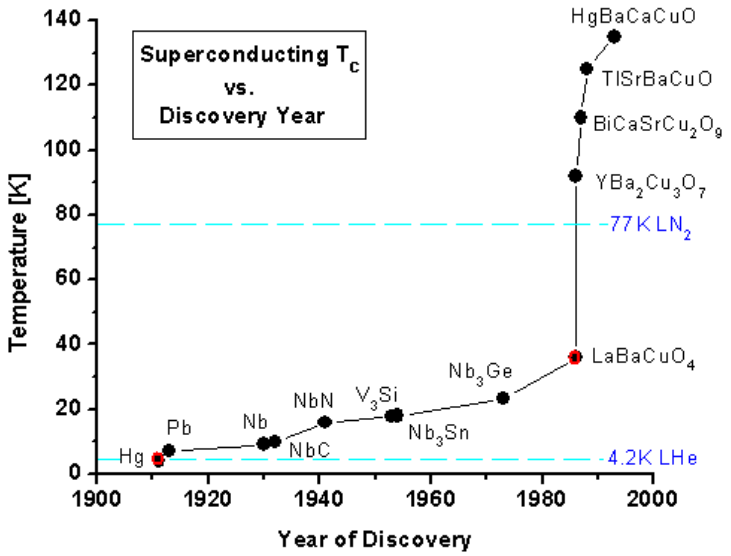

Figure 2.2: Discovery of superconducting materials over the last century [9].

2.1.2 Meissner effect

The critical magnetic field (H_c), is the field below which the material is in the superconducting state and above which it is in the normal state. When a superconductor is cooled below the critical temperature (T_c) in a magnetic field below H_c [4], the applied field will be excluded from entering the sample. Under those conditions, even the field in an originally normal sample is expelled from the sample interior [10], as seen in Figure 2.3. This diamagnetism is another fundamental aspect of superconductors which was discovered by Meissner and Ochsenfeld in 1933 and is called the Meissner effect [4].

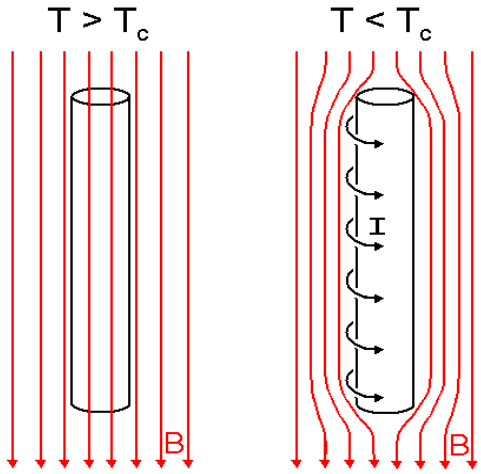

Figure 2.3: Magnetic field expulsion below H_c [9].

2.1.3 Type I and type II superconductors

Superconductors can be classified into two types according to the change from the superconducting state to the normal state. In type I superconductors, which are mainly pure elements like Al, Hg, etc., a magnetic field can not penetrate when it is below H_c, and the superconductor is characterised by perfect conductivity and perfect diamagnetism. The magnetic field is completely screened by the Meissner effect, where screening currents are induced in the surface to keep the field out of the interior of the sample, and zero resistance is maintained up to H_c [4, 10].

In 1956, the subject of type II superconductors was created by Abrikosov [11]. This type of superconductor is characterised by two critical magnetic fields; H_{c1} and H_{c2} [12]. Abrikosov showed that in addition to the flux expulsion by the Meissner effect, type II superconductors exhibit a mixed state [11] in which the magnetic flux penetrates the sample between H_{c1} and H_{c2}. Below H_{c1} the superconductor is in the Meissner state and above H_{c2} the superconductivity will be destroyed even at $T<T_c$ [13]. Figure 2.4 shows the difference between type I and type II superconductors.

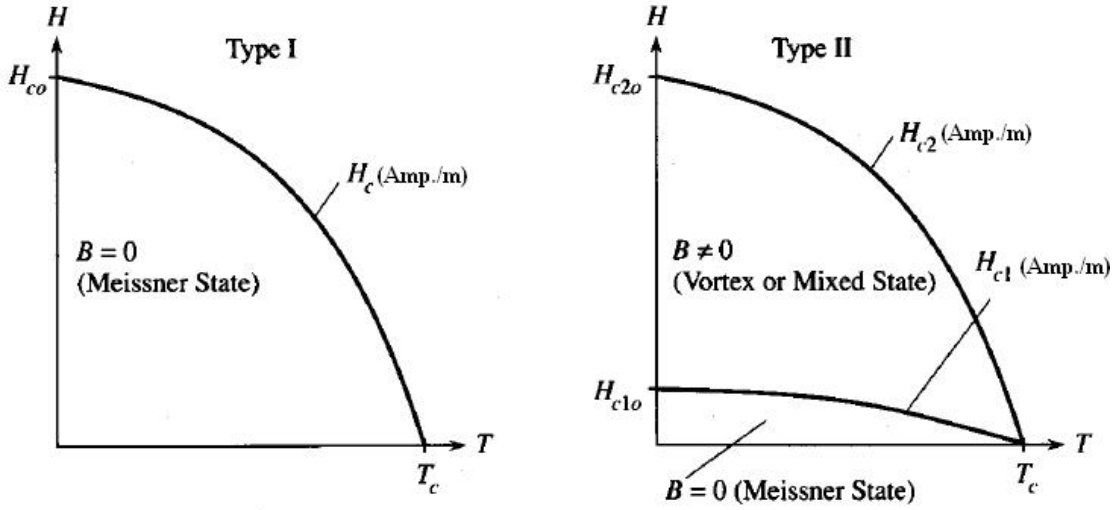

Figure 2.4: Schematic diagram for type I and type II superconductors [14].

2.1.4 Coated conductor tapes

The discovery of high temperature superconductors (HTS) led to an explosion of research and development efforts world wide, because of the significant potential for practical applications offered by these materials. There are two generations of HTS wires and tapes [15], the first generation was based on BSCCO superconducting filaments in a silver matrix [16, 17]. The expensive fabrication method of

superconducting tapes with BSCCO and silver is known as the powder-in-tube (PIT) process. A high-purity mixture of Bi_2O_3, $SrCO_3$, CaO and CuO powder is filled into a silver tube and continuously drawn into a narrow cylinder of about 1 mm diameter. Such filaments are rolled together and deformed into a tape. Then a final annealing (sintering) procedure is performed to react and obtain tapes with good superconducting properties [18, 19]; the sintering temperature is very close to the partial melting temperature of BSCCO, therefore, partial melting of the ceramic at the silver-ceramic interface occurs causing enhancement in grain coarsening. As a consequence, grains grow with their c-axes perpendicular to the interface leading to texture evolution [18, 20]. The first generation of HTS wires had modest superconducting properties and high production cost [15]. Wu and co-workers achieved a T_c of 93K (-180.2°C) by the discovery of YBCO [8, 21] which is the superconducting constituent of the second generation of HTS tapes, also referred to as coated conductors [15, 22]. The main interest is centred on $Y_1Ba_2Cu_3O_{7-x}$ due to a number of factors: it has a high critical current density (J_c) performance in magnetic fields at 77K, has an advantage of replacing BSCCO wires with lower cost [18], can be produced with high degree of biaxial texture, it has no high angle grain boundaries [23, 24] and it is easy to prepare single phase $YBa_2Cu_3O_{7-x}$ under normal temperature and pressure conditions [25]. More details about the significance of biaxial texture and the structure of YBCO will be found in sections 2.1.4.1 and 2.1.4.3, respectively.

To develop an appropriate conductor, the manufacturing process consists of the following (Figure 2.5):

- Preparation of the substrate layer.
- Preparation of the buffer layer(s).
- Preparation of the HTS material. [26]

Coated conductors are typically formed of a 50 μm thick metallic substrate (mainly Ni or Ni alloy), one or more insulating oxide buffer layers with a thickness of 0.5-1 μm, and an HTS film thicker than 1μm [27].

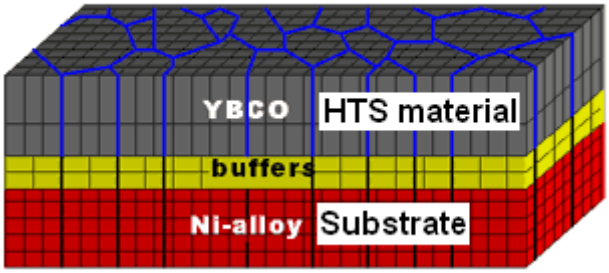

Figure 2.5: Superconductor architecture [28].

2.1.4.1 The substrate layer

For the development of a reliable deposition technology for high-quality HTS thin films, the choice of substrate material is of primary importance. The basic requirements for the substrate can be summarised as follows [29].

- Crystallographic lattice match between the HTS film and substrate.
- Similar thermal expansion coefficients of HTS and substrate.
- No chemical interaction at the interface between HTS and substrate, and
- Suitably polished surface, stable and reasonably robust.

Generally two classes of substrates can be distinguished: a) compatible substrates onto which HTS can be deposited without a buffer layer such as $LaAlO_3$, $SrTiO_3$ and MgO for YBCO deposition; however, buffer layers may be added for some compatible substrates to reduce the probability of a-axis growth as is the case of depositing a CeO_2 buffer on $LaAlO_3$ substrates, and b) non-compatible substrates which have to be covered with an epitaxial buffer layer prior to the deposition of the HTS film owing to a large lattice mismatch and/or chemical interaction between substrate and HTS material or owing to missing in-plane orientation as is the case to get biaxially oriented YBCO on polycrystalline substrates. Table 2.1 lists some important properties of different materials, which can be used as substrates as well as buffers or interlayers [29].

Table 2.1: Properties of substrate materials suitable for the preparation of YBCO thin films [29].

Substrate materials	Attainable dielectric properties		Thermal expansivity (10^{-6} °C^{-1})	Melting temperature (°C)	Available substrate size (mm)	Crystallinity		Chemical stability	Mechanical strength	Notes
	ε	$\tan\delta$ at 10 GHz, 77 K				Misfit to YBCO (%)	Twinning			
$SrTiO_3$	300	$\sim 2\times10^{-2}$	9.4	2080	30–50	1.4				
YSZ	27–33	$> 6\times10^{-4}$	11.4	2550	Diameter 100	6				
$NdAlO_3$				2070						
MgO	9.6–10	6.2×10^{-6}	14	2825	> 30	9	No	Good	Poor	Hygroscopic
α-Al_2O_3 (sapphire)	9.4–11.6 anisotropic	10^{-8}	9.4	2049	Diameter 100	6–11 (r cut) 18 (m cut)	No	Poor	Good	Requires buffering
YSZ buffered r-cut sapphire	27–33 (for YSZ)	$> 6\times10^{-4}$ (for YSZ)		2550 (for YSZ)		6	No	Good	Good	
CeO_2 buffered r-cut sapphire	21.2 (for CeO_2)			2600 (for CeO_2)	Diameter 100	0.7	No	Good	Good	
Y_2O_3	14			2400	Diameter 30	3	No	Expected to be good	Fair	
$YAlO_3$	16	10^{-5}		1875	Diameter 30	3.5	No	Fair	Fair	
$LaAlO_3$	20.5–27	7.6×10^{-6}–3×10^{-4}	10–13	2100	Diameter 100	2	Yes	Good	Fair	
$LaGaO_3$	25		9	1715	Diameter 40	2	Yes	Good	Fair	
$NdGaO_3$	23	4×10^{-4}	9–11	1670	Diameter 50	0.04	No	Good	Fair	
$PrGaO_3$	24		7–8	1680	Diameter 10	0.3	Yes	Good		

The lattice misfit is normalized to the YBCO lattice for c-axis orientation, the thermal expansivity of c-axis-oriented YBCO is (1–1.3) $\times$ 10^{-5} K^{-1}, YSZ refers to yttrium (~9 mol% of Y_2O_3) stabilized ZrO_2. Other candidates, which are not listed here, are e.g. $CaNdAlO_4$ or $XAlO_3$ (with X = SrLa, Y, Gd, Eu, Sm, Nd or Pr).

The fabrication of high temperature superconductors into useful forms with acceptable superconducting properties has been hindered by many intrinsic material problems, such as superconducting weak links and poor mechanical properties [15]. It is known that high angle grain boundaries reduce the potential critical current density (J_c) value (Figure 2.6) of the superconductor [30, 31], by impeding long range current flow [6]. Such problems have led to the development of the second generation HTS tapes which have the potential to carry 100-1000 times the current without resistance losses of comparable copper wire. HTS power engineering equipment has the potential to be half the size of conventional alternatives with the same or higher power rating and less than one half the energy losses [15]. Three methods have been invented to produce flexible metallic substrates, which were also crystallographically biaxially textured and resembled a long, mosaic pseudo-single crystal, upon which epitaxial growth of the superconducting layer was possible to realize a single-crystal-like HTS tape [15]. These methods are, rolling assisted biaxially textured substrates (RABiTS) [16, 24, 32-34], Ion beam assisted deposition (IBAD) [33, 35-38] and inclined substrate deposition (ISD) [39-42].

The RABiTS process involves a thermomechanical [43, 44] biaxial texturing of a metal or alloy [16]; hot rolling [26] or cold rolling [32, 45] followed by annealing [26, 32], and then epitaxial deposition of the buffer layers and the superconductor [16]. The buffer layers are required to prevent Ni diffusion into YBCO which degrades the superconducting properties. The whole process is demonstrated in Figure 2.7.

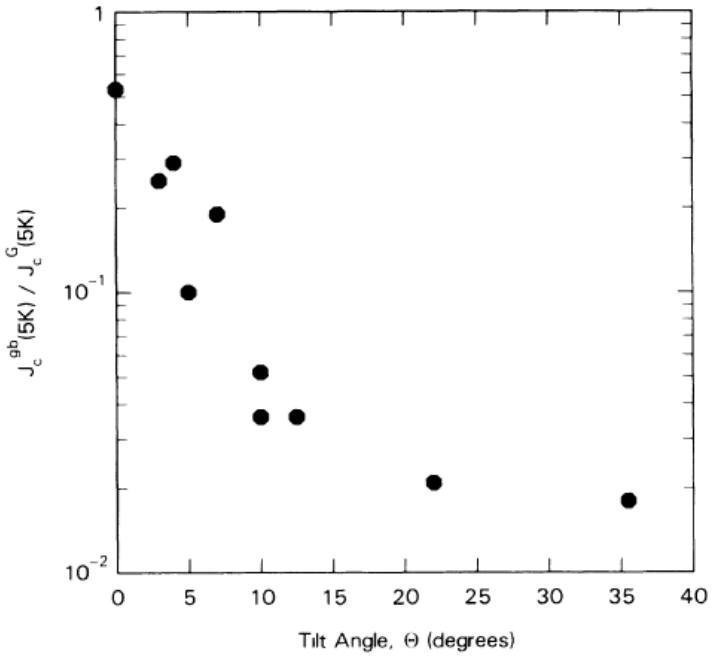

Figure 2.6: Ratio of grain boundary critical current density J_C^{gb} to the average value of the critical current density J_C^G as a function of the misorientation angle [30].

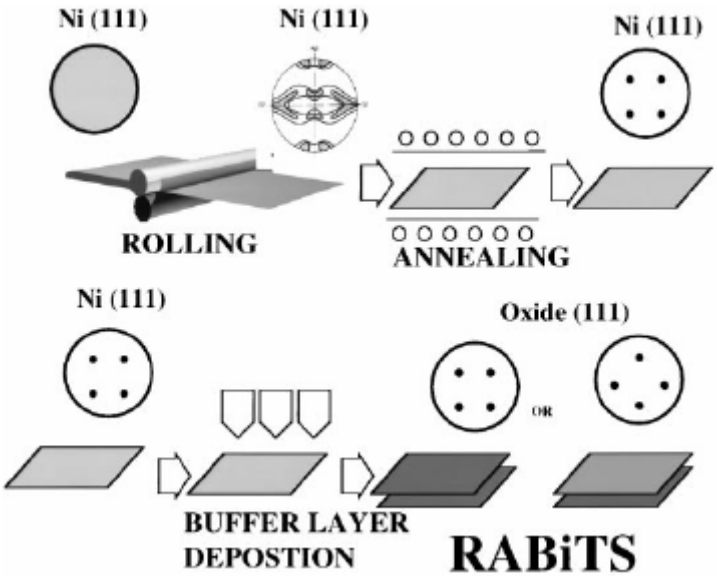

Figure 2.7: Schematics of the RABiTS technique. Starting with a randomly oriented Ni bar/plate, cold-rolling is used to produce a distinct rolling texture (see schematic pole figures). This is followed by recrystallisation to a cube texture. Epitaxial metal and/or oxide buffer layer(s) are then deposited on the textured Ni [43, 46].

The IBAD process differs from the RABiTS in that the texture is developed in the first buffer layer rather than in the polycrystalline metallic substrate [26]. This is

accomplished by using an ion beam [47, 48] impinging on the buffer layer (Figure 2.8) which is being laid down simultaneously [15] by vapour phase deposition [26].

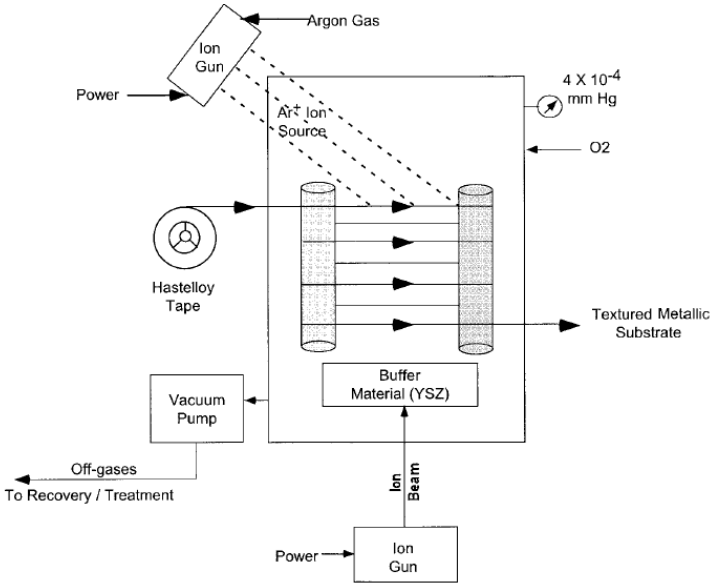

Figure 2.8: Textured substrate preparation by IBAD [26].

The biaxial alignment in the ISD method is obtained by inclining the substrate (Figure 2.9) under specific conditions of pulsed laser deposition (PLD), using Excimer laser [49], without ion beam assistance [49, 50]. The ISD was first developed in 1996 to deposit YSZ (yttria stabilised zirconia) on Ni based substrates by PLD [49], and in 2002, biaxially textured (MgO) on polycrystalline substrates has been grown successfully by ISD [51] using electron beam evaporation [52, 53].

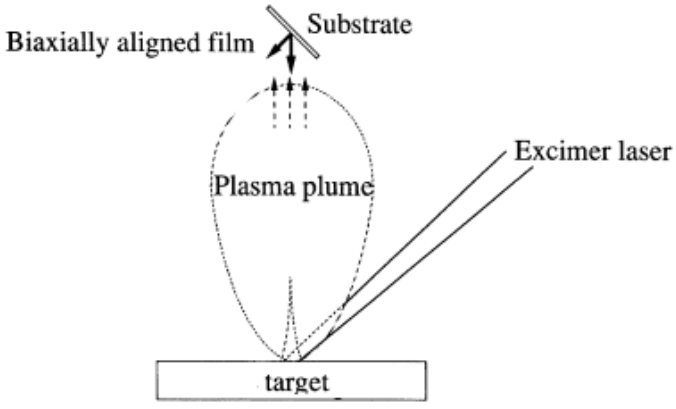

Figure 2.9: Schematic diagram of inclined substrate deposition (ISD) [49].

2.1.4.2 The buffer layer

The role of the buffer layers, which are commonly ceramic oxides, is mainly to extend the texture of the substrate into the superconducting film by gradually

adjusting the lattice mismatch between them [54]. The buffer layers also chemically isolate the HTS film from the substrate [55] to prevent diffusion between them [56], and also prevent surface oxidation of the substrate during YBCO deposition [57]. There are many buffer layers which are chemically and structurally compatible with HTS YBCO [54], such as $LaAlO_3$ which is one of the most widely used substrates for HTS due to the development of proper epitaxy [58], $SrTiO_3$ which is used as a single buffer layer for RABiTS YBCO [59], YSZ [60], CeO_2 [61-64], and the subject of this study MgO [53, 65-68].

MgO has a NaCl structure (rock salt structure) with a lattice constant of 4.213A° (Figure 2.10). A unit cell for this crystal structure (Figure 2.10) is generated from an FCC arrangement of anions with one cation situated at the cube center and one at the center of each of the 12 cube edges. An equivalent crystal structure results from a face-centered arrangement of cations. Thus, the rock salt crystal structure may be thought of as two interpenetrating FCC lattices, one composed of the cations, the other of anions. Each of the cations and anions has a coordination number of 6 [69, 70]. It is used in the semiconductor industry [71-75] as a dielectric material [74], as an intermediate buffer layer for growth of ferroelectric materials on semiconductors [76], and as a potential gate dielectric for Si [77]. MgO thin films have been also used widely as chemically stable buffer layers for high T_c superconductor [65] and ferroelectric applications [71]. This is because MgO has a low chemical reactivity [72], a wide band gap, a low optical loss [65], and low dielectric constant [78].

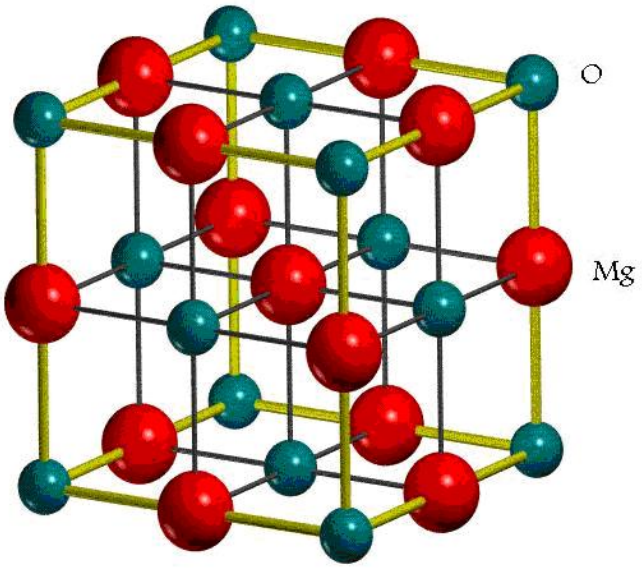

Figure 2.10: Unit cell for MgO having NaCl structure [79].

MgO thin films have been prepared by many techniques, either physical [16, 26], such as pulsed laser deposition [65, 80, 81], electron beam evaporation [75, 82], or chemical [26, 83, 84], such as metal organic chemical vapour deposition [56, 85] and spray pyrolysis, on Si (100), Si (111), NaCl (100) single crystals, polycrystalline Al_2O_3 substrates and glass substrates [56, 65, 67, 72, 78, 86]. More details on the deposition of MgO by spray pyrolysis will be found in section 2.5.

2.1.4.3 The superconducting layer

YBCO is the most obvious candidate material for conductor applications because of its high irreversibility field [87]. Biaxially textured YBCO thin films have been successfully deposited by many techniques such as sputtering [88] and PLD [49, 89]. Those techniques need high vacuum [90]. The non-vacuum methods include sol-gel [91], metal organic deposition [92], and spray pyrolysis [23, 24, 87, 93, 94].

The YBCO superconductor has a layered perovskite-like and highly anisotropic structure with a thermal expansion coefficient of $13x10^{-6}°C^{-1}$ [95]. $YBa_2Cu_3O_{7-x}$ (YBCO-123) is the extensively studied high-temperature superconductor (HTS) for which T_c exceeds the boiling point of liquid nitrogen (77K at 1atm). It is oxygen deficient with ordered vacancies, consisting of three unit cells, with four different layers stacked sequentially as BaO-CuO-BaO-CuO_2-Y-CuO_2-BaO-CuO-BaO (Figure 2.11). The presence of one or more CuO_2 planes in the unit cell is a common feature of all cuprate superconductors. The $Y_1Ba_2Cu_3O_{7-x}$ has both orthorhombic ($x<0.5$), the superconducting phase, and tetragonal ($x\geq0.5$) structures. The lattice parameters for $YBa_2Cu_3O_7$ are a= 3.8185Å, b=3.8856Å and c=11.68047Å. A slight difference between a and b lattice constants in the orthorhombic superconducting phase is caused by oxygen vacancy ordering in the CuO layer (chains) sandwiched between BaO layers. The relation between oxygen deficiency (x) and the superconducting transition temperature is shown in Figure 2.12. Besides the high transition temperature of the HTSCs (T_c=93K), they also have a pronounced anisotropy. Such anisotropy originates from the fact that superconductivity occurs mainly in the CuO_2 planes [13, 21, 96].

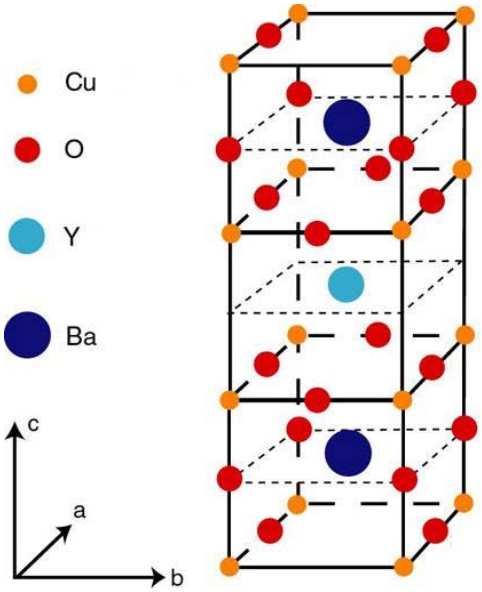

Figure 2.11: The unit cell of YBCO-123 [97].

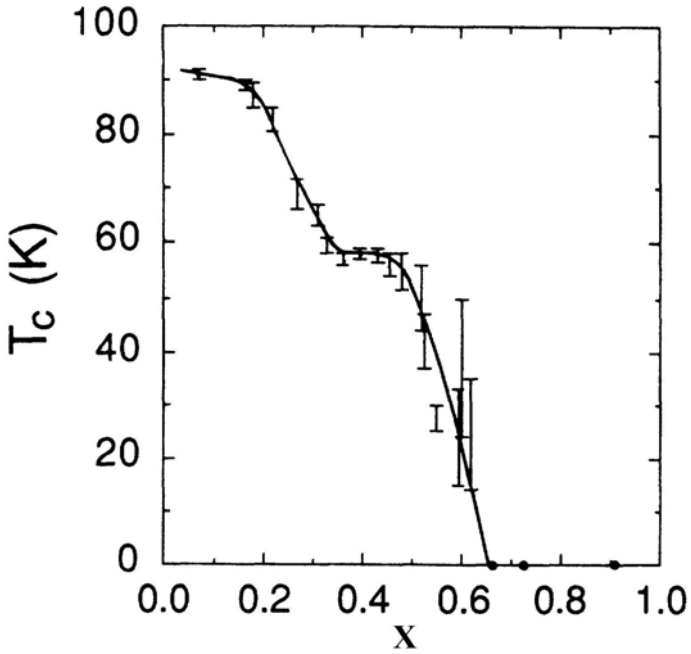

Figure 2.12: Superconducting transition temperature (T_c) as a function of oxygen content for $YBa_2Cu_3O_{7-x}$ [98].

Oxide superconductors like YBCO are brittle ceramic materials and therefore are not amenable to common forming operations. To overcome this problem, YBCO has been deposited as a thin film on flexible metallic substrates [32]. The growth of YBCO films on metallic substrates, such as stainless steel or Ni-based superalloys, is desirable for wires, cables, electromagnetic shields etc. [99]; however, YBCO

deposited directly on such substrates exhibits poor superconducting properties [100] because of interdiffusion problems [99]. For this reason, buffer layers are required.

Some of the HTS applications include: high-power transmission cables, high-field magnets, magnetic shields and large scale microwave devices [40], HTS cables assembled by YBCO tapes are also used for AC transmission cables [101], and many other applications.

2.2 Thin film technology

Thin film deposition is made onto the substrate to obtain properties which are unattainable or not easily attainable in the substrate alone; for example, Cr coatings used on plastic parts for automobiles impart hardness, metallic luster, and protection against ultraviolet light. This functionality is also achieved in the same part made from bulk metal but on the expense of cost and weight. Another example is titanium nitride (TiN) coatings on cutting tools which offer hardness, low friction, and chemical barrier to alloying of the tool with the workpiece. Such properties are unattainable in a bulk material; since the bulk material must also offer high strength and toughness in the cutting tool application. Table 2.2 lists some of the required properties for some of the applications at hand. Usually, multiple properties are obtainable simultaneously from the same film and additional functionality in thin films can be obtained by depositing multiple layers of different materials. The films can be either thin or thick. Thin film involves individual molecule-deposition, while the thick ones involve particle deposition as in painting and plasma spraying. It is to be mentioned that the thick film technique does not offer the control or the material quality of the thin film techniques. Also the films deposited by thin film techniques can be thicker than those obtained by a thick film technique, such as graphite plates several millimetres thick deposited by thermal decomposition (pyrolysis) of hydrocarbon vapours [102].

Table 2.2: Thin film applications [102].

Thin film property category	Typical applications
Optical	Decoration, Memory discs(CDs)
Electrical	Insulation, Conduction, Semiconductor devices
Magnetic	Memory discs
Chemical	Barrier to diffusion or alloying, Protection against oxidation or corrosion
Mechanical	Wear resistance coating, Hardness, Adhesion
Thermal	Barrier layer, Heat sinks

All thin film processes contain main sequential steps. A source of film material is provided, the material is transported to the substrate, deposition takes place, and sometimes the film is subsequently annealed. The source of the film-forming material may be a solid, liquid, vapour or gas. Solid materials need to be vaporised to transport them to the substrate. This can be achieved by heat or by energetic beam of electrons, photons (laser ablation), or positive ions (sputtering). These methods are categorised as physical vapour deposition (PVD). Thin film processes involving the use of gases, evaporating liquids, or chemically gasified solids as the source material, are categorised as chemical vapour deposition (CVD) where the chemical composition of the product is different from the starting material. In both PVD and CVD, contamination and supply rate are the major source-material issues. Contamination is also an issue in the transport and deposition steps. Supply rate is important because film properties vary with deposition rate and with the ratio of elements supplied to compound films. The major issue in transporting the film-forming material to the substrate is the uniformity of arrival rate over the substrate area. The factors affecting this uniformity are very different, depending on whether the transport medium is a high vacuum, as in high vacuum PVD, or a fluid (i.e. gaseous medium), as in fluid-CVD. In vacuum, the molecules travel from the source to the substrate in straight lines, while in fluid, there are many collisions among molecules during the transport. According to that, the uniformity of arrival rate at the substrate in high vacuum medium is determined by geometry. In a fluid medium, it is determined by

gas flow patterns and by diffusion of the source molecules through the other gases present. The advantage of using a high-vacuum transport medium is easy access to the deposition surface, and it allows energy input from an ion beam and allows the use of analytical techniques involving electron beams, such as electron diffraction and Auger spectroscopy. The fluid medium has the advantage that it uses atmospheric pressure or an easily-achieved moderate vacuum level.

The deposition behaviour of the thin film onto the substrate is determined by the source, transport factors and by conditions at the deposition surface. The surface factors include: substrate surface conditions, reactivity of the arriving material and energy input. Substrate surface condition includes roughness, level of contamination, degree of chemical bonding with the arriving material and crystallographic parameters in the case of epitaxy. The reactivity is the probability of arriving molecules to react with the surface and becoming incorporated into the film. This probability is termed the sticking coefficient (α_s) which varies from unity to less than 10^{-3}. It is usually lower for CVD than for PVD processes, the low values of α_s aids in coating convoluted shapes and in deposition on selected areas.

The energy input into the surface can come in many forms. It has a large effect on the reactivity of the arriving material, the composition and structure of the film. The basic source of energy input is the substrate temperature. Other sources include photons, and chemical energy carried by reactive source molecules and by molecules that have been dissociated in the course of vaporisation. So, the substrate condition, reactivity and energy input, all work together with the arriving fluxes to determine the structure and composition of the deposited film which in turn determine the film properties [102].

2.2.1 Epitaxy

Woodcock [103] made a survey for the term epitaxy. He found that many definitions were given to epitaxy. The Longman Dictionary of Physics gives it as: ‘‘A method of growing a thin layer of material upon a single crystal substrate so that the lattice structure is identical to that of the substrate’’. The Oxford Dictionary of Physics defined epitaxy as: ‘‘Growth of a layer of one substance on a single crystal of another, such that the crystal structure in the layer is the same as that in the substrate’’. This implies that the film deposited on a BCC substrate, for example,

would only be called as epitaxial if it also had a BCC structure as well. On the contrary, the term epitaxial is also used to describe YBCO films, which have an orthorhombic crystal structure, on polycrystalline or biaxially textured metallic substrates buffered with cubic oxides [44, 89, 100, 104, 105].

Woodcock [103] found that the dictionary definitions and common usages of the term epitaxial differ considerably and some clarification of the parameters used to assign films as epitaxial is needed. He defined, epitaxy (or epitaxial growth) as: ‘‘Growth of a film exhibiting a characteristic orientation relationship with a substrate, dictated by the minimisation of structural disorder at the film/substrate interface’’. Thus, epitaxial growth of a film on a textured substrate will result in a textured film.

Epitaxy also means that the crystallographic order of the film is being significantly influenced by that of the substrate as a result of some degree of matching between the two along the interface [102]. It is also defined as the condition in which lattice planes on one side of a boundary are parallel to those on the other [106]. Another definition is the growth process of a solid film on a crystalline substrate in which the atoms of the growing film mimic the arrangement of the atoms of the substrate.

The growth processes of thin epitaxial films are essentially the same as that of bulk crystals, except for the influence of the substrate at the initial stages. This influence comes from the lattice misfit and thermal stresses, from the defects appearing at the substrate-film interface and from the chemical interactions between the film and the substrate. Frankenheim [107] was the first to successfully obtain epitaxy of alkali-halide deposits from a solution onto a cleaved mica surface.

Five possible modes of crystal growth can be distinguished in epitaxy (Figure 2.13): Volmer-Weber, Frank-van der Merve, Stranski Krastanov, columnar and step flow mode. The mode by which the epitaxial film grows depends upon the lattice misfit between substrate and film, the growth temperature and adhesion energy.

During island or Volmer Weber growth, small clusters are nucleated directly on the substrate surface. The clusters then grow into islands, which in turn coalesce to form a continuous film. This type of growth occurs when the film atoms, or molecules, are more strongly bound to each other than to the substrate as in the case for metal films growing on insulators. Layer-by-layer, or Frank-van der Merve, growth occurs when the binding between film atoms is less than that between the film atoms and the substrate. Examples of layer-by-layer growth are the metal on metal

system as well as the semiconductor on semiconductor system. The third growth mode often referred as Stranski-Krastanov, or layer plus island growth mode, is an intermediate case. In this case after forming one or more monolayers, further layer growth becomes unfavourable and islands are formed on top of this intermediate layer. The transition from layer-by-layer to island growth is not completely understood. The columnar growth mode shows some similarities with the Stranski Krastanov and Volmer Weber modes, but it is fundamentally different. In the case of the Stranski Krastanov and Volmer Weber growth, when the film thickens, the condensed phase islands characteristic to these modes tend to merge and to cover the whole substrate surface. In contrast the columns are not merging when the film is grown according to the columnar growth mechanism. As a result, columns usually remain separated throughout the growth process of the film, and the film grown in this way is easily fractured. The columnar growth mode occurs where low atomic mobility over the substrate surface leads to the formation of highly defective atomic columns of the deposited material on this surface.

Beside these described growth modes, in many cases of high quality epitaxy, the so-called step-flow growth mode is observed. When the substrate wafer is cut slightly misoriented from a low-index plane in a specific direction, its surface breaks up into monoatomic steps with precisely oriented low-index terraces and edges. Nucleation may occur on the terraces when the substrate temperature is sufficiently low or the flux of the constituent elements of the growing film is high enough to prohibit fast surface migration of the species adsorbed on the terraces. In this case the film may grow on the terraces in the Frank-van der Merve or Stranski Krastanov mode. However, when the substrate temperature is high enough or the flux is sufficiently low, then the adatoms can be so mobile that they become incorporated directly into the step edges. In this case growth of the epitaxial film occurs by the advancement of steps along the terraces [107-109].

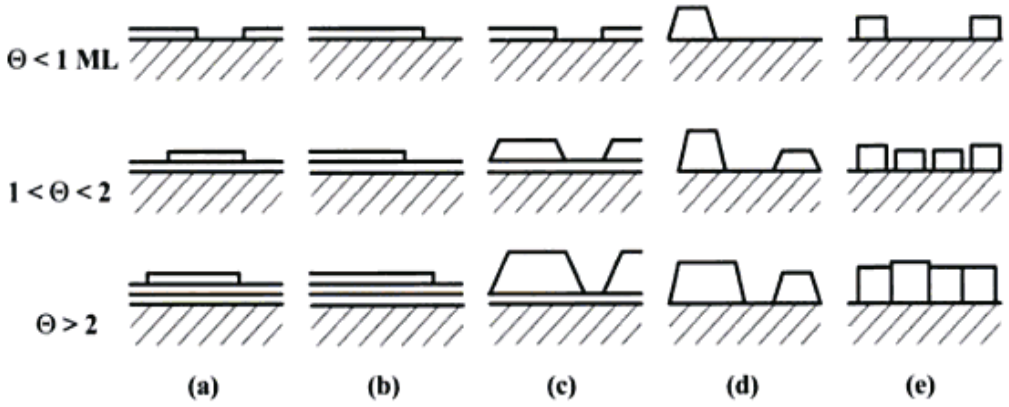

Figure 2.13: Schematic representation of the five crystal growth modes frequently occurring on flat surfaces of substrate crystals: (a) layer-by-layer or Frank-van der Merve, (b) step flow, (c) layer plus island or Stranski-Krastanov, (d) island or Volmer-Weber, (e) columnar growth mode. θ represents the coverage in monolayers (ML) [108].

2.3 Spray pyrolysis for film formation

Aerosol (used to describe solid or liquid particles suspended in a gas) routes are used mainly for particle formation but they can also be used for the fabrication or modification of films. However, relative to aerosol routes for particle formation, the routes used for film fabrication are less well understood.

Many criteria must be considered when fabricating films. Most applications require high purity films to optimise electrical, magnetic and optical properties. Metal films, for example must possess low resistivities which cannot be attained when carbon and oxygen impurities are present. The microstructure is another criterion that must be considered, for instance, high temperature superconducting ceramics must be single crystal films to maximize their current-carrying capacity. The film morphology has a profound effect on film properties. Even if the film may be of high purity; poorly connected grains can be formed, leading to high resistivities for metals. In the case of superconductors, it should consist of highly connected grains to reduce the resistance. Controlled stoichiometry, precursor cost, and many more factors must also be considered [110].

Spray pyrolysis is defined as the aerosol process that atomises a solution and heats the droplets to produce solid products [111]. Spray pyrolysis (droplet deposition) involves the deposition of evaporating droplets containing reactants onto surfaces, followed by further solvent evaporation and chemical reaction on the surface

[110]. Since the pioneering work by Chamberlin and Skarman in 1966 [112] on cadmium sulphide films for solar cells, many studies have been performed on spray pyrolysis for the preparation of thin films of noble metals, metal oxides, spinel oxides and superconducting compounds [113]; because it is a simple, inexpensive [114], non-vacuum technique [115], and it has a high deposition rate [87]. Spray pyrolysis is used for the preparation of thin and thick films, and it is employed for the deposition of dense and porous films and for powder production [84]. Typical spray pyrolysis equipment consists of [84] (Figure 2.14):

- Atomiser
- Precursor solution
- Substrate heater
- Temperature controller

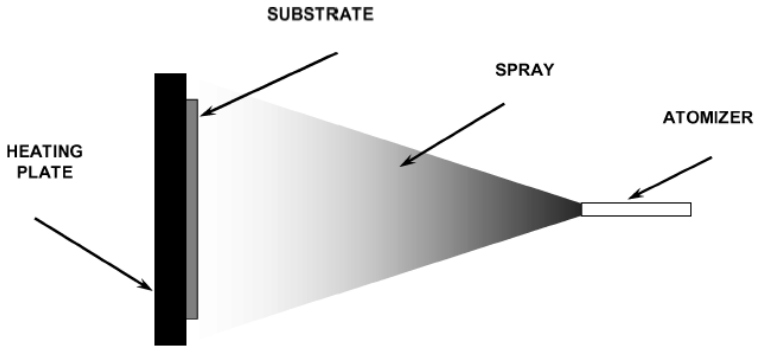

Figure 2.14: Schematic diagram of the spray pyrolysis equipment [84].

Many atomisers (also called nebulizers) are used to convert bulk liquids into droplets during spray pyrolysis. Some of them will be mentioned briefly here and the focus will be on the ultrasonic nebulizer; the one used in this work.

In the pneumatic nebuliser, the solution is exposed to air blast [116] where the energy of the air or a carrier gas is used to break up sheets or jets of a liquid. Pneumatic atomisers are the most complex of the atomisers because the liquid and gas phases interact in a complex manner [110]. In the electrostatic nebuliser, DC voltage is applied between an electrically conductive substrate and a metal capillary nozzle, which is connected to a precursor solution, to generate the spray which moves toward the heated substrate by the electrostatic force [117]. The electrostatic atomisation depends on the electrical conductivity of the liquid and produces droplet sizes in the range of sub-microns to millimetres and is used mainly on the laboratory scale

because it does not allow simultaneous high liquid flow rates and submicron droplets. However they have the advantage that the charged droplets can be deposited onto surfaces even in the presence of thermophoretic forces, which drive the particles away from hot surfaces [110].

The ultrasonic nebuliser, which is used in this work, is used to obtain uniformly distributed micrometer and submicron-size droplets [118] by using ultrasonic frequencies to produce short wavelengths that are necessary for fine atomisation [84]. The atomised droplets are then transported to the heated substrate through a pipe by a neutral gas (e.g. Argon) [113]. Ultrasonic atomisers use an ultrasonic transducer that vibrates at ultrasonic frequencies (usually, 50 KHz – 2.4 MHz) to produce the short wavelengths required for liquid atomisation. The ultrasonic atomisers are used extensively in aerosol methods for generating films and powders at laboratory and industrial scale. The reason behind that is the low spray velocity of the ultrasonic atomisers, the small amount of carrier gas required to operate them and the small droplet size produced. This makes it easy to carry small droplets at a high concentration towards a surface without using a high gas flow [110].

There are three classes of ultrasonic atomisers. In the first class, the liquid passes through a tube that is driven ultrasonically. In the second class, the liquid comes into contact with an ultrasonic horn. In the third class, an ultrasonic transducer is submerged in the liquid. The principle of operation in all of the classes is the same. When a liquid comes into contact with an ultrasonically driven surface, a wave pattern appears on the surface of the liquid. When the amplitude of the vibration is sufficient, the wave height is sufficient for the wave crest in the film to become unstable. This instability drives the formation of droplets, which are ejected from the surface. A carrier gas can then be used to sweep the droplets away from the surface.

The submerged ultrasonic transducers, the one adapted in this work, can provide 1 to 5μm droplets for frequencies of 1.5 to 2.4MHz with low gas flow rates that correspond to high droplet concentrations. The sizes produced by the submerged ultrasonic transducers are much smaller than those produced with the other ultrasonic types, which produce droplets with mass median diameters of 20 μm and larger. The droplet size depends on the surface tension and density of the fluid, and frequency of the ultrasonic source according to the following equation [110]:

$$d_p = \left(\frac{\pi\sigma}{4\rho f_t^{\,2}} \right)^{1/3} \quad \textbf{(Eq. 2.1)}$$

where d_p is the droplet diameter (cm), σ is the surface tension (erg/cm^2), ρ is the fluid density (g/cm^3) and f_t is transducer frequency (Hz). Figure 2.15 shows the dependence of the droplet diameter on frequency and Figure 2.16 shows droplet size distributions produced by ultrasonic atomisers. It is also worthy to mention that the ultrasonic atomisers exhibit a dependence of the aerosol output on the level of the liquid above the transducer, as shown in Figure 2.17, therefore, a constant liquid level should be maintained.

The advantages of the ultrasonic generators with submerged transducers are [110]:

- Narrow droplet size distribution
- Simplicity
- High concentration of droplets
- Droplet size appropriate for spray pyrolysis

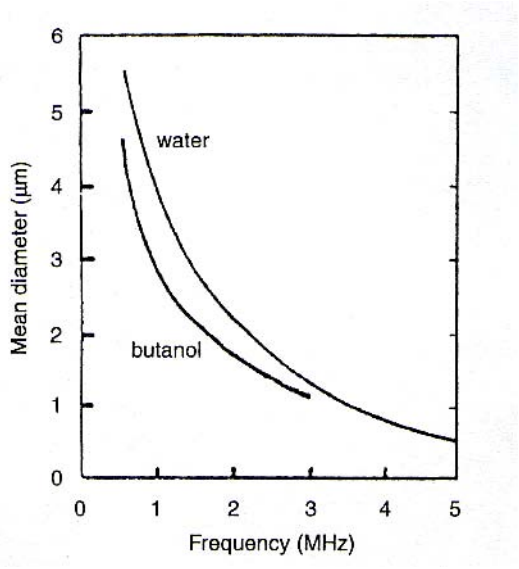

Figure 2.15: Dependence of droplet size on transducer frequency [110].

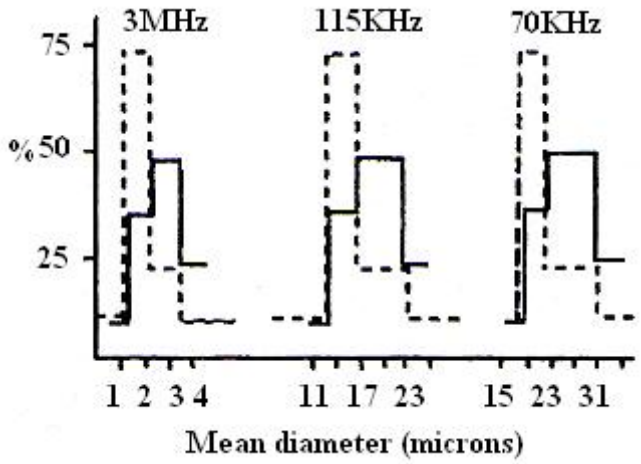

Figure 2.16: Number (dotted)) and volume (solid) distribution of water droplets [119, 120].

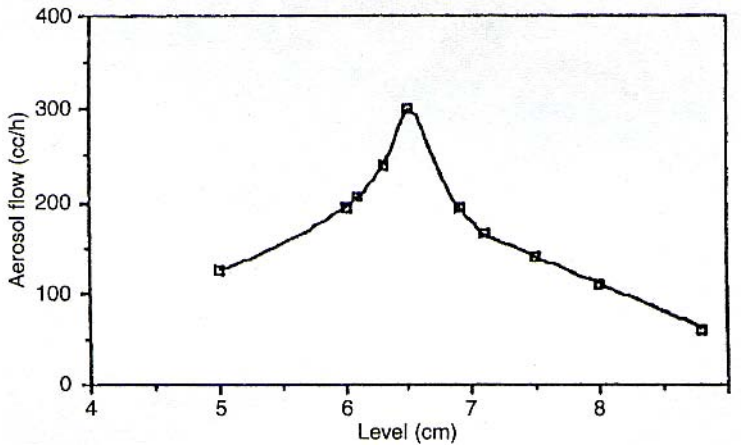

Figure 2.17: Dependence of aerosol flow as a function of liquid level above transducer [119].

Undesirable situations may occur during droplet deposition. As the droplet approaches the heated substrate, solvent will evaporate and if the evaporation is enough, only solid particles of the precursor(s) will deposit to form the film. This situation is unfavourable as it results in porous films. Particles that became sufficiently small in the gas phase may not deposit if their inertia is low enough to avoid impaction and the particles follow the gas flow away from the substrate (Figure 2.18). It is also important to mention that in spray pyrolysis, the rate of deposition decreases with increasing temperature as a result of the different mechanism of deposition; the thermophoretic velocity driving the droplets away from the surface is higher at higher substrate temperatures and the droplet evaporation is more rapid, leading to smaller droplets that are better able to flow with the gas [110].

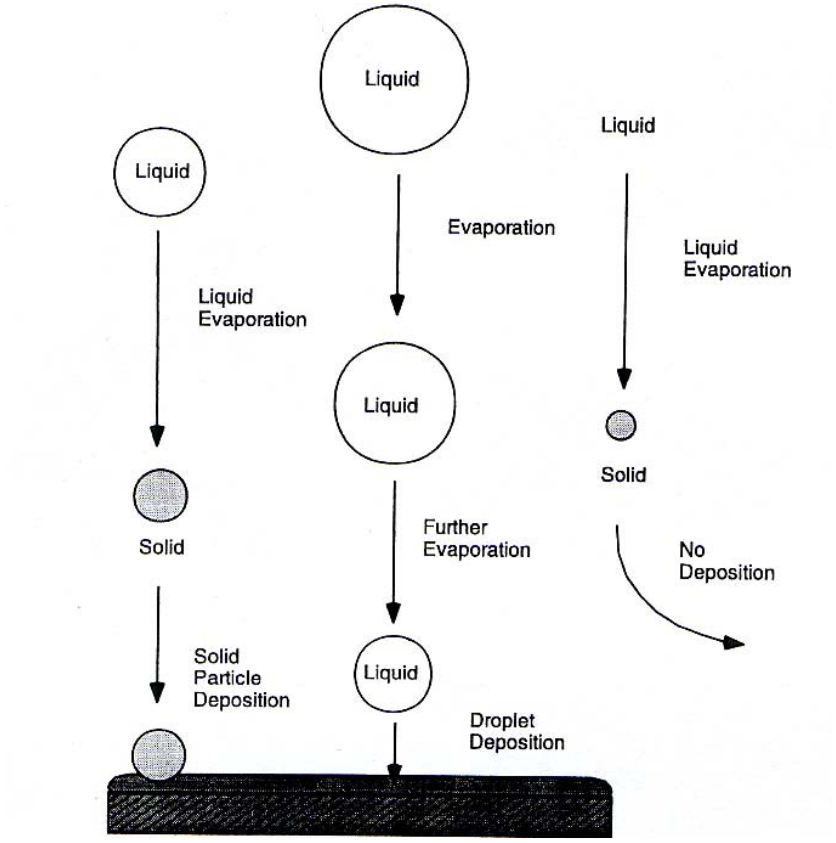

Figure 2.18: Droplets of different sizes can behave differently during deposition [110].

To synthesize thin films of the required material, it is important to know the details of the deposition conditions as well the details of the chemical thermal decomposition processes [83]. There is no clear explanation of the processes occurring during deposition. However, four modes for the deposition and decomposition processes may be distinguished (Figure 2.19) [83, 120].

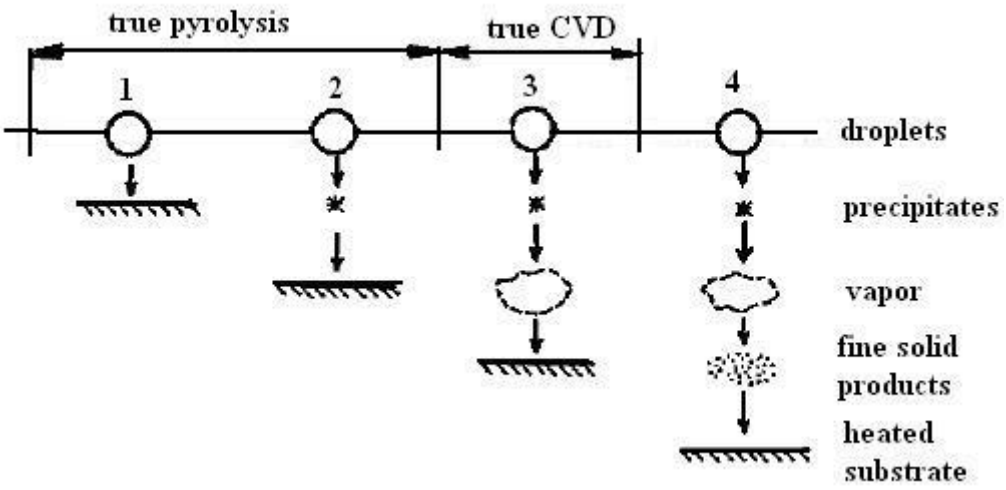

Figure 2.19: Possible working modes that may occur during deposition [83].

"In the first mode (1), the aerosol droplets splash on the surface of the heated substrate, the solvent vaporizes and the decomposition of already dry precipitates directly on the substrate follows. In the second mode (2), rather similar to the first one, only dry precipitates come to the surface, where thermal decomposition takes place. We may designate the decomposition processes of these two working modes as ''true pyrolysis'', because the thermal decomposition takes place on the surface of a heated substrate only. As a true CVD 'chemical vapour deposition' mode we consider the third mode (3), when thermal decomposition of dry precipitates starts on their way to the substrate. In this case mainly vapour arrives at the substrate surface. In the fourth mode (4), the full thermal decomposition takes place outside the substrate and only finely divided solid product arrives at the substrate surface. Also it is to be noted that the actual working mode depends not only on the substrate temperature, but also on the temperature of the working surrounding" [83].

Thin films can also be deposited by AACVD which involves chemical vapour deposition onto a heated substrate with aerosol delivery of precursors, whether in solution or solid-particle form. The major distinction between spray pyrolysis and AACVD is that in AACVD the precursor also evaporates and then adsorbs and reacts on the surface to form a film. The droplets are usually formed by spray routes in which volatile precursors are dissolved in liquids that are atomised. Alternatively, solid particles of the reactant can be entrained in a gas to form an aerosol that evaporates at least partially before reaching the substrate. This process is then followed by CVD [110]. The main distinction between AACVD and CVD is the method by which the precursors are delivered to the substrate. The theory of CVD is well developed, however, no full models have been developed to describe AACVD.

One of the largest applications for AACVD technique is the deposition of multicomponent films. Figure 2.20 shows the different modes of behaviour of AACVD, where three cases can be distinguished for precursors A, B and C. The simplest case is evaporation of the precursor followed by CVD. Another case is incomplete evaporation of the precursor particles. In the last case, the precursors evaporate either partially or completely and then react in the gas phase to give products (D, E and F) that deposit on the surface or perhaps also form particles in the gas phase.

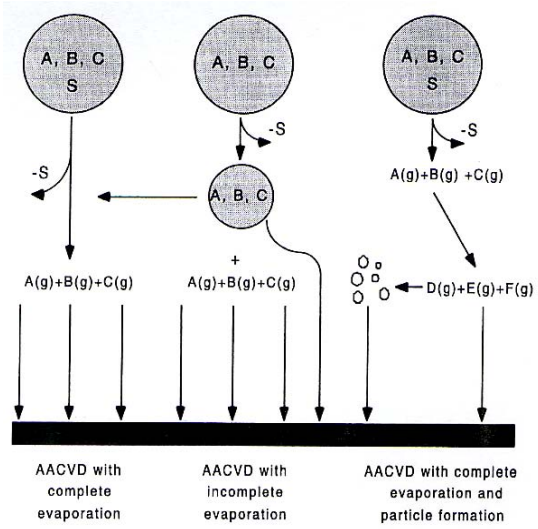

Figure 2.20: Possible behaviour modes of AACVD [110].

2.4 Aerosol techniques

Aerosol techniques are the science involved in the synthesis and processing of powders and films. Historically, the term aerosol is used to describe solid or liquid particles suspended in a gas and it can be formed as a result of wide variety of processes. Those processes can be classified into physical and chemical ones. An example of the physical processes, where the chemical composition of material is the same before and after processing but the form of the material is changed from bulk to particles, is the direct ejection of particles from surfaces into a gas. An example of the chemical processes, where the composition of the precursor is different from that of the final product, is the chemical vapor deposition of volatile species being evaporated from an aerosol and spray pyrolysis, the subject of this work.

Materials produced by aerosol processes may be a single crystal, which is an extreme case, may exhibit a preferred orientation (in the case of films), or, at the opposite end, may be amorphous. The crystallinity of the film or powder can be controlled through the processing conditions, mainly temperature and time history of the process [110, 111].

It should be mentioned that the equations mentioned in this section are used for giving the reader an idea about the different processes occurring during spray pyrolysis. However, non of them are applicable to the spray pyrolysis system used in this work due to different reasons; the increase in the droplet life time due to the presence of solute in droplets and the increase in the evaporation rate due to heating of

the gas above the substrate were neglected. These effects would affect the deposition process as will be seen in the following sections.

2.4.1 Technologies for generating powders and films

The technologies for generating powders and films can be divided, according to how the final product is produced, into gas-to-particle conversion, intraparticle reaction processes and bulk-to-particle direct ejection or entrainment processes.

An example of bulk-to-particle direct ejection is the laser ablation and sputtering in certain modes of operation [110]. PLD is used to deposit thin films of buffer materials or YBCO and in this work it is used to deposit YBCO and CeO_2. The laser beam is focused down by a lens and hits a target of the desired material at ~45° angle. The incident laser beam creates a plume of the material perpendicular to the target surface. The heated substrate is placed in the plume path. PLD is very suitable for the controlled deposition of complex multi-elemental thin films with a desired stoichiometry. The deposited material can range from nano-particles to thin films (amorphous, polycrystalline, single crystal) [121, 122].

2.4.1.1 Gas to particle conversion

In this approach condensable gaseous (atomic or molecular) species are used to form supersaturated vapor (the atoms or molecules of a given species present at partial pressure higher than the vapor pressure of that species) by either a chemical reaction that creates new species or as a result of physical processes such as cooling that reduce the vapor pressure of condensable species. Due to the supersaturation, new particles form by homogenous nucleation. The particle growth can then follow by physical condensation of vapor onto particles, by chemical reaction on the particle surface, or by diffusion of the reactant into a particle, followed by reaction within the bulk of the particle. At high particle concentration and normally at high temperatures, coalescence can occur to form a single spherical particle. Finally agglomeration results from collisions between particles to form a collection of particles [110].

Gas-to-particle conversion processes can be coupled with particle deposition from the gas phase to provide methods for fabricating films. Such deposition can be accomplished by mechanisms that include [110]:

- Thermophoresis, where particle motion is induced by a temperature gradient in a gas by which the particles move from high to low temperature regions. It is

responsible for particle deposits at cold spots on reactor walls and exhaust tubes. It reduces the deposition rates during aerosol assisted CVD, droplet deposition, and solid particle deposition onto heated surfaces. In thin films, thermophoresis provides, when the substrate temperature is greater then that of the gas, the driving force to keep particles that are suspended in a cool gas stream from striking a hot surface, keeping them from penetrating into hotter regions of the gas where their evaporation rates would be increased [123].

- Electrophoresis: it is the charging of particles by an electric field to increase the transport rate of particles to regions near to the hot surface, where the precursors can evaporate.
- Diffusion of particles is a mechanism by which collisions occur between particles larger than the gas mean free path (is to be explained in more details in section 2.4.1.1.1), and it is a mechanism of particle deposition onto surfaces when the particle size is sufficiently small and diffusion distance sufficiently short, as in CVD processes in which particles can be formed just above the surface of a material.
- Deposition can also be achieved by impaction. Particles follow the gas stream lines, neglecting other forces such as electrophoretic and thermophoretic, until the fluid stream changes direction, as in the case of a bend or obstruction in a pipe or aerosol spraying of a substrate using a jet of gas. Large particles cannot follow this change; inertia forces them to move in the original direction and impact. On the other hand, small particles follow the gas flow (Figure 2.21). The impaction technique is used to form films by the depositing droplets onto surfaces during spray pyrolysis [110].

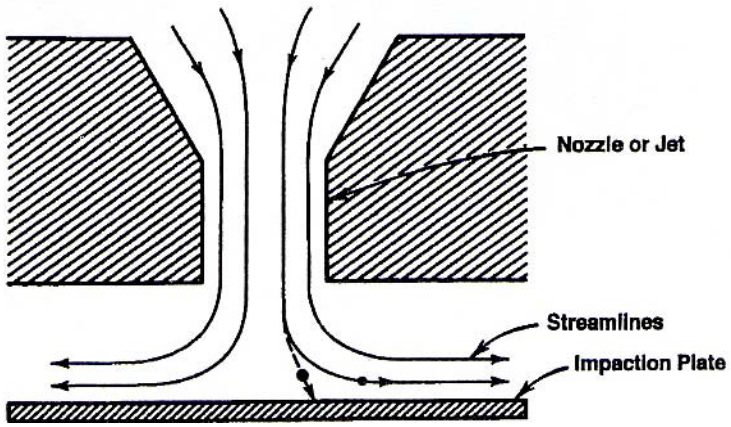

Figure 2.21: Schematic of the impaction mechanism [123].

The above basic deposition phenomena are also common to a variety of film generation routes including solid-particle deposition, spray pyrolysis, and aerosol assisted chemical vapour deposition (AACVD) (Figure 2.22). The mechanisms underlying these phenomena are shown in Figure 2.23.

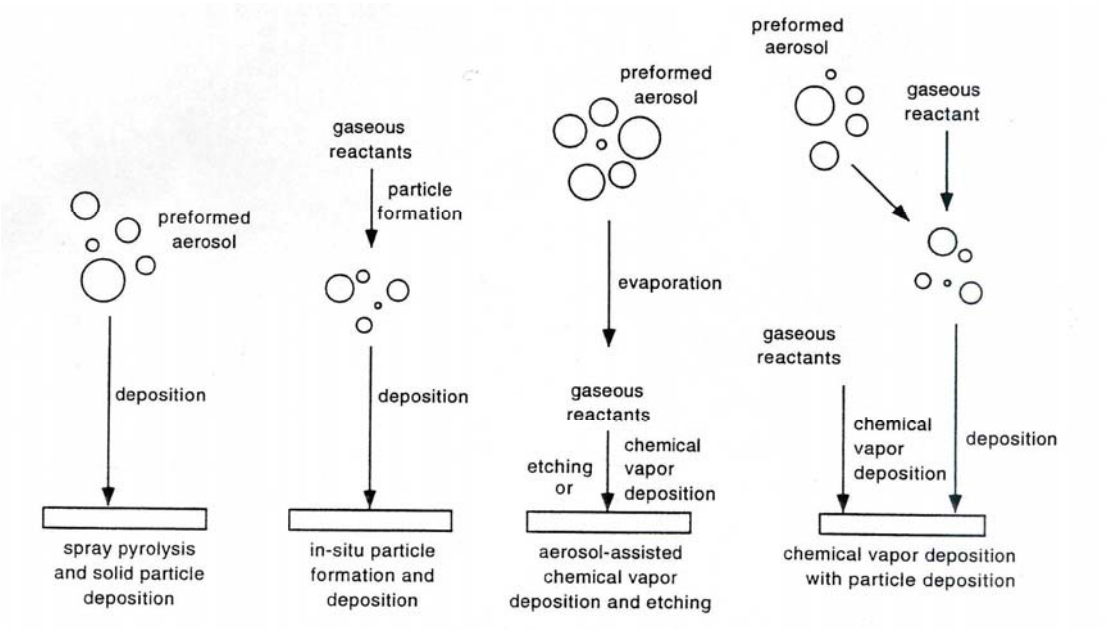

Figure 2.22: Role of particle deposition in various processes for film fabrication [110].

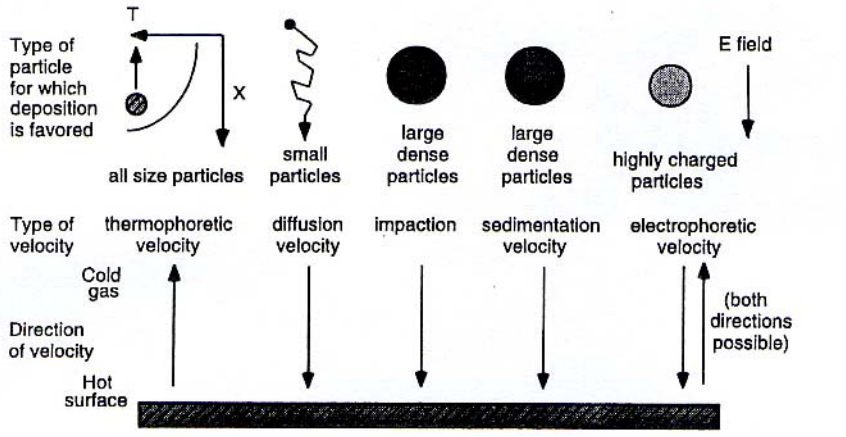

Figure 2.23: Particle transport phenomena [110].

2.4.1.1.1 Mean free path of the gas

To describe aerosol processes, several variables, such as precursor and product characteristics, must be considered. More specifically, particle size distribution and composition (which determine vapor pressure, for example) are the most important parameters. Control of the aerosol processes for the production of materials also

requires understanding the interaction between the aerosol components i.e. gas and particles. The nature of this interaction is largely determined by the particle size and mean free path of the gas [124].

The mean free path of a gas (λ) is one of the most important characteristics associated with an aerosol. It is the average distance that a molecule or atom of the gas travels before colliding with another atom, another molecule, or the walls. A major difference between gases and liquids is that the λ for gas molecules is larger; as a consequence gas molecules travel relatively long distances before colliding with each other. This is because the molecules and atoms in liquids are separated by distances roughly equal to molecular or atomic diameters, while the molecules and atoms in gases are separated by distances much larger than that.

The average distance (cm) traveled by the molecules between collisions is given by:

$$\lambda = \frac{2.00\mu}{\rho \bar{C}} \quad \textbf{(Eq. 2.2)}$$

where μ (g/cm sec) and ρ (g/cm^3) are the gas viscosity and density, respectively. $\bar{C}$ (cm/sec) is the average of the velocities of all the gas molecules.

When the particle diameter is much larger than the mean free path ($d_p >> \lambda$), the particle sees the gas as a continuous medium. However, when ($d_p << \lambda$), in this case each particle behaves as if it were in a rarefied medium in which the particles do not influence the velocity distribution of surrounding molecules and atoms (Figure 2.24).

The Knudsen number ($Kn = 2\lambda/d_P$) is used to simplify analysis involving particle size and gas mean free path. It is defined as the ratio of the mean free path of the gas to the particle radius. When Kn << 1 the particles are said to be in the continuum regime and when Kn >> 1, the particles are in the free molecular regime. For the case where $0.1\lambda < d_P < 10\lambda$, the particles are in the transition-slip regime, since the particles slip effectively between the gas molecules.

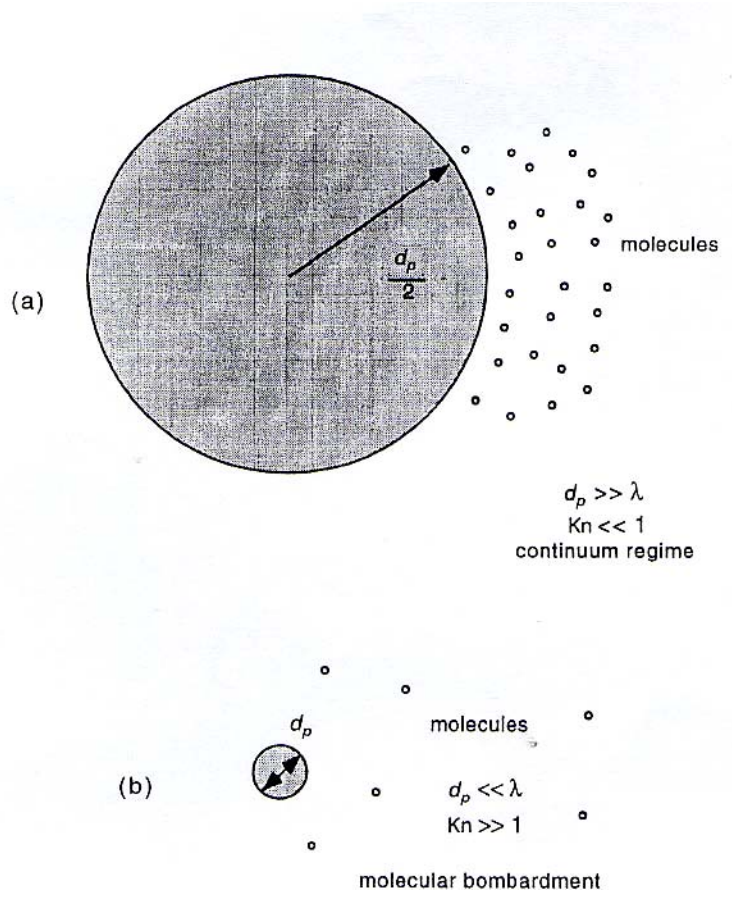

Figure 2.24: Relation between particle sizes and mean free path for a) continuum regime and b) free molecular regime [110].

2.4.1.2 Intraparticle reaction processes

Some of these processes are called evaporative decomposition, spray roasting and spray pyrolysis, the subject of this work. Intraparticle processes are important during powder formation by spray pyrolysis, vacuum atomization of molten metals, droplet-phase reactions to form liquid or solid products. It is also important for film formation by AACVD when the volatile precursor in each droplet reacts before evaporating. In Intraparticle reaction processes the particles containing the precursor are formed mechanically by a droplet or particle generator. The precursor is then reacted with a gas or pyrolysed in the particle to form the product. This can be done with the aid of a hot wall, a flame or any energy source that heats the particles [110].

There are several classes of Intraparticle processes, as follows:

- Gas-solid reactions: they occur at the interface of particles with a gas, or the gaseous species can diffuse into a porous solid, where the reaction occurs. Such reactions are important for the formation of materials, especially for

nanometer-sized metal oxide particles. An example is the conversion of Al to Al_2O_3 by reaction with oxygen [125].

- Gas-liquid reactions which occur at or near the droplet-gas interface, as well as within the droplet as the conversion of liquid reactant aerosol droplets to solid products during spray pyrolysis and the decomposition of volatile precursors in aerosol droplets during aerosol delivery of precursors for CVD. Spray pyrolysis can be used for film production (Figure 2.25) where the droplets are deposited on a heated substrate followed by decomposition of the precursor. Further heating results in the formation of the product film. Other situations may be encountered in spray pyrolysis where solid particles form in the gas phase, then deposit on the substrate and finally sinter to form the ceramic thin film. Another variation is to use volatile reactants that evaporate from the solid particles or droplets into the gas phase and deposit material into the substrate by chemical vapor deposition (CVD). Such approach is called aerosol CVD, spray CVD and spray pyrolysis [110].
- Phase transformations which involve materials going from liquid to solid, as in the solidification of molten metal droplets, amorphous to crystalline, and crystalline to crystalline phases.
- Crystal growth which follows the precipitation of solutes during spray pyrolysis. Crystallites in solids grow at high temperatures, leading in some cases to the formation of single-crystal particles. An example is the formation of single-crystal precious metal particles during spray pyrolysis [126, 127].
- Transport of gaseous reactants and products into and out of particles.

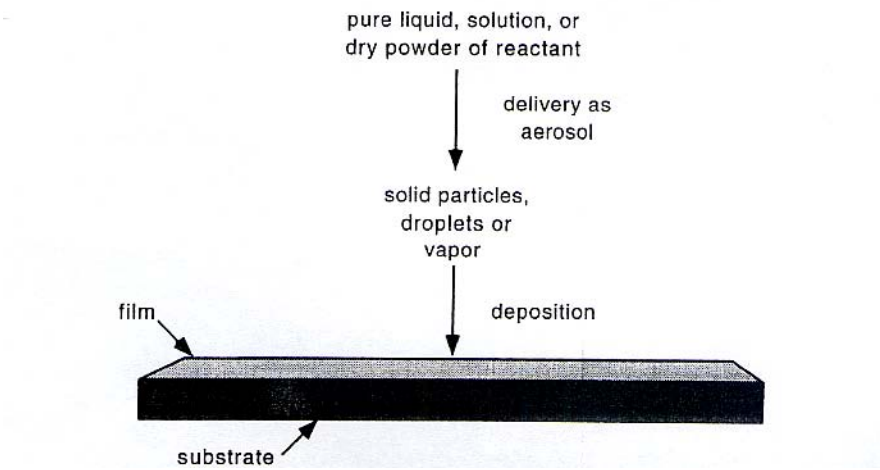

Figure 2.25: Production of thin films by spray pyrolysis [110].

Diffusion is the mechanism by which transport occurs during intraparticle processes. Diffusive transport, the movement of species due to their random thermal motion in a concentration gradient, occurs in solids, liquids and gases. Reactants are transported into the interior of particles and reaction products are removed from the interior of the particles by diffusion. Diffusion is also the process that enables crystal growth inside particles after solute precipitation in droplets. Diffusion processes are often driven by concentration gradients caused by reactions inside particles or droplets or by transport processes outside the particles. They can also be driven by surface curvature. In spray pyrolysis, particles are formed by the diffusion of the solvent through the droplet to the surface, where it then evaporates and diffuses into the gas phase. At the same time, the solute must diffuse towards the center of the particle. This results in concentration gradients of the solute in the droplet that are the cause of precipitation of species at the droplet surface, which can lead to formation of a shell. The diffusing species must then also diffuse through this shell [128].

2.4.2 Chemistry of aerosol processes

Chemical processes that occur during the aerosol synthesis of materials can be classified in terms of the final product (i.e. film or powder) or according to the phase in which they occur (i.e. solid, liquid, or gas). Whichever classification is used, there is a significant amount of overlap between each classification. In addition to that, it is difficult to determine whether gas-phase, liquid-phase or solid-state reactions occur during aerosol synthesis of material. For example, film deposition can occur by simultaneous particle deposition or CVD.

Film deposition can occur by spray pyrolysis (droplet deposition), solid particle deposition, and CVD. In spray pyrolysis, a droplet composed of the solvent and the metal-containing precursor is delivered to a heated substrate, where the solvent evaporates and the precursor react to form a film of the desired material. In this case, the solubilities and volatilities of the metal-containing precursors, their reactivities individually and with each other on the heated substrate are all important; the reactivity of the metal-containing precursor is crucial to the purity, composition and value of the product of the process. Also it is desirable that the precursor be non-volatile to avoid gas-phase processes and retain control over the deposition process. The volatility of a given species increases with increasing the temperature and with decreasing the molecular weight. The solvent may also play a role in

determining the purity and composition of the produced film. CVD involves the delivery of vapour-phase precursors using an aerosol delivery process to the surface where reaction to deposit a film occurs. Gas-phase reaction can lead to the formation of undesired particles which may be deposited on the surface. In CVD it is important that the precursors be volatile and capable of reacting on the substrate surface to form high purity films. When complex materials are to be deposited, the relative vapour pressures (volatility) and reactivities of the precursors are again important.

The solubility of a solute in a solvent is important in aerosol processes in which the solute (or metal containing precursor) is first dissolved in a solvent in order to deliver the solute to the system. Two such processes are spray pyrolysis and AACVD. Solubility can affect particle morphology through different solubilities of the reagent, compositional homogeneity during powder formation and different transport rates during film deposition. Water is often a choice as a solvent for spray pyrolysis because it exhibits a high dielectric constant, i.e. has high ability to dissolve ionic species and is used mainly to dissolve metal nitrates. Another solvent property which should be considered is the donor or coordinating ability of the solvent i.e. its ability to coordinate to a particular metal (acceptor) center, which depends on the nature of the solvent and the metal center to which electrons are being donated and is an important aspect of dissolving a metal-containing compound. The donor/acceptor ability of solvents has been quantified using donor/acceptor numbers. A higher numerical value indicates a stronger donor or acceptor; this can be used as a guide to help dissolve reagents by choosing a better donor solvent over a weaker donor solvent to improve solubility [129].

Table 2.3 shows an example of donor and acceptor numbers. The donor number is the negative of the standard reaction enthalpy for the reaction between the donor in question with the acceptor $SbCl_5$ in 1,2-dichloroethane. The acceptor number is an arbitrary number derived from the change in nuclear magnetic resonance (NMR) chemical shift when trimethylphosphine oxide (Me_3PO) is used as a reference base and given a value of 0, while a value of 100 is given to the acceptor $SbCl_5$. The solubilities of common reagents in water are given in Table 2.4.

Table 2.3: Donor and acceptor numbers for various solvents at 298K [110].

Solvent	Donor number	Acceptor number
Acetic acid	-	52.9
Acetone	17.0	12.5
Benzene	0.1	8.2
Carbon tetrachloride	-	8.6
Diethyl ether	19.2	3.9
Dimethylsulfoxide	29.8	19.3
Ethanol	19.0	37.1
Pyridine	33.1	14.2
Tetrahydrofuran	20.0	8.0
Water	18	54.8

Table 2.4: Solubilities of some metal-containing compounds at 298K. (Superscripts are in °C) [110].

Name of Compound	Formula	Solubility in Water (g/100 g of water)
Aluminum (III) chloride	$AlCl_3$	46.6
Aluminum (III) nitrate	$Al(NO_3)_3$	81.8
Aluminum (III) sulfate	$Al_2(SO_4)_3$	40.4
Barium acetate	$Ba(OAc)_2 \cdot 3H_2O$	75
Barium chloride	$BaCl_2 \cdot 2H_2O$	38.1
Barium formate	$Ba(O_2CH)_2$	31.9
Barium hydroxide	$Ba(OH)_2$	5.6
Barium nitrate	$Ba(NO_3)_2$	11.5
Barium sulfate	$Ba(SO_4)$	insoluble
Cadmium chloride	$CdCl_2 \cdot H_2O$	135
Cadmium nitrate	$Cd(NO_3)_2$	167
Cadmium sulfate	$CdSO_4$	77
Calcium acetate	$Ca(OAc)_2 \cdot 2H_2O$	33.8
Calcium chloride	$CaCl_2 \cdot 6H_2O$	100
Calcium nitrate	$Ca(NO_3)_2 \cdot 4H_2O$	152
Calcium sulfate	$CaSO_4 \cdot 2H_2O$	0.26
Cerium(III) sulfate	$Ce_2(SO_4)_3 \cdot 9H_2O$	7.3
Chromium (III) nitrate	$Cr(NO_3)_3$	152.35
Cobalt (II) chloride	$CoCl_2$	59.7
Cobalt (II) nitrate	$Co(NO_3)_2$	111
Cobalt (II) sulfate	$CoSO_4$	42
Copper (II) chloride	$CuCl_2$	77.3
Copper (II) nitrate	$Cu(NO_3)_2$	156
Copper (II) sulfate	$CuSO_4 \cdot 5H_2O$	37.8
Iron (II) chloride	$FeCl_2$	66.7
Iron (III) chloride	$FeCl_3 \cdot 6H_2O$	106.8
Iron (II) nitrate	$Fe(NO_3)_2 \cdot 6H_2O$	266^{60}
Iron (III) nitrate	$Fe(NO_3)_3 \cdot 9H_2O$	137.7^{20}
Iron (II) sulfate	$FeSO_4 \cdot 7H_2O$	60
Lanthanum nitrate	$La(NO_3)_3$	168^{40}
Lead (II) acetate	$Pb(OAc)_2$	69.8
Lead (II) nitrate	$Pb(NO_3)_2$	64.4
Magnesium acetate	$Mg(OAc)_2$	68.6
Magnesium chloride	$MgCl_2$	55.8
Magnesium nitrate	$Mg(NO_3)_2$	73.6
Magnesium sulfate	$MgSO_4$	38.9
Nickel chloride	$NiCl_2$	70.6
Nickel nitrate	$Ni(NO_3)_2$	105
Nickel sulfate	$NiSO_4 \cdot 6H_2O$	44
Silver acetate	AgOAc	1.2
Silver chloride	AgCl	insoluble
Silver nitrate	$AgNO_3$	216^{20}
Silver sulfate	Ag_2SO_4	0.9
Strontium acetate	$Sr(OAc)_2$	39.5
Strontium chloride	$SrCl_2$	58.7
Strontium nitrate	$Sr(NO_3)_2$	88.7
Strontium sulfate	$SrSO_4$	0.0138
Zinc chloride	$ZnCl_2$	437
Zinc nitrate	$Zn(NO_3)_2$	138
Zinc sulfate	$ZnSO_4$	66.5

2.4.2.1 Thermal decomposition of precursors

Compounds such as metal nitrates, carbonates and sulfates have been employed extensively for the formation of metal-oxide-based materials by aerosol processes, such as spray pyrolysis. Metal nitrates are the most commonly used precursor for metal oxides because of their lack of carbon, hence avoiding carbon contamination. Therefore, the discussion in this section will concentrate on the metal nitrates which are used in this work - the precursor materials and their thermal decomposition

behaviour. Metal acetates were also used as a precursor in this work and will be represented in section 8.2.1.

Although the reaction mechanisms have not been studied in detail during aerosol-processing experiments, a great deal is known about the thermal decomposition of metal nitrates in the solid state. In general, metal nitrates decompose thermally, by heating, to form the corresponding metal oxide, together with NO_2, NO and O_2, in various stoichiometries:

$$M(NO_3)_2 \rightarrow MO + xNO_2 + yNO + zO_2 \quad \textbf{(Eq. 2.3)}$$

$$MO \rightarrow M + \frac{1}{2}O_2 \quad \textbf{(Eq. 2.4)}$$

Noble metals such as Ag and Pd, tend to react further and lose O_2 at higher temperatures, forming the corresponding metals.

It is worth mentioning that the solvent has a potential importance in a thermal decomposition reaction and may play a significant role in the composition and phase evolution of the system. As an example, nickel nitrate, $Ni(NO_3)_2$, thermally decomposes in a single process to form NO_2, O_2 and NiO. However, the corresponding hydrate, $Ni(NO_3)_2.2H_2O$, decomposes thermally in two steps; first by forming a mixture of $Ni(NO_3)_2$ and $Ni(OH)_2$ and second by dehydration and loss of NO_2 and O_2 which results in the formation of NiO [130].

2.4.2.2 Surface processes

During the deposition of thin films on heated surfaces, many surface processes are involved. The deposition process starts by the transport of molecular species to the surface where they can physically adsorbed by the formation of a weak interaction between the surface and the molecules. This can then be followed by chemical adsorption, in which bonds in the molecular species are broken and new bonds are formed between fragments of the molecular species and the surface. The species formed on the surface are usually very reactive and can undergo further chemical reactions, which results in the formation of reactive species, such as metal atoms and organic by-products. The metal nuclei generally possess high diffusion coefficients at the deposition temperature and migrate freely across the substrate surface to positions of greater thermodynamic stability, which is often another atom or part of a growing film. This migration ultimately results in additional film growth. The organic by-products can be rearranged on the surface resulting in their entrainment on the

growing film, which is undesirable since it can lead to contamination of the film through the formation of metal carbides, or the incorporation of carbon into the film, which may be detrimental to its properties [131]

2.4.3 Particle growth, evaporation and nucleation phenomena in aerosols

2.4.3.1 Introduction

Growth of particles, evaporation of droplets and formation of new particles are all exhibited by aerosol processes. Evaporation and condensation of gaseous species from and onto particles can occur for both droplets and solid particles and it is one of the ways particles grow and shrink in size after they are formed, often by nucleation. In droplets, condensation and evaporation occur onto and from a liquid and require a change in phase from vapour to liquid or vice versa. For solid particles, atomic and molecular species can physically or chemically adsorb onto the surfaces. On one hand, the physical adsorption involves the formation of weak attractions such as van der Waals and is important only for species with partial pressures near their vapour pressure. On the other hand, the chemical adsorption involves the formation of chemical bonds with the surfaces and can occur at any temperature and partial pressure. This is the mechanism by which many solid particles grow.

Condensation and evaporation is an important concept in a wide variety of aerosol processes for the synthesis and processing of materials. Film formation by the deposition of droplets onto surfaces (spray pyrolysis) involves directing the droplets at hot surfaces. The gas temperature rises as the droplets approach the surface, resulting in evaporation of the liquid and result in a decrease in the size of droplet. In aerosol assisted chemical vapour deposition (AACVD), volatile precursors, either in solution or as a pure liquid, are transported by droplets to a region where the solvent and precursor evaporate to form a vapour of the reactant on the surface to form a film or, in the gas phase, to form particles.

Spray pyrolysis for the production of powder involves converting a liquid containing a precursor, in a solution or as a suspension, into aerosol droplets. A heated gas is used to evaporate the droplets, yielding particles of the reactant. The final product is then obtained by decomposition of the particles at high temperatures. The particles can grow and shrink by condensation and sublimation, respectively. Such

particles can be used to deliver precursors for chemical vapour deposition (CVD) processes in the same manner to that for aerosol assisted chemical vapour deposition (AACVD) with droplets. Solid particles of volatile reactants can be deposited onto surfaces if they do not evaporate before deposition. Surface reaction is a particle growth mechanism in which volatile reactants chemically adsorb on particle surfaces and react to form a product with a low vapour pressure, which then remains on the particle surface. The transportation and chemical adsorption of co-reactants such as oxygen are required for such reactions to take place.

The transport of gaseous species onto particle surfaces by evaporation and condensation also play central roles in the theory of gas-phase nucleation, that is, the formation of new particles [110, 132].

2.4.3.2 Qualitative particle growth

Before addressing the details of particle formation and growth, a summary of how the various phenomena are related would be useful. For the example of particle formation followed by growth, the overall process begins with the formation of new particles by homogenous nucleation; the one when condensation of vapour takes place on clusters of similar vapour molecules [132]. In situations when collisions do not occur, growth often occurs by vapour condensation. After the formation of the particles, vapour diffusion takes place, with a much shorter time than growth.

The transport of atomic and molecular species to and from particle surfaces is encountered in many material-processing applications and is the start point to the theory of condensation, evaporation and surface reaction [133]. The simplest case of molecular transport to a particle surface is when the particle size is much smaller than the gas mean free path i.e. in the free molecular regime ($d_p << \lambda$), where the molecules arrive at the particle surface in a ballistic fashion (Figure 2.26). This occurs for particles smaller than 10nm at standard temperature and pressure. Physically, the particle is so small that it fits into the spaces between gas molecules and atoms and behaves like a large molecule.

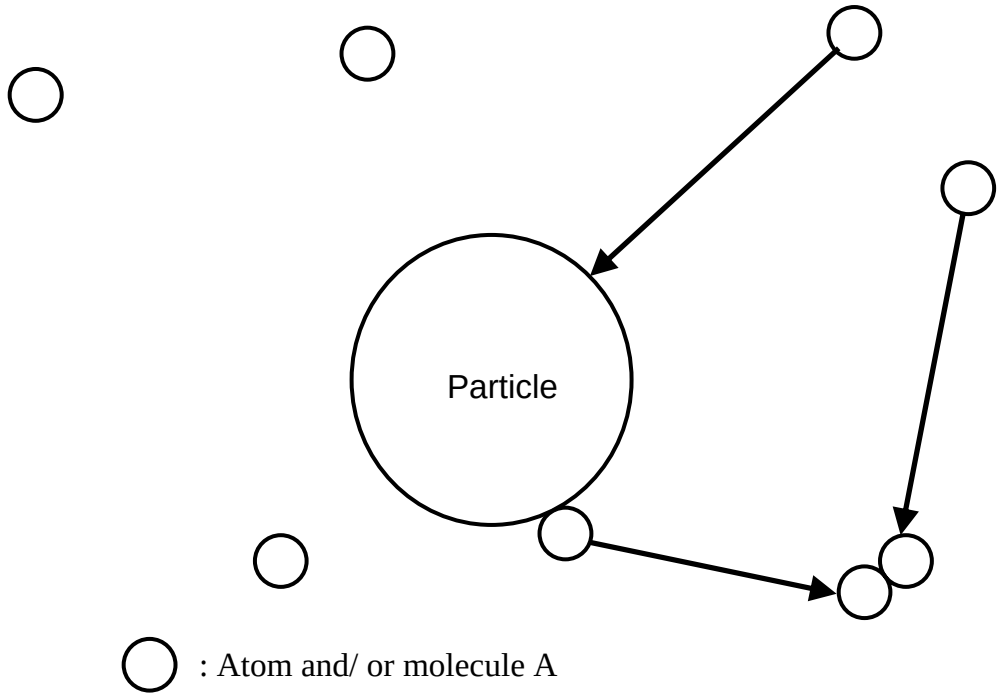

Figure 2.26: Schematic of atoms and / or molecules (A) colliding with a particle in the free molecular regime [110].

From the kinetic theory of gases, the rate of change of the particle (solid or liquid) diameter with time at temperature T in the free molecular regime (Kn>>1) is given by:

$$\frac{dd_p}{dt} = \frac{2\alpha_s \nu_1 (p_1 - p_d)}{(2\pi m_1 k_B T)^{1/2}} F_1 \quad \textbf{(Eq. 2.5)}$$

Where:

d_p: the particle diameter.

t : the time.

α_s: the sticking coefficient.

ν_1: is the volume of transported molecule or atom in the particle = m_1 / ρ_1.

$m_1 = M / N_A$, the mass of transported molecule or atom in the particle.

ρ_1: is the density of the material in the particle in the solid or liquid state.

M: the molecular weight.

N_A: Avogadro's number.

p_1: the partial pressure of the vapour for species 1 far from the particle.

p_d: the partial pressure at the particle surface.

k_B: Boltzmann's constant.

T: the temperature.

F_1: correction factor.

In the continuum regime, the transport mechanism by which atoms and molecules move to and from a particle's surface is diffusion, which occurs when the particle size is much larger than the gas mean free path, or about 1000 nm at standard temperature and pressure. The gaseous species being transported undergo numerous collisions with other gas molecules on its way to or from the particle surface (Figure 2.27). In addition, during condensation, evaporation or sublimation, a concentration gradient can be established around the particles.

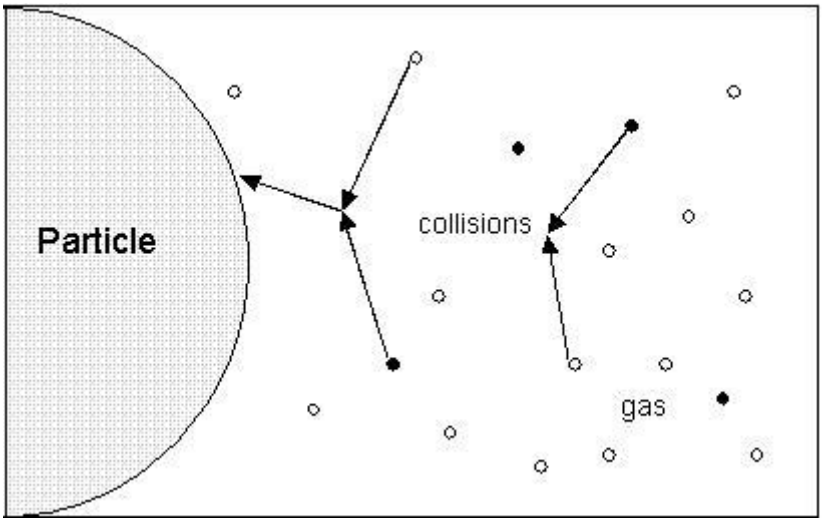

Figure 2.27: Schematic illustrating how atoms and molecules are transported to a particle surface by diffusion in the continuum regime [110].

The rate of change of particle diameter with time at a temperature T in the continuum regime is given by:

$$\frac{dd_p}{dt} = \frac{4D\,v_1(p_1 - p_d)}{k_B T d_p} F_2 \quad \textbf{(Eq. 2.6)}$$

where: D (cm^2/sec) is the diffusivity of the gas or vapour (diffusion coefficient).

F_2: correction factor.

For many applications of aerosols in material synthesis and processing, on the one hand, it is not of interest to know the detailed evolution of particle size for the processes of condensation and evaporation. On the other hand, it is often of interest to know the time required for particles to grow or shrink a certain amount. The characteristic time for evaporation or condensation is defined as the time required to halve the particle diameter by evaporation or sublimation or to double it by condensation. In the continuum limit (Kn<<1), for large particles such that $p_d = p_e$

(i.e. the vapour pressure over a curved surface = the vapour pressure over a flat surface), and neglecting the correction factor, the characteristic time τ_{GC} is given by:

$$\tau_{GC} = \frac{3k_B T d_{po}^2}{32D(p_1 - p_e)\nu_1} \quad \textbf{(Eq. 2.7)}$$

where d_{po} is the initial particle diameter.

In the free molecule limit (Kn>>1) and with $p_d = p_e$, the characteristic time for particle condensation or evaporation τ_{GF}, neglecting the correction factor and the sticking coefficient, is given by:

$$\tau_{GF} = \frac{(2\pi m_1 k_B T)^{1/2}}{4\nu_1(p_i - p_e)} \quad \textbf{(Eq. 2.8)}$$

where p_i is the partial pressure of species (i) corresponding to complete evaporation.

In equations 2.4 and 2.5, the reduction in vapour pressure and, therefore, increase in droplet lifetime due to the presence of solutes in droplets was neglected. Another effect which was neglected is the increase in the evaporation rate due to heating of the gas above the substrate. This is a complicated problem, as the thermophoresis keeps the particle from approaching the substrate too closely, and the large volume of water vapour produced by evaporation on the substrate results in a net gas velocity away from the substrate [134].

2.4.3.2.1 Chemical reactions

Chemical reactions at the surface of, or inside, particles are often exploited for the generation or modification of materials by introducing gaseous reactant into the aerosol stream to convert the precursor to the product. However, a distinction must be made between the relative rates of transport of gaseous reactants to the particle and chemical reactions on or in the particle i.e. surface reaction or volume reaction. An example of surface reaction is the growth of the particle by CVD. In contrast, the volume reaction occurs in cases where the particle consists of one reactant material that must be converted to a product by chemical reaction throughout the particle, not just at an interface.

If the rate of reaction on the particle surface is able to consume the reactants faster than it can be supplied to the particle by vapour transport, then transport limits the growth rate. If, however, the rate of consumption of the gaseous reactant is slower

than the maximum rate at which vapour can be supplied by gas-phase transport, then the particle growth rate is determined by the chemical reaction rate, regardless of whether the reaction takes place on the surface or inside the particle.

The rate of particle growth by surface reaction is given by:

$$\frac{dd_p}{dt} = \frac{2k_s p_{1s} \nu_1}{k_B T} \quad \textbf{(Eq. 2.9)}$$

where:

k_s: is the surface reaction rate constant (cm/sec).

p_{1s}: is the reactant partial pressure at the particle surface.

ν_1: the volume of the reaction product.

The characteristic time for particle growth by surface reaction is given by:

$$\tau_{GSR} = \frac{k_B T d_{po}}{2k_s p_1 \nu_1} \quad \textbf{(Eq. 2.10)}$$

However, when the maximum rate of gas-phase transport to the particles is rapid relative to the reaction rate, and the reaction occurs homogenously throughout the particles, the rate of particle growth is limited by the reaction rate inside the liquid or solid in the particles. An example of the volume-reaction-limited growth is that of a reactant dissolved in water droplets (or droplets of some other solvent) and a gaseous co-reactant. The co-reactant enters the particles and reacts with dissolved reactant to form a product, thereby increasing the volume of the droplet.

The rate of particle growth by volume reaction is given by:

$$\frac{dv}{dt} = \frac{r_v \nu M}{\rho_p} \quad \textbf{(Eq. 2.11)}$$

Where:

r_v : the rate of reaction per unit volume (moles/cm^3 sec).

M: the molecular weight.

ρ_p: the particle density.

ν : the particle volume.

The characteristic time for particle growth by volume reaction is given by:

$$\tau_{GV} = \frac{3(\ln 2)\rho_p k_B T}{k_v H p_1 M} \quad \textbf{(Eq. 2.12)}$$

where:

k_v : the reaction rate constant.

H: Henry's constant which relates the concentration in the liquid to the partial pressure in the gas (L.atm/mole) [135].

2.4.3.3 Droplet evaporation

Particle formation by evaporation from solution droplets takes place during spray pyrolysis to form both films and powders where the vapour pressure at the particle surface is no longer that of pure liquid, but is reduced by the suspended or dissolved species. The presence of the solute lowers the vapour pressure of the solvent. This effect is caused, first, by the presence of nonvolatile molecules near the droplet surface, thus reducing the area for evaporation, and second, by the development of chemical forces between solute and solvent molecules.

During the evaporation of solution droplets, there are two competing effects. As the solvent evaporates, the solute concentration increases and the solvent vapour pressure over the droplet decreases. At the same time, evaporation of the solvent reduces the droplet size, increasing the droplet curvature and therefore increasing the solvent vapour pressure for droplets with diameters less than or equal to approximately 0.1μm. This is because the molecules near the particle surface have fewer nearest neighbours than they would in a flat surface, this results in less energy being required to remove an atom or molecule from a curved surface into the gas phase. Thus, in material processing, the main concern is the reduction of vapour pressure; which forces the use of longer residence times or higher process temperatures for complete removal of the solvent.

Droplet evaporation plays an important role in droplet and solid particle deposition, as well in the aerosol delivery of volatile precursors for CVD. If the solvent evaporates before the droplets strikes the substrate, solid precursor particle deposition will then lead to rough films. If the precursor does not evaporate fully, after solvent evaporation, during the aerosol delivery of precursors for CVD, deposition rates are reduced and some of the precursor is not utilised. Furthermore, partial evaporation of the precursor can lead to rather complex temperature dependences for the deposition rate.

In droplet deposition (also called spray pyrolysis), the deposition is accompanied by some degree of solvent (sometimes also with solute) evaporation. In the case of water droplets containing small amounts of a dissolved species, droplet lifetime accounting for the lowering of the temperature due to the latent heat of

evaporation for droplet diameters of 0.1, 1, and 10μm are $5x10^{-5}$, $2x10^{-3}$, and 0.15 seconds, respectively, at atmospheric pressure, 50% relative humidity and 20°C. These calculations assume no increase in the relative humidity of the surrounding gas as the water evaporates, a situation that is sometimes unrealistic. Those lifetimes can be reduced when solvents of higher vapour pressures are used; the lifetimes for ethanol droplets of the same diameters are $1x10^{-5}$, $3x10^{-4}$, and 0.03 seconds, respectively, at 20°C and one atmosphere [123].

The above examples can be used as a qualitative guide to determine when a process occurs by droplet deposition or by some other mechanism such as vapour deposition, when vapour solutes and precursors are used. The given evaporation times suggest that droplet deposition without appreciable solvent evaporation requires that the droplet diameter be greater than roughly 10 μm for droplet residence times of about 0.1 second before impaction. Thus initial droplet diameter of 100 μm or greater usually ensures droplet deposition before evaporation. Conversely, experiments carried out with certain classes of ultrasonic atomisers, using droplets less than 5 μm in diameter, will provide solvent evaporation well before a droplet reaches a surface. In such cases, deposition can occur by solid particles for non-volatile solutes or by CVD for volatile solutes.

In contrast to droplet deposition (spray pyrolysis), complete solvent and precursor evaporation is required for the aerosol delivery of volatile precursors in CVD without particle or droplet deposition. In this case the evaporation of the solvent and the precursor must occur before the droplet or particle reaches the substrate. Therefore, droplet diameters of less than 10 μm are used to ensure evaporation of the solvent within the residence time of the droplets in the system. However, the precursor may not evaporate fully during aerosol delivery of CVD precursors unless the vapour pressure is high enough (use high temperature) and the residence time is long enough. This explains the motivation for adding a preheated section before the deposition chamber in AACVD processes, to increase both the temperature and residence time of the droplet in the gas phase. It is also important to note that the droplet generator, which controls the size and concentration, plays an important role in film formation processes based on droplet or vapour deposition. Unless sufficiently high precursor solubility in the solvent and sufficiently high droplet concentrations are used, the solute will not have sufficient time to evaporate in the deposition system. This is because the time required to saturate the gas with the evaporating droplets

increases by decreasing the particle diameter and by decreasing droplet concentration according to the following equation:

$$\tau_{sat} = \frac{1}{(2\pi d_p D N_\infty)} \quad \textbf{(Eq. 2.13)}$$

where D is the diffusion coefficient (cm^2/sec) and N_∞ is the droplet concentration per unit volume.

2.4.3.4 Nucleation

Gas-phase nucleation is to be discussed here because it is related to the concepts described by the equation for particle growth in the free-molecular regime. Gas-phase nucleation is the process by which gas atoms or molecules are transformed into liquid or solid particles and is the basis for gas-to-particle conversion processes. Also it plays a role in spray-based aerosol processes. Two mechanisms with different driving forces occur, physical and chemical nucleation, although the distinction between the two phenomena is often not clear.

In the physical nucleation, the particles are built up from monomer units that have the same or nearly the same form and composition, both in the gas phase and as particles. An example is the formation of metal particles from a metal vapour by cooling. The chemical nucleation is the result of chemical reactions between a molecule and a growing oligomer (several monomers bonded to each other). An example is the formation of particles during CVD, where the precursor may react in the gas phase to form oligomers with low vapour pressures that in turn nucleate to form particles. The particles then grow by the reaction between monomers. In the chemical nucleation there may be only a few sites on the oligomer (also called clusters which are small collections of molecules or atoms formed by random collisions between two or more molecules or atoms) where further reaction can take place. In contrast, a monomer can add to any location on a cluster during physical nucleation.

A situation intermediate between physical and chemical nucleation is the formation of oligomers by the reaction of several monomer units. The oligomers that are formed may have such low vapour pressures that they nucleate to form particles. Thus, the particles are composed of partially reacted species.

Nucleation can also be homogenous or heterogeneous. The homogenous nucleation occurs without the presence of foreign phase (only with existing particles).

In contrast, the heterogeneous nucleation requires the presence of a foreign body, usually aerosol particles of some other material onto which nucleation takes place. This is most common in atmospheric processes.

It is worth mentioning that for the vast majority of cases of aerosol material synthesis in the literature, the nucleation mechanism responsible for particle formation is not discussed, and the parameters required to evaluate the critical particle size required for the particle formation i.e. for nucleation and growth of the particle, are not available. However for almost all conditions of practical importance, particle formation and growth occurs by chemical reactions and collisions or coagulation. The coagulation is the process by which two particles collide and stick together to form a new, large particle. However, coagulation is not important in spray processes for powders and films, because the particle concentration is not high enough to result in particle collisions during a typical process residence time [136-139].

2.4.4 Advantages and disadvantages of aerosol processes for thin film deposition

Aerosol routes to manufacturing films have some advantages and disadvantages with respect to the material they produce and the process itself. In the case of spray pyrolysis, the process is simple, reproducible and cheap; only a substrate heater and an atomizer are needed and the operation is generally at atmospheric pressure. Many choices for liquid-phase precursors can be used including nitrates, chlorides and acetates...etc., it is possible to use low-volatility precursors, and high deposition rates can be obtained ranging from 0.1-1µm/min. Films obtained by aerosol deposition can be produced with single and polycrystalline forms with high purity and controlled film thickness, and by using multicomponent materials. An advantage of aerosol routes to films, compared to liquid-phase routes such as dip coating, is that many aerosol processes are dry and only vapor or solid particles contact the surface. This advantage is important for applications in which high purity films are required as in the manufacturing of optical fibers.

The disadvantages of aerosol processes for film formation may be summarized by: potential contamination by solvent, dilute process i.e. large volumes of gases per quantity of product, residual particles may remain after droplet evaporation during aerosol delivery of volatile reactants. Particle formation and deposition lead to porous films and degraded properties [110].

In section 2.4, a distinction between spray pyrolysis (droplet deposition) and AACVD was made, however, AACVD is referred to in the literature as spray pyrolysis, spray metal-organic CVD, pyrolysis process and low temperature CVD [83, 110, 120]. Figure 2.28 shows the effect of temperature on the decomposition of spray pyrolysis solution. It can be seen that if the temperature is high enough to vaporise the solution and the precursor, a CVD can be obtained (resembles the third mode of deposition in Figure 2.19) and this may be called as AACVD. So no distinction will be made after this point.

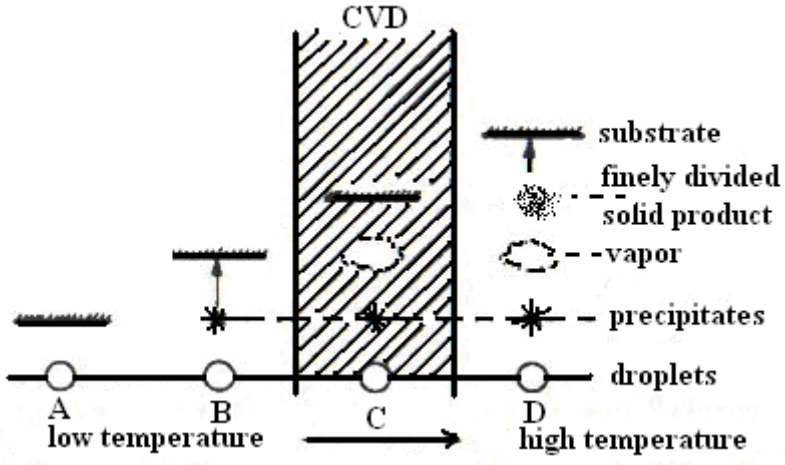

Figure 2.28: Decomposition as a function of temperature [120].

2.5 Spray pyrolysis of magnesium oxide (MgO)

In order to grow good quality films, one should optimize the following working parameters: the substrate temperature [120], substrate-nozzle distance (SND) [140], spray rate, and solution concentration [113].

2.5.1 Substrate temperature, carrier gas flow rate and spray rate

There are few reports on the deposition of MgO by spray pyrolysis on single crystal and glass substrates, however, none were found on metallic substrates. The following studies investigated the effect of substrate temperature on the produced films. Ji Ming et al [65] deposited MgO on (100) Si substrate. 0.5M of magnesium acetate was selected as the precursor solution. Filtered air was used as the carrier gas. SND was fixed at 10 cm and using a nozzle diameter of 8 mm. The deposition was done at a temperature range of 580°C-680°C. After deposition, the films were annealed at 700°C in oxygen for 10 min to reduce the crystalline defects and remove

the residual organic matter, which resulted in a well-crystallised structure. They found that the deposition rate decreased with increasing the substrate temperature. This was explained by the diminishing of mass transport to the substrate at higher temperature due to gas convection from the substrate pushing the droplets of the precursors away. Malle Krunks et al [141] explained similar results for the deposition of ZnO in the same way. They also gave another reason for the low deposition rate; this was attributed to the increased rate of re-evaporation at higher temperatures. Ji Ming et al [65] found that the film density increased with the decrease of film deposition rate at high temperature. This was attributed to the higher diffusion energy supplied by the higher temperature which is considered to be beneficial for the particles to fill in the internal defects, and this results in the formation of denser films. They also found that the (200) plane became the dominant one as the substrate temperature increased. At 680°C, the MgO film was strongly textured with preferential orientation along the (200)-axis. The relationship between the degree of orientation and substrate temperature was explained, in the same way as Xiaorog Fu et al [72], by the absorbed Mg and O atoms with a higher mobility, enhanced at higher substrate temperatures, able to easily move to equilibrium atomic sites on the surface. Thus, the increase of (200)-preferred orientation occurred while the substrate temperature was high enough. Ji Ming et al [65] noticed a morphology change from island growth and rough film surfaces to a layered one as the temperature was increased from 580°C to 680°C. At 580°C, it is possible that the droplets of $Mg(CH_3COO)_2.4H_2O$ evaporated before they reached the substrate surface, and the resulted precipitates impinge on the surface where decomposition occurred. The growth in the vertical direction was faster than in the horizontal direction because of the high deposition rate and low migration of the absorbed molecules on the growing surface. At 680°C, the droplets evaporated to form solid particles as they approached the substrate surface, and the particles melted and vaporized. Then, the solid vapour diffused to the substrate to undergo a heterogeneous reaction there. The film exhibited the characteristics of layer growth mechanism because of the low deposition rate and high migration of the absorbed molecules on a growing surface. Stryckmans et al [142] showed that, for the deposition of MgO (at temperatures of 300°C-550°C) on alumina substrate using hydrated magnesium acetylacetonate dissolved in isopropanol as a precursor, at low temperatures, the deposition was limited by the heterogeneous chemical reaction kinetics process at or near the substrate surface. At high temperatures, however, the

reaction kinetics were controlled by the diffusion process through the boundary layer owing to the rapid reaction kinetics at the surface. In other words, the reaction kinetics were so fast that the surface reaction became controlled by mass transfer of the reactant. They also found that the texture of the MgO films developed with thickness, where no preferred orientation was observed in the first crystallite layer. The films with high degree of (200) preferred orientation showed smooth surfaces and reduced number of cracks. They also found that the film thickness increased with increasing the temperature.

DeSisto and Henry [143] studied the effect of substrate temperature on the produced films using different substrates. They produced thin films of MgO on Si (100), sapphire and fused silica at temperatures between 400°C and 550°C. They used magnesium acetylacetonate, $Mg(CH_3COCHCOCH_3)_3$, as a precursor. The operating frequency of the ultrasonic nebulizer was 60 kHz which gave a median droplet size of 30 μm. On one hand, they found that MgO films on sapphire crystallized with a strong (100) orientation after annealing at 700°C and 930°C in flowing oxygen. On the other hand, MgO films on Si and fused silica developed cracks after the annealing process. They attributed that to the difference in the thermal expansion between the film and substrate (3, 0.55 and 13.8 x 10^{-6}/°C for Si, SiO_2 and MgO, respectively). They also found that the films prepared outside the range of 400°C-550°C had a slight roughness in appearance. Stampolova et al [67] used low temperatures for the deposition. They used a water-ethanol solution of $Mg(NO)_3.6H_2O$ as a precursor to deposit MgO on alumina and glass substrates at 300°C-350°C using SND of 10 cm. After a single spraying/annealing cycle, the films produced on alumina were porous. Therefore, many deposition cycles were followed by annealing at 970°C in order to grow well-crystallised films. Dense polycrystalline films were produced on alumina and those produced on glass exhibited fine grain structure.

Another spraying parameter was studied by Xiaorong Fu et al [72]. They studied the effect of oxygen flow rate and substrate temperature on the produced films. MgO was deposited on (100) Si substrate using magnesium acetate as a starting reactant. They found that at a flow rate of 2.5 l/min of oxygen, (200) oriented MgO films were produced. However, the films were polycrystalline when the flow rate was adjusted at 3.5 l/min. They also found that the crystallinity was increased with increasing the substrate temperature from 380°C to 600°C. At 600°C, a strong MgO (200) peak was observed with no other peaks, which means that the MgO film has

grown preferentially with the MgO (200) parallel to the Si (100) substrate surface with a thickness of 0.28 μm. The heating energy of the substrate provided the migration energy for surface atoms to form stable (200) preferential layer. The atomic force microscopy (AFM) observations showed that the films were smooth and homogeneous. The root mean square (RMS) surface roughness values were used to indicate the film surface roughness values. RMS values were 26.5, 65.4, 69.6 and 118 Å (corresponding to 2.65, 6.54, 6.96 and 11.8 nm, respectively) for films deposited at 380°C, 470°C, 540°C and 600°C, respectively. They concluded that the factors contributed to lowering the deposition rate were higher substrate temperature and lower oxygen flow rate. The relationship between the MgO orientation and the deposition rate may be discussed in terms of the migration of molecules on a growing surface. At low deposition rate, sufficient migration occurred to form the (200) plane of MgO which is energetically stable. According to lattice coincidence between (100) Si and MgO, a lattice mismatch for (200) MgO is smaller than that of (111) and (220) MgO corresponding to (100) Si substrate. At higher deposition rate, insufficient migration tends to form the energetically unstable (111) or (220) planes of MgO.

It is found that in the growth of FCC oxides that the (200) orientation minimizes the surface free energy and is therefore more energetically favourable. However, the (111) orientation has been shown to predominate as the fastest growing phase through an evolutionary process when the growth rate is sufficiently high. The (200) orientation was formed when the growth rate was low enough to allow surface diffusion to occur, resulting in the formation of the most densely packed phase parallel to the substrate. When the growth rate was increased, generally by increasing the flow rate of matter to the substrate, the mechanisms of film growth become dominated by the incoming precursor adhering to one crystal plane in preference to another. This phenomenon resulted in an evolutionary process where the fastest growing plane dominates, and eventually becomes the preferred orientation of the final film [144, 145]. O. Renault and M. Labeau [146] deposited MgO on glass substrates from magnesium acetate precursor at 400°C using the aerosol assisted chemical vapour deposition technique. <111> oriented films were obtained when using an air flow rate of 0.4μm/hr and a <200> oriented film when using a 0.12μm/hr air flow rate. They reported that as the growth of MgO thin films with a preferred (111) orientation is a competitive process it has been suggested that an amorphous layer was required to be deposited prior to a preferred orientation developing. This

merely suggests that the initial film layer is of random orientation and the preferential orientation develops as the deposition process continues. They found that films thinner than 150nm appear to be X-ray amorphous with no detectable peaks after which the (111) orientation was seen to develop preferentially. This first 150 nm may be composed of very small grains which are smaller than the coherence length of the X-rays and hence unable to be detected by XRD.

Pavlopoulos D. et al [147-149] deposited CeO_2 on glass substrates by spray pyrolysis using $Ce(NO_3)_3.6H_2O$ as a precursor. (111) oriented films were obtained when using an Ar flow rate of 3l/min regardless of the deposition temperature (325°C-450°C) and a (200) oriented films when using an Ar flow rate of 10 l/min at high temperatures (350°C-550°C). He also found that in the temperature range between 250°C-450°C, the thickness increased almost linearly with temperature indicating that the deposition rate was limited by the reaction kinetics. In the temperature range between 450°C-550°C, the thickness slightly decreased with increasing temperature. This was attributed to the fact that the reaction kinetics were so fast that the growth rate was mass transfer controlled. The thickness was also increased by increasing the concentration. It was also found that as the thickness of the film increased, the (200) texture coefficient rose. The texture coefficient was also decreased as the solutions became more diluted or by decreasing the substrate temperature. They also deposited MgO films on (100) Si oriented single crystals at 650°C from 0.078M magnesium nitrate as a precursor and using an Ar flow rate of 10l/min. They found that the thickness of the films increased linearly with increasing the deposition time while the roughness increased. They also found that inclined substrate deposition (ISD) resulted in thinner films when increasing the inclination angle.

And to summarise, different deposition variables and their effects on the deposited films are summarised in Table 2.5.

2.5.2 Substrate- nozzle distance (SND)

The effect of the substrate to nozzle distance was studied by Xie Yi et al [78]. MgO was deposited on (111) Si using ethanol-water solution of magnesium acetylacetonate. The solution was sprayed in the temperature range of 400C°- 450°C using an air flow rate of 3.5-4.01 l/min. They found that thin films of high quality could be deposited using substrate to nozzle distance (SND) between 8cm - 9cm. The

produced films were dense, smooth and homogeneous without pores and defects. Prince et al [140] (deposited In_2O_3 by spray pyrolysis and will be mentioned in more details later) found that the SND affected the thickness of the deposited layer. At distances larger than the optimum SND, the accumulation of thermal energy by each droplet is so high that it evaporates most of the solvent molecules well above the substrate surface which gives thin films. At shorter distances, heat absorbed by solvent molecules in the droplet is not enough to vaporise them completely. This will be coated over the substrate as a very thin layer which reduced the substrate temperature drastically and led to the formation of thin films as well.

2.5.3 Solution concentration

Few reports were found for the effect of precursor solution concentration on the MgO films deposited by spray pyrolysis. O. Stryckmans et al [142] deposited MgO films on polycrystalline Al_2O_3 substrates using magnesium acetyacetonate as a precursor at 300°C -550°C. The films were fully oriented at 400°C and non-oriented films were obtained at higher and lower temperatures. This texture evolution was observed for depositions from 0.035M and 0.05M but not for depositions from 0.01M and 0.02M. The study of the film microstructure for the MgO films as a function of the deposition temperature for solutions of 0.05 M was investigated. At 250°C, the MgO film microstructure presents individual, quasi-spherical grains. From 250°C to 420°C, the surface became gradually smoother and more cracked. For substrate temperatures higher than 400°C, the surface became irregular again with spherical grains at 500°C. This trend was similar for a concentration of 0.035M of the precursor. The different thermal expansion coefficients of MgO and alumina may explain the cracks in the MgO layer. However, this explanation was not sufficient since MgO layers deposited on MgO substrates also show cracks. Pavlopoulos, D. [147] deposited MgO films on (100) Si substrates from different concentrations of $Mg(CH_3COO)_2.4H_2O$ at 650°C. A strained (200) preferred orientation with a small MgO (220) peak was obtained when using 0.093M. A concentration of 0.139M resulted in formation of strained and unstrained (200) MgO in addition to small MgO (220) peak while a concentration of 0.186M resulted in the formation of strained MgO (200) and (220) peaks.

The effect of precursor concentration on MgO films deposited by other techniques in addition to the effect of precursor concentration on the properties of different films will be found in the following sections.

2.5.4 Different methodological approaches for the deposition of MgO

The electrostatic nebuliser was used by Soo Gil Kim et al [86]. They deposited MgO on SiO_2/Si (100) by the electrostatic spray pyrolysis method in the temperature range 400°C-500°C. The used precursor was bis(2,2,6,6-tetramethyle-3,5-heptanedionato) magnesium (II) dissolved in 90% ethyl alcohol and 10% acetic acid. The acetic acid played a role to prevent the source from being oligomerized in the solvent. They found that the MgO was deposited with a (100) preferred orientation regardless of the substrate temperature. The MgO films deposited at higher substrate temperatures showed better crystallinity, even though they were thinner due to lower deposition rate, than those deposited at lower temperatures. This was explained in the same way as done before [66, 79]. Soo Gil Kim et al [86] also found that the growth rate decreased with increasing the substrate temperature because of source depletion caused by homogenous reaction. SEM images showed that the surface roughness of the films increased with increasing the substrate temperature. After the solvent in a droplet was completely evaporated, the decomposition rate of the Mg precursor in a droplet also increased with the temperature. Therefore, large MgO particles occurred by homogenous nucleation before the Mg gas phase source arrived on a substrate in the case of a film deposited at 500°C compared to those deposited at 400°C- 450°C. Hence, large particles on the film surface are obtained.

In 2001 Rhee et al [56] deposited highly oriented MgO films on Si (111) and amorphous glass substrates at temperatures below 400°C using the charged liquid cluster beam technique. The precursor solution of MgO was prepared by sol-gel processing of magnesium acetate in ethanol using an acid catalyst. The Si substrate was etched with diluted HF (20%) to remove the surface oxide layer. However, since it is most likely that the Si (111) substrate will be oxidized before the deposition, when a high substrate temperature is used, it is very possible that the MgO film will be deposited on SiO_2. MgO films started to crystallize below 300°C and became more highly oriented in the [100] direction as the substrate temperature was increased.

2.5.5 Spray pyrolysis of other ceramic oxides

Not many studies were conducted into the deposition of CeO_2 by Spray pyrolysis. Shengyue Wang et al [150-152] deposited CeO_2 as a buffer layer on Si (100) using $Ce(CH_3COCHCOCH_3)_3$ in a 50% ethanol / water mixture as a precursor using ultrasonic spray pyrolysis. They found that appropriate control of the ratio of pulse time to interval time was necessary for obtaining high texture quality and greater crystallite size cerium (IV) oxide thin films. The crystallite size decreased with increasing the ratio of pulse time to interval time. Shengyue Wang et al [152] used cerium acetylacetonate, $Ce(CH_3COCHCOCH_3)_3$, for the deposition of cerium oxide (IV) on Si (100) substrates at 450°C. They found that low ratios of pulse time to interval time are very necessary to obtain rich crystallite thin films. In the initial stage of deposition, the nucleation and growth rate of the nuclei compete with each other. At large ratios, the generation reaction rate was high and the rate of nuclei formation exceeded that of the growth of nucleation. While at low ratios, the growth rate of nucleation predominated and hence the increase of crystallite sizes predominated. Konstantinov et al [62] deposited CeO_2 on fused-silica substrates at 350°C-500°C using $Ce(NO_3)_3.6H_2O$ as a precursor. The best uniform ceria films with nanometric scale grains were prepared at a substrate temperature of 400°C with 0.5 h annealing of the deposit at 500°C. At lower spraying temperatures large CeO_2 crystallites have been observed on the film surface along with the fine grains. When the substrate temperature exceeded 400°C, numerous cracks caused by thermal stresses appeared in the films. Petrova et al [63] used $Ce(NO_3)_3.6H_2O$, $CeCl_3.7H_2O$, anhydrous citric acid, tartaric acid and ethylene glycol as the initial materials for the preparation of the starting solutions of the spray pyrolysis. They deposited CeO_2 on β-quartz at 350°C-500°C, and found that post deposition annealing led to bigger crystallites. The deposited films were polycrystalline except the ones deposited from ethylene glycol solution of $Ce(NO_3)_3$ which show a preferred orientation along the [100] direction. The relatively poor XRD patterns of some of the films (produced at higher substrate temperature) were due to the rather small thickness of the films. The latter was a result of the evaporation of the aerosol liquid phase and dissipation of the material. They also found that the roughness increased with the increase in film thickness. Also the higher substrate temperature led to higher rate of evaporation and accordingly, to higher supersaturation and bigger number and smaller size of the crystals formed.

Pavlopoulos et al [148, 153] deposited CeO_2 on borosilicate glass using $Ce(NO_3)_3.6H_2O$ as a precursor. They found that the texture of CeO_2 improved with increasing temperature. Elidrissi et al [154] prepared CeO_2 thin films on glass substrates using cerium chloride or cerium nitrate as the starting material. The spray rate was 5 ml/min, air was used as the carrier gas and the substrate temperature was between 300°C to 500°C. For the case of using magnesium chloride, the films were amorphous at 300°C. As the substrate temperature was increased, the films became more crystalline as indicated by the increase of the (200) peak intensity. The optimum temperature was found to be 500°C. A similar effect was also observed on CeO_2 prepared from cerium nitrate. The films obtained from the chloride solution showed large grain size and important density of porosity. However, the morphology aspect of the surface, for the films prepared from the nitrate solution, was less pronounced with very small grains and no pores. In 2005, Ming Wei and Choy [155] used electrostatic spray-assisted vapour deposition (ESAVD) to deposit cerium oxide films on Si (100) and glass substrates at temperatures between 400°C and 600°C. ESAVD involves spraying atomised precursor droplets across an electric field where the droplets undergo decomposition and chemical reaction in the vapour phase near the vicinity of the heated substrate [156, 157]. Ming Wei and Choy [155] found that the orientation relationships between CeO_2 film and Si substrate were $001_{CeO2}//001_{Si}$ and $111_{CeO2}//111_{Si}$, however, no distinct alignment was observed in the CeO_2 films deposited on glass. Ming Wei et al [54] later in the same year, deposited CeO_2 by the same method on textured Ni tapes at the same temperature range. Cerium nitrate (99.9%, Aldrich) was employed as a chemical precursor, which was dissolved in an aqueous alcohol solvent (the mixture of ethanol and de-ionized water) to form a solution with a molar concentration between 0.005 and 0.05M. The deposition temperature was within the range of 400°C -600°C and the used electric potential was 5 and 20KV. The orientation relationships between CeO_2 and Ni substrate were 001_{CeO2} //001_{Ni} and 110_{CeO2} //100_{Ni}. However, the intensity of the CeO_2 peaks from the phi scan were very low; besides that, they did not mention if the deposition was made on buffered Ni or directly on Ni tapes.

Other oxide films which were deposited by spray pyrolysis include In_2O_3, ZnO and SnO_2 and others. Prince et al [140] deposited In_2O_3 using indium chloride as a precursor. They found that low precursor concentration resulted in thin and amorphous film. A linear increase in the growth rate was observed with the increase

in the precursor concentration up to certain limit then it slows down. The flow rate was found to affect the crystallinity of the produced films; a flow rate of 5l/min showed a sign of transformation from amorphous to crystalline nature and a flow rate of 15 l/min showed a well-crystallized phase with uniform surface. They also found that the smoothness, uniformity and grain size of the produced films increased with increasing the substrate temperature up to 380°C and then deteriorated. C. H. Lee and C. S. Huang [158] deposited In_2O_3 by spray pyrolysis on Si wafers using $InCl_3$-methanol solution as the source material. They found that in the lower temperature range (≤300°C) the growth rates increased with growth temperature because of the increase in reaction rates of hydrolysis of the $InC1_3$ solute molecules. They reach a maximum at about 300°C and then decreased as the temperature further increased, because of depletion of reactants owing to volume reaction. They also found that the thickness increased with increasing the concentration and that the growth rate increased with increasing the flow rate because of the greater amount of reactant participating in the deposition process. At higher flow rates the rate of increase of the growth rate was slower due to the phenomenon of reactant saturation effect. P.K. Manoj et al [159] deposited indium oxide thin films on glass substrates from precursor solution of indium chloride. They found that the preferential orientation of the film changed from (222) to (400) on increasing the temperature. They also observed a decrease in film thickness with increasing temperature due to stronger re-evaporation at higher temperatures. The same thickness dependence was also observed by Malle Krunks and Enn Mellikov [141]. They deposited ZnO films on glass substrates from $Zn(CH_3CO_2)_2.2H_2O$. This observed dependence of thickness on temperature can be explained by the diminished mass transport to the substrate at higher temperatures due to gas convection from the bath pushing the droplets of the precursor away. Additionally, the decrease in film thickness can be attributed to an increase in the rate of re-evaporation at higher temperatures. They also found that the (002) texture became more dominant at high temperatures due to the higher chemical purity of the film prepared at high temperatures where the purity of the film was controlled by the level of thermal decomposition.

Paraguay et al [114] prepared ZnO thin films by spray pyrolysis onto glass substrate from zinc acetates. They found that the surface morphology and microstructural characteristics of the films were highly dependant on deposition temperature. A critical temperature was found to be around 610K (337°C); above this

temperature, the deposition rate was constant where the growth rate was mass transport controlled; the reaction kinetics were so fast that the surface reaction finally became controlled by mass transfer of the reactants, and the concentration of the reactants on the surface was the limiting parameter. They also found that at temperatures below 610K, the deposition rate increased with increasing temperature where the deposition rate was limited by the reaction kinetics process at or near the substrate surface, and found that the growth rate was limited by surface diffusion. K. E. Elangovan et al [160] deposited thin films of fluorine-doped tin oxide (SnO_2:F) on glass by spray pyrolysis technique from an economic stannous chloride ($SnCl_2$) precursor. They revealed that the preferred orientation of the films varied with film thickness and that the deposition rate and film thickness increased linearly with increasing the concentration. E. Elangovan and K. Ramamurthi [161] deposited SnO_2 by spray pyrolysis on glass substrates from $SnCl_2$-$2H_2O$. The deposition rate increased with increasing precursor concentration and the preferred orientation was changed from (211) to (200) by increasing the concentration and thickness. G. Korotcenkov et al [162] deposited SnO_2 by spray pyrolysis on (100) Si and glass substrates. Amorphous films were obtained at low deposition temperatures (<350°C). (110) and (200) peaks were obtained between 350°C and 450°C. They also found that the texture became (200) when the film thickness increased to more than 160nm. Zaouk et al [117] deposited SnO_2 by electrostatic spray pyrolysis on glass substrates using $SnCl_4.5H_2O$ as a precursor. They found that the crystallinity of the films depends on the substrate temperature.

Gurumurugan et al [163] deposited CdO on glass substrates by spray pyrolysis from cadmium nitrate at different temperatures. They found an increase in the film thickness with increasing the temperature. J. Morales et al [164] deposited CuO on stainless steel substrates by spray pyrolysis from an aqueous copper acetate solutions at temperatures over 200°C–300°C. The heating temperature was found to have little limited effect on the particle size and thickness of the films, which, however, increased significantly by increasing deposition time.

Katherine D. et al [165] and Shigetoshi Ohshima et al [166] deposited CeO_2 films on Al_2O_3 films by PLD. They found that the surface roughness increased with increasing the film thickness and with increasing pulse frequency.

Almost no reports were found for the preparation of thin films on metallic substrates using the spray pyrolysis technique. Also no reports were found for MgO

deposition on metallic substrates by spray pyrolysis. Only one paper was found for CeO_2 deposition on textured Ni by ESAVD [54] and another one for CuO deposition on stainless steel substrates by spray pyrolysis from an aqueous copper acetate solution at temperatures over 200°C–300°C [164].

ISD deposition using e-beam evaporation was found to be beneficial to deposit biaxially textured MgO films on polycrystalline substrates. This is important for the subsequent deposition of high J_c YBCO superconducting films as seen from the survey in section 2.6. However, there are no reports for the deposition of MgO by ISD using spray pyrolysis; except Pavlopoulos [147] who deposited MgO on Si (100) substrates, using 0.078M of magnesium nitrate as a precursor at 650°C at different inclination angle (10°, 25° and 45°). He found that the lowest FWHM for the out-plane-texture was for the film deposited at zero inclination angle and that the thickness decreased with increasing the inclination angle. The roughness decreased up to 25° then increased with increasing the inclination angle to 45°.

Different deposition variables and their effects on the deposition of different films are summarised in Table 2.5.

Table 2.5: Summary of different spray pyrolysis deposition variables and their effects on the deposition of different films.

Thin film material	Precursor	Substrate temperature °C	Substrate material	Carrier gas	Effects
MgO [65]	0.5M magnesium acetate in water	580 -680	(100) Si	Filtered air	Deposition rate decreased with increasing temperature; due to gas convection from the substrate pushing the droplets of the precursors away, and film density increased with increasing temperature due to the higher diffusion energy. Also the texture improved with increasing the temperature. The film morphology was changed from island growth and rough film surfaces to a smoother and layered one by increasing the temperature from 580°C to 680°C.
MgO [72]	magnesium acetate in ethylene glycol monomethyl ether	380-600	(100) Si	Pure O_2 2.5-3.5 l/min.	Texture was found to improve with increasing the substrate temperature; however the surface roughness was increased (2.65nm at 380°C and 11.8nm at 600°C).

					Low flow rates of O_2 resulted in textured MgO films and the high flow rates resulted in polycrystalline films.
MgO [142]	magnesium acetylacetonate in isopropanol	300-550	Poly-crystalline Al_2O_3	Nitrogen gas	The texture of the MgO films was found to develop with thickness, where no preferred orientation was observed in the first crystallite layer. The films with high degree of (200) preferred orientation show smooth surfaces and reduced number of cracks. The film thickness and roughness were found to increase with increasing the substrate temperature. RMS roughness of about 150nm was obtained at a deposition temperature of 500°C.
MgO [143]	magnesium acetylacetonate i.e. $Mg(CH_3COCHCOCH_3)_3$	400-550	(100) Si, sapphire and fused silica	O_2	MgO films deposited on sapphire crystallized with a strong (100) orientation after annealing at 700°C and 930°C in flowing oxygen. On the other hand, MgO films on Si and fused silica developed cracks after the annealing process. The films prepared outside the range

					of 400°C -550°C had a slight roughness in appearance.
MgO [67]	$Mg(NO)_3.6H_2O$ in water-ethanol solution	300-350	Al_2O_3 and glass	Ar gas (40 ml/min.)	Dense polycrystalline films were produced on alumina and those produced on glass exhibited fine grain structure.
MgO [146]	magnesium acetate in water	400	Glass	Air	Flow rate of carrier gas was found to affect the texture of the produced films in terms of the preferred orientation; a low deposition rate resulted in (200) oriented films and high deposition rates resulted in (111) oriented films. The texture was also found to develop with increasing thickness. The film roughness was found to decrease with increasing film thickness; for a (200) oriented film, the roughness was about 9nm for a film thickness 80nm and 6.3nm for a film thickness of 250nm.
MgO [147,	$Mg(NO)_3.6H_2O$ in water	650	(100) Si	Ar gas	The thickness of the films increased linearly with the

149]					deposition time while the roughness increased. The films deposited at 650°C from 0.078M solution resulted in RMS value of about 20-25nm for a deposition time of 32 minutes and 40-45nm for a deposition time of 64 minutes. They also found that inclined substrate deposition (ISD) resulted in thinner films when increasing the inclination angle.
ZnO [141]	Zinc acetates i.e. $Zn(CH_3CO_2).2H_2O$ in mixture of distilled water and isopropyl	200-425	Glass	Compressed air	Deposition rate decreased with increasing temperature due increased rate of re-evaporation. The (002) texture became more dominant at high temperatures. The film thickness was found to decrease with increasing the substrate temperature.
CeO_2 [147, 148, 153]	Cerium nitrates i.e. $Ce(NO_3)_3.6H_2O$ in water	200-600	Borosilicate glass	Ar gas 3 and 10 l/min.	Low flow rates resulted in (111) oriented films in the temperature range 325°C-450°C. (200) oriented films were obtained when using high flow rates in the

					temperature range 450°C-550°C. In the temperature range between 250°C-450°C, the thickness increased almost linearly with temperature. In the temperature range between 450°C-550°C, the thickness slightly decreased with increasing temperature. The thickness was also found to increase with increasing the precursor concentration and the texture improved with increasing thickness and temperature. The texture was found to improve with increasing the temperature but on the expense of roughness. The thickness was found to increase with temperature up to 450°C then decreased. The thickness of the film increased with increasing the precursor concentration.
CeO_2 [150-152]	Cerium acetylacetonate i.e. $Ce(CH_3COCHCOCH_3)_3$ in a 50% ethanol / water	450	(100) Si	Compressed air	Appropriate control of the ratio of pulse time to interval time was necessary for obtaining high texture quality and greater crystallite size cerium (IV) oxide thin films. The crystallite size was found to decrease with increasing the ratio of pulse time to interval time. At large ratios, the

					generation reaction rate was high and the rate of nuclei formation exceeded that of the growth of nucleation. While at low ratios, the growth rate of nucleation predominated and hence the increase of crystallite sizes predominated. Therefore, short pulse time and relative long pulse-interval time could provide enough time to grow smooth and high density films.
CeO_2 [62]	$Ce(NO_3)_3.6H_2O$ in 50% water-ethanol mixture	350-500	Fused silica	-	The best uniform ceria films with nanometric scale grains (20nm) were prepared at a substrate temperature of 400°C with 0.5 h annealing of the deposit at 500°C. At lower spraying temperatures large CeO_2 crystallites have been observed on the film surface along with the fine grains. When the substrate temperature exceeded 400°C, numerous cracks caused by thermal stresses appeared in the films.
CeO_2 [63]	$Ce(NO_3)_3.6H_2O$, $CeCl_3.7H_2O$, in ethylene glycol	350-500	B-quartz	-	The deposited films were polycrystalline except the ones deposited from ethylene glycol solution of $Ce(NO_3)_3$ which show a preferred orientation along the [100] direction. The relatively poor XRD patterns of some of

					the films (produced at higher substrate temperature) were due to the rather small thickness of the films. The roughness increased with the increase in film thickness. Also the higher substrate temperature led to higher rate of evaporation and accordingly, to higher supersaturation and bigger number and smaller size of the crystals formed. For a substrate temperature of 350°C-500°C, the crystallite size was in the range of 10-60nm.
CeO_2 [154]	cerium chloride, cerium nitrate	300-500	Glass	Air	When using magnesium chloride, the films were amorphous at 300°C. As the substrate temperature was increased, the films became more crystalline as indicated by the increase of the (200) peak intensity. A similar effect was also observed on CeO_2 prepared from cerium nitrate. The films obtained from the chloride solution showed large grain size and important density of porosity. However, the morphology aspect of the surface, for the films prepared from the nitrate solution, was less pronounced with very small grains and no pores.

CeO_2 [155]	Cerium nitrate in a mixture of methanol and de-ionised water	400-600	(100) Si, glass and Ni tapes	-	The orientation relationships between CeO_2 film and Si substrate were $001_{CeO2}//001_{Si}$ and $111_{CeO2}//111_{Si}$, however, no distinct alignment was observed in the CeO_2 films deposited on glass. The orientation relationships between CeO_2 and Ni substrate were 001_{CeO2} //001_{Ni} and 110_{CeO2} //100_{Ni}. However, the intensity of the CeO_2 peaks from the phi scan were very low, besides that, they did not mention if the deposition was made on buffered Ni or directly on Ni tapes.
In_2O_3 [140]	Indium chloride in ethanol-water mixture	300-500	Glass	Air	They found that low precursor concentration resulted in thin and amorphous film. A linear increase in the growth rate was observed with the increase in the precursor concentration up to certain limit then it slows down. The flow rate was found to affect the crystallinity of the produced films; a flow rate of 15 l/min showed a well-crystallized phase with uniform surface. They also found that the smoothness, uniformity and grain size of the produced films increased with increasing the substrate temperature up to 380°C and then deteriorates.

In_2O_3 [158]	$InCl_3$ in methanol	200-375	Oxidised (100) Si wafers	-	In the lower temperature range (≤300°C) the growth rates increased with growth temperature because of the increase in reaction rates of hydrolysis of the $InC1_3$ solute molecules. They reach a maximum at about 300°C and then decreased as the temperature further increased. The thickness increased with increasing the concentration and that the growth rate increased with increasing the flow rate because of the greater amount of reactant participating in the deposition process. At higher flow rates the rate of increase of the growth rate was slower due to the phenomenon of reactant saturation effect.
In_2O_3 [159]	Indium chloride in ethanol-distilled water	425	Glass	Compressed air	The preferential orientation of the film changed from (222) to (400) by increasing the temperature. They also observed a decrease in film thickness with increasing temperature due to stronger re-evaporation at higher temperatures.
ZnO [114]	Zinc acetates in water	207-437	Glass	Air	The surface morphology and microstructural characteristics of the films were highly dependant on

					deposition temperature. A critical temperature was found to be around 610K (337°C).
SnO_2 [160]	$SnCl_2$ in HCl diluted in methanol	400	Glass	-	The preferred orientation of the films varied with film thickness and that the deposition rate and film thickness increased linearly with increasing the concentration.
SnO_2 [161]	$SnCl_2$-$2H_2O$ in HCl diluted in methanol	400	Glass	-	The deposition rate increased with increasing precursor concentration and the preferred orientation changed from (211) to (200) by increasing the concentration and thickness.
SnO_2 [162]	$SnCl_4$-$5H_2O$ in alcohol	400-900	(100) Si	-	Amorphous films were obtained at low deposition temperatures (<350°C). A (110) and (200) peaks were obtained between 350°C and 450°C. They also found that the texture became (200) when the film thickness increased to more than 160nm.
CdO [163]	Cadmium nitrate in alcohol	450-550	Glass	-	Film thickness increased with increasing temperature.
CuO [164]	$Cu(CH_3COO)_2$	200-300	Stainless steel	Air	The heating temperature was found to have little limited effect on the particle size and thickness of the films, which, however, increased significantly by increasing

					deposition time (from 30 to 60 minutes). However, for the deposition time of 30 minutes, the thickness was found to increase with decreasing the deposition temperature. Besides that, the films obtained with a deposition time of 30 minutes were rougher than those obtained with a deposition time of 60 minutes.

2.6 ISD deposition of MgO using e-beam evaporation

The basic requirements of a buffer layer are to be biaxially textured with suitable lattice parameters and non reactive with a HTS layer [167]. Moreover, biaxially textured MgO can be grown on non-textured metallic tapes by the inclined-substrate-deposition (ISD) technique [41, 168] using e-beam evaporation [168-171] for the fabrication of coated superconductor wires [172]. By this method, the MgO (200) is grown with the c-axis being tilted from the substrate normal due to the shadowing effect [173-175]. The deposited YBCO film on top of that MgO also grows with the (00l) being tilted from the substrate normal, which has led to low J_c values. Higher J_c and T_c values are obtained by growing untilted YBCO films by depositing YSZ and CeO_2 buffers on top of the tilted MgO film [169, 176, 177]. The biaxial texture is achieved by many techniques (2.1.4.1) and for MgO it is achieved mainly by the inclined substrate deposition (ISD). It was first reported by K. Hasegawa et al [49, 167, 178] in 1996 to deposit biaxially aligned YSZ films on untextured Hastelloy (Ni base alloy) tapes; by using an off-axis pulsed laser ablation, ISD led to in-plane alignment of YSZ films. Later on, in 1999, Bauer et al [179] grew biaxially aligned MgO buffer on Hastelloy C276 from a sintered MgO target using e-beam evaporation. In 2000, M.P. Chudzik et al [180] from the Argonne National Laboratory succeeded in depositing biaxially textured MgO on continuously moving Hastelloy C tapes by e-beam evaporation and found that the texture improved by increasing the inclination angle.

Therefore, e-beam evaporation can be used to deposit MgO by the inclined substrate deposition [173, 174]. By this method, the MgO (200) is grown with the c-axis being tilted from the substrate normal due to the shadowing effect as can be seen from the schematic diagram in Figure 2.29 [173-175, 180, 181]. The deposited YBCO film on top of that MgO also grows with the (005) being tilted from the substrate normal, which led to low J_c values. M. Bauer et al [179] found that for the tilted YBCO films, the current can flow in two different directions i.e. in the a-b plane (in-plane) and along the c-axis which resulted in lower J_c values. Higher J_c and T_c values were obtained by growing untilted YBCO films by depositing YSZ and CeO_2 buffers on top of the tilted MgO film [169, 176, 177].

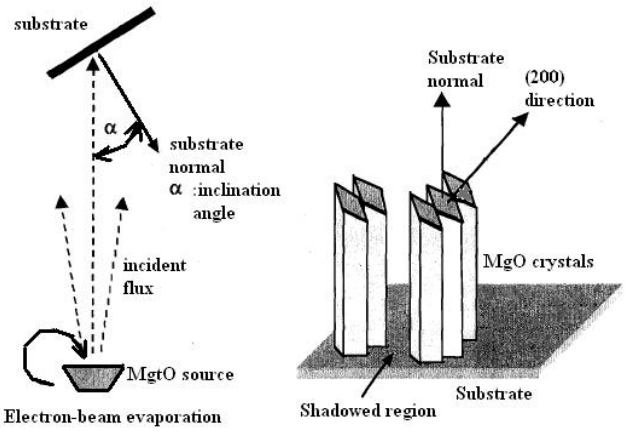

Figure 2.29: Schematic diagram showing the principle of ISD deposition (left) and schematic diagram showing the growth of crystals truncated by (200) planes (right) [175].

Ralf Metzger et al [173] deposited biaxially textured MgO, as a buffer material, on Hastelloy C276 by the inclined substrate deposition using e-beam evaporation. Starting from numerous single crystalline nuclei with random orientation, each nucleus grew by epitaxial alignment of MgO from the vapour phase. The inclined direction of incidence of the arriving vapour caused some orientations to grow faster in height than others. The taller columns can shadow some of their smaller neighbours resulting in the extinction of the latter. Therefore, MgO (200) grew tilted with respect to the substrate normal. M.P. Chudzik et al [175] found that the texturing of MgO, deposited on metal foils, was a selective growth process where the texture improved with increasing film thickness and with increasing the inclination angle. They found that the creation of biaxial texture in the MgO film was due to the combined effect of the cubic equilibrium crystal habit of MgO and columnar self-shadowing. The columns grew nominally parallel to the substrate normal despite the highly inclined angle of the atomic flux. The top of such columns were truncated by (200) planes. Beihai Ma. et al [39, 41, 50, 169, 171, 177, 182, 183] deposited MgO by ISD on Hastelloy C276 with e-beam evaporation. The ISD MgO films revealed a roof tile structure and the in-plane texture of the MgO film improved with increasing thickness and the films became smoother with increasing the thickness. Yttria-stabilised zirconia (YSZ) buffer layer, ceria cap layer and YBCO films were subsequently deposited on the ISD-MgO-buffered metallic substrates by PLD. The MgO (200) was tilted with respect to the substrate normal. However the YBCO films were biaxially textured with the c-axis parallel to the substrate normal. A sharp T_c of 91K was obtained. In another study, they found that further improvement in the MgO texture

and a decrease in surface roughness were obtained by depositing a homoepitaxial MgO layer on the ISD MgO layer at elevated temperature and flat angle. The same group also found that the type of buffer on top of the ISD MgO films affected the texture of the deposited YBCO films. The use of $SrTiO_3$ (STO) as a buffer layer on top of the ISD MgO resulted in epitaxial growth of YBCO films with the c-axis tilted with respect to the substrate normal. The deposition of YBCO directly on the ISD-MgO resulted also in the growth of YBCO with the c-axis tilted from the substrate normal. However, when using YSZ and CeO_2 instead of STO, a c-axis untilted YBCO films were obtained. They revealed that CeO_2 controls the orientation of the YBCO films grown on ISD-MgO buffered metal substrates. They also found that there was an optimal CeO_2 thickness (10 nm), above and below that thickness, the YBCO texture was bad. Similar dependence of the YBCO texture on the CeO_2 thickness was found by Méchin et al [95]. Develos et al [165] found that the surface morphology of CeO_2 was changed by changing the thickness. Shi et al [184] found that the CeO_2 growth mode changed on changing the deposition temperature and thickness i.e. the growth mode was layer-by-layer at 790°C (up to a thickness of 100nm) which gave smooth surfaces and island growth was experienced at 775°C and 805°C (by a thickness of 100nm) and layer-by-layer (up to a thickness of 10nm).

Y Xu et al [174] deposited MgO templates on Hastelloy C276, buffered with YSZ, in an electron beam (e-beam) evaporation system by inclined substrate deposition. The MgO in-plane texture was formed by the preferred growth direction of [11n] // substrate normal and one of the MgO {200} planes rotated to the in-flux direction. They found that the texture evolved faster and the films were thinner and rougher, due to the formation of voids and loose structure, at high inclination angles compared to that at lower inclination angles. They also found that the texture improved with thickness and with increasing the inclination angle.

Rachel E. Koritala et al [185] deposited biaxially textured MgO films by ISD using e-beam evaporation on Hastelloy C substrates. They found that the roughness increased with increasing thickness. High roughness values were also obtained at low and high inclination angles and the lowest roughness values were obtained for inclination angles of 20°-55° where the roughness was not affected by the inclination angle in this range.

In 2002, Balachandran et al [53] grew biaxially textured MgO films by inclined substrate deposition (ISD), with electron beam evaporation, at deposition rates of

20-100 Å/s on Hastelloy C276. The substrate inclination angle was varied between 10° to 70°. Columnar grain structures with roof-tile-shaped surfaces were observed for the films deposited at room temperature with an inclination angle of 55°. The films exhibited good biaxial texture. In the same year, Ma et al [40, 50] deposited MgO by the same method. In order to reduce the surface roughness, a thin layer of MgO was deposited at 0°. They noticed the same columnar grain structure with MgO being biaxially textured. Therefore, MgO deposited by ISD is an excellent candidate for fabrication of high-quality YBCO coated conductors.

2.7 MgO deposition on Si substrates by PLD

Atsushi Masuda et al [186] deposited [100] oriented MgO buffer layers by pulsed laser deposition on (100) Si substrates using ceramic MgO pellets as the target. They used an ArF excimer laser operating at wavelength of 193nm for which the optical absorption coefficient is high in MgO. The fluence used was 7 J/cm^2 and the deposition temperature ranged from 550°C-800°C under 0.13 mbar (~0.1 torr) and 1x10^{-7} mbar (7.5x10^{-8} torr) O_2. (200) oriented films were obtained under 0.13 mbar and amorphous films were obtained under high vacuum (1x10^{-7} mbar or 7.5x10^{-8} torr). X. Li et al [187] deposited MgO on Si (100) substrates by PLD, using an energy fluence of 4 J/cm^2, from Mg and MgO targets. High vacuum (5x10^{-6} torr) resulted in amorphous MgO films when using the MgO target, however, Mg targets resulted in (100) textured MgO films under same sort of vacuum and the strongest MgO peak was obtained at 650°C. This difference was attributed to different nucleation processes for the MgO crystals when using different targets; when the Mg atoms were offered to the substrate surface by using a Mg target, the migration of Mg atoms and the reaction of Mg with O_2 on the substrate surface promote the growth of MgO at the desired orientation more effectively than when a MgO target was used. Other researchers deposited MgO films on different substrates using Mg targets under different conditions [188-190].

2.8 MgO surface optimization for $YBa_2Cu_3O_7$ (YBCO) thin film growth and YBCO defects

High temperature annealing was reported to form steps on the MgO substrate surfaces which favour YBCO deposition by pulsed laser deposition. It was also found that the annealing controls the production of in-plane orientation of c-axis YBCO

films. However, in some cases, YBCO films sputtered on annealed MgO substrates were found to contain a high density of 45° misoriented grains [191-193].

B. H. Moeckly et al [193] found that annealing of MgO substrates in air or oxygen to 1100°C-1200°C for 12-24 hours resulted in the formation of a high density of atomic steps on the substrate surface, and subsequently the deposited YBCO films were biaxially textured. M. Grant et al [192] annealed (001) MgO substrates in air at 1350°C for 10 minutes to form a series of steps on the surface. They found that the steps form as a result of lowering the total free energy of the system. Degardin et al [191] studied the effect of annealing temperature, time and atmosphere on MgO morphology. The annealing was made at 900°C-1100°C for times of 2-10hrs using air and pure oxygen. They found that the surface morphology depends on the annealing conditions. The optimal annealing condition for MgO in terms of the quality of the deposited YBCO films was to use 1000°C for 5hrs under pure oxygen where they found that substrate surface reconstruction occurs at this temperature. This resulted in (001)-oriented terraces bounded by (100)-oriented steps on the MgO surfaces. The deposited YBCO films exhibited 0° misorientation and high J_c (0.75×10^6 A/cm^2) compared to the un-annealed samples (0.01×10^6 A/cm^2) and to the samples annealed under other conditions (0.2 to $< 0.75 \times 10^6$ A/cm^2).

It is known that MgO is hygroscopic [194]. Simulations made by Walter Langel and Michele Parrinello [195] revealed that the dissociation of water could proceed very quickly on MgO stepped surfaces. Thus, the formation of hydroxyl groups or magnesium carbonates after exposure of MgO to air may reduce the quality of subsequently deposited films [191, 196]. B. I. Kim et al [196] found that high-temperature annealing (1000°C) in dry oxygen removed carbon contamination from degraded MgO substrates stored in moist air for several days.

The effect of storage and humidity on the produced films was studied by Balkenende et al [116]. They found that MgO layers, deposited by spray pyrolysis using magnesium acetates as a precursor, were easily degraded by air while in storage. This is caused by the reaction of magnesium oxide with water and carbon dioxide in air and form a surface layer of magnesium carbonate and magnesium hydroxide. However, heating the contaminated layer briefly at a temperature of 450°C in air was sufficient to regenerate the MgO surface [116].

J Du et al [197, 198] found that MgO substrates, after weeks of exposure to laboratory environment, were degraded by the formation of hydroxyl groups,

carbonates and other possible carbon compounds. YBCO films grown on these contaminated or degraded MgO substrates showed an increased degree of 45° in-plane grain misorientation, which reduces the film critical current density from $3x10^6$ A/cm^2 (for a fresh MgO substrate) to $0.005x10^6$ A/cm^2. The effect of annealing at 760°C in mixed 1:15 oxygen : argon gas at pressure of 50 Pa was studied by XPS. The main O 1s peak at 529.5 eV is due to the original substrate MgO oxygen atoms and the shoulder at a higher binding energy (HBE) in the range 531–532 eV is due to oxygen of other oxygen-bearing compounds. It is well established in the literature that hydroxylation of MgO (i.e formation of ($Mg(OH)_2$) causes the O 1s core level to shift to a higher binding energy by about 2.2 eV or sometimes 3eV [199-201]. J Du et al found that annealing improved the surface quality by removing many contaminants, mostly hydroxides $Mg(OH)_2$ and carbonates $MgCO_3$. Subsequent YBCO films grown on MgO with this pre-treatment showed perfect grain alignment and high critical current densities ($2.4x10^6$ A/cm^2). Fares Khairallah and Antonella Glisente [202] used XPS to characterize nanoscale magnesium oxide. O 1s and Mg 2P were used to differentiate between MgO and $Mg(OH)_2$. Mg 2P is used to confirm the presence of Mg as an oxide or hydroxide which occurs at 49.3-49.5eV. The O 1s reveals the presence of Mg and confirms if present as MgO (529.6-529.8eV) or as hydroxide i.e. as $Mg(OH)_2$ (531.1-531.3eV). Similar results were found by others [201, 203, 204].

Defects in YBCO films have a great influence on the superconducting properties and on the surface smoothness and some of them will be mentioned here. Grain boundary misorientation was found to affect the superconducting properties. D. T. Verebelyi et al and Z. G. Ivanov [205, 206] found that the critical current density reduced exponentially with increasing the misorientation angle beyond 4° (~ $4x10^6$ A/cm^2) up to 40° (~ $1x10^2$ A/cm^2). The dependence of the critical current density on the misorientation angle was also found by others [197, 198, 207].

T.J. Jackson et al [208] deposited YBCO films on STO (001) substrates by pulsed laser deposition. They found that the films frequently exhibited holes which were correlated with the incidence of epitaxial yttria (Y_2O_3) precipitates within the film and with suppression of twining of YBCO films. All the films have a superconducting transition onset temperature of about 90K. The films with holes, which are as deep as the film thickness, have wide transition temperatures of about 7K, while films with shallow holes have transition widths less than 1K. They also found that it is still unclear why a minority of films prepared under apparently

identical conditions can be obtained without holes and precipitates. R. Krupke et al [209] related the formation of holes in YBCO film deposited on $LaAlO_3$ (LAO) to Y_2O_3 as well. The formation of such Y_2O_3 inclusions was also observed by others [210, 211]. However, Develos et al [212] related the formation of the pores in YBCO films deposited on LAO substrates to yttrium rich composition (BaY_2O_4). This off-stoichiometry in the composition of the films was attributed to the scattering of the ablated species with the oxygen ambient. They found that nucleation and enlargement of the barium yttrium oxide phase obstructs the YBCO growth and eventually caused pore formation.

The effect of film thickness on the critical current density of YBCO films on CeO_2/YSZ/CeO_2 buffered rolling assisted biaxially textured Ni substrates was studied by K. J. Leonard et al [213]. They found that the critical current density decreased with increasing the film thickness (~ $2.5x10^6$ A/cm^2 for a film thickness of ~ 0.2µm and ~ $0.5x10^6$ A/cm^2 for a film thickness of ~ 3µm), due to the formation of more randomly oriented grains in the upper portion of the YBCO film surface, resulting in less cube texture. In addition, an increase in mismatch across the boundaries of the c-axis grains with increasing time during deposition, along with the development of $BaCeO_3$ and Y_2BaCuO_5 phases at the YBCO/CeO_2 buffer interface, contributed to the degradation of film properties where misoriented YBCO growth occurs above such phases.

MgO deposition by PLD requires high vacuum and high fluence. PLD and other depositing techniques are considered relatively expensive compared to spray pyrolysis. Therefore, in sections 2.5-2.7, a literature survey was made in an attempt to put the main key factors in depositing MgO and other films by spray pyrolysis and by other deposition techniques available for the reader. The effect of the main depositing variables on the properties of the produced films was mentioned. However, it is to be mentioned that not many reports were found for MgO deposition by spray pyrolysis.

It was found that, for MgO deposition by spray pyrolysis on different ceramic substrates from different precursors, the substrate temperature affects texture evolution and surface morphology of the deposited films and that the properties of films depend on the used substrate. The texture of films was found to develop with thickness and that the thickness either increased or decreased with increasing temperature but increased with increasing the deposition time. The texture was also found to improve with increasing precursor concentration; however, it was found in

some reports that there is a concentration limit above and below which the texture deteriorates. Flow rate was found to affect the preferred orientation for MgO and other films. For MgO films deposited by other techniques it was found that the films grew with (100) orientation irrespective of the substrate temperature but the texture was found to improve and the roughness deteriorates with increasing temperature. However, no reports were found for MgO deposition on metallic substrates; consequently, the effects of different depositing variables need to be investigated. In addition, no reports were found for YBCO deposition on top of the spray pyrolysed MgO to evaluate its performance.

For other films deposited by spray pyrolysis it was found that the thickness increased and the texture improved with increasing precursor concentration and increasing temperature. Others found that amorphous films were obtained at low temperature and low thicknesses. It was found that pulse time to interval time affects the quality of the texture. Flow rate was found to affect the crystallinity of the produced films. Smoothness, uniformity and grain size of the produced films were found to increase with increasing the substrate temperature up to certain temperature and then deteriorate. Film properties were found to change by changing the substrate or precursor even when using the same deposition conditions. The film thickness was found to decrease with increasing temperature. However, others found that the temperature have limited effect on the thickness.

ISD deposition of MgO was done mainly by e-beam evaporation to deposit biaxially textured MgO films on polycrystalline Hastelloy C276 substrates. This is important for the subsequent deposition of high J_c YBCO superconducting films. By this method, the MgO (200) is grown with the c-axis being tilted from the substrate normal due to the shadowing effect and this led to YBCO films with low J_c and T_c values. Texture was found to improve with increasing thickness and with increasing inclination angle. However, no reports were found for MgO deposition by ISD using spray pyrolysis.

Annealing of the MgO substrates was found to be beneficial to control the in-plane texture of the subsequent YBCO films by the formation of atomic steps on the surface which lowers the total free energy of the system. This approach was not found in the literature for MgO films deposited by spray pyrolysis.

3 Experimental details

3.1 The spray pyrolysis unit

The spray pyrolysis system consists of an ultrasonic nebulizer, to atomize the chemical solution, and a reactor where the chemical reactions and the deposition process take place.

The nebuliser (OMRON model NE-U17 with ultrasonic frequency of 1.7 MHz) transmits the energy of ultrasonic vibration from the vibrator into the chemical solution through the water in the water tank. This results in the emission of the chemical solution from the cup as a dispersed aerosol, solid or liquid particles suspended in a gas [110], (Figure 3.1). Argon gas was used to carry the nebulised solution onto the heated substrate. The quantity of the chemical solution that can be used is up to 150 ml, the amount of water in the water tank is 375 ml, the nebulisation rate is 0-3 ml/min and the size of the produced aerosol particles is 4.4 μm mass median aerodynamic diameter (MMAD) according to the nebuliser specifications based on cascade impaction particle size measurements method according to BS EN 13544-1:2001.

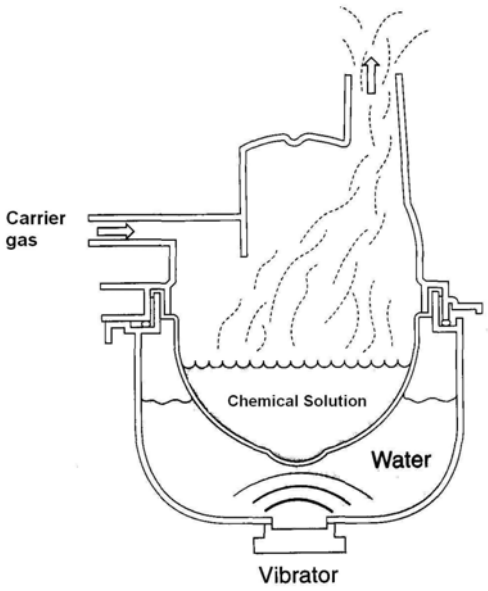

Figure 3.1: Schematic of the ultrasonic nebuliser [214].

The pyrolysis reactor used during this work was built by Pavlopoulos. D. [147] for the purpose of controlling the temperature of the substrate. In this system, the substrate was attached to a stainless steel holder which was positioned in the middle of a tubular furnace; where the temperature was highest. Two K-type thermocouples were used to measure the temperature. The first one was placed behind the substrate,

which is going to represent the deposition temperature in this work, i.e., the substrate temperature, and the other one was placed in the mid-height of the furnace close to the wall. The nozzle diameter was 1 cm and the substrate to nozzle distance (SND) was fixed at 7 cm. Figure 3.2 and Figure 3.3 show a schematic and an image of the used spray pyrolysis system, respectively.

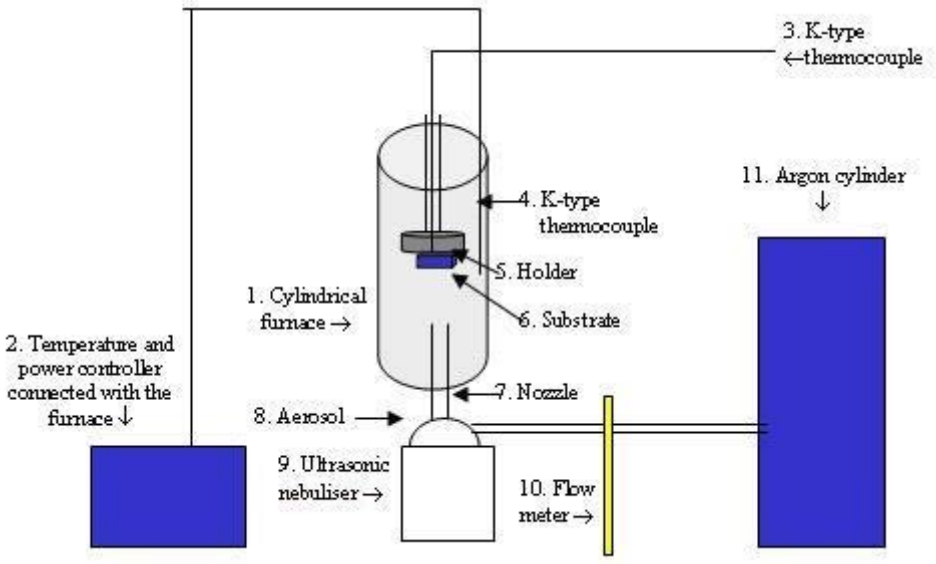

Figure 3.2: Schematic of the spray pyrolysis reactor [147].

Figure 3.3: A photograph of the spray pyrolysis system showing, from left to right, the gas flow meter, the thermocouple, the temperature controller, the tubular furnace and the ultrasonic nebuliser.

MgO deposited by inclined substrate deposition (ISD) using e-beam evaporation was found to be an excellent candidate for fabrication of high-quality YBCO coated conductors (section 2.5). Therefore, ISD was investigated using spray pyrolysis as no reports were found addressing this issue. Inclined substrate deposition (ISD) was made by inclining the substrate relative to the aerosol flow as can be seen in Figure 3.4.

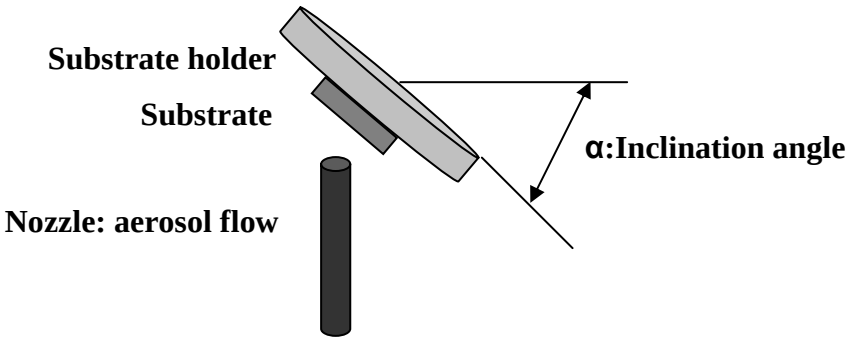

Figure 3.4: Schematic of the ISD setup.

During the spray pyrolysis deposition process, the temperature of the holder was observed to drop by 10°C-30°C. Therefore, the ratio of pulse time to interval time was set at 1 to 7, i.e. 15 seconds deposition after which the gas flow was turned off; 105 seconds needed for the heater to stabilise to the set temperature. This process was repeated for any required period of time. The furnace was then turned off and the sample was left to be furnace cooled down to room temperature. The parameters which were fixed for all of the depositions during this work are summarised in Table 3.1 while Table 3.2 lists the examined parameters.

Table 3.1: Deposition parameters that are kept fixed during deposition.

Deposition parameter	Deposition conditions
Argon flow rate	5,10 and 15 l/min
Pulse time	15 seconds
Interval time	105seconds
Substrate-nozzle distance	7 cm
Nozzle diameter	1 cm
Precursor solvent	Distilled water
Cooling of samples	Furnace cool in atmosphere
Heating rate	3°C/min.

Table 3.2: The examined deposition parameters.

Substrate temperature	Type of the substrate
Type of the precursor (nitrate, acetate)	Substrate inclination angle
Concentration of solution	Deposition time

3.1.1 The deposition substrates

MgO was deposited on different substrates i.e. on (100) oriented Si single crystal wafers (10mm X 10mm X 340µm), on Ni- 5at%W (10mm X 10mm X 100µm) rolling assisted biaxially textured substrates (RABiTS) and on polycrystalline technical substrates which include wrought 310-austenitic stainless steel and Hastelloy C276 (10mm X 10mm X 2mm). The RABiTS and the technical substrates were mechanically polished down to a roughness of about 2-5nm.

Substrates were cleaned using acetone (CH_3COCH_3), then ethanol (CH_3CH_2OH), in an ultrasonic bath for a period of 10 min each. They were then dried with Argon gas.

3.1.2 MgO film deposition

The MgO buffer or template layer was deposited by the Spray Pyrolysis technique using magnesium nitrate [$Mg(NO_3)_2.6H_2O$] or magnesium acetate [$Mg(CH_3COO)_2.4H_2O$] as precursors. The required concentrations were made by dissolving a specific amount (in grams) of each precursor in distilled water (e.g. 2 grams of each precursor were dissolved in 100ml of distilled water to give a concentration of 0.093M of magnesium acetate and 0.078M of magnesium nitrate, respectively). The decomposition temperature of the precursors was measured by thermogravimetrical analysis (TGA) which will be explained in section 3.3.1.

3.2 Pulsed laser deposition (PLD)

The pulsed laser deposition (PLD) was used, as a well established route to high quality films [19, 20], to deposit the superconducting $YBa_2Cu_3O_7$ (YBCO) layer on the MgO-buffered substrates. This was done to evaluate the MgO performance as a buffer, although spray pyrolysis of the YBCO layer should also be a possibility in the

future [24, 25, 69, 174, 175]. CeO_2 was also deposited by PLD on top of the MgO-buffered substrates in an attempt to improve the in-plane texture of YBCO.

For YBCO deposition by PLD (using YBCO target with 99.9% purity bought from PI-KEM), an excimer laser (Lambda Physik, LPX 300) with a wavelength of 248 nm was used. The laser was focused on a rotating YBCO target with a raster movement at an energy density of 2 and 2.75 J/cm^2 (the energy of the beam was measured inside the deposition chamber prior to each deposition and the target was ground to a smooth finish before each deposition). Substrates were mounted on a heatable sample stage with silver paste, the chamber was then evacuated, the target was then cleaned and conditioned with a 1000 laser pulses under vacuum with a shutter being positioned over the substrate. The substrate was then heated to 780°C at a rate of 20°C/min. The distance between the target and the substrates was 56 mm, and an oxygen background pressure of 450 mtorr (0.6 mbar) was employed during the deposition. 5000 pulses at pulse repetition rate of 4 Hz were employed for YBCO deposition. Cooling of the substrates was at a rate of 10°C/min under an oxygen background pressure of 525 torr (0.7 bar) which was introduced into the chamber over 8 minutes while maintaining the substrate temperature. Other deposition parameters were used as well and will be mentioned when necessary, however, 1000 pulses at pulse repetition rate of 2 Hz was employed for CeO_2 deposition. Figure 3.5 and Figure 3.6 show a schematic of the PLD system and an image of the used PLD machine, respectively.

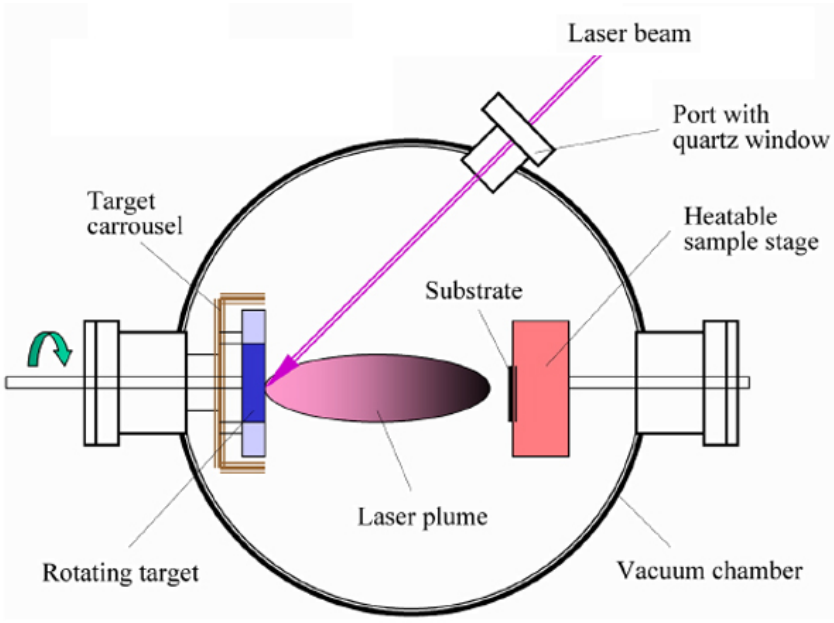

Figure 3.5: Schematic of the PLD system [215].

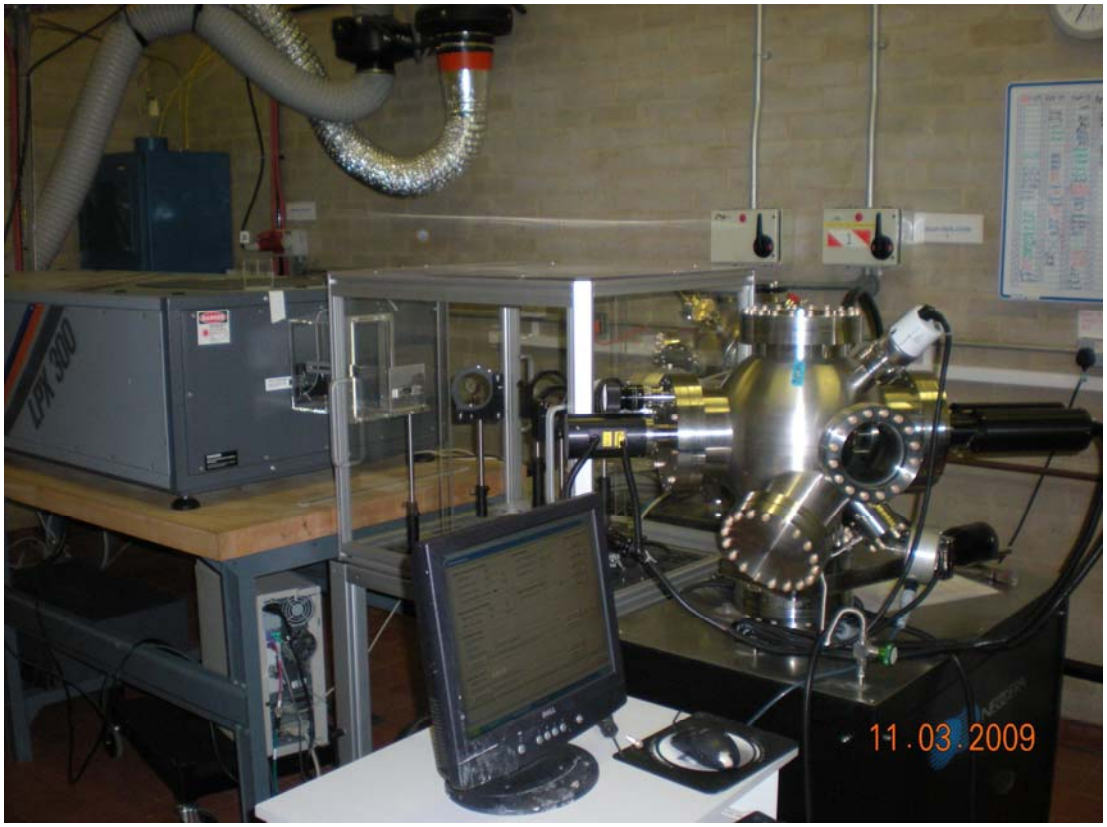

Figure 3.6: Image of the used PLD system.

3.3 Characterization techniques

The techniques used to characterise the precursors, the substrate and/or the deposited thin films are to be described briefly below.

3.3.1 Thermogravimetrical analysis

Thermogravimetrical analysis (TGA) of the decomposition of the precursors was used as a guideline temperature for the thin film deposition. This is a technique where the mass (weight) of the sample is monitored as a function of temperature or time, while the sample is subjected to a controlled temperature program [216], also it determines the extent of a reaction and detects species such as water. This technique is often sample-mass sensitive because of the necessity of the species to diffuse into and out of the bed of particles [110]. The result of a thermogravimetrical analysis test is a thermal analysis curve; its features (peaks, discontinuities, changes of slopes, etc.) are related to thermal events in the sample [217]. Therefore a final decomposition temperature of the precursor can be identified.

In this work, 7 mg of each precursor was placed in an alumina crucible. The TGA analysis was performed in 75cm^3/min flow of Argon from 25°C to 750°C at a constant heating rate of 10°C/min. using a NETZSCH apparatus model STA 449 C.

3.3.2 X-ray diffraction (XRD)

For a diffraction to occur, the Bragg law must be satisfied i.e.:

$$n\lambda = 2d\sin\theta \quad \textbf{(Eq. 3.1)}$$

where n is an integer and called the order of diffraction, λ is the wavelength of an incident monochromatic X-ray beam, d is the interplanar spacing and θ is called the Bragg angle, the angle between the incident X-ray beam and the particular crystal plane under consideration. Figure 3.7 shows a schematic of the X-ray diffractometer [218].

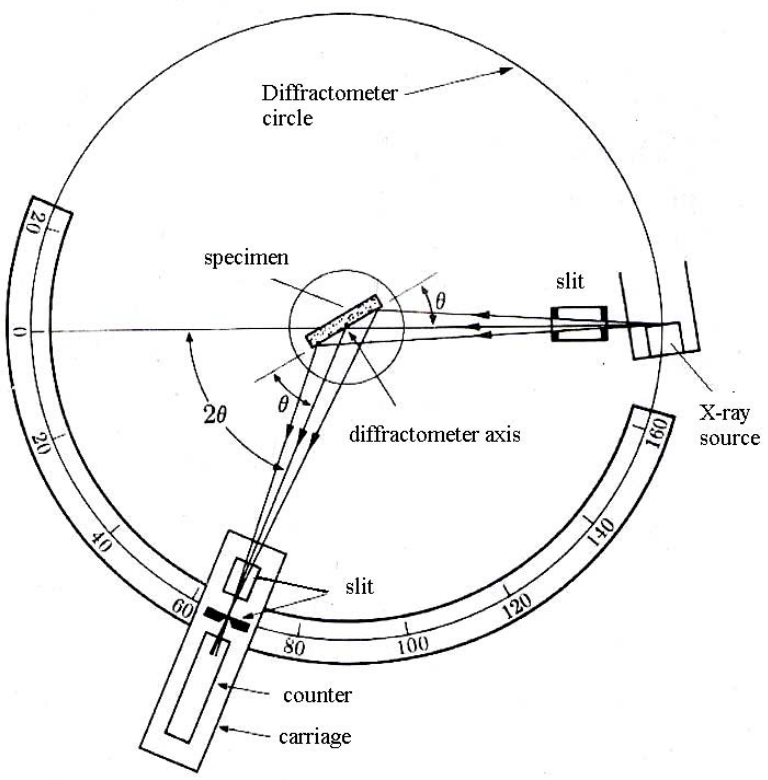

Figure 3.7: Schematic of X-ray diffractometer [218].

In θ-2θ scans, a rotation of the detector through 2θ degrees is automatically accompanied by a rotation of the sample through θ degrees [218]. In this work this was carried out using a two circle Philips machine with a monochromatic Cu Kα radiation having a wavelength of 1.54Å. Phase identification and crystal structure information can be obtained from such a scan. Moreover, qualitative information

about the out-of-plane texture can be obtained as well. However, for quantitative information, rocking curves analysis (ω scan) is required. This scan is similar to the θ-2θ scan mode but the movement of the sample and the detector is decoupled, where a sample at a position θ is rocked about the diffractometer axis within a range (θ+Δθ) (Figure 3.7) while the detector is kept fixed at the corresponding 2θ. The full width at half maximum (FWHM) can then be measured to characterise the quality of the crystal.

Qualitative in-plane and out-of-plane information can be obtained by performing a pole figure measurement scan. The pole figure is a stereographic projection, with a specified orientation relative to the specimen, that shows the variation of pole density with pole orientation for a selected set of crystal planes [218]. The pole figure is often plotted in polar coordinates consisting of the tilt and rotation angles with respect to a given crystallographic orientation. A pole figure scan is performed at a fixed θ and 2θ and consists of a series of in-plane rotation (ϕ rotation) around the center of the sample, i.e. a rotation of the sample in its own plane about an axis normal to its surface, at different tilt (ψ) angles [218, 219] as illustrated in Figure 3.8.

A 3-circle Hiltonbrooks X-ray diffractometer with Cu Kα radiation having a wavelength of 1.54Å was used for the pole figure scan measurements.

Pole figure measurements give qualitative information about the in-plane texture. For quantitative information, a phi (ϕ) scan is needed. The scan is performed by rotating the sample 360° through ϕ at a fixed (ψ, θ and 2θ) which belongs to a plane satisfying the Bragg condition. The in-plane texture quality is then evaluated by measuring the FWHM.

The rocking curve and the ϕ scans were performed using a four circle Siemens D5000 diffractometer with Cu Kα radiation having a wavelength of 1.54Å.

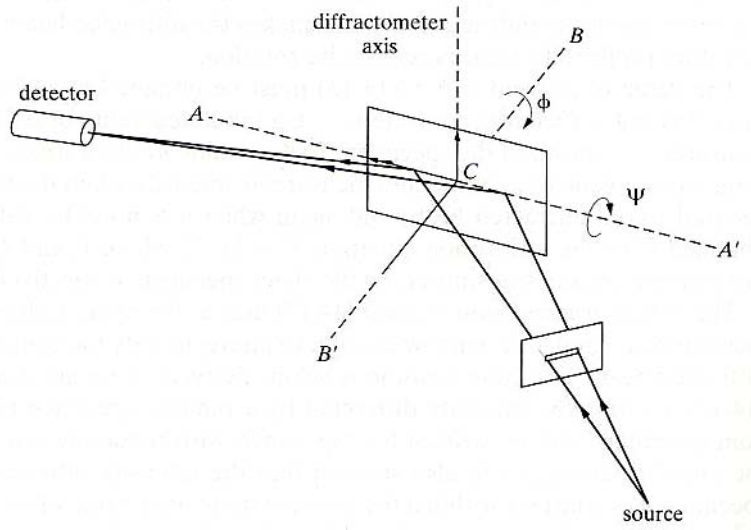

Figure 3.8: Schematic showing the ϕ and ψ rotations during pole figure measurements [218]**.**

3.3.3 Scanning electron microscopy (SEM)

Scanning electron microscopy is one of today's most important material microstructural characterization techniques. It produces images over a wide range of magnification; additionally, the variety of electron induced signals can yield a great deal of morphological, textural and chemical information about a specimen.

One of the scanning electron microscopy components is the electron gun which produces a focused beam of electrons that strikes the specimen for the production of a high resolution image, where an electrical potential is established between a negatively charged filament (cathode) and a positively charged plate (anode). This electrical potential is referred to as the accelerating voltage. The simplest and the widely used electron gun is the thermionic emission gun (conventional hairpin-shaped tungsten and fine-tipped LaB_6 filaments) where electrons are emitted from a heated filament and then accelerate towards the anode.

The image in a scanning electron microscope is improved (better resolution) by reducing the filament tip diameter. This was achieved in the field emission gun, which uses a short piece of specifically oriented, single crystal tungsten wire electrolytically etched to a very sharp tip, where the electrons are drawn by an electrical field. This results in enhanced electron emission relative to the thermionic sources.

The scanning electron microscope utilizes a focused beam of high energy electrons that systematically scans across the surface of the specimen. The interaction of the beam with the specimen produces a large number of signals at or near the specimen surface. Figure 3.9 shows the possible signals generated by the primary

electron beam-specimen interaction in the scanning electron microscope. These interactions include low energy electrons, termed secondary electrons. The low energy of secondary electrons (due to inelastic scattering and can only escape near the surface of a specimen) makes them a conveniently collected signal for scanning electron microscopy since they can be easily drawn to a positively biased detector system. The electron signal is eventually converted to an electronic signal which is portrayed on cathode ray tube (essentially a television screen) giving information about the surface structure; this also provides high resolution imaging of fine surface morphology, as the intensity of secondary electrons reaching the detector is influenced by the surface topography. The interactions also include high energy electrons termed backscattered electrons, as a result of elastic scattering, and can escape from greater depths within the sample, so giving topographical information but not as accurately resolved as for secondary electron imaging. It also provides image contrast as a function of elemental composition i.e. atomic number contrast. X-rays are generated much deeper below the sample surface and are used for chemical analysis [220-222].

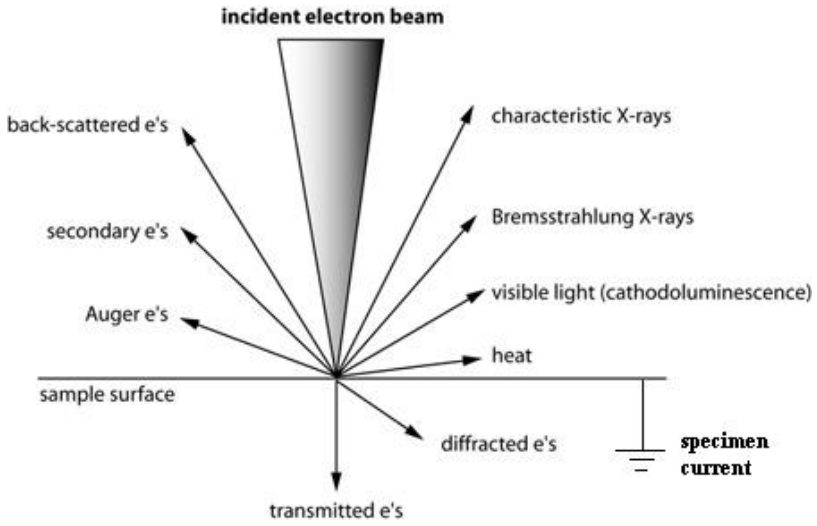

Figure 3.9: Electron beam-specimen interaction [220].

The scanning electron microscope may be facilitated by microanalytical tools which include wavelength dispersive spectroscopy (WDS) and energy dispersive spectroscopy (EDS). It may also be facilitated by the electron backscattered diffraction (EBSD) texture measurement tool. Figure 3.10 shows a JEOL JSM-7000F with a field emission gun scanning electron microscope, facilitated with EDS, WDS and EBSD, which was used during this work for high resolution images (e.g. for

thickness measurement of a thin film) and texture analysis. JEOL JSM-6060LV with a tungsten thermionic gun facilitated with EDS was also used for low magnification images and chemical microanalysis.

Figure 3.10: A JEOL 7000 scanning electron microscope.

3.3.3.1 Energy dispersive spectroscopy (EDS)

X-rays are one of the most widely used products of the electron beam-sample interaction. Analytical electron microscopy is accomplished by the coupling of an X-ray analysis device (EDS) with a scanning electron microscope. The analysis can be performed quickly and most importantly it is non-destructive to the sample [221].

The sample consists of atoms, and the atoms consists of a central nucleus surrounded by electrons lying in various shells (K, L, M,…). If an electron from an electron beam hitting the sample has sufficient kinetic energy, it can knock an electron out from the K shell, leaving the atom in an excited, high energy state. One of the outer electrons immediately falls into the vacancy in the K shell, emitting energy in the process, and the atom is once again in its normal energy state. The energy emitted is in the form of radiation of a definitive wavelength and is, in fact, characteristic K radiation. The K shell may be filled by an electron from the L or M

shells giving rise to K_α and K_β, respectively. L characteristic lines originate in a similar way [223] and so on.

The X-rays produced from the electron beam-sample interaction have energies (wavelengths) characteristic of the elements in the sample. These wavelengths are separated by the EDS on the basis of their energies by means of a Si(Li) counter and a multichannel analyzer (MCA).

When an X-ray strikes the semiconductor Si(Li) counter, electrons in the crystal each absorb a given amount of energy. The higher the energy of the X-ray, the higher the number of excited electrons. This excitation creates free electrons in the conduction band and free holes in the valence band, and if a high voltage is maintained across opposite faces of the silicon crystal, the electrons and holes will be swept to these faces, creating a small pulse in the external circuit proportional in height to the energies of the incident beam. The MCA then sorts out the various pulses heights which are then plotted as intensity vs. energy (KeV) [221, 223]. Figure 3.11 is a schematic of the energy dispersive spectrometer.

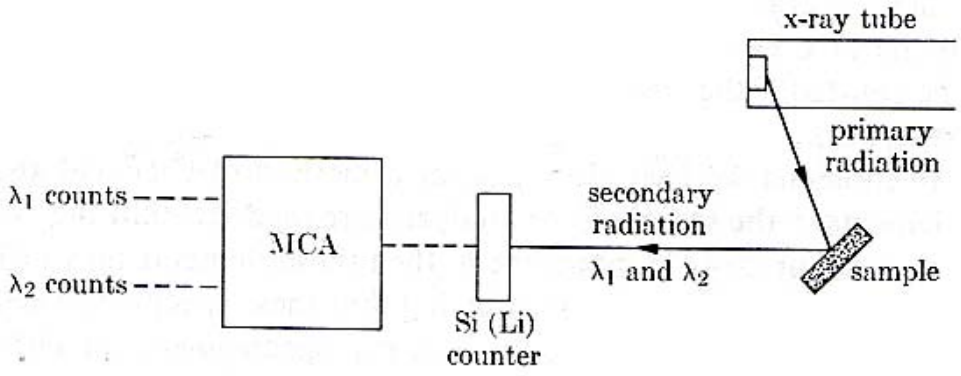

Figure 3.11: Schematic of the energy dispersive spectrometer [223].

It is to be mentioned that the EDX is a semi-quantitative measurement tool especially when dealing with light elements like magnesium and oxygen. The EDX was used in this work to give a rough indication of the amount of the elements present. Besides that, the EDX detector used was not windowless which may also affect the accuracy of the semi-quantitative measurements.

3.3.3.2 Electron backscattered diffraction (EBSD)

The ability to obtain microstructure-level information implies that the probe size formed by X-rays or electrons must be smaller than the size of the microstructural

units themselves. Therefore, this rules out X-ray diffraction as an experimental tool for microstructure measurements. Electrons are ideal for combined microstructural / crystallographic studies and TEM was the major technique used for such work. Since then, a more convenient SEM-based technique for microstructure has been developed, known as electron backscattered diffraction.

Electron Backscatter Diffraction (EBSD) is a technique which allows crystallographic information to be obtained from samples in the SEM. In EBSD a stationary electron beam of electrons is directed onto a tilted crystalline sample; a tilt of 70° from the horizontal so the angle between the incident electron beam and the specimen surface is 20° to optimise both the fraction of escaped backscattered electrons scattered from the sample and the contrast in the diffraction pattern. The electrons undergo various interactions with the atoms in the crystal lattice and some of the electrons emerge from the sample. If a fluorescent phosphor screen is placed close to the sample (Figure 3.12) a pattern is formed on the screen because the intensity of the emerging electrons varies slightly with direction. This pattern is called a diffraction pattern which is characteristic of the crystal structure and orientation of the sample region from which it was generated.

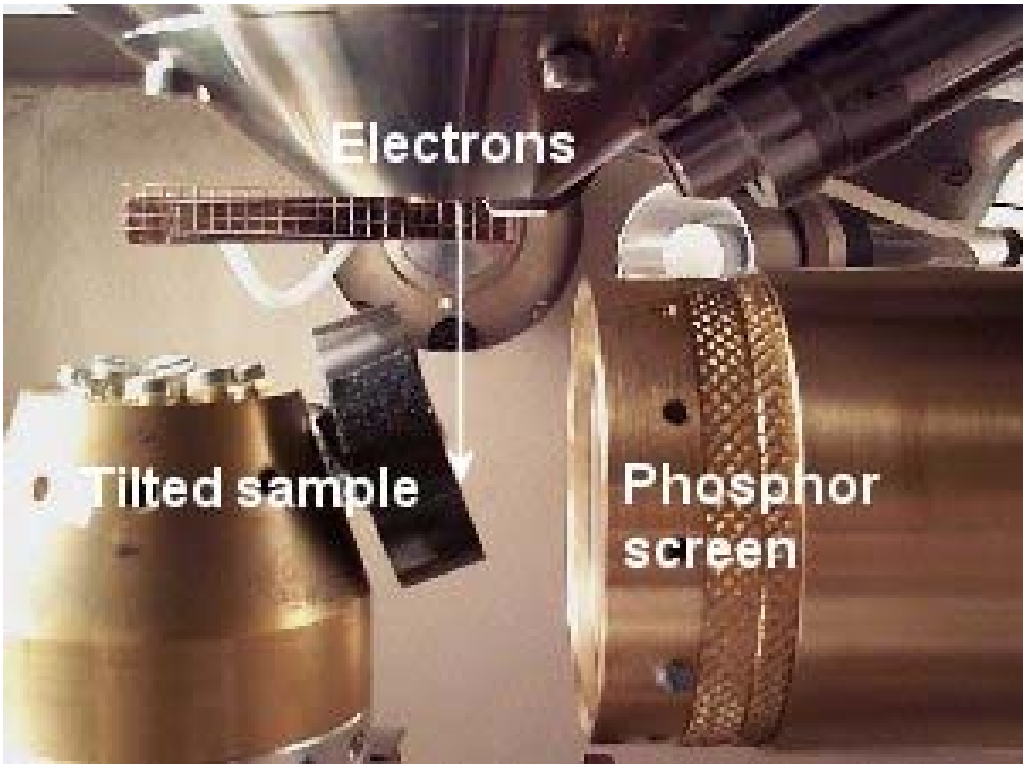

Figure 3.12: An image showing a tilted sample and a phosphorous screen in SEM chamber [224].

The mechanism by which the diffraction patterns are formed is as follows: the atoms in the material inelastically scatter a fraction of the electrons with a small loss of energy to form a divergent source of electrons close to the surface of the sample. Some of these electrons are incident on atomic planes at angles which satisfy the Bragg equation. Since diffraction of the electrons through the Bragg angle is occurring in all directions, these electrons are diffracted to form a set of paired large angle cones corresponding to each diffracting plane. When used to form an image on the fluorescent screen the regions of enhanced electron intensity between the cones produce the characteristic Kikuchi bands of the electron backscatter diffraction pattern (Figure 3.13).

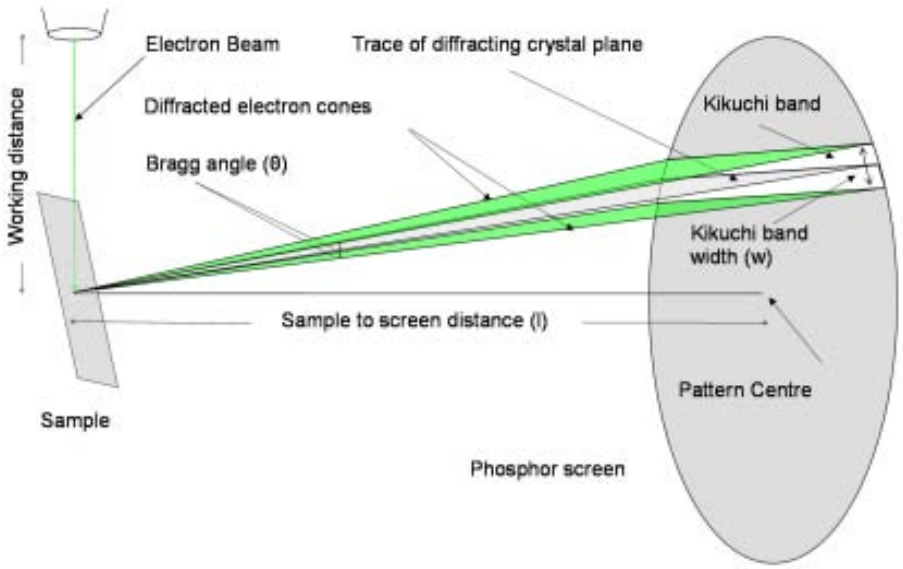

Figure 3.13: EBSD geometry [224].

The diffraction pattern can be used to measure the crystal orientation, measure grain boundary misorientations as it can characterise the boundary by the difference in orientation on either side of the boundary, discriminate between different materials, and provide information about local crystalline perfection. The symmetry and appearance of the diffraction pattern is related intimately to the crystal structure at the point where the beam meets the sample. If the crystal rotates (in other words its orientation changes) the diffraction pattern will be seen to move. If a different type of material is placed under the beam, the diffraction pattern will change completely. So the diffraction pattern can be used to measure crystal orientations and to identify materials. When the beam is scanned in a grid across a polycrystalline sample and the crystal orientation measured at each point, the resulting map will reveal the

constituent grain morphology, orientations, and boundaries. This data can also be used to show the preferred crystal orientations (texture) present in the material, for example, as pole figure.

Because EBSD measures crystal orientation, and hence used to analyse the sample texture, then EBSD is complementary to the standard method of measuring texture using X-ray diffraction. However, EBSD goes further because it can relate the texture (or textures) present to the microstructure of the material. In addition, textures which vary from place to place in a sample can be studied easily. The way in which textures develop can be studied at the level of the microstructure with EBSD [224, 225].

3.3.4 Atomic force microscopy (AFM)

Scanning probe microscopy (SPM) consists of a family of microscopy forms and the primary two are scanning tunnelling microscopy (STM) and atomic force microscopy (AFM) which also called scanning force microscopy (SFM).

Since its inception in the mid-1980s, SPM has become a very well-accepted technique for characterizing surfaces and interfacial processes with nanometer-scale resolution and precision.

There are three modes of AFM i.e., contact mode AFM, non contact mode AFM and tapping mode AFM. In this work the contact mode was adopted.

Contact mode AFM operates by scanning a tip (with a nominally atomically sharp tip, typically pyramidal in shape, which is mounted on the underside of an extremely sensitive cantilever) across the sample surface while monitoring the change in cantilever deflection with a split photodiode detector. Precise control over the tip-sample separation distance is what provides the AFM (SPM) technique with its high spatial resolution. One can then generate a surface contour map that reflects relative differences in interaction intensity as a function of surface position.

The tip contacts the sample surface and a feedback loop maintains a constant deflection between the cantilever and the sample by vertically moving the scanner at each (x, y) data point to maintain a "setpoint" deflection (Figure 3.14). By maintaining a constant cantilever deflection, the force between the tip and the sample remains constant. The force is calculated from Hooke's Law: where

$$F = -kx \quad \textbf{(Eq. 3.2)}$$

F = Force

k = spring constant

x = cantilever deflection.

Spring constants usually range from 0.01 to 1.0 N/m, resulting in forces ranging from nN to μN in an ambient atmosphere. The distance the scanner moves vertically at each (x, y) data point is stored by the computer to form the topographic image of the sample surface. Operation can take place in ambient and liquid environments.

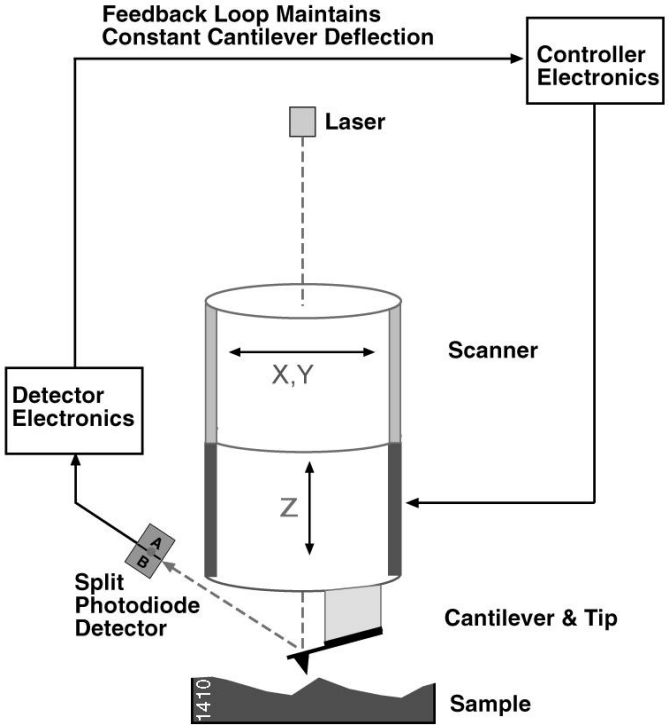

Figure 3.14: Schematic of the contact mode AFM [226].

The roughness of the film can be calculated from the AFM image. The Root Mean Square (RMS) Roughness is the standard deviation of the Z values within a given area and is given by [226, 227]:

$$\text{RMS} = \sqrt{\frac{\sum_{i=1}^{N}(Z_i - Z_{ave.})^2}{N}} \quad \textbf{(Eq. 3.3)}$$

$Z_{ave.}$: is the average Z value within the given area.

Z_i: is the current Z value.

N: is the number of points within a given area.

The atomic force microscope used in this study was a Nanoscope^{R} IIIa (Digital Instruments, Dimension^{TM} 3100, Veeco Metrology group). Contact mode AFM was employed at ambient conditions using silicon nitride probes with a nominal tip radius

of curvature of 20 nm and spring constant of 0.12N/m. A scan rate of 1 Hz was employed.

3.3.5 AC susceptibility

There are two classic ways to define superconductivity, one involving the property of zero resistance and the other based on perfect diamagnetism, i.e. AC susceptibility, which became popular with the advent of high temperature superconductivity. In this test magnetisation currents are induced in the sample, by the application of a small varying magnetic field (H_{AC}) with the aid of a primary coil, and the flux variation due to the sample is picked up by a sensing (pickup) coil surrounding the sample, the resulting magnetic moment or susceptibility induced in the coil is detected by a lock-in amplifier which also separates the χ' and χ''. Figure 3.15 is a schematic of the AC susceptibility apparatus used in this work.

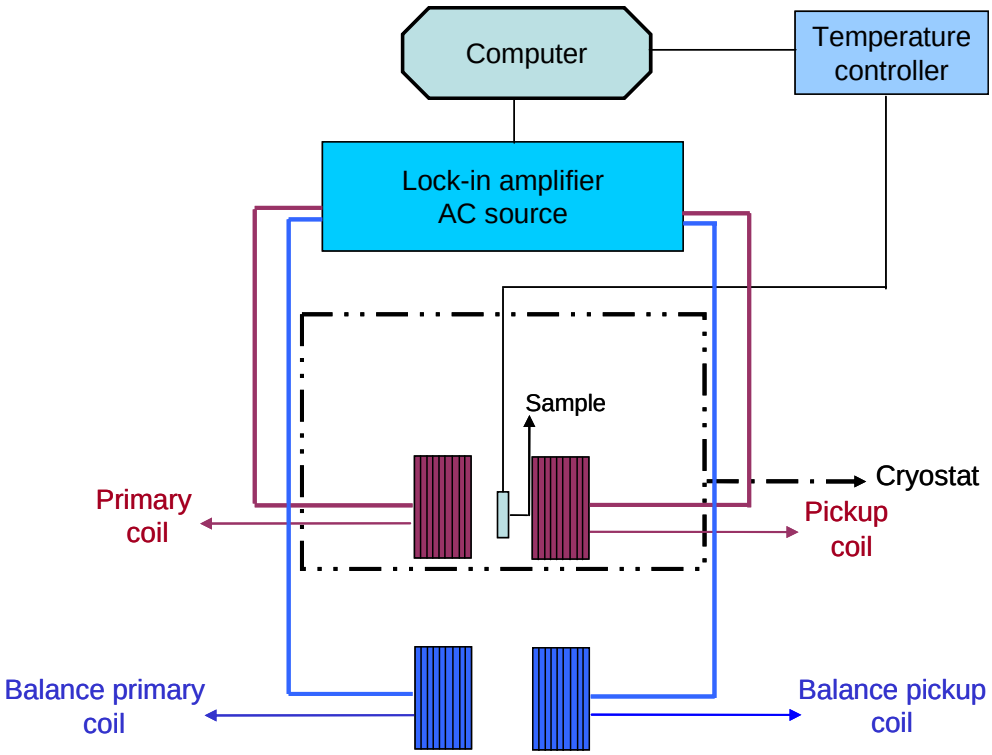

Figure 3.15: Schematic of AC susceptibility apparatus.

Figure 3.16 shows the real (χ') and the imaginary (χ''), also called the first derivative, susceptibilities. The point at which the first derivative reaches its maximum value could be selected as defining T_c. The width ΔT between the points where the first derivative curve is half of its maximum value, is a good quantitative

measure of the width of the transition. The figure also shows the definition of the T_c onset and the T_c midpoint.

The susceptibility measurements determine the magnetic state of the entire sample, and also give a better indication of the extent to which the sample has transformed to the superconducting state. On the one hand, χ' gives quantitative expression for the amount of magnetic flux penetration into the sample; $\chi' = -1$ for a complete Meissner expulsion and $\chi' = 0$ for a full flux penetration. On the other hand, $\chi'' = 0$ in the superconducting state and <1 in the mixed state. When χ'' >1 then it reflects AC losses. This is based on SI units, where numerical results must be corrected for any sample demagnetising factor [228-233].

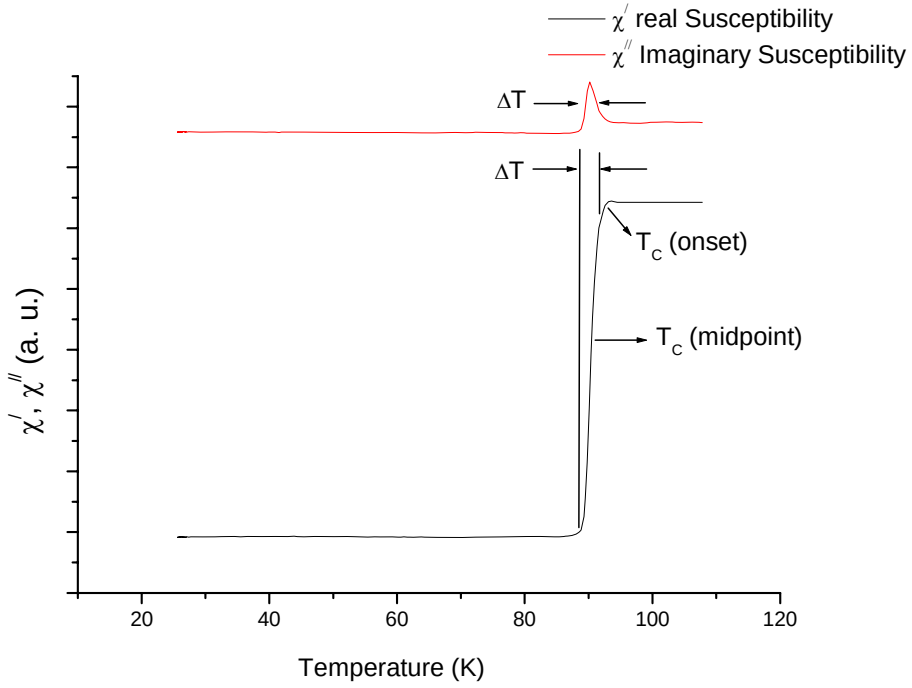

Figure 3.16: χ' and χ'' for YBCO deposited on MgO single crystal with a T_c onset of 90.2K.

The volume magnetic susceptibility (χ) is defined by the relationship:

$$\chi = dM / dH \quad \textbf{(Eq. 3.4)}$$

where in SI units:

M: is the magnetization of the material (the magnetic dipole moment per unit volume) measured in Amp/m.

H: is the magnetic field strength also measured in Amp./m [232, 234].

3.3.6 X-ray photoelectron spectroscopy (XPS)

XPS is a surface chemical analysis technique based on the binding energies of the electrons. Electrons are emitted from a metallic surface after the absorption of energy from electromagnetic radiation, such as X-rays, having a frequency above a certain threshold frequency (typically visible light). The emitted electrons can be referred to as photoelectrons. In an XPS experiment electrons are photoionized from the core levels by X-rays. The surface is irradiated with photons from a soft X-ray source, most commonly Al Kα (1486.6eV) but also Mg Kα (1253.6eV) is used as well. By the law of conservation of energy, the electron absorbs the energy of the photon and if sufficient, the electron can escape the material with a finite kinetic energy. A single photon can only eject a single electron as the energy of one photon can only be absorbed by one electron. The cornerstone of XPS is the measurement of the kinetic energy E_k of the outgoing electrons. This energy is related to the electron binding energy E_B, according to the basic XPS equation which was first made by Rutherford, and was then modified to:

$$E_K = h\upsilon - E_B \quad \textbf{(Eq. 3.5)}$$

where E_K is the kinetic energy of the ejected photo-electron, $h\upsilon$ is the incident photon energy and E_B is the electron binding energy [235-237].

From those binding energies, the state of a specific element can be determined, i.e. present as an oxide, hydroxide, carbonate…etc.

In this work, the XPS spectra were recorded with a standard Mg Kα source (20 pass energy, 0.1 step, and 0.1 seconds per step for the detailed spectra) using XPS VG Scientific ESCALAB MKII spectrometer with a spatial resolution of 100μm.

4 Spray pyrolysis of MgO on silicon single crystals using magnesium nitrate as a precursor

4.1 Introduction

In this chapter Si single crystals were used for the optimization of the spray pyrolysis parameters for further deposition on RABiTS and polycrystalline metallic substrates which will be presented in the following chapters. In addition to that they have been used due to their low cost. The deposition of MgO thin films by spray pyrolysis, on (100) oriented silicon (Si) single crystal wafers which has a cubic diamond structure [223], will be introduced using magnesium nitrate as a precursor. Before the deposition, the wafers (330µm thick) were cut into 10mm x10mm and then cleaned in acetone, then ethanol for 10 minutes each in an ultrasonic bath, then dried with Ar gas. A pulse time to interval time of 1:7 was applied and the deposition time was 32 minutes. The used Ar flow rate was 10 l/min.

To evaluate the performance of the MgO films, YBCO was deposited by PLD on top of MgO films deposited by spray pyrolysis on Si and on top of MgO films deposited by PLD on Si. Therefore, YBCO deposition parameters were first optimised by depositing YBCO by PLD on MgO single crystals.

Thermal decomposition of the precursor (was used as a guideline temperature for the thin film deposition) was presented, the effect of the precursor concentration, substrate temperature and inclination angle on the quality of the spray pyrolysed MgO films on Si were all investigated. In addition to that, MgO was deposited by PLD on Si to compare the produced films with those deposited by spray pyrolysis.

It is to be mentioned that X-ray scans for the MgO films deposited by spray pyrolysis on Si detected only MgO (200) peaks from the MgO films. Therefore, we could not quantify the level of texture as no other peaks were detected to reference to. Accordingly, it was assumed that an increase in the intensity of MgO (200) peak reflects an improvement in texture.

4.2 Thermal decomposition of the nitrate precursor

Before depositing MgO by spray pyrolysis, a thermogravimetrical analysis (TGA) of the decomposition of the nitrate precursor was used as a guideline temperature for the thin film deposition. For this purpose, a sample of magnesium nitrate hexahydrate, $Mg(NO_3)_2.6H_2O$, with a mass of 7 mg was placed in an alumina crucible. The thermogravimetric (TGA) analysis was performed in a flow of Argon

from 25°C to 750°C. The TGA measurement was performed at a constant heating rate of 10°C/min. Figure 4.1 shows the TGA curve for the tested $Mg(NO_3)_2.6H_2O$ sample.

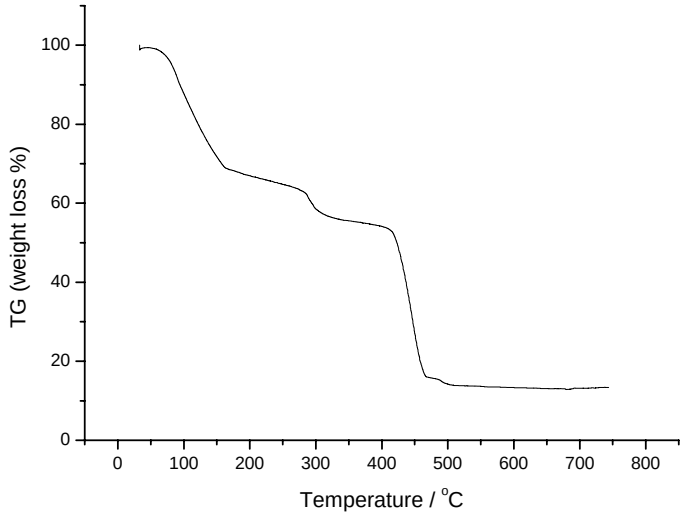

Figure 4.1: TGA curve for $Mg(NO_3)_2.6H2O$.

The decomposition of $Mg(NO_3)_2.6H_2O$ takes place in three steps as can be seen from Figure 4.1, the first two are dehydration and the third one is the decomposition of anhydrous $Mg(NO_3)_2$ to MgO, $1\frac{1}{2}O_2$ and 2NO [238]. The decomposition finished at about 500°C which is close to that obtained by Migdal [238] under the same conditions. He found that the decomposition finished at 770K (496.8°C).

It was found that storage and humidity degrades the MgO films by the formation of magnesium hydroxide [116]. However, heating the contaminated layer briefly at a temperature of 450°C in air is sufficient to regenerate the MgO surface [116], a condition that will be met during YBCO deposition. However, the analysis (EDX, SEM, XRD…etc.) was always carried out on fresh samples.

4.3 MgO deposition by spray pyrolysis on Si (100) substrates

In this section the deposition of MgO on (100) oriented Si single crystal was performed using 0.078M and 0.0078M of magnesium nitrate. These concentrations were used because a PhD thesis was found where MgO was deposited by spray pyrolysis on (100) oriented Si single crystal using 0.078M of magnesium nitrate. In order to widen the investigation in this work, 0.0078M was used as well.

4.3.1 Effect of substrate temperature and precursor concentration on MgO film properties

Figure 4.2 and Figure 4.3 illustrate the XRD patterns for the MgO films deposited in the temperature range of 600°C-700°C using 0.0078M and 0.078M of magnesium nitrate hexahydrate, respectively. The MgO (200), MgO (111), Si (400), and Si (111) peaks are at 2θ of 42.9°, 36.93°, 69.17° and 28.42°, respectively, according to the JCPDS PDF files 00-045-0946 and 00-005-0565, respectively. The lattice parameters for the cubic Si and MgO are 5.4301Å and 4.2112Å, respectively according to the same PDF files.

The lattice mismatch between MgO and Si is 22.44% tensile in-plane shifting the out-of-plane MgO (200) peak towards higher 2θ angles. If MgO is rotated by 45°, the lattice mismatch is then 9.7% compressive in-plane and the resulting lattice mismatch strain would shift the MgO (200) peak (representing out-of-plane texture) towards lower 2θ angles when compared to the PDF files. Besides that, the thermal expansion coefficients are 3.0-3.8x10^{-6}/K for Si [97, 145] and 13.8x10^{-6}/K for MgO [143, 239]. Therefore, during cooling, an MgO film deposited on Si will be under tension in-plane and under compression out-of-plane due to the thermal expansion mismatch. Accordingly, the MgO (200) peak will be shifted towards higher 2θ angles when compared to the PDF files; due to the compression of the out-of-plane lattice parameter. Therefore, the shift in the MgO (200) peak towards higher 2θ angles is either because the lattice mismatch, or because of the thermal expansion mismatch between the MgO film and the Si substrate. It can be seen from Figure 4.2 that only the Si (200) and (400) peaks are detected and the strained (200) MgO peaks appeare at 43.9° compared with an unstrained 2θ value of 42.9°. The same MgO (200) peak shift was seen by Pavlopoulos [147]. Korotcenkov et al [240] also observed a similar strain for the case of depositing In_2O_3 by spray pyrolysis on Si substrates. The strain was attributed to the lack of coincidence in the thermal expansion coefficients between the substrate and the deposited layer [240]. Figure 4.2 shows that the MgO, deposited from the 0.0078M solution, has a (200) preferential orientation. This texture became more pronounced as the temperature was increased from 600° to 700°C; this can be explained by the mobility of the absorbed Mg and O atoms which is enhanced at higher substrate temperatures, and therefore, could easily move to equilibrium atomic sites on the surface. The heating energy of the substrate provides the migration energy

for surface atoms to form a stable and energetically stable (200) preferential layer [66, 79]. The texture improvement with temperature can be also explained by reaction kinetics, which is controlled by the diffusion process through the boundary layer at high temperatures. Because the reaction kinetics and diffusion were enhanced at high temperatures, then a stronger texture was obtained [142]. Another explanation is due to the higher chemical purity of the film prepared at high temperatures where the purity of the film is controlled by the level of thermal decomposition [141]. The improvement of texture with increasing temperature was also observed by others [56, 86]. This texture improvement with temperature was also observed for other films deposited from a range of different precursors and using different deposition processes [117, 147, 154, 159, 162]. It can be concluded that epitaxial growth was achieved since the obtained peaks correspond only to the (200) of MgO (Figure 4.2 and Figure 4.3) and this will be confirmed by the pole figures later in this chapter.

At 600°C, a very low peak intensity of MgO (200) was noticed at both of the used concentrations (Figure 4.2 and Figure 4.3), i.e., at 0.078M and 0.0078M; therefore, the temperature range selected for this work according to the TGA test was reasonable, i.e., going to lower deposition temperatures was not necessary. Strained (200) MgO peaks, at 650°C and 700°C using an 0.078M solution (Figure 4.3), was also obtained as in the case of the 0.0078M solution. The only difference was in the intensity of the MgO (200) peaks, which were lower at 0.0078M. This was attributed to the lower growth rate at the lower concentration, which in turn resulted in low intensity peaks [114, 140]. Pavlopoulos [147] saw that the preferred orientation of the films became stronger as the concentration increased. This was when using temperatures up to 650°C, for the deposition of MgO on STO substrates. Other researchers deposited different films on different substrates and found that the texture improved by increasing the concentration [147, 158, 160, 161].

However, it is should be pointed out that a large debate on texture behaviours of different films at different temperatures and concentrations were observed by researchers. A complete survey about the subject can be found in sections 2.5 and 2.6.

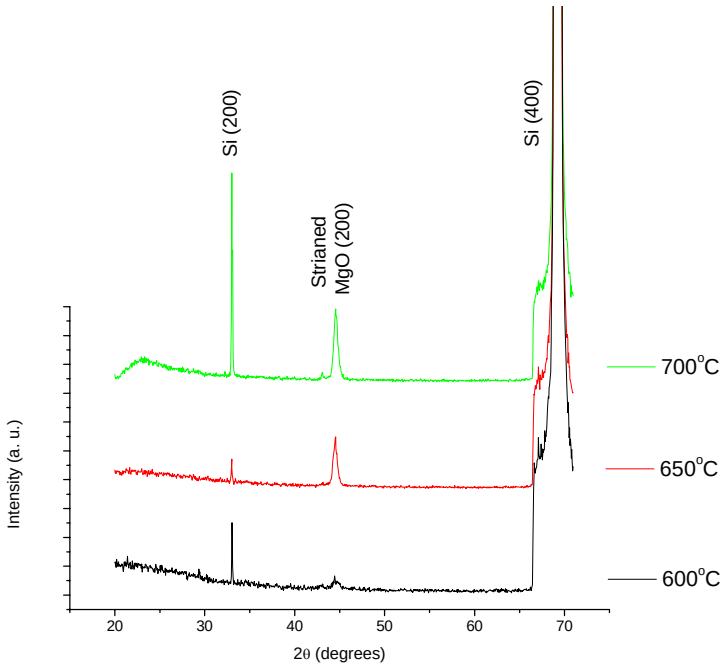

Figure 4.2: XRD patterns of the MgO films deposited with zero inclination angle, at different temperatures, from 0.0078M $Mg(NO_3)_2.6H_2O$ solution.

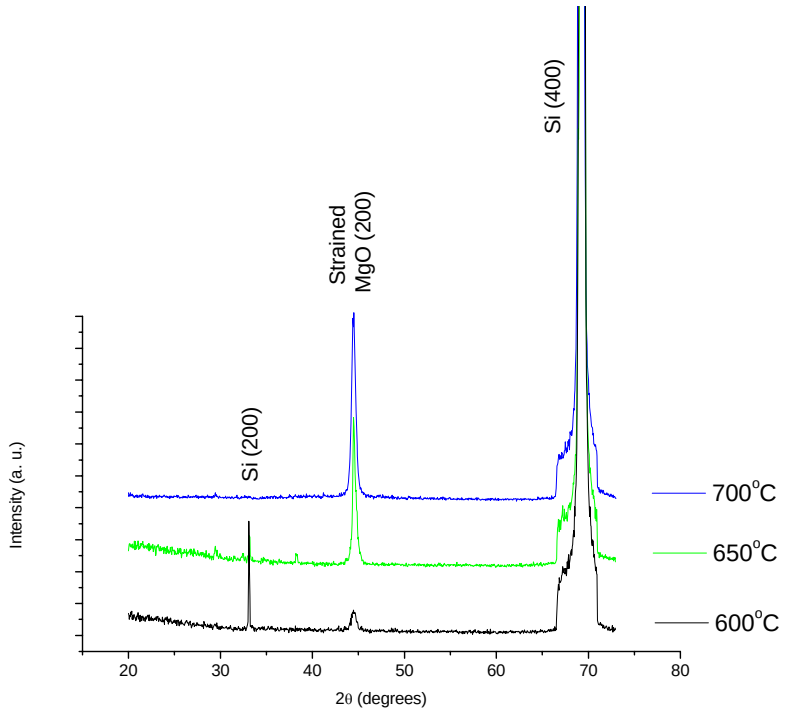

Figure 4.3: XRD patterns of the MgO film deposited with zero inclination angle, at different temperatures, from 0.078M $Mg(NO_3)_2.6H_2O$ solution.

4.3.2 Surface morphology

SEM images of the MgO films deposited at 650°C and 700°C are shown in Figure 4.4 to Figure 4.7. It can be seen that the film morphologies depend on the substrate temperature and the concentration of the precursor. At 650°C, the surface roughness decreased with increasing the concentration from 0.0078M to 0.078M. The corresponding average (of three readings) root mean square (RMS) roughness values (from the AFM images in Figure 4.8 and Figure 4.9) are 19.2 and 10.8 nm, respectively, compared to a roughness value of around 20 nm for the film deposited at 0.078M by Pavlopoulos [147]. At 0.0078M, the surface was rougher than that at 0.078M due to the presence of overgrown particles of MgO on the surface as can be seen by comparing Figure 4.4 and Figure 4.5. This could be attributed to the low nucleation rate at low concentration; therefore the growth rate of the particles was larger compared to that at higher concentration. The same result was observed by Shengyue Wange et al [98] at low ratios of pulse time to interval time. The low ratio gave large crystallite sizes due to the predominance of the growth rate over the nucleation rate. Figure 4.5 shows a smooth and uniform surface morphology and this is supported by Figure 4.9 which shows the AFM image at 0.078M. Therefore, the film with high degree of preferred orientation (the ones deposited from 0.078M) show smoother surface and this observation was also observed by Stryckmans et al [142]. At 700°C, the average (of three readings) RMS roughness values are 31.76 and 47.16 nm at 0.0078M and 0.078M, respectively. This means that the roughness increased by increasing the temperature from 650°C to 700°C. This increase in roughness by increasing the temperature was attributed to the higher growth rate of the nuclei which gives large crystallite sizes [152]. Xiaorong Fu et al [72] and Soo Gil Kim et al [86] also found that the roughness increased with increasing the substrate temperature. After the solvent in a droplet was completely evaporated, the decomposition rate of the Mg precursor in a droplet increased with the temperature, too. Therefore, large MgO particles occurred by homogenous nucleation before the MgO gas phase source arrived on the substrate. Hence, large particles on the film surface were obtained. However, Prince et al [140] found that the smoothness of In_2O_3 films increased with increasing the substrate temperature up to 380°C and then deteriorates at higher temperatures. Petrova et al [63] found that the roughness of CeO_2 films decreased with increasing the substrate temperature due to higher rate of evaporation and

accordingly, to higher supersaturation and bigger number and smaller size of the crystals formed.

And to continue, at 700°C, the roughness increased with increasing the concentration. This may be explained as follows. At high temperatures, the decomposition rate of the Mg precursor in droplets increased, therefore, large MgO particles occured by homogenous nucleation before the MgO gas phase source arrived at the substrate. Hence, large particles on the film surface were obtained [86]. This effect increased by increasing the concentration from 0.0078M to 0.078M. This can be seen by comparing Figure 4.6 and Figure 4.7, which is also supported by the AFM images in Figure 4.10 and Figure 4.11.

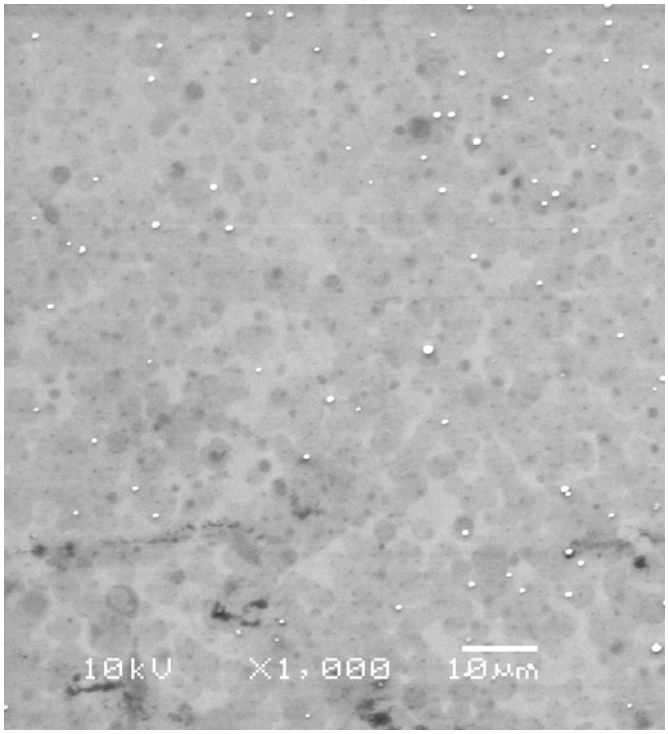

Figure 4.4: SEM image of the MgO film deposited with a zero inclination angle at 650°C from 0.0078M $Mg(NO_3)_2.6H_2O$ solution.

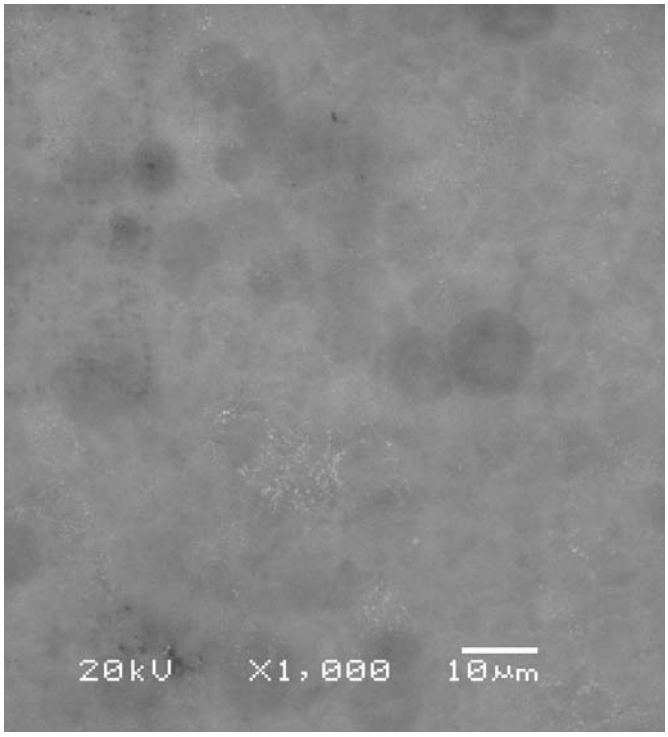

Figure 4.5: SEM image of the MgO film deposited with a zero inclination angle at 650°C from 0.078M $Mg(NO_3)_2.6H_2O$ solution.

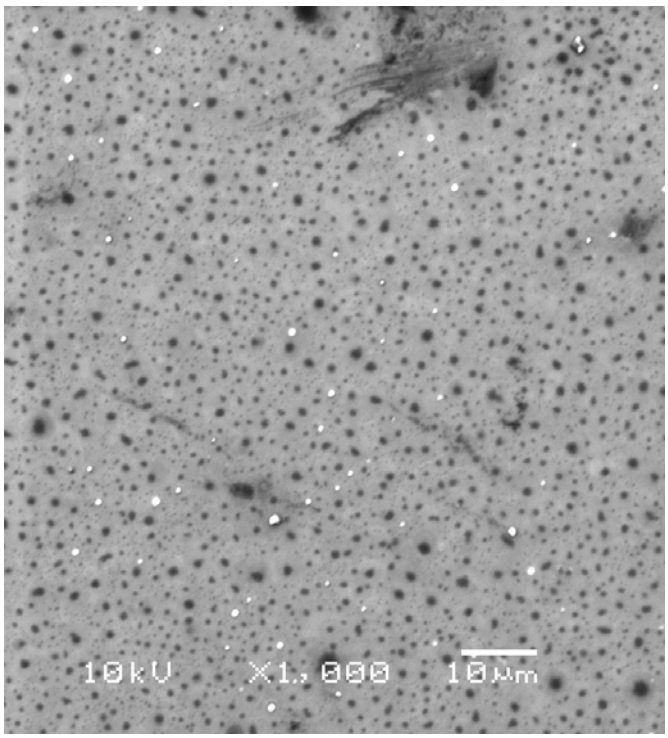

Figure 4.6: SEM image of the MgO film deposited with a zero inclination angle at 700°C from 0.0078M $Mg(NO_3)_2.6H_2O$ solution.

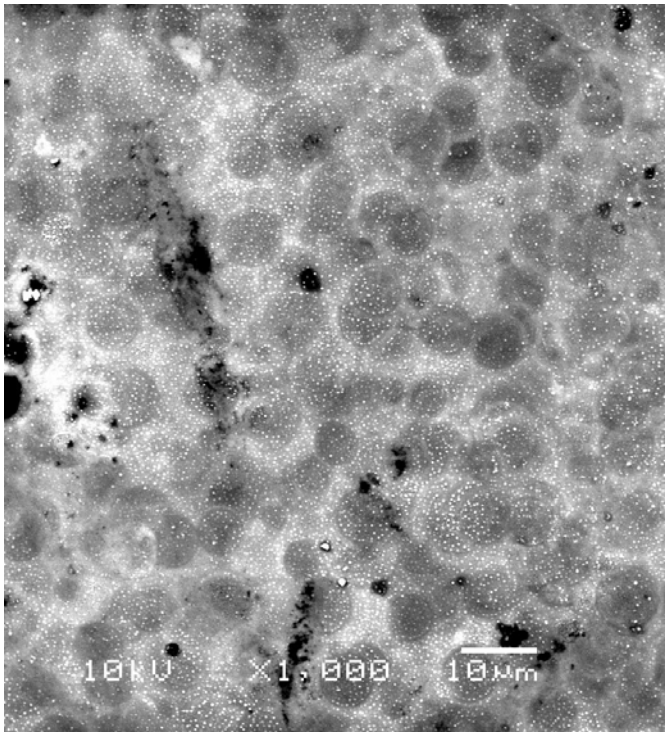

Figure 4.7: SEM image of the MgO film deposited with a zero inclination angle at 700°C from 0.078M $Mg(NO_3)_2.6H_2O$ solution.

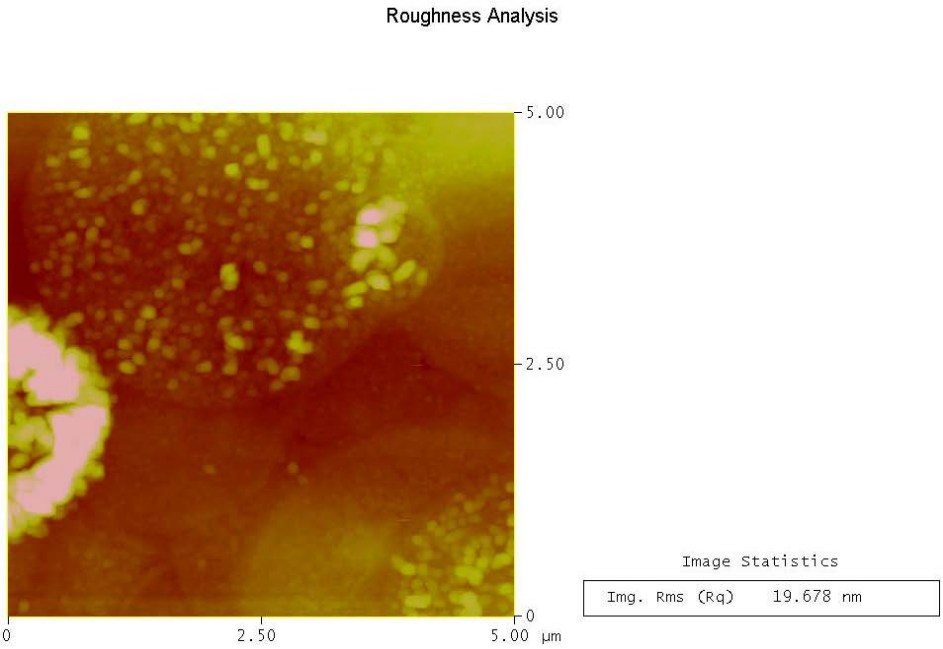

Figure 4.8: A 5x5µm^2 AFM image of the MgO film deposited with a zero inclination angle at 650°C from 0.0078M $Mg(NO_3)_2.6H_2O$ solution.

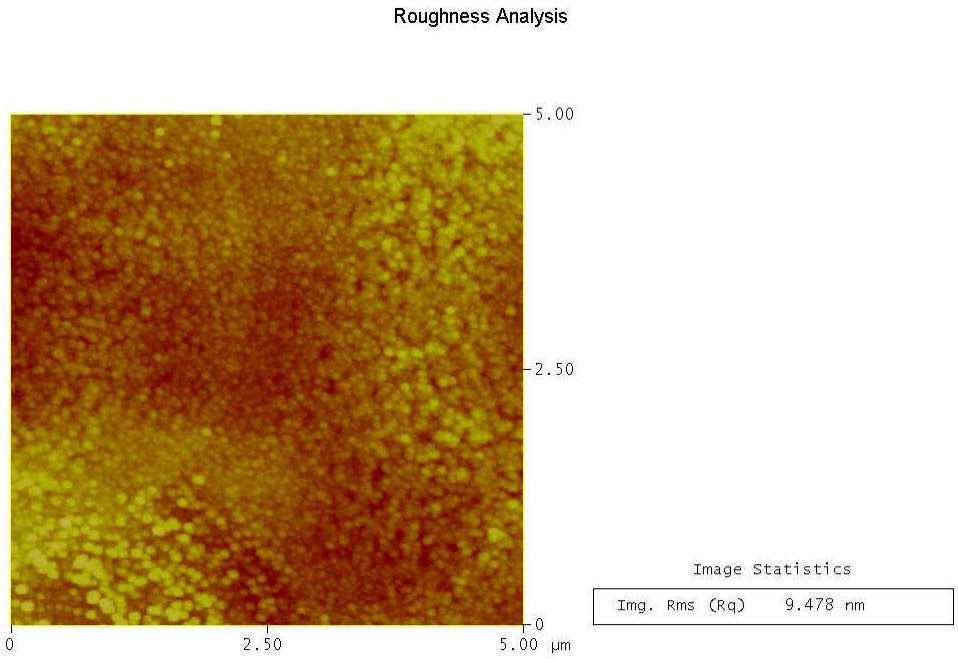

Figure 4.9: A 5x5µm^2 AFM image of the MgO film deposited with a zero inclination angle at 650°C from 0.078M $Mg(NO_3)_2.6H_2O$ solution.

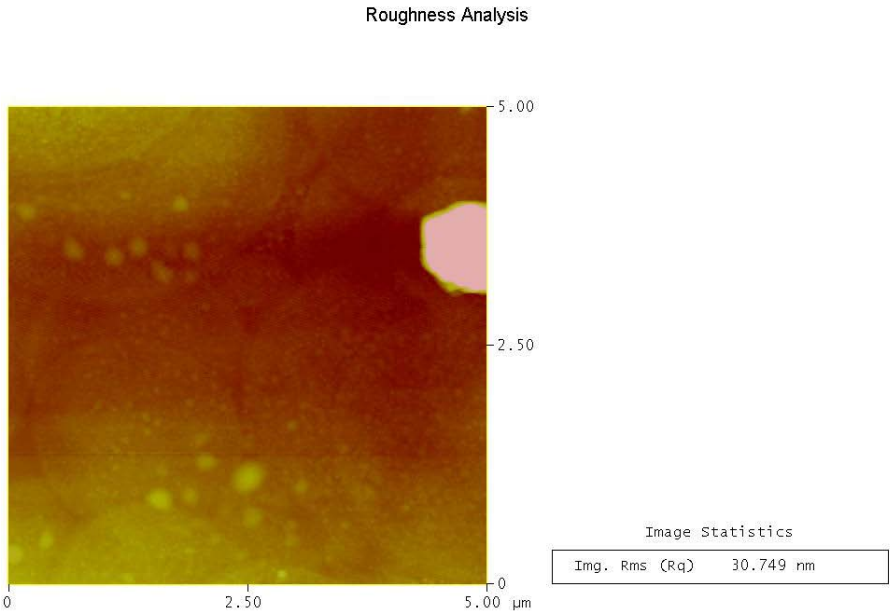

Figure 4.10: A 5x5µm^2 AFM image of the MgO film deposited with a zero inclination angle at 700°C from 0.0078M $Mg(NO_3)_2.6H_2O$ solution.

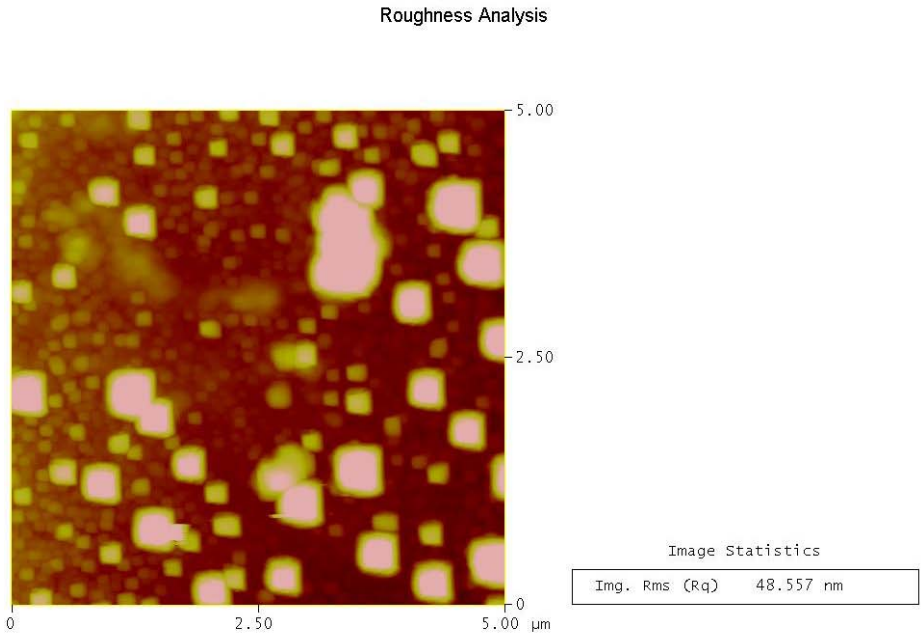

Figure 4.11: A 5x5µm^2 AFM image of the MgO film deposited with a zero inclination angle at 700°C from 0.078M $Mg(NO_3)_2.6H_2O$ solution.

AFM section profile images are shown in Figure 4.12 and Figure 4.13 for MgO films deposited from 0.078M solution at 650°C and 700°C, respectively. For the sample deposited at 650°C, when comparing Figure 4.5 and Figure 4.9 to Figure 4.12, it can be seen that the surface is homogenous and smooth and most of the film is located on the same layer as can be seen from Figure 4.12. However, the film deposited at 700°C shows particles or grains which are located on different layers relative to the rest of the film (Figure 4.7, Figure 4.11, and Figure 4.13). The films deposited at 650°C and 700°C from the 0.0078M solution showed similar growth behaviour. The optimum deposition conditions for the case of MgO deposition on Si single crystals were to use 0.078M at 650°C which resulted in epitaxial MgO films (section 4.3.3)

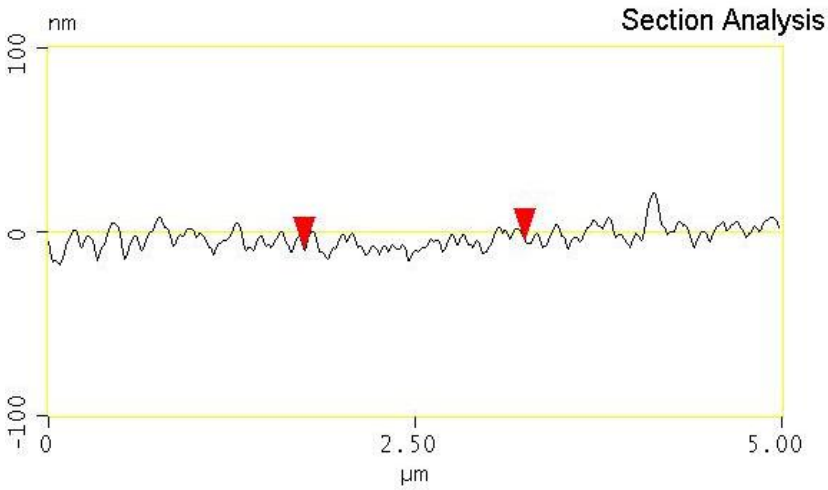

Figure 4.12: AFM section profile image of the MgO film deposited with a zero inclination angle at 650°C from 0.078M $Mg(NO_3)_2.6H_2O$ solution.

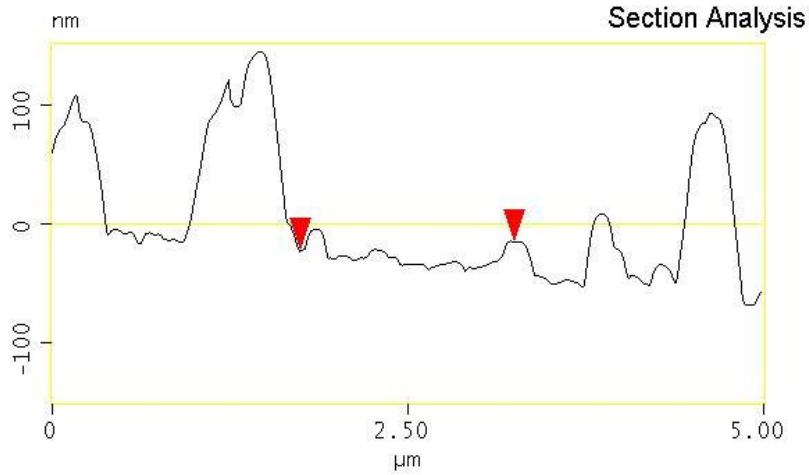

Figure 4.13: AFM section profile image of the MgO film deposited with a zero inclination angle at 700°C from 0.078M $Mg(NO_3)_2.6H_2O$ solution.

When depositing at 650°C using a precursor concentration of 0.078M, the surface was smooth and homogenous, therefore the best mode which gives this result is the third mode; when thermal decomposition of dry precipitates starts on their way to the substrate. The deposition modes mentioned in section 2.3, were described with respect to an increase in the deposition temperature. However, it is possible to manipulate that explanation by keeping the temperature constant while increasing the concentration. The nebuliser produces droplets almost of the same size; therefore, at low concentration the droplet will contain less solute than at high concentration. The lifetime required for evaporation increases by increasing the amount of solute in the droplet [110]; therefore, increasing the concentration has the same effect as

decreasing the temperature. According to that, at 0.0078M, the lifetime to evaporate the droplet is shorter and the possibility of forming oxide particles from the vapour phase before deposition, as in the fourth mode (where the full thermal decomposition takes place before reaching the substrate and only finely divided solid products arrive at the substrate surface), is more probable. From this, it was assumed that the fourth mode of deposition applies to the films deposited at 0.0078M and the third mode applies to the films deposited at 0.078M. This explains the rough surface with distinct particles obtained at 650°C using 0.0078M and the smooth one obtained at 0.078M.

At 700°C, as mentioned earlier, the roughness increased by increasing the concentration from 0.0078M to 0.078M. In this case, it is difficult to determine which mode of deposition applies compared to that occurring at 650°C, as the temperature difference is not large enough to change the mode of deposition. However, in this case, the temperature may be high enough that we have the fourth mode of deposition at both of the used concentrations. Accordingly, the higher the concentration the rougher the produced film.

4.3.3 Composition of films and texture analysis

The chemical analysis results obtained from the EDX test, using an accelerating voltage of 4KV (Figure 4.14 and Table 4.1), for the sample deposited at 650°C from 0.078M solution, suggest that the atomic percentage of magnesium to that for oxygen is very close to 1:1 and this suggests that a stoichiometric MgO film was obtained. The detected Si peak is coming from the interaction of the X-ray beam with Si substrate.

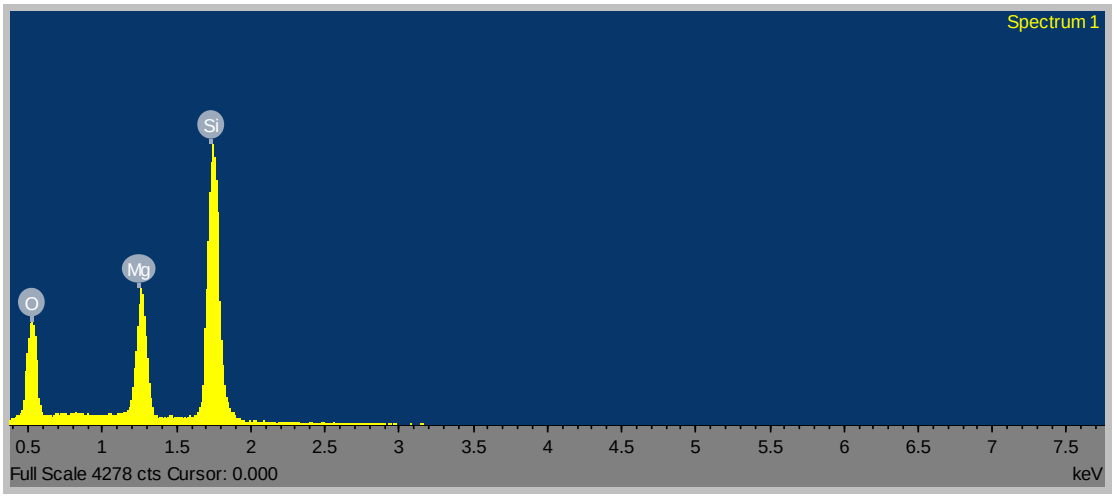

Figure 4.14: EDX spectrum for the sample deposited at 650°C from 0.078M solution using an accelerating voltage of 4KV.

Table 4.1: Atomic % of magnesium and oxygen as obtained from the EDX spectrum using an accelerating voltage of 4kV for the sample deposited at 650°C using 0.078M.

Element	Atomic%
O K	17.15
Mg K	17.55
Si K	65.30
Totals	100

The X-ray pole figure of Figure 4.15 shows that the Si single crystals are biaxially textured as it should be. The (200) pole figure of Figure 4.16 confirms that the MgO film for the sample deposited at 650°C using 0.078M was grown with a (200) texture. At the same time, the (111) pole figure in Figure 4.16 shows that the film has an in-plane texture along the a-b plane (in-plane). This indicates that the MgO film was grown epitaxially on Si, i.e. biaxially textured, as is required for the deposition of YBCO. From Figure 4.15 and Figure 4.16, it can be seen that MgO was not rotated relative to the Si substrate during deposition to reduce the lattice mismatch; but a cube-on-cube epitaxial relation was obtained. Therefore, the straining in this case is to be attributed mainly to the thermal expansion mismatch between MgO and Si. A similar texture relation between spray pyrolysed film and the substrate was observed by Ming Wei and Choy [155]. They used electrostatic spray-assisted vapour deposition to deposit cerium oxide films on Si (100) and glass substrates at temperatures between 400° and 600°C. The orientation relationships between CeO_2 film and Si substrate were $001_{CeO2}//001_{Si}$ and $111_{CeO2}//111_{Si}$. However, Wei et al [54] later on, deposited CeO_2 by the same method on textured Ni tapes in the same temperature range. The orientation relationships between CeO_2 and Ni substrate were 001_{CeO2} //001_{Ni} and 110_{CeO2} //100_{Ni}. This gave a 45° rotation of CeO_2 relative to the substrate.

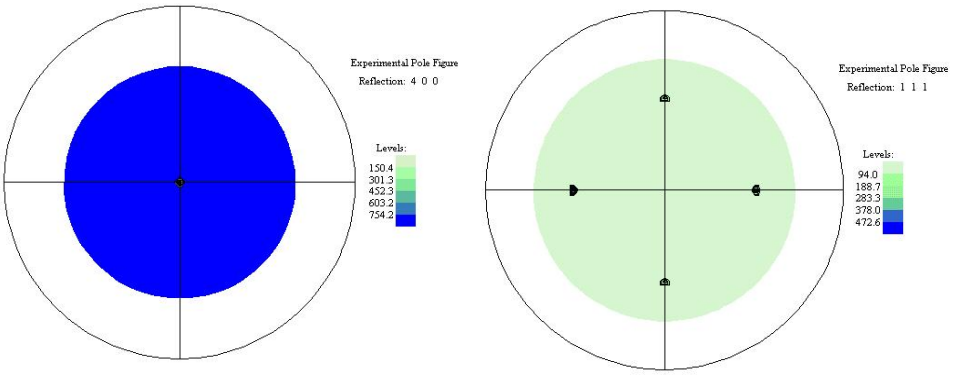

Figure 4.15: (400), left, and (111), right, X-ray pole figures, at 2θ of 69.17° and 28.42°, respectively, of Si (100) substrate deposited with MgO film at 650°C using 0.078M solution.

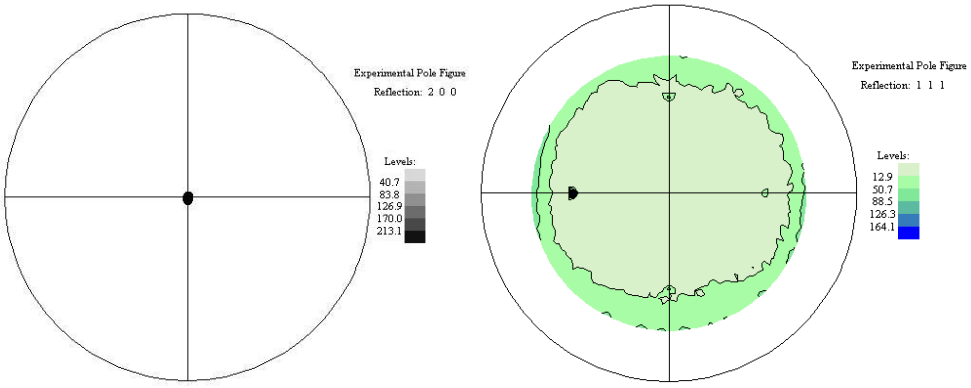

Figure 4.16: (200), left, and (111), right, X-ray pole figures, at 2θ of 43.85° and 36.93°, respectively, of the MgO film deposited at 650°C using 0.078M solution.

4.3.4 Effect of inclination angle on MgO film properties

The XRD patterns of the films deposited at 650°C at different inclination angles from the 0.0078M and 0.078M solutions are shown in Figure 4.17 and Figure 4.18, respectively. The peaks are identified according to the JCPDS PDF files 00-045-0946 and 00-005-0565 for MgO and Si, respectively.

Only the peaks corresponding to the Si substrate and strained MgO (200) can be seen from the XRD patterns of Figure 4.17 and Figure 4.18. The same result was obtained for the films deposited at a zero inclination angle and was attributed to the thermal expansion mismatch between MgO and Si, not to the lattice mismatch, the case if MgO rotates. This will be confirmed later from the pole figure measurements. Once more, all the films have a (200) texture and the intensity increased with increasing the concentration. No reports were found for ISD deposition of MgO by spray pyrolysis. However, it is to be noted in this work that inclining the substrate led to untilted MgO films with (200) grown parallel to the substrate normal and did not result in the shadowing effect which was observed for MgO and YSZ films deposited

by ISD method using PLD and e-beam evaporation [39-41, 49, 50, 53, 167, 169, 173-175, 177-183].

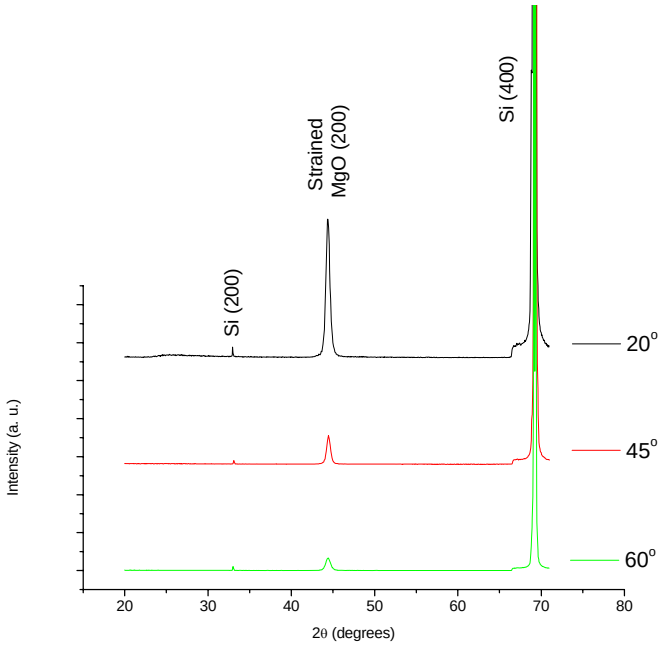

Figure 4.17: XRD patterns of the MgO films deposited at different inclination angles, at 650°C from a 0.0078M $Mg(NO_3)_2.6H_2O$ solution.

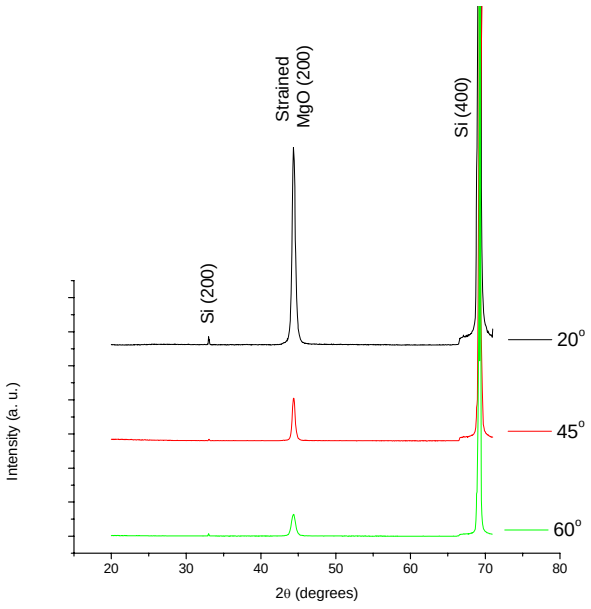

Figure 4.18: XRD patterns of the MgO films deposited at different inclination angles, at 650°C from a 0.078M $Mg(NO_3)_2.6H_2O$ solution.

The RMS roughness values (Figure 4.19) for the MgO films deposited at 650°C from 0.0078M decreased with increasing the inclination angle from zero to 20°. However, the roughness became independent of the inclination angle from 20° to 60°. At zero inclination angle, the aerosol flow impacts on the surface directly resulting in

rough films compared to that with substrate being inclined, where the probability of direct impact is less, resulting in smoother films. When using 0.078M solution (Figure 4.19), however, the roughness values are almost independent of the inclination angles. This disagrees with findings of Pavlopoulos [147], for the films deposited from 0.078M at 650°C, who found that the RMS values decreased by increasing the inclination angle from zero to 10° and to 25° but they increased at 45°. The corresponding roughness values were 34, 12, 8 and 54 nm, respectively. He attributed the high roughness value at 45° to the formation of overgrown particles on the film surface. However, the findings of this work agrees with the findings of Ratcheva and Nanobva [241]. They found that in the case of In_2O_3:Te films prepared by spraying on Si substrates, no influence of the spraying angle on the grain growth rate and grain size was observed for two spraying angles, namely, 30° and 90°, and hence no influence on the roughness. Rachel E. Koritala et al [185] found for the case of biaxially textured MgO films deposited by ISD using e-beam evaporation on Hastelloy C substrates that high roughness values was obtained at low and high inclination angles and the lowest roughness values were obtained for inclination angles of 20°-55° where the roughness was not affected by the inclination angle in this range. In the present work, the roughness dependence (between 0.0078M and 0.078M) on the inclination angle can be attributed to the large difference in the used concentrations. At 0.0078M, the concentration was low enough that a small change in the inclination angle affects the aerosol delivery to the substrate leading to a roughness variation between 0° and 20° which is not the case when using 0.078M.

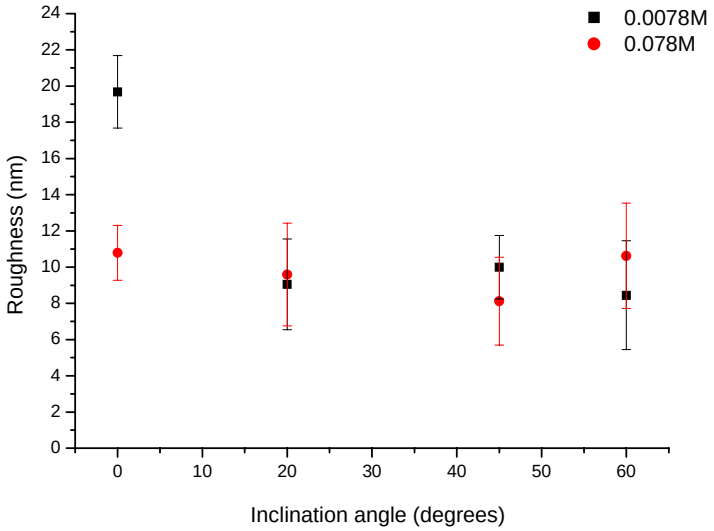

Figure 4.19: RMS roughness of the MgO films deposited at 650°C from 0.0078M and 0.078M $Mg(NO_3)_2.6H_2O$ solution.

Figure 4.20 to Figure 4.25 show the SEM images for the samples deposited from 0.0078M and 0.078M solutions at 650°C and at different inclination angles. At 0.0078M and with an inclination angle of 45°, more white particles can be seen throughout the surface which explains the slight increase in roughness compared to that at 20° and 60° (Figure 4.20-Figure 4.22). However, the surface morphology for the samples with MgO deposition using the 0.078M solution was almost the same regardless of the inclination angle, but a more homogenous surface is obtained with an inclination angle of 60° as can be seen from its SEM and AFM images, respectively (Figure 4.25 and Figure 4.26).

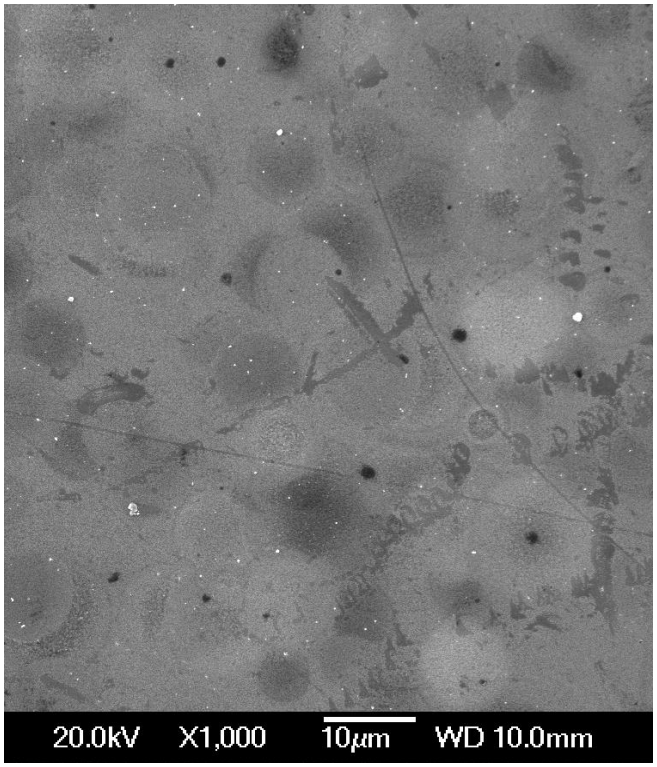

Figure 4.20: SEM image of the MgO film deposited at 650°C from a solution of 0.0078M at an inclination angle of 20°.

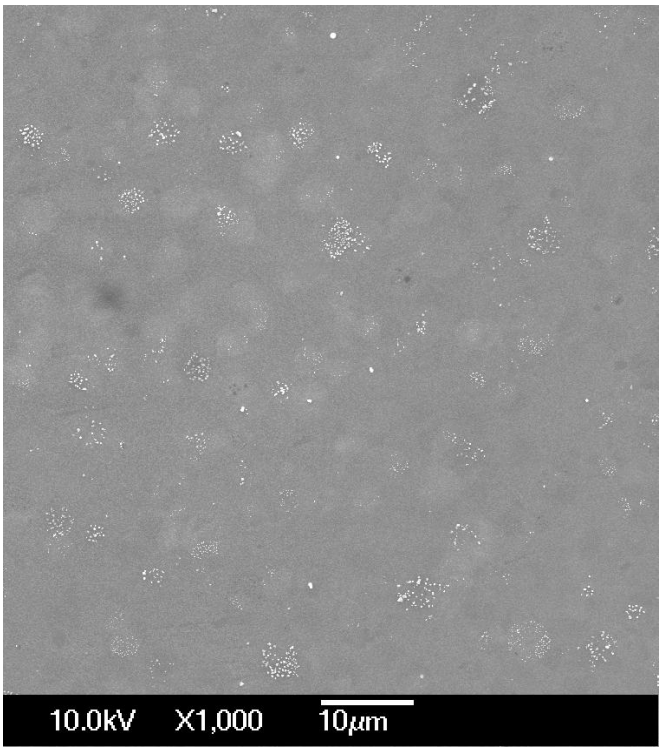

Figure 4.21: SEM image of the MgO film deposited at 650°C from a solution of 0.0078M at an inclination angle of 45°.

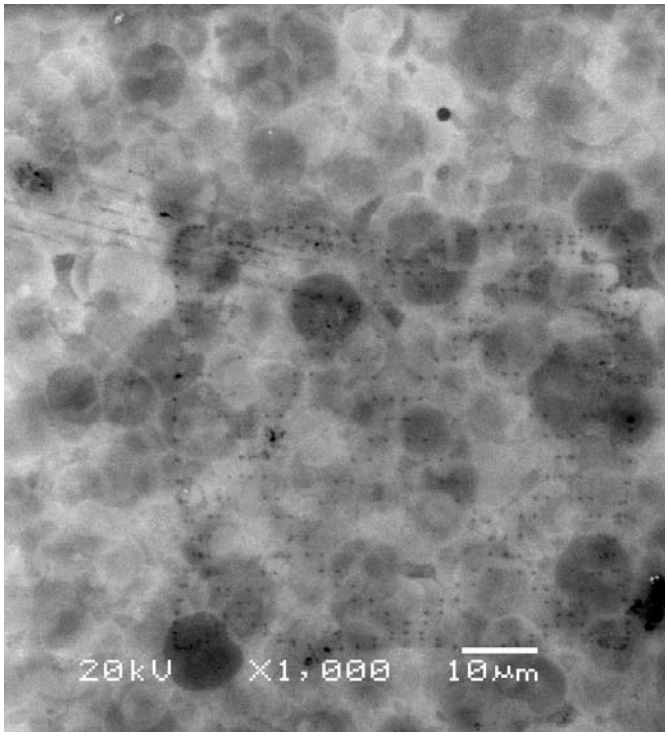

Figure 4.22: SEM image of the MgO film deposited at 650°C from a solution of 0.0078M at an inclination angle of 60°.

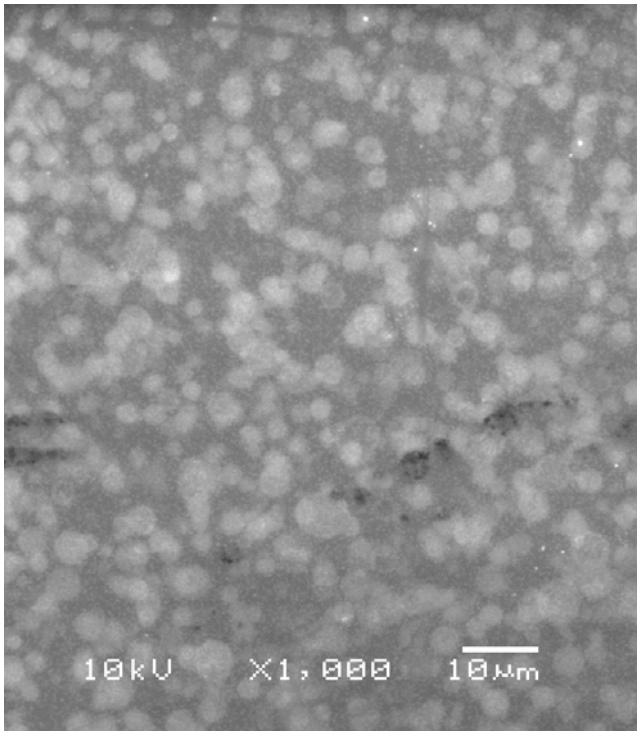

Figure 4.23: SEM image of the MgO film deposited at 650°C from a solution of 0.078M at an inclination angle of 20°.

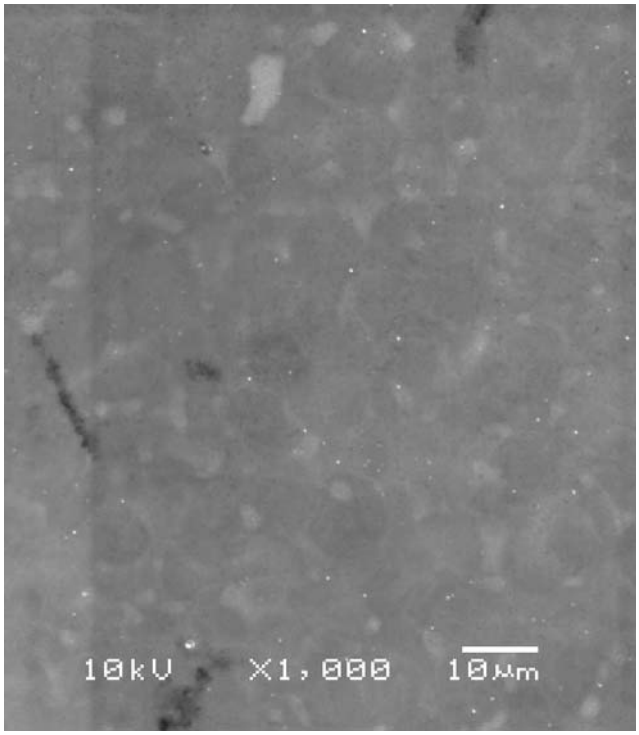

Figure 4.24: SEM image of the MgO film deposited at 650°C from a solution of 0.078M at an inclination angle of 45°.

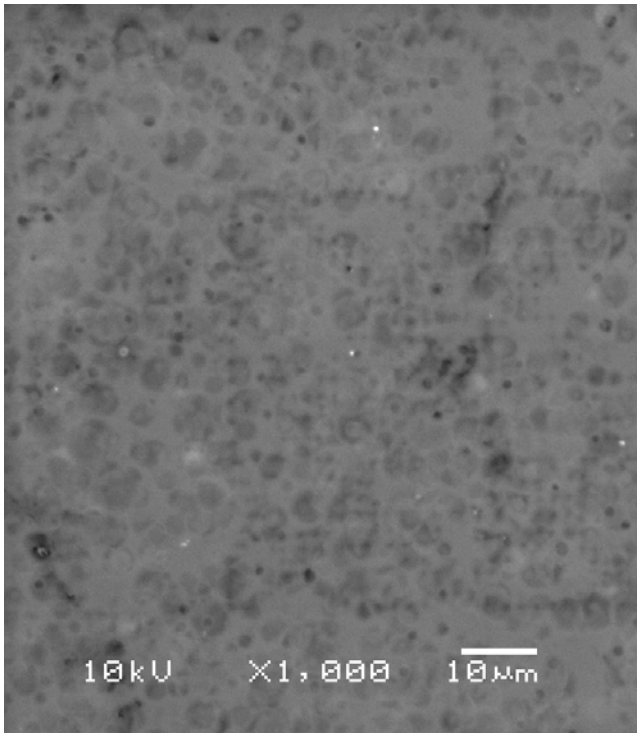

Figure 4.25: SEM image of the MgO film deposited at 650°C from a solution of 0.078M at an inclination angle of 60°.

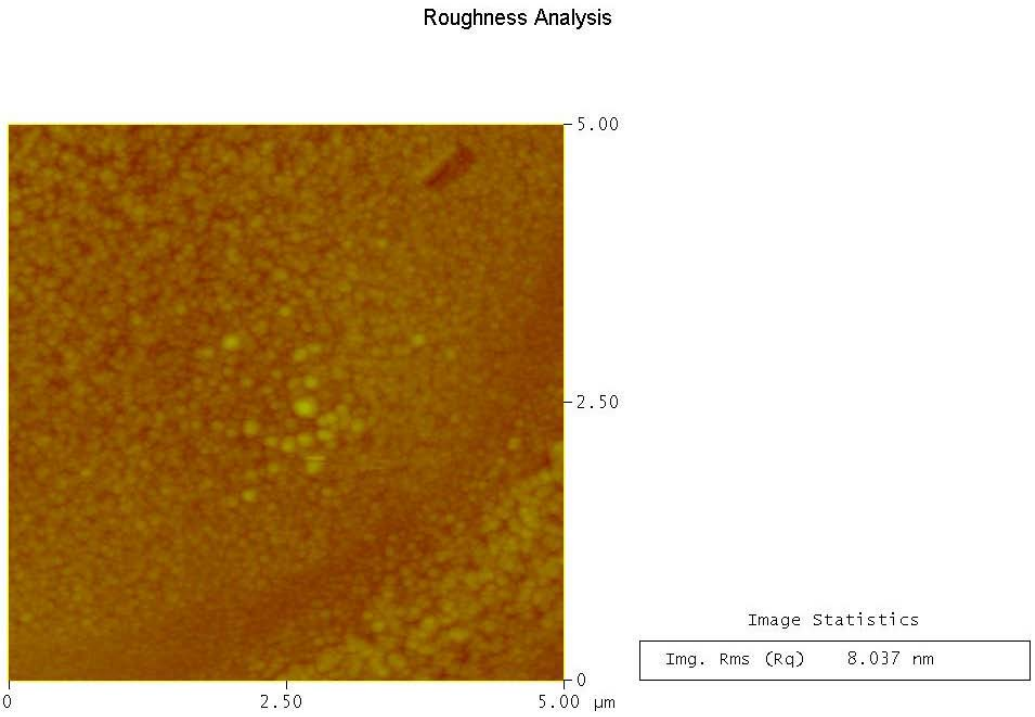

Figure 4.26: A 5x5µm^2 AFM image of the MgO film deposited at 650°C from a solution of 0.078M at an inclination angle of 60°.

The chemical analysis results for the MgO film deposited at 650°C from a solution of 0.078M at an inclination angle of 20° suggest a stoichiometric MgO film as was obtained for the MgO film deposited at zero inclination angle.

As was the case for the MgO film deposited at zero inclination angle, the film deposited at an inclination angle of 20° was grown with a (200) texture. From the X-ray pole figures in Figure 4.27 and Figure 4.28 it can be seen that MgO was not rotated during deposition and an in-plane texture along the a-b plane (in-plane) was obtained. Hence a cube-on-cube epitaxial relationship was obtained between MgO and Si.

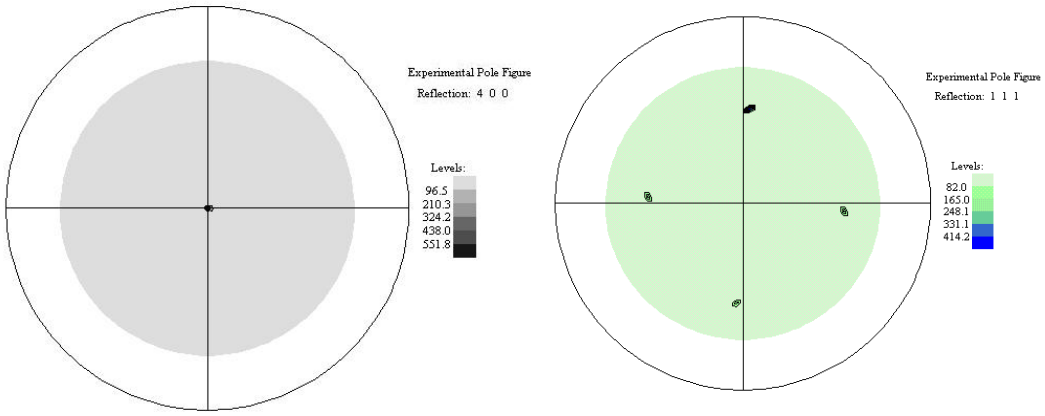

Figure 4.27: (400), left, and (111), right, X-ray pole figures, at 2θ of 69.17° and 28.42°, respectively, of Si (100) substrate deposited with MgO film at 650°C from a solution of 0.078M at an inclination angle of 20°.

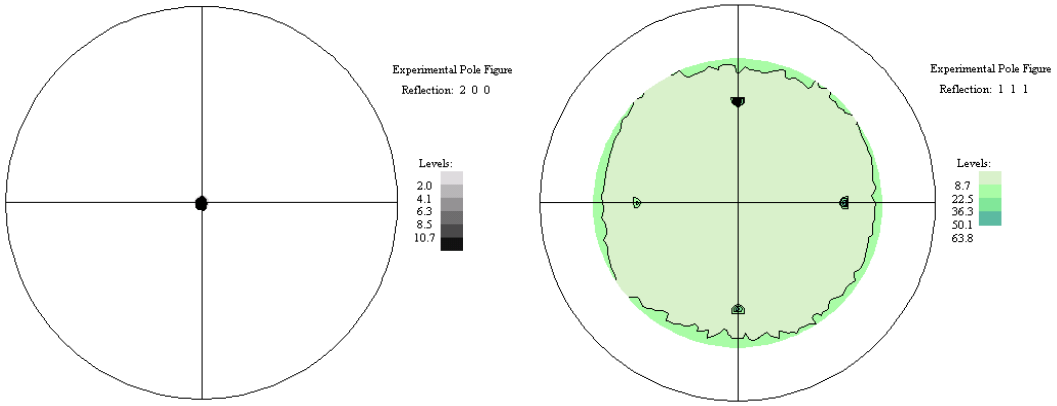

Figure 4.28: (200), left, and (111), right, X-ray pole figures, at 2θ of 43.82° and 36.93°, respectively, of the MgO film deposited at 650°C from a solution of 0.078M at an inclination angle of 20°.

Further investigation of the effect of the inclination angle on the properties of the MgO films was made at 700°C. The XRD patterns (Figure 4.29 and Figure 4.30) show that the films have a (200) texture with no tilt from the c-axis. The patterns for the films deposited at an angle of inclination of 60° show very weak intensity of the strained MgO (200) peaks compared to that with an inclination angle of 20° and 45°. At high substrate temperatures, the gas convection from the substrate pushes the droplets of the precursor away from it [65, 141]. This effect increased by increasing the inclination angle from 20° to 60°, regardless of the used concentration. This effect was also observed for films deposited at 650°C (Figure 4.17 and Figure 4.18) and the intensity increased with increasing the concentration as was the case at 650°C.

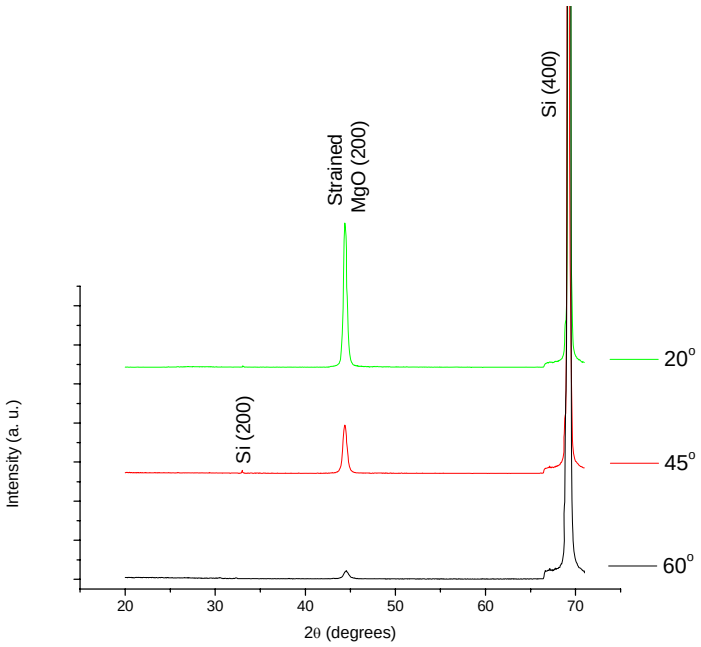

Figure 4.29: XRD patterns of the MgO films deposited at different inclination angles, at 700°C from a 0.0078M $Mg(NO_3)_2.6H_2O$ solution.

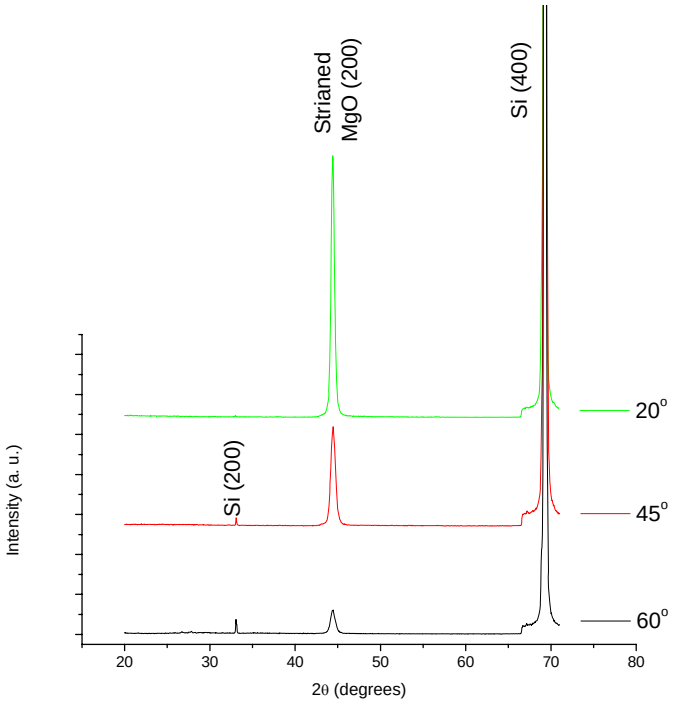

Figure 4.30: XRD patterns of the MgO films deposited at different inclination angles, at 700°C from a 0.078M $Mg(NO_3)_2.6H_2O$ solution.

The RMS values (Figure 4.31) show that the roughness, at 0.0078M and 0.078M, decreased by increasing the inclination angle from zero to 60°. Hence, in spray pyrolysis the ISD affects the crystallinity and roughness of the deposited MgO films. It can also be seen that the roughness values of the MgO films deposited at

0.078M were higher than those obtained from the 0.0078M solution, although the difference was not large. The mode of deposition at high temperature (700°C in this case) was recognised to be the fourth mode of deposition, where particles are deposited on the substrate instead of vapour of the precursor. In addition to that, the gas convection from the substrate pushing the droplets of the precursors away is increased at high temperature. This effect also increased by increasing the inclination angle. Therefore, a change in the deposition mode and pushing of the precursor away from the substrate at the high temperature led to this trend in the roughness values compared to that at 650°C.

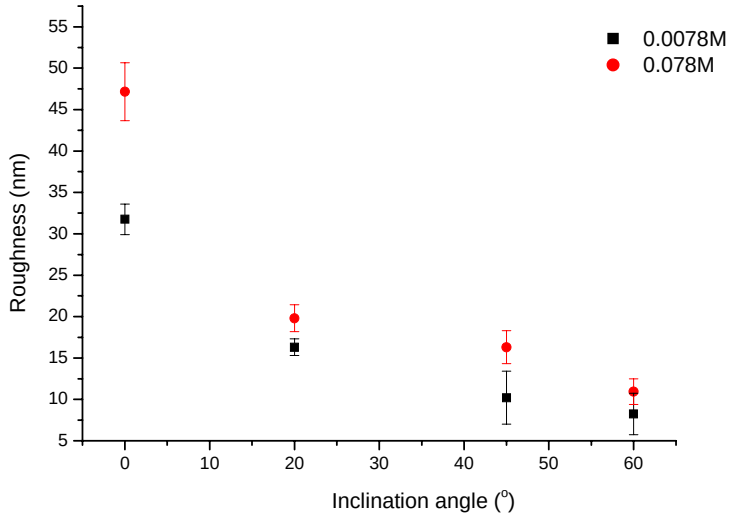

Figure 4.31: RMS roughness of the MgO films deposited at 700°C from 0.0078m and 0.078M $Mg(NO_3)_2.6H_2O$ solution.

The SEM images (Figure 4.32 to Figure 4.37) show that in almost all of the cases particles were formed on the surface of the substrate; this confirms that at 700°C the fourth mode of deposition is the dominant one.

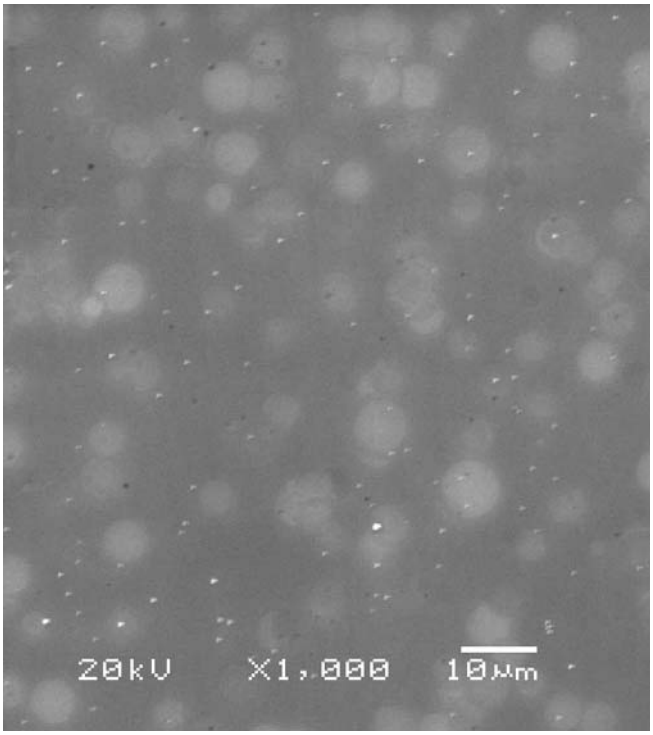

Figure 4.32: SEM image of the MgO film deposited at 700°C from a solution of 0.0078M at an inclination angle of 20°.

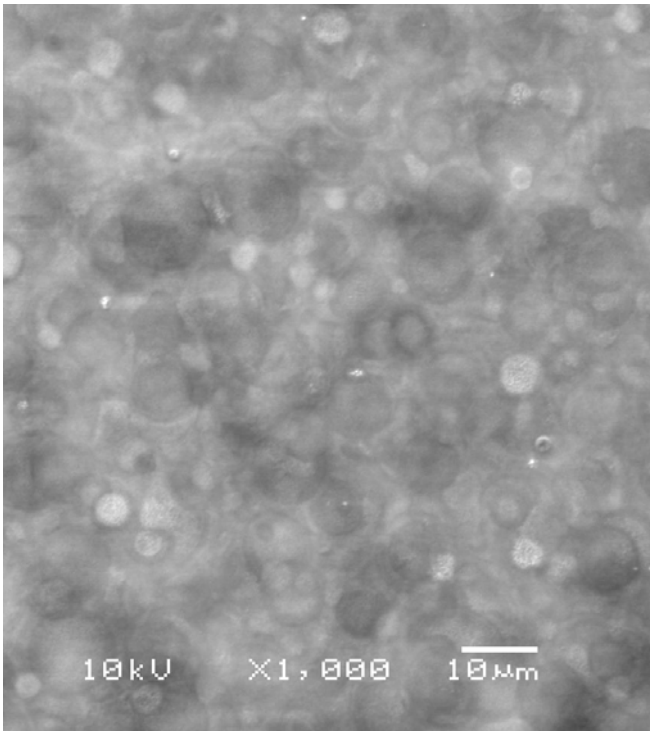

Figure 4.33: SEM image of the MgO film deposited at 700°C from a solution of 0.0078M at an inclination angle of 45°.

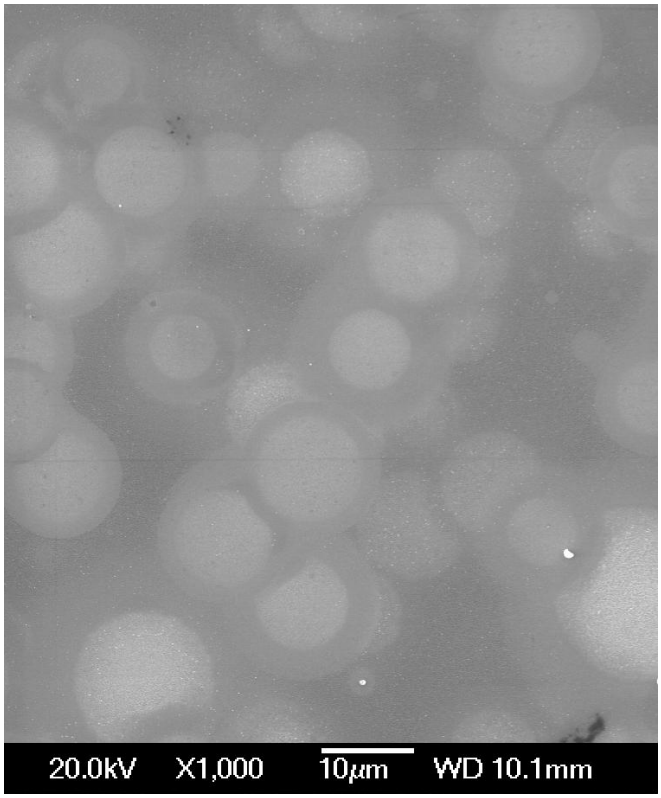

Figure 4.34: SEM image of the MgO film deposited at 700°C from a solution of 0.0078M at an inclination angle of 60°.

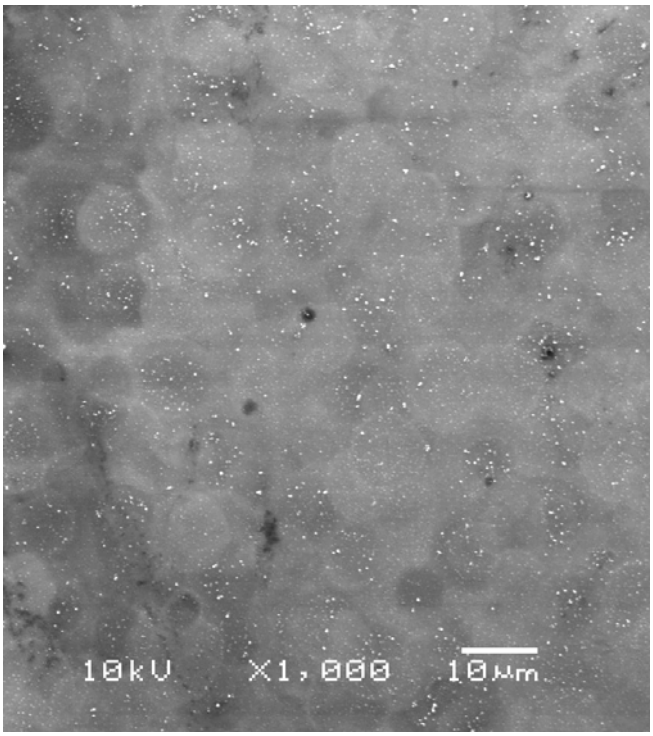

Figure 4.35: SEM image of the MgO film deposited at 700°C from a solution of 0.078M at an inclination angle of 20°.

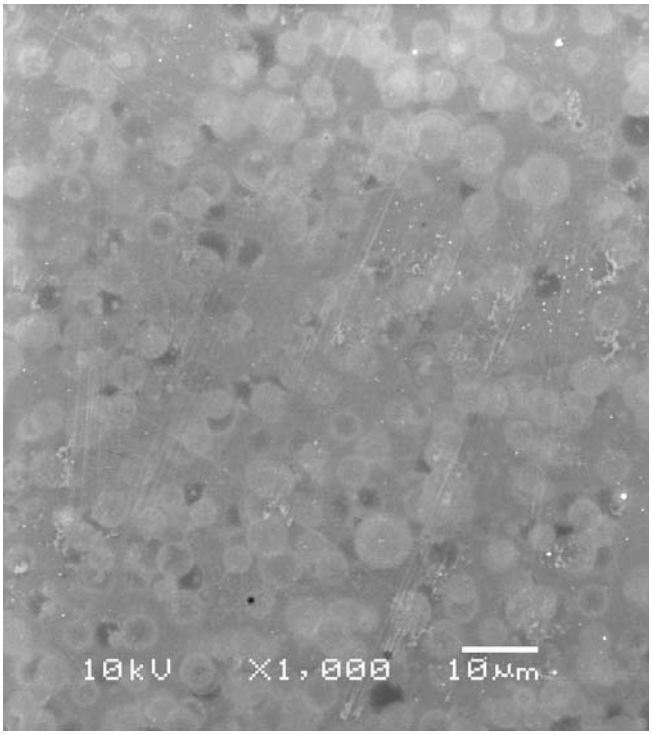

Figure 4.36: SEM image of the MgO film deposited at 700°C from a solution of 0.078M at an inclination angle of 45°.

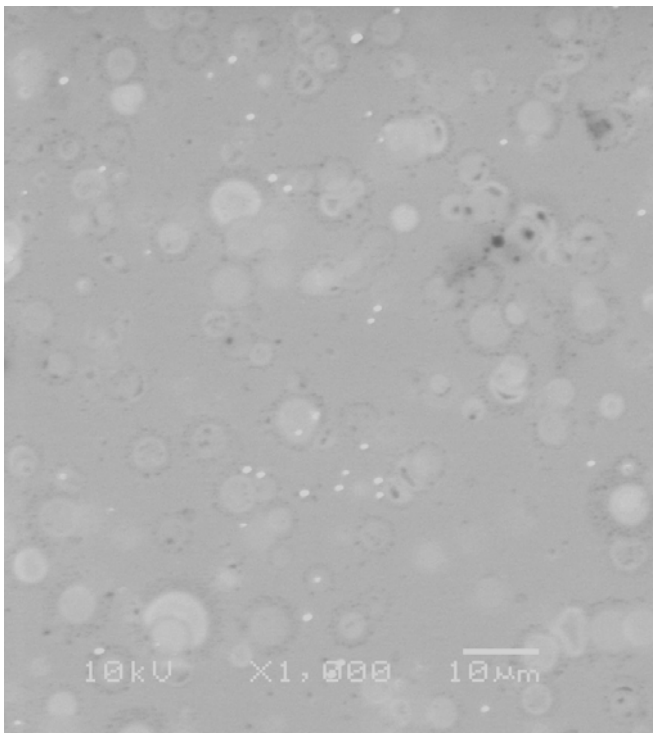

Figure 4.37: SEM image of the MgO film deposited at 700°C from a solution of 0.078M at an inclination angle of 60°.

Irrespective of the inclination angle and the used concentration, the deposited MgO films have almost 1:1 ratio of Mg:O as suggested from the EDX tests. Also the films have out-of-plane and in-plane texture. As an example, the X-ray pole figure for the MgO film deposited at 700°C from a solution of 0.078M at an inclination angle of 20° is shown in Figure 4.39 together with the X-ray pole figure of the Si substrate which is shown in Figure 4.38. The MgO film has a cube-on-cube texture relative to the Si substrate, where no rotation of the MgO film was noticed relative to the Si substrate to reduce the lattice mismatch.

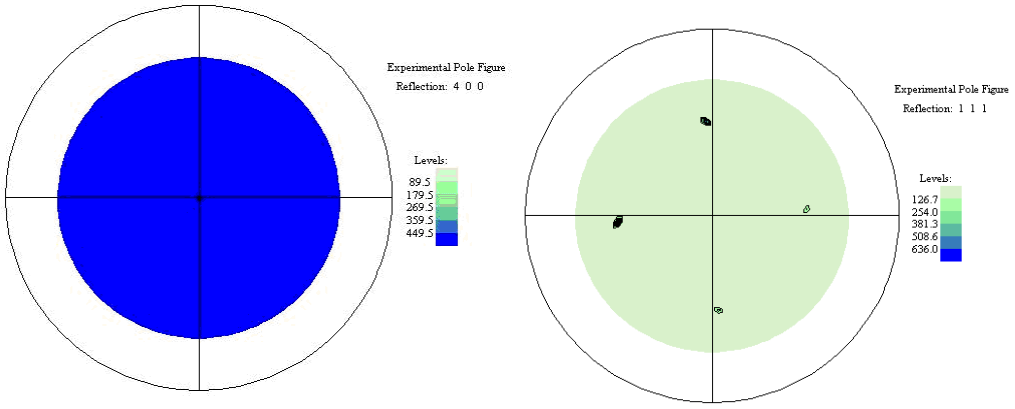

Figure 4.38: (400), left, and (111), right, X-ray pole figures, at 2θ of 69.17° and 28.42°, respectively, of Si (100) substrate deposited with MgO film at 700°C from a solution of 0.078M at an inclination angle of 20°.

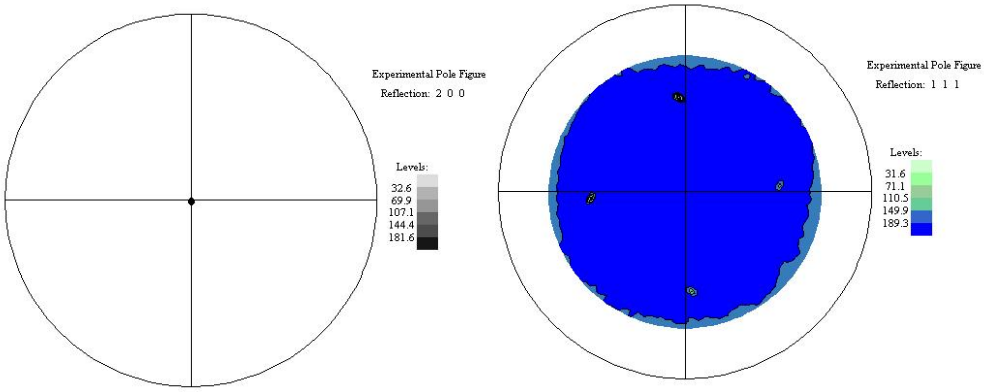

Figure 4.39: (200), left, and (111), right, X-ray pole figures, at 2θ of 43.96° and 36.93°, respectively of the MgO film deposited at 700°C from a solution of 0.078M at an inclination angle of 20°.

It is known that ISD deposition is applied, either by PLD or e-beam, to grow MgO thin films to improve the in plane texture for YBCO deposition. However, from Figure 4.17, Figure 4.18, Figure 4.29, and Figure 4.30, it can be seen that the MgO has only a (200) texture. This means that the ISD deposition by spray pyrolysis is not

giving the shadowing effect observed by others. In spray pyrolysis, the ISD is just affecting the crystallinity, roughness and thickness (as will be discussed in section 4.3.5) of the deposited MgO films.

4.3.5 Effect of deposition parameters on MgO film thickness

The thickness measurements were done by SEM on sample cross sections. It can be seen from Figure 4.40 that the thickness increased almost linearly with increasing the deposition temperature. It was also increased by increasing the precursor concentration. Figure 4.41 is a cross sectional SEM image of the MgO film deposited from 0.0078M solution at 600°C. The effect of the deposition temperature on the thickness of MgO and different films from different precursors were studied by others where different thickness dependencies were obtained [65, 114, 141, 142, 146, 147, 158, 159, 163, 164]. The reasons for increasing thickness with increasing temperature are many. The deposition rate, which is limited by the reaction kinetics process at or near the substrate surface, and the growth rate, which is limited by surface diffusion, both increase with increasing temperature and hence resulted in a thickness increase. Another explanation is due to the decomposition rate of the precursor which is higher at the higher temperature. The increase of the thickness with increasing the concentration was attributed to the growth rate, deposition rate was constant, where it was mass transport controlled; the reaction kinetics were so fast that the surface reaction finally becomes controlled by mass transfer of the reactants, and the concentration of the reactants on the surface was the limiting parameter. Other researchers also found that the thickness of different films increased with increasing the concentration due to similar reasons [147, 158, 160].

From the thickness measurements it can also be concluded that, for the same precursor concentration, the texture of the MgO films developed with thickness (Figure 4.2, Figure 4.3 and Figure 4.40). The thinner films obtained using the low concentration i.e. 0.0078M, showed reasonably textured MgO films but at higher temperatures. Therefore, the texture improves by increasing the thickness and the deposition temperature. However, quite thick films may not be strongly textured at low temperatures as was the case for the film deposited from 0.078M solution at 600°C. The texture dependence of MgO and different films on the deposition temperature and film thickness was investigated by others [72, 86, 141, 142, 146, 147, 159, 161, 162, 174, 183, 242, 243]. From Figure 4.40 it can be concluded that the

deposition rate depends on the deposition temperature and concentration. It ranged from 4.75Å/sec (114Å/240sec) for the film deposited from 0.0078M solution at 600°C to 33Å/sec for the film deposited from 0.078M solution at 700°C. The deposition rate for the film deposited from 0.078M solution at 650°C with zero inclination angle was about 30Å/sec.

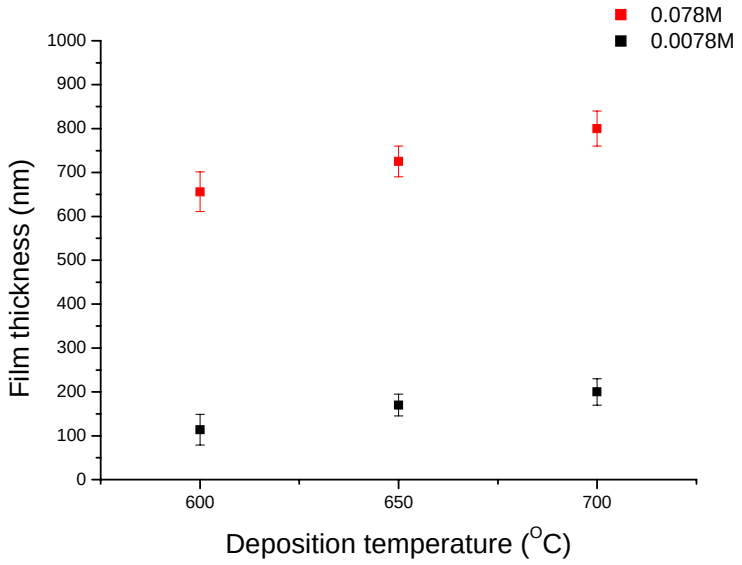

Figure 4.40: Effect of deposition temperature and precursor concentration on MgO film thicknesses deposited with zero inclination angle.

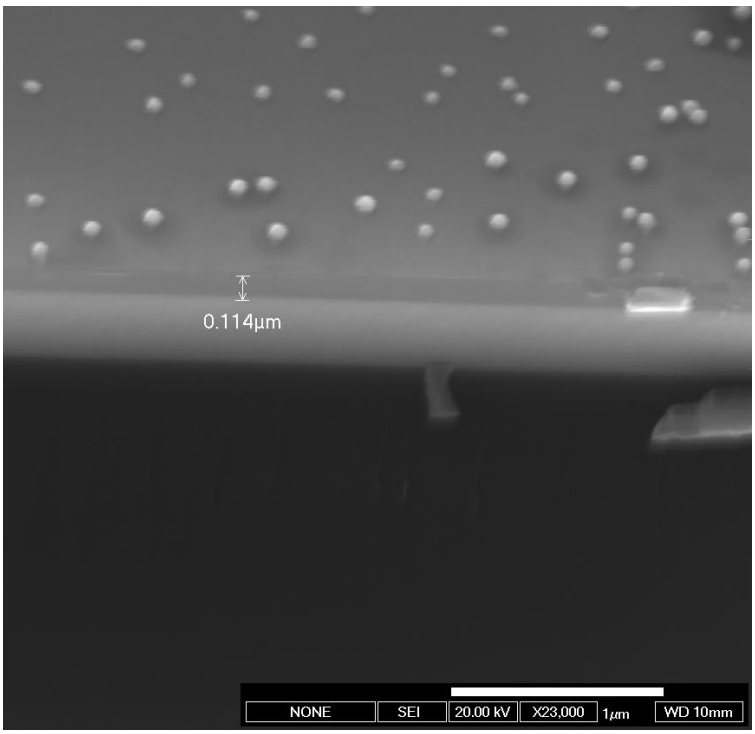

Figure 4.41: A cross sectional SEM image for MgO film deposited at 600°C from 0.0078M solution.

The effect of inclination angle on MgO film thicknesses was also studied. A cross sectional SEM image for the MgO film deposited at 650°C from 0.078M solution with an inclination angle of 45° is shown in Figure 4.42. Figure 4.43 shows that the film thickness, at 650°C, decreased with increasing the inclination angle irrespective of the used concentration. The higher the concentration and the lower the inclination angle resulted in thicker (Figure 4.43) and rougher (Figure 4.19) MgO films and the stronger the MgO (200) peaks i.e. better texture (Figure 4.17 and Figure 4.18). Similar thicknesses and observations were seen by Pavlopoulos D. [147] for the films deposited from 0.078M at 650°C who found that film thicknesses decreased almost linearly by increasing the inclination angle from 0° to 45°. The film prepared with no inclination angle was around 750nm while the thinnest film around 200nm was obtained when the inclination angle was set to 45^0 .Other researchers (using e-beam evaporation to deposit MgO films) found that the texture evolved faster and the films were thinner and rougher, due to the formation of voids and loose structure, at high inclination angles compared to that at lower inclination angles. They also found that the texture improved with thickness and with increasing the inclination angle [39, 41, 50, 169, 174, 175, 177, 180, 182, 183]. Rachel E. Koritala et al [185] found that, for MgO films deposited by e-beam on Hastelloy C276, the roughness increased with increasing thickness. High roughness values were also obtained at low and high inclination angles and the lowest roughness values were obtained for inclination angles of 20°-55° where the roughness was not affected by the inclination angle in this range. Develos et al [165] and Shigetoshi Ohshima et al [166] deposited CeO_2 films on Al_2O_3 films by PLD. They found that the surface roughness increased with increasing the film thickness.

Figure 4.44 shows the effect of inclination angle and precursor concentration on MgO film thicknesses at 700°C where it shows similar behaviour to those deposited at 650°C. Figure 4.45 is a cross sectional image for MgO film deposited at 700°C from 0.078M solution with an inclination angle of 20°.

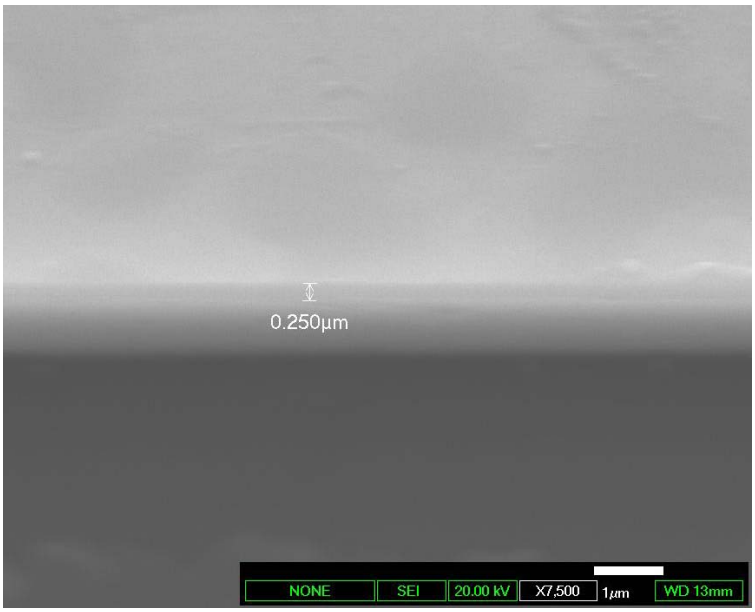

Figure 4.42: A cross sectional SEM image for MgO film deposited at 650°C from 0.078M solution with an inclination angle of 45°.

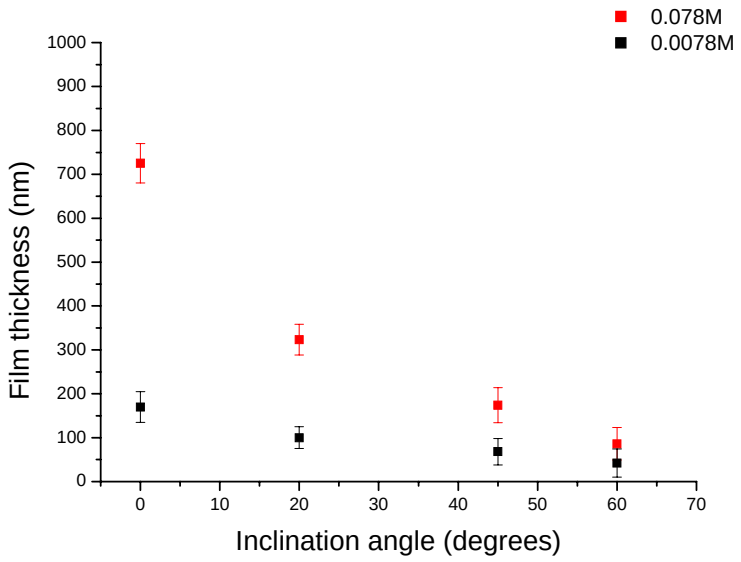

Figure 4.43: Effect of inclination angle and precursor concentration on MgO film thicknesses (at a deposition temperature of 650°C).

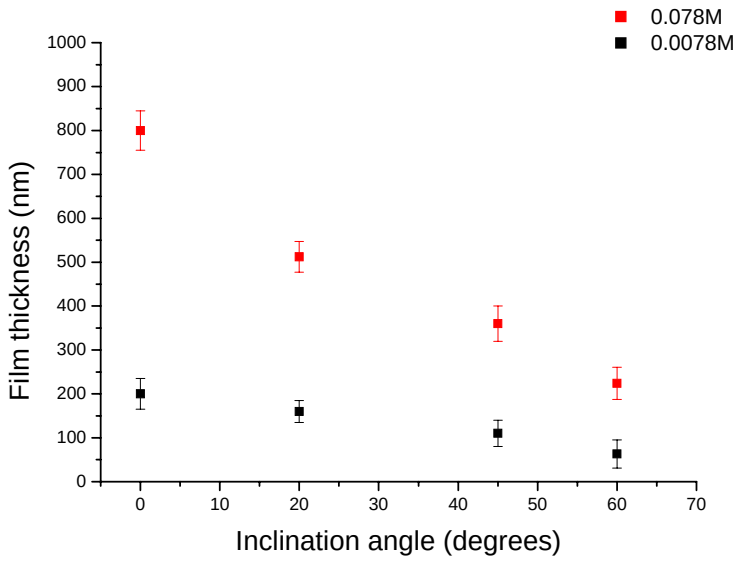

Figure 4.44: effect of inclination angle and precursor concentration on MgO film thicknesses (at a deposition temperature of 700°C).

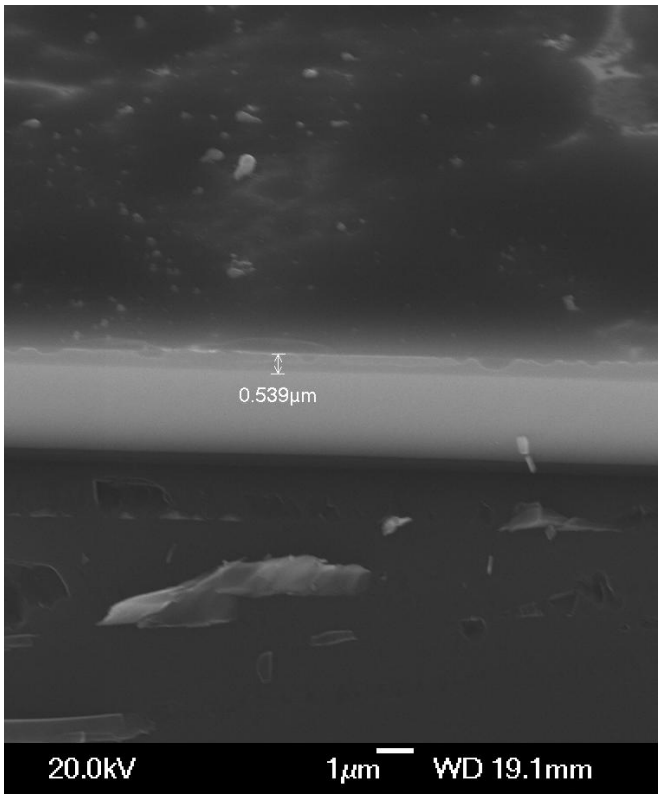

Figure 4.45: A cross sectional image for MgO film deposited at 700°C from 0.078M solution with an inclination angle of 20°.

4.4 MgO deposition by pulsed laser deposition on Si (100) substrates

To evaluate the quality of MgO films deposited by spray pyrolysis, PLD was used to deposit MgO films on the Si (100) substrates from MgO targets (99.95% purity bought from THEVA). An excimer laser with a wavelength of 248nm was utilised for the deposition. The MgO deposition parameters were:

- The deposition temperature: 750°C.
- Substrate target distance: 47mm.
- Deposition pressure: 0.13mbar (~ 0.1 torr) O_2.
- Energy fluence: 3.0-3.45 J/cm^2 (the energy of the beam was measured inside the deposition chamber prior to each deposition and the target was ground to a smooth finish before each deposition).
- Number of pulses 4000.
- Pulse frequency: 4Hz
- Heating and cooling rates: 20°C/min and 4°C/min, respectively.

The Si substrates were cleaned in acetone and ethanol then loaded in the deposition chamber; evacuation of the chamber was obtained by pumping down to $5x10^{-6}$ mbar ($3.75x10^{-6}$ torr), the target was then cleaned and conditioned with a 1000 laser pulses under vacuum with a shutter being positioned over the substrate. After heating to 750°C, the substrates were first deposited with MgO by 100 pulses under high vacuum to minimise the formation of silicon oxides; then 0.13mbar of oxygen was introduced. The deposition under high vacuum was made because the introduction of O_2 just before the deposition yields amorphous MgO layers [186]. This suggests that O_2 gas introduced before the deposition of MgO films forms an oxide layer on the substrate, which leads to the degradation of the crystallinity of the MgO films [186]. For comparison another MgO deposition was completely made under 0.13mbar oxygen pressure. Cooling of the substrate was under 0.7 bar O_2 which was introduced in the chamber over 8 minutes while maintaining the substrate temperature.

Figure 4.46 shows the XRD patterns for the MgO films deposited by PLD on Si (100) substrates at different energy fluencies and compared to the MgO film deposited by spray pyrolysis from 0.078M magnesium nitrate solution at 650°C with zero inclination angle. It was clear that the intensity of MgO increased by increasing the

laser energy fluence from 3 to 3.45J/cm^2. But still, the intensity of MgO was much lower compared to the MgO film deposited by spray pyrolysis. It can be seen however, that the MgO (200) peaks deposited by spray pyrolysis were shifted towards higher 2θ angles (43.9°) due to the strain as was discussed before. In contrast, the MgO peaks for the films deposited by PLD were strained to a lesser extent (43.15°) when compared to the JCPDS PDF files 00-045-0946. This was due to the cooling procedure applied. During spray pyrolysis, the samples were left to be furnace cooled after the deposition where the tubular furnace was open to the atmosphere and this would cool the sample quite rapidly at the beginning, which gives rise to thermal strains and hence a shift in the peaks. However, in the PLD deposition, the samples were cooled in a closed system under controlled rate which may reduce the effect of the thermal strains.

On the one hand, the MgO films deposited on Si (100) by PLD using an energy fluence of 3.45J/cm^2 was a little smoother (Figure 4.47 and Figure 4.48) compared to the MgO film spray pyrolysed at 650°C from 0.078M magnesium nitrate solution (Figure 4.5 and Figure 4.9). On the other hand, the texture of the MgO film deposited by spray pyrolysis had a well defined in-plane and out of-plane-texture (Figure 4.16) in contrast to the MgO film deposited by PLD which had a good out-of-plane texture but no in-plane texture (Figure 4.49).

It is to be mentioned that the MgO films with the first 100 pulses deposited under high vacuum, and the rest of pulses under 0.13mbar, were the same as the films deposited completely under 0.13mbar in terms of the MgO (200) peak intensities. The reason for having the low intensity peaks of MgO (200) deposited by PLD was the low fluence used. The system used in this work for PLD deposition operates with excimer laser with a wavelength of 248nm and this makes it difficult to get energy fluence higher than 3.45J/cm^2 even by changing the laser path, reducing the spot size as much as possible and by using new lenses and mirrors. However, other researchers were using an ArF laser with a wavelength of 193nm which have high optical absorption coefficient for MgO and using a fluence of 4-7J/cm^2 which is more efficient in depositing MgO films [186, 187].

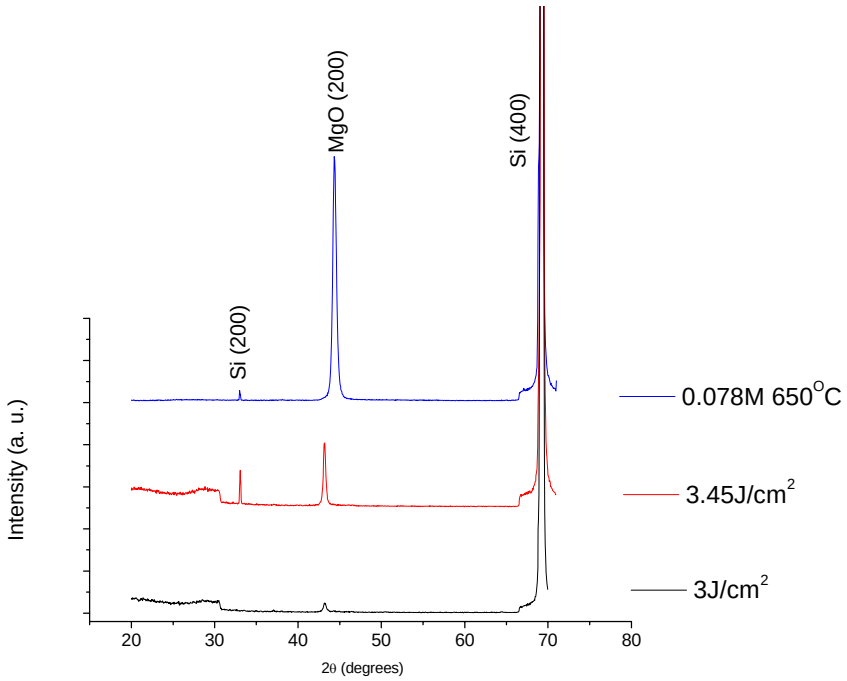

Figure 4.46: XRD patterns for MgO deposition on Si (100) substrate by PLD at different fluencies and compared to MgO deposition by spray pyrolysis using 0.078M of magnesium nitrate at 650°C with zero inclination angle.

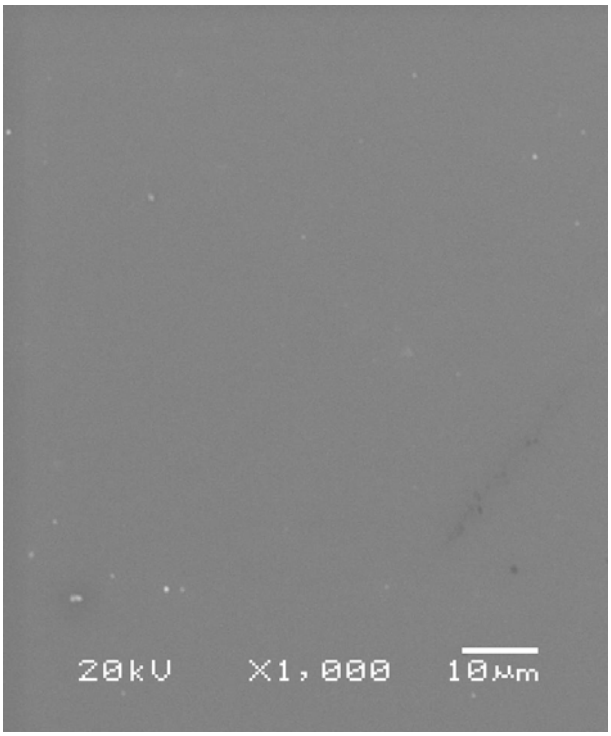

Figure 4.47: SEM image for MgO film deposited by PLD on Si (100) at an energy fluence of 3.45J/cm^2.

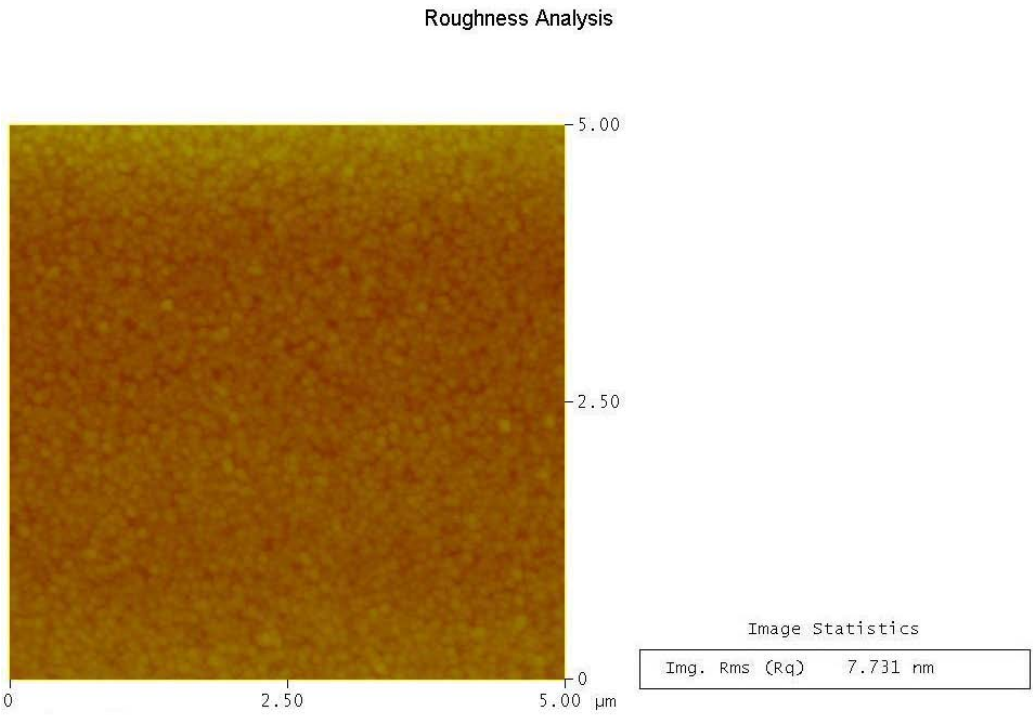

Figure 4.48: A 5x5µm^2 AFM image for MgO film deposited by PLD on Si (100) at an energy fluence of 3.45J/cm^2.

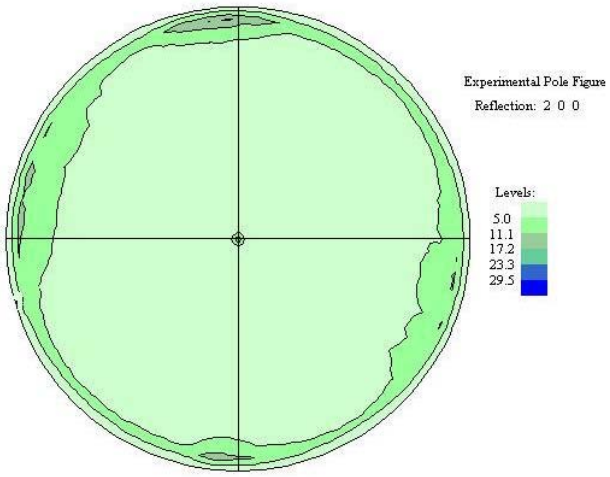

Figure 4.49: (200) X-ray pole figure at 2θ=43.10° of the MgO film deposited by PLD on Si (100) at an energy fluence of 3.45J/cm^2.

4.5 Optimisation of YBCO deposition parameters

To evaluate the performance of the spray pyrolysed MgO films as a buffer, YBCO films were deposited by PLD on top of them. This is a well established route to high quality films [244, 245], although spray pyrolysis of the YBCO layer should also be a possibility in the future [23, 24, 87, 93, 94].

YBCO deposition by PLD needs to be optimised, for this purpose, YBCO deposition on MgO single crystals was utilised before depositing YBCO by PLD on MgO films deposited either by spray pyrolysis or by PLD. The MgO single crystals are (h00) oriented (Figure 4.50). They have an RMS of about 1.5nm (Figure 4.51 and Figure 4.52). Figure 4.53 shows the EBSD pole figure patterns for the MgO single crystal. It is clear that it is biaxially textured. The out-of-plane and in-plane texture were quantitatively measured by the rocking curve (ω-scan) (Figure 4.54) and phi scan (Figure 4.55), respectively. The FWHM was 0.025° for the out of plane-texture and 0.038° for the in-plane-texture.

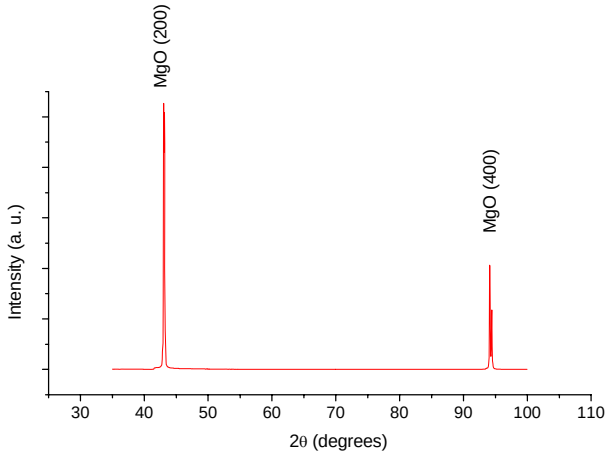

Figure 4.50: XRD pattern of the as received MgO single crystal.

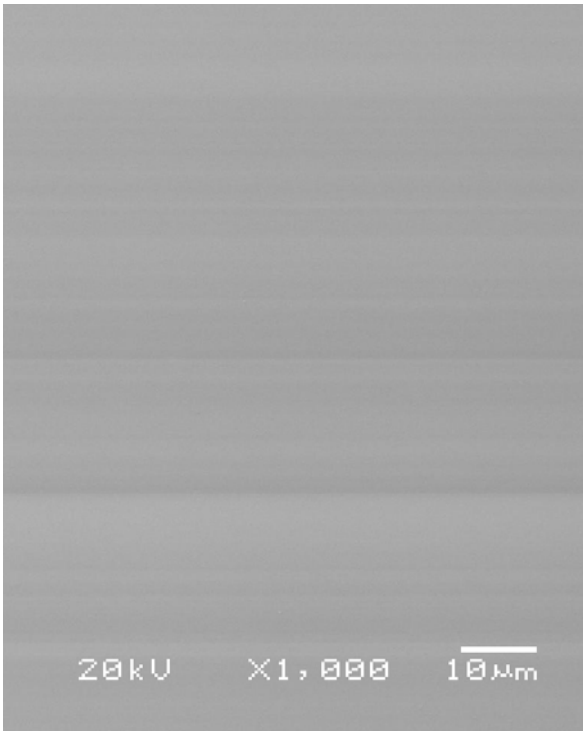

Figure 4.51: SEM image of the as received MgO single crystal.

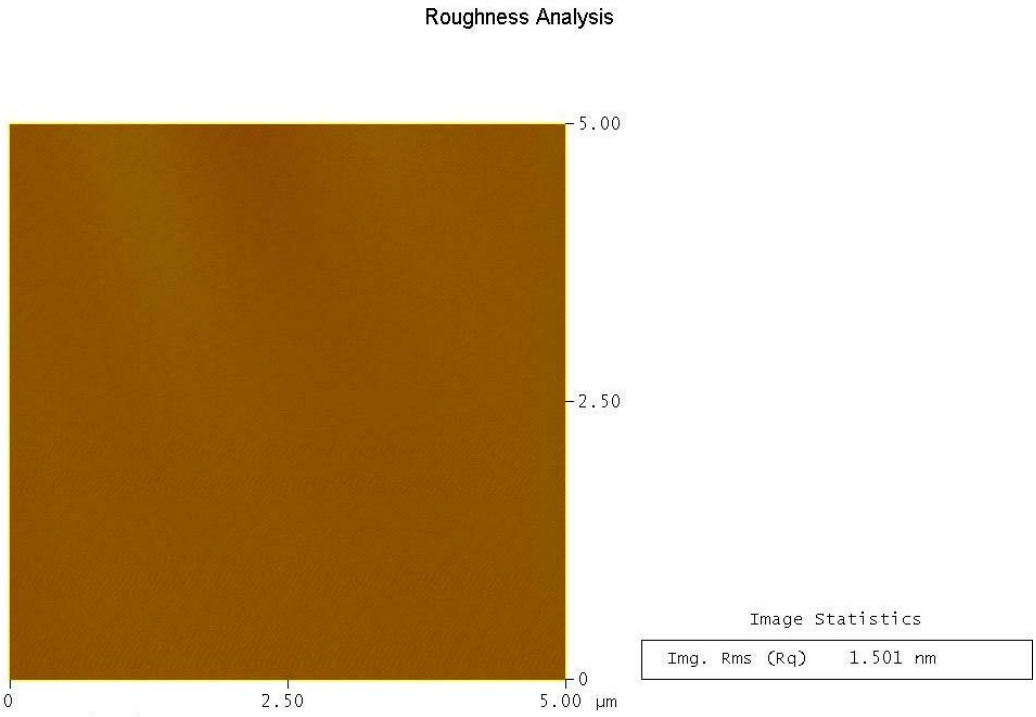

Figure 4.52: A 5x5µm^2 AFM image of the as received MgO single crystal.

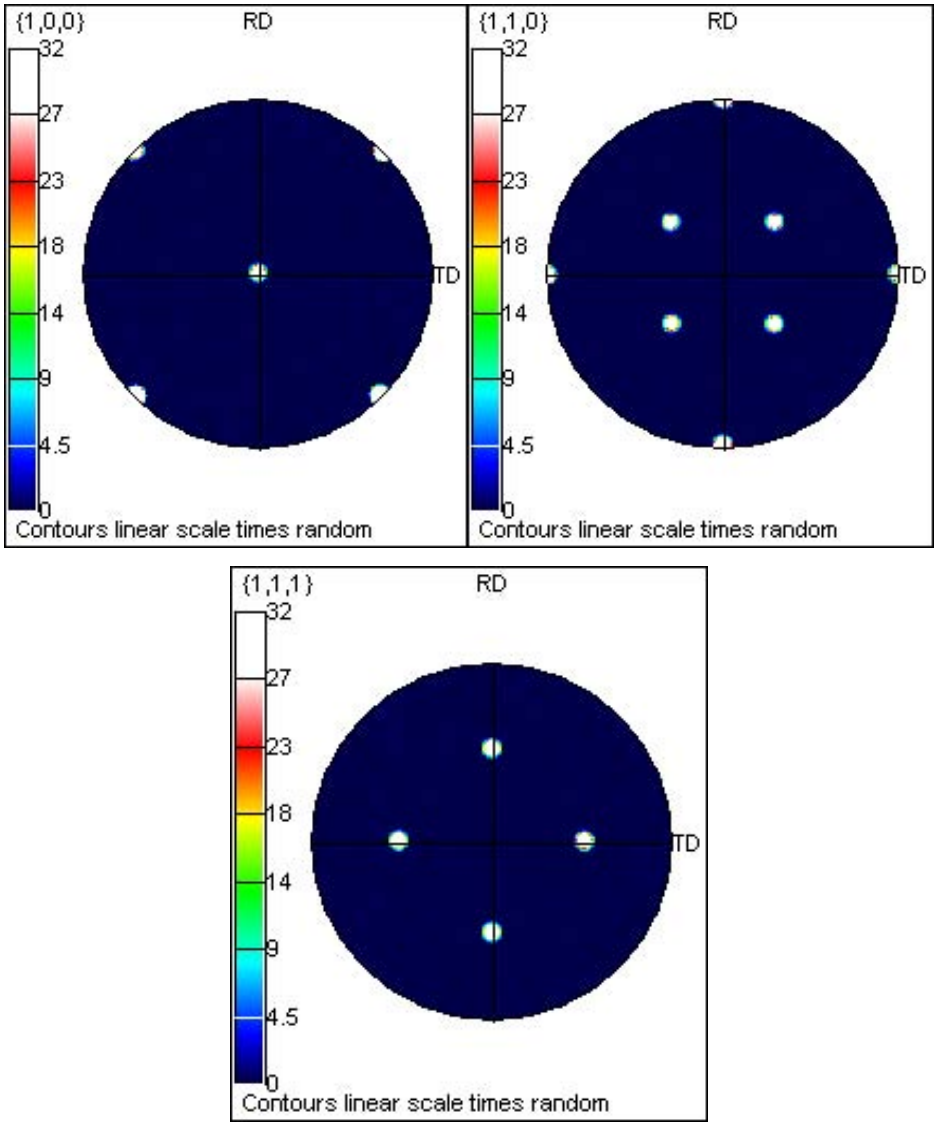

Figure 4.53: EBSD pole figure patterns for MgO single crystal showing the MgO {100}, {110} and {111} planes.

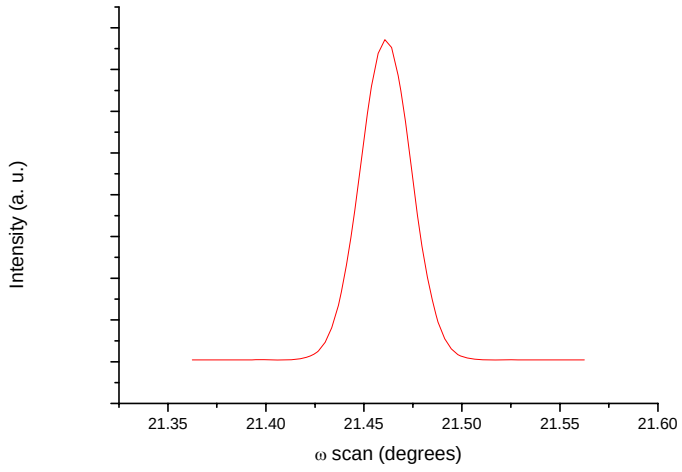

Figure 4.54: X-ray diffraction ω–scan for MgO (200) with a FWHM of 0.025°.

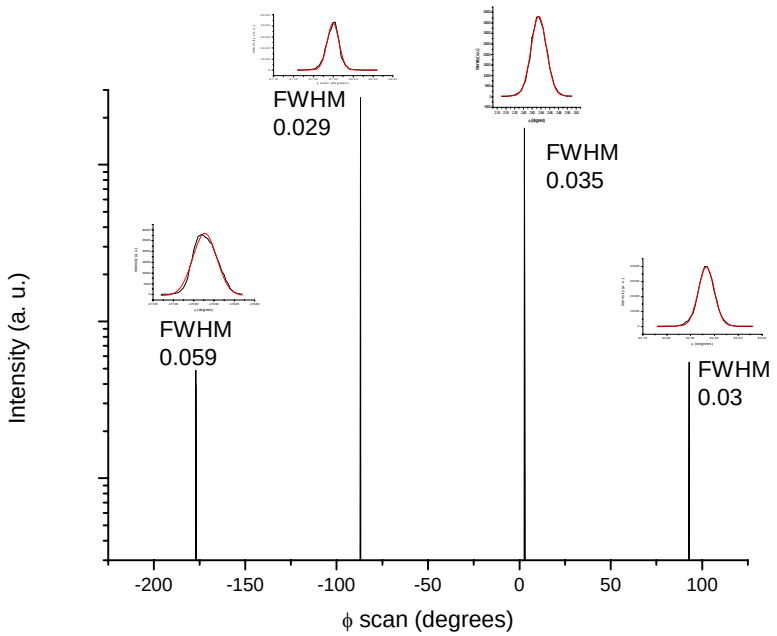

Figure 4.55: X-ray diffraction Φ–scan for MgO (220) with a FWHM of about 0.038°.

4.5.1 YBCO deposition by pulsed laser deposition on MgO single crystals

YBCO was deposited on MgO single crystals using different fluencies (J/cm^2) and different number of pulses (i.e. different thicknesses) under 450 mtorr O_2 which was utilized during deposition. The deposition temperature was 780°C, the heating and cooling rates were 20°C/min and 10°C/min, respectively. The target-substrate distance was fixed at 56mm and the used pulse frequency was 4Hz.

Figure 4.56 shows the XRD patterns for YBCO films deposited on MgO single crystals at 2 and 2.75J/cm^2 and using 2000, 5000 and 10000 pulses. The MgO and YBCO peaks were indexed according to the JCPDS PDF files 00-045-0946 and 00-038-1433, respectively. YBCO has an orthorhombic structure with lattice parameters of a= 3.8185Å, b=3.8856Å and c=11.6804Å according to the JCPDS PDF file 00-038-1433. The (001), (002), (003), (004), (005), (006), (007), (103), (113), (115), (116) are at 2θs of 7.55°, 15.17°, 22.83°, 30.62°, 38.51°, 46.63°, 54.99°, 32.89°, 40.38°, 51.49°, 58.21°, respectively. The thermal expansion coefficient of YBCO is 13.0-13.4x10^{-6}/K [95, 246]. It can be seen that all of the YBCO films are 00l oriented with the (006) peak being the strongest. A log scale pattern for YBCO films (Figure 4.57) shows the formation of a weak YBCO (103) peak which was believed to be a nucleation problem during YBCO deposition.

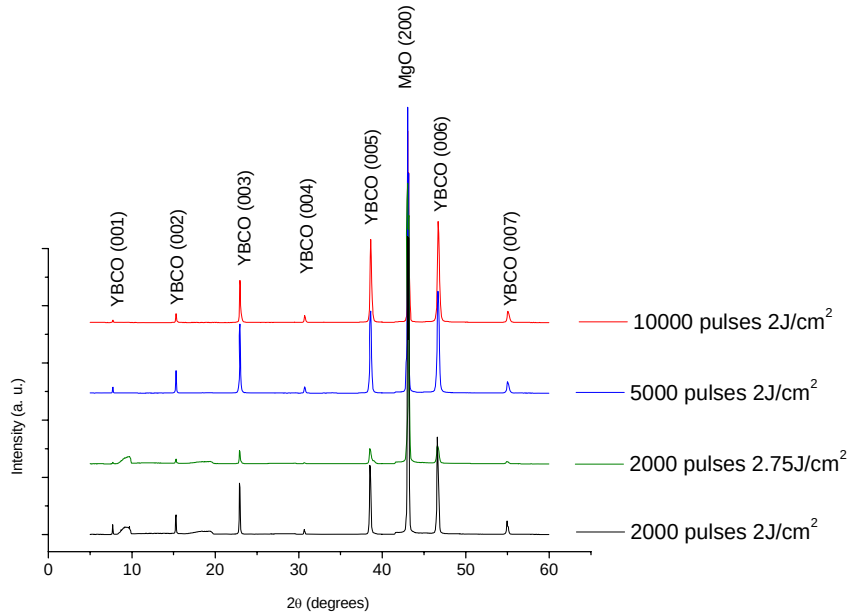

Figure 4.56: XRD patterns for YBCO films deposited on MgO single crystal using different number of pulses and different fluencies.

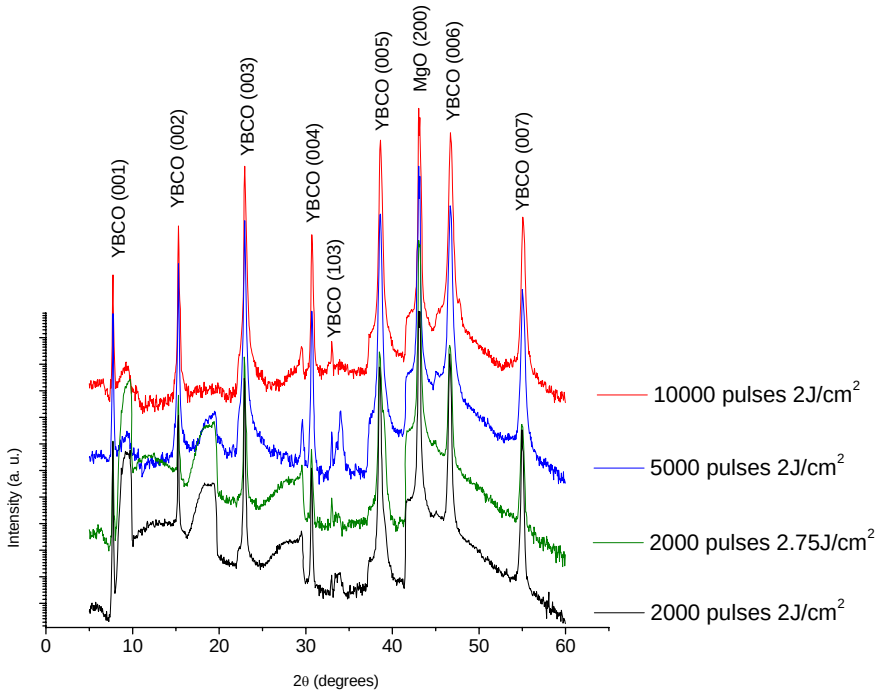

Figure 4.57: XRD patterns in log scale for YBCO films deposited on MgO single crystal using different number of pulses and different fluencies.

The films deposited with 2000 pulses show that the intensity of YBCO (006) decreased with increasing the fluence from 2 to 2.75J/cm^2. At high fluence, more

material should be ablated from the target; this may also be combined by the formation of molten droplets or particulates which makes the ablation process less efficient and affects the film quality [245, 247-249] where it may affect the nucleation and growth process, hence disturbing the texture of the YBCO film. The SEM and AFM images (Figure 4.58-Figure 4.61) show that the films are porous and that the roughness increased by increasing the fluence from 2.0-2.75 J/cm^2. Such porous films were noticed by others where it was attributed to the formation of Y_2O_3 precipitates or yttrium rich secondary phase i.e. BaY_2O_4 [208, 209, 212].

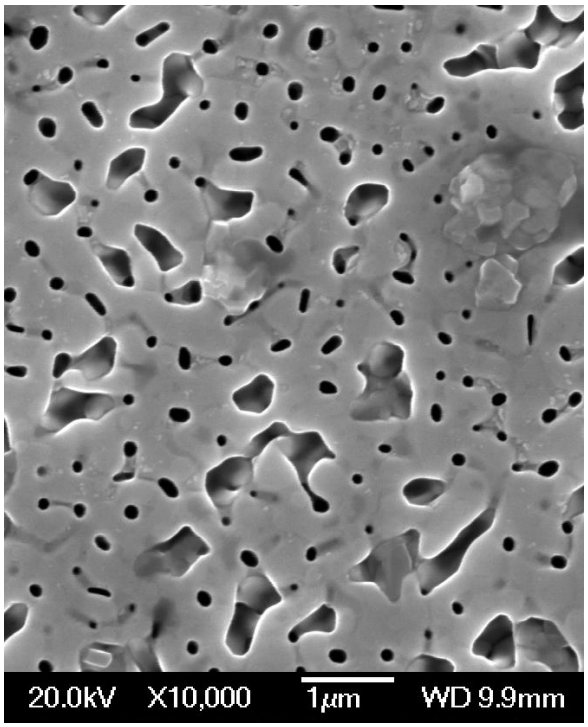

Figure 4.58: SEM image for a 2000 pulses YBCO film deposited on MgO single crystal using a fluence of 2 J/cm^2.

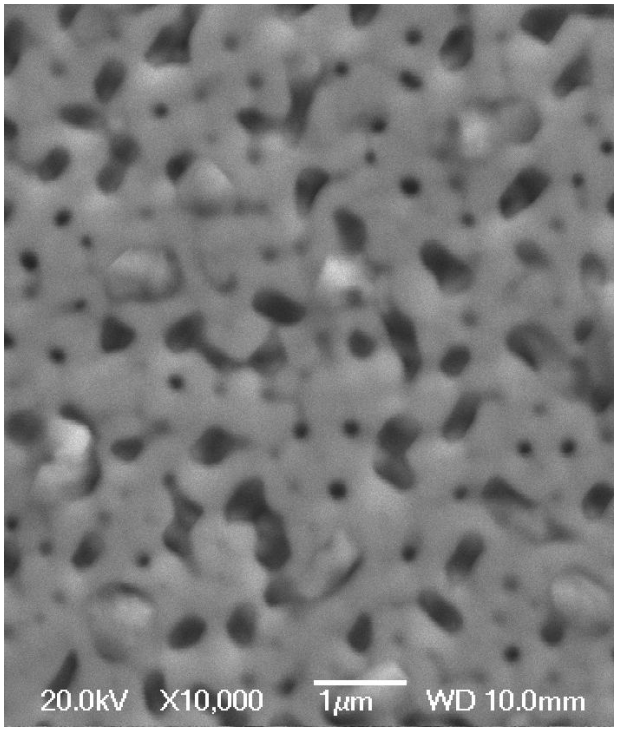

Figure 4.59: SEM image for a 2000 pulses YBCO film deposited on MgO single crystal using a fluence of 2.75 J/cm^2.

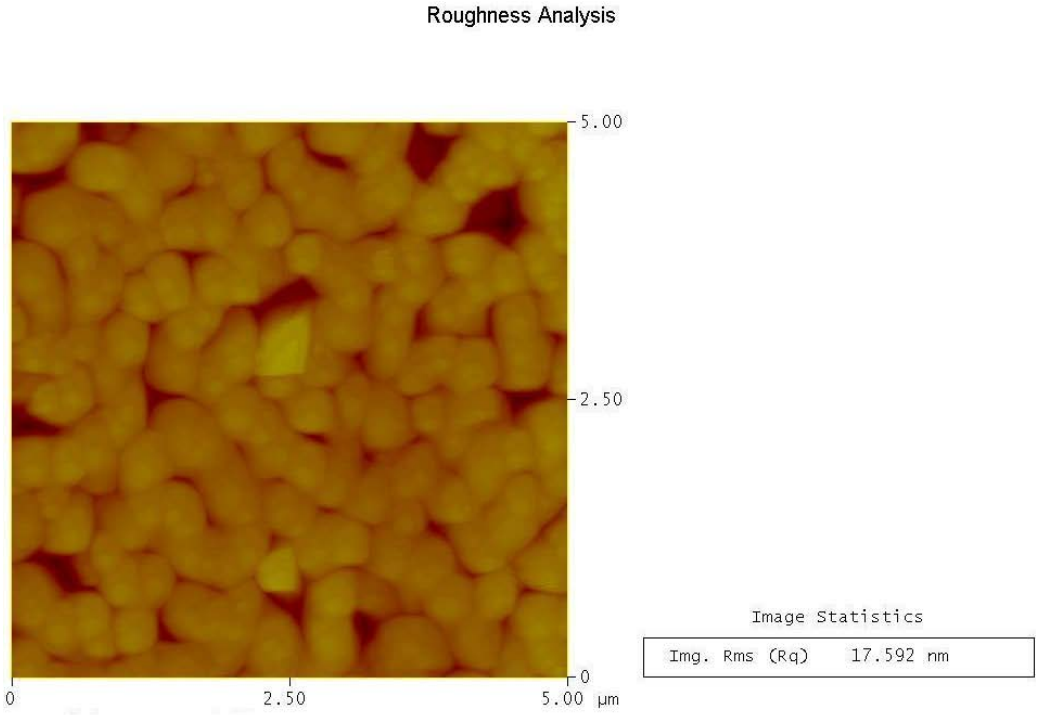

Figure 4.60: A 5x5μm^2 AFM image for a 2000 pulses YBCO film deposited on MgO single crystal using a fluence of 2 J/cm^2.

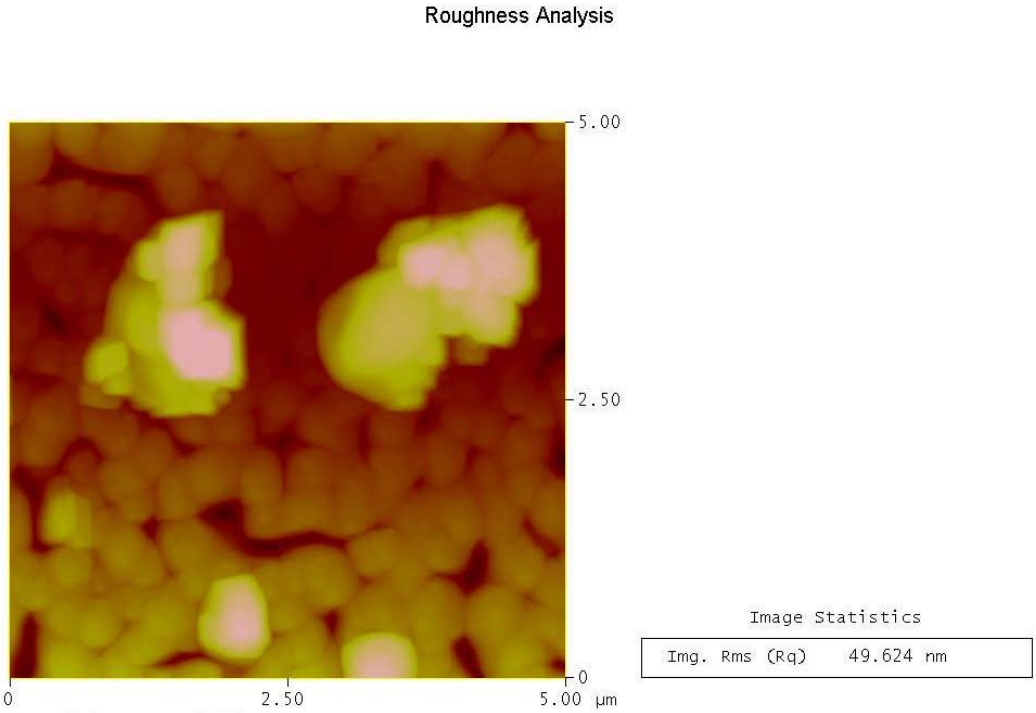

Figure 4.61: A 5x5µm^2 AFM image for a 2000 pulses YBCO film deposited on MgO single crystal using a fluence of 2.75 J/cm^2.

Both of the YBCO films deposited using 2000 pulses have a well defined in-plane and out-of-plane texture as can be seen from the EBSD pole figure patterns in Figure 4.62 and Figure 4.63. However, large grain misorientation in the film deposited using 2.75 J/cm^2 (Figure 4.65) was worse compared to the film deposited using 2 J/cm^2 (Figure 4.64). Large grain misorientation is known to affect the superconducting properties [30, 197, 198, 205-207].

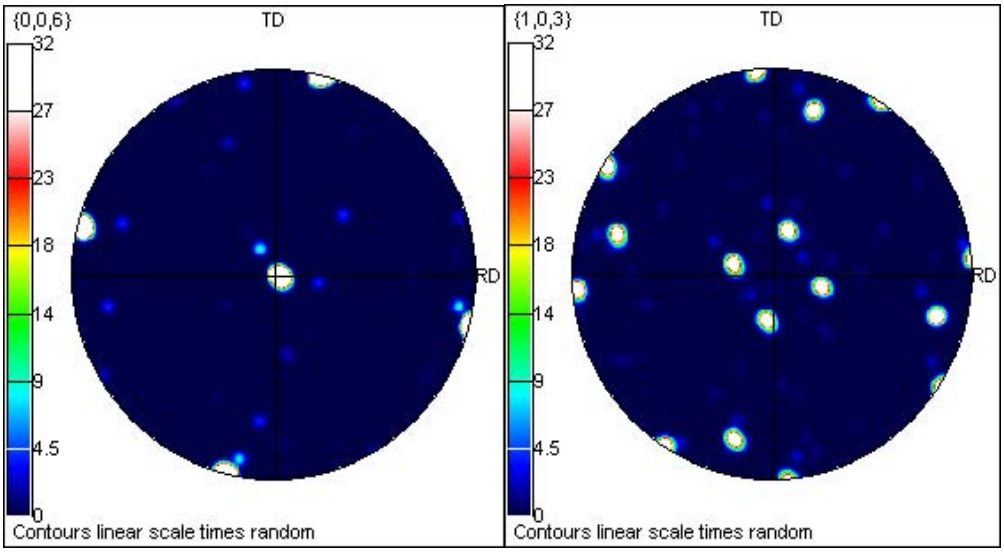

Figure 4.62: EBSD pole figure patterns for a 2000 pulses YBCO film deposited on MgO single crystal using a fluence of 2 J/cm^2 showing the YBCO {006} and {103} planes.

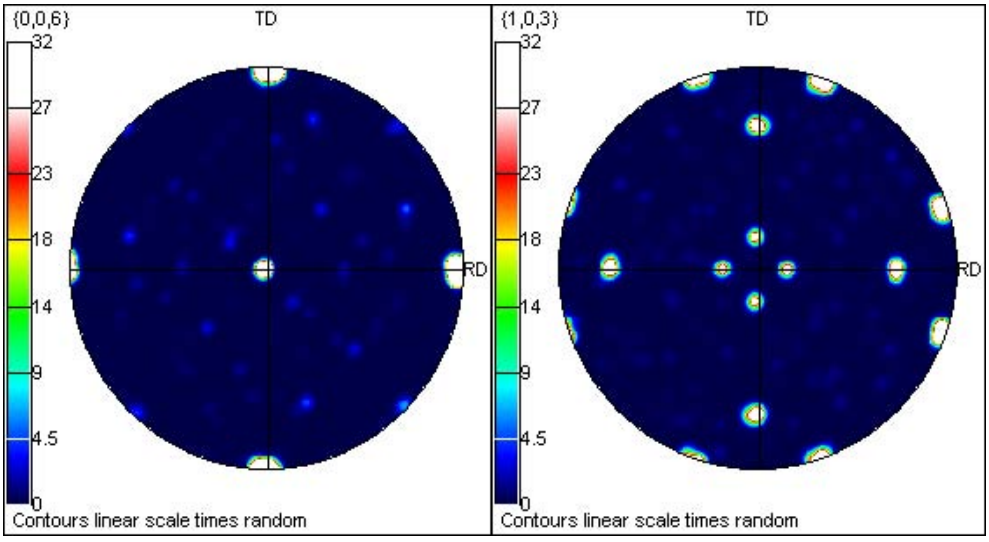

Figure 4.63: EBSD pole figure patterns for a 2000 pulses YBCO film deposited on MgO single crystal using a fluence of 2.75 J/cm^2 showing the YBCO {006} and {103} planes.

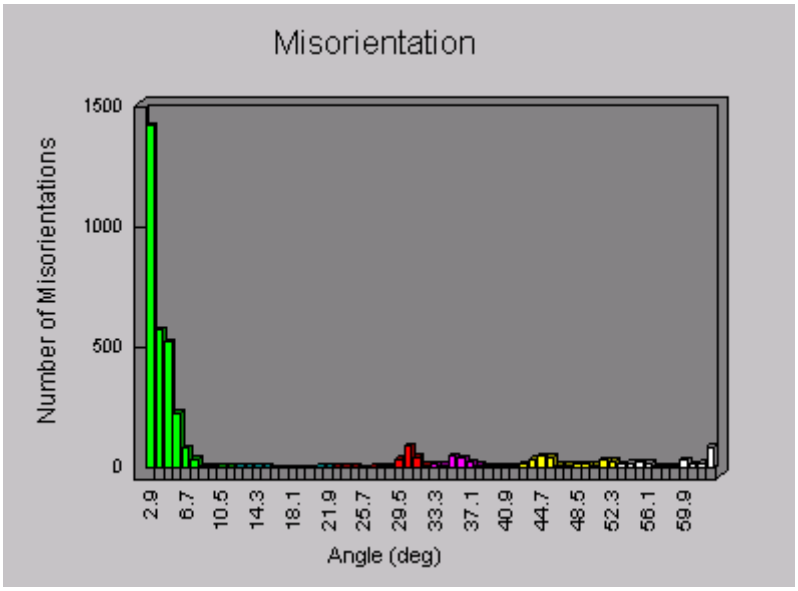

Figure 4.64: EBSD histogram for a 2000 pulses YBCO film deposited on MgO single crystal using a fluence of 2J/cm^2 showing misorientation angles.

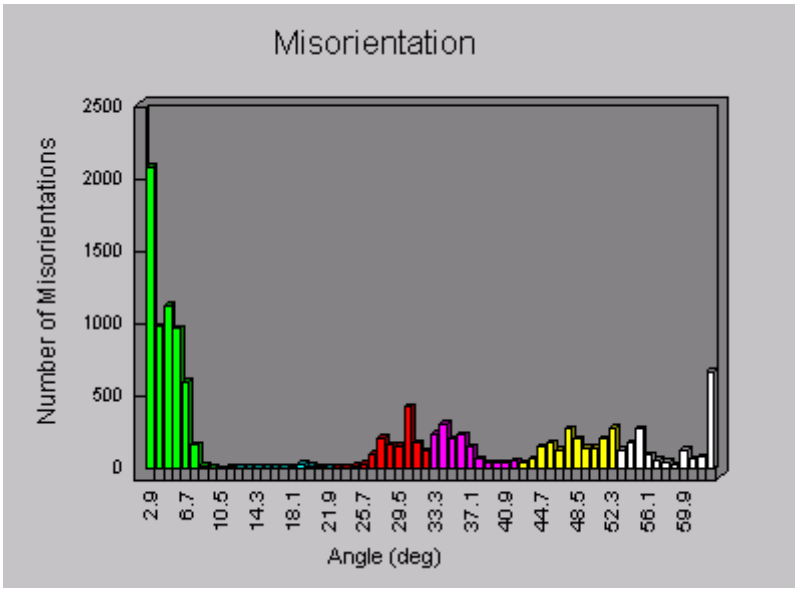

Figure 4.65: EBSD histogram for a 2000 pulses YBCO film deposited on MgO single crystal using a fluence of 2.75J/cm^2 showing misorientation angles.

The AC susceptibility test (Figure 4.76) showed a broad superconducting transition temperature for the film deposited with 2.75 J/cm^2 with a T_c onset of 86.9K whereas a sharp transition temperature with a T_c onset of 87.4K was obtained for the film deposited at 2 J/cm^2. This confirms that the optimum fluence for YBCO deposition in the used system during this work is 2J/cm^2.

By increasing the number of pulses to 5000 and 10,000 while keeping the fluence at 2 J/cm^2, the intensity of YBCO (006) was the same for both films (Figure 4.57). The SEM and AFM images (Figure 4.66-Figure 4.69) show that the films are less porous compared to films with 2000 pulses (Figure 4.58). Figure 4.70 is a cross sectional SEM image for an YBCO film deposited with 10,000 pulses showing a film thickness of 1.922µm which gives a deposition rate of (19220/10000) = 1.922Å/pulse. Therefore, the film deposited with a 5000 pulses should have a thickness of 0.96µm where the measured thickness was about 1.01µm. The film roughness increased by increasing the number of pulses from 5000 to 10,000 (Figure 4.68 and Figure 4.69), although both films had a well defined in-plane and out-of-plane texture (Figure 4.71 and Figure 4.72). Both films also had sharp transition temperatures of 91.9K for the 5000 pulses film and 92K for the 10,000 pulses film (Figure 4.76). The out-of-plane and in-plane texture for the 5000 pulses film were measured quantitatively using the rocking curve and phi scans, respectively. The out-of-plane texture was found to have

a FWHM of 1.03° (Figure 4.73) and that for the in-plane texture of 1.8° (Figure 4.74). The film was also found to consist mainly of low angle grains (Figure 4.75).

From the above, and as the critical current density decreases with increasing YBCO thickness [213], it can be concluded that the optimum conditions for YBCO deposition, which gives highest T_c, smoothest film, low angle grains and high quality in-plane and out-of plane texture were to use 5000 pulses and a fluence of 2 J/cm^2.

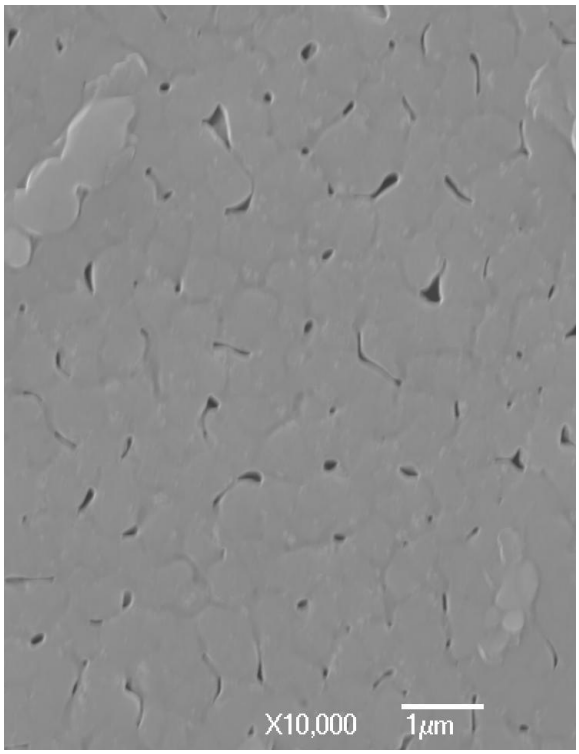

Figure 4.66: SEM image for a 5000 pulses YBCO film deposited on MgO single crystal using a fluence of 2 J/cm^2.

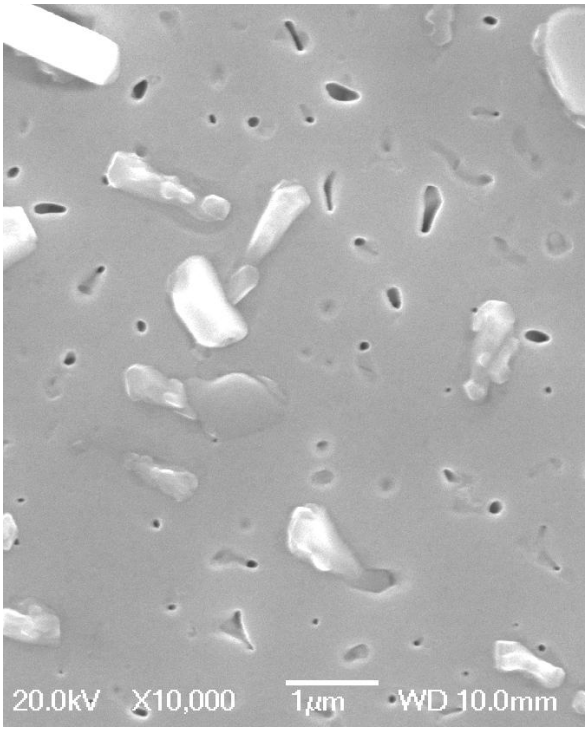

Figure 4.67: SEM image for a 10000 pulses YBCO film deposited on MgO single crystal using a fluence of 2 J/cm^2.

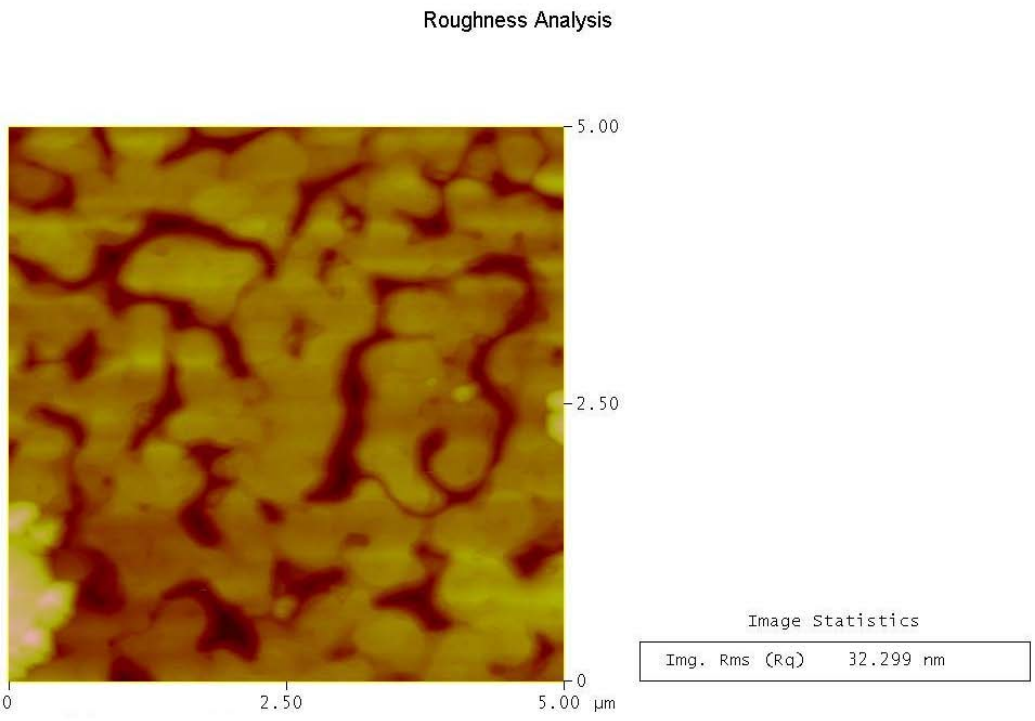

Figure 4.68: A 5x5μm^2 AFM image for a 5000 pulses YBCO film deposited on MgO single crystal using a fluence of 2 J/cm^2.

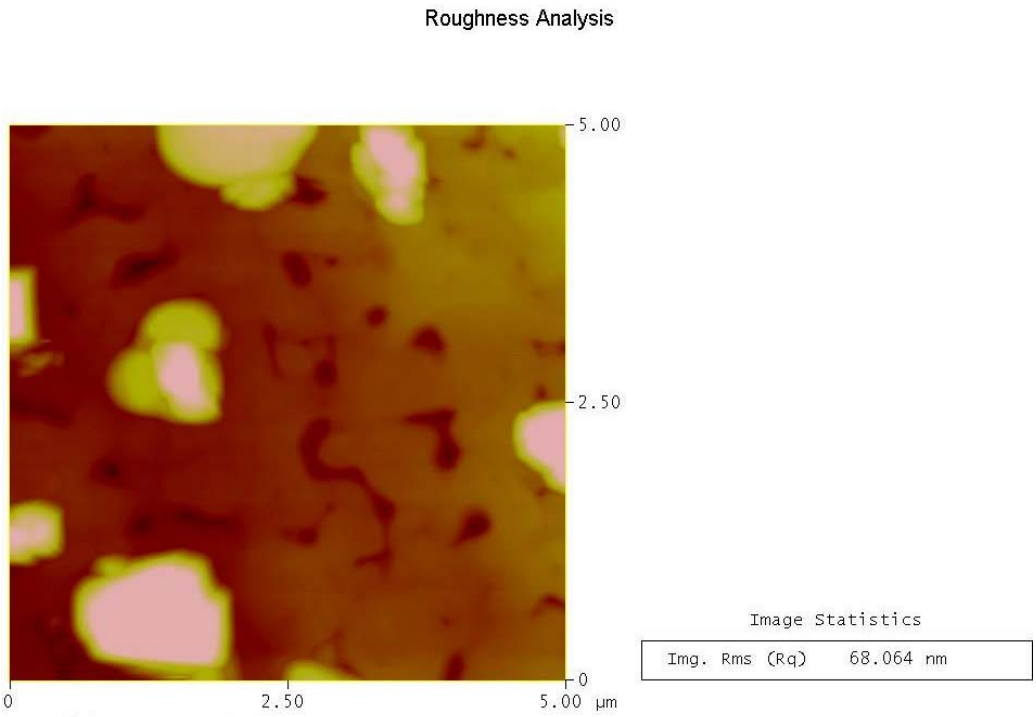

Figure 4.69: A 5x5µm^2 AFM image for a 10000 pulses YBCO film deposited on MgO single crystal using a fluence of 2 J/cm^2.

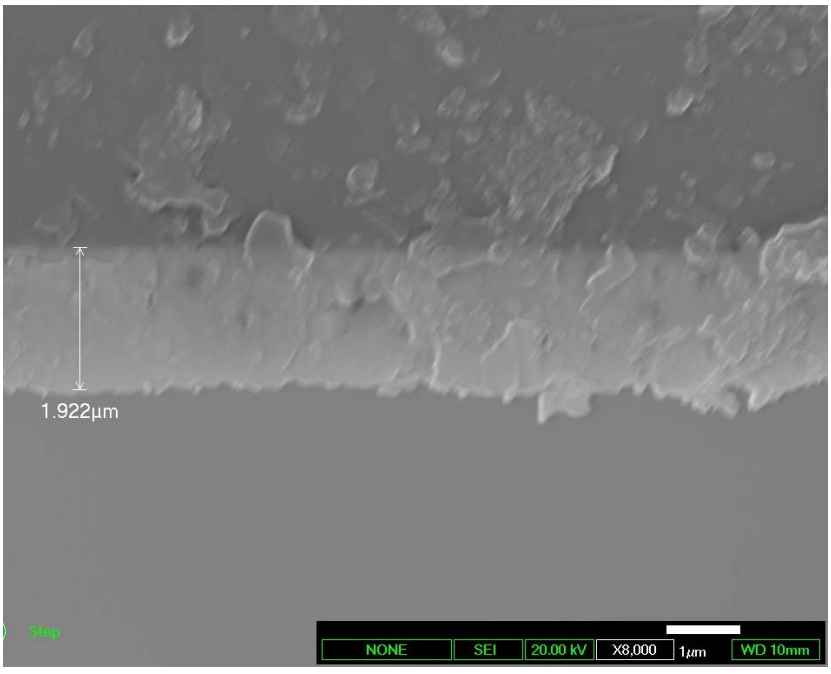

Figure 4.70: A cross sectional SEM image for a 10000 pulses YBCO film deposited on MgO single crystal using a fluence of 2 J/cm^2.

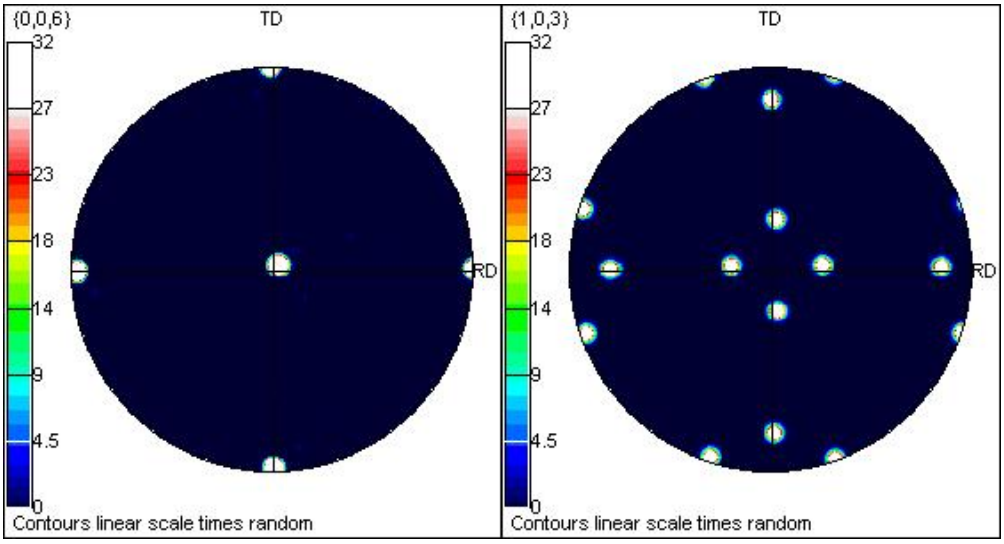

Figure 4.71: EBSD pole figure patterns for a 5000 pulses YBCO film deposited on MgO single crystal using a fluence of 2 J/cm^2 showing the YBCO {006} and {103} planes.

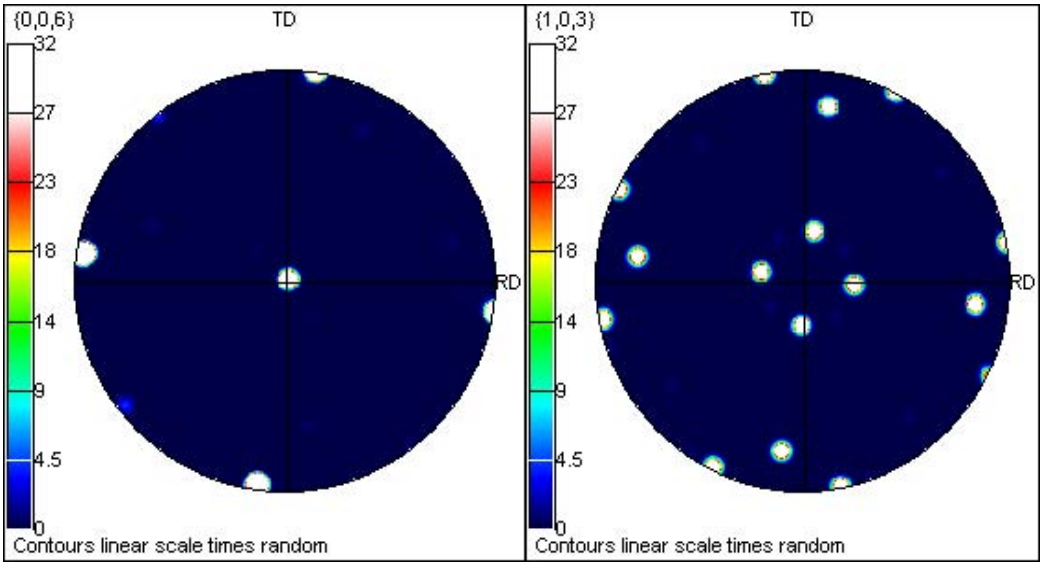

Figure 4.72: EBSD pole figure patterns for a 10000 pulses YBCO film deposited on MgO single crystal using a fluence of 2 J/cm^2 showing the YBCO {006} and {103} planes.

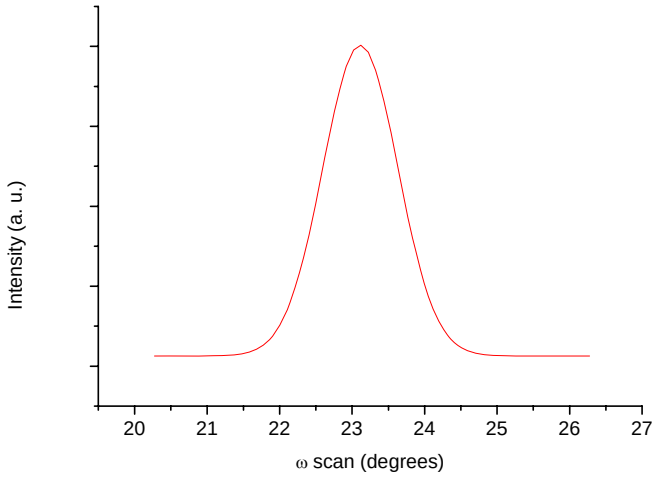

Figure 4.73: X-ray diffraction ω–scan for a 5000 pulses YBCO film deposited on MgO single crystal using a fluence of 2J/cm^2 showing a FWHM of 1.03^o.

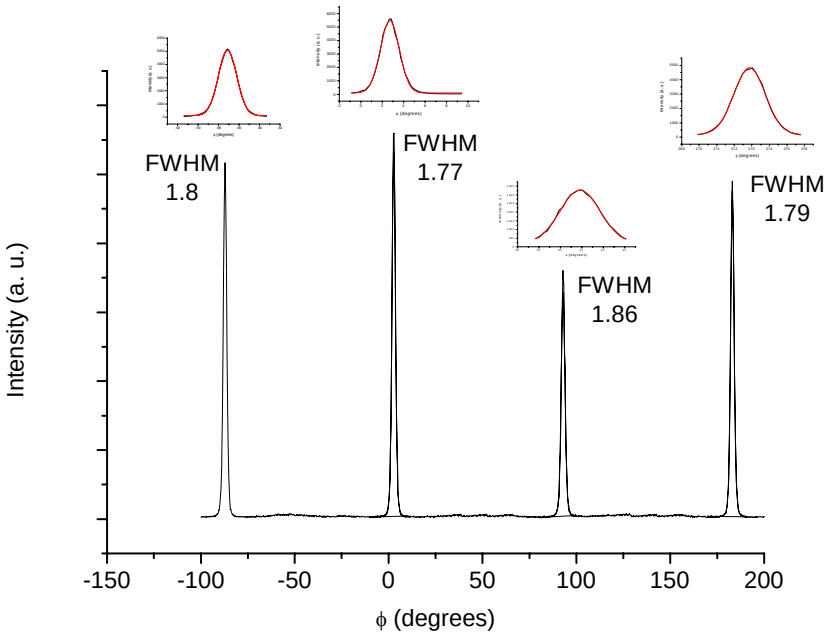

Figure 4.74: X-ray diffraction Φ–scan for a 5000 pulses YBCO film deposited on MgO single crystal using a fluence of 2J/cm^2 showing a FWHM of 1.8^o.

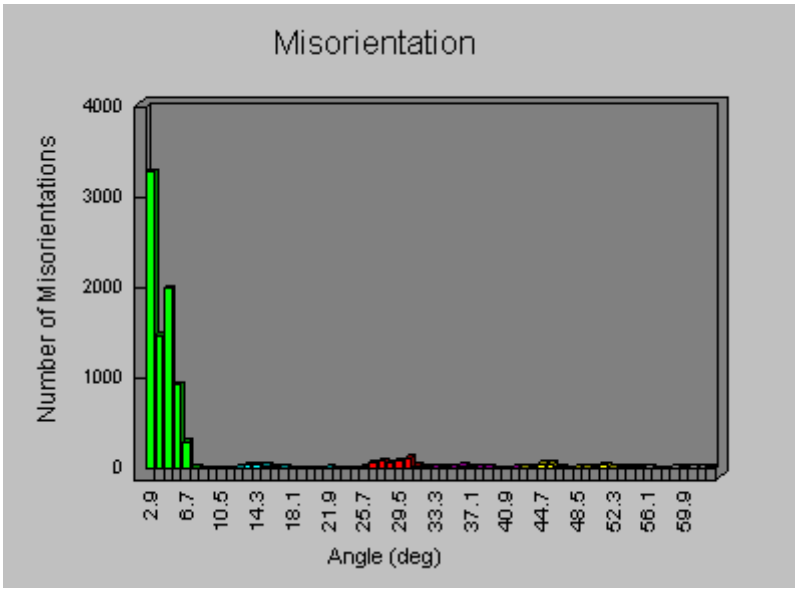

Figure 4.75: EBSD histogram for a 5000 pulses YBCO film deposited on MgO single crystal using a fluence of 2J/cm^2 showing misorientation angles.

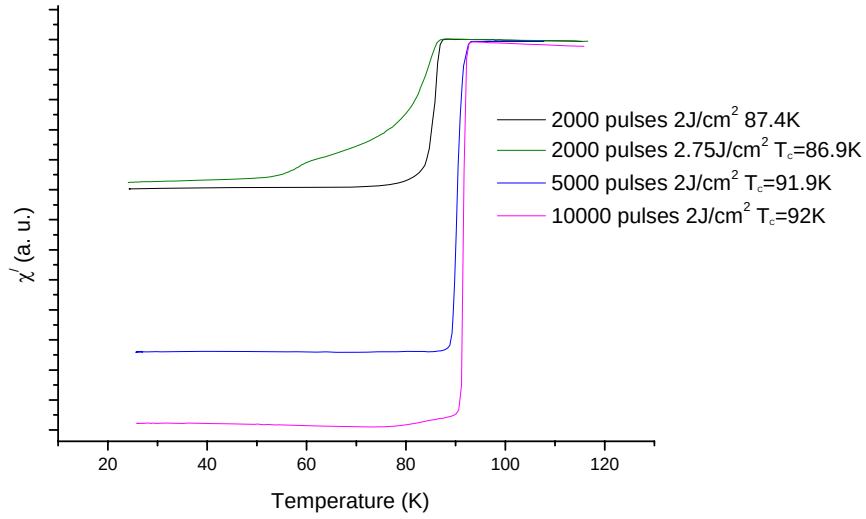

Figure 4.76: AC susceptibility test showing χ' for YBCO films deposited on MgO single crystal at different number of pulses and different fluencies.

4.6 YBCO deposition by pulsed laser deposition on Si (100) substrates buffered with MgO

To evaluate the performance of the MgO films deposited by spray pyrolysis and PLD, YBCO was deposited by PLD on top of them. This is a well established route to high quality films [244, 245], although spray pyrolysis of the YBCO layer should also

be a possibility in the future [23, 24, 87, 93, 94]. The optimised parameters for YBCO deposition were obtained by first depositing YBCO on MgO single crystal (section 4.5.1). The optimised and used YBCO deposition parameters were:

- The deposition temperature: 780°C.
- Substrate target distance: 56mm.
- Deposition pressure: 450mtorr oxygen.
- Energy fluence: 2J/cm^2.
- Number of pulses: 500 and 5000.
- Pulse frequency: 4Hz
- Heating rates: 20°C/min and the used cooling rate was 5°C/min, instead of 10°C/min to avoid film cracking due to thermal and lattice mismatch with silicon.

Some researchers limited the deposition of YBCO films on Si substrates, buffered with CeO_2 and YSZ, to 40-50nm to minimise the effect of thermal stresses which decrease the film's critical temperature and current density [95, 250, 251]. Therefore, in this work YBCO deposition was first applied using 500 pulses. However, no YBCO peaks were detected irrespective of the YBCO deposition conditions. Others found that films with less than 50nm resulted in strained YBCO films with distorted unit cells [252]. Therefore, YBCO deposition will be limited to 5000 pulses.

Figure 4.77 shows the XRD pattern for an YBCO film deposited on Si (100) buffered with MgO spray pyrolysed at 650C using 0.078M solution of magnesium nitrate at zero inclination angle. It is clear that the film has a strong texture along the c-axis, however, a strong (103) peak was obtained as well (weak (103) peaks were obtained when depositing YBCO on MgO single crystals as can be seen in Figure 4.57). This was not surprising because the MgO film deposited on Si was under tension in-plane and under compression out-of-plane due to the thermal expansion mismatch. Therefore, it was believed that the strained MgO layer disturbed the YBCO deposition and led to this kind of partial texture. Therefore, the film had out-of-plane texture but no in-plane texture (Figure 4.78). The surface roughness after YBCO deposition (Figure 4.79 and Figure 4.80) was increased compared to the roughness of the MgO buffer (Figure 4.5 and Figure 4.9) and the YBCO film had a broad superconducting transition temperature (Figure 4.81). YBCO films deposited on MgO

spray pyrolysed from 0.078M at 650°C and 700°C with an inclination angle of 20° resulted in polycrystalline YBCO films with no T_c. The YBCO film deposited on MgO film, deposited on Si (100) by PLD using and energy fluence of 3.45J/cm^2, was polycrystalline as well with no T_c. This time it was attributed to the weak texture of MgO film.

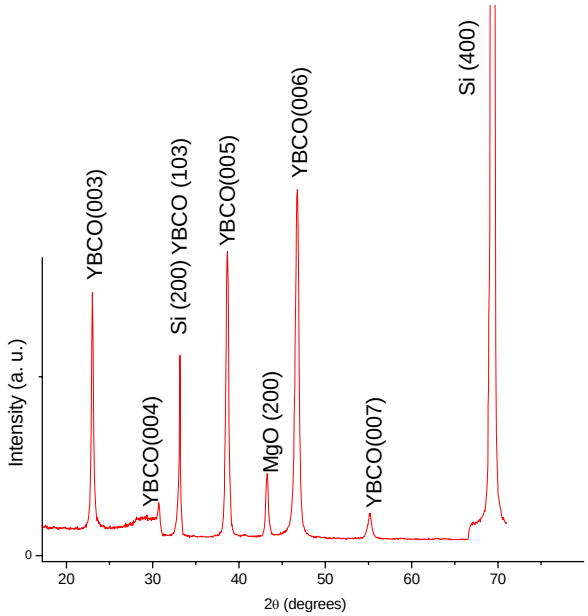

Figure 4.77: XRD pattern for YBCO film deposited on Si (100) buffered with MgO spray pyrolysed at 650°C using 0.078M solution of magnesium nitrate at zero inclination angle.

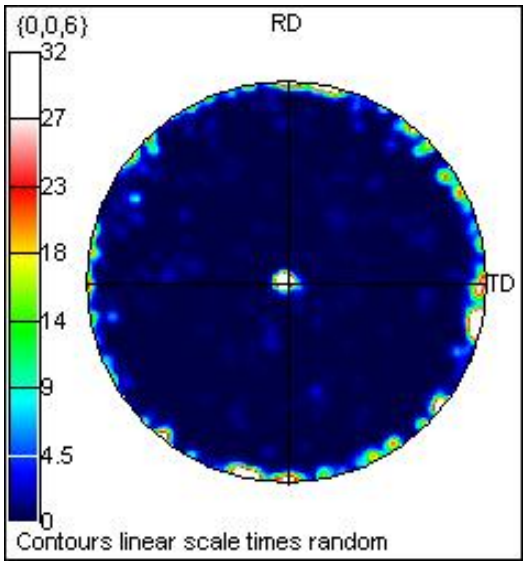

Figure 4.78: EBSD pole figure pattern showing the {006} planes for YBCO film deposited on Si (100) buffered with MgO spray pyrolysed at 650°C using 0.078M solution of magnesium nitrate at zero inclination angle.

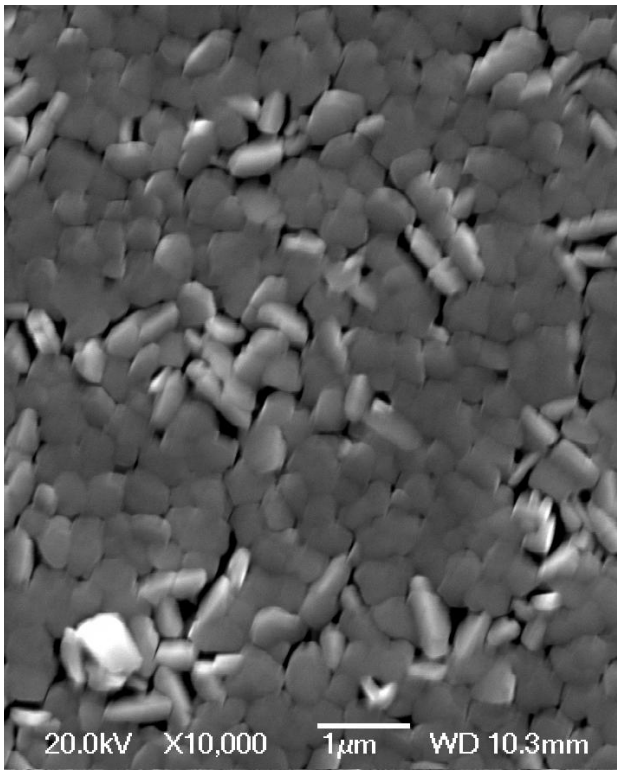

Figure 4.79: SEM image for YBCO film deposited on Si (100) buffered with MgO spray pyrolysed at 650°C using 0.078M solution of magnesium nitrate at zero inclination angle.

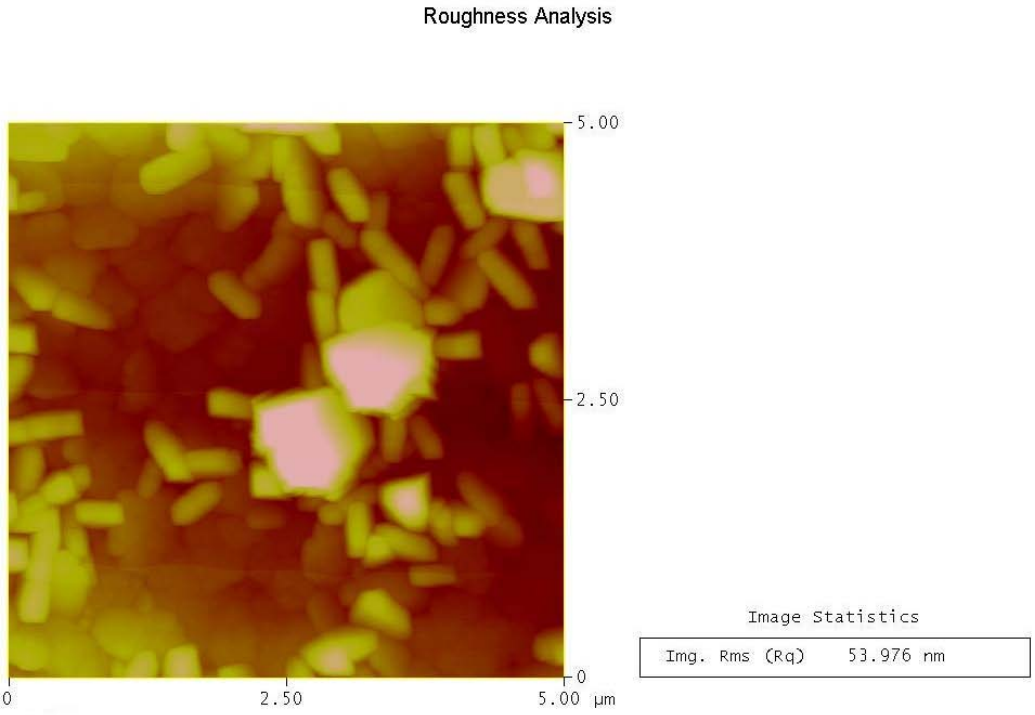

Figure 4.80: A 5x5μm^2 AFM image for YBCO film deposited on Si (100) buffered with MgO spray pyrolysed at 650°C using 0.078M solution of magnesium nitrate at zero inclination angle.

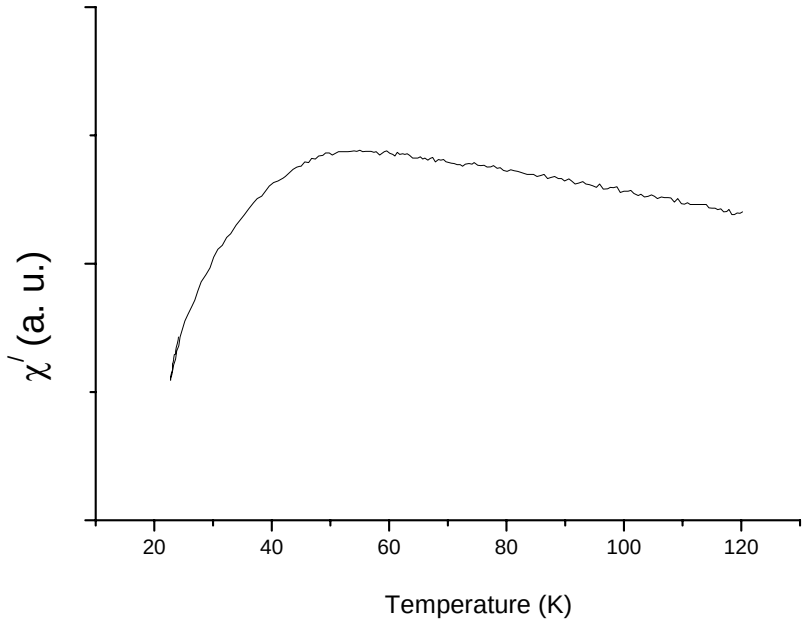

Figure 4.81: AC susceptibility test showing χ' for YBCO film deposited on Si (100) buffered with MgO spray pyrolysed at 650°C using 0.078M solution of magnesium nitrate at zero inclination angle.

5 Spray Pyrolysis of MgO on RABiTS NiW

5.1 Introduction

In this chapter the deposition of MgO thin films by spray pyrolysis on NiW RABiTS will be introduced using mainly magnesium nitrate as a precursor. NiW tape (100µm thick) was cut into 10mm x 10mm substrates. The samples were polycrystalline; therefore, they were heat treated for recrystallisation. Some of them were then mechanically polished down to a roughness of 2-5 nm, and then they were cleaned in acetone, then ethanol for 10 minutes each in an ultrasonic bath, then dried with Ar gas. In the spray pyrolysis deposition, a pulse time to interval time of 1:7 was applied for 32 minutes; however, the precursor concentration was varied. The used Ar flow rate was 10 l/min. In addition to that, MgO deposition was also applied on an epitaxial oxide i.e. NiO (200) formed on top of the NiW tapes by oxidation.

As far as we know, no reports have been found for MgO deposition on metallic substrates by spray pyrolysis. The aim of depositing MgO by spray pyrolysis is to reduce the cost of production instead of using the relatively expensive methods for the buffer layer deposition, such as electron beam evaporation [82] and pulse laser deposition [80]. In section 4.5.1 YBCO was deposited on MgO single crystals to demonstrate that MgO was a good substrate for YBCO deposition where a sharp transition temperature was obtained with a T_c onset of about 91K. Therefore, a further objective of the work was to grow MgO as the only buffer layer before YBCO deposition in an attempt to make the process a cost-effective one by reducing the usual multi-layer buffer architecture to a single layer.

5.2 NiW substrates

The chemical composition of the NiW substrates, as received from the supplier, was checked by the EDX (using an accelerating voltage of 20 KV).

Table 5.1 shows that the chemical composition of the as received substrates was about Ni-5at%W.

Table 5.1: Chemical composition of the as received NiW substrates.

Element	Chemical composition, at% (EDX, 20KV)
Ni K	94.78
W L	5.22

The surface roughness of the as received substrates, as shown from the AFM image in Figure 5.1, shows that the roughness was about 50nm.

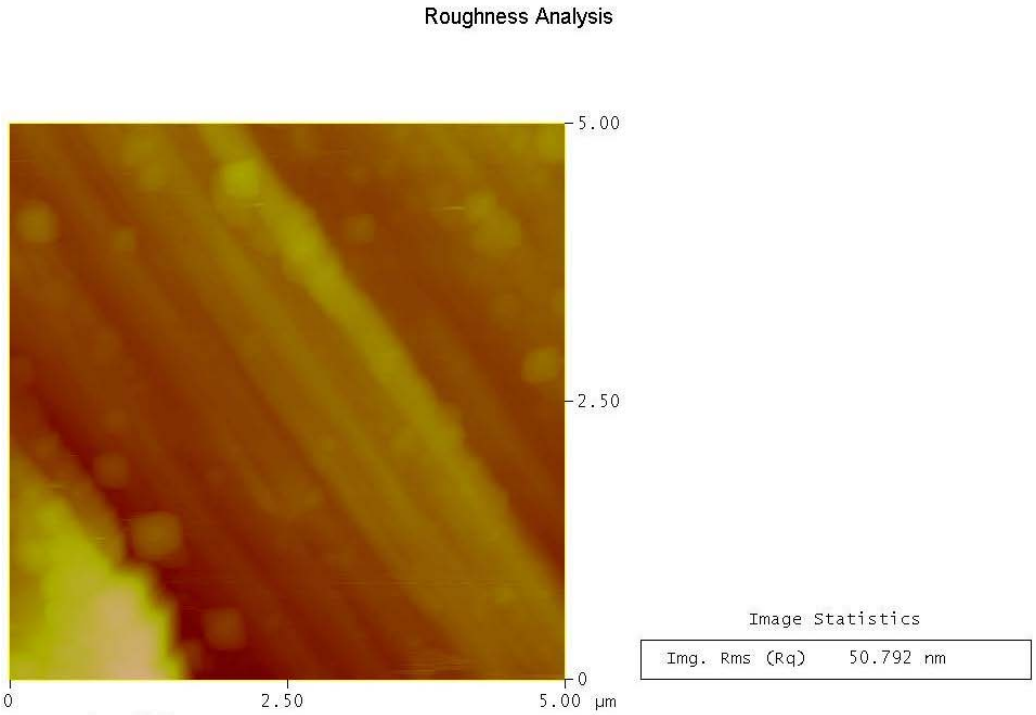

Figure 5.1: A 5x5µm^2 AFM image of the as received NiW substrates.

Figure 5.2 shows the XRD pattern taken from the NiW substrate with the peaks being indexed according to the JCPDS PDF file 00-004-0850 where the lattice parameter is 3.5238Å (The 2θs for Ni (111), Ni (200), Ni (220), Ni (311) and Ni (400) are 44.50°, 51.85°, 76.37°, 92.95° and 121.94°, respectively). From the XRD pattern it is clear the substrates are polycrystalline with the Ni (220) being the strongest peak.

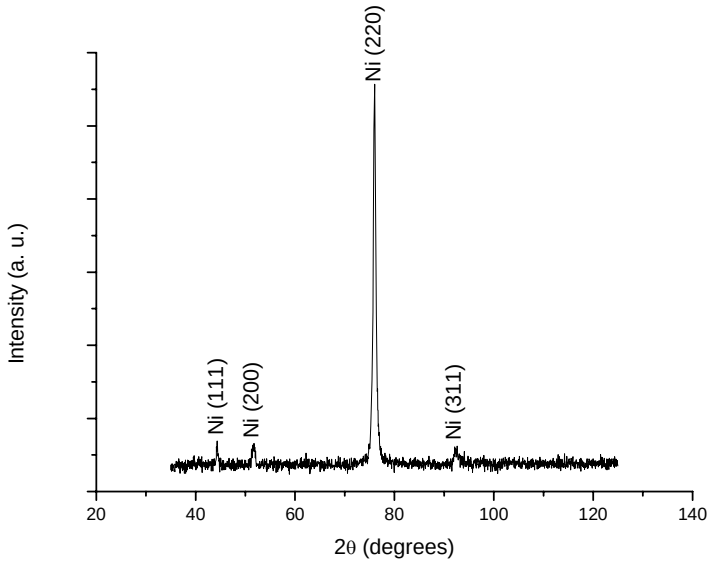

Figure 5.2: XRD pattern of the as received NiW substrates.

5.3 Recrystallisation treatment of NiW substrates

Goyal A. et al [44] obtained a {100}<001> cube texture in pure nickel by recrystallisation at 1000°C for 4 hours in a vacuum of ~ 10^{-6} torr. Kaname Matsumoto et al [253-255] also obtained a {100}<001> cube texture in pure nickel plates by a recrystallisation treatment at 800°C -1100°C for 3 hours but they did not mention in which atmosphere. A (200) oriented NiO film was then obtained by oxidising the cube textured Ni plates at 900°C-1300°C for times ranging from 5min-3hours in 1atm of purified oxygen or in a flowing Ar gas at a flow rate of 500ml/min. The grown NiO oxide had in-plane FWHM of 10°-14°. YBCO films were then deposited at temperatures between 700°C -750°C under 200-300 mtorr O_2. This gave a T_c onset of 87K, a J_c of 4-6x10^4 A/cm^2 and in-plane FWHM of 10°-12°. To improve the superconducting properties, they deposited a thin cap layer of MgO by PLD on top of the NiO layer. By this way, a T_c of 88K and J_c of 3x10^5 A/cm^2 (77K, 0 T) were obtained for YBCO films. The epitaxial growth of (100)-oriented cube oxides on a Ni (001) surface is inhibited by the formation of NiO (111) at the oxide-metal interface [256]. David P. Norton et al [257] obtained a cube textured Ni by annealing under 4%H_2-96% Ar atmosphere for later growth of cube textured oxide layers such CeO_2, YSZ and YBCO which were deposited by PLD. They found that the CeO_2 and YSZ principal crystallographic axes were rotated 45° relative to the in-plane Ni (100) axis,

whereas YBCO was rotated 45° with respect to YSZ, however, they produced several films with J_c (77 K, H = 0) greater than 600,000 A/cm^2. R.I. Chakalova et al [258] deposited YBCO on biaxially textured Ni tapes using YSZ and CeO_2 in different combinations. To prevent the oxidation of the Ni substrate, 4% H_2 in Ar was used. A T_c of 80k-90K was obtained depending on the used buffer architecture. Y L Cheung et al [259] deposited multilayer YBCO film insulated with STO on NiW RABiTS using CeO_2/YSZ/CeO_2 buffer architecture. 4% H_2 in Ar was introduced in the chamber during heating to prevent oxidation of the substrate. The YBCO films separated with STO were found to have a higher T_c and smaller transition width than YBCO films separated using CeO_2 and Y_2O_3 insulating layers. E Maher et al [260] succeeded in depositing YBCO films on curved Ni tapes as a principle of multi-layer coil fabrication. Y L Cheung et al [261] also succeeded in depositing YBCO films on buffered curved NiW RABiTS by pulsed laser deposition to demonstrate the feasibility of fabricating in-situ a multi-turn superconducting coil on a cylindrical heated former. T. G. Woodcock et al [262, 263] grew biaxially textured NiO films on biaxially textured Ni substrates by thermal oxidation at 1200°C for 1 hour in flowing oxygen. The NiO films were (200) oriented, however, small NiO (111) peaks were obtained as well. They found that up-quenching to the oxidation temperature and down-quenching after holding for 1 hour gave rough surfaces compared to that when the sample was ramped at 300°C/hour and furnace cooled after holding at the oxidation temperature. This latter heating cycle gave smoother surfaces and therefore more suitable for the deposition of subsequent functional layers. They also found that the cube textured material appears to grow with a grain size very similar to that of the substrate material, suggesting that an epitaxial growth mechanism may be in operation. This may not be the case, as the observed orientation relationship would result in a highly strained interface due to the large lattice misfit (18%) between Ni and NiO. Khoi et al [256] grew (100) NiO on (100) Ni cylinders between 500°C-800°C, however, there was a 45° rotation of the NiO film relative to the substrate i.e. (110) NiO // (100) Ni. They also found that the orientation of the oxide layer changed with thickness.

The recrystallisation treatments in this work were carried out in a tube furnace rated to 1200°C. The treatment was carried out at 1100°C for 3 hours under Ar-5%H_2 atmosphere. The gas mixture was supplied from a compressed gas cylinder through copper tubing. The gas flow was controlled and was set at 100ml/min for a furnace

volume of 1630ml. Before heating, the gas mixture was supplied to the furnace for one hour which means that the furnace volume was replaced 3.7 times. The heating was then carried out at a rate of 300C°/hr. After heating to the required temperature and holding for the required time, the furnace was switched off to allow the samples to be furnace cooled under the same atmosphere. Figure 5.3 shows the XRD pattern for the sample after the recrystallisation treatment. It can be seen that the sample was strongly (200) textured with no other peaks and was biaxially textured (Figure 5.4). Figure 5.5 shows the SEM image of the sample after the recrystallisation treatment where the grain boundaries were revealed due to the thermal etching effect. The revealing of the grain boundaries at high temperatures was even seen during pulsed laser disposition of YBCO on NiW RABiTS by Y L Cheung et al [259, 261]. The thermal etching effect on Ni RABiTS was also seen by others [32, 264, 265]. The roughness after the recrystallisation treatment was about 14nm as can be seen from the AFM image in Figure 5.6.

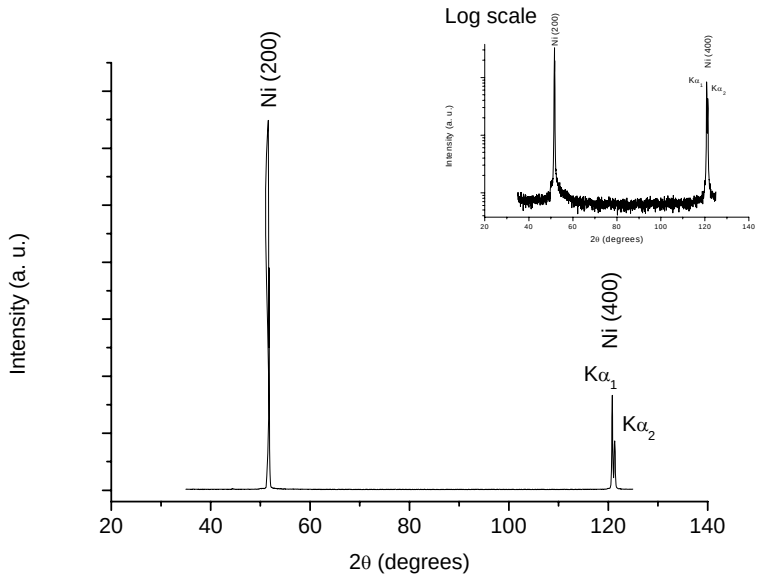

Figure 5.3: XRD pattern of the as received NiW substrates after the recrystallisation treatment.

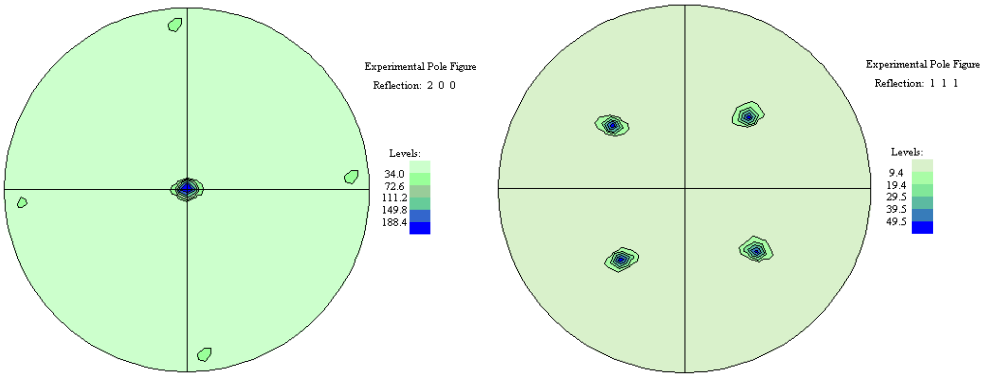

Figure 5.4: (200), left, and (111), right, X-ray pole figures, at 2θ of 51.6° and 44.5°, respectively, of the as received NiW substrates after the recrystallisation treatment.

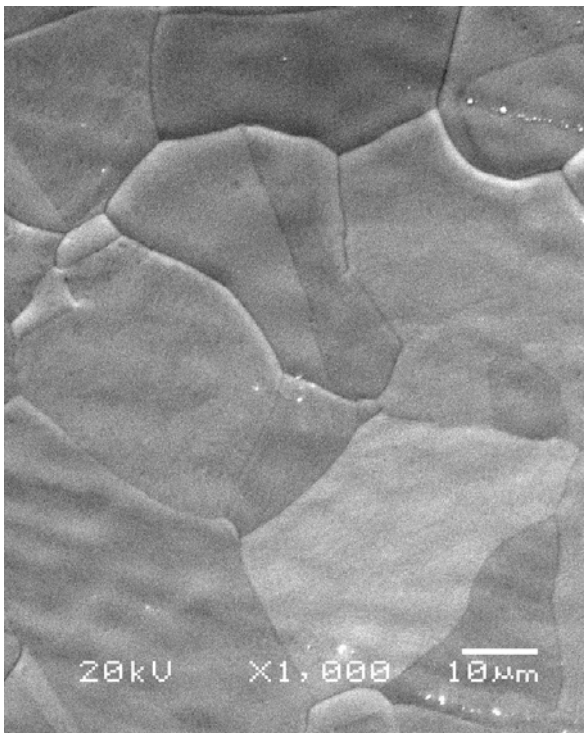

Figure 5.5: SEM image of the as received NiW substrate after the recrystallisation treatment.

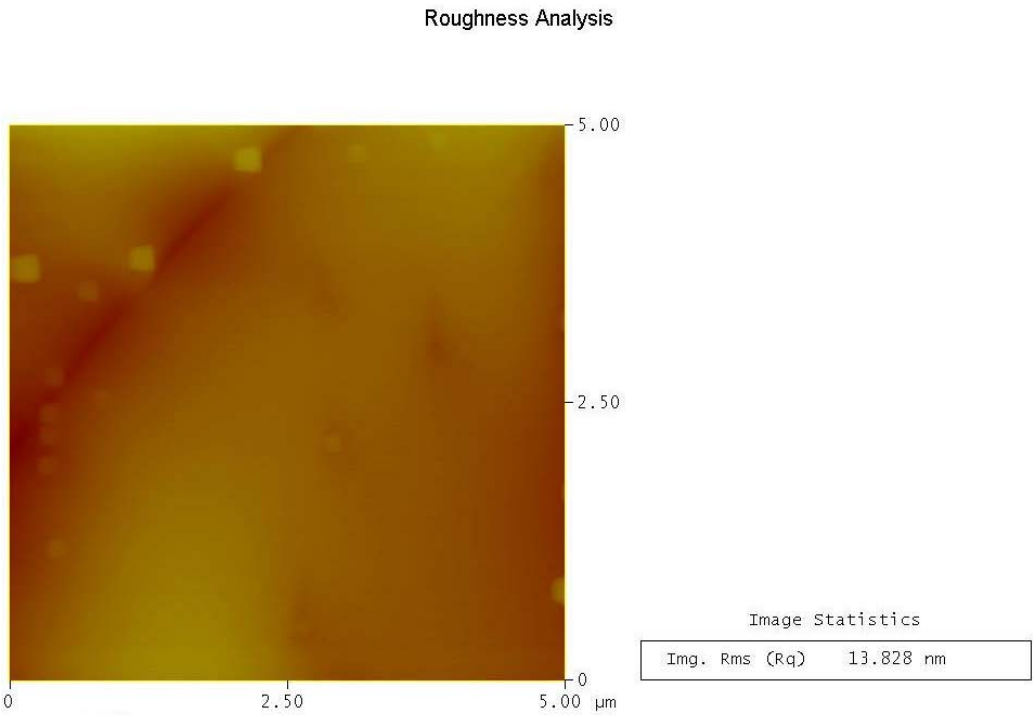

Figure 5.6: A 5x5µm^2 AFM image of the as received NiW substrates after the recrystallisation treatment.

After the recrystallisation treatment, the substrates were mechanically polished down to a roughness of 2-5nm (Figure 5.7 and Figure 5.8) and this had no effect on the texture of the NiW substrate.

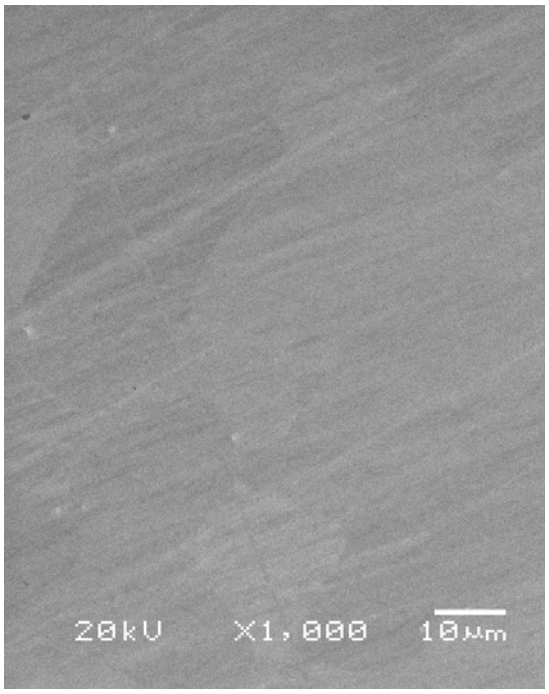

Figure 5.7: SEM image of the as received NiW substrates after the recrystallisation treatment and mechanical polish.

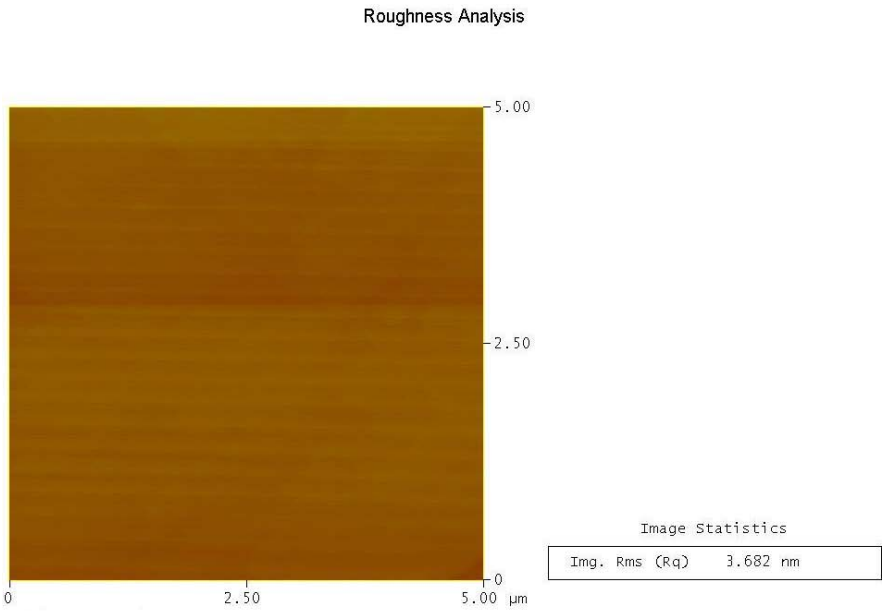

Figure 5.8: A 5x5µm^2 AFM image of the as received NiW substrates after the recrystallisation treatment and mechanical polish.

5.4 MgO deposition on NiW RABiTS by spray pyrolysis using magnesium nitrate precursor

After the recrystallisation treatment, MgO was deposited on NiW tapes by spray pyrolysis using $Mg(NO_3)_2.6H_2O$ as a precursor. The deposition was carried out at 650°C using 0.078M-0.468M of the precursor on the polished and unpolished NiW substrates. No MgO XRD peaks were detected, even when using the high solution concentration, as can be seen from the XRD patterns in Figure 5.9 for the polished and unpolished substrates. Even it can be seen that the texture of the substrate was disturbed by the formation of a small Ni (111) peak in addition to the formation of a polycrystalline oxide layer with NiO peaks indexed according to the JCPDS PDF file 00-004-0835 where the lattice parameter is 4.1769Å (The 2θs for NiO (111), NiO (200), NiO (220), and NiO (400) are 37.28°, 43.30°, 62.92° and 95.08°, respectively). The NiO oxide was stronger (had higher NiO peaks) on the unpolished substrate and this can be explained by the larger surface area of the unpolished substrate, therefore makes it more susceptible to oxidation. The SEM images (Figure 5.10 and Figure 5.11) show that the surface roughness after the deposition was almost the same (for substrate background) except more MgO particles (detected by EDX) were formed on the unpolished substrate. The unpolished substrates are rougher compared to the polished ones, this provides more sites for heterogonous nucleation and growth of

MgO particles. The EDX test showed the presence of Mg on both the polished and the unpolished substrates and this suggests the presence of an amorphous MgO film. The EDX spectrum for MgO deposited on the polished substrate is shown in Figure 5.12. The instability of the NiW tape during the spray pyrolysis deposition conditions, due mainly to the formation of oxides, disturbed the deposition process of MgO and resulted in an amorphous MgO thin film, although it could be that the Mg reacted to form other phases.

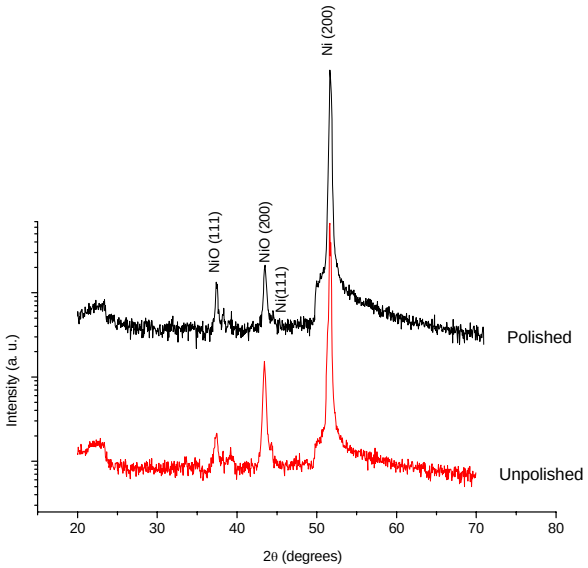

Figure 5.9: log scale XRD patterns for MgO deposition on polished and unpolished NiW substrate tapes by spray pyrolysis at 650°C using 0.468M $Mg(NO_3)_2.6H_2O$ for 32 minutes.

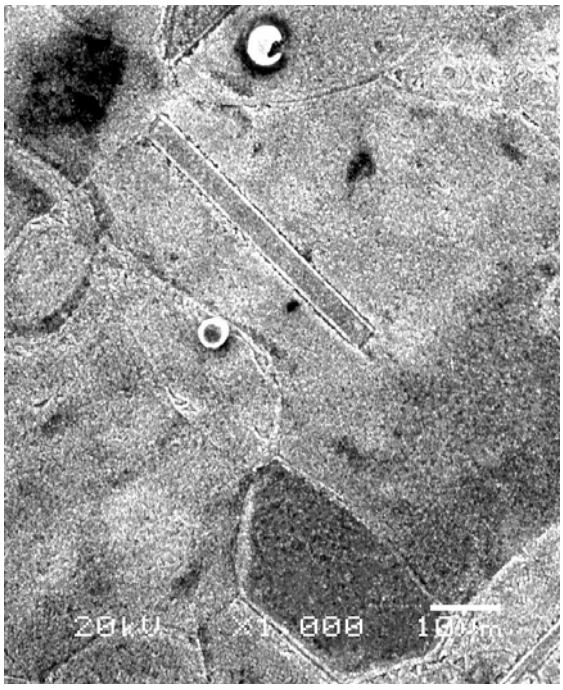

Figure 5.10: SEM image for the unpolished NiW tape deposited with 0.468M at 650°C with a deposition time of 32 minutes.

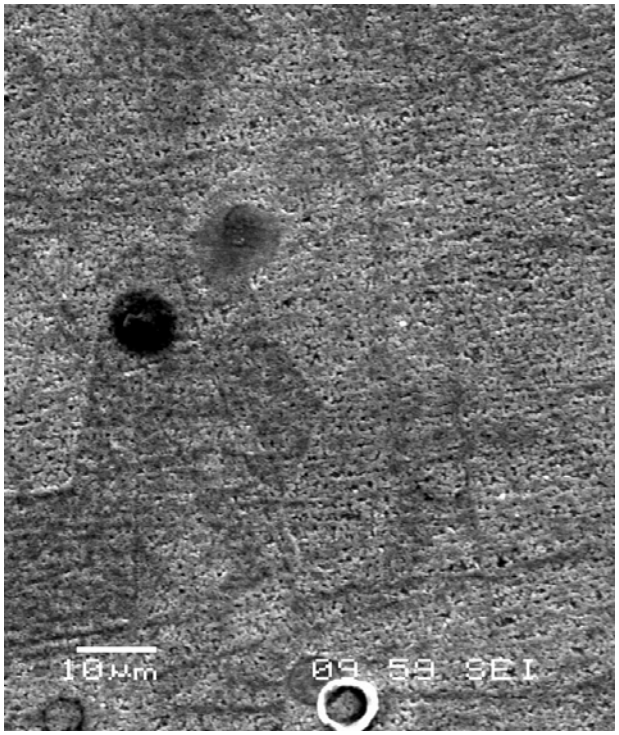

Figure 5.11: SEM image for the polished NiW tape deposited with 0.468M at 650°C with a deposition time of 32 minutes.

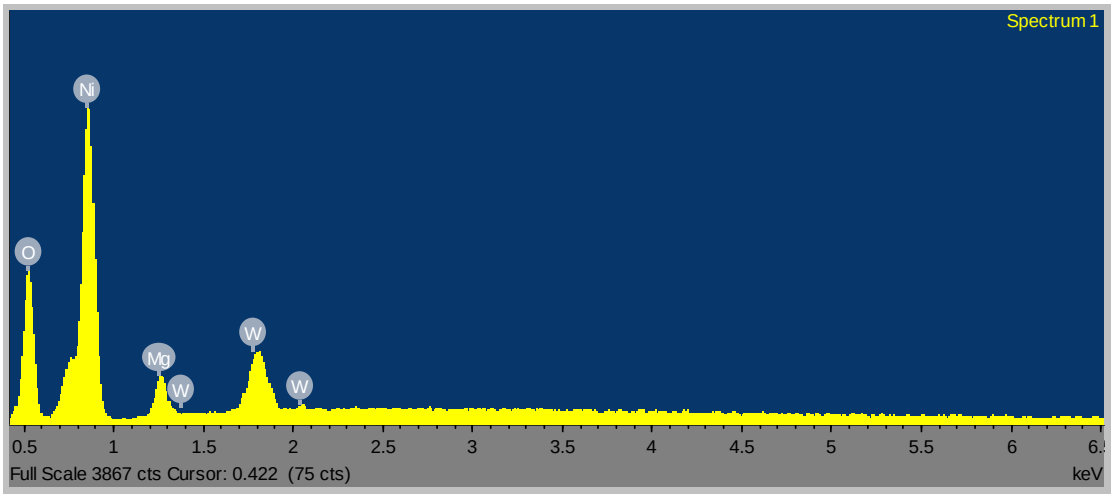

Figure 5.12: EDX spectrum, using an accelerating voltage of 4KV, for the polished NiW tape deposited with 0.468M at 650°C with a deposition time of 32 minutes.

As the substrates were unstable during MgO deposition by spray pyrolysis due to the formation of an oxide layer, then the substrates were oxidised on purpose to deposit MgO on an epitaxial NiO (200) oxide layer.

5.5 Growth of textured NiO films on NiW RABiTS

Textured NiO was grown on Ni and NiW tapes by others for later deposition of YBCO [253-255, 257, 262, 263]. In this work the oxidation was done to get a more stable surface for MgO deposition by spray pyrolysis. The oxidation treatment was done in a tubular furnace similar to the one where the recrystallisation treatment was performed. The treatment was carried out at 1200°C for 1 and 3 hours under O_2 atmosphere. The O_2 was supplied from a compressed gas cylinder through copper tubing. The gas flow was controlled and was set at 100ml/min for a furnace volume of 1630ml. Before heating, the O_2 gas was supplied to the furnace for one hour which means that the furnace volume was replaced 3.7 times. The heating was then carried out at a rate of 300C°/hr. After heating to the required temperature and holding for the required time, the furnace was switched off to allow the samples to be furnace cooled under the same atmosphere. Figure 5.13 shows the XRD patterns for the unpolished and recrystallised NiW substrates after the oxidation in addition to the XRD pattern for the unpolished and recrystallised-NiW RABiTS. The NiO peaks were indexed according to the JCPDS PDF file 00-004-0835 and have a lattice parameter of 4.1769Å. It is clear that the NiO oxide layer grew with a (200) texture irrespective of the oxidation time and only very weak NiO (111) was detected on the log scale. This was better than the texture obtained by T. G. Woodcock et al [262, 263] where a considerable NiO (111) peak was obtained in their case. The NiO (200) peak (Figure 5.13) was stronger when the oxidation was carried out for three hours; however, this was at the expense of the surface smoothness (Figure 5.14-Figure 5.17) and it was clear that the NiO had flat crystal faces as was also observed by Kaname Matsumoto et al [254]. X-ray pole figure measurements were done on the sample oxidized for 1 hour (Figure 5.18 and Figure 5.19). It was clear that the NiO had a biaxial texture and was epitaxial with the underlying NiW substrate. However, the NiO was rotated 45° relative to the substrate. This was attributed to the lattice misfit (18.5%) between NiW and NiO. The lattice parameters for NiW and NiO are 3.5238Å and 4.1769Å, respectively. From one hand, Kaname Matsumoto et al did not observe any rotation for NiO films deposited on Ni tapes and they got a cube-on-cube epitaxial relationship [253-255]. On the other hand, T. G. Woodcock et al [262, 263] raised this issue without showing the texture relation between the substrate and the growing oxide layer. On one occasion they did not observe the rotation and found a cube-on-cube

relationship and on another occasion they mentioned the 45° rotation and explained that as a result of the lattice misfit with the substrate which decreased from 18.5% to 16.2% by the rotation. The same 45° rotation was observed by Khoi et al [256]. Rotations of this kind in order to reduce lattice misfit are also common in RABiTS architectures [257].

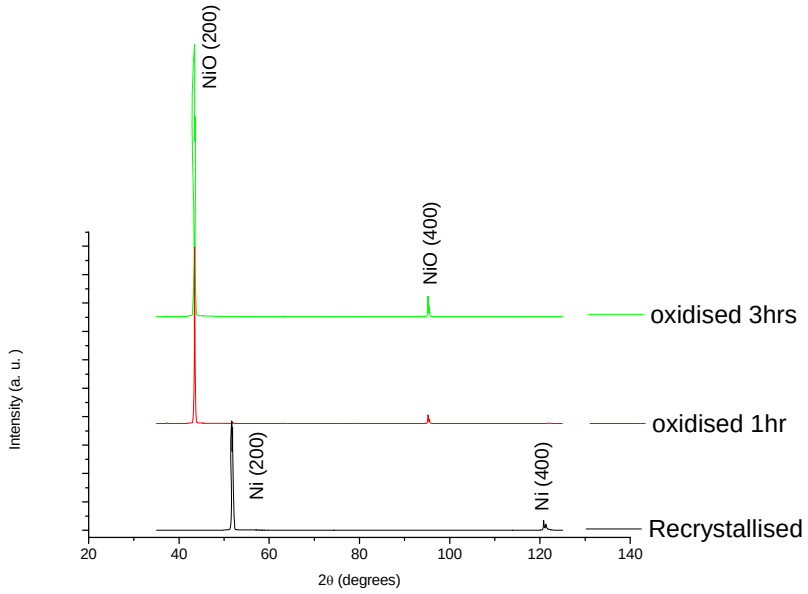

Figure 5.13: XRD patterns for the unpolished NiW after recrystallisation and after recrystallisation and oxidation at different times.

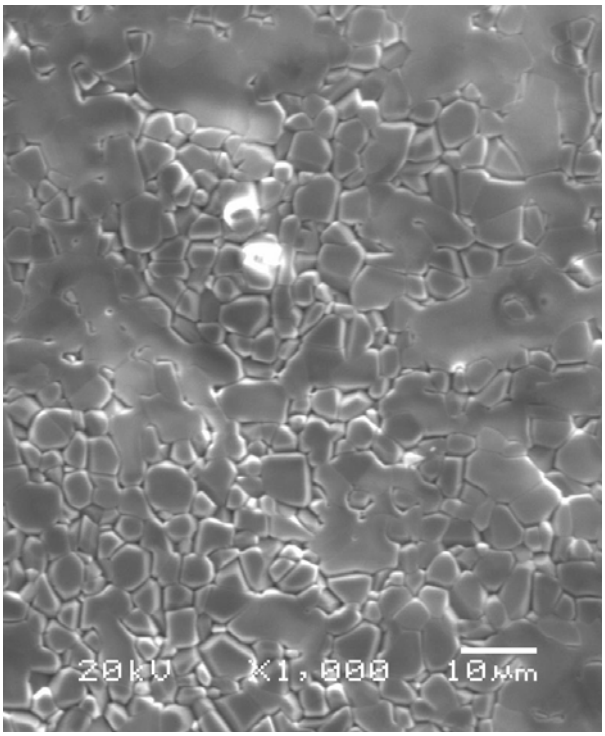

Figure 5.14: SEM image for recrystallised NiW RABiTS after oxidation for 1 hour.

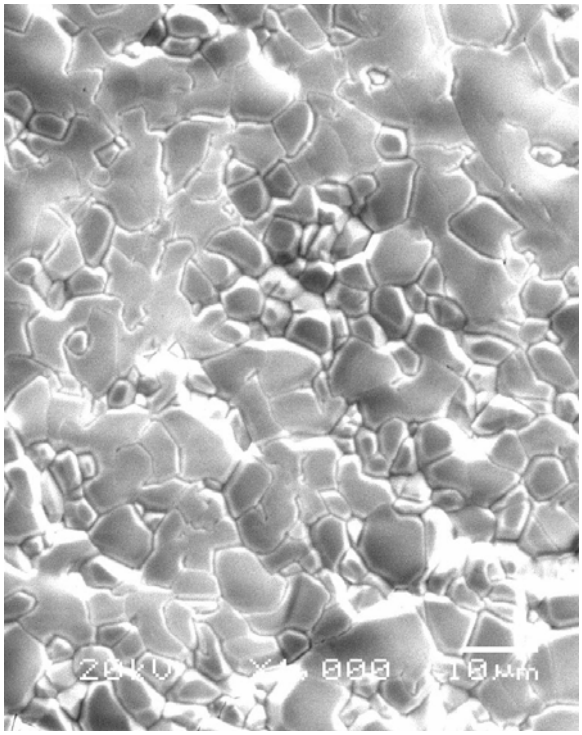

Figure 5.15: SEM image for recrystallised NiW RABiTS after oxidation for 3 hours.

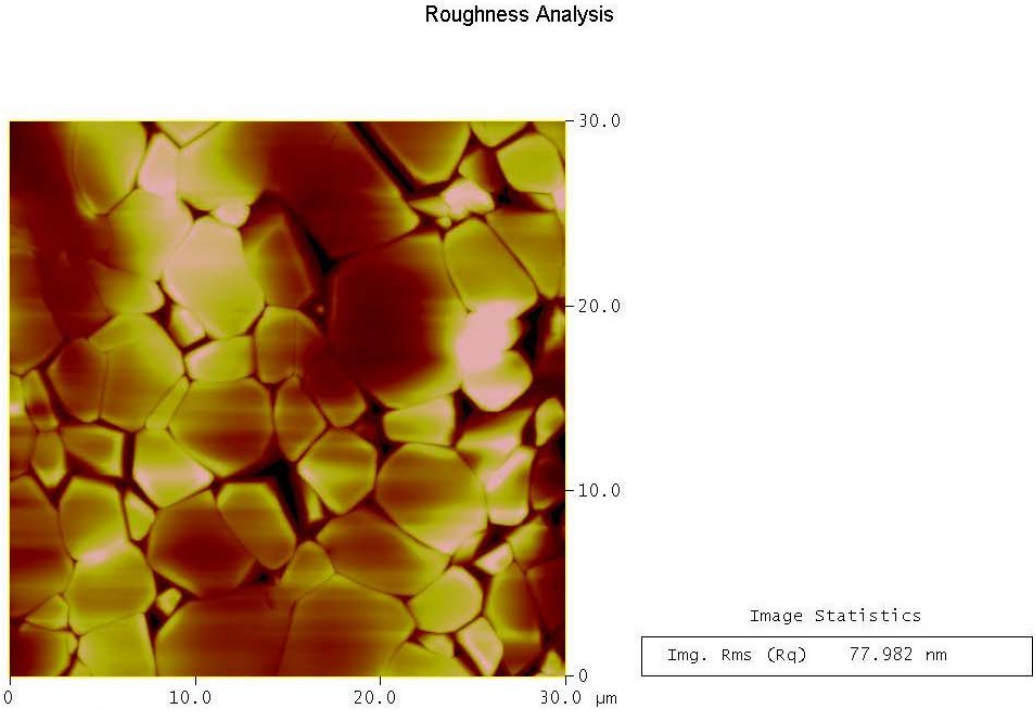

Figure 5.16: A 30x30µm^2 AFM image for recrystallised NiW RABiTS after oxidation for 1 hour.

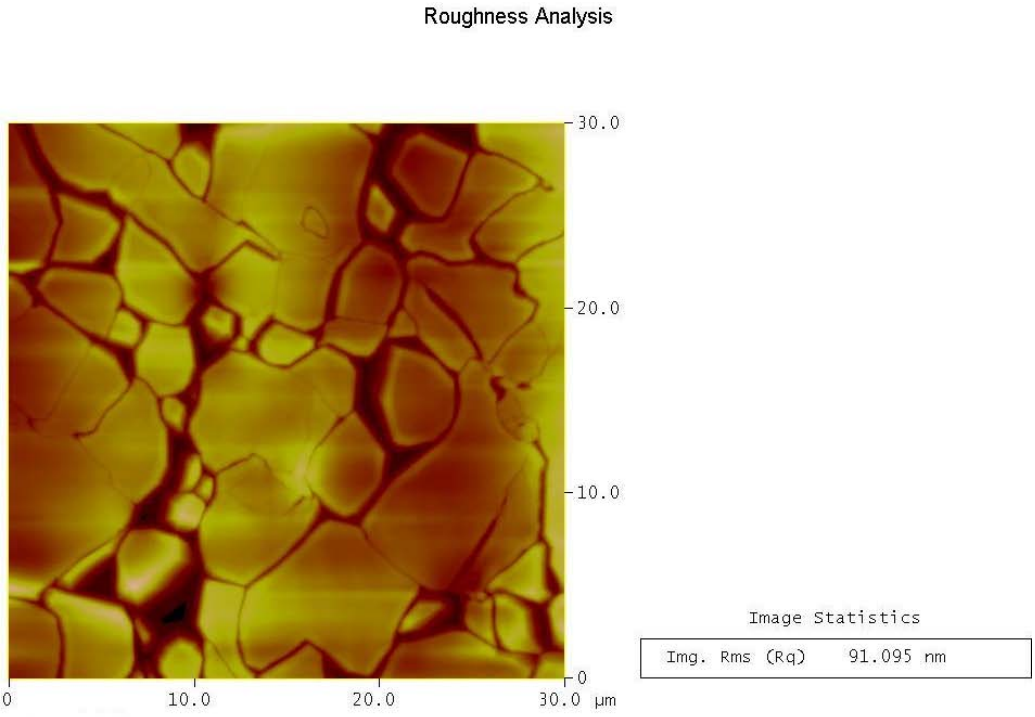

Figure 5.17: A 30x30µm^2 AFM image for recrystallised NiW RABiTS after oxidation for 3 hours.

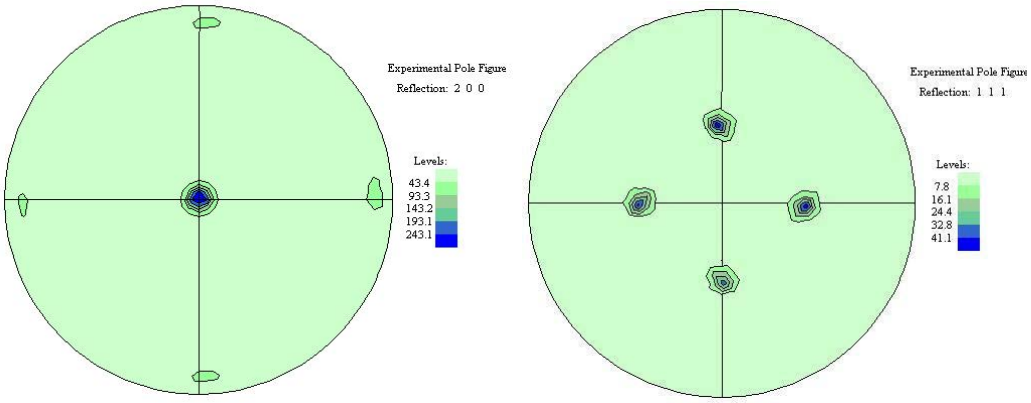

Figure 5.18: (200), (left), and (111), (right), X-ray pole figures, at 2θ of 51.6° and 44.5°, respectively, of NiW after the recrystallisation treatment.

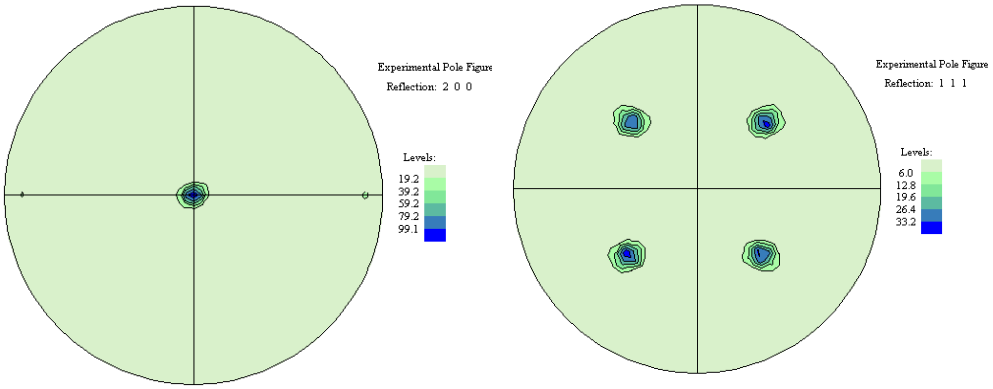

Figure 5.19: (200), (left), and (111), (right), X-ray pole figures, at 2θ of 43.3° and 37.3°, respectively, of NiO oxide layer (oxidised for 1 hour) on top of the recrystallised NiW shown in Figure 5.18.

NiO was also grown on the recrystallised and polished NiW substrates. The same texture was obtained as that for the unpolished substrates, however with a smoother surface (about 40nm).

Before presenting MgO deposition on this NiO layer, the stability of the surface under the conditions used for YBCO deposition by PLD was investigated first. This was done by applying the same thermal cycle and the same atmosphere as when YBCO will be deposited and was done on the grown NiO layer on the polished and the unpolished recrystallised NiW substrates. Therefore, the samples were loaded in the PLD chamber, the chamber was then pumped down to about $1.3x10^{-6}$ mbar ($1x10^{-6}$ torr), they were heated to 780°C (at a rate of 20°C/min.) under 0.6 mbar (450 mtorr) for the same period of time as when YBCO is to be deposited. The samples were then cooled to room temperature at a rate of 10°C/min.

It was found that the texture of NiO on the unpolished surface was not changed and this confirms the stability of the oxide layer. However, the NiO layer on the polished substrate showed a mixed orientation after the thermal cycle (Figure 5.20). It was clear that the texture changed from (200) to a mixed texture of (200) and (111). This may be attributed to the mechanical stresses created on the surface of the polished substrate during mechanical polishing which in turn disturbed the stability of the oxide film texture at 780°C. The surface smoothness was also deteriorated from 40nm before the thermal cycle to about 65nm after the thermal cycle. Therefore, MgO will not be deposited on such an oxide layer grown on polished substrates. Figure 5.21 is the SEM image of the recrystallised and polished NiW substrate after the thermal cycle.

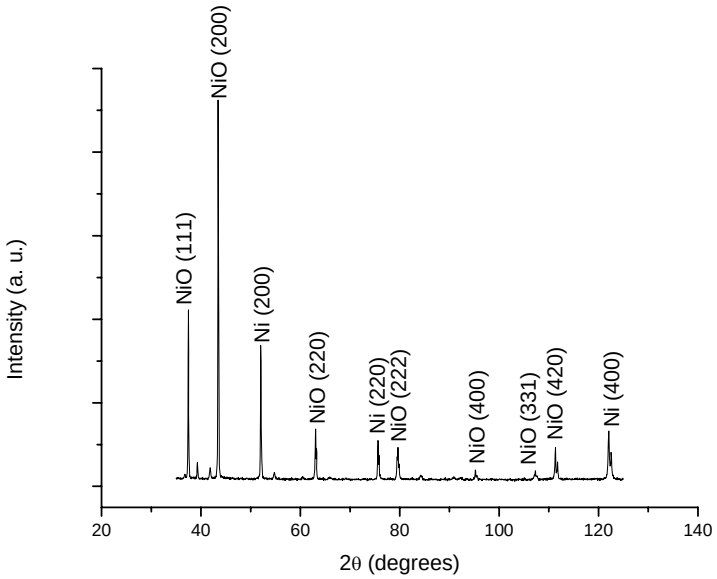

Figure 5.20: XRD pattern of the recrystallised and polished NiW substrate after YBCO-thermal cycle.

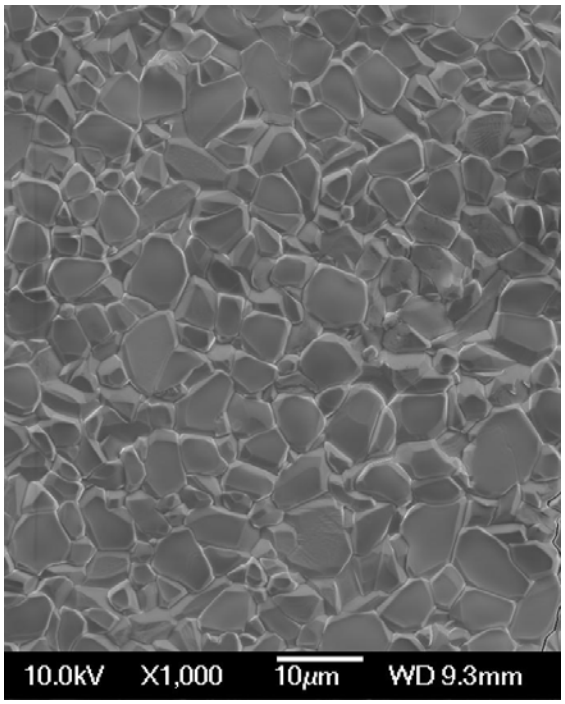

Figure 5.21: SEM image of the recrystallised and polished NiW substrate after YBCO-thermal cycle.

5.6 MgO deposition on (200) textured NiO by spray pyrolysis using magnesium nitrate precursor

It was found that NiO texture was unstable, when grown on a polished and recrystallised NiW substrate, when subjected to YBCO-thermal cycle. Therefore, MgO was deposited only on NiO films grown on the recrystallised and unpolished

NiW substrates. The oxidation of NiW substrates was done under O_2 for one hour as it gave a smoother film compared to that when using three hours.

MgO deposition was performed at 650°C for 32 minutes using 0.078M-0.468M $Mg(NO_3)_2.6H_2O$. No MgO XRD peaks were detected even when using the high concentration of 0.468M (Figure 5.22). EDX test (at 4KV) showed the presence of Mg and this suggests that the deposited MgO film was amorphous, although it could be that the Mg reacted to form other phases. The particles formed on the surface (Figure 5.23) were detected by EDX as MgO particles and this increased the roughness of the substrate to about 170nm (Figure 5.24) compared to about 70nm (Figure 5.16) before MgO deposition.

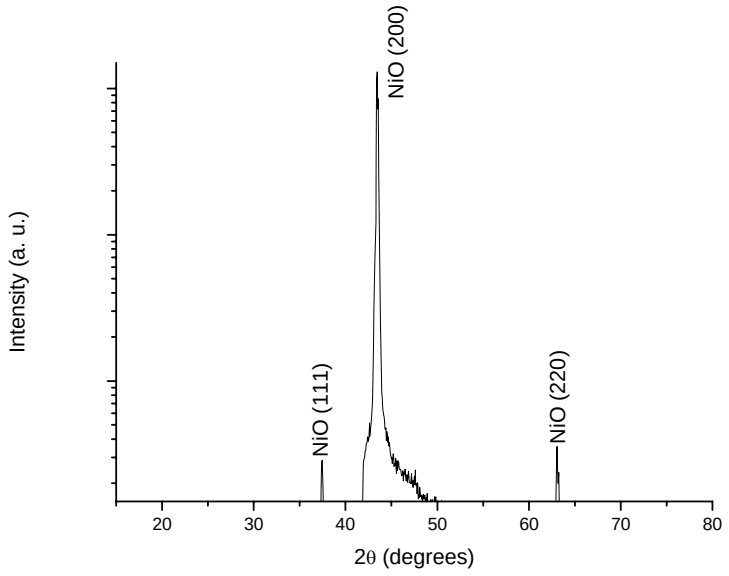

Figure 5.22: log scale XRD pattern for MgO deposition on NiO grown on unpolished and recrystallised NiW substrate tape by spray pyrolysis at 650°C using 0.468M $Mg(NO_3)_2.6H_2O$ for 32 minutes.

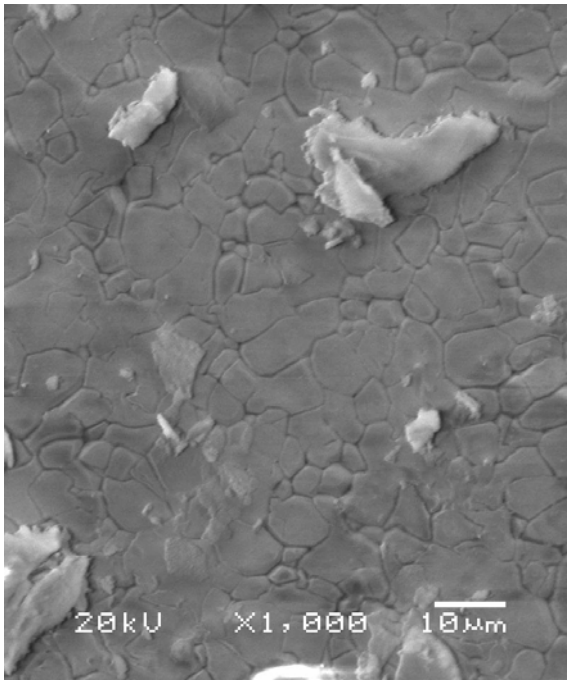

Figure 5.23: SEM image for MgO deposition on NiO grown on unpolished and recrystallised NiW substrate tape by spray pyrolysis at 650°C using 0.468M $Mg(NO_3)_2.6H_2O$ for 32 minutes.

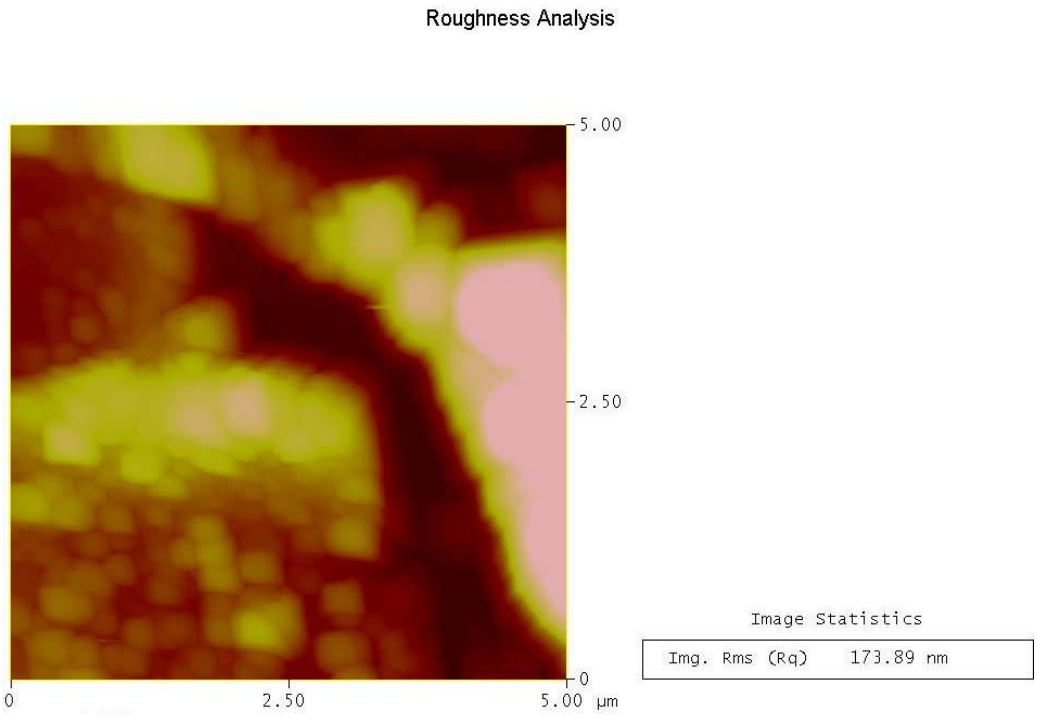

Figure 5.24: A 5x5µm^2 AFM image for MgO deposition on NiO grown on unpolished and recrystallised NiW substrate tape by spray pyrolysis at 650°C using 0.468M $Mg(NO_3)_2.6H_2O$ for 32 minutes.

The reason for not detecting any MgO peaks was not very clear, however, it may be attributed to the surface instability of the oxide during the spray pyrolysis

deposition conditions. Even when MgO deposition was applied from acetate precursors (its thermal decomposition is discussed in section 8.2.1) at 550°C and 650°C using 0.093M and 0.279M solutions, although, no MgO peaks were detected as well. Therefore, MgO deposition by spray pyrolysis on NiW RABiTS or on NiO was not successful due to the surface instability of the substrate and/or the oxide layer under the spray pyrolysis deposition conditions. Although, Ming Wei et al [54] deposited CeO_2 by the ESAVD on textured Ni tapes. However, there are some differences in the two cases; in this work we are depositing MgO not CeO_2 by spray pyrolysis not by ESAVD. In addition to that, Ming Wei et al did not mention whether CeO_2 films were deposited directly on Ni tapes or on pre- buffered ones.

6 Spray pyrolysis of MgO on 310-austenitic stainless steel using magnesium nitrate as a precursor

6.1 Introduction

In this chapter the deposition of MgO thin films by spray pyrolysis on wrought polycrystalline 310-austenitic stainless steel, using magnesium nitrate as a precursor, will be introduced. The 310-stainless steels (StSt) (100mm x100mm x 2mm) were bought from Goodfellow. The substrates were then cut into 10mm x10mm x 2mm using the wire electric discharge machine (WEDM). The samples were then mechanically polished down to a roughness of 2-5 nm, and then they were cleaned in acetone, then ethanol for 10 minutes each in an ultrasonic bath, then dried with Ar gas. In the spray pyrolysis deposition, an Ar flow rate of 10 l/min was used, a pulse time to interval time of 1:7 was applied; however, the deposition temperature, deposition time, and precursor concentration were varied.

As far as we know, no reports have been found for MgO deposition on metallic substrates by spray pyrolysis. The aim is to reduce the cost of production by using spray pyrolysis instead of the relatively expensive methods for the buffer layer deposition, such as electron beam evaporation [82] and pulse laser deposition [80]. As in the previous chapter an objective of this work is to grow MgO as the only buffer layer before YBCO deposition in an attempt to make the process a cost-effective one by reducing the usual multi-layer buffer architecture to a single layer.

6.2 310-stainless steel substrates

The chemical composition of the 310-austenitic stainless steel substrates, as received from the supplier, was checked using EDX (using an accelerating voltage of 20 KV) and compared to the American Iron and Steel Institute (AISI) standards [266].

Table 6.1 shows that that the chemical composition of the substrates as received from the supplier is within a good approximation to the AISI standards and to the one obtained from the EDX test.

Table 6.1: Chemical composition of the 310-St. St.

Element	Chemical composition, wt% (Goodfellow)	Chemical composition, wt% (AISI)	Chemical composition, wt% (EDX, 20KV)
Cr	24-26	24-26	26.08
Ni	19-22	19-22	19.83
Mn	<2	2	1.55
Si	<1	1.5	0.58
C	<0.25	0.25	0.22
Fe	Balance	Balance	Balance

The surface roughness of the polished substrates, as shown from the AFM image in Figure 6.1, shows that the roughness is in the order of 2-5nm. Figure 6.2 is the SEM image of the substrate after polishing.

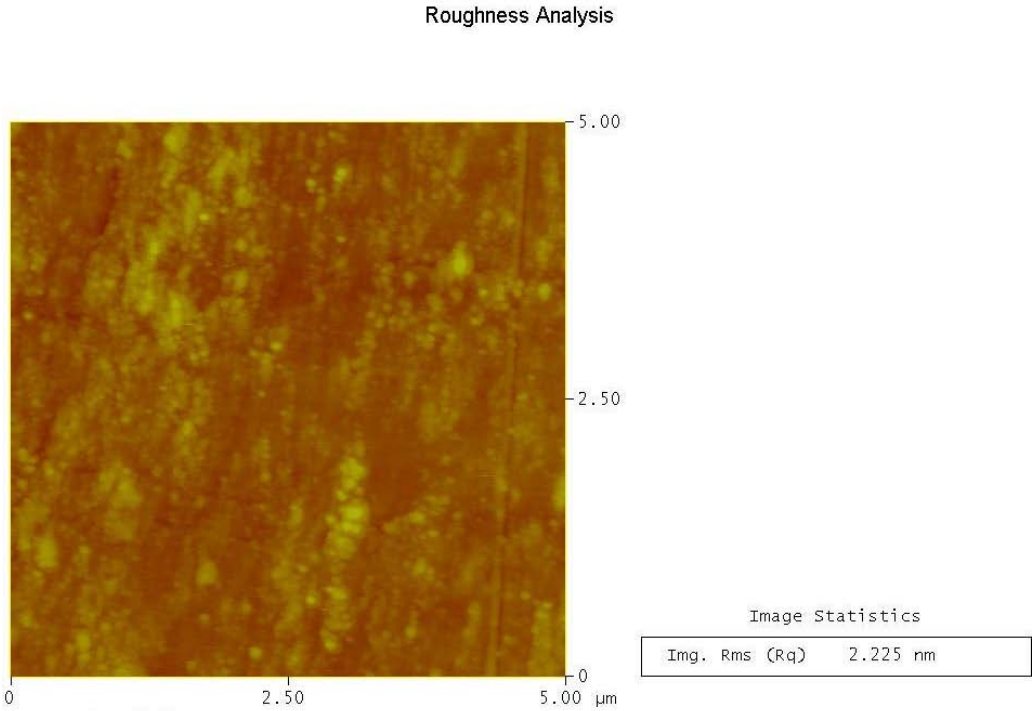

Figure 6.1: A 5x5µm^2 AFM image of the mechanically polished 310-St. St substrate.

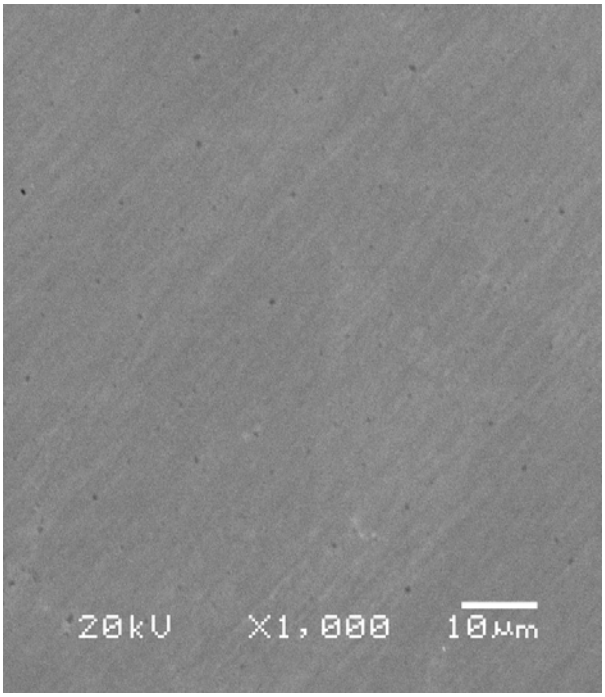

Figure 6.2: SEM image of the mechanically polished 310-St. St. substrate.

From the JCPDS PDF files, we could not find any XRD patterns for these specific substrates, i.e. the 310-stainless steels substrates. Figure 6.3 shows the XRD pattern for the 310-stainless steel substrates with the XRD peaks being indexed according to the structure factor rule (the (111), (200) and (220) peaks are at 2θs of 43.60°, 50.85° and 74.78°, respectively). From the sequence of the peaks, double-single, it was recognised that the structure of the 310-stainless steel is FCC with a calculated lattice parameter of 3.58Å and having a thermal expansion coefficient of 16-18x10^{-6}/K as given by the supplier [267]. It was also clear from the XRD pattern that the substrates were polycrystalline with (111) being the strongest peak.

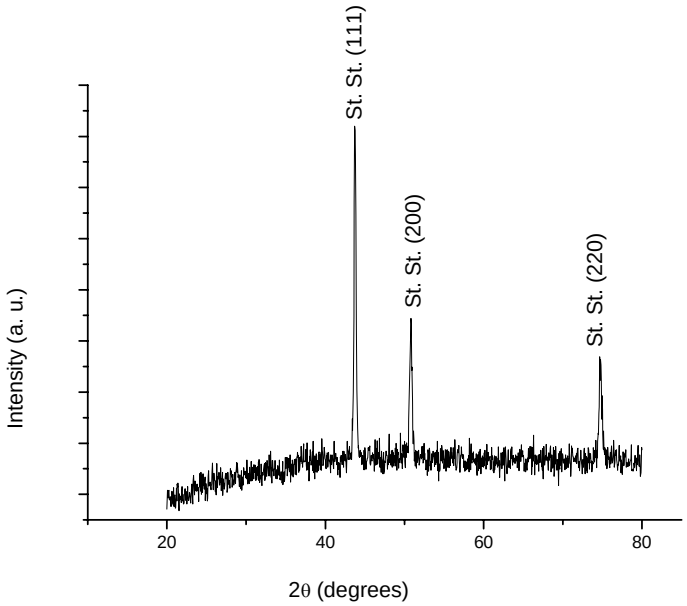

Figure 6.3: XRD pattern of the mechanically polished 310-St. St. substrate with the peaks being indexed according to the structure factor rule.

6.3 Spray pyrolysis of MgO on 310-austenitic stainless using magnesium nitrate precursor

6.3.1 Effect of deposition temperature and time on MgO film properties

MgO was spray pyrolysed on the 310-austenitic stainless steel substrates using $Mg(NO_3)_2.6H_2O$ as a precursor. The deposition was done using 0.078M at different temperatures for 32 minutes. The XRD patterns after the deposition are shown in Figure 6.4 where it can be seen that no MgO XRD peaks were detected regardless of the substrate temperature.

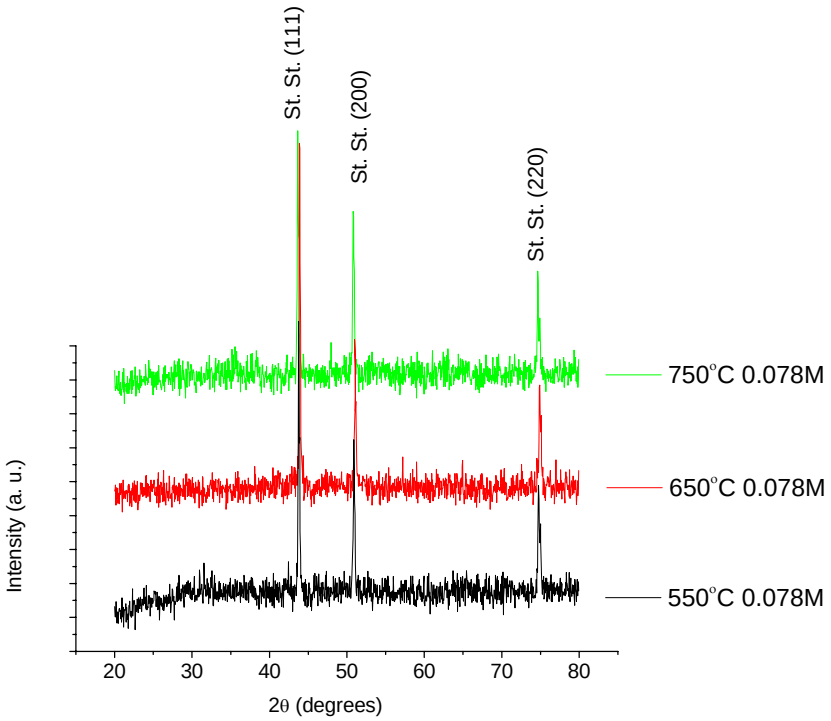

Figure 6.4: XRD patterns for MgO deposited on 310-St. St. using 0.078M of $Mg(NO_3)_2.6H_2O$ at different temperatures for 32 minutes.

Further investigation on the deposited MgO films was made by performing an EDX test. The results obtained suggest that Mg and O are present in almost stoichiometric ratio. The EDX result, using an accelerating voltage of 4KV, for the sample deposited at 650°C from 0.078M is shown in Table 6.2. From this, and from the XRD patterns in Figure 6.4, it is suggested that the deposited MgO films were amorphous, although it could be that the Mg reacted to form other phases.

Table 6.2: Summary of the EDX chemical composition result for the 310-St. St. deposited with 0.078M at 650°C for 32 minutes.

Element	at %
O K	23.99
Mg K	19.21
Fe L	34.17
Cr L	15.41
Ni L	7.22

In an attempt to deposit (200) oriented MgO films, the deposition time was increased to 96 minutes for the sample deposited at 650°C. Even by increasing the deposition time three times more compared to those in Figure 6.4, no MgO XRD peaks were detected as can be seen from Figure 6.5. As was the case for the sample deposited with 0.078M at 650°C for 32 minutes (Table 6.2), the EDX result for the sample with a deposition time of 96 minutes showed the presence of Mg and O. Therefore, the deposited MgO film was again amorphous, although it could be that the Mg reacted to form other phases.

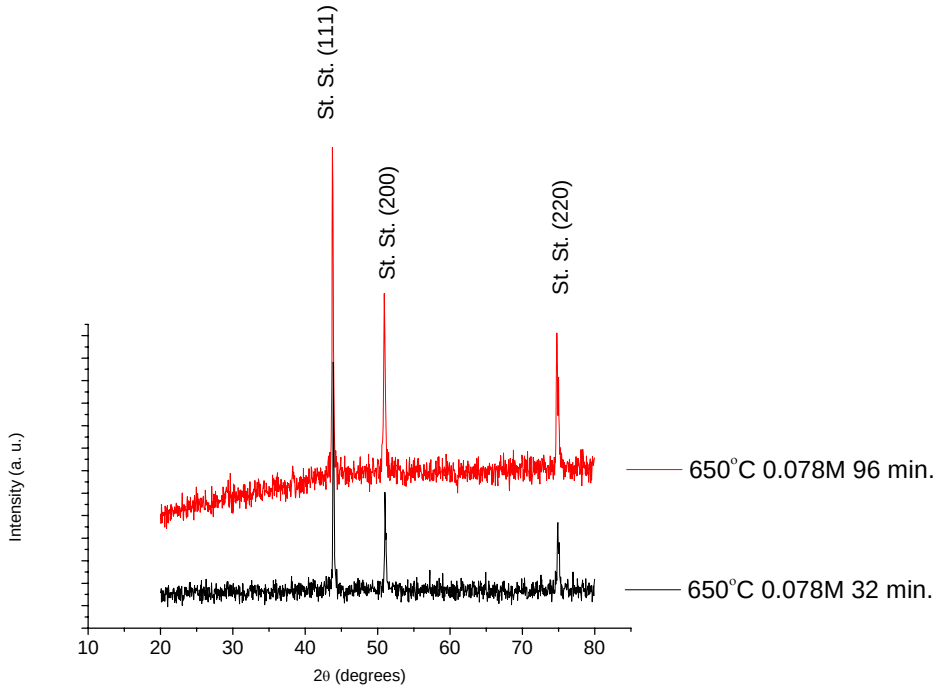

Figure 6.5: XRD patterns for MgO deposited on 310-St. St. using 0.078M of $Mg(NO_3)_2.6H_2O$ at 650°C with different deposition times.

The SEM images for the samples deposited at different temperatures and at different deposition times (i.e. those shown in Figure 6.4 and Figure 6.5) are shown in Figure 6.6 to Figure 6.9. It is clear that the MgO thin film was decorating the substrate when the temperature was higher than 550°C, where the film was copying the surface morphology of the substrate grains. The decoration was more pronounced as the temperature was higher than 550°C or the deposition time was higher than 32 minutes. In addition to that, the roughness increased by increasing the temperature or the deposition time as can be seen from the SEM images (Figure 6.6 to Figure 6.9).

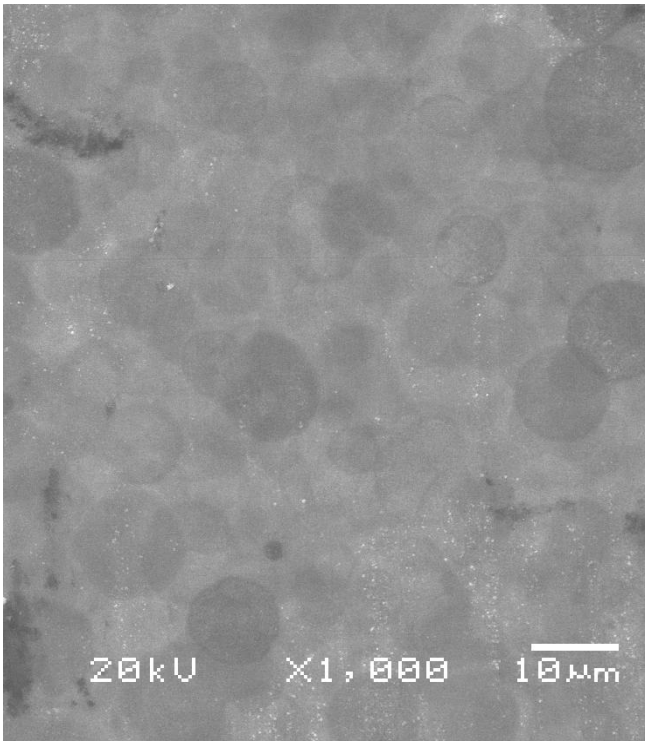

Figure 6.6: SEM image of the MgO film deposited on 310-St. St. at 550°C from a solution of 0.078M of $Mg(NO_3)_2.6H_2O$ with a deposition time of 32 minutes.

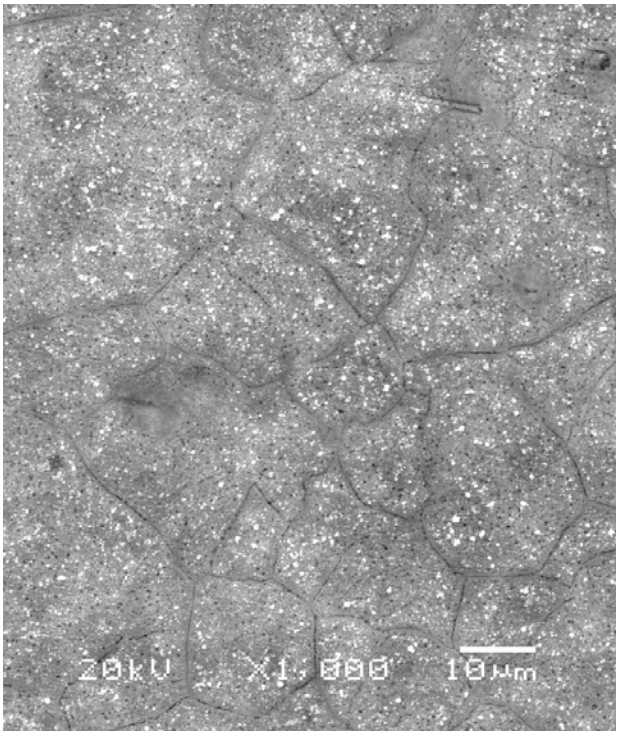

Figure 6.7: SEM image of the MgO film deposited on 310-St. St. at 650°C from a solution of 0.078M of $Mg(NO_3)_2.6H_2O$ with a deposition time of 32 minutes.

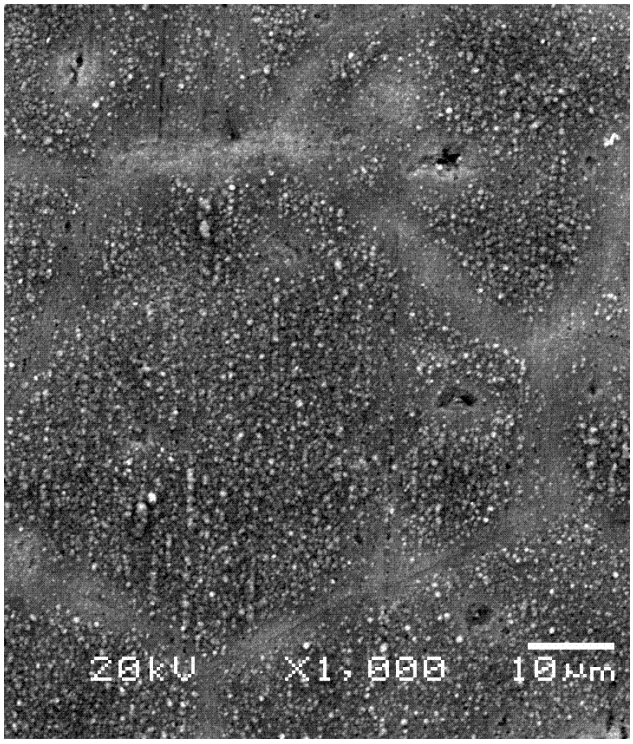

Figure 6.8: SEM image of the MgO film deposited on 310-St. St. at 750°C from a solution of 0.078M of $Mg(NO_3)_2.6H_2O$ with a deposition time of 32 minutes.

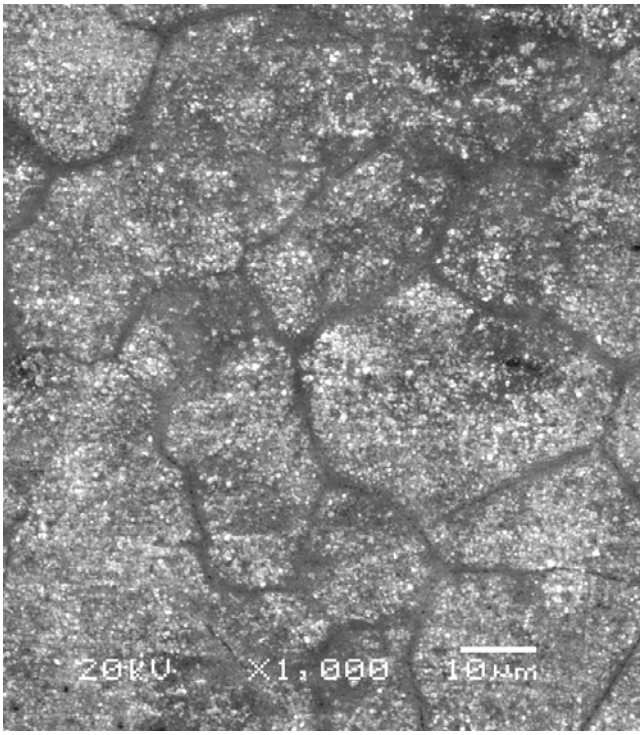

Figure 6.9: SEM image of the MgO film deposited on 310-St. St. at 650°C from a solution of 0.078M of $Mg(NO_3)_2.6H_2O$ with a deposition time of 96 minutes.

6.3.2 Effect of precursor concentration on MgO film properties

In order to grow (200) oriented MgO films, the concentration and deposition times were increased once again. The deposition time was increased to 48 minutes and the concentration was increased to 0.468M and 0.78M. However, as can be seen from the XRD patterns in Figure 6.10, no MgO XRD peaks were detected. As was the case for the samples deposited from 0.078M solution, the MgO films for the samples deposited from 0.468M and 0.78M solutions were decorating the substrate and copying their grain morphology (Figure 6.11 and Figure 6.12, respectively). The EDX result, for the sample deposited from 0.468M solution (Figure 6.13 and Table 6.3), suggests that the substrate was deposited with a stoichiometric MgO film. However, from the EDX and XRD results, it was concluded that such a film was amorphous, although it could be that the Mg reacted to form other phases. The MgO film deposited from 0.78M solution was found to be amorphous as well. The EDX tests performed on the particles (Figure 6.11 and Figure 6.12) show that such particles were MgO.

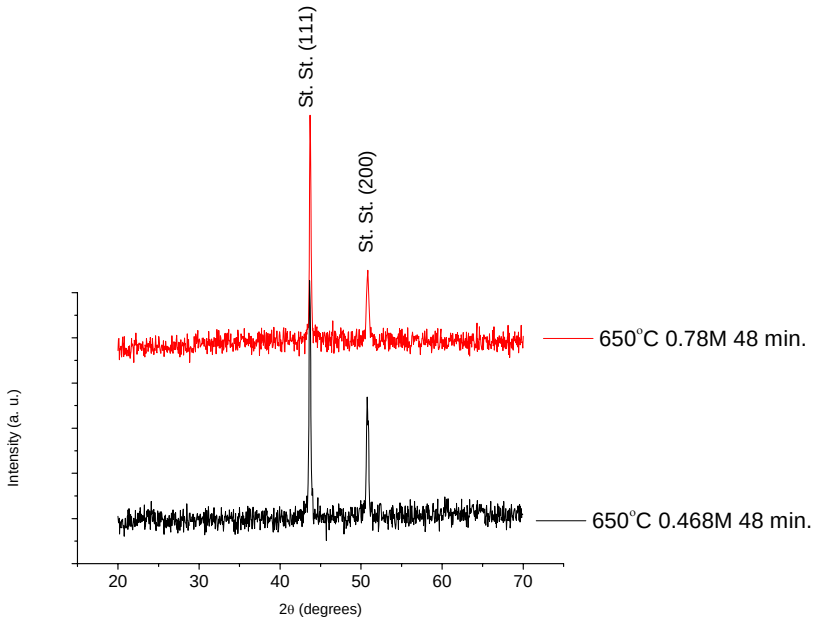

Figure 6.10: XRD patterns for MgO deposition on 310-St. St. at 650°C using different deposition concentrations of Mg(NO3)2.6H2O.

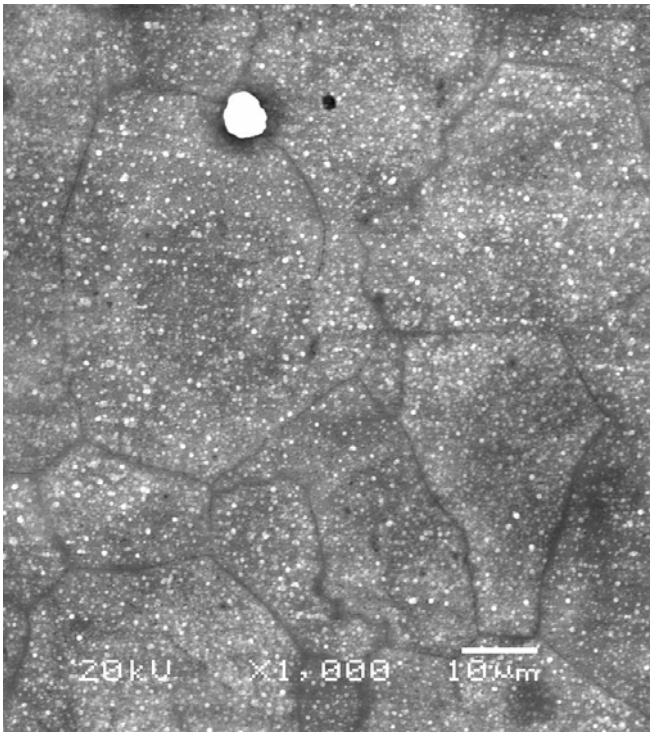

Figure 6.11: SEM image of the MgO film deposited on 310-St. St. at 650°C from a solution of 0.468M of $Mg(NO_3)_2.6H_2O$ with a deposition time of 48 minutes.

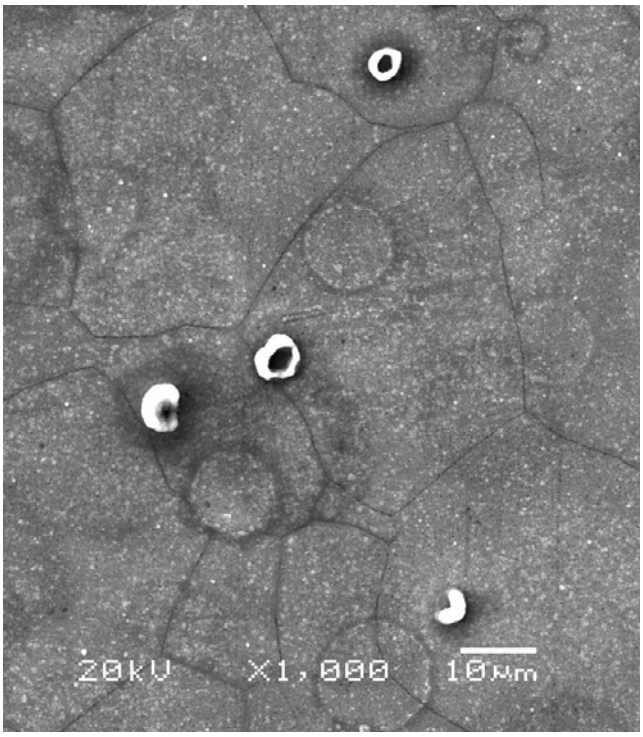

Figure 6.12: SEM image of the MgO film deposited on 310-St. St. at 650°C from a solution of 0.78M of $Mg(NO_3)_2.6H_2O$ with a deposition time of 48 minutes.

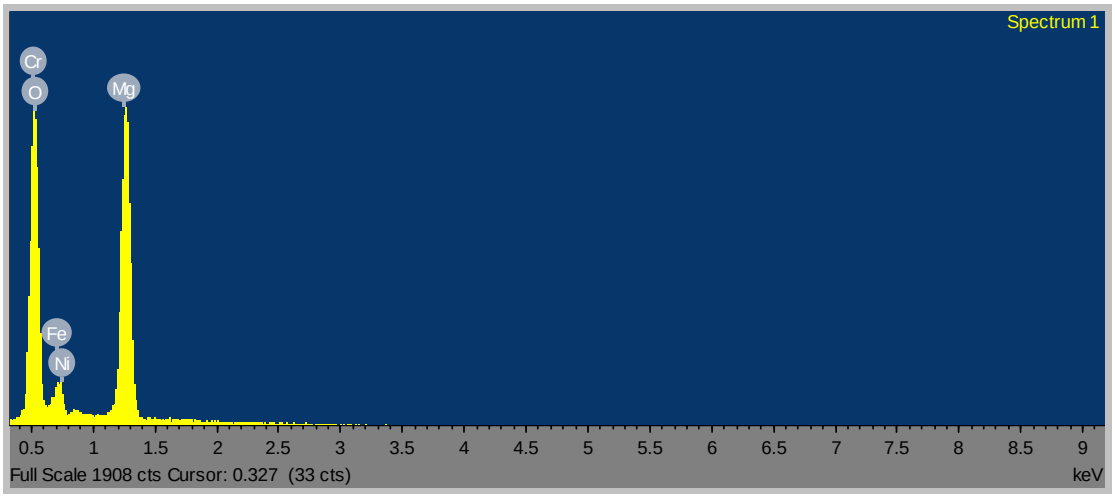

Figure 6.13: EDX spectrum, using an accelerating voltage of 4KV, for the 310-St. St. deposited with 0.468M at 650°C with a deposition time of 48 minutes.

Table 6.3: Summary of the EDX chemical composition results, using an accelerating voltage of 4KV, for the 310-St. St. deposited with 0.468M at 650°C with a deposition time of 48 minutes.

Element	at %
O K	45.44
Mg K	45.88
Fe L	7.08
Cr L	1.03
Ni L	0.57

The above results show that regardless of the substrate temperature, precursor concentration or the deposition time, no MgO XRD peaks were detected. This initiated further investigation and analysis on the 310-austenitic stainless steel substrates.

6.4 Detecting susceptibility to intergranular attack in 310-austenitic stainless steel

Austenitic stainless steels are non-magnetic, resistant to corrosion, exhibit excellent ductility, formability and toughness [268]. Ordinarily, the corrosion occurs in the presence of water and oxygen, and usually it does not take place in the absence of either of these. Rapid corrosion may take place in water; the corrosion rate is accelerated by the velocity or the acidity of the water, by the motion of the metal, and by an increase in the temperature or aeration [269]. The corrosion resistance of

Stainless Steel is therefore required during spray pyrolysis of MgO due to the relatively high temperature used during deposition and the wet environment encountered.

Steels are said to be stainless when they resist corrosion; this is achieved by dissolving sufficient chromium in the iron to produce a coherent, adherent, insulating and regenerating chromium oxide protective film on the surface. It is not surprising therefore that they are used in the harsh environments where corrosion resistance is an important design criterion. The stainless character occurs when the concentration of chromium exceeds about 12 wt%. However, even this is not adequate to resist corrosion in acids such as HCl or H_2SO_4.

In normal conditions, austenitic stainless steels are given a high-temperature heat-treatment, often called a solution-treatment, which gives a fully austenitic solid solution. However, at temperatures below about 800°C, there is a tendency to precipitate chromium-rich carbides as the alloy enters the carbide plus austenite phase field. The carbon content in stainless steel is believed to play a key role in the precipitation of Cr carbides. The main carbide phase is $M_{23}C_6$, where the 'M' stands for a mixture of metal atoms including iron, molybdenum, chromium and manganese, depending on the steel composition and heat-treatment. These carbides require long-range diffusion in order to precipitate and hence can be avoided by rapid cooling from the solution-treatment temperature. The precipitation of $M_{23}C_6$ and M_7C_3 occurs primarily at the austenite grain surfaces which are heterogeneous nucleation sites; it can occur in a matter of minutes at temperatures around 750°C. The chemical composition in the vicinity of the grain boundaries can be altered by the precipitation of the chromium-rich particles. The resulting chromium-depleted zone at the grain boundaries makes them susceptible to intergranular anodic-attack even under stress-free conditions. Once again, the anodic regions present a much smaller area (grain boundaries) compared with the rest of the exposed surface which is cathodic; the localised rate of corrosion at the boundaries is therefore greatly exaggerated. This is the essence of sensitisation. In addition, precipitation of nitrides along the grain boundaries, such as Cr_2N, due to excess of N may also lead to a localised depletion of Cr and hence induce localised corrosion around them [270, 271]. This situation may also be valid during MgO deposition from the nitrate precursor.

In section 6.3, MgO was deposited on 310-stainless steel at various temperatures, deposition times and different concentrations of the $[Mg(NO_3)_2.6H_2O]$

precursor. However, no XRD peaks were detected for MgO and it was concluded that the deposited MgO films were amorphous, although it could be that the Mg reacted to form other phases. From the surface morphologies of the MgO films, when the temperature is higher than 550°C, in Figure 6.7-Figure 6.9, Figure 6.11 and Figure 6.12, it can be seen that grooves were formed along the grain boundaries of the substrates which were decorated by the amorphous MgO layer. Such morphologies are similar to the morphologies encountered in sensitised austenitic stainless steels [271-273].

At temperatures between 425^{o}C-900^{o}C, there is a tendency to precipitate chromium-rich carbides mainly along the grain boundaries. The resulting chromium-depleted zone close to the grain boundaries make them susceptible to intergranular corrosion (Figure 6.14) [266, 273-275]. For this reason, the substrate materials were investigated for the sensitisation effect as will be discussed in the next section.

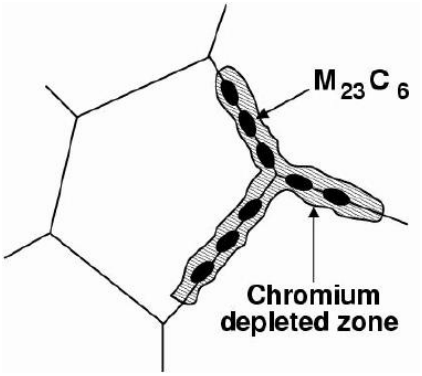

Figure 6.14: Mechanism of sensitisation [274].

6.4.1 ASTM A 262: practice A-oxalic acid etch of austenitic stainless steels

The ASTM test (practice A 262) for detecting the susceptibility to intergranular corrosion (IGC) was adopted [275]. This test detects the susceptibility to intergranular attack associated with the precipitation of chromium carbides. It is a rapid and simple method of identifying the specimens that are free of susceptibility to intergranular attack by means of their etch structures.

The test requires a source of direct current and a cylindrical piece of stainless steel, as large as the specimen to be etched, working as a cathode. The specimen to be tested (etched) is made the anode. The solution used for etching is prepared by adding

100 g of reagent grade oxalic acid crystals ($H_2C_2O_4.2H_2O$) to 900 ml of distilled water and stirring until all crystals are dissolved. The Amperes used during the test should be equal to the total immersed area of the specimen measured in square centimetres and applied for 1.5 minutes. Thus, for the substrates with 10mm x10mm x 2mm, the total area is 2.8 cm^2, therefore, 2.8A were applied for 1.5 minutes in this work. Following etching, the specimens should be rinsed thoroughly in hot water and in acetone or alcohol to avoid crystallisation of oxalic acid on the etched surfaces during drying.

The etch structures are classified into the following types:

- Step structure where only steps are formed between grains.
- Dual structure where some ditches are formed at grain boundaries in addition to steps, but no single grain completely surrounded by ditches.
- Ditch structure where one or more grains completely surrounded by ditches.

6.4.2 Oxalic acid etch of 310-austenitic stainless steel

In performing the test, a specimen should be representing as nearly as possible the surface of the material as it will be used in service. In this work, the surface of the samples to be tested by the oxalic acid etch should represent the surface after the spray pyrolysis deposition. For this reason and for the sake of being able to tell the difference in results, the as received substrates, the substrates after the spray pyrolysis deposition and the substrates free of sensitisation must all be tested by the oxalic acid test.

To simulate the spray pyrolysis deposition conditions during the oxalic etch test, the substrates were first deposited with 0.078M solution at 550°C, 600°C and 650°C for 32 minutes. A sample free from sensitisation can be obtained by heat treating at 1095°C for 1 hr then water quenching to bring the chromium carbides into solution [266], and this is called a solution annealing treatment [271]. Another sample was heated to 650°C for 24 hrs then furnace cooled to study the effect of heat treating time. All of the samples were then polished and etched by the oxalic acid etch one at a time.

In the absence of chromium carbides a step structure is formed, while ditches are formed at the grain boundaries as evidence of chromium carbide precipitates. If the ditches do not envelope any one grain completely, the etch is classified as dual structure and, if one or more grains are completely surrounded, as ditch structure

[272]. In the oxalic acid etch test, conditions for acceptable and unacceptable etch structures are specified. Acceptable etch structures (Figure 6.15-Figure 6.19 which show step and dual structures) are immune to intergranular attack. Unacceptable etch structures (Figure 6.20 which show a ditch structure) indicate that the specimen may be subject to intergranular attack where ditches are surrounding the grains [273]. So, from Figure 6.17-Figure 6.19, severe intergranular corrosion in 310-stainless steel, under the deposition conditions used during spray pyrolysis, is not observed. However, from Figure 6.18 and Figure 6.19, some carbides are still being formed as can be seen from the grooves (ditches) formed at the grain boundaries. It can also be noted, especially in Figure 6.18 and Figure 6.19, that the twin boundaries were not attacked by the acid, indicating to some extent that the twin boundaries exhibit a better corrosion resistance than the grain boundaries. X. Q. Wu et al [271] found similar groove (or ditch) structure in 316L austenitic stainless steel after being given a sensitisation treatment at 650°C for 2 hours. The XRD patterns did not show any peaks corresponding to Cr precipitates in the steel but their presence caused degradation of the corrosion resistance of grain boundaries.

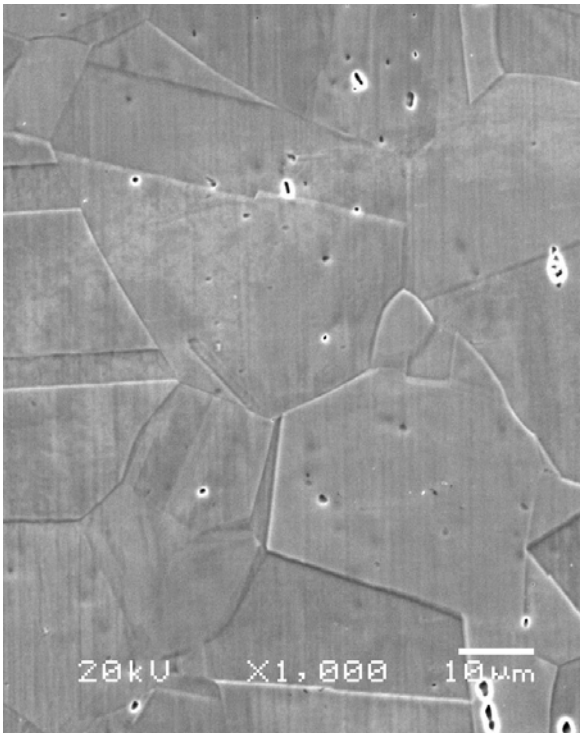

Figure 6.15: SEM image after the oxalic acid test for detecting the (IGC) in as received 310-St. St. showing a step structure.

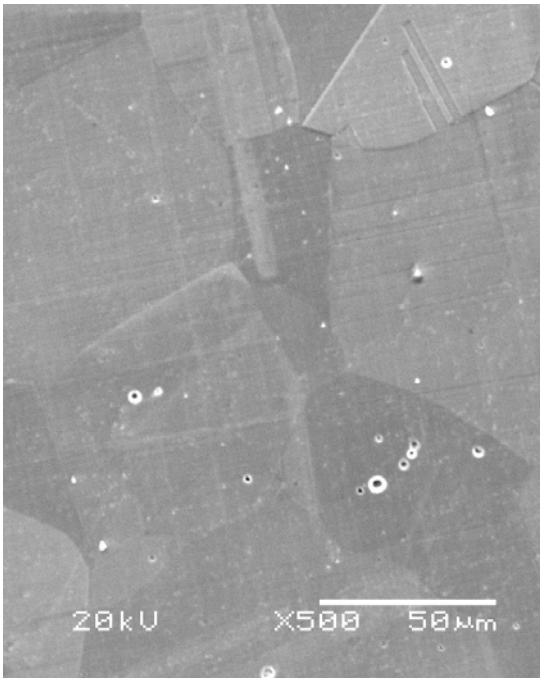

Figure 6.16: SEM image after the oxalic acid test for detecting the (IGC), in 310-St. St. heated to 1095°C for 1 hr then water quenched then polished, showing a step structure.

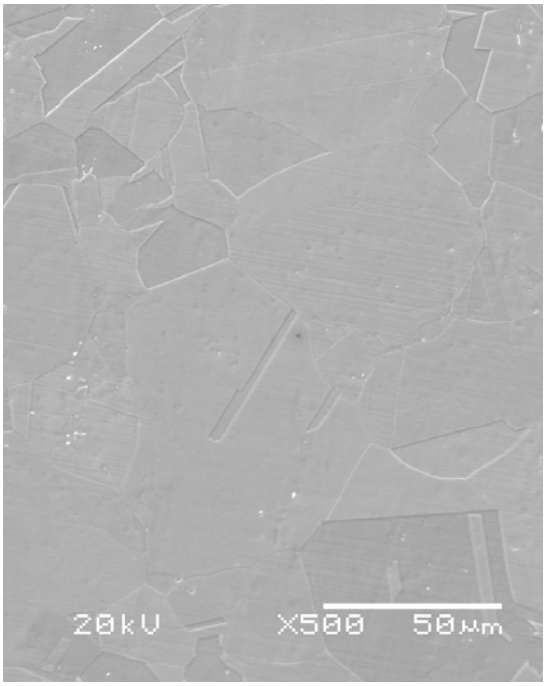

Figure 6.17: SEM image after the oxalic acid test for detecting the (IGC), in 310-St. St. deposited with MgO at 550°C from 0.078M solution of $Mg(NO_3)_2.6H_2O$ with a deposition time of 32 minutes then removed by polishing, showing a step structure.

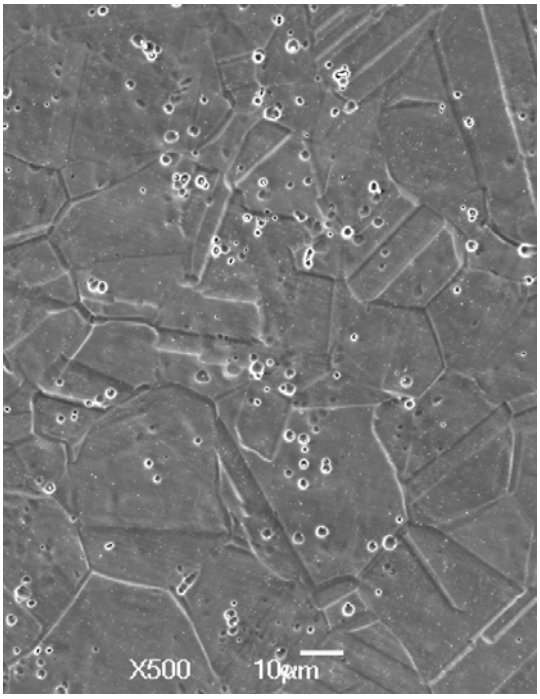

Figure 6.18: SEM image after the oxalic acid test for detecting the (IGC), in 310-St. St. deposited with MgO at 600°C from 0.078M solution of $Mg(NO_3)_2.6H_2O$ with a deposition time of 32 minutes, then removed by polishing, showing a dual structure.

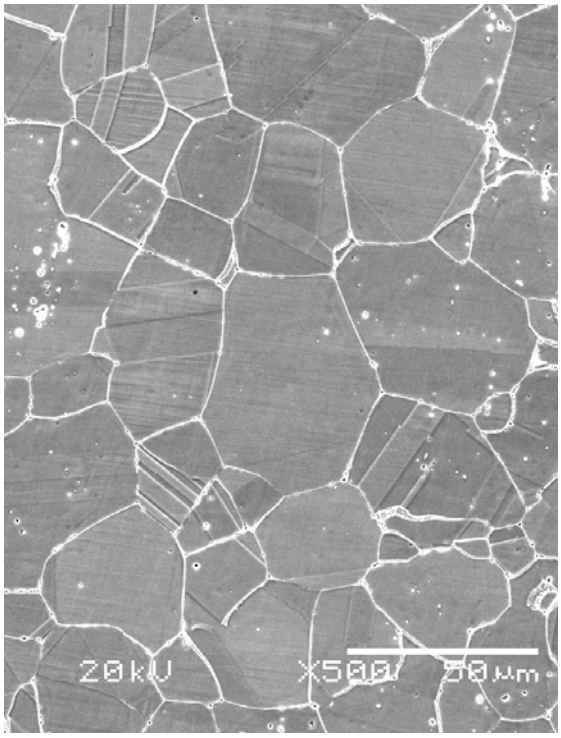

Figure 6.19: SEM image after the oxalic acid test for detecting the (IGC), in 310-St. St. deposited with MgO at 650°C from 0.078M solution of $Mg(NO_3)_2.6H_2O$ with a deposition time of 32 minutes then removed by polishing, showing a dual structure.

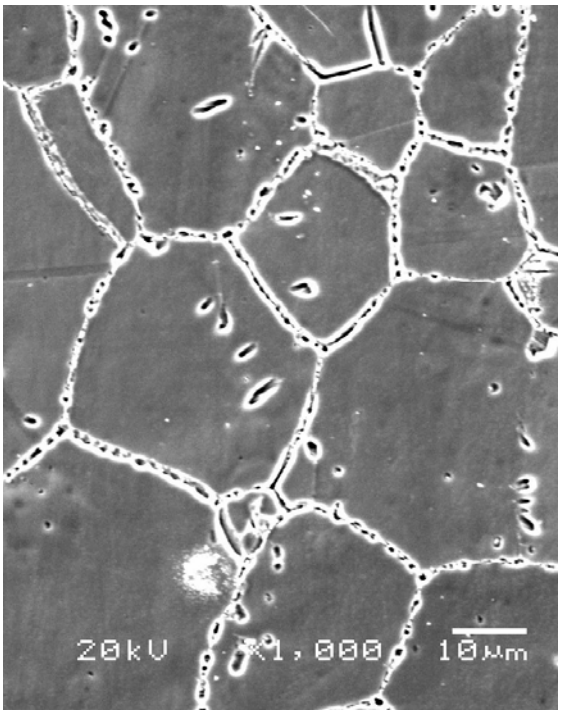

Figure 6.20: SEM image after the oxalic acid test for detecting the (IGC), in 310-St. St. heated to 650°C ,without any depositions, for 24 hrs then furnace cooled and polished, showing a ditch structure.

As the surface quality of the substrates, such as roughness, cleanliness and grain boundary grooving, play a significant role for the buffer and the YBCO growth and also may affect the superconducting properties [61, 167, 264, 265], it was concluded that the substrate surface is not stable for thin film deposition and that 310-St. St. is not a good candidate as a substrate material for buffer layer deposition using the spray pyrolysis technique due to the thermal instability of the surface during deposition at relatively high temperature and wet environment.

7 Spray pyrolysis of MgO on Hastelloy C276 from nitrate precursor

7.1 Introduction

This chapter is divided mainly into two. In the first part, the stability of the substrate for thin film deposition will be investigated in terms of the susceptibility to intergranular corrosion. In the second part of this chapter, the deposition of MgO from a nitrate precursor, at different deposition temperatures, precursor concentrations, deposition times, inclination angles, Ar-flow rates and different annealing treatments will be investigated. To evaluate the performance of the MgO films, YBCO was then deposited by PLD on top of MgO film deposited by spray pyrolysis on Hastelloy C276. In an attempt to improve the in-plane texture of YBCO, CeO_2 was also deposited by PLD on top of MgO film deposited by spray pyrolysis on Hastelloy C276.

7.2 Susceptibility of Hastelloy C276 to intergranular corrosion

7.2.1 Introduction

Hastelloy is a non-magnetic candidate substrate material [32], which exhibits good resistance to sea-water corrosion, excellent pitting and crevice corrosion resistance [268], and it is has good resistance to creep, fatigue and erosion [276]. As for 310 austenitic stainless steel (section 6.4), the corrosion resistance of Hastelloy C276 is required during spray pyrolysis of MgO due to the relatively high temperature used during deposition and the wet environment encountered. Therefore, before depositing MgO films, examination of the surface stability of Hastelloy C276 for thin film deposition was given the priority this time. This was done by applying a standard test to study the susceptibility of Hastelloy C276 to intergranular corrosion as will be explained in section 7.2.3.

7.2.2 Hastelloy C276 substrates

The Hastelloy C276 (HC) (100mm x100mm x 2mm) was bought from Goodfellow. The substrates were then cut into 10mm x10mm x 2mm using the wire electric discharge machine (WEDM). The samples were then mechanically polished down to a roughness of 2-5 nm, and then they were cleaned in acetone, then ethanol for 10 minutes each in an ultrasonic bath, then dried with Ar gas.

The chemical composition of the wrought Hastelloy C276 substrates, as received from the supplier, was checked using the EDX (using an accelerating voltage of 20 KV) and compared to the American Iron and Steel Institute (AISI) standards

[266]. Table 7.1 shows that the chemical composition of the substrates as received from the supplier is, with a good approximation, close to the AISI standards and to the one obtained from the EDX test.

Table 7.1: Chemical composition of the as received Hastelloy C276.

Element	Chemical composition, wt% (Goodfellow)	Chemical composition, wt% (AISI)	Chemical composition, wt% (EDX, 20KV)
Cr	13-17.5	15.5	15.67
Ni	Balance	59	58
Mo	16-18	16	15.81
W	3.7-5.3	3.7	4.23
C	<0.15	0.02	0.12
Fe	4.5-7	5	6.17

The surface roughness of the substrates, as shown from the AFM image in Figure 7.1, shows that the roughness was in the order of 2-5 nm. Figure 7.2 is the SEM image of the substrate after polishing and Figure 7.3 is the SEM image of the sample after being polished and etched with kalling's reagent (10 g $CuCl_2$, 50 ml HCl, and 50 ml ethanol) to reveal the microstructure.

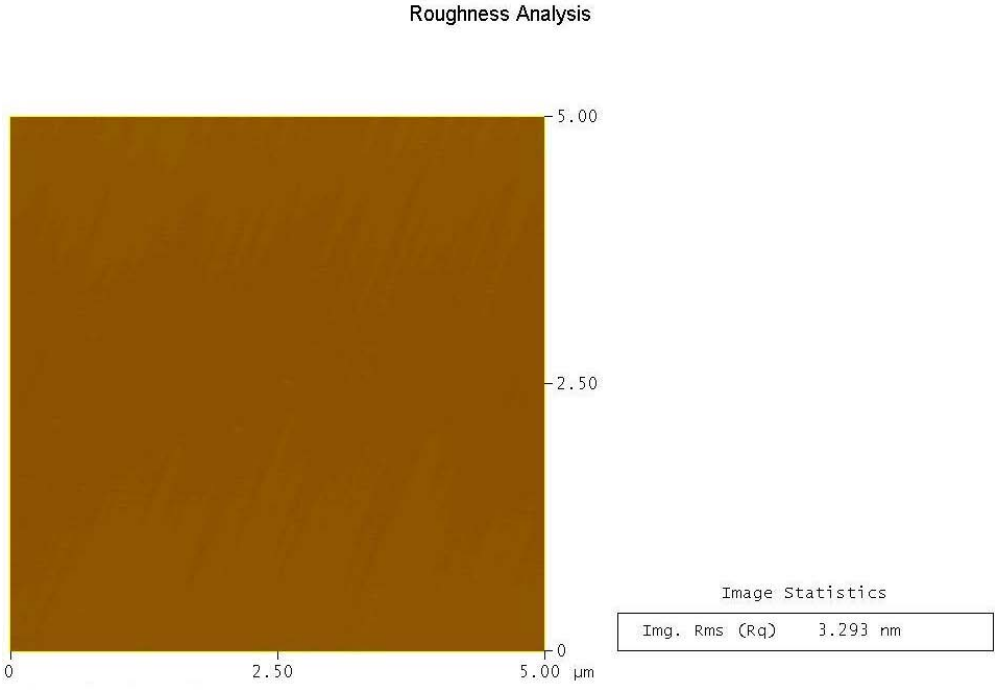

Figure 7.1: A 5x5µm^2 AFM image of the mechanically polished Hastelloy C276 substrate.

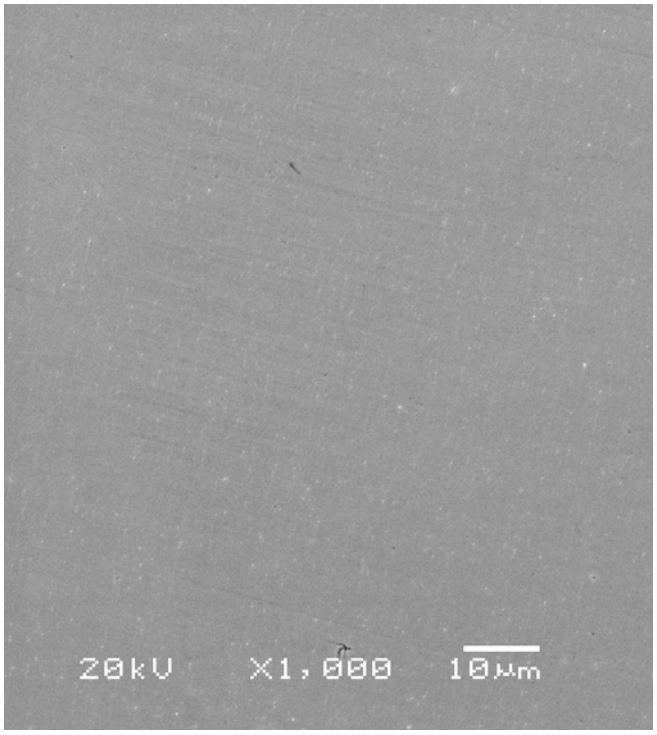

Figure 7.2: SEM image of the mechanically polished Hastelloy C276 substrate.

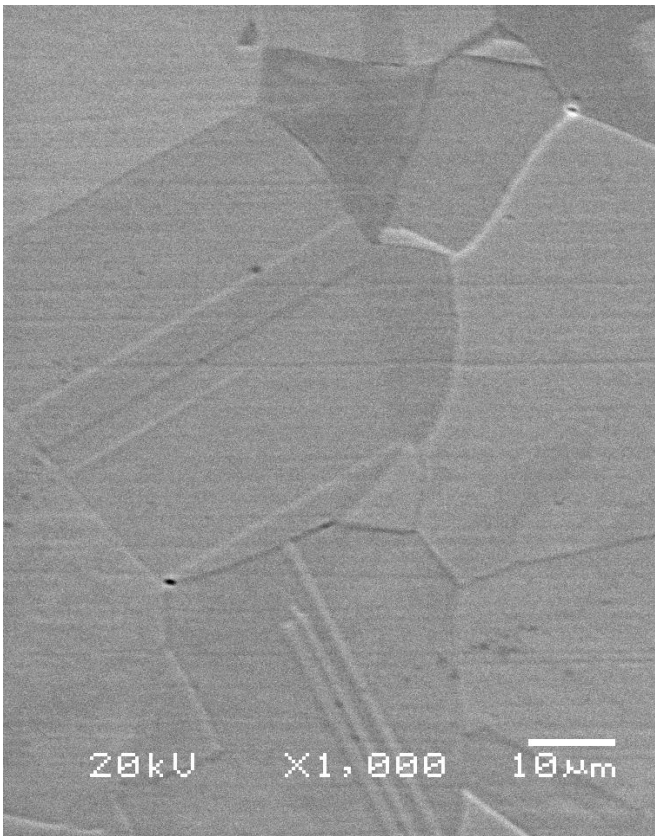

Figure 7.3: SEM image of the mechanically polished Hastelloy C276 substrate and etched with the kalling's reagent.

From the JCPDS PDF files, we could not find any XRD patterns for these specific substrates, i.e. the Hastelloy C276 substrates. Figure 7.4 shows the XRD pattern for Hastelloy C276 substrates with the XRD peaks being indexed according to the structure factor rule (the (111), (200) and (220) peaks are at 2θs of 43.55°, 50.65° and 74.45°, respectively). From the sequence of the peaks, double-single, it was recognised that the structure of Hastelloy C276 is FCC with a calculated lattice parameter of 3.595Å and having a thermal expansion coefficient of 10.8-11.3x10^{-6}/K as given by the supplier [267]. It was also clear from the XRD pattern that the substrates were polycrystalline with the (111) being the strongest peak.

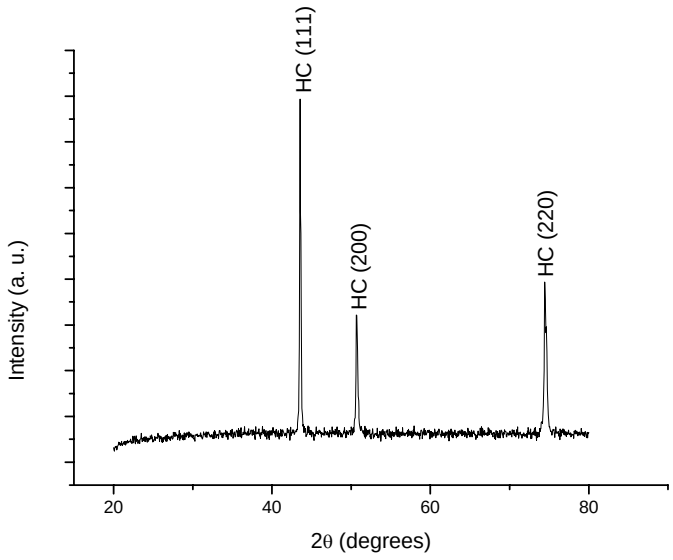

Figure 7.4: XRD pattern of the mechanically polished Hastelloy C276 substrate with the peak being indexed according to the structure factor rule.

7.2.3 Detecting susceptibility to intergranular attack in Hastelloy C276

The carbon content in nickel based alloys is less than that in stainless steels (Table 6.1 and Table 7.1). Besides that, in nickel base alloys, the solubility of carbon in the matrix decreases as the nickel content rises. This low carbon content is beneficial for resistance to intergranular corrosion. The nickel alloys susceptible to intergranular corrosion sensitization include:

- Inconel alloy 600
- Inconel alloy 800
- Inconel 800H
- Nickel 200

- Hastelloy alloys B and C

Hastelloy C alloys are susceptible to intergranular corrosion after being heated at 500°C-705°C, which is in the range of the spray pyrolysis deposition temperatures. Many investigations were carried out on the nature of the precipitates formed in alloy C. The identified precipitates were Ni_7Mo_6, Mo_6C, $M_{23}C_6$, and M_2C [275]. These intermetallic compounds and carbides are rich in molybdenum, tungsten and chromium and therefore create adjacent areas of alloy depletion that can be selectively attacked. Carbide precipitation can be retarded considerably by lowering carbon and silicon; and this is the principle behind the use of Hastelloy C276 which has low carbon and Si content (Table 7.1); the Si is an impurity which may segregate along the grain boundaries, which is deleterious in oxidizing environments, and alter the corrosion properties. However, the Hastelloy C alloys are made immune by heat treatment at 1210°C-1240°C to put the carbides in solid solution, followed by rapid cooling in air or water, this treatment is called solution annealing [266, 275].

7.2.3.1 BSI BS EN ISO 9400:1995, method A (corresponds to the ASTM standard G28, method A)

It is the iron (III) sulfate-sulfuric acid test for the determination of the susceptibility of wrought (not cast) nickel-based, chromium-bearing alloys to intergranular corrosion as influenced by variation in processing or composition, or both. It is also used to evaluate the effect of subsequent heat treatment. In this test, the specimens should represent as nearly as possible the surface of the material used in service. The recommended apparatus, and which was used in this work, is shown in Figure 7.5. The chemical solution was placed in a flask which was heated by an electrical hot plate for continuous boiling of the test solution.

A 600 ml of the test solution was prepared by measuring 400 ml (cm^3) of distilled water and pour into the Erlenmeyer flask. A 236 cm^3 of reagent grade 95 to 98% sulfuric acid was then measured and added slowly to the water in the Erlenmeyer flask to avoid boiling by the heat evolved. 25 g of reagent grade iron (III) sulfate [$Fe_2(SO_4)_3.9H_2O$] was then added to the sulfuric acid solution. The solution after that was boiled until the entire iron (III) sulfate was dissolved. The samples were then immersed in the flask and it was continued for 24 hours, for alloys containing less than 18% chromium (the case for Hastelloy C276) and 120 hours for alloys containing

more than 18% chromium (not applicable for the substrates used in this work). After that the samples were removed, rinsed in water and acetone then dried.

The effect of the test solution on the material can be measured by determining the loss of mass of the specimen. The corrosion rate can be calculated as follows:

$$\text{Corrosion rate} = \frac{k\Delta m}{At\rho} \quad \textbf{(Eq. 7.1)}$$

Where

K : is a constant and its value depends on the corrosion rate unit, ex. 8.76×10^4 if the corrosion rate is in mm/yr.

t : is the exposure time in hours.

A : is the exposed area in square centimetres.

Δm: is the mass loss in grams.

ρ : is the density in grams per cubic centimetre (8.87 g/cm^3 for C276).

The criterion for passing the test is the corrosion rate. The maximum allowable corrosion rate in Hastelloy C276 is 1 mm/month [275]. As an alternative or in addition to calculating a corrosion rate from mass loss data, metallographic examination may be used to evaluate the degree of intergranular attack.

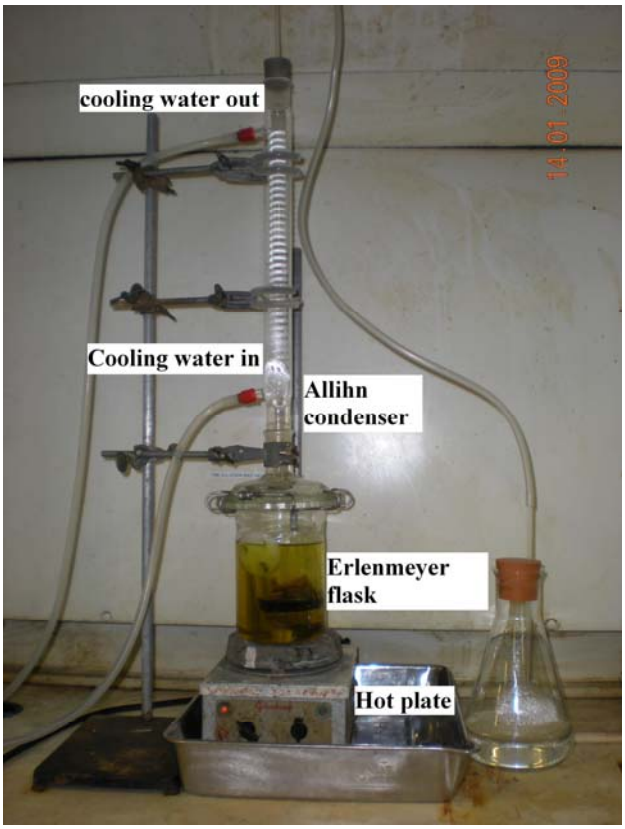

Figure 7.5: Apparatus for Ferric sulfate – sulfuric acid test.

7.2.3.2 Ferric sulfate – sulfuric acid test for Hastelloy C276

In performing the test, a specimen should be representing as nearly as possible the surface of the material as it will be used in service. In this work, the surface of the samples to be tested by the ferric sulfate-sulfuric acid test should represent the surface after the spray pyrolysis deposition. For this reason and for the sake of being able to tell the difference in results, the as received substrates, the substrates after the spray pyrolysis deposition and the substrates free of sensitisation must all be tested by the ferric sulfate-sulfuric acid test.

To simulate the spray pyrolysis deposition conditions during the ferric sulfate-sulfuric acid test, the substrates were first deposited with 0.078M solution at 500°C, 550°C, 600°C and 650°C for 48 minutes. A sample free from sensitisation can be obtained by heat treating at 1215°C for 1 hr then water quenched (WQ) to bring the chromium carbides into solution, and this is called a solution annealing [266, 275]. Another sample was heated to 650°C for 24 hrs then furnace cooled to study the effect of heat treating time. All of the samples were then polished and subjected to the boiling ferric sulfate-sulfuric acid test.

Table 7.2 shows the corrosion rate results in mm/month. According to the American Society for Metals (ASM), the corrosion rate should exceed 1 mm/month for the samples to be considered susceptible to IGC [275]. According to that, none of the Hastelloy samples, regardless of the spray pyrolysis deposition conditions, which were applied before the test, or the applied heat treatment, were susceptible to intergranular corrosion; as the corrosion rate was less than 1mm/month. The highest corrosion rate was found for the sample heated to 650°C for 24 hours then furnace cooled, even though the corrosion rate was less than 1mm/month (0.76mm/month). This slight increase in the corrosion rate compared to the other samples may be attributed to the long heating time which led to the formation of some chromium carbides at grain boundaries.

Table 7.2: Corrosion rates as obtained from the Ferric sulfate-sulfuric acid test.

	Exposed area (cm^2)	Weight before test (g)	Weight after test (g)	Weight loss (g)	Corrosion rate (mm/month)
As received	2.732	1.6654	1.62490	0.0405	0.51
500°C	2.619	1.53027	1.48946	0.04081	0.53
550°C	2.775	1.61239	1.56902	0.04337	0.54
600°C	2.799	1.70467	1.65983	0.04484	0.55
650°C	2.748	1.63630	1.59240	0.0439	0.55
1215°C (WQ)	2.743	1.66740	1.62711	0.04029	0.5
650°C (24 hrs)	2.667	1.61126	1.55212	0.05914	0.76

The SEM images for the samples after the ferric sulfate-sulfuric acid test are shown in Figure 7.6-Figure 7.12. From the SEM images, it can be seen that all of the samples have the same structure except the one heated to 1215°C then water quenched (Figure 7.7) and the one heated at 650°C for 24 hours then furnace cooled (Figure 7.12). Those structures agree with the corrosion rate values, where the sample heated to 650°C for 24 hours had the highest corrosion rate and the SEM image showed that it was the most attacked one. However, the sample heated to 1215°C had the lowest corrosion rate and the SEM image showed that it is the least attacked one.

It is known that the carbon content in stainless steel plays a key role in the precipitation of Cr carbides [271]. By taking into consideration the low percentage of carbon in Hastelloy C276 (0.02% max.) compared to that in 310-stainless steel (0.25%) [266], (Table 6.1 and Table 7.1, respectively), the SEM images in Figure 7.6-Figure 7.12 show pits formed on grain boundaries from the long contact with the acid, not ditches or grooves as was seen in Figure 6.18-Figure 6.20, which was as a result of the sensitisation effect due to the formation of Cr-carbides. Therefore, it was clear that the Hastelloy under the spray pyrolysis deposition conditions used in this study was not susceptible to IGC. Therefore, it was concluded that C276 can be used as a substrate for MgO deposition, by spray pyrolysis, in terms of the surface stability.

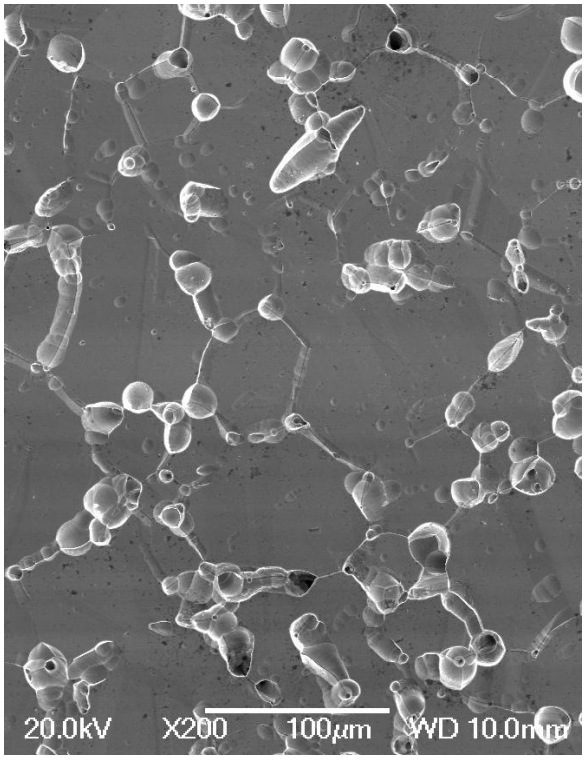

Figure 7.6: SEM image after the ferric sulfate-sulfuric acid test for detecting the (IGC) in the as received Hastelloy C276.

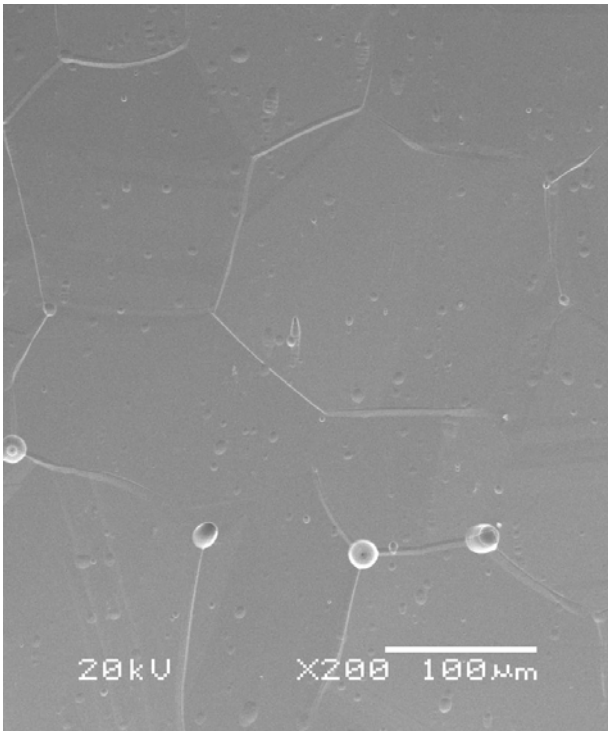

Figure 7.7: SEM image after the ferric sulfate-sulfuric acid test for detecting the (IGC), in Hastelloy C276 heated to 1215°C for 1 hr then water quenched then polished.

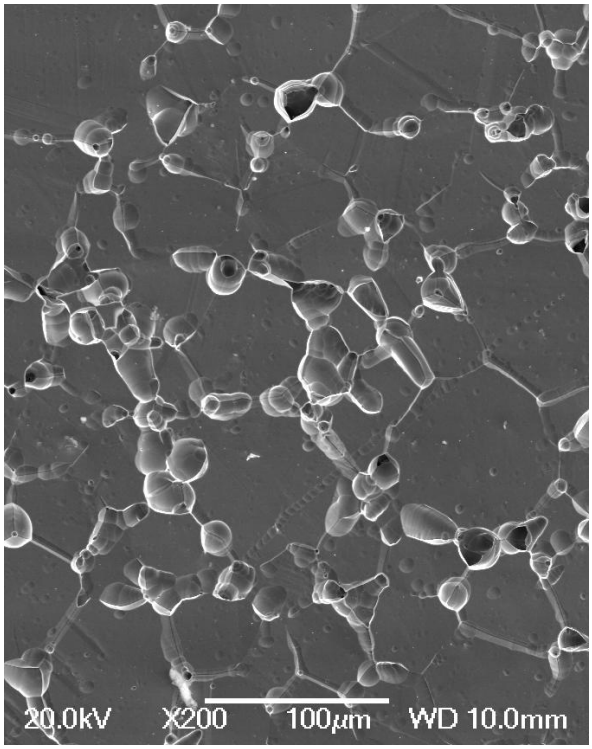

Figure 7.8: SEM image after the ferric sulfate-sulfuric acid test for detecting the (IGC), in Hastelloy C276 after deposition of MgO at 500°C from 0.078M solution of $Mg(NO_3)_2.6H_2O$ with a deposition time of 48 minutes which was then removed by polishing.

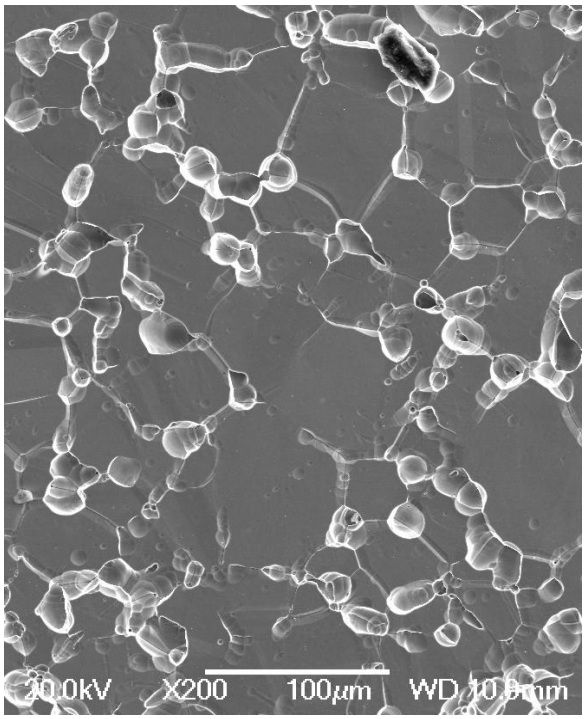

Figure 7.9: SEM image after the ferric sulfate-sulfuric acid test for detecting the (IGC), in Hastelloy C276 after deposition of MgO at 550°C from 0.078M solution of $Mg(NO_3)_2.6H_2O$ with a deposition time of 48 minutes which was then removed by polishing.

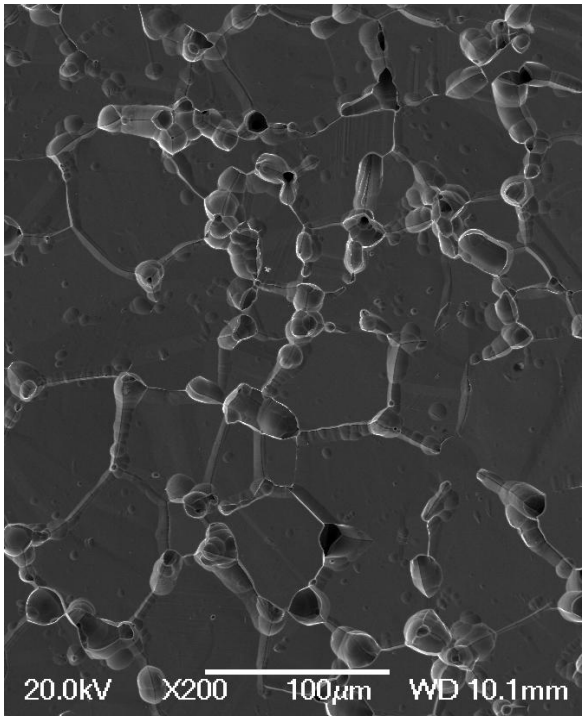

Figure 7.10: SEM image after the ferric sulfate-sulfuric acid test for detecting the (IGC), in Hastelloy C276 after deposition of MgO at 600°C from 0.078M solution of $Mg(NO_3)_2.6H_2O$ with a deposition time of 48 minutes which was then removed by polishing.

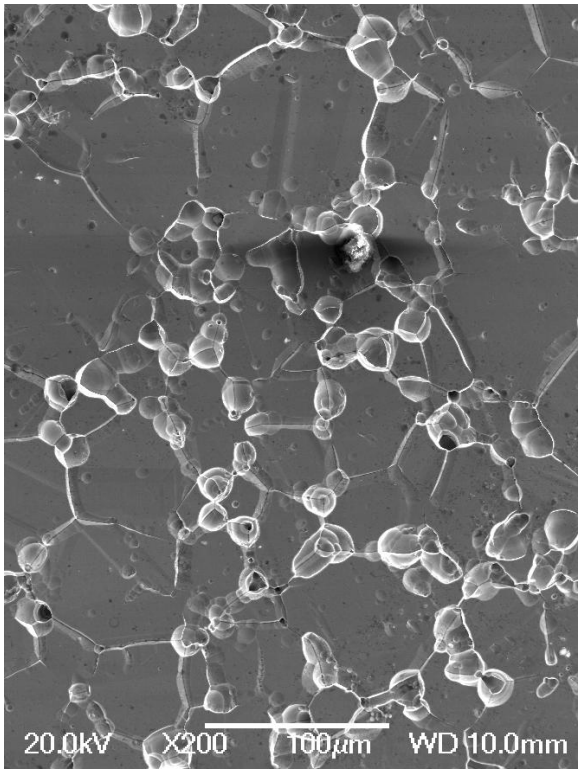

Figure 7.11: SEM image after the ferric sulfate-sulfuric acid test for detecting the (IGC), in Hastelloy C276 after deposition of MgO at 650°C from 0.078M solution of $Mg(NO_3)_2.6H_2O$ with a deposition time of 48 minutes which was then removed by polishing.

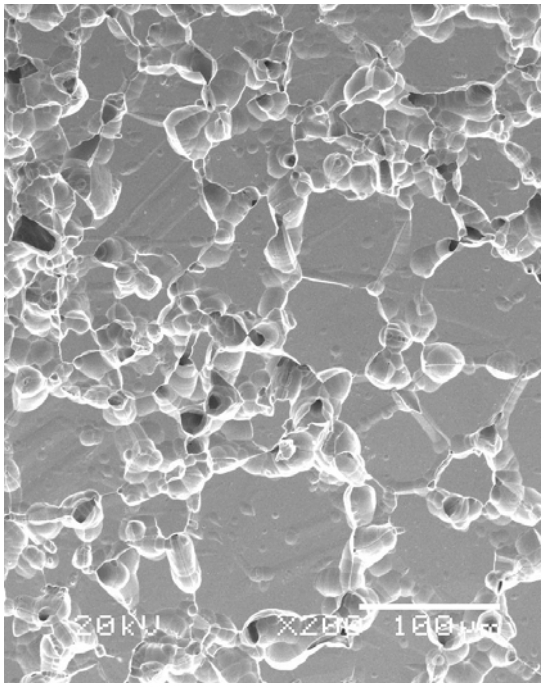

Figure 7.12: SEM image after the ferric sulfate-sulfuric acid test for detecting the (IGC), in Hastelloy C276 heated to 650°C, without any depositions, for 24 hrs then furnace cooled then polished.

7.3 Spray pyrolysis of MgO from the nitrate precursor

In this section the deposition of MgO thin films by spray pyrolysis on wrought polycrystalline Hastelloy C276, using magnesium nitrate as a precursor, will be introduced. The Hastelloy C276 (HC) (10mm x10mm x 2mm) substrates were mechanically polished down to a roughness of 2-5 nm, and then they were cleaned in acetone, then ethanol for 10 minutes each in an ultrasonic bath, then dried with Ar gas. In the spray pyrolysis deposition, a pulse time to interval time of 1:7 was applied; however, the effect of deposition temperature, precursor concentration, deposition time, the deposition inclination angle, Ar flow rate, and the effect of different annealing treatment on the properties of MgO films deposited by spray pyrolysis on Hastelloy C276 were all investigated. Finally, YBCO and CeO_2 were deposited by PLD to evaluate the performance of the MgO films deposited by spray pyrolysis on Hastelloy C276.

As far as we know, no reports have been found for MgO deposition on metallic substrates by spray pyrolysis using nitrate precursor. The aim (as mentioned for 310-austenitic stainless steel) is to reduce the cost of production by using spray pyrolysis instead of the relatively expensive methods for the buffer layer deposition, such as electron beam evaporation [82] and pulse laser deposition [80]. As in the previous chapters a further objective of this work is to grow MgO as the only buffer

layer before YBCO deposition in an attempt to make the process a cost-effective one by reducing the usual multi-layer buffer architecture to a single layer.

It is to be mentioned that X-ray scans for the MgO films deposited by spray pyrolysis on Hastelloy C276 detected only MgO (200) peaks from the MgO film. Therefore, we could not quantify the level of texture as no other peaks were detected to reference to. Accordingly, it was assumed that an increase in the intensity of MgO (200) peak reflects an improvement in texture

7.4 Effect of deposition temperature on MgO film properties

Magnesium nitrate [$Mg(NO_3)_2.6H_2O$] as a precursor was used to deposit MgO by spray pyrolysis on Hastelloy C276 substrates. The deposition was done using 0.078M at different temperatures for 32 minutes and using an Ar flow rate of 10 l/min. The XRD patterns after the deposition are shown in Figure 7.13 where it can be seen that no MgO XRD peaks were detected regardless of the substrate temperature.

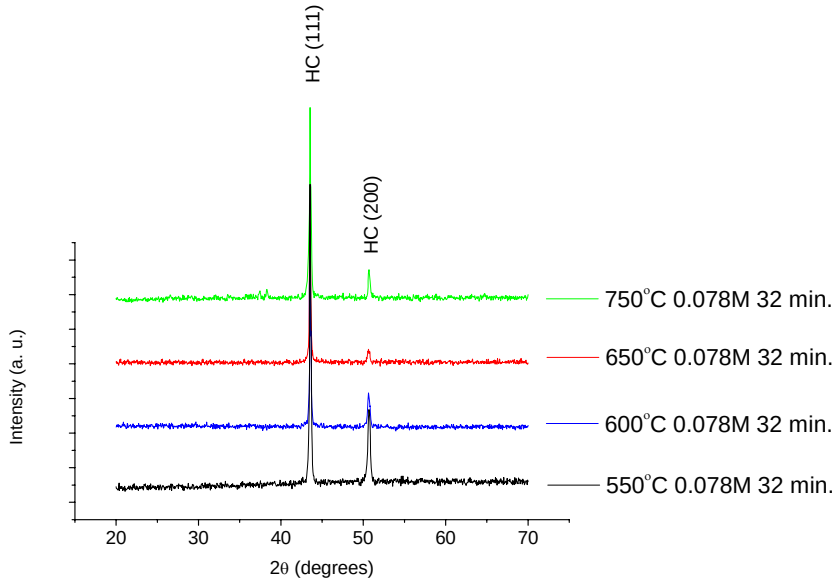

Figure 7.13: XRD patterns for MgO deposition on Hastelloy C276 using 0.078M of $Mg(NO_3)_2.6H_2O$ at different temperatures for 32 minutes.

The SEM images in Figure 7.14-Figure 7.16 show microstructures which are very similar to the one obtained for MgO deposition on Si single crystal from 0.078M solution at 650°C (Figure 4.5). This confirms that the microstructure of the deposited MgO films depends on the used substrate; similar microstructures were obtained on different substrates but by using different deposition temperatures. The SEM image for the films deposited at 750°C (Figure 7.17) show a different microstructure where

the grain boundaries of the substrate were revealed (compare to Figure 7.3). This can be attributed to the thermal etching effect, not due to any sensitisation effects. As from the boiling acid test it was found that the substrates were not susceptible to sensitisation. The revealing of the grain boundaries at high temperatures was even seen during pulsed laser deposition of YBCO on NiW RABiTS by Y L Cheung et al [259, 261]. The thermal etching effect on Ni RABiTS was also seen by others [32, 264, 265].

The EDX tests performed on the films deposited on Hastelloy C276 at 550°C to 650°C show the presence of Mg. However, no MgO XRD peaks were detected (Figure 7.13) and this suggests that the deposited MgO films were amorphous. It was believed that this was due to the low thickness of the deposited MgO films. For MgO deposition on Si, it was found that the texture of MgO improved with increasing thickness. More details on thickness will be found in section 7.8. It will be found that thinner films were obtained on C276 compared to those obtained on Si single crystals, and this shows the dependence of MgO film deposition on the used substrate. MgO and other films were deposited by researchers on ceramic substrates; they found that amorphous films were obtained at low thicknesses and that the texture developed with thickness [114, 140, 146, 147, 154, 158, 160-162]. O. Renault and M. Labeau [146] found that MgO films thinner than 150 nm were amorphous. Stryckmans et al [142] found that the texture of MgO deposited on alumina substrates from magnesium acetylacetonate precursor developed with thickness. James R. Groves et al [242] found the same behaviour for MgO films deposited by ion beam assisted deposition (IBAD). Elidrissi B et al [154] found that CeO_2 films prepared on glass substrates at low temperatures by spray pyrolysis were amorphous. Joseph Prince J et al [140] found that low precursor concentration resulted in the formation of amorphous In_2O_3 films.

The EDX test for the sample deposited at 750°C suggested a ratio of Mg:O of about 1:10. This would be attributed to the high deposition temperature where the lifetime required for evaporation would be shorter compared to that when using 0.078M at 650°C. Besides that, it was believed that at high temperatures, the gas convection from the substrates will be more pronounced which makes the residence time of droplets in the spray pyrolysis system shorter; where the time will not be enough for nucleation and growth to proceed to completion. This combined effect of shorter evaporation lifetime and higher gas convections results in the formation of

small particles that will follow the gas flow away from the substrate. The same behaviour of small particles was explained by Toivo [110]. As a consequence, the high temperature used made the droplet to be pushed away due to gas convection from the substrate [64, 113]. Therefore, the high deposition temperature (in our case 750°C) resulted in Mg deficiency.

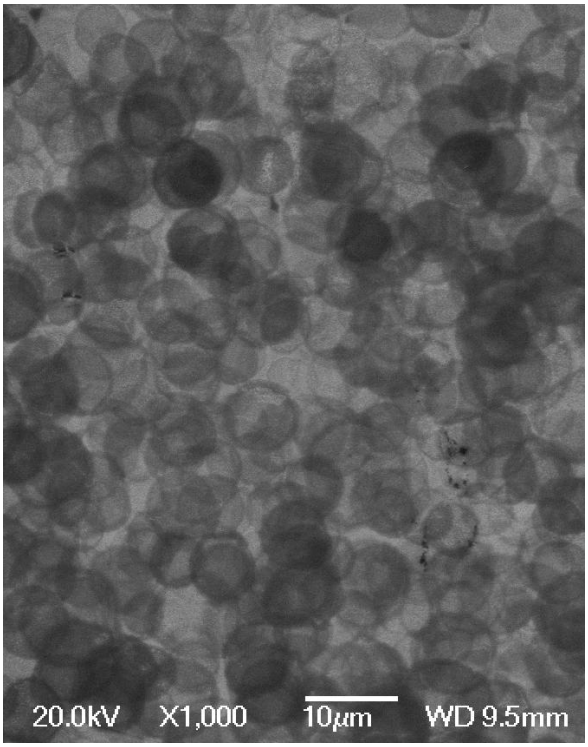

Figure 7.14: SEM image for the MgO film deposited on Hastelloy C276 using 0.078M of $Mg(NO_3)_2.6H_2O$ at 550°C with a deposition time of 32 minutes.

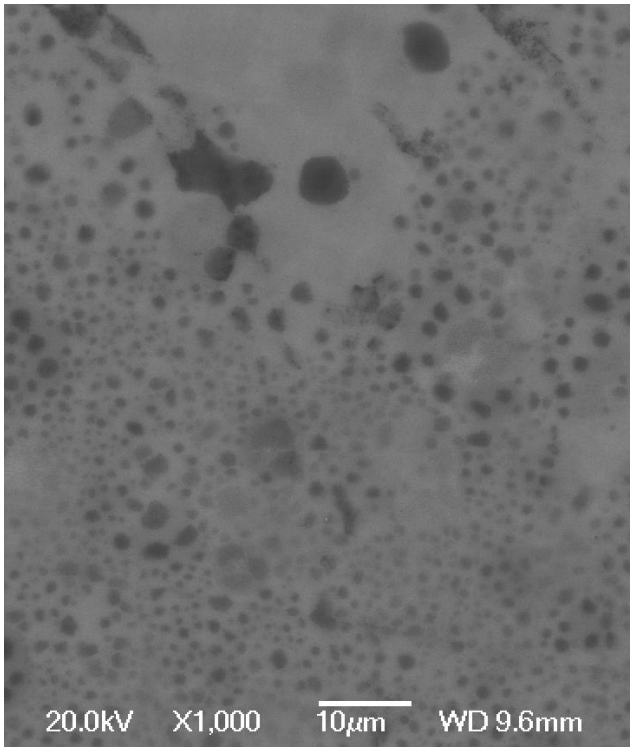

Figure 7.15: SEM image for the MgO film deposited on Hastelloy C276 using 0.078M of $Mg(NO_3)_2.6H_2O$ at 600°C with a deposition time of 32 minutes.

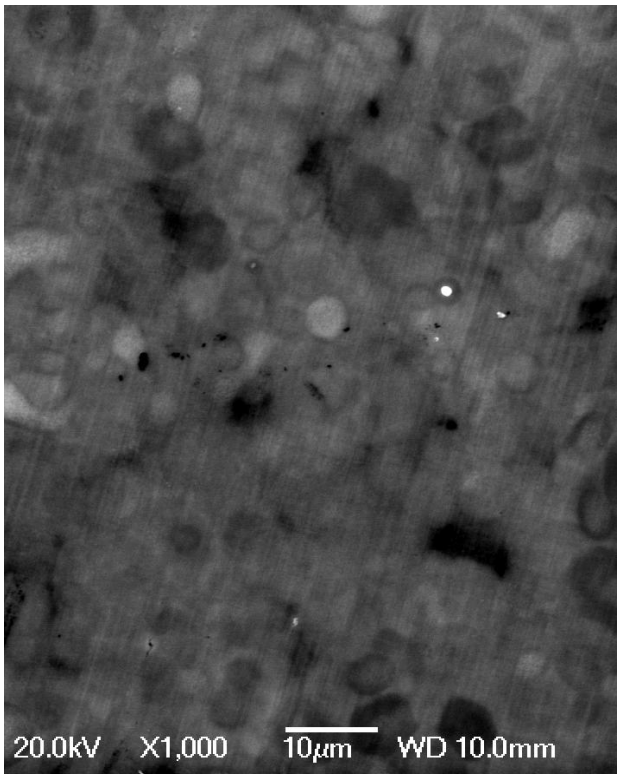

Figure 7.16: SEM image for the MgO film deposited on Hastelloy C276 using 0.078M of $Mg(NO_3)_2.6H_2O$ at 650°C with a deposition time of 32 minutes.

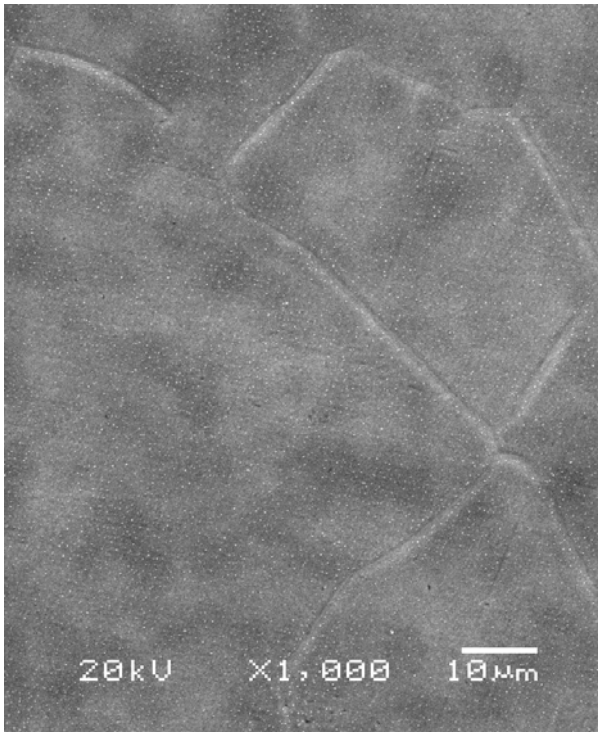

Figure 7.17: SEM image for the MgO film deposited on Hastelloy C276 using 0.078M of $Mg(NO_3)_2.6H_2O$ at 750°C with a deposition time of 32 minutes.

7.5 Effect of deposition time on MgO film properties

The effect of the deposition time on MgO film deposition by spray pyrolysis was studied at different temperatures, using an Ar flow rate of 10 l/min, as can be seen in Figure 7.18 and Figure 7.19. It can be seen that at 0.078M solution, no MgO XRD peaks were detected irrespective of the deposition temperature or the deposition time. The EDX results show the presence of Mg, therefore, the deposited MgO films were amorphous. Amorphous films of MgO, CeO_2, In_2O_3 deposited by spray pyrolysis on different substrates were obtained by others [140, 146, 154]. Others found that the texture of MgO developed with thickness [142, 242, 243].

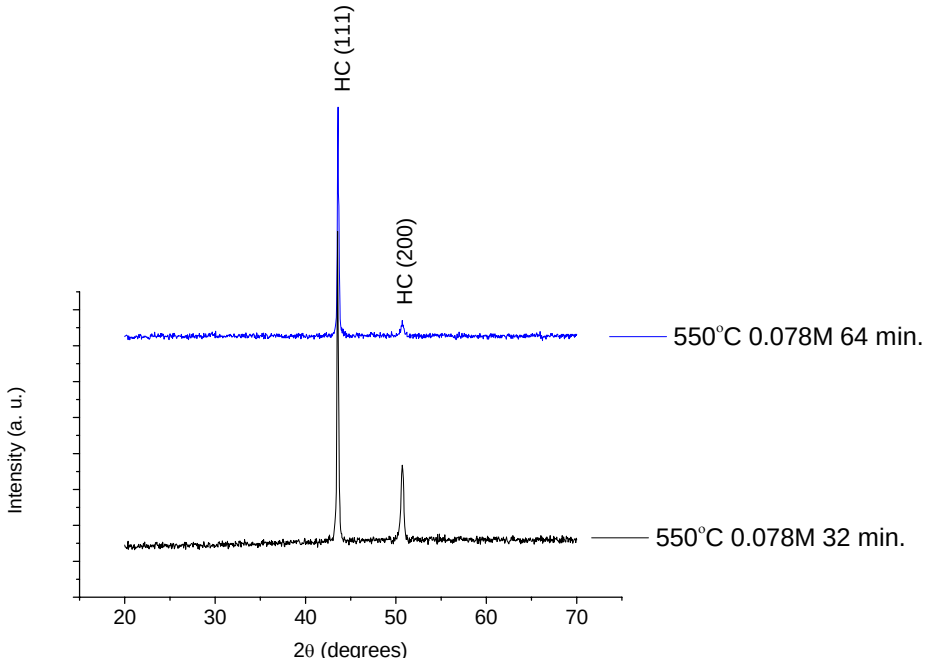

Figure 7.18: XRD patterns for MgO deposition on Hastelloy C276 using 0.078M of $Mg(NO_3)_2.6H_2O$ at 550°C and at different deposition time.

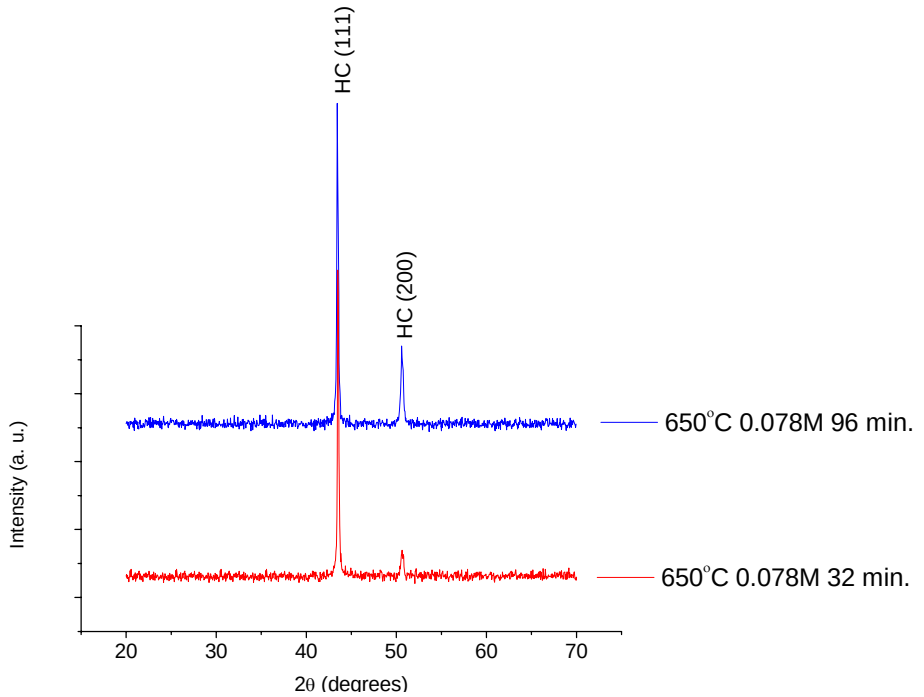

Figure 7.19: XRD patterns for MgO deposition on Hastelloy C276 using 0.078M of $Mg(NO_3)_2.6H_2O$ at 650°C and at different deposition time.

The SEM image for the films deposited at 550°C for 64 minutes (Figure 7.20) was almost the same as the one deposited for 32 minutes (Figure 7.14) except it has some particles being formed on the surface. The MgO film deposited at 650°C (Figure 7.21) show the formation of overgrown particles as was the case for the MgO film

deposited on Si single crystal at 700°C (Figure 4.7), but it was more pronounced in the case of MgO deposition on Hastelloy C276. By increasing the deposition time, the particles have enough time to grow regardless of the substrate temperature and this may explain the formation of particles at 550°C and 650°C (Figure 7.20 and Figure 7.21) when increasing the deposition time to 64 minutes and 96 minutes, respectively, relative the films deposited at the same temperatures but for 32 minutes (Figure 7.14 and Figure 7.16).

The formation of amorphous MgO films even by increasing the deposition time gave an indication that the thickness of the deposited films was still low. This implied that the used concentration was not high enough to develop a textured MgO film by the deposition of thick films.

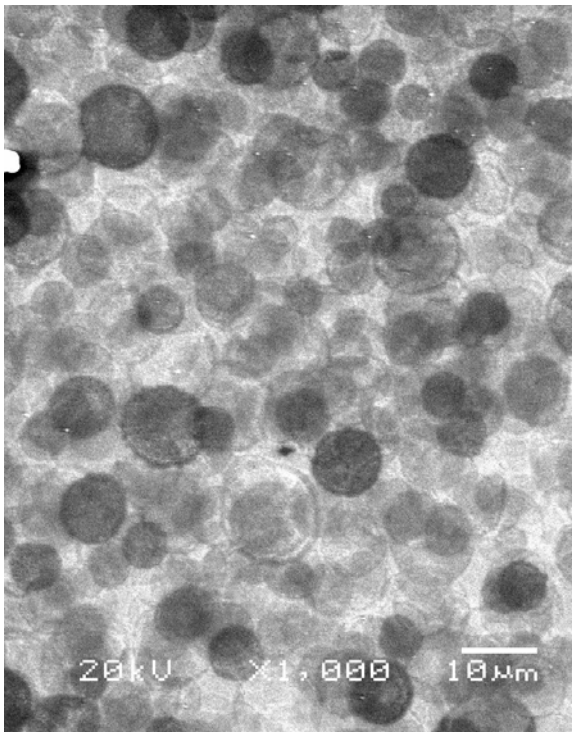

Figure 7.20: SEM image for the MgO film deposited on Hastelloy C276 using 0.078M of $Mg(NO_3)_2.6H_2O$ at 550°C with a deposition time of 64 minutes.

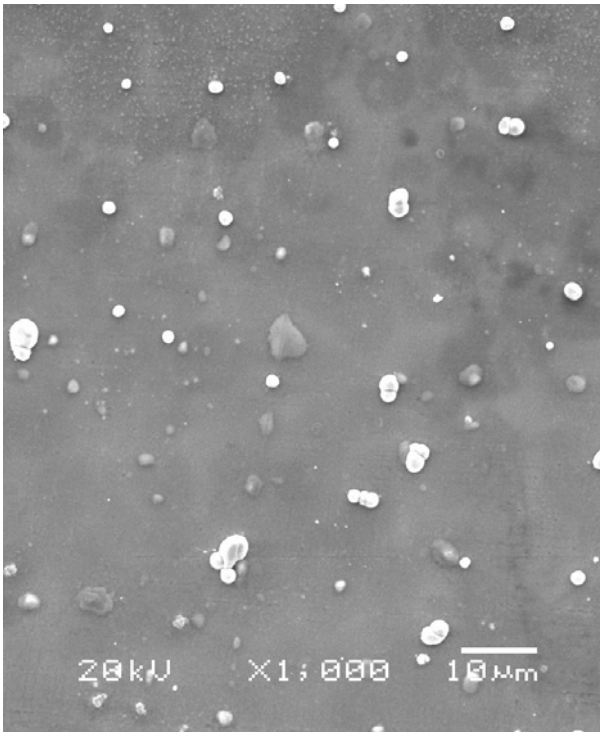

Figure 7.21: SEM image for the MgO film deposited on Hastelloy C276 using 0.078M of $Mg(NO_3)_2.6H_2O$ at 650°C with a deposition time of 96 minutes.

7.6 Effect of precursor concentration on MgO film properties

The deposition of MgO films on Hastelloy C276 was then performed at higher concentrations, using 0.468M and 0.78M solutions. The used Ar flow rate was 10 l/min, and the deposition was done at different temperatures and deposition times as can be seen from the XRD patterns in Figure 7.22. This time MgO peaks were successfully observed. A weak MgO (200) peak, the only detected one, started to appear normal to the substrate surface. The MgO peaks were indexed according to the JCPDS PDF file 00-045-0946 where MgO (200) is at 2θ of 42.9°. The thermal expansion coefficients of Hastelloy C276 and MgO are 10.8-11.3x10^{-6} /°C and 13.8 x 10^{-6}/°C, respectively [143, 267]. The lattice parameter for MgO is 4.2112Å and for Hastelloy C276, as calculated from Bragg's law, is 3.5952Å and this gives a lattice mismatch of 17.1%. This explains the shift of MgO peaks in Figure 7.22 to 43.15°; however, this shift is not much compared to that obtained when depositing MgO on Si single crystals. It can be seen from Figure 7.22 that the peak intensity increased by increasing the deposition time, the deposition temperature or by increasing the concentration. However, this was at the expense of the film smoothness as can be seen

from the SEM images (Figure 7.23-Figure 7.28) and Figure 7.29. The smoothest films were deposited at 650°C for 32 and 48 minutes using 0.468M $Mg(NO_3)_2.6H_2O$ which show an RMS of about 20 nm (Figure 7.30 and Figure 7.31). An AFM section profile image is shown in Figure 7.32 for MgO films deposited from 0.468M solution at 650°C for 32 minutes. When comparing Figure 7.23 and Figure 7.30 to Figure 7.32, it can be seen that the surface is homogenous and smooth and most of the film was located on the same layer as can be seen from Figure 7.32. The same was also observed for the film deposited from 0.468M solution at 650°C for 48 minutes. However, all of the other MgO films shown in Figure 7.22 show particles or grains which were located on different layers relative to the rest of the film.

According to the deposition modes of spray pyrolysis [83], the smooth surface for both films (i.e. the ones deposited using 0.468M at 650°C for 32 and 48 minutes) were deposited according to the third mode of deposition; when the thermal decomposition of dry precipitates starts on their way to the substrate. However, by increasing the deposition time more than 48 minutes, by increasing the deposition temperature to 700°C or by increasing the concentration to 0.78M, overgrown particles were formed on the surface (Figure 7.25-Figure 7.28), which led to an increase in the roughness (Figure 7.29). The fourth mode of deposition leads to the formation of particles on the surface by increasing the temperature, where the full thermal decomposition takes place outside the substrate and only finely divided solid product arrives at the substrate surface; therefore, at 700°C, the deposition was carried out according to the fourth mode of deposition. It is also to be pointed out that the actual working mode depends not only on the substrate temperature, but also on the temperature of the working surrounding [83]. By increasing the deposition time to 64 minutes (Figure 7.25) and 96 minutes (Figure 7.26) the growth of the particles dominates the nucleation, leading to the formation of overgrown particles. However, no sound explanation was found to relate this behaviour with the type of the deposition mode that might be applied to this situation and further investigation is required. The lifetime required for evaporation increases by increasing the amount of solute in the droplet [110]; therefore, by increasing the concentration to 0.78M, the time is not enough to evaporate both the solvent and the solute, a situation similar to that encountered in the second mode of deposition where dry precipitates come to the surface [83].

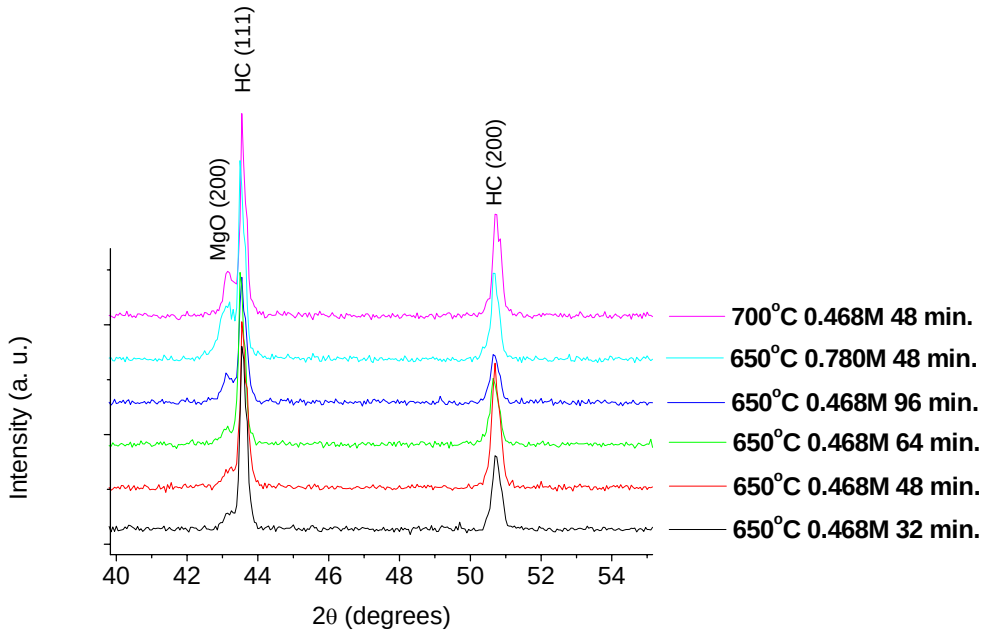

Figure 7.22: XRD patterns for MgO deposition on Hastelloy C276 using 0.468M and 0.78M of $Mg(NO_3)_2.6H_2O$ at different deposition temperatures and different deposition times.

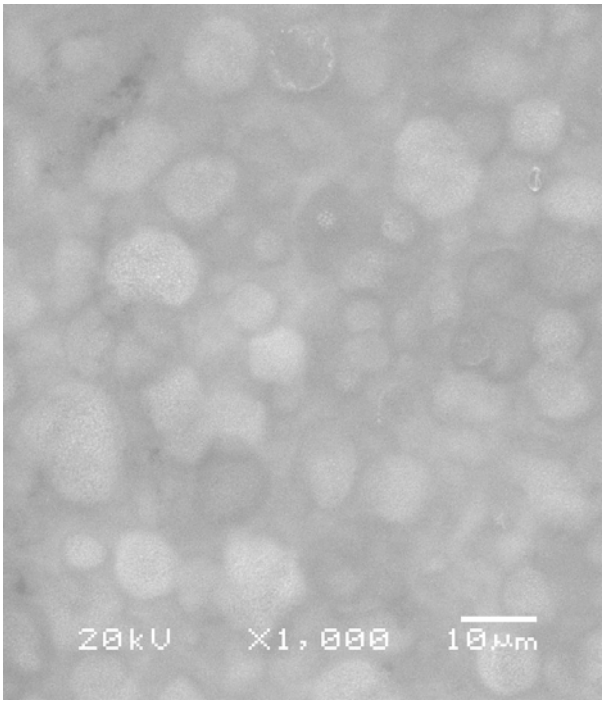

Figure 7.23: SEM image for the MgO film deposited on Hastelloy C276 using 0.468M of $Mg(NO_3)_2.6H_2O$ at 650°C for 32 minutes.

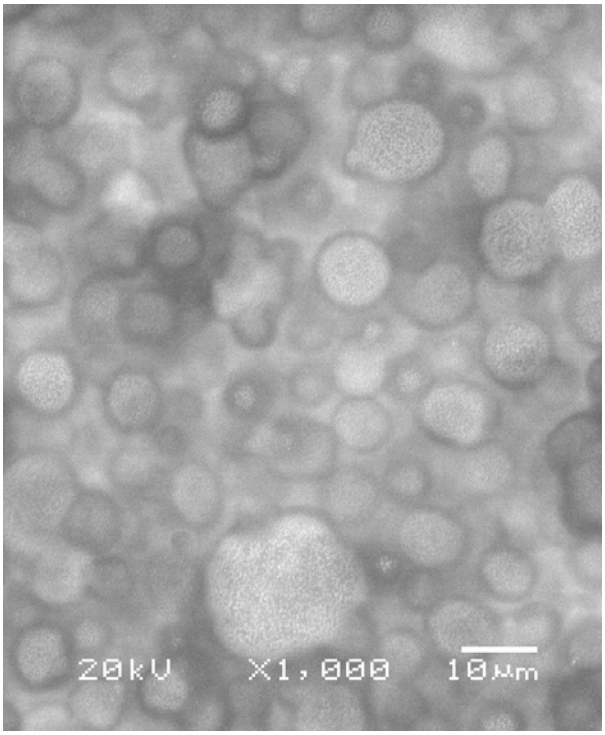

Figure 7.24: SEM image for the MgO film deposited on Hastelloy C276 using 0.468M of $Mg(NO_3)_2.6H_2O$ at 650°C for 48 minutes.

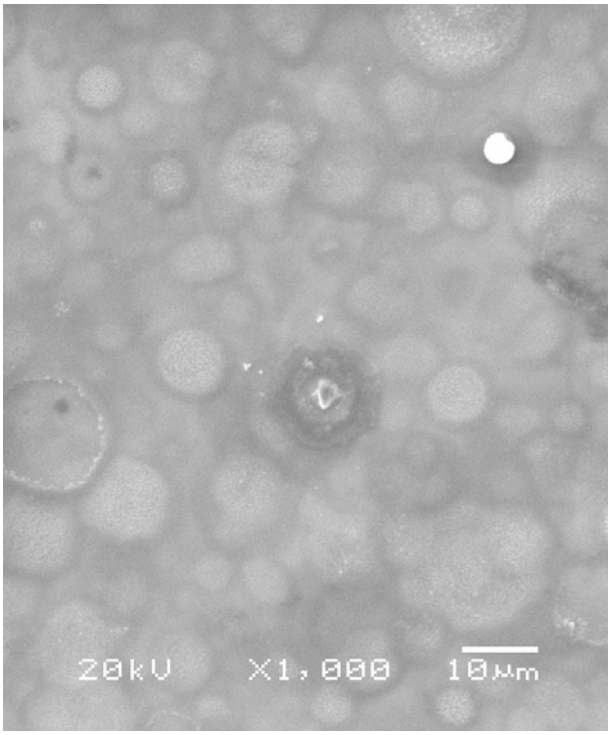

Figure 7.25: SEM image for the MgO film deposited on Hastelloy C276 using 0.468M of $Mg(NO_3)_2.6H_2O$ at 650°C for 64 minutes.

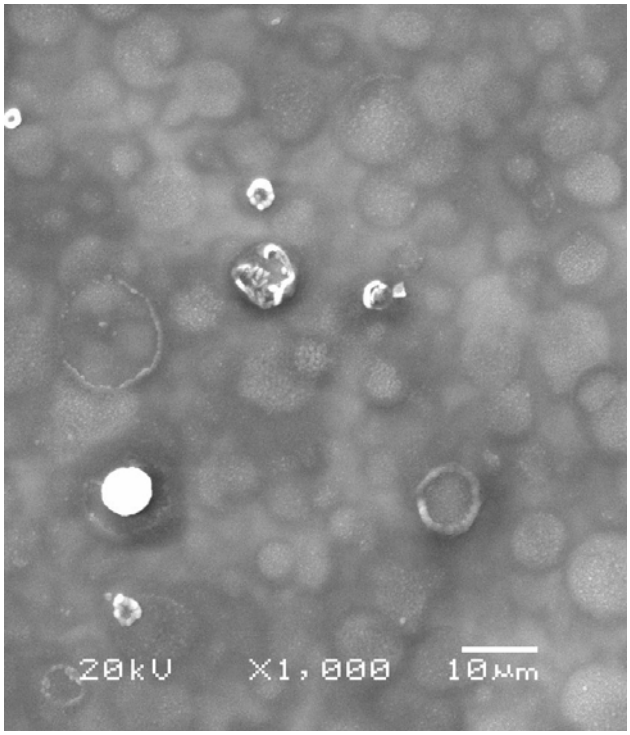

Figure 7.26: SEM image for the MgO film deposited on Hastelloy C276 using 0.468M of $Mg(NO_3)_2.6H_2O$ at 650°C for 96 minutes.

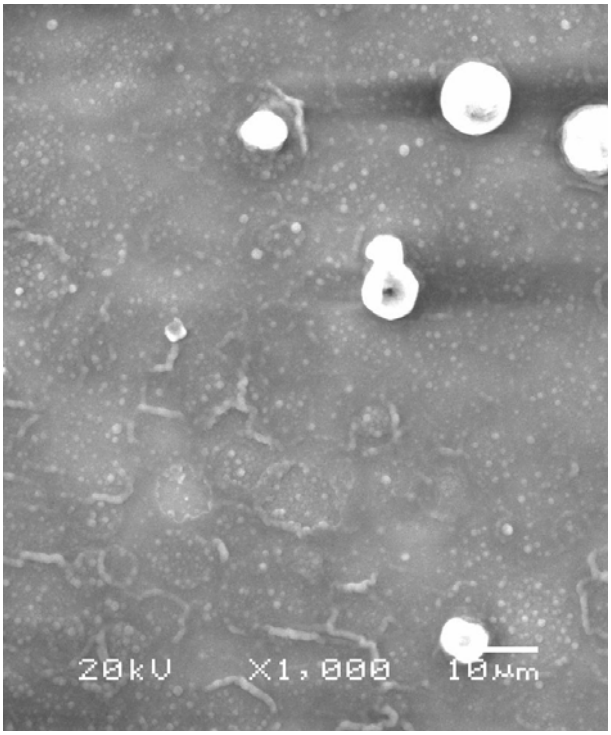

Figure 7.27: SEM image for the MgO film deposited on Hastelloy C276 using 0.78M of $Mg(NO_3)_2.6H_2O$ at 650°C for 48 minutes.

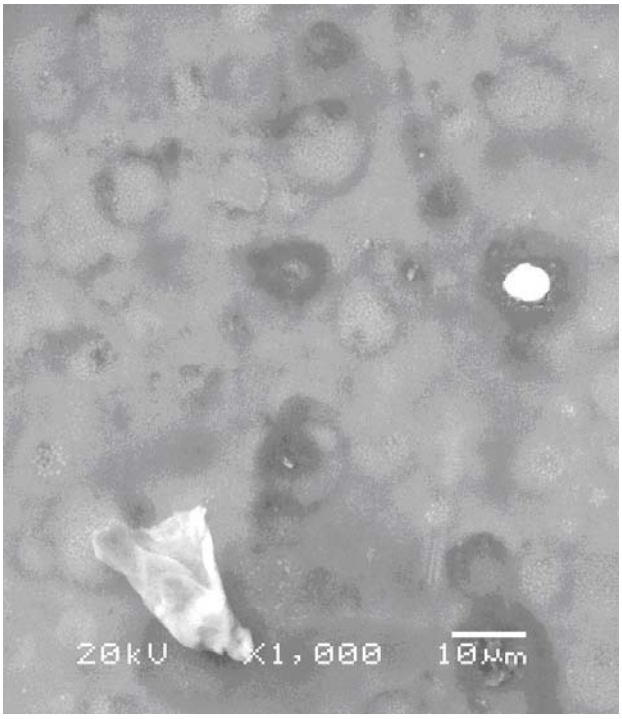

Figure 7.28: SEM image for the MgO film deposited on Hastelloy C276 using 0.468M of $Mg(NO_3)_2.6H_2O$ at 700°C for 48 minutes.

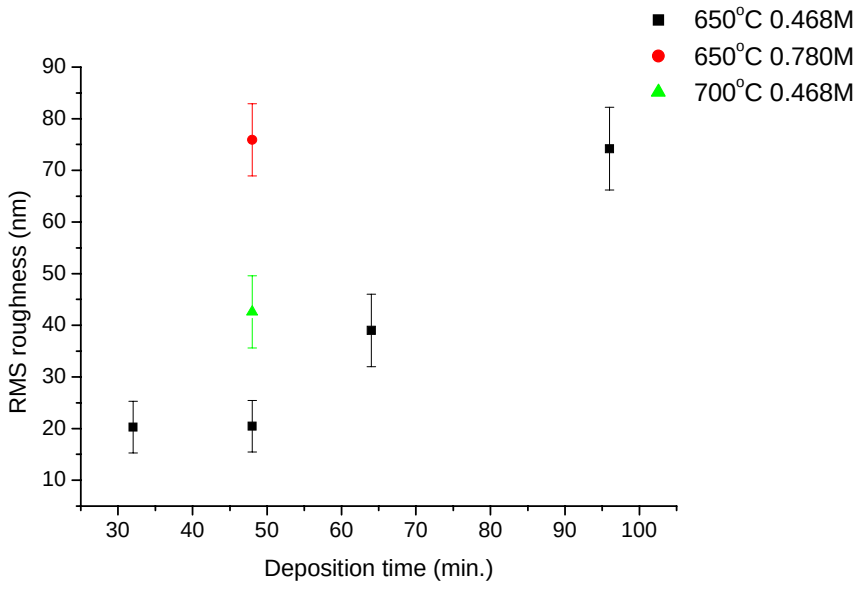

Figure 7.29: The effect of deposition time on MgO film roughness at different deposition temperatures and different precursor concentrations.

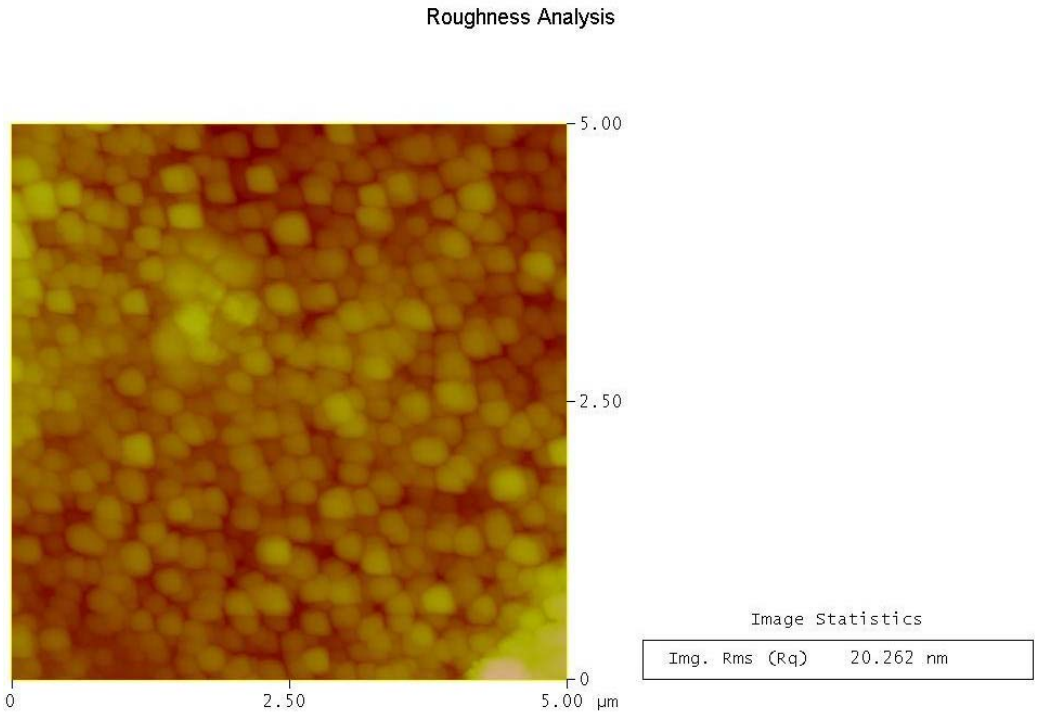

Figure 7.30: A 5x5µm^2 AFM image for the MgO film deposited on Hastelloy C276 using 0.468M of $Mg(NO_3)_2.6H_2O$ at 650°C for 32 minutes.

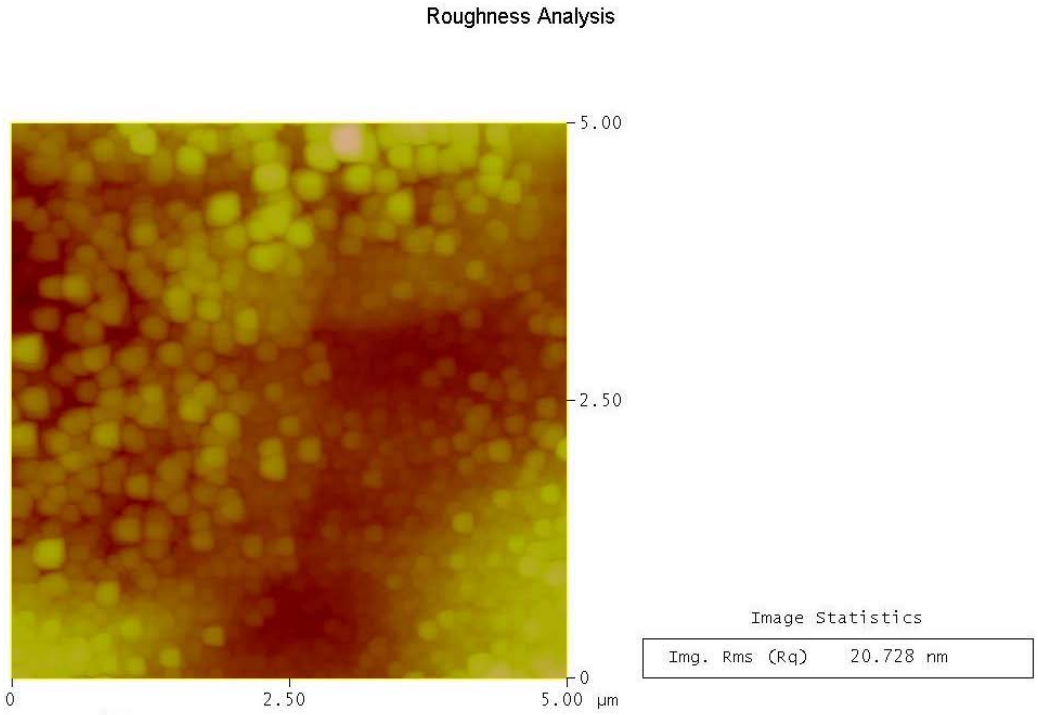

Figure 7.31: A 5x5µm^2 AFM image for the MgO film deposited on Hastelloy C276 using 0.468M of $Mg(NO_3)_2.6H_2O$ at 650°C for 48 minutes.

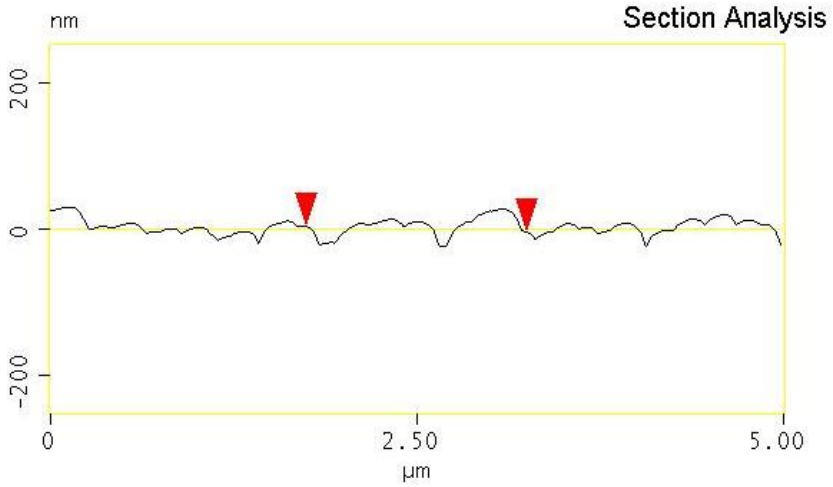

Figure 7.32: AFM section profile image for the MgO film deposited on Hastelloy C276 using 0.468M of $Mg(NO_3)_2.6H_2O$ at 650°C for 32 minutes.

The EDX results, using an accelerating voltage of 4KV, suggest that all of the films (shown in Figure 7.22) were almost stoichiometric MgO. An example is shown in Figure 7.33 and Table 7.3 for the sample deposited at 700°C for 48 minutes from 0.468M solution. The particles were nearly stoichiometric MgO as well.

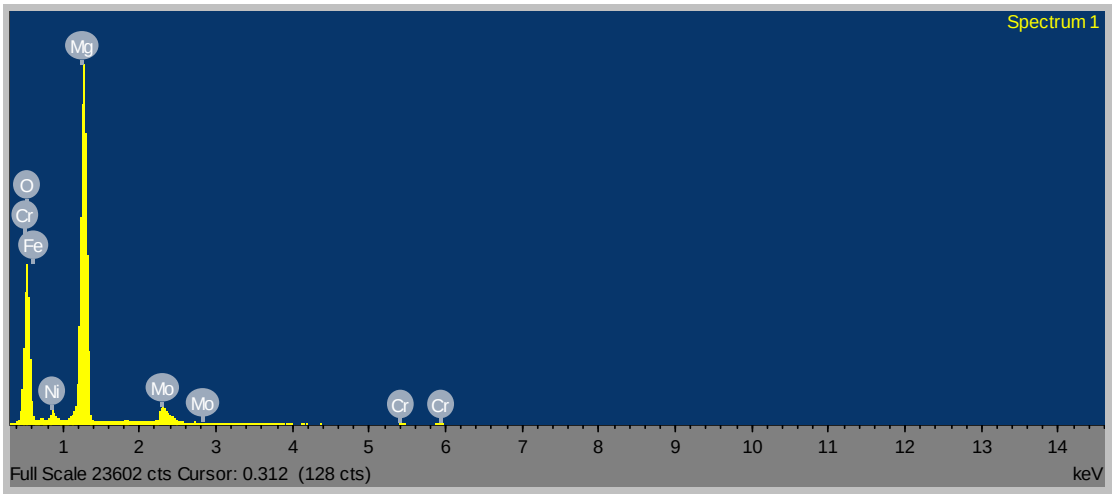

Figure 7.33: EDX spectrum, using an accelerating voltage of 4KV, for the Hastelloy C276 deposited with 0.468M at 700°C with a deposition time of 48 minutes.

Table 7.3: Summary of the EDX chemical composition results, using an accelerating voltage of 4KV, for the Hastelloy C276 deposited with 0.468M at 700°C with a deposition time of 48 minutes.

Element	at %
O K	47.21
Mg K	45.25
Fe L	0.7
Cr L	2.78
Ni L	1.63
Mo L	2.43

The texture of MgO was not strong as can be expected from the XRD patterns in Figure 7.22. This was confirmed from the X-ray pole figure measurements. An MgO (200) pole figure measurement for the sample deposited at 650°C for 48 minutes from 0.468M solution is shown in Figure 7.34. It can be seen that there is a weak out-of-plane texture and no in-plane texture (no definite poles were obtained at the circumference but a ring was obtained instead).

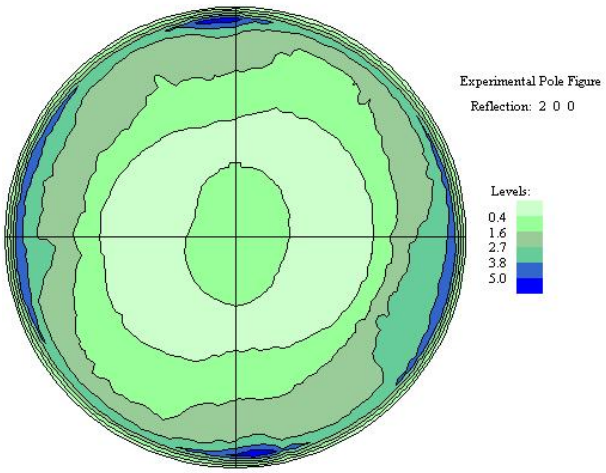

Figure 7.34: : (200) X-ray pole figure, at 2θ of 43.15°, of the MgO film deposited at 650°C from a solution of 0.468M for 48 minutes.

In an attempt to improve the texture of the MgO (200) peak, a double deposition was made. This means that the sample was deposited under certain conditions, left to be furnace cooled to room temperature, then deposited again at the same conditions. This was done at 650°C for 48 minutes each using 0.468M solution. The XRD pattern in Figure 7.35 show that the intensity of MgO peak increased by the double deposition. This was almost similar to increasing the deposition time to 96 minutes

(Figure 7.22). If it is assumed that the thickness of MgO film increased with increasing the deposition time, then it can be concluded that the texture improved slightly with thickness. Similar behaviour was found by other researchers [142, 146, 175]. More details on thickness are found in section 7.8. However, this slight improvement in texture with the double deposition was at the expense of the surface smoothness as can be seen from the SEM and AFM images in Figure 7.36 and Figure 7.37, respectively compared to the film deposited at 650°C from 0.468M for 48 minutes (Figure 7.31).

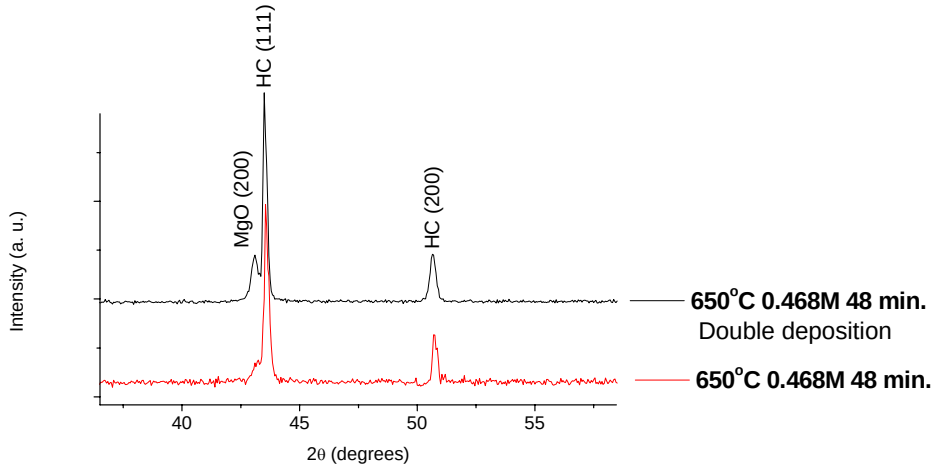

Figure 7.35: XRD patterns for MgO deposition on Hastelloy C276 showing the double deposition effect using 0.468M $Mg(NO_3)_2.6H_2O$ at 650°C for 48 minutes.

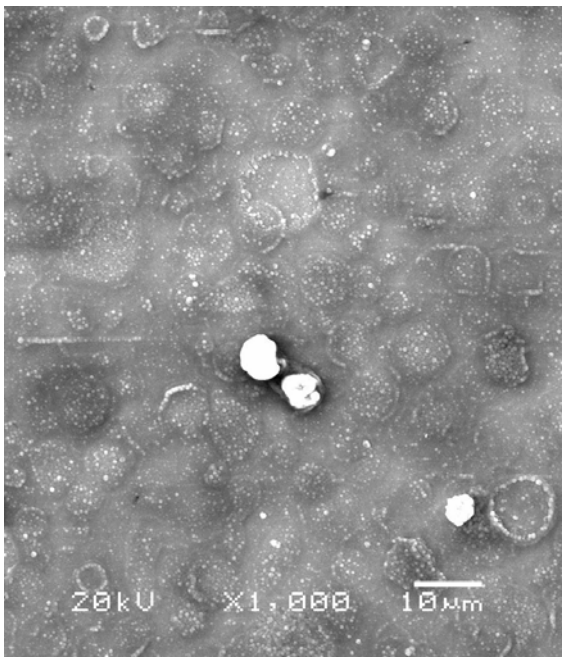

Figure 7.36: SEM image for MgO on Hastelloy C276 with the double deposition using 0.468M $Mg(NO_3)_2.6H_2O$ at 650°C for 48 minutes.

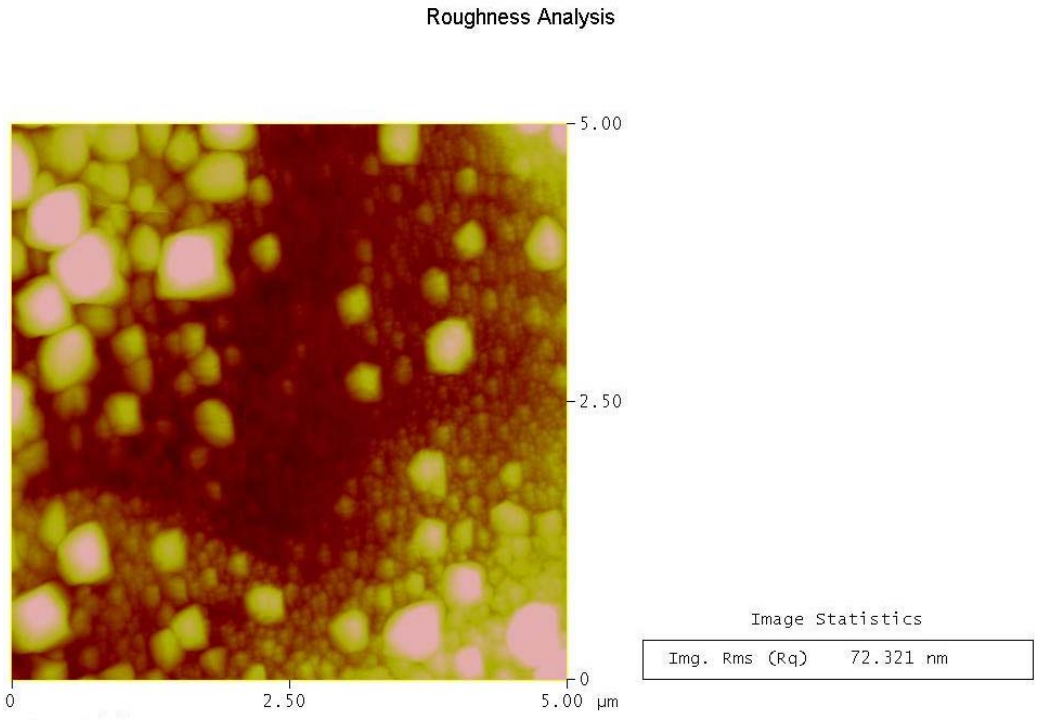

Figure 7.37: A 5x5µm^2 AFM image for MgO on Hastelloy C276 with the double deposition using 0.468M $Mg(NO_3)_2.6H_2O$ at 650°C for 48 minutes.

7.7 X-ray photoelectron spectroscopy (XPS) test

The sample deposited from 0.468M at 650°C for 48 minutes using 10 l/min Ar flow rate was tested for surface contamination using the XPS. The XPS spectra were recorded with a standard Mg Kα source using 20 pass energy, 0.1 eV step, and 0.1 seconds per step for the detailed spectra. For Mg 2P, the scan was from 40-60eV, the Mg 2P peak was found to be at 50.1eV (Figure 7.38) and it is due to the contribution of magnesium oxide/hydroxide. For the O 1s, the scan was from 520-550eV and two peaks were obtained at 530.8eV and at 532.6eV (Figure 7.39); one for magnesium oxide and the other for magnesium hydroxide. This indicates that the surface of MgO was contaminated with hydroxides as was expected as MgO is hygroscopic [194]. A similar result was found by others [197-204]. However, heating the contaminated layer briefly at a temperature of 450°C in air is sufficient to regenerate the MgO surface [116]; in our experiments this condition will be met during subsequent YBCO deposition. Although, the sample analysis was carried out on fresh samples to minimise the effect of storage.

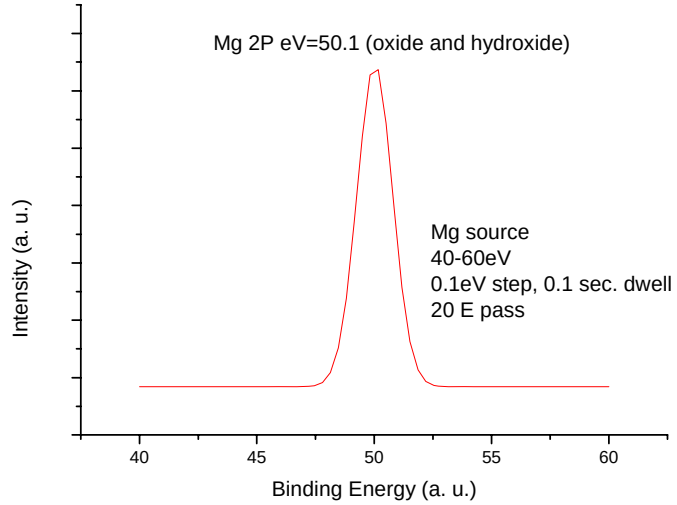

Figure 7.38: XPS spectrum for the MgO thin film deposited on Hastelloy C276 substrate using 0.468M $Mg(NO_3)_2.6H_2O$ at 650°C for 48 min. showing the Mg 2P.

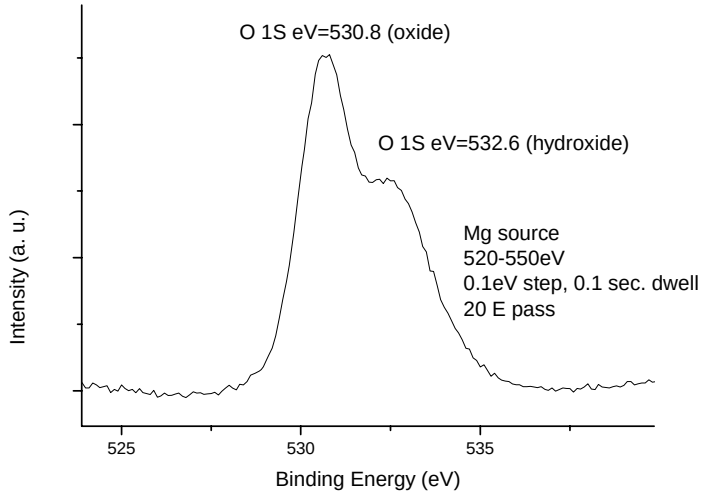

Figure 7.39: XPS spectrum for the MgO thin film deposited on Hastelloy C276 substrate using 0.468M $Mg(NO_3)_2.6H_2O$ at 650°C for 48 min. showing the O 1S.

7.8 Effect of deposition parameters on MgO film thickness

The thickness measurements for the MgO films deposited on metallic substrates, i.e. Hastelloy C276, was not straight forward. Three methods were tried for the thickness measurements, using a high resolution SEM. The first one was to cut a cross section of the sample with the spark machine followed by mechanical polishing. However, this process increased the thickness of the films as the sample was submerged in oil. The second method was to mount the samples and polish them through at least one third of the sample width. This resulted sometimes in polishing

away of the thin film as well. In other occasions, smearing was the result of the mechanical polishing process which made the thickness measurement not accurate. The third method was to stick a special kind of tape on the thin film followed by milling the back of the substrate down to half of its thickness. The sample was then bent and the tape was removed taking with it the thin film from the bent area. The areas of the thin film next to the removed tape were now exposed and can be used to measure the thickness. However, this process was not very reliable as the film was usually destroyed during the milling process due to overheating of the tape. Therefore, studying the effect of the thickness on MgO films was not feasible on metallic substrates. A non destructive thickness measurement using Ellipsometry was also applied; however this method was not accurate for thicknesses in the range of 200 nm, besides thickness measurements for MgO and YBCO films simultaneously made the measurement process rather complex and inaccurate. After many trials, thickness measurement by mechanically polishing the sample deposited at 650°C from a solution of 0.468M for 32 minutes, using an Ar flow rate of 10 l/min, was achieved as can be seen in Figure 7.40 which shows a 0.262 μm thick MgO film. This gives a deposition rate of 10.92 Å/sec (2620Å/240sec.). This deposition rate is lower than the deposition rate obtained for MgO films deposited on Si from 0.078M at 650°C with zero inclination angle. This confirms that film deposition by the spray pyrolysis technique is a function of substrate material, precursor concentration, and temperature. Unfortunately, it was not successful to measure the thickness for any of the samples deposited from the 0.078M solution.

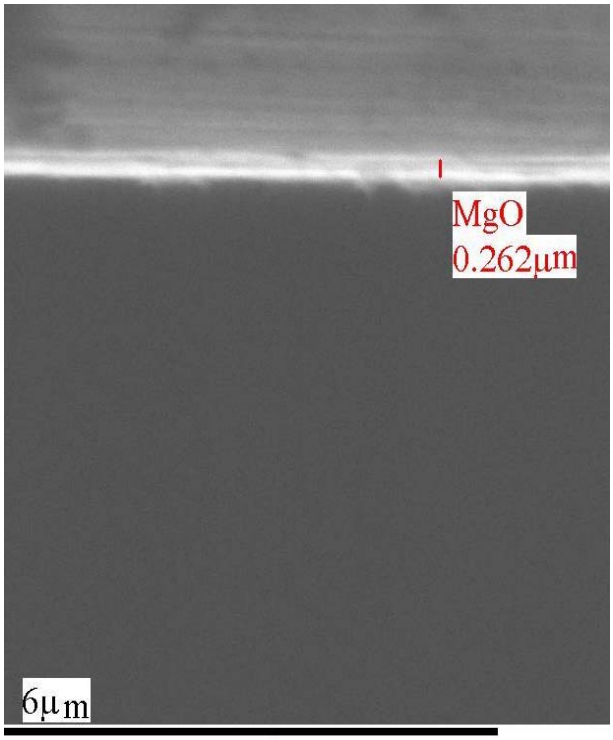

Figure 7.40: SEM cross section for MgO film spray pyrolysed on Hastelloy C276 using 0.468M $Mg(NO_3)_2.6H_2O$ at 650^oC for 32 minutes.

It was found, when depositing MgO films on Si substrates that the texture improved with increasing thickness and the thickness was found to increase with increasing the concentration. Therefore, it was believed that at low thicknesses (as was the case when depositing MgO on C276 using 0.078M solution), the MgO texture was not developed yet and amorphous films were obtained. Therefore no MgO XRD peaks were detected for the samples deposited from the 0.078M solution irrespective of the deposition temperature (Figure 7.13) or the deposition time (Figure 7.18 and Figure 7.19) as the concentration was low enough that sufficiently thick films for the growth of textured MgO was not obtainable. However, by increasing the concentration to 0.468M, sufficiently thick film was deposited and this resulted in the deposition of MgO with a weak (200) peak. Amorphous films of MgO, CeO_2, In_2O_3 deposited by spray pyrolysis on different substrates were obtained by others [140, 146, 154]. Others found that the texture of MgO develops with thickness [142, 183, 242]. When the concentration was increased to 0.468M, the thickness increased and the texture was developed leading to the detection of MgO peaks (Figure 7.22). O. Renault and M. Labaeu [146] deposited MgO on glass substrates using the aerosol

assisted-metallorganic chemical vapour deposition technique. They found that the texture orientation changed with thickness which in turn was dependent on the type of solvent which affected the deposition rate. James R. Groves et al [242] deposited MgO on Si wafers using IBAD. They found that the in-plane texture of MgO films improved by increasing the thickness up to 10 nm then decayed. M.P. Chudzik et al [175] found that the texturing of MgO, deposited on metal foils by e-beam evaporation, is a selective growth process where the texture improved with increasing film thickness and with increasing the inclination angle. A complete survey about the texture development with thickness can be found in sections 2.5 and 2.6.

7.9 Effect of inclination angle (ISD) on MgO film properties

The effect of inclination angle on the texture development of MgO thin films was studied by some researchers. They found that the shadowing effect is the mechanism which drives texture formation in MgO films by inclining the substrate, during pulsed laser deposition or e-beam evaporation, relative to the flux direction (section 2.6). To our knowledge, no reports were found investigating the effect of angle inclination on the texture development of MgO thin films deposited by the spray pyrolysis technique. For this purpose, MgO deposition at 20°, 45°, and 60° using 0.468M solution at 650°C for 48 minutes was utilised for the investigation. The used Ar flow rate was 10 l/min. The XRD patterns in Figure 7.41 show that the intensity of MgO (200) decreased by increasing the inclination angle from 0° to 45°. The peak was then disappeared when increasing the inclination angel to 60°. In spite of this, the EDX results show the presence of Mg, therefore the deposited MgO film was amorphous. Amorphous films of MgO, CeO_2, In_2O_3 deposited by spray pyrolysis on different substrates were obtained by others [140, 146, 154]. The decrease of peak intensity with increasing the inclination angle was also observed when depositing MgO on Si single crystal and this was attributed to the lower thickness at higher inclination angles (section 4.3.4). It was found that the intensity of MgO (200) deposited on Si substrates at 650°C and 700°C from a 0.0078M and 0.078M $Mg(NO_3)_2.6H_2O$ decreased by increasing the inclination angle from 20° to 60°(Figure 4.17, Figure 4.18, Figure 4.29 and Figure 4.30) where the gas convection from the substrate pushed the droplets of the precursor away from it [65, 141] and this effect increased by increasing the inclination angle. Therefore, for the case of MgO deposition on C276, the lower intensity of MgO peaks at high inclination angles was

also attributed to the low thickness of MgO. Others found that the texture of MgO developed with thickness [142, 242].

However, it is to be noted in this work that inclining the substrate led to untilted MgO films with (200) direction parallel to the substrate normal and did not result in the shadowing effect which was observed for MgO and YSZ films deposited by ISD method using PLD and e-beam evaporation [39-41, 49, 50, 53, 167, 169, 173-175, 177-183]. One more point should be mentioned. As was said before, MgO can be deposited by inclined substrate deposition (ISD) using e-beam evaporation [173, 174]. By this method, the MgO film had the (200) with the c-axis being tilted from the substrate normal due to the shadowing effect [173-175]. The deposited YBCO film on top of that MgO also grows with the (00l) being tilted from the substrate normal, which has led to low J_c values. Higher J_c and T_c values are obtained by growing untilted YBCO films by depositing YSZ and CeO_2 buffers on top of the tilted MgO film [169, 176, 177]. In this work MgO was deposited from nitrate precursor by inclining the substrate relative to the nozzle. This led to untilted MgO films with (200) direction parallel to the substrate normal; no shadowing effect was observed. However, this was at the expense of MgO (200) peak intensity. In all cases, spray pyrolysis gave MgO (200) peaks parallel to the substrate normal whether ISD was utilised or not. YBCO films grown on top of MgO deposited by spray pyrolysis (as will be seen later in this chapter) had the (006) of YBCO // (200) of MgO. Thus, spray pyrolysis offers an alternative method of depositing a single MgO buffer layer with no tilting for later YBCO deposition.

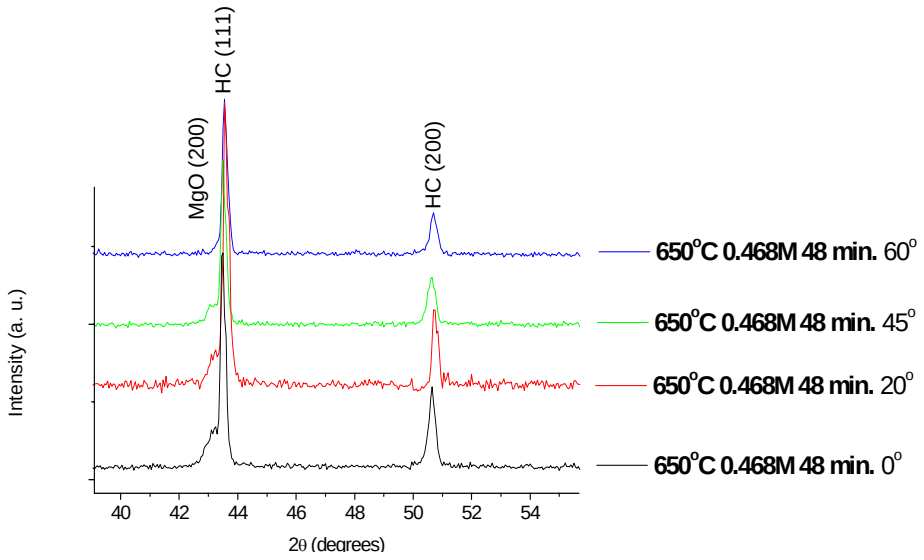

Figure 7.41: XRD patterns for MgO deposition on Hastelloy C276 using 0.468M $Mg(NO_3)_2.6H_2O$ at 650°C for 48 minutes and at different inclination angles.

Figure 7.42-Figure 7.45 show that the roughness decreased with increasing the inclination angel from 20° to 60°; similar behaviour was found for MgO deposition on Si single crystals (Figure 4.31). This behaviour can be attributed to pushing of droplets of the precursor away from the substrates, and by increasing the inclination angle, smoother films were obtained. However, for MgO deposition on Si, the RMS of the film deposited with no inclination angle was rougher than the ones deposited with an inclination angle. A different situation was encountered when depositing MgO on Hastelloy C276. At zero inclination angle, the surface roughness was about 20nm, and by increasing the inclination angle to 20°, the surface roughness increased to about 48nm then decreased by increasing the inclination angle to 45° and 60°. This increase in the roughness at 20° may be attributed to a flow turbulence at the substrate surface leading to the formation of particles and hence to an increase in the roughness. This turbulence decreased by increasing the inclination angle, and therefore to a decrease in the roughness values. This behaviour was not really understood and needs further investigation. Rachel E. Koritala et al [185] found that for the case of biaxially textured MgO films deposited by ISD using e-beam evaporation on Hastelloy C substrates that high roughness values was obtained at low and high inclination angles and the lowest roughness values were obtained for inclination angles of 20°-55° where the roughness was not affected by the inclination angle in this range.

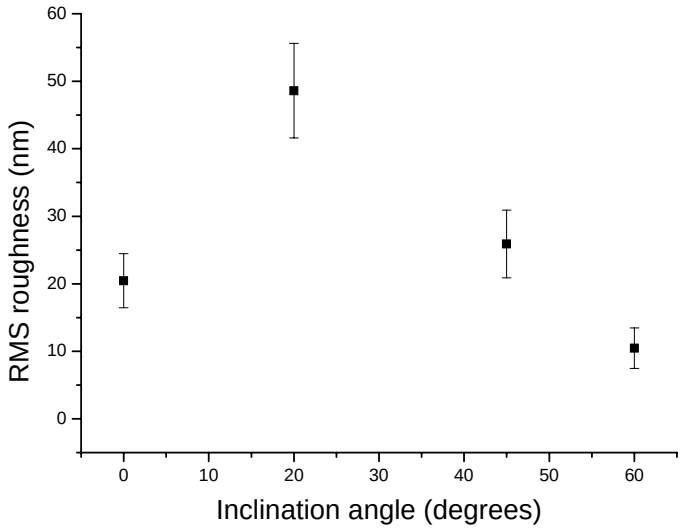

Figure 7.42: The effect of inclination angle on the film roughness of MgO films deposited from 0.468M solution at 650°C for 48 minutes.

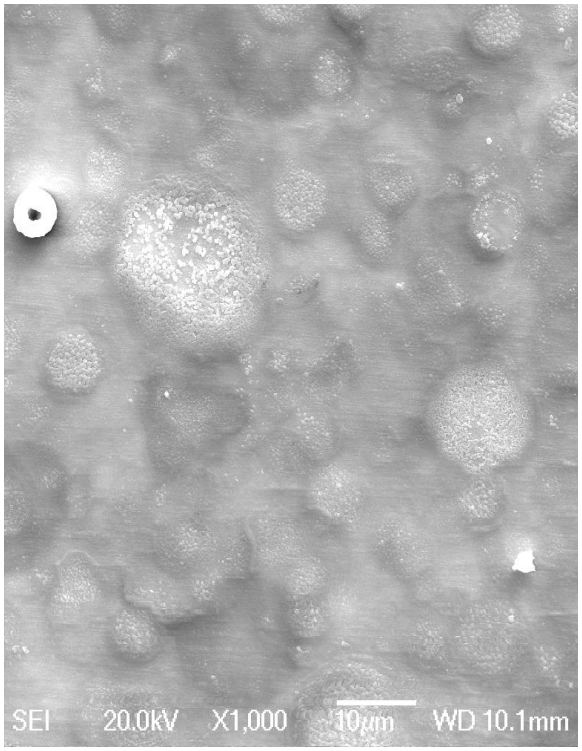

Figure 7.43: SEM image for MgO film deposited on Hastelloy C276 using 0.468M $Mg(NO_3)_2.6H_2O$ at 650°C for 48 minutes and at an inclination angle of 20°.

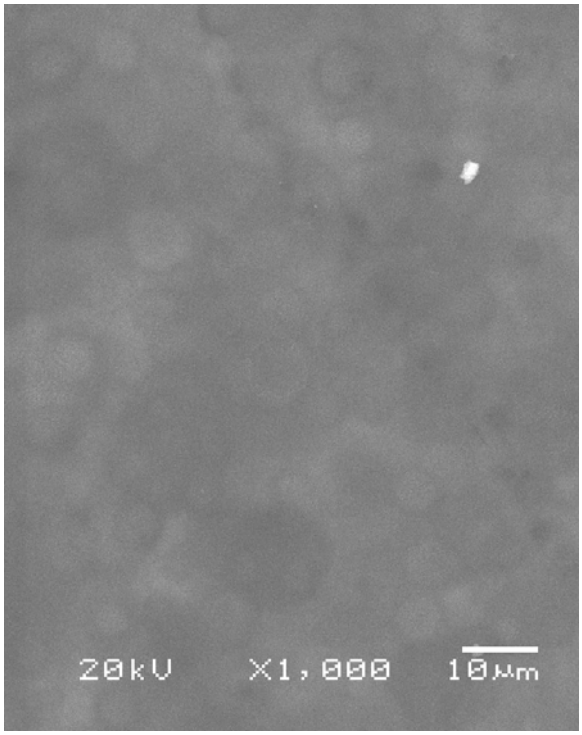

Figure 7.44: SEM image for MgO film deposited on Hastelloy C276 using 0.468M $Mg(NO_3)_2.6H_2O$ at 650°C for 48 minutes and at an inclination angle of 45°.

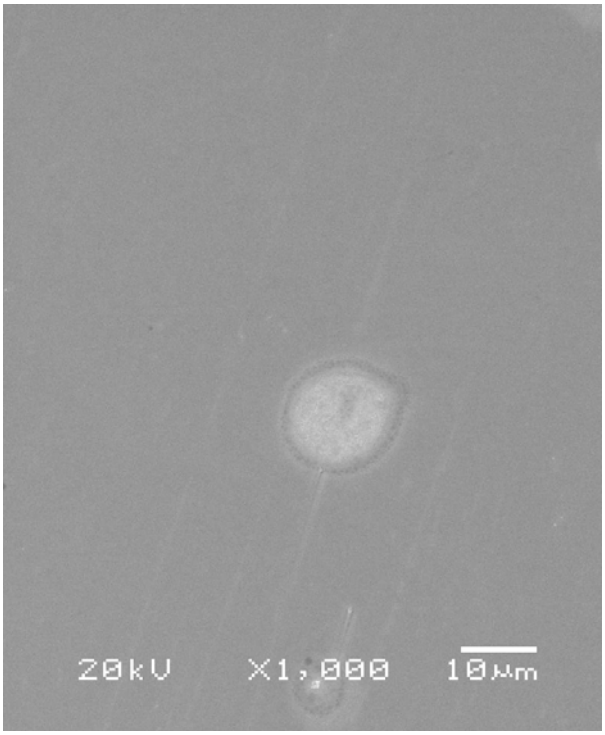

Figure 7.45: SEM image for MgO film deposited on Hastelloy C276 using 0.468M $Mg(NO_3)_2.6H_2O$ at 650°C for 48 minutes and at an inclination angle of 60°.

It is known that ISD deposition is applied, either by PLD or e-beam, to grow MgO thin films to improve the in plane texture for YBCO deposition. However, from Figure 7.41, it can be seen that the MgO (200) peak is not tilted relative to the substrate normal. This means that the ISD deposition by spray pyrolysis is not giving the shadowing effect observed by others. In Spray pyrolysis, the ISD is just affecting the crystallinity, roughness and thickness of the deposited MgO films.

7.10 Effect of Ar flow rate on MgO film properties

The effect of Ar flow rate on the spray pyrolysis deposition of MgO was investigated using 5 l/min, 10 l/min, and 15 l/min. The depositions were made using 0.468M solution at 650°C for 48 minutes. The XRD patterns in Figure 7.46 show that low Ar flow rate (5l/min.) did not result in any MgO peaks. The EDX results (Figure 7.47 and Table 7.4) show the presence of Mg, this suggests that an amorphous MgO film was obtained when using an Ar flow rate of 5 l/min. This was assumed to be as a result of the low thickness of the deposited MgO film when using low Ar flow rates. Amorphous films of MgO, CeO_2, In_2O_3, SnO_2 deposited by spray pyrolysis on different substrates were obtained by others [140, 146, 154, 162]. Others found that the texture of MgO developed with thickness [142, 242]. However, by increasing the

flow rate to 10 l/min and 15 l/min, only MgO (200) peak was detected. The high flow rate (15 l/min) has no effect on the quality of the texture as the MgO peak was not improved compared to that when using an Ar flow rate of 10 l/min. This is in disagreement with what found by Xiaorong Fu et al [72] and O. Renault and M. Labeau [146]. They found that the flow rate changed the preferred orientation. This was also found by others for different films [144, 145]. Pavlopoulos D. also found a change of the preferred orientation by changing the flow rate in the case of depositing CeO_2 on borosilicate glass. Joseph Prince J et al [140] found that crystallinity changed with the flow rate in the case of depositing In_2O_3. In addition to that, in this work the high flow rate (15 l/min) did not improve the intensity of MgO (200) peak and this was attributed to the saturation effect. C. H. Lee and C. S. Huang deposited In_2O_3 by spray pyrolysis on Si wafers using $InCl_3$-methanol solution as the source material [158], they found that at high flow rates, the growth rate was slow due to the reactant saturation effect. Other researchers [86] found that, for MgO films deposited on Si (100) substrates by electrostatic spray pyrolysis, the growth rate decreased with increasing the substrate temperature, others [114] found that, for ZnO films deposited on glass substrates by spray pyrolysis, at high temperatures the deposition rate was constant (saturated) where the growth rate is mass transport controlled; the reaction kinetics are so fast that the surface reaction finally becomes controlled by mass transfer of the reactants, and the concentration of the reactants on the surface is the limiting parameter.

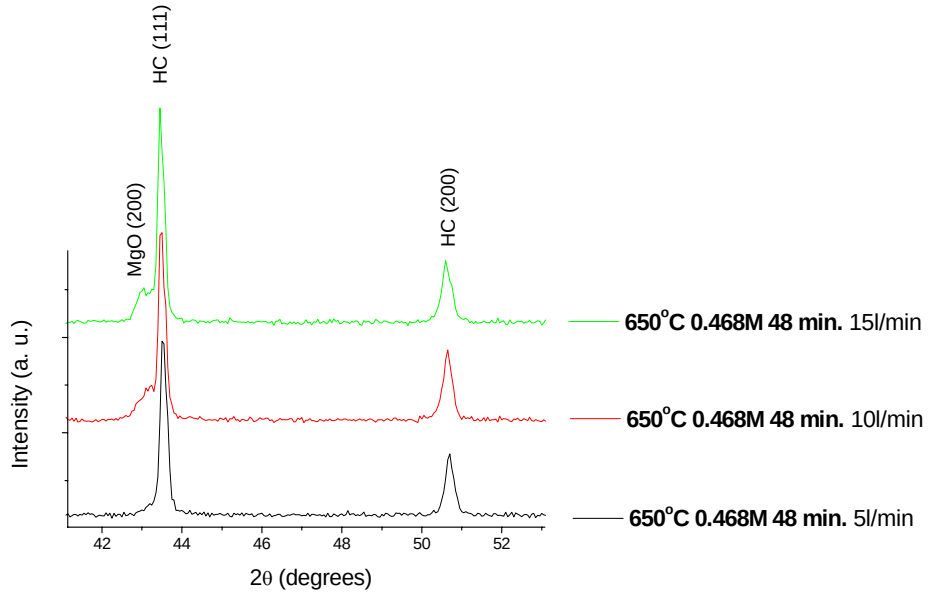

Figure 7.46: XRD patterns for MgO deposited on Hastelloy C276 using 0.468M $Mg(NO_3)_2.6H_2O$ at 650°C for 48 minutes and at different Ar flow rates.

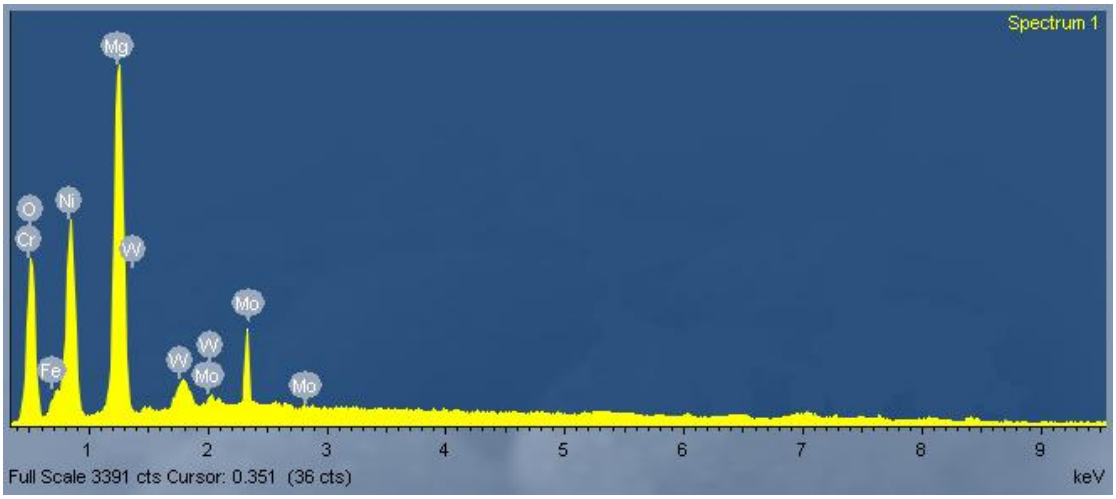

Figure 7.47: EDX spectrum, using an accelerating voltage of 4KV, for the Hastelloy C276 deposited with 0.468M at 650°C with a deposition time of 48 minutes and using an Ar flow rate of 5l/min.

Table 7.4: Summary of the EDX chemical composition results, using an accelerating voltage of 4KV, for the Hastelloy C276 deposited with 0.468M at 650°C with a deposition time of 48 minutes and using an Ar flow rate of 5l/min.

Element	at %
O K	25.19
Mg K	30.68
Ni L	26.92
Cr L	8.85
Mo L	4.51
Fe L	3.29
W M	0.56

The SEM images (Figure 7.24, Figure 7.48) and Figure 7.49 show that the smoothest film was obtained when using an Ar flow rate of 10 l/min and this was confirmed by the RMS reading obtained from the AFM as shown in Figure 7.50. On the one hand, the high flow rate (15 l/min) means more precursor material will reach the substrate, so it resembles increasing the concentration, where the time is not enough to evaporate both the solute and the solvent, which in turn leads to a rough MgO films. On the other hand, at low flow rate (5l/min), fewer precursor droplets arrive at the substrate; hence the growth rate may dominate the nucleation which in turn gives rough surfaces as well. Therefore, it was found that the optimum flow rate is 10 l/min which gives detectable MgO peaks and smoothest MgO films.

Figure 7.48: SEM image for the Hastelloy C276 deposited with 0.468M at 650°C with a deposition time of 48 minutes and using an Ar flow rate of 5 l/min.

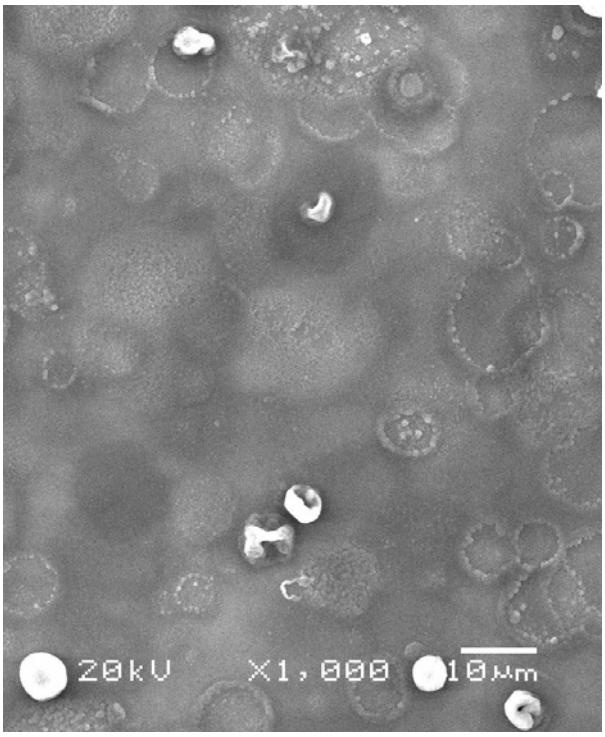

Figure 7.49: SEM image for the Hastelloy C276 deposited with 0.468M at 650°C with a deposition time of 48 minutes and using an Ar flow rate of 15 l/min.

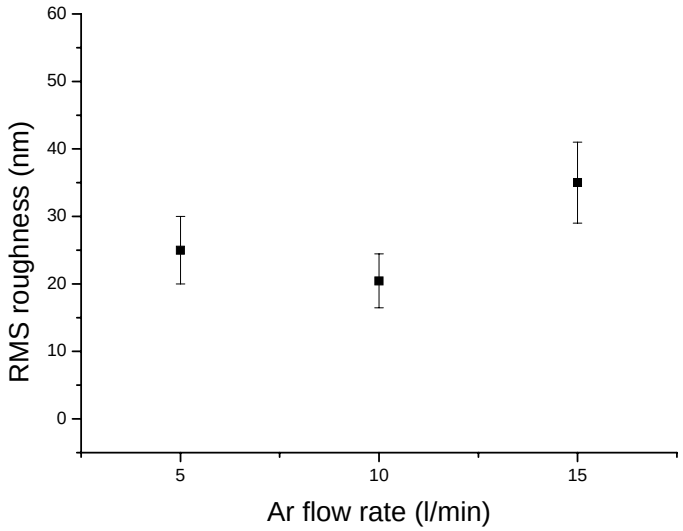

Figure 7.50: The effect of Ar flow rate on the film roughness of MgO film deposited from 0.468M solution at 650°C for 48 minutes.

7.11 Effect of annealing on the texture of MgO films

YBCO films deposited on annealed MgO buffers/substrates had improved in-plane texture and superconducting properties [191-193]. Therefore, an attempt to improve the texture of MgO films, annealing in different environments, at different temperatures and different annealing times were performed.

7.11.1 Annealing under O_2 atmosphere

The annealing experiments were carried out in a tube furnace rated to 1200°C. Pure oxygen was supplied from a compressed gas cylinder through copper tubing. The gas flow was controlled and was set at 100 ml/min for a furnace volume of 1630ml. Before heating, the oxygen was open for one hour which means that the furnace volume was replaced 3.7 times. The heating was carried out at a rate of 300°C/hr. After heating to the required temperature and holding for the required time, the furnace was switched off to allow the samples to be furnace cooled under O_2 atmosphere as well. Figure 7.51 shows the XRD patterns for the sample deposited at 650°C for 48 minutes from a 0.468M solution after being annealed under O_2 atmosphere at different temperatures and times. A narrow XRD scan is given in Figure 7.52. It can be seen that annealing at temperatures of 400°C-650°C for three hours did not affect the texture of the MgO (200) peak. The surface morphology and roughness were the same as that before the annealing (Figure 7.24 and Figure 7.29).

This was expected as the annealing temperatures did not exceed the deposition temperatures used during spray pyrolysis. This also confirms the stability of MgO film up to 650°C even under O_2 atmosphere. However, when the annealing temperature was increased to 800°C for a deposition time of three hours and 1000°C for a deposition time of three and five hours, other oxides started to appear (Figure 7.51). Those oxides were mainly chromium and nickel oxides indexed according to the JCPDS PDF files 00-032-0285 and 00-004-0835, respectively. The oxides were more pronounced by annealing at 1000°C for three and five hours. Some other peaks could not be indexed and were referred to as complex oxides. At 800°C, the MgO (200) was a little improved but this was at the expense of substrate oxidation and roughness as will be seen below.

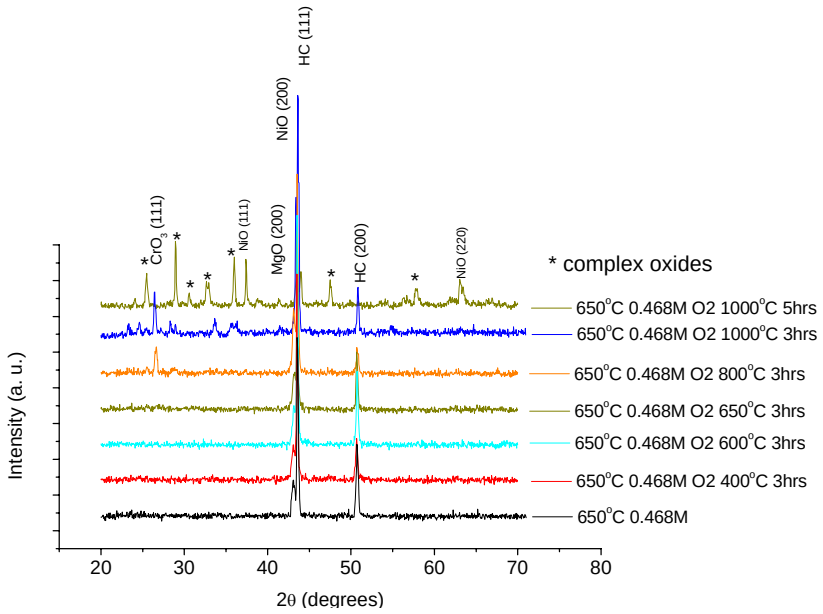

Figure 7.51: XRD patterns for Hastelloy substrates deposited with MgO from 0.468M at 650°C for 48 minutes after O_2 anneal at different temperatures and times.

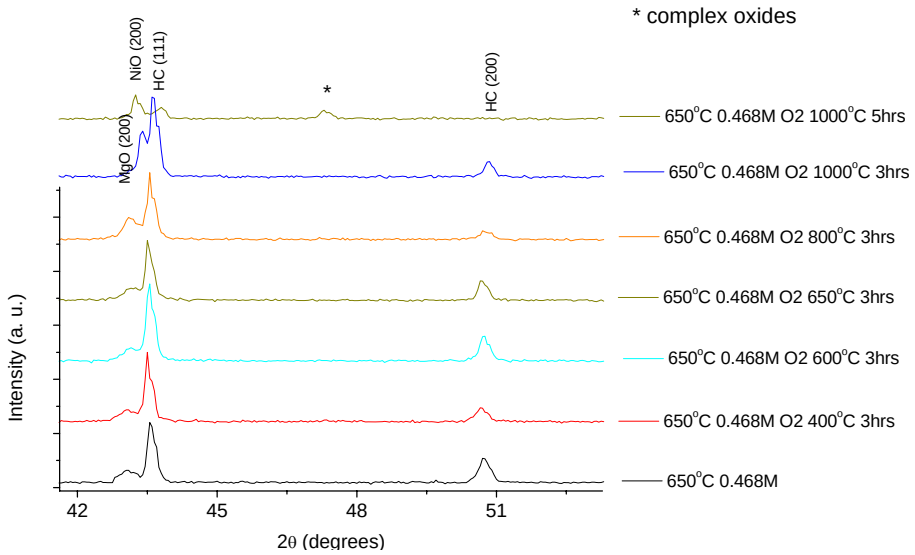

Figure 7.52: XRD patterns with a narrow scan for the Hastelloy substrates deposited with MgO from 0.468M at 650°C for 48 minutes after O_2 anneal at different temperatures and times.

The SEM images for the samples annealed at 800°C and 1000°C for three hours are shown in Figure 7.53 and Figure 7.54, respectively. It can be seen that the surface roughness increased by annealing. It was 20 nm for the sample before annealing (Figure 7.31) and became 63 nm for the sample annealed at 800°C for three hours and 130 nm for the sample annealed at 1000°C for three hours. The EDX test at 4KV showed an increase in the Cr and Ni content in addition to the presence of Mg, and this can be used to suggest the presence of oxides.

From this, it is clear that annealing up to 650C was not improving the texture nor deteriorating the MgO film. However, annealing at 800°C-1000°C affected the surface stability by the oxidation of the substrate.

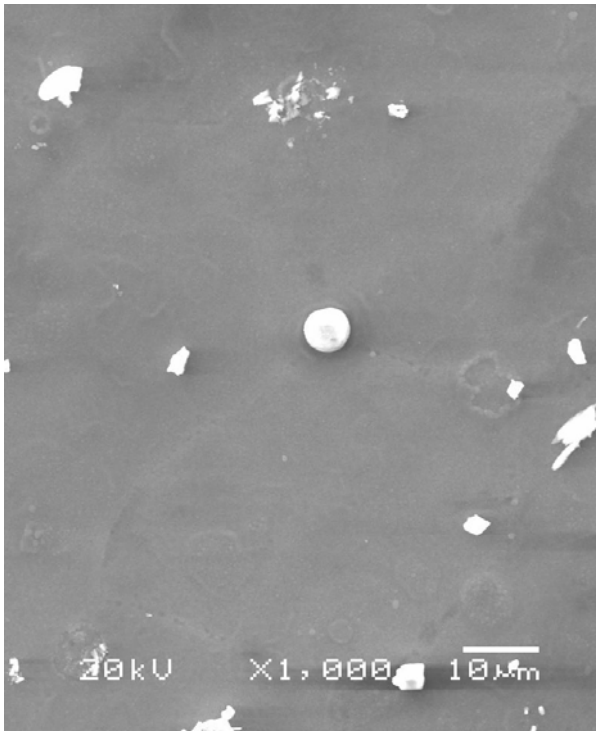

Figure 7.53: SEM image for the Hastelloy substrate deposited with MgO at 650°C for 48 minutes from 0.468M solution then annealed at 800°C under O_2 for three hours.

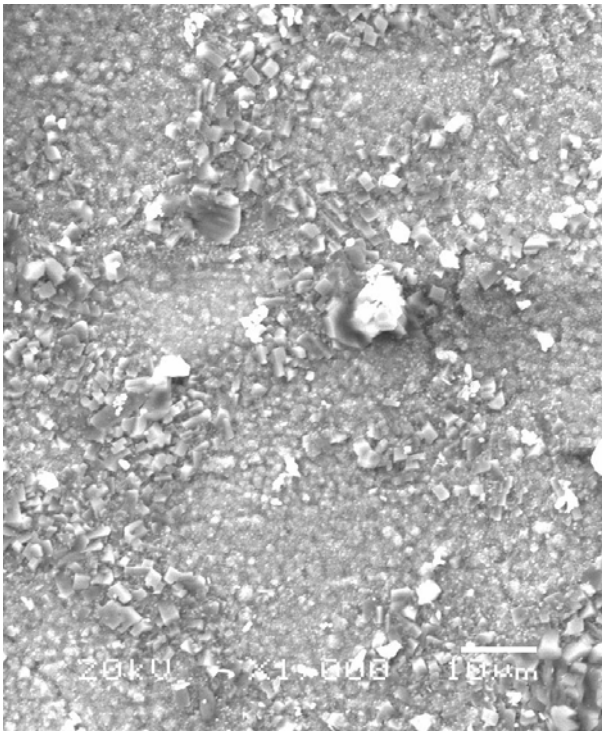

Figure 7.54: SEM image for the Hastelloy substrate deposited with MgO at 650°C for 48 minutes from 0.468M solution then annealed at 1000°C under O_2 for three hours.

To study the effect of annealing on MgO films deposited with higher concentration, the annealing was applied to the samples deposited from a 0.78M solution at 650°C and for 48 minutes. The same procedures used for annealing the samples deposited from the 0.468M solution were exactly used to anneal the samples deposited from the 0.78M solution. Figure 7.55 shows the XRD patterns for the samples after being annealed under O_2 atmosphere at different temperatures and times. A narrow XRD scan is given in Figure 7.56. It can be seen that annealing at temperatures of 400°C-650°C for three hours did not affect the texture of the MgO (200) peak. The surface morphology and roughness were the same as before the annealing (Figure 7.27 and Figure 7.29). This was expected as the annealing temperatures did not exceed the deposition temperature during spray pyrolysis. This also confirms the stability of MgO film up to 650°C even under O_2 atmosphere. Therefore, annealing at 400°C-650°C did not play a role in improving the texture of MgO (200) and this was also obtained when using 0.468M. However, when the annealing temperature was increased to 800°C for a deposition time of three hours, an increase in the intensity of MgO (200) was observed with no evidence of any oxides being detected. This may be attributed to the higher concentration of the precursor which in turn gives a thicker MgO layer which protected the substrate from oxidation. However, this slight improvement in the texture was at the expense of surface roughness as can be seen from the SEM and AFM images in Figure 7.57 and Figure 7.58, respectively, where the roughness is 130 nm compared to about 75nm (Figure 7.29) before annealing. This increase in roughness was due to the high annealing temperature under O_2 flow and the high precursor concentration. This may enhance diffusion processes in the MgO film leading to the formation of rough background in addition to the formation of MgO particles (Figure 7.57) which was confirmed by an EDX test. Oxides started to appear when the annealing temperature increased to 1000°C for annealing time of three and five hours (Figure 7.55). The same oxides were formed when annealing the samples deposited from 0.468M solution (Figure 7.51). Those oxides were mainly chromium and nickel oxides indexed according to the JCPDS PDF files 00-032-0285 and 00-004-0835, respectively. The oxides were more pronounced by annealing at 1000C for five hours. Some other peaks could not be indexed and were referred to as complex oxides. The SEM image for the sample annealed at 1000°C for three hours is shown in Figure 7.59 which shows a very rough

surface. The EDX test showed an increase in the Cr and Ni content in addition to the presence of Mg, and this can be used to suggest the presence of oxides.

From this, it is clear that annealing up to 650C was not improving the texture nor deteriorating the MgO film irrespective of the precursor concentration used for depositing MgO films. However, for the precursor concentration of 0.78M, annealing at 800°C, showed a slight improvement in the intensity of MgO (200) but this was at the expense of roughness. Annealing at 1000°C affected the surface stability by the oxidation of the substrate.

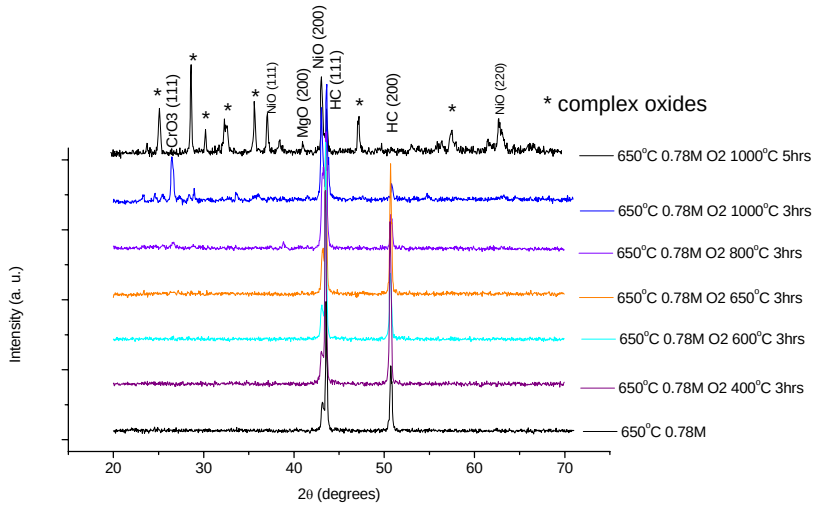

Figure 7.55: XRD patterns for the Hastelloy substrates deposited with MgO from 0.78M at 650°C for 48 minutes after O_2 anneal at different temperatures and times.

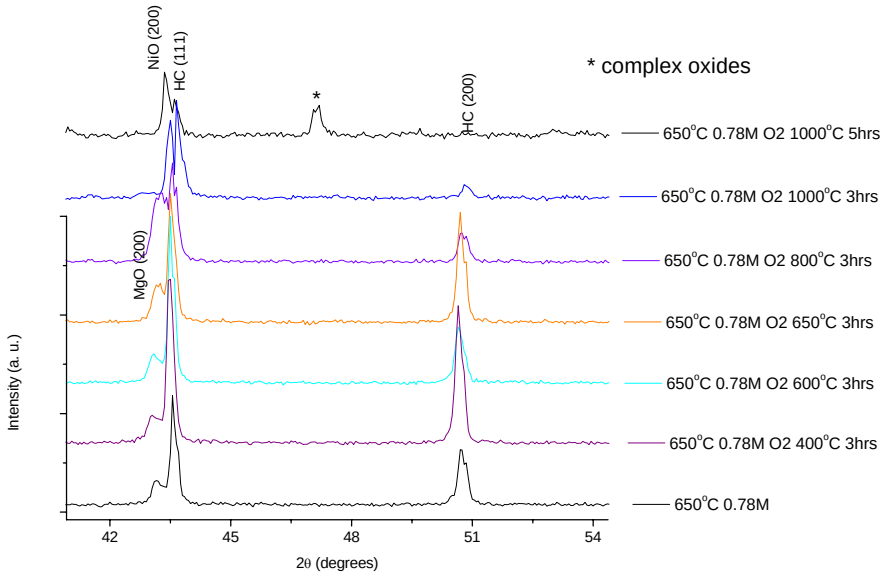

Figure 7.56: XRD patterns with a narrow scan for the Hastelloy substrates deposited with MgO from 0.78M at 650°C for 48 minutes after O_2 anneal at different temperatures and times.

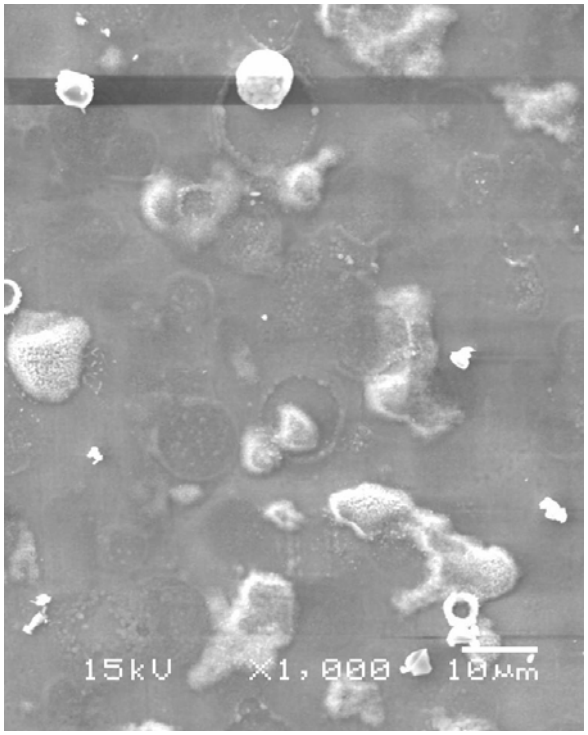

Figure 7.57: SEM image for the Hastelloy substrate deposited with MgO at 650°C for 48 minutes from 0.78M solution then annealed at 800°C under O_2 for three hours.

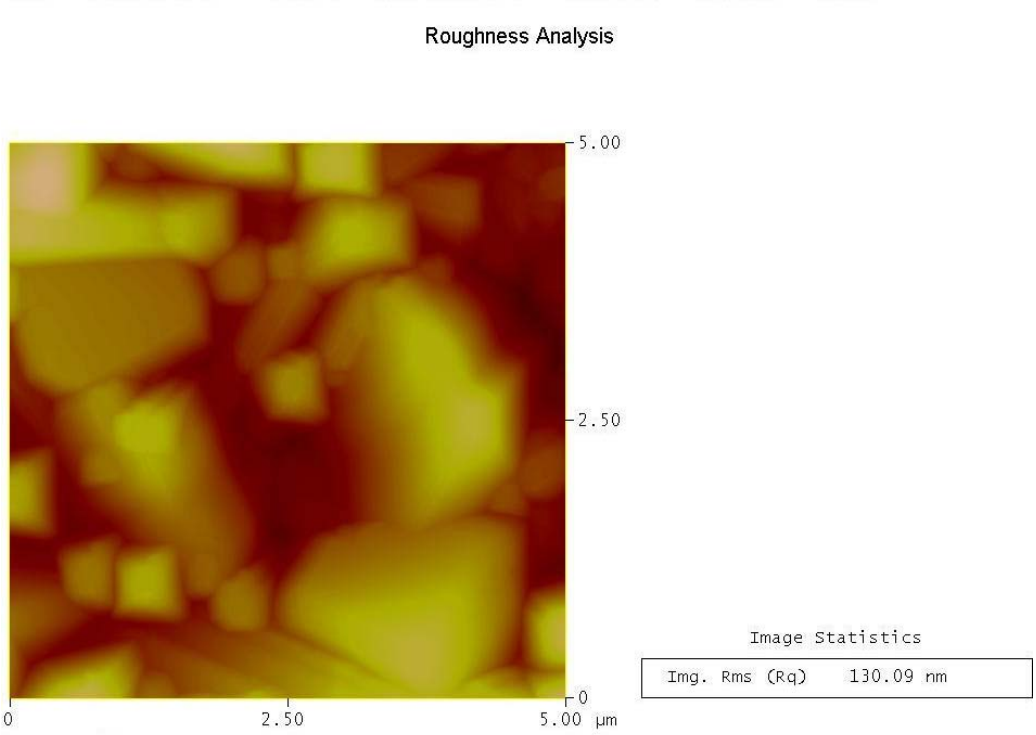

Figure 7.58: A 5x5µm^2 AFM image for the Hastelloy substrate deposited with MgO at 650°C for 48 minutes from 0.78M solution then annealed at 800°C under O_2 for three hours.

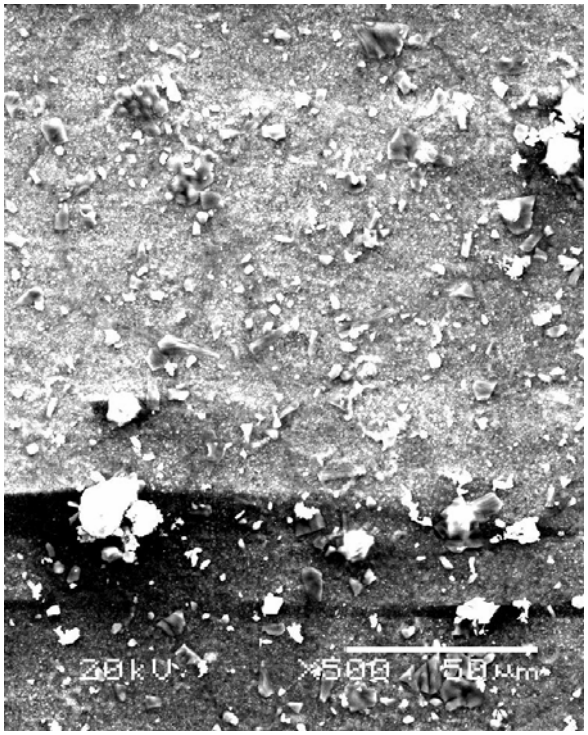

Figure 7.59: SEM image for the Hastelloy substrate deposited with MgO at 650°C for 48 minutes from 0.78M solution then annealed at 1000°C under O_2 for three hours.

7.11.2 Annealing under vacuum

It was found that high temperature annealing under O_2 resulted in substrate oxidation. Therefore, to protect the substrate from oxidation, high temperature annealing will be done in an O_2-free environment. This suggests doing the annealing under vacuum.

The vacuum annealing experiments were carried out in a tube furnace connected to pumping system; which consists of rotary and turbo pumps. The furnace was rated to 1200°C. Before heating, the system was pumped down to about $5x10^{-7}$ mbar ($3.75x10^{-7}$ torr). The heating was carried out at a rate of 300C°/hr. After heating to the required temperature and holding for the required time, the furnace was switched off to allow the samples to be furnace cooled under vacuum atmosphere as well.

Figure 7.60 shows the XRD patterns for the samples deposited at 650°C for 48 minutes from a 0.468M solution after being annealed under vacuum (~ $2x10^{-6}$ mbar) at different temperatures and times. A narrow XRD scan is given in Figure 7.61. It can be seen that up to 800°C with annealing time of three hours, no oxides were formed but at the same time, no improvement in the MgO (200) texture was obtained. The surface morphology and roughness were the same as that before annealing (Figure 7.24 and Figure 7.31). This confirms that the MgO film is stable under

vacuum atmosphere up to 800°C which is good for later YBCO deposition which is carried out under 450 mtorr O_2 at 780°C as will be seen in section 7.12. By increasing the annealing temperature to 1000°C, the MgO (200) peak disappeared, and the SEM image (Figure 7.62) for the sample annealed at 1000°C for three hours shows that the MgO film was severely affected where grain boundaries of the substrate were revealed as a result of thermal etching. The EDX test showed that the formed particles were MgO (Figure 7.63 and Table 7.5). However, the area between the particles showed Mg deficiency (Figure 7.64 and Table 7.6). The surface roughness of the sample increased from 20 nm before annealing (Figure 7.31) to 64.8 nm after annealing (Figure 7.65). This increase in roughness was due to the high annealing temperature. This may enhance diffusion processes to occur in the MgO film leading to the formation of rough background in addition to the formation of MgO particles. As was the case when annealing MgO films deposited from 0.468M solution, annealing for the films deposited from 0.78M solution had no effect on the texture and smoothness between 650°C-800°C. However, rough surfaces and Mg deficiency were noticed when annealing at 1000°C.

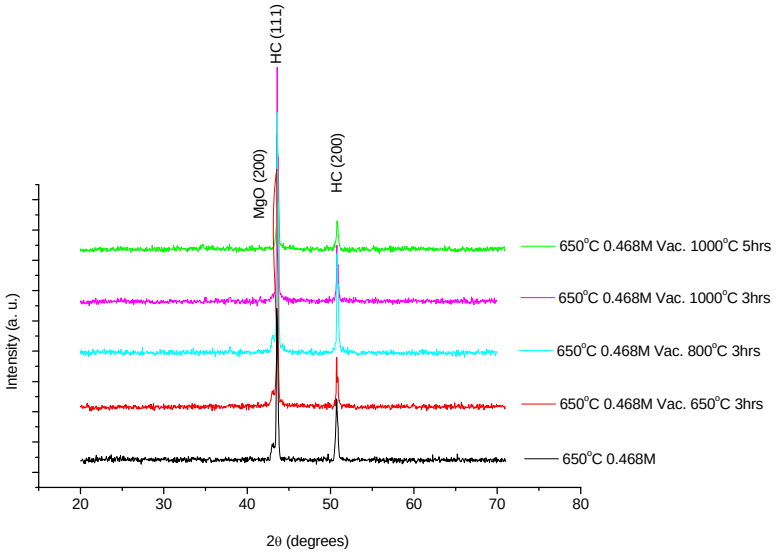

Figure 7.60: XRD patterns for the Hastelloy substrates deposited with MgO from 0.468M at 650°C for 48 minutes after vacuum anneal at different temperatures and times.

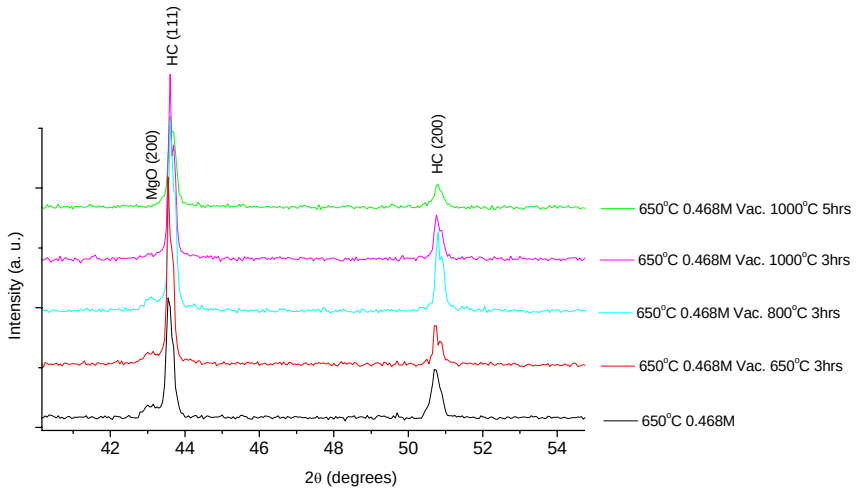

Figure 7.61: XRD patterns with a narrow scan for the Hastelloy substrates deposited with MgO from 0.468M at 650°C for 48 minutes after vacuum anneal at different temperatures and times.

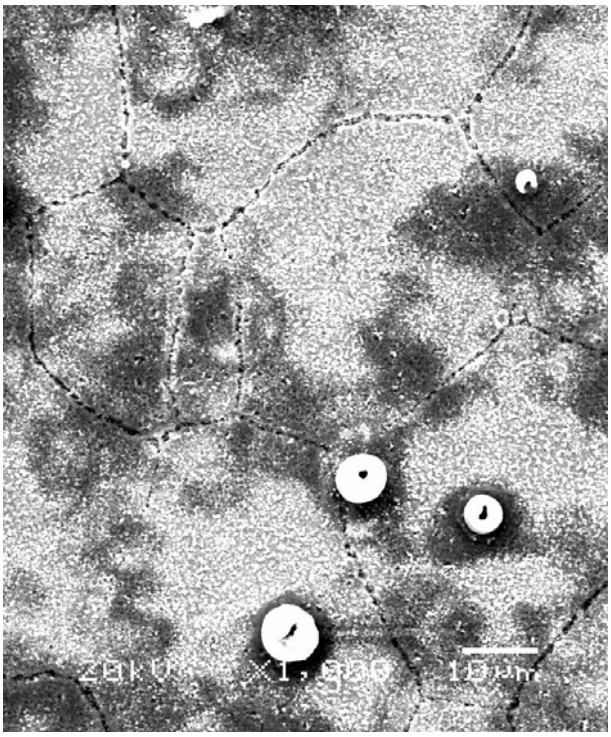

Figure 7.62: SEM image for the Hastelloy substrate deposited with MgO at 650°C for 48 minutes from 0.468M solution then annealed at 1000°C under vacuum for three hours.

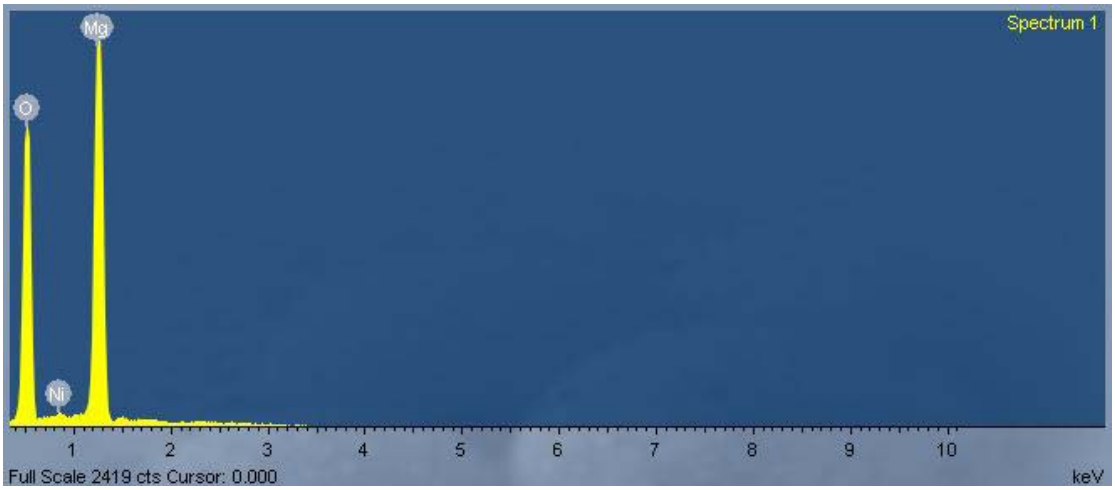

Figure 7.63: EDX spectrum, using an accelerating voltage of 4KV, for the particles formed on Hastelloy C276 deposited with 0.468M at 650°C with a deposition time of 48 minutes after being annealed at 1000°C under vacuum for 3 hours.

Table 7.5: Summary of the EDX chemical composition results, using an accelerating voltage of 4KV, for the particles formed on Hastelloy C276 deposited with 0.468M at 650°C with a deposition time of 48 minutes after being annealed at 1000°C under vacuum for 3 hours.

Element	at %
O K	48.33
Mg K	51.23
Ni L	0.44

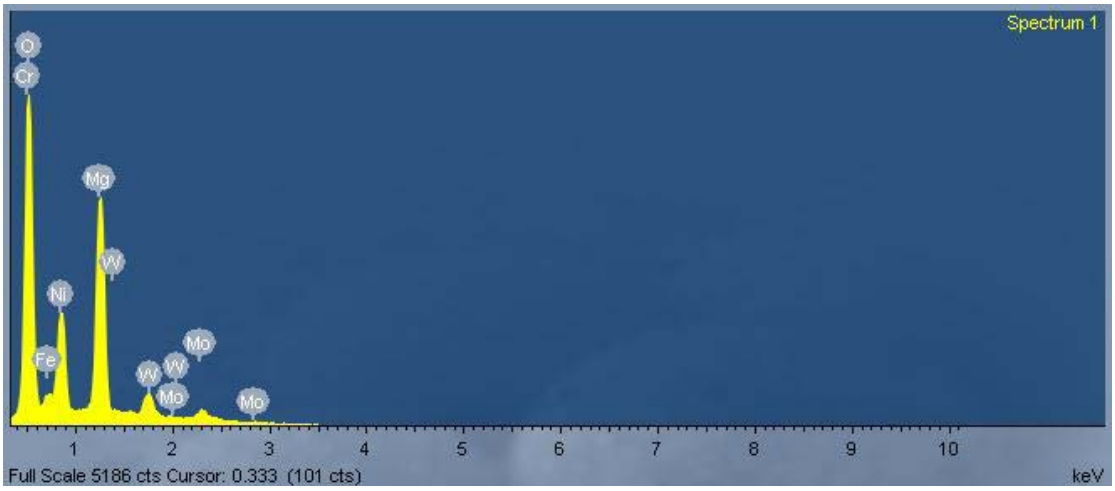

Figure 7.64: EDX spectrum, using an accelerating voltage of 4KV, for the area between particles formed on Hastelloy C276 deposited with 0.468M at 650°C with a deposition time of 48 minutes after being annealed at 1000°C under vacuum for 3 hours.

Table 7.6: Summary of the EDX chemical composition results, using an accelerating voltage of 4KV, for the area between particles formed on Hastelloy C276 deposited with 0.468M at 650°C with a deposition time of 48 minutes after being annealed at 1000°C under vacuum for 3 hours.

Element	at %
O K	41.91
Mg K	26.7
Cr L	10.65
Fe L	1.42
Ni L	14.32
Mo L	3.94
W M	1.06

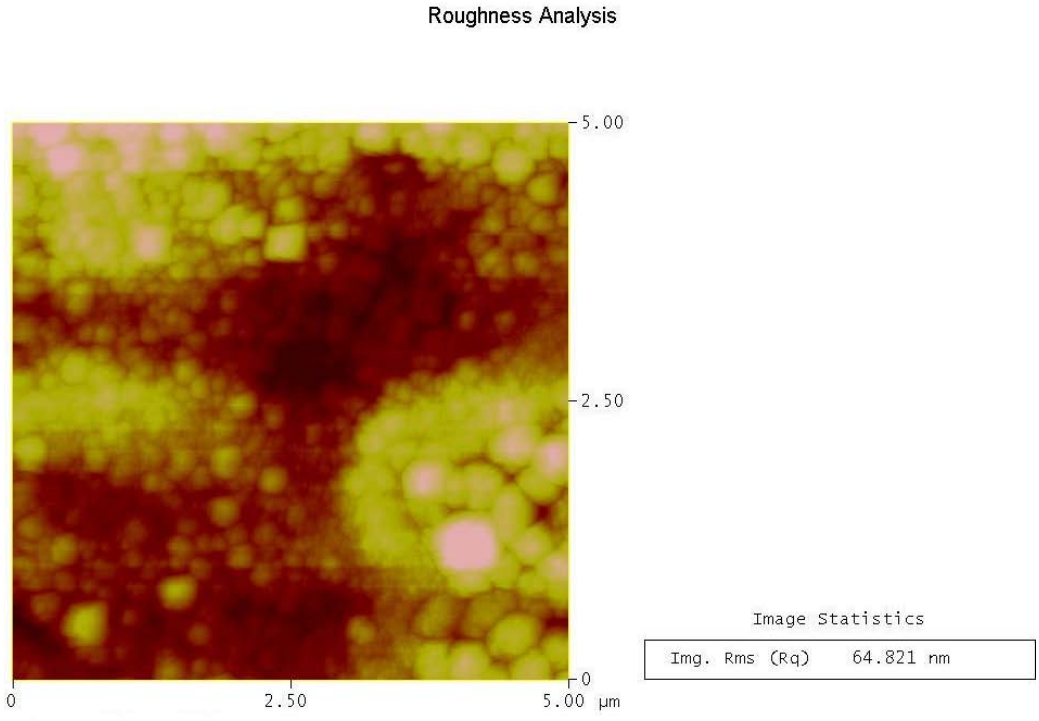

Figure 7.65: A 5x5µm^2 AFM image for the Hastelloy substrate deposited with MgO at 650°C for 48 minutes from 0.468M solution then annealed at 1000°C under vacuum for three hours**.**

To study the effect of high temperature annealing (1000°C) under vacuum and its relation to Mg deficiency, MgO single crystals were annealed under the same conditions, i.e. under vacuum and at 1000°C for three hours.

Figure 7.66 shows the XRD patterns for MgO single crystal before and after vacuum annealing at 1000°C for three hours. It was clear that no change happened

due to the annealing process in terms of peak intensity or the formation of any extra peaks. This was expected as the X-ray beam will interact deeply with the sample; as it was believed that if any change will occur due to vacuum annealing, it will be confined to a thin layer on the surface. This was confirmed by the SEM images in Figure 7.67-Figure 7.69 which reveal a morphological change after the annealing process. It can also be seen from the SEM images that a vacuum anneal made the surface rougher compared to that before annealing. This was also confirmed by the AFM images in Figure 7.70 and Figure 7.71. This increase in roughness was also noticed on the MgO films (deposited on Hastelloy) after annealing at 1000°C for three hours (Figure 7.65) relative to that before annealing (Figure 7.31). To make the picture clearer, an EDX test was performed on the as received and annealed MgO single crystals using an accelerating voltage of 4KV; which will interact only with a thin layer on the surface. Table 7.7 and Table 7.8 confirms that vacuum ($3.75x10^{-7}$ torr) anneal at 1000°C resulted in Mg deficiency. Therefore we can confirm that under such conditions of high temperature and high vacuum, Mg tends to evaporate leading to Mg deficient films. This behaviour was not mentioned by researchers who applied annealing treatments on MgO substrates [191-193]. However, some groups found that annealing MgB_2 resulted in Mg evaporation. K. A. Yates et al found that annealing MgB_2 (in vacuum) at 500°C resulted in significant Mg loss [277]. Z. Y. Fan et al [278] found that the onset of significant Mg evaporation under vacuum (10^{-9} torr) was observed near 425°C.

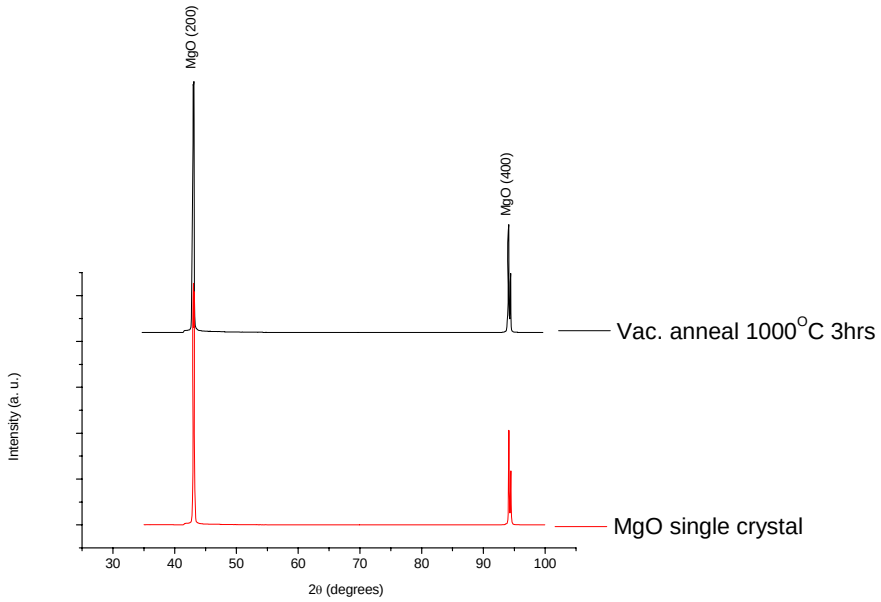

Figure 7.66: XRD patterns for MgO single crystal before and after vacuum annealing at 1000°C for 3 hours.

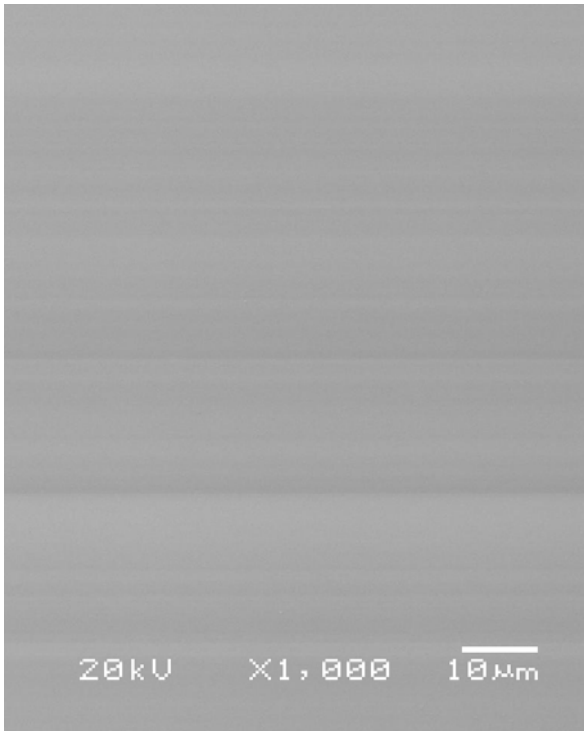

Figure 7.67: SEM image of the as received MgO single crystal.

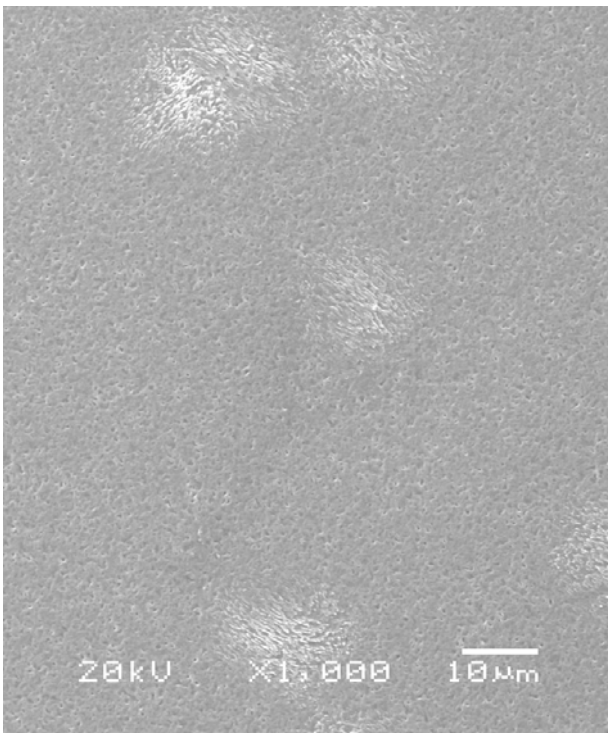

Figure 7.68: SEM image of the as received MgO single crystal after vacuum anneal at 1000°C for 3 hours.

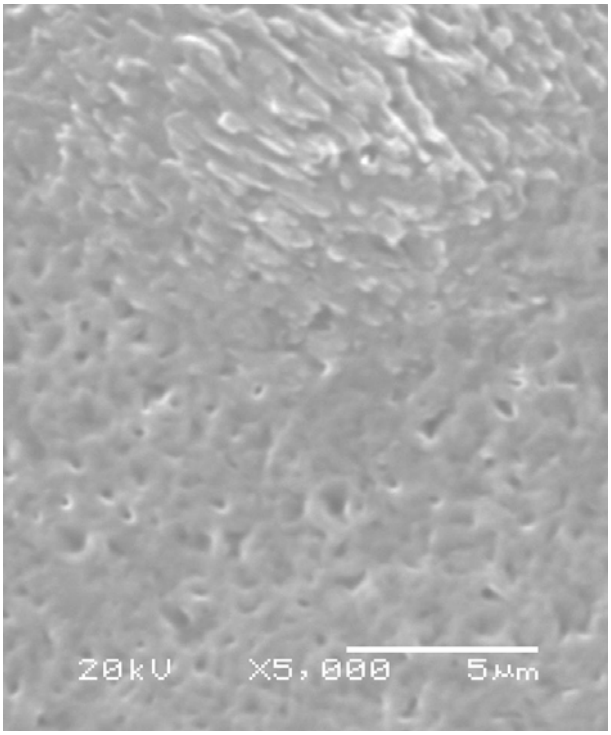

Figure 7.69: Higher magnification SEM image of the as received MgO single crystal after vacuum anneal at 1000°C for 3 hours.

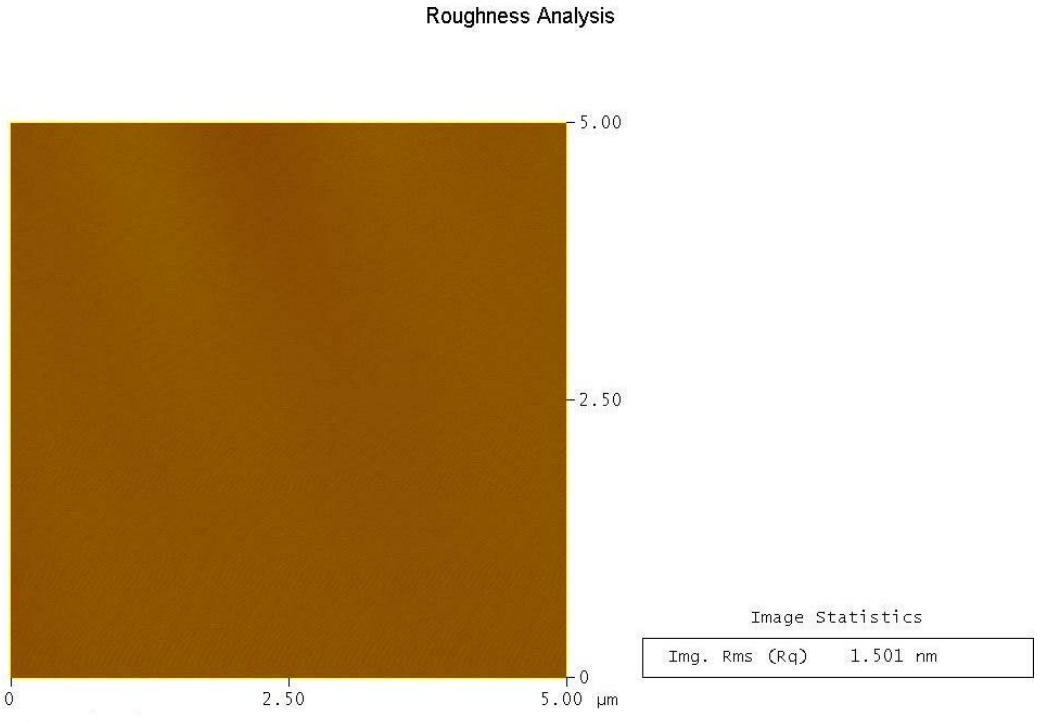

Figure 7.70: A 5x5µm^2 AFM image of the as received MgO single crystal

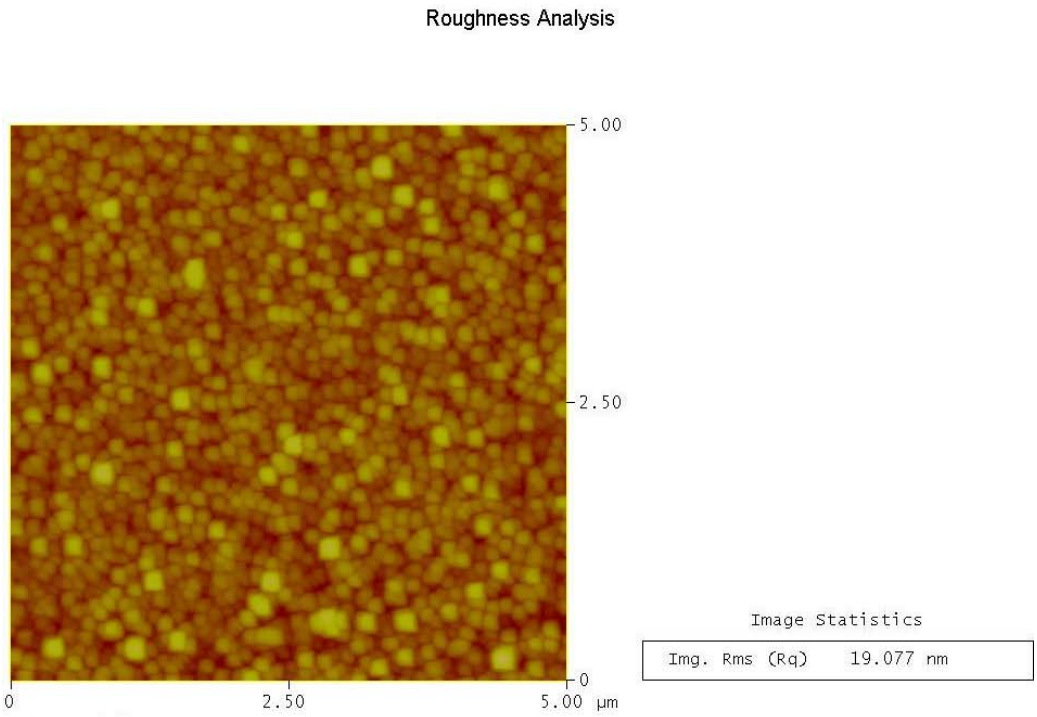

Figure 7.71: A 5x5µm^2 AFM image of the as received MgO single crystal after vacuum anneal at 1000°C for 3 hours.

Table 7.7: Summary of the EDX chemical composition results (using an accelerating voltage of 4KV) of the as received MgO single crystal.

Element	at %
O K	49.95
Mg K	50.05

Table 7.8: Summary of the EDX chemical composition results (using an accelerating voltage of 4KV) of the as received MgO single crystal after vacuum anneal at 1000°C for 3 hours.

Element	at %
O K	52.34
Mg K	37.8

In order to confirm that Mg evaporation needs high vacuum and high temperature to evaporate, a high temperature anneal using purified Ar was applied. After pumping the system to 3.75x10^{-7} torr, 0.25 bar (0.246 atm.) of purified Ar was purged to the system. The purification was made to get rid of any traces of oxygen or

moisture that may present in Ar. After that, the sample was heated to 1000°C at a rate of 300°C/hr and holds for three hours, the sample was then furnace cooled.

The XRD patterns in Figure 7.72 show that annealing under purified Ar, for the sample deposited from 0.468M solution at 650C for 48 minutes, did not result in the elimination of the MgO (200) as a result of Mg evaporation as was the case during vacuum anneal (Figure 7.61). The same result was obtained for the film deposited from the 0.78M solution. This confirms that the high temperature of annealing should be combined with high vacuum to lead to Mg evaporation irrespective of the precursor concentration used for MgO deposition. It can also be noticed that very little improvement in the intensity of MgO (200) was obtained, but the surface smoothness deteriorated (Figure 7.73 and Figure 7.74) compared to the sample before annealing (Figure 7.31). This was also observed for the film deposited from the 0.78M solution. This may be attributed to the high temperature anneal which enhances diffusion processes leading to the formation of tiny particles which in turn contribute to the deterioration of the surface smoothness.

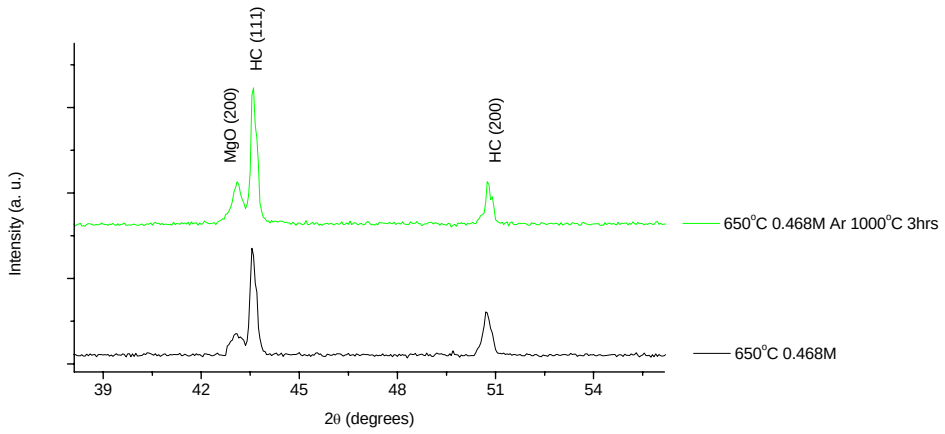

Figure 7.72: XRD patterns for the Hastelloy substrates deposited with MgO from 0.468M solution at 650°C for 48 minutes then annealed under 0.25 bar purified Ar at 1000°C for three hours.

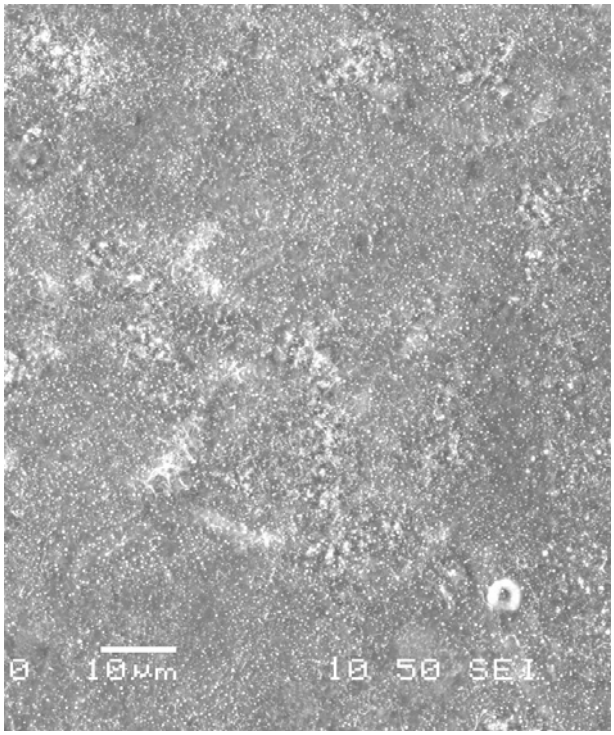

Figure 7.73: SEM image for the Hastelloy substrate deposited with MgO from 0.468M solution at 650°C for 48 minutes then annealed under 0.25 bar purified Ar at 1000C for three hours.

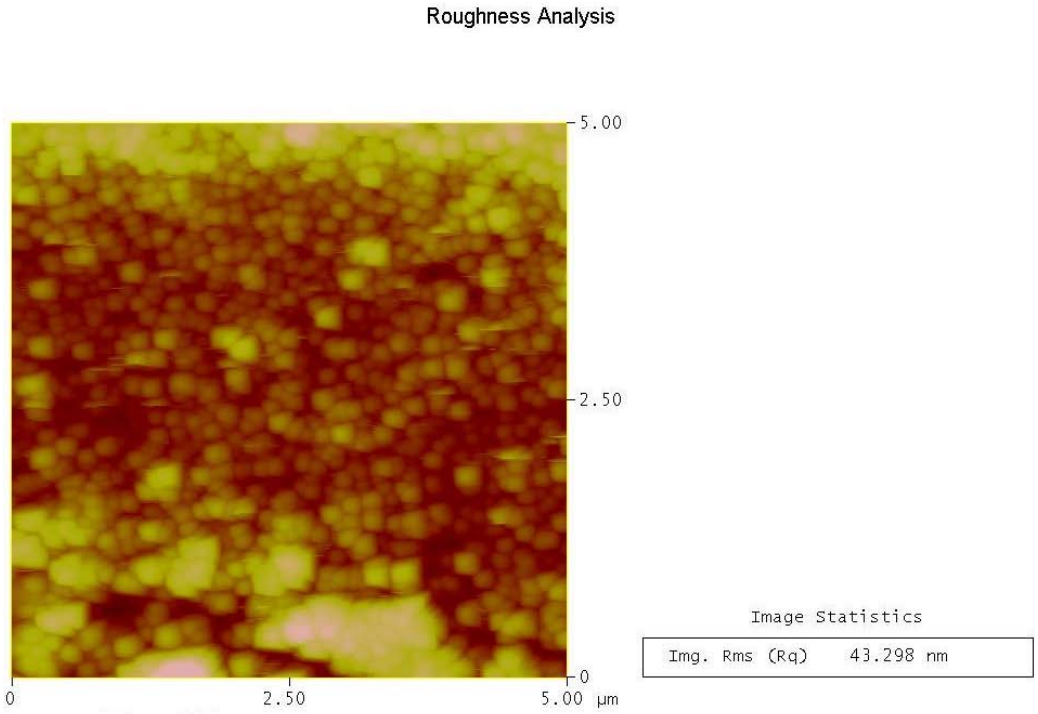

Figure 7.74: A 5x5µm^2 AFM image for the Hastelloy substrate deposited with MgO from 0.468M solution at 650°C for 48 minutes then annealed under 0.25 bar purified Ar at 1000C for three hours.

7.12 YBCO, MgO and ceria (CeO_2) deposition by PLD

7.12.1 Introduction

Before YBCO deposition, the MgO films deposited from 0.468M for 32 and 48 minutes at 650°C were heated in the YBCO deposition chamber at the same conditions used for YBCO deposition to see the stability of MgO films. It was found that the intensity of MgO (200) peak, surface morphology and surface smoothness were the same before and after the heating. This confirmed the stability of MgO films during YBCO deposition.

As in the previous chapters an objective of this work is to grow MgO as the only buffer layer before YBCO deposition in an attempt to make the process a cost-effective one by reducing the usual multi-layer buffer architecture to a single layer. To evaluate the performance of the MgO as a buffer the YBCO films were deposited by PLD. This is a well established route to high quality films [244, 245], although spray pyrolysis of the YBCO layer should also be a possibility in the future [23, 24, 87, 93, 94]. The optimised parameters for YBCO deposition were obtained by first depositing YBCO on MgO single crystal (section 4.5.1). The YBCO deposition and optimised parameters were:

- The deposition temperature: 780°C.
- Substrate target distance: 56mm.
- Deposition pressure: 450mtorr oxygen.
- Energy fluence: 2J/cm^2.
- Number of pulses 5000.
- Pulse frequency: 4Hz
- Heating and cooling rates: 20°C/min and 10°C/min, respectively.

7.12.2 YBCO deposition on MgO films spray pyrolysed at different temperatures, precursor concentrations and deposition times

YBCO was deposited by PLD on MgO films spray pyrolysed under different conditions (see Figure 7.22). The MgO and YBCO peaks were indexed according to the JCPDS PDF files 00-045-0946 and 00-038-1433, respectively. Figure 7.75 shows that YBCO films deposited on MgO films spray pyrolysed at 650°C at different precursor concentrations and deposition times were polycrystalline. The film deposited at 700°C from 0.468M solution with a deposition time for 48 minutes was

polycrystalline as well. Figure 7.76 and Figure 7.77 show that YBCO films deposited on MgO spray pyrolysed at 650°C using 0.468M for 64 and 96 minutes had granular structure. The same structure was also observed for YBCO films deposited on MgO spray pyrolysed at 650°C using 0.78M for 48 minutes and for the film spray pyrolysed at 700°C using 0.468M for 48 minutes (Figure 7.78 and Figure 7.79, respectively). It was also found that the roughness trend found for MgO films (Figure 7.29) was also observed for YBCO films; however, in this case the roughness values were higher (Figure 7.80-Figure 7.83).

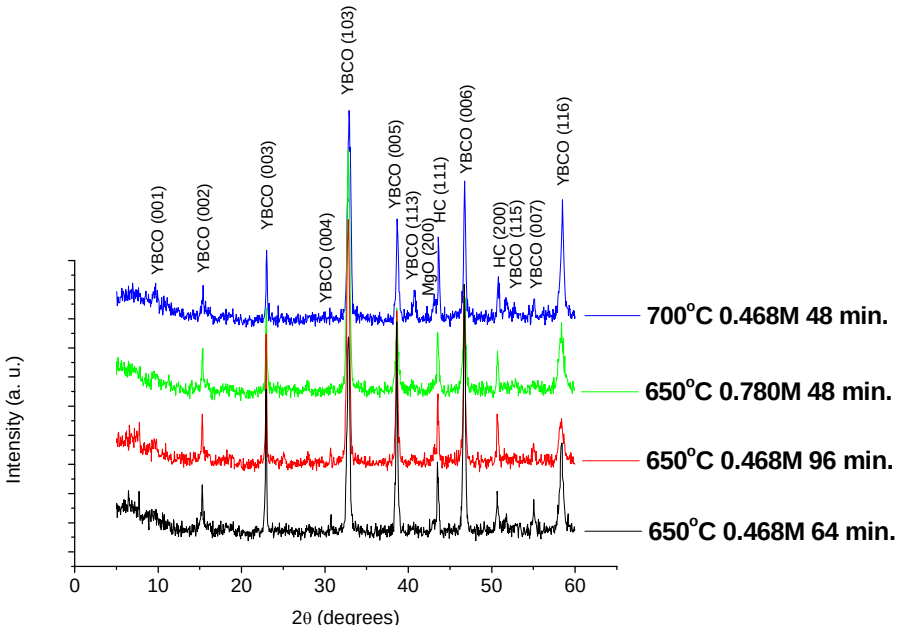

Figure 7.75: XRD patterns for YBCO films deposited by PLD on the MgO films spray pyrolysed at different conditions.

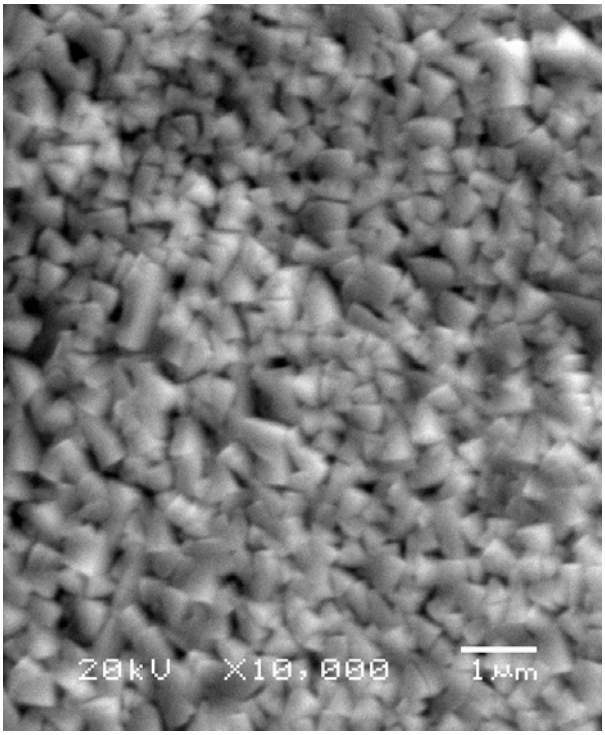

Figure 7.76: SEM image for YBCO film deposited on MgO film spray pyrolysed on Hastelloy C276 using 0.468M of $Mg(NO_3)_2.6H_2O$ at 650°C for 64 minutes.

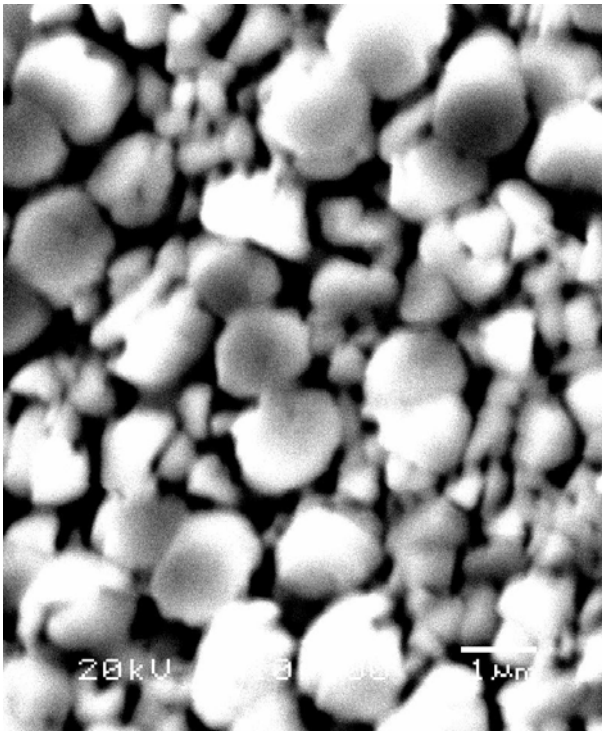

Figure 7.77: SEM image for YBCO film deposited on MgO film spray pyrolysed on Hastelloy C276 using 0.468M of $Mg(NO_3)_2.6H_2O$ at 650°C for 96 minutes.

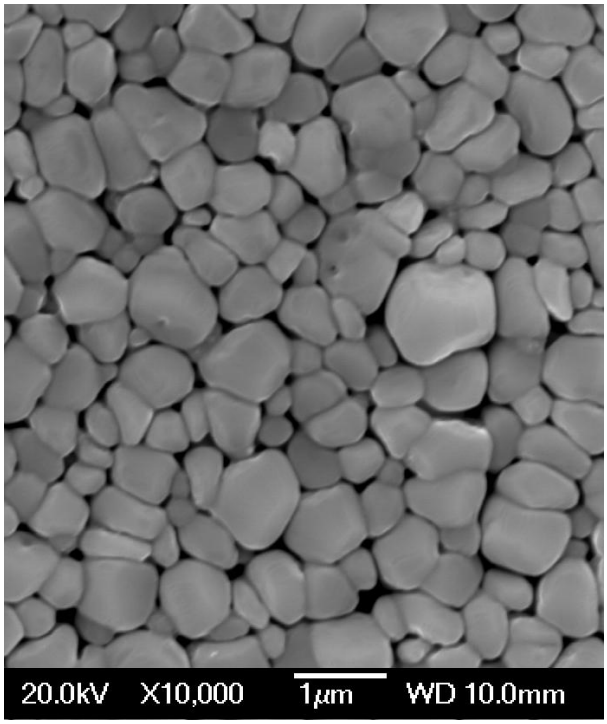

Figure 7.78: SEM image for YBCO film deposited on MgO film spray pyrolysed on Hastelloy C276 using 0.78M of $Mg(NO_3)_2.6H_2O$ at 650°C for 48 minutes.

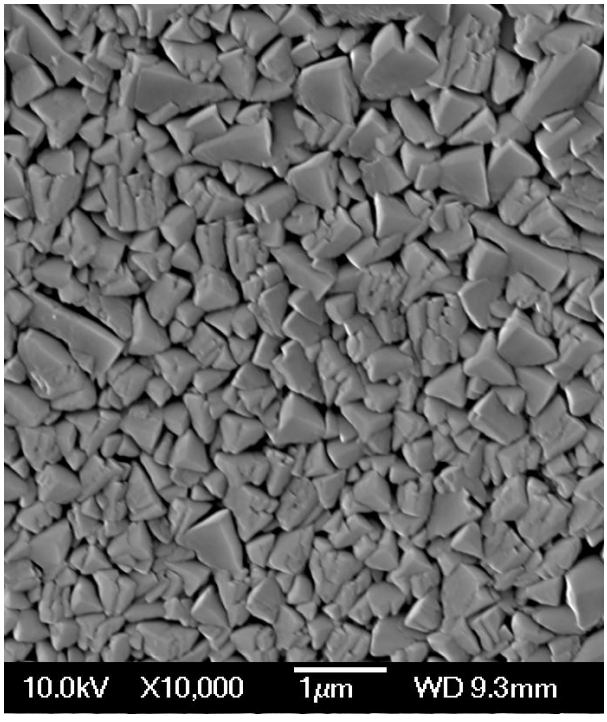

Figure 7.79: SEM image for YBCO film deposited on MgO film spray pyrolysed on Hastelloy C276 using 0.468M of $Mg(NO_3)_2.6H_2O$ at 700°C for 48 minutes.

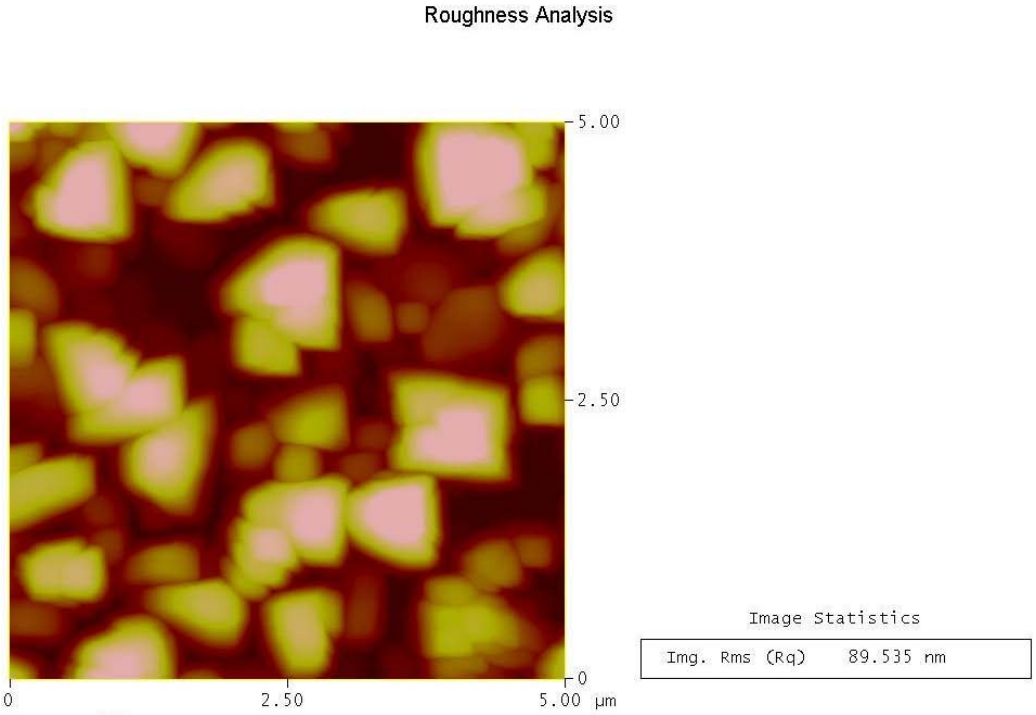

Figure 7.80: A 5x5µm^2 AFM image for YBCO film deposited on MgO film spray pyrolysed on Hastelloy C276 using 0.468M of $Mg(NO_3)_2.6H_2O$ at 650°C for 64 minutes.

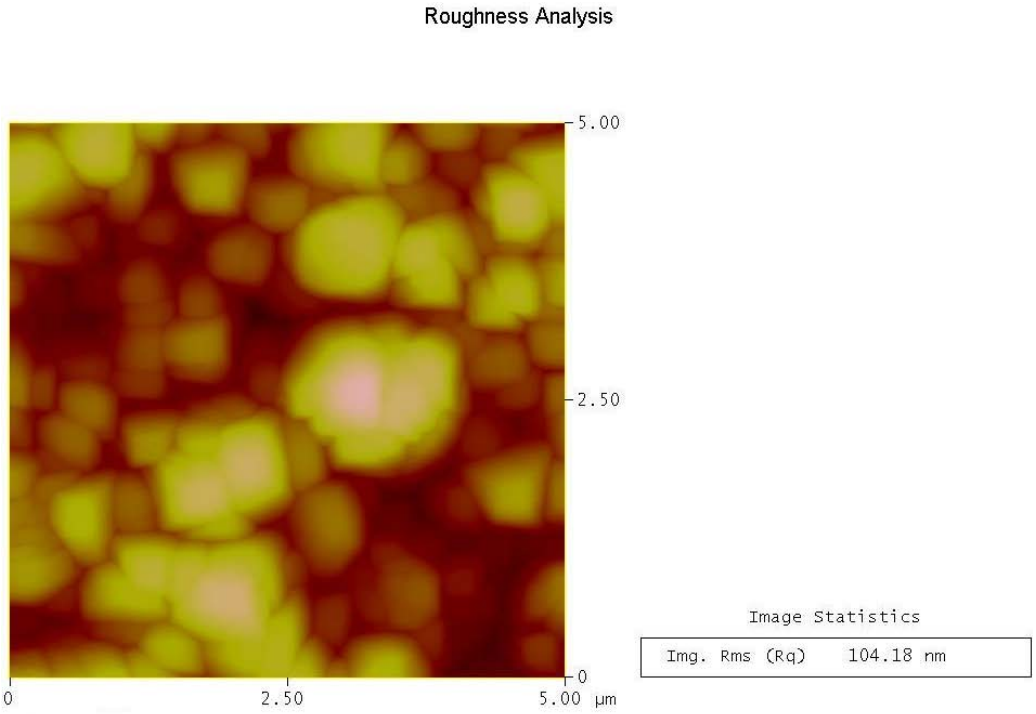

Figure 7.81: A 5x5µm^2 AFM image for YBCO film deposited on MgO film spray pyrolysed on Hastelloy C276 using 0.468M of $Mg(NO_3)_2.6H_2O$ at 650°C for 96 minutes.

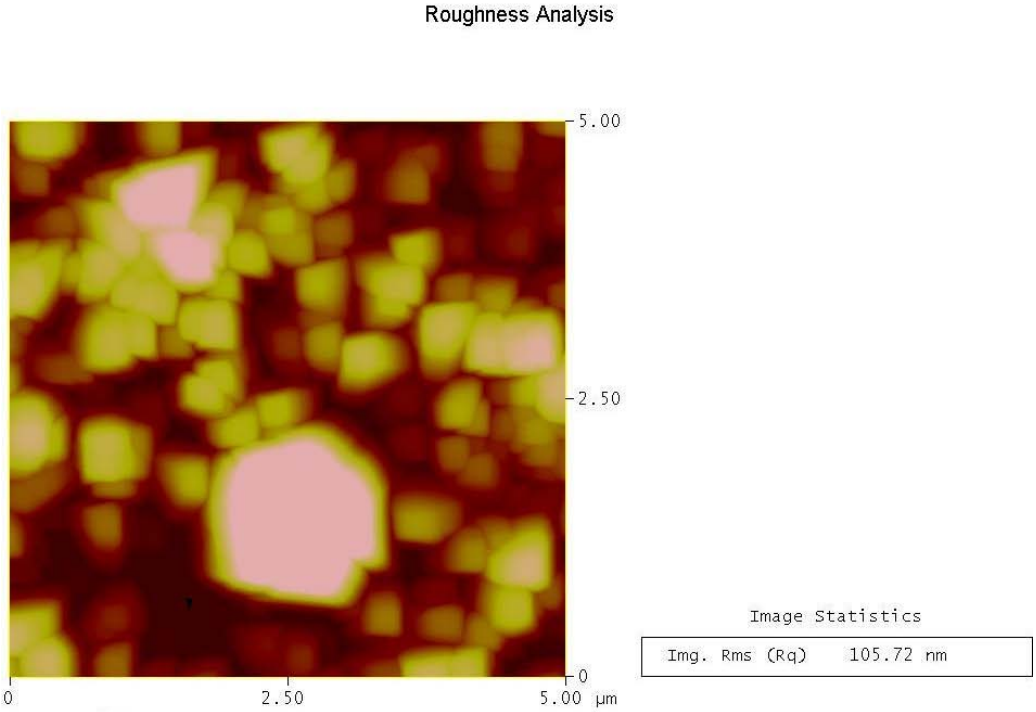

Figure 7.82: A 5x5µm^2 AFM image for YBCO film deposited on MgO film spray pyrolysed on Hastelloy C276 using 0.78M of $Mg(NO_3)_2.6H_2O$ at 650°C for 48 minutes.

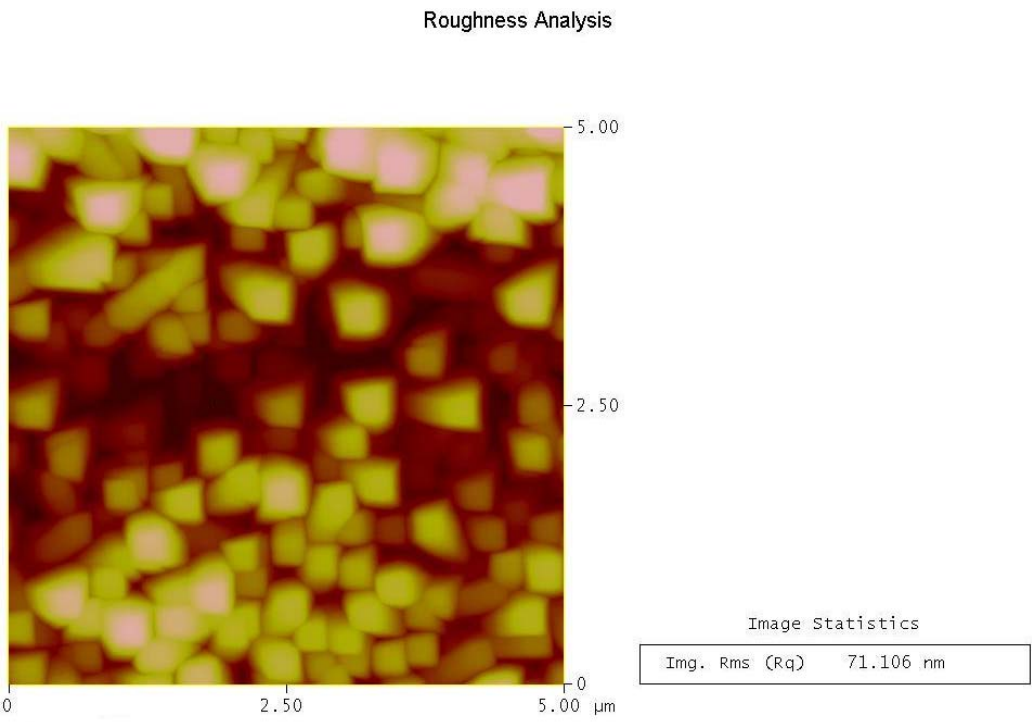

Figure 7.83: A 5x5µm^2 AFM image for YBCO film deposited on MgO film spray pyrolysed on Hastelloy C276 using 0.468M of $Mg(NO_3)_2.6H_2O$ at 700°C for 48 minutes.

From the above, it was clear that the MgO films with RMS roughness greater than 20 nm resulted in polycrystalline YBCO films (Figure 7.29 and Figure 7.75). Only the smoothest MgO films (Figure 7.29), i.e. the ones deposited at 650°C using 0.468M for 32 and 48 minutes, showed a well textured YBCO films (Figure 7.84), although, a weak 103 peak was obtained which was believed to be due to nucleation problems during the PLD deposition of YBCO. Such a peak was even seen for YBCO films deposited on MgO single crystals (Figure 4.57). This demonstrates the critical role of the surface smoothness of MgO films, deposited by spray pyrolysis from the nitrate precursors, on the subsequent growth of YBCO films. The SEM images for YBCO films show that the films were more continuous (Figure 7.85 and Figure 7.86) and smoother (Figure 7.87 and Figure 7.88) compared to YBCO films deposited on MgO films deposited by spray pyrolysis under different conditions (Figure 7.76-Figure 7.83). The film deposited at 650°C from 0.468M solution for 48 minutes was found to be a little smoother (RMS of about 30 nm, Figure 7.88) compared to the film deposited for 32 minutes (RMS of about 40 nm, Figure 7.87). However, pores were formed on both films. Such porous films were noticed by others where it was attributed to the formation of Y_2O_3 or BaY_2O_4 [208, 209, 212]. The MgO (200) peaks detected for the films deposited from 0.468M solution at 650°C for 32 and 48 minutes had low intensity (Figure 7.22) which indicates from one hand a weak out-of-plane and in-plane texture as was shown qualitatively by the X-ray pole figure in Figure 7.34 for the sample with 48 minutes of deposition. On the other hand, the YBCO film deposited on the spray pyrolysed MgO for 48 minutes had a better out-of-plane texture but a weak in-plane texture (Figure 7.89) and was confirmed by the EBSD pole figure pattern in Figure 7.90. This implied that the texture of the underlying MgO layer was copied by the growing YBCO film.

AC susceptibility at zero field showed a broad superconducting transition temperature, for the films deposited from 0.468M at 650°C for 32 and 48 minutes, with a T_c onset of about 84.5K (Figure 7.91). From the AC curves it can be seen that the YBCO film deposited on the MgO film deposited by spray pyrolysis for 48 minutes show a slightly better transition which can be attributed to the continuous and smoother YBCO film deposited on that MgO film compared to YBCO film deposited on the MgO film deposited by spray pyrolysis for 32 minutes. YBCO films shown in Figure 7.75 had no T_c.

The effect of inclination angle, flow rate, annealing under O_2, vacuum or Ar atmospheres resulted either in rough surfaces or in decreasing the intensity of MgO (200) peak. YBCO films deposited on such samples were polycrystalline with no T_c. Polycrystalline YBCO films were also deposited on bare Hastelloy substrates and showed no T_c.

It is to be noted in this work that inclining the substrate led to untilted MgO films with (200) direction parallel to the substrate normal and did not result in the shadowing effect which was observed for MgO and YSZ films deposited by ISD method using PLD and e-beam evaporation [39-41, 49, 50, 53, 167, 169, 173-175, 177-183]. In this work, spray pyrolysis gave MgO (200) peaks parallel to the substrate normal whether ISD was utilised or not. It was found by researchers that YBCO deposition on c-axis tilted MgO resulted in c-axis tilted YBCO films. The tilt was found to affect the superconducting properties, i.e. J_c and T_c [169, 176, 177]. In this work YBCO films grown on top of MgO deposited by spray pyrolysis have the (006) of YBCO // (200) of MgO. Thus, spray pyrolysis offers an alternative method of depositing a single MgO buffer layer with no tilting for YBCO deposition.

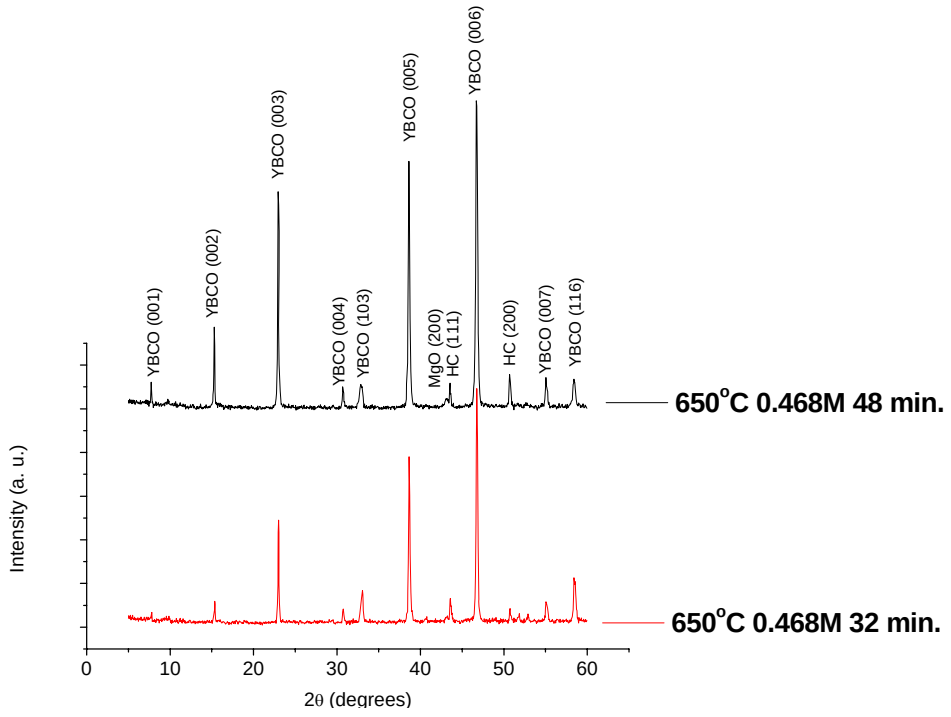

Figure 7.84: XRD patterns for YBCO films deposited by PLD on the MgO films deposited by spray pyrolysis at 650°C from 0.468M solution for different deposition times.

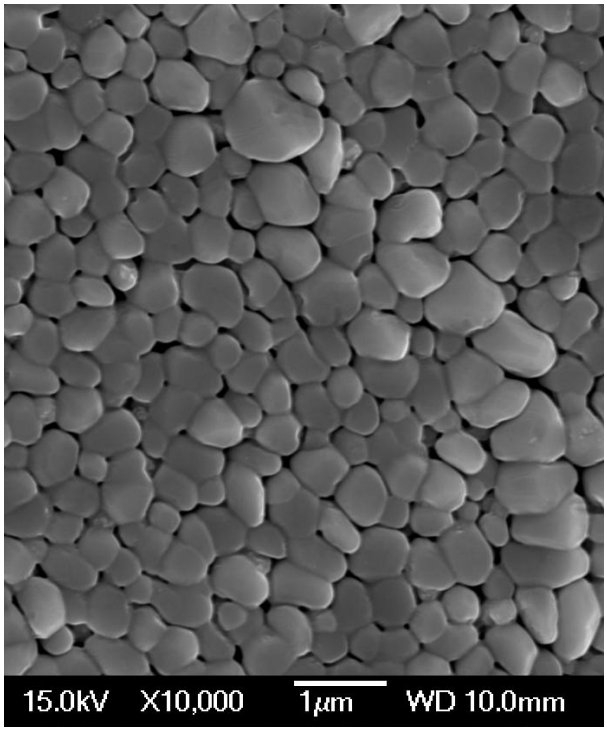

Figure 7.85: SEM image for YBCO film deposited on MgO film spray pyrolysed on Hastelloy C276 using 0.468M of $Mg(NO_3)_2.6H_2O$ at 650°C for 32 minutes.

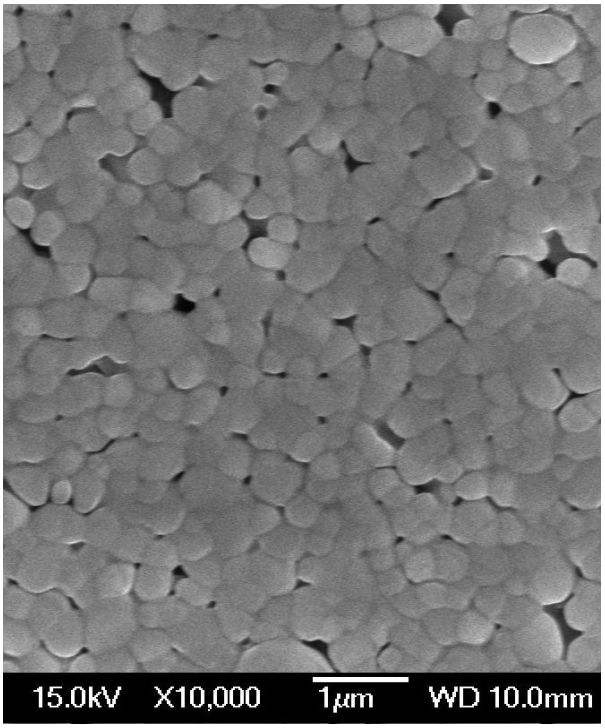

Figure 7.86: SEM image for YBCO film deposited on MgO film spray pyrolysed on Hastelloy C276 using 0.468M of $Mg(NO_3)_2.6H_2O$ at 650°C for 48 minutes.

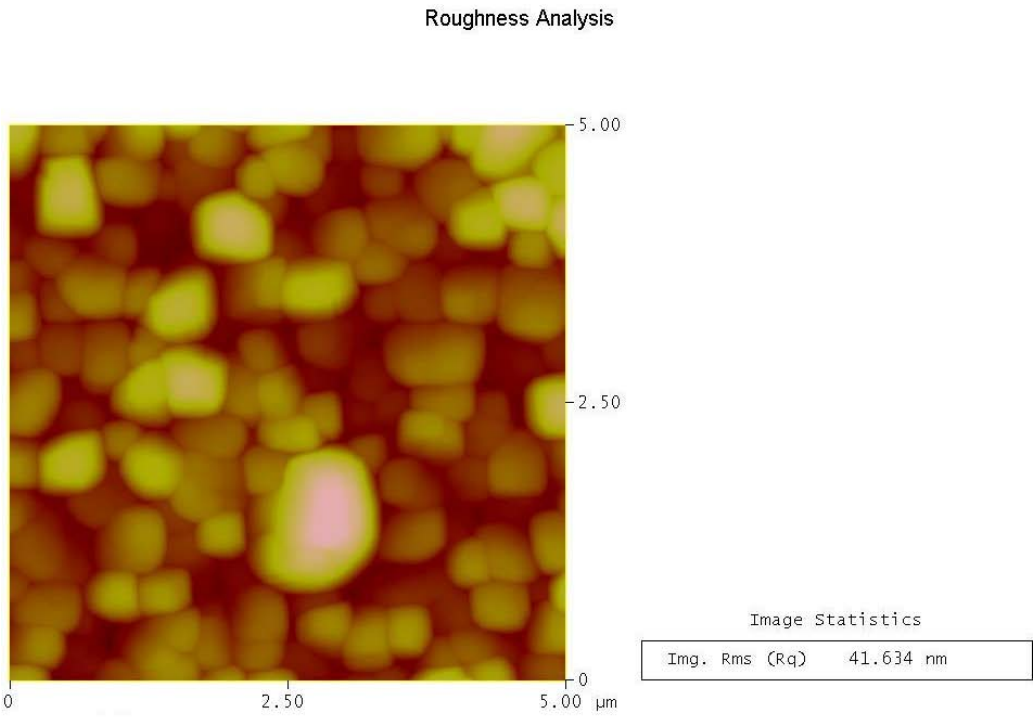

Figure 7.87: A 5x5µm^2 AFM image for YBCO film deposited on MgO film spray pyrolysed on Hastelloy C276 using 0.468M of $Mg(NO_3)_2.6H_2O$ at 650°C for 32 minutes.

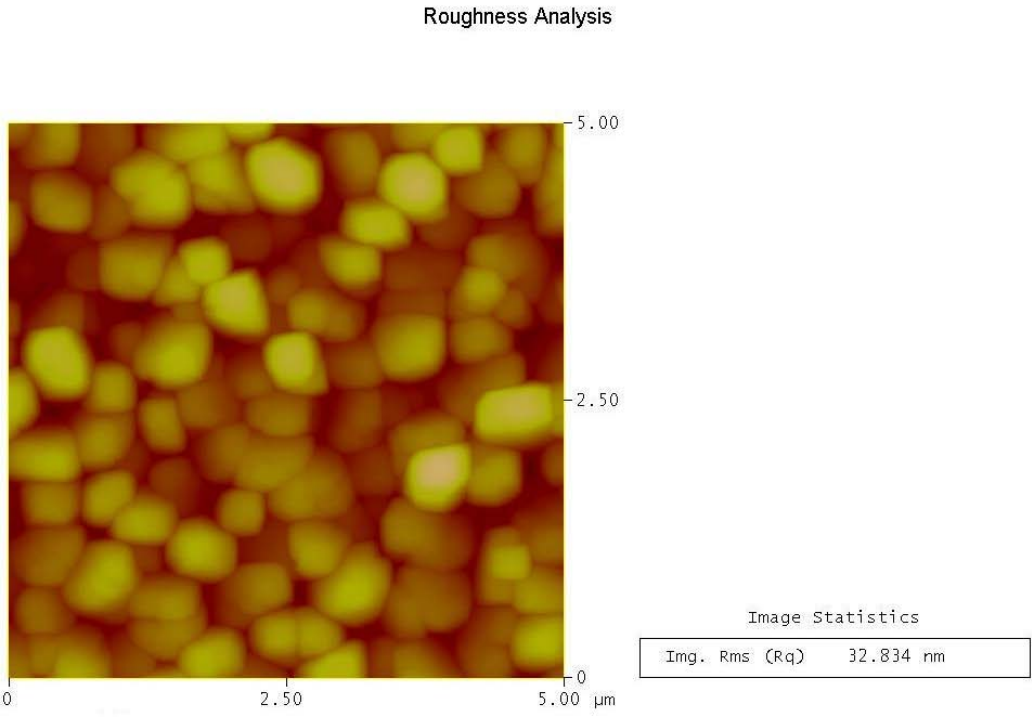

Figure 7.88: A 5x5µm^2 AFM image for YBCO film deposited on MgO film spray pyrolysed on Hastelloy C276 using 0.468M of $Mg(NO_3)_2.6H_2O$ at 650°C for 48 minutes.

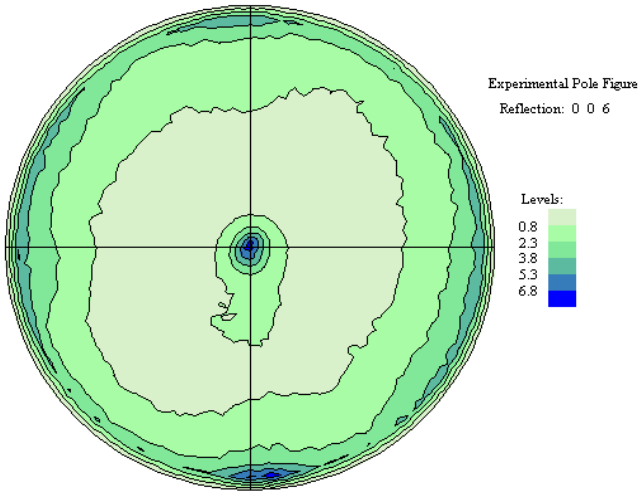

Figure 7.89: : (001) X-ray pole figure showing YBCO {006} planes, at 2θ of 46.65°, for YBCO film deposited by PLD on Hastelloy substrate buffered with MgO deposited by spray pyrolysis at 650^{o}C from the nitrate precursor using 0.468M concentration for 48 minutes.

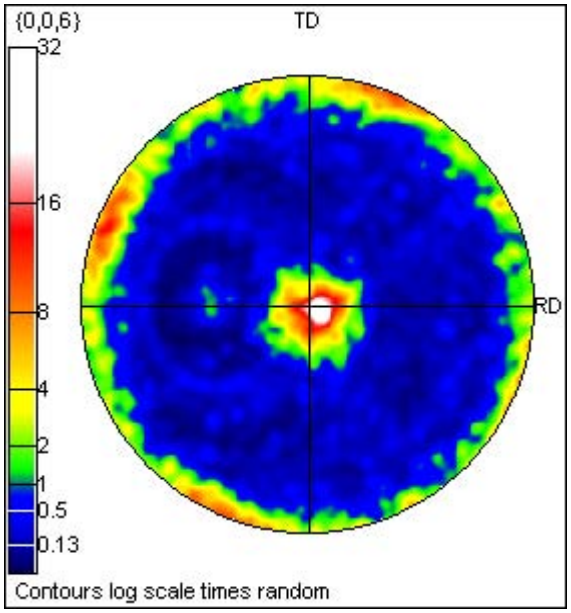

Figure 7.90: EBSD pattern showing the {006} planes for YBCO film deposited by PLD on Hastelloy substrate buffered with MgO deposited by spray pyrolysis at 650^{o}C from the nitrate precursor using 0.468M concentration for 48 minutes.

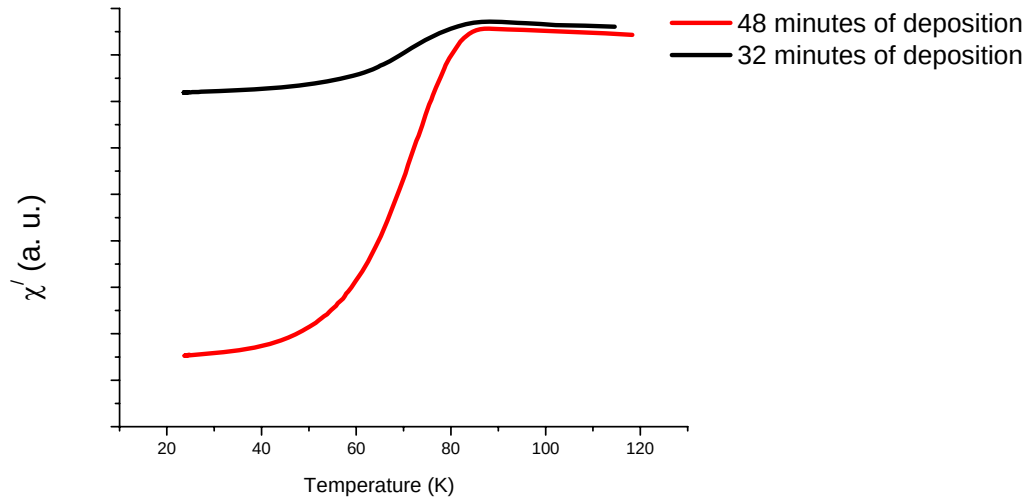

Figure 7.91: AC susceptibility measurement for YBCO deposited at 780°C on the MgO buffer layer deposited by spray pyrolysis at 650°C at different times using 0.468M $Mg(NO_3)_2.6H_2O$.

7.12.3 Pulsed laser deposition of MgO on bare Hastelloy substrates

It was found (section 7.12.2) that YBCO deposition on MgO films deposited by spray pyrolysis resulted in YBCO films having very weak in-plane texture and broad superconducting transition temperatures. In an attempt to establish a good in-plane texture, MgO was deposited by PLD on bare Hastelloy C276 (i.e. polished and cleaned but with no buffer layers) under the same deposition conditions for MgO on Si (100) (section 4.4).

Figure 7.92 shows the XRD patterns for MgO deposited on bare Hastelloy C276 by PLD using an energy fluence of 3-3.2J/cm^2. As was mentioned in section 4.4, we could not get energy fluence more than 3.45J/cm^2 and some times not more than 3.2J/cm^2 depending on how newly the laser was refilled. Therefore, this low energy was not enough for obtaining textured MgO peaks. The EDX tests show the presence of Mg, therefore, this suggests the presence of amorphous MgO film. Because of this, PLD deposition of MgO will not be utilised any more in this work.

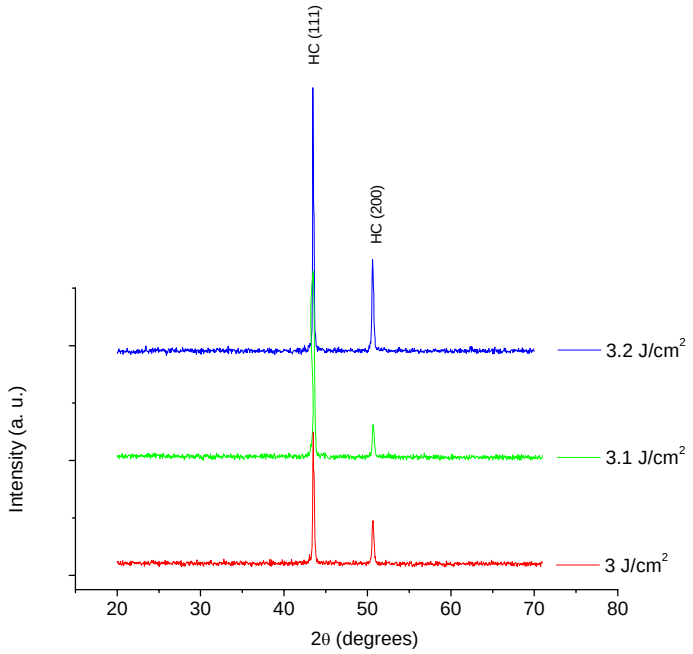

Figure 7.92: XRD patterns for MgO deposited by PLD on bare Hastelloy C276 under different energy fluencies.

7.12.4 Pulsed laser deposition of ceria (CeO_2) and YBCO on MgO deposited by spray pyrolysis

It was found (section 7.12.2) that YBCO deposition on MgO films deposited by spray pyrolysis resulted in YBCO films having very weak in-plane texture and broad superconducting transition temperatures. In an attempt to establish a good in-plane texture, researchers found that the deposition of CeO_2, on top of MgO deposited by the ISD approach using e-beam evaporation, will lead to a well defined and good in-plane textured YBCO films [39, 41, 50, 95, 169, 176, 177, 182, 183]. They deposited CeO_2 at different conditions. The deposition temperature ranged from 700°C-800°C using an energy fluence of 1.5-2 J/cm^2 and under O_2 pressure ranging from 2x10^{-4}-0.6 mbar (0.15-450 mtorr) or under reducing conditions in the case of using Ni or NiW RABiTS substrates [39, 95, 169, 177, 182, 259-261, 279, 280]. It was found that the CeO_2 deposition conditions and film thickness affects the structure and properties of YBCO films and that more work is still needed to better understand the mechanisms of the dependences of YBCO film properties on CeO_2 thicknesses [169]. Some researchers found that the optimum CeO_2 thickness for YBCO deposition is 10-40 nm [95, 169, 250, 258] while others found it to be in the range of 100 nm-150 nm [258, 259]. For this reason, CeO_2 was deposited by PLD on top of MgO films

deposited by spray pyrolysis followed by YBCO deposition by PLD as well in an attempt to improve the texture and superconducting properties of YBCO.

CeO_2 has a cubic (fluorite, CaF_2) structure with a lattice constant at room temperature of 5.411Å with a cation coordination number of 8. In CaF_2 calcium ions are positioned at the centers of cubes, with fluorine ions at the corners. One unit cell consists of eight cubes, as indicated in Figure 7.93. CeO_2 is very stable even at very high temperature. The large lattice mismatch between CeO_2 and YBCO is reduced by rotation of 45° in the CeO_2 a-b lattice plane (in-plane). This way, the lattice mismatch will be 0.16% and 1.7% along the a and b axis of YBCO, respectively. Besides that, it is important to have (100) oriented CeO_2 in order to grow c-axis oriented, epitaxial YBCO films [70, 169, 184, 279, 281].

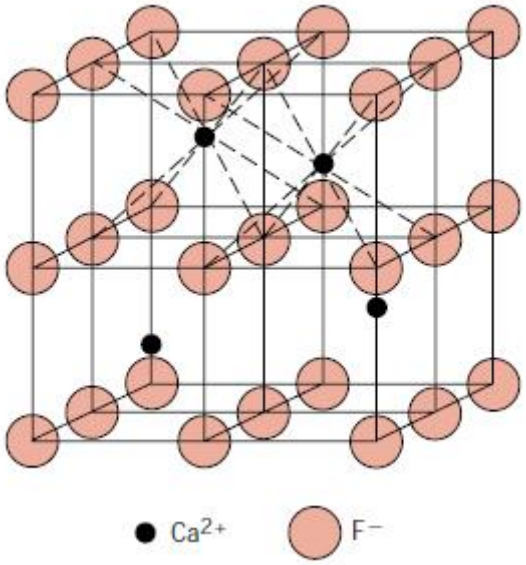

Figure 7.93: A unit cell for the fluorite crystal structure [70].

In this work CeO_2 was deposited at two different conditions. The used energy fluence was 2 J/cm^2, the distance between the target and the substrate was fixed at 56 mm, 500 and 1000 pulses were applied as it was found by researchers that cracks will form in 100-200nm thick CeO_2 films [282-284]. The first deposition was made at 780°C using 0.6 mbar O_2 and the second one was made at 710°C using $2x10^{-4}$ mbar O_2. The YBCO deposition conditions were the same as those mentioned in section 7.12.1. The depositions were made on the MgO films deposited by spray pyrolysis from 0.468M solution at 650°C for 48 minutes.

The samples deposited with 500 pulses of CeO_2 show very weak CeO_2 peaks. Therefore, the deposition proceeded from now on with only 1000 pulses. Figure 7.94

shows the XRD patterns for CeO_2 films deposited on top of MgO films deposited by spray pyrolysis. The CeO_2 peaks were indexed according to the JCPDS PDF file 00-004-0593 where the (111), (200), (220), and the (311) peaks occur at 2θs of 28.55°, 33.07°, 47.49°, and 56.32°, respectively. It can be seen that none of the CeO_2 deposition conditions resulted in a perfectly (200) oriented films. However, the deposition at 780°C using 0.6 mbar O_2 resulted in a stronger CeO_2 (200) peak compared to the film deposited at 710°C using $2x10^{-4}$ mbar O_2. The surface roughness was increased after the CeO_2 deposition as was clear from the SEM and AFM images (Figure 7.95-Figure 7.98) compared to that before the deposition (Figure 7.24 and Figure 7.29). The EDX test suggested that the formed particles were composed of Mg and O with a ratio of Mg:O of 1:1.50.

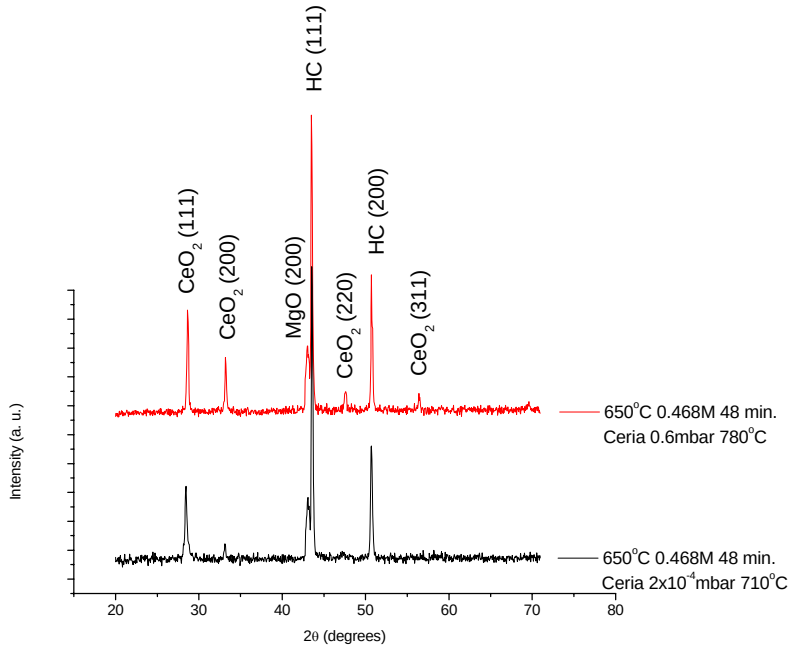

Figure 7.94: XRD patterns for CeO_2 films deposited by PLD at different conditions on the MgO films spray pyrolysed at 650°C from 0.468M for 48 minutes**.**

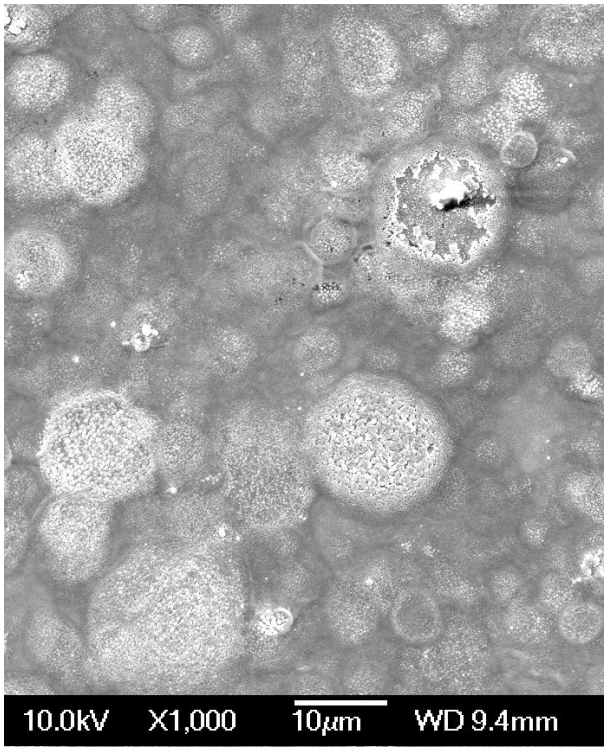

Figure 7.95: SEM image for CeO_2 film deposited by PLD at 710°C using $2x10^{-4}$ mbar O_2 on the MgO film deposited by spray pyrolysis at 650°C from 0.468M for 48 minutes**.**

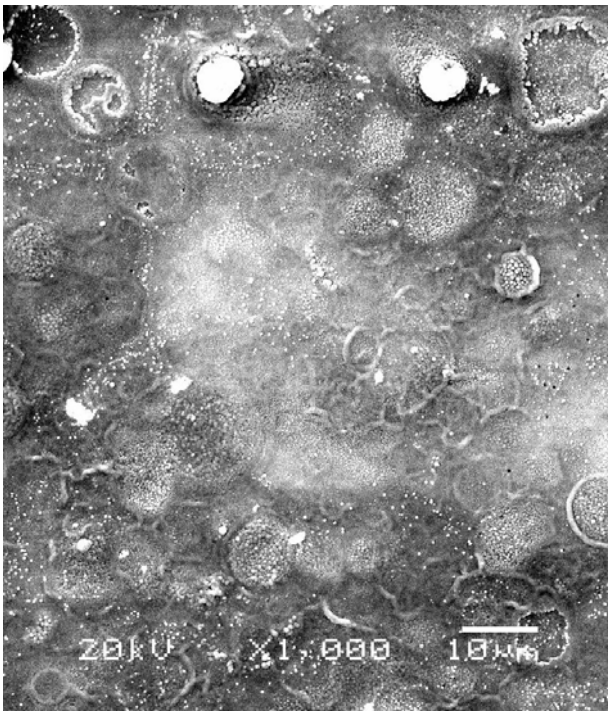

Figure 7.96: SEM image for CeO_2 film deposited by PLD at 780°C using 0.6 mbar O_2 on the MgO film deposited by spray pyrolysis at 650°C from 0.468M for 48 minutes**.**

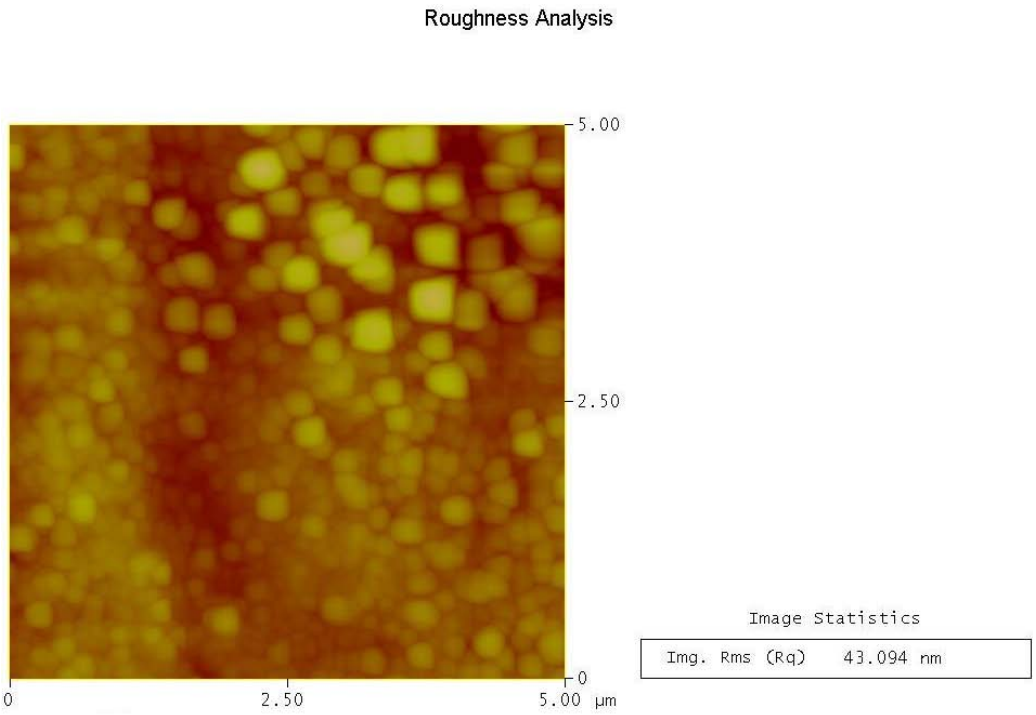

Figure 7.97: A 5x5µm^2 AFM image for CeO_2 film deposited by PLD at 710°C using 2x10^{-4} mbar O_2 on the MgO film spray pyrolysed at 650°C from 0.468M for 48 minutes**.**

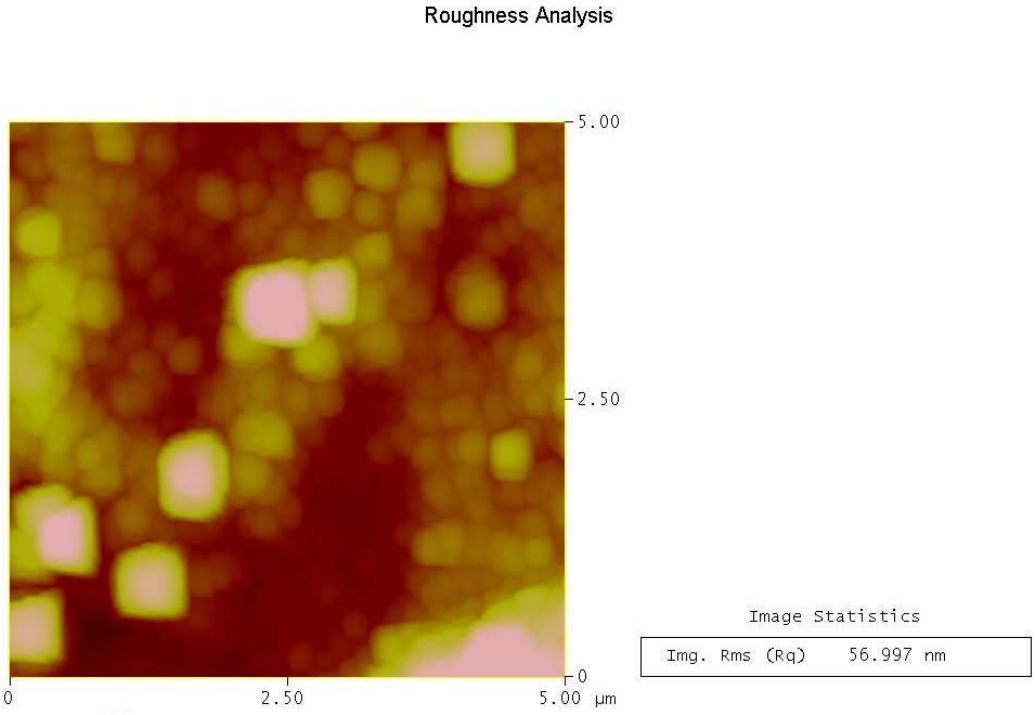

Figure 7.98: A 5x5µm^2 AFM image for CeO_2 film deposited by PLD at 780°C using 0.6 mbar O_2 on the MgO film spray pyrolysed at 650°C from 0.468M for 48 minutes**.**

To see the influence of the deposited CeO_2 film (even the surface was quite rough) on the properties of the superconducting layer, YBCO was deposited on each

of the samples shown in Figure 7.94. Figure 7.99 shows the XRD patterns for YBCO films deposited on CeO_2. It is clear that the YBCO film had a stronger (006) peak on the CeO_2 film deposited at 780°C using 0.6 mbar O_2. However, the YBCO films were rougher as can be seen from the SEM images (Figure 7.100 and Figure 7.101) and AFM images (Figure 7.102 and Figure 7.103), respectively, compared to the YBCO film deposited directly on the MgO film deposited by spray pyrolysis (Figure 7.86 and Figure 7.88). CeO_2 film deposited at 780°C using 0.6 mbar resulted in smoother YBCO film when compared to the CeO_2 film deposited at 710°C using $2x10^{-4}$ mbar. This can be attributed to the stronger CeO_2 (200) peak deposited at 780°C using 0.6 mbar which gave a stronger YBCO (006) peak and hence smoother film. The cross sectional SEM image in Figure 7.104 show that YBCO, CeO_2 and MgO films had thicknesses of about 1.384μm, 99nm and 342nm respectively. This means that the deposition rate of YBCO was 13840 Å /5000 pulses = 2.7Å/pulse, and for CeO_2 990Å/1000 pulses = 0.99Å/pulse and for MgO 3420 Å / (360sec) = 9.5Å/sec.

The pole figure in Figure 7.105 shows that YBCO has a good weak out-of-plane texture but still no in-plane texture (no definite poles were obtained at the circumference but a ring was obtained instead). This means that CeO_2 deposition on the MgO films deposited by spray pyrolysis had no effect in improving the in-plane texture of the subsequent YBCO layer which disagrees with what was found by other researchers [39, 41, 50, 95, 169, 176, 177, 182, 183]. In addition to that, both samples shown in Figure 7.99 had no T_c.

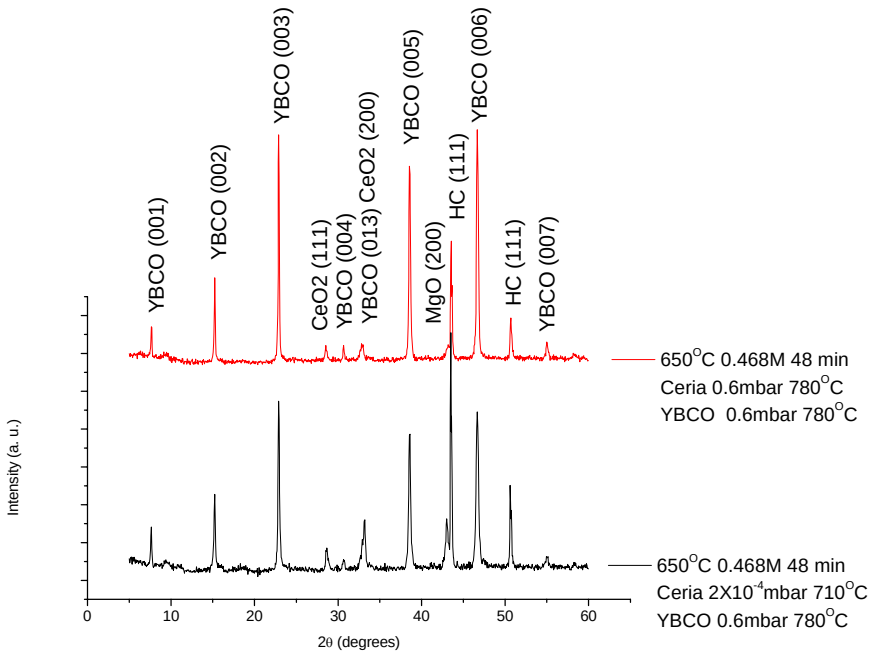

Figure 7.99: XRD patterns for YBCO and CeO_2 films deposited by PLD at different conditions on the MgO films spray pyrolysed at 650°C from 0.468M for 48 minutes**.**

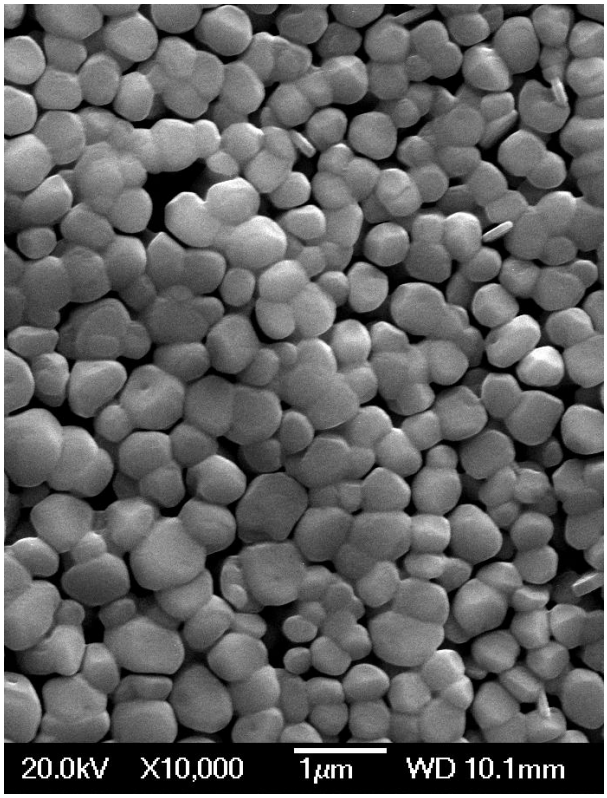

Figure 7.100: SEM image for YBCO on CeO_2 film deposited by PLD at 710°C using $2x10^{-4}$ mbar O_2 on the MgO film spray pyrolysed at 650°C from 0.468M for 48 minutes**.**

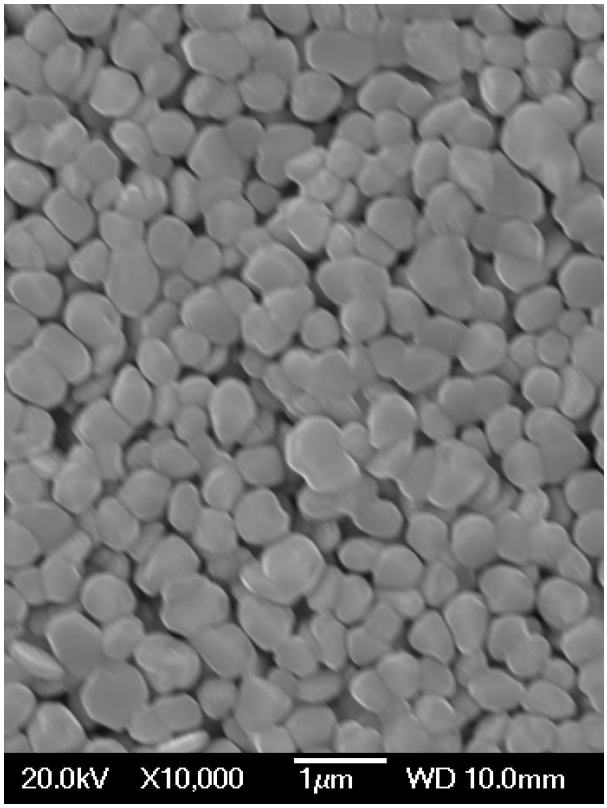

Figure 7.101: SEM image for YBCO on CeO_2 film deposited by PLD at 780°C using 0.6 mbar O_2 on the MgO film spray pyrolysed at 650°C from 0.468M for 48 minutes.

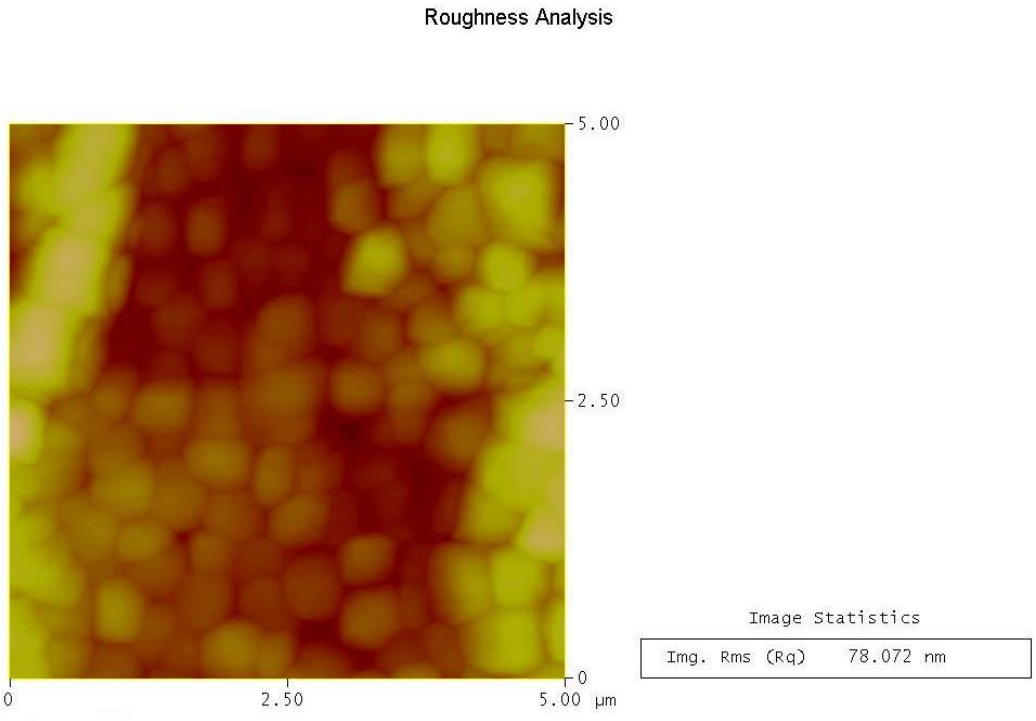

Figure 7.102: A 5x5μm^2 AFM image for YBCO on CeO_2 film deposited by PLD at 710°C using $2x10^{-4}$ mbar O_2 on the MgO film spray pyrolysed at 650°C from 0.468M for 48 minutes**.**

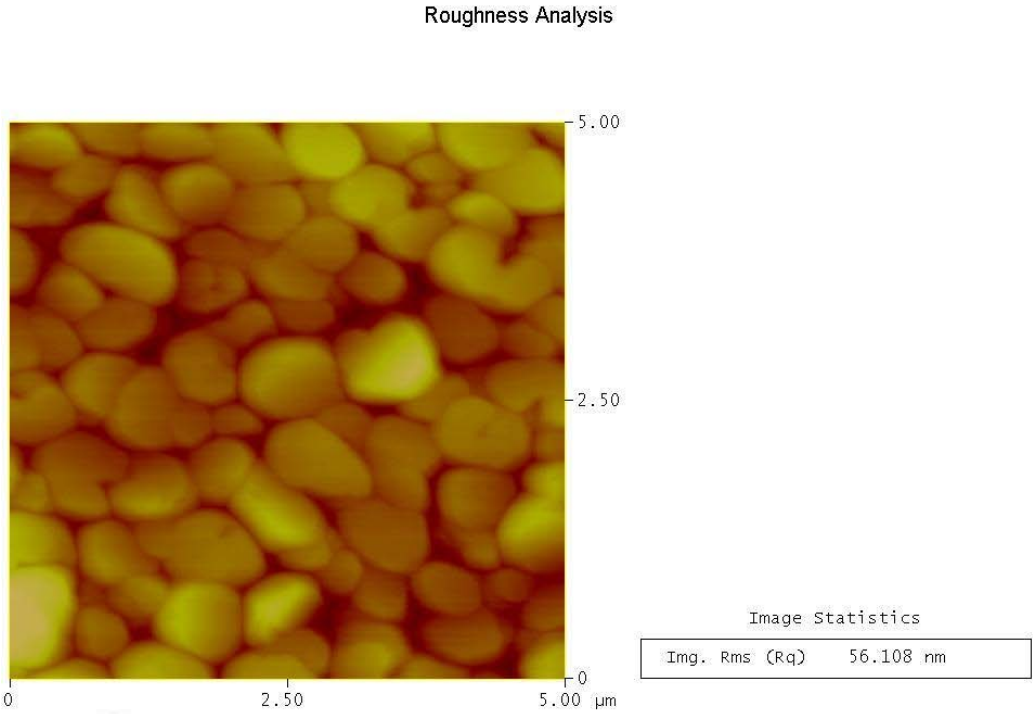

Figure 7.103: A 5x5µm^2 AFM image for YBCO on CeO_2 film deposited by PLD at 780°C using 0.6 mbar O_2 on the MgO film spray pyrolysed at 650°C from 0.468M for 48 minutes.

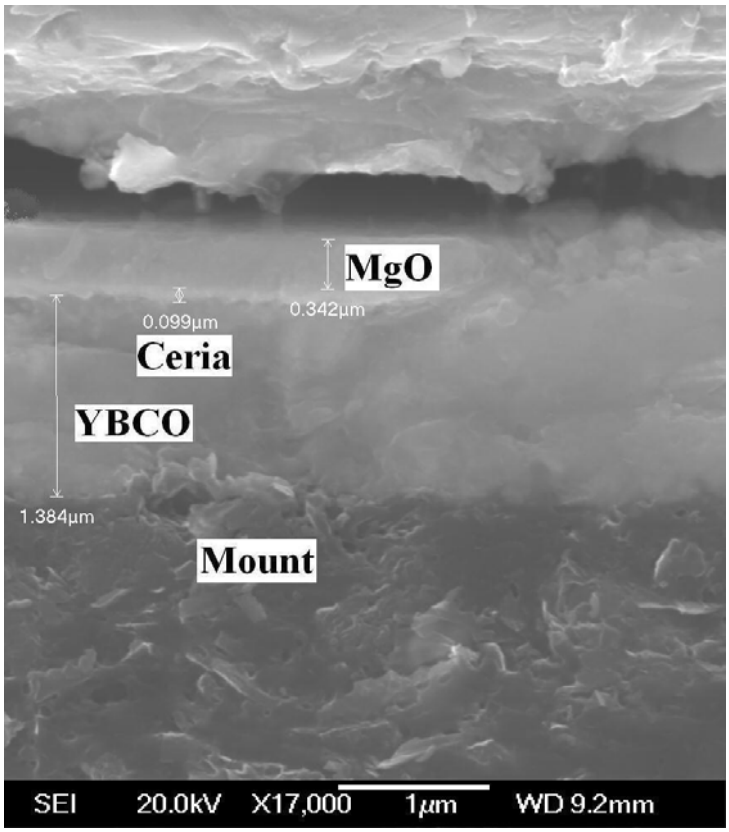

Figure 7.104: Cross sectional SEM image for YBCO on CeO_2 film deposited by PLD at 780°C using 0.6 mbar O_2 on the MgO film spray pyrolysed at 650°C from 0.468M for 48 minutes.

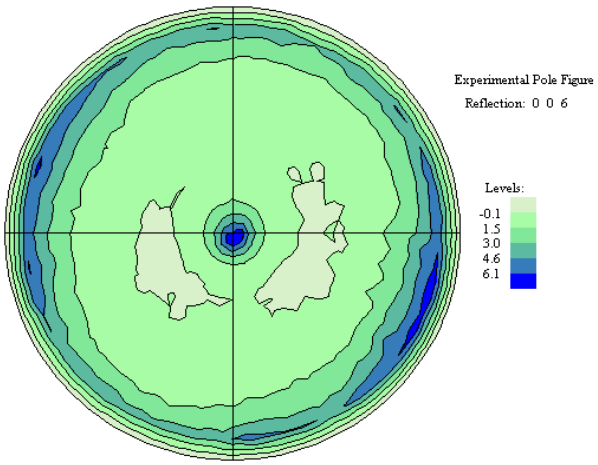

Figure 7.105: (001) X-ray pole figure showing the YBCO {006} planes, at 2θ of 46.65°, for YBCO deposited on CeO_2 film which was deposited by PLD at 780°C using 0.6 mbar O_2 on the MgO film deposited by spray pyrolysis at 650°C from 0.468M for 48 minutes.

8 Spray pyrolysis of MgO on Hastelloy C276 from acetate precursor

8.1 Introduction

As was the case for MgO deposition using the nitrate precursor, the deposition of MgO thin films from acetate precursor by spray pyrolysis was done on wrought polycrystalline Hastelloy C276. The sample dimensions and sample preparation for the deposition were the same as mentioned in section 7.2.2. Before the deposition the substrates were cleaned in acetone, then ethanol for 10 minutes each in an ultrasonic bath, then dried with Ar gas. In the spray pyrolysis deposition, a pulse time to interval time of 1:7 was applied; however, the effect of deposition temperature, precursor concentration, deposition time, the deposition inclination angle, Ar flow rate, and the effect of different annealing treatment on the properties of MgO films were all investigated. Finally, YBCO and CeO_2 were deposited by PLD to evaluate the performance of the MgO films deposited by spray pyrolysis on Hastelloy C276.

As far as we know, and as was the case for MgO deposition from nitrate precursor, no reports have been found for MgO deposition on metallic substrates by spray pyrolysis using acetate precursor. The aim (as mentioned for 310-austenitic stainless steel) is to reduce the cost of production by using spray pyrolysis instead of the relatively expensive methods for the buffer layer deposition, such as electron beam evaporation [82] and pulse laser deposition [80]. As in the previous chapters a further objective of this work is to grow MgO as the only buffer layer before YBCO deposition in an attempt to make the process a cost-effective one by reducing the usual multi-layer buffer architecture to a single layer.

It is to be mentioned that X-ray scans for the MgO films deposited by spray pyrolysis on Hastelloy C276 detected only MgO (200) peaks from the MgO film. Therefore, we could not quantify the level of texture as no other peaks were detected to reference to. Accordingly, it was assumed that an increase in the intensity of MgO (200) peak reflects an improvement in texture.

8.2 MgO deposition on Hastelloy C276 from acetate precursor

Before depositing MgO by spray pyrolysis, a thermogravimetrical analysis (TGA) of the decomposition of the acetate precursor was used as a guideline temperature for the thin film deposition.

8.2.1 Thermal decomposition of the acetate precursor

A sample of magnesium acetate, $Mg(CH_3COO)_2.4H_2O$, with a mass of 7 mg was placed in an alumina crucible. The thermogravimetric (TGA) analysis was performed in a flow of Argon from 25°C to 750°C. The TGA measurement was performed at a constant heating rate of 10°C/min. Figure 8.1 shows the TGA curve for the tested $Mg(CH_3COO)_2.4H_2O$ sample.

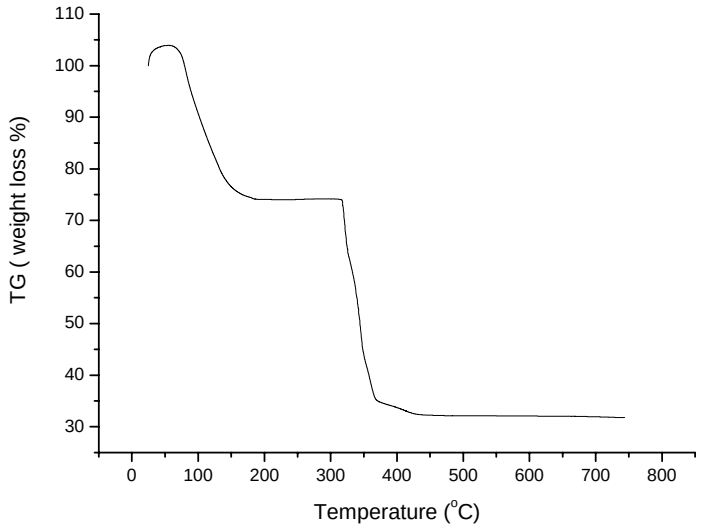

Figure 8.1: TG curve for $Mg(CH_3COO)_2.4H_2O$**.**

The decomposition of magnesium acetate takes place in three steps according to the following equations [285]:

$$Mg(CH_3COO)_2.4H_2O \rightarrow Mg(CH_3COO)_2 + 4H_2O \quad \textbf{(Eq. 8.1)}$$

$$Mg(CH_3COO)_2 \rightarrow MgCO_3 + (CH_3)_2.CO \text{ (acetone) (g)} \quad \textbf{(Eq. 8.2)}$$

$$MgCO_3 \rightarrow MgO + CO_2 \text{ (g)} \quad \textbf{(Eq. 8.3)}$$

Dehydration occurs in the first step. The decomposition of the acetates proceeds in the next two steps, by the release of acetone and CO_2 to yield MgO. It can be seen from Figure 8.1 that the decomposition finished at about 400°C and beyond about 450°C no weight loss takes place, suggesting the formation of stoichiometric MgO. Similar results were obtained by A. Moses et al and McAdie et al [285, 286]. Therefore, the deposition of MgO was done at temperatures higher than 450°C.

8.3 Effect of deposition temperature on MgO film properties

Magnesium acetate [$Mg(CH_3COO)_2.4H_2O$] as a precursor was used to deposit MgO by spray pyrolysis on Hastelloy C276 substrates. The deposition was done using 0.093M solution at different temperature for 32 minutes and using an Ar flow rate of 10 l/min. The XRD patterns after the deposition are shown in Figure 8.2 where MgO (200) oriented XRD peaks were detected using a much lower concentration compared to the nitrate precursor (Figure 7.22). The MgO peaks were indexed according to the JCPDS PDF files 00-045-0946 where MgO (200) is at 2θ of 42.9°. As was the case with the nitrate precursor, the MgO (200) peak, the only detected one, was normal to the substrate surface. The thermal expansion coefficients of Hastelloy C276 and MgO are 10.8-11.3x10^{-6} /°C and 13.8 x 10^{-6}/°C, respectively [143, 267]. The lattice parameter for MgO is 4.2112Å and for Hastelloy C276, as calculated from Bragg's law, is 3.5952Å and this gives a lattice mismatch of 17.1%. This explains the shift of MgO peaks to 43.12°, however, this shift is not much compared to that obtained when depositing MgO on Si single crystals. No MgO peaks were detected at 500°C, although the EDX results (Figure 8.3 and Table 8.1) showed the presence of Mg, therefore, the deposited MgO film was suggested to be amorphous. Figure 8.4 is the SEM image for the sample deposited at 500°C. The intensity of the MgO (200) was enhanced by increasing the temperature from 550°C to 600°C and to 650°C; however, that was at the expense of the surface roughness as shown from the SEM images in Figure 8.5-Figure 8.7 and Figure 8.8. Figure 8.9 is an AFM image for the MgO film deposited at 550°C. The SEM images in Figure 8.4-Figure 8.6 show microstructures which are very similar to the one obtained during MgO deposition on Si single crystal from 0.078M solution at 650°C (Figure 4.5). This confirms that the microstructure of the deposited MgO films depends on the substrate used; similar microstructures were obtained on different substrates but by using different deposition temperatures and different precursor. An AFM section profile image is shown in Figure 8.10 for MgO film deposited from 0.093M solution at 550°C for 32 minutes. When comparing Figure 8.5 and Figure 8.9 to Figure 8.10, it can be seen that the surface was homogenous and smooth and most of the film was located on the same layer as can be seen from Figure 8.10. The same was also observed for the film deposited from 0.093M solution at 500°C and 600°C. However, The MgO film deposited at 650°C showed particles or grains which were located on different layers relative to the rest of

the film. According to the deposition modes of spray pyrolysis [83], the smooth surfaces for the films deposited at 500°C, 550°C and 600°C (Figure 8.4-Figure 8.6) were consistent with the third mode of deposition; when thermal decomposition of dry precipitates starts on their way to the substrate. However, at 500°C, the temperature was not high enough to form textured MgO films. The film deposited at 650°C (Figure 8.7) which showed higher roughness due to the formation of particles on the surface was deposited according to the fourth mode of deposition; where the full thermal decomposition takes place before reaching the substrate and only finely divided solid products arrive at the substrate surface.

The EDX results for the films deposited at 550°C-650°C suggest that the deposited MgO was almost stoichiometric with a ratio of Mg:O very close to 1:1 as can be seen from Figure 8.11 and Table 8.2 for the MgO film deposited at 600°C from 0.093M solution for 32 minutes.

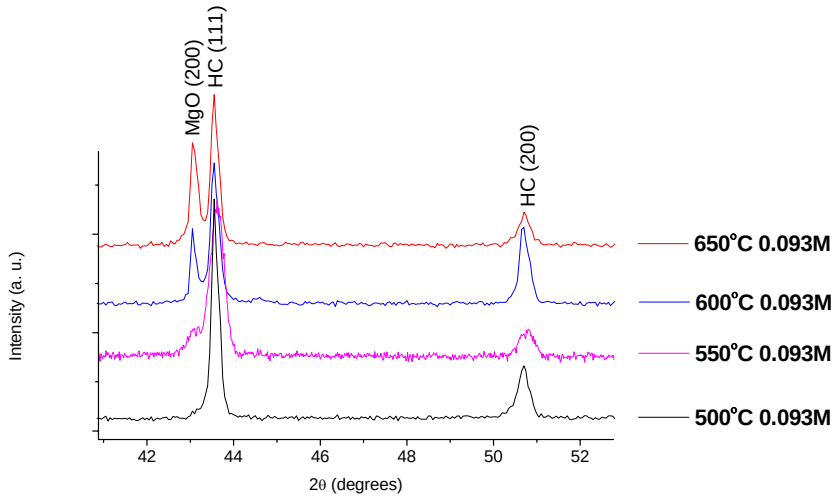

Figure 8.2: XRD patterns for MgO deposition on Hastelloy C276 using 0.093M of $Mg(CH3COO)_2.4H_2O$ at different temperatures for 32 minutes.

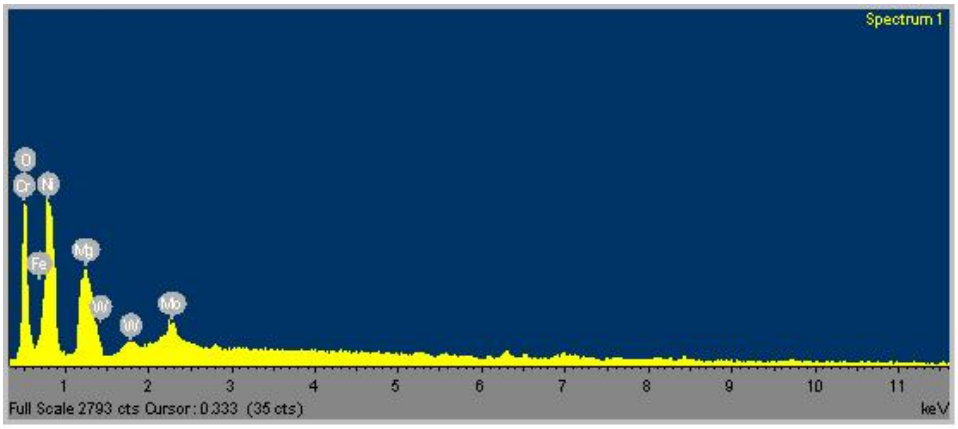

Figure 8.3: EDX spectrum, using an accelerating voltage of 4KV, for MgO with 0.093M at 500°C with a deposition time of 32 minutes.

Table 8.1: Summary of the EDX chemical composition results, using an accelerating voltage of 4KV, for MgO with 0.093M at 500°C with a deposition time of 32 minutes.

Element	at %
O K	30.42
Mg K	18.97
Cr L	10.00
Fe L	3.66
Ni L	30.84
W M	0.77
Mo L	5.34

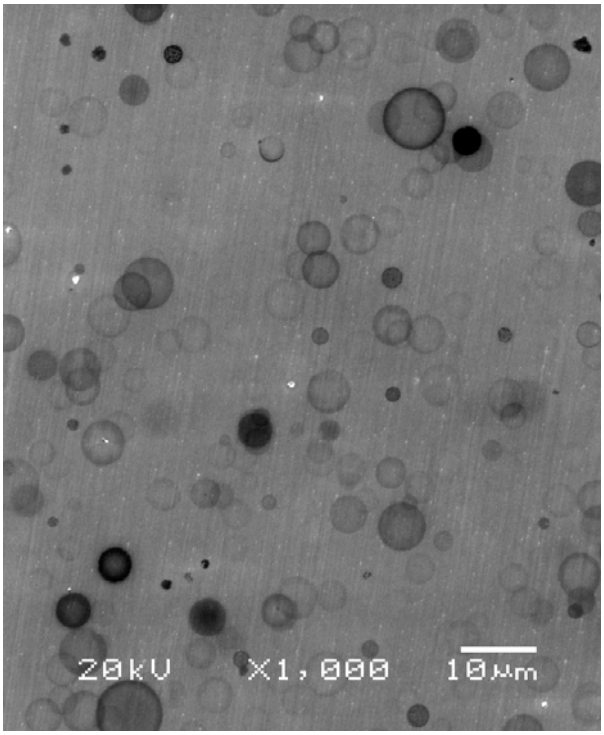

Figure 8.4: SEM image for the MgO film deposited on Hastelloy C276 using 0.093M of $Mg(CH3COO)_2.4H_2O$ at 500°C for 32 minutes.

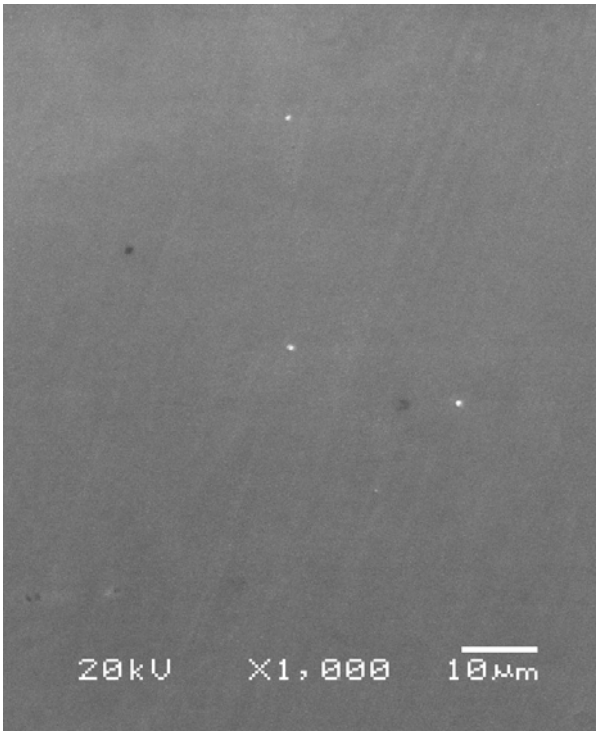

Figure 8.5: SEM image for the MgO film deposited on Hastelloy C276 using 0.093M of $Mg(CH3COO)_2.4H_2O$ at 550°C for 32 minutes.

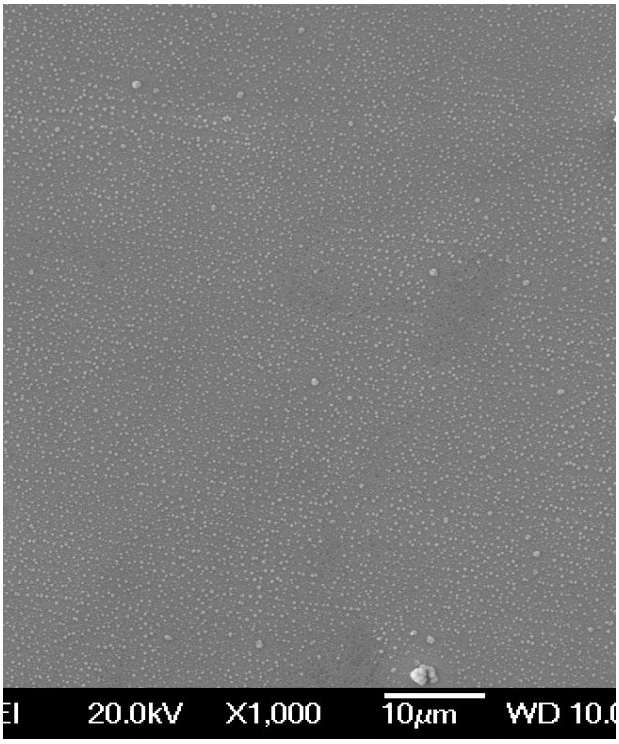

Figure 8.6: SEM image for the MgO film deposited on Hastelloy C276 using 0.093M of $Mg(CH3COO)_2.4H_2O$ at 600°C for 32 minutes.

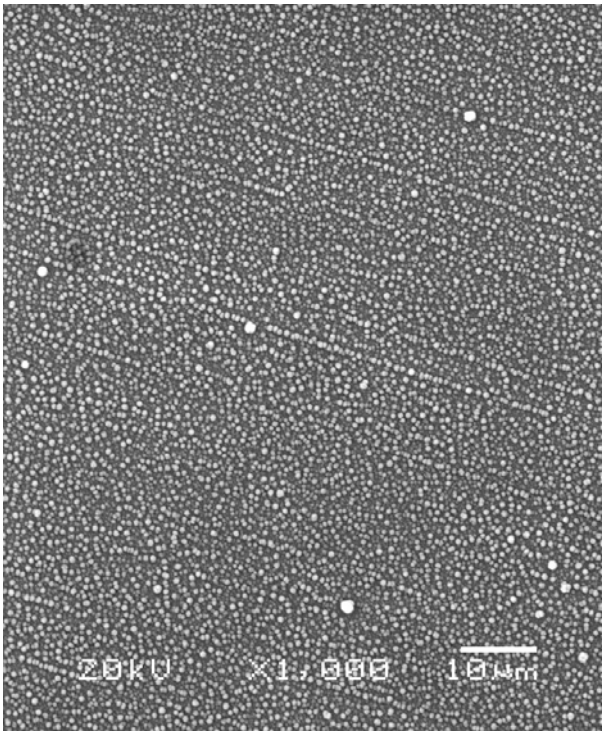

Figure 8.7: SEM image for the MgO film deposited on Hastelloy C276 using 0.093M of $Mg(CH3COO)_2.4H_2O$ at 650°C for 32 minutes.

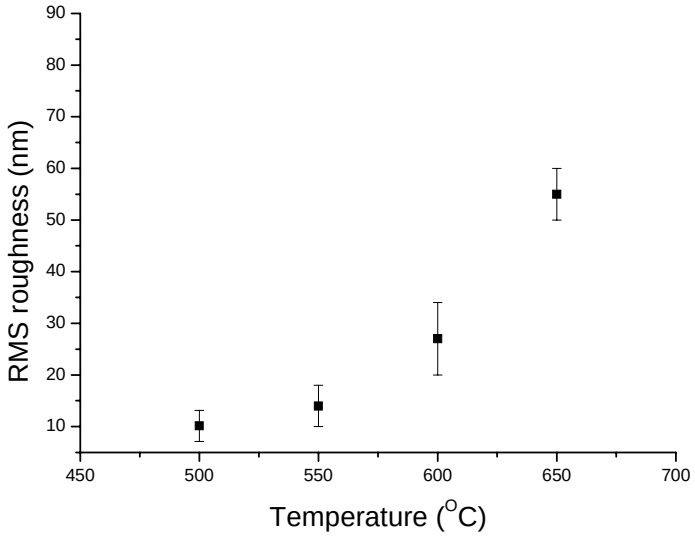

Figure 8.8: The effect of deposition temperature on MgO film roughness for the films deposited from 0.093M $Mg(CH3COO)_2.4H_2O$ for 32 minutes.

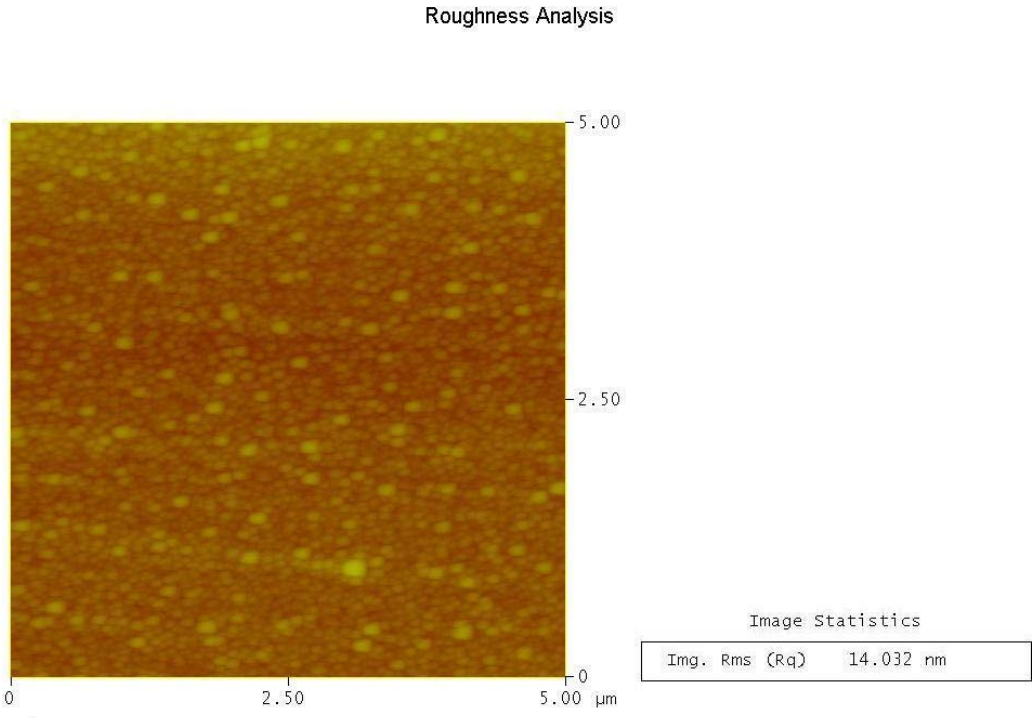

Figure 8.9: A 5x5µm^2 AFM image for the MgO film deposited on Hastelloy C276 using 0.093M of $Mg(CH3COO)_2.4H_2O$ at 550°C for 32 minutes.

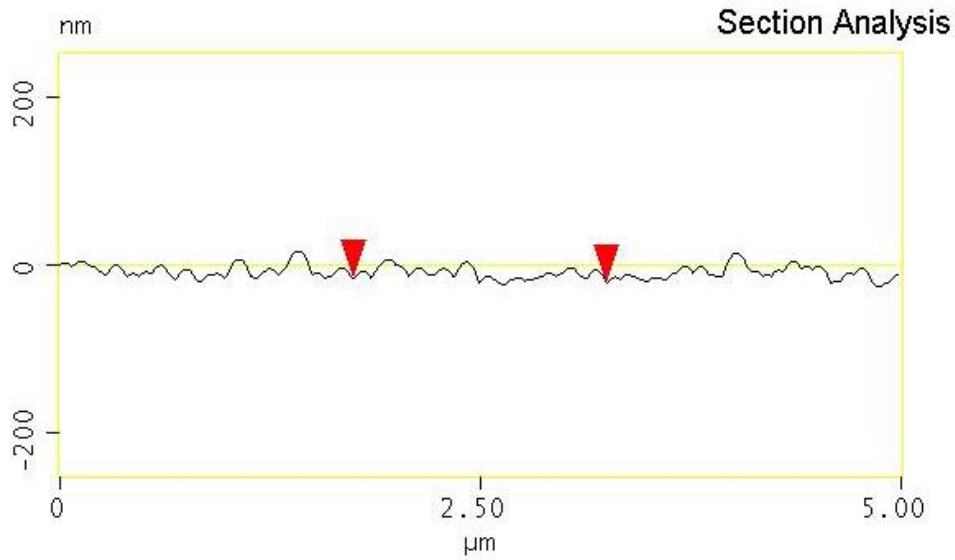

Figure 8.10: AFM section profile image for the MgO film deposited on Hastelloy C276 using 0.093M of $Mg(CH3COO)_2.4H_2O$ at 550°C for 32 minutes.

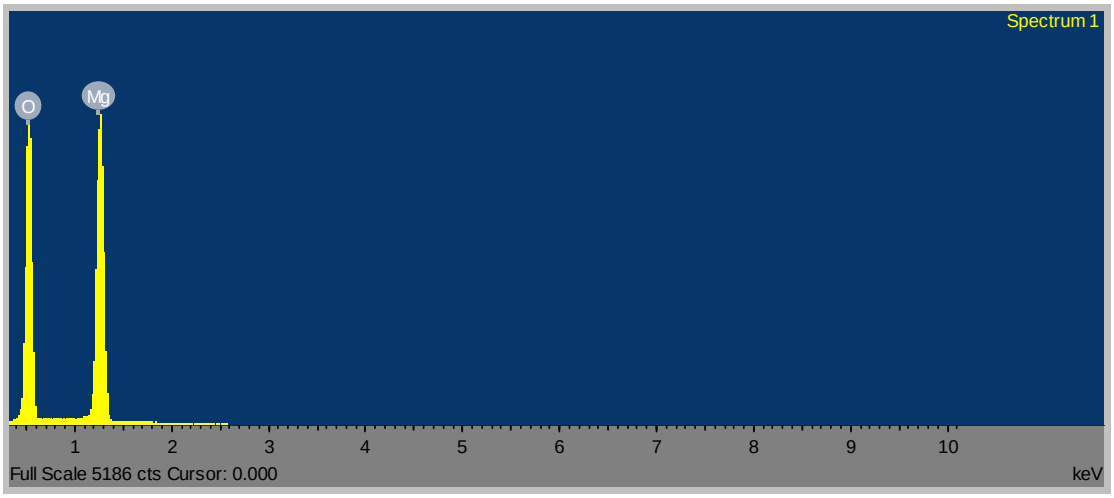

Figure 8.11: EDX spectrum, using an accelerating voltage of 4KV, for MgO film deposited with 0.093M solution at 600°C for a deposition time of 32 minutes.

Table 8.2: Summary of the EDX chemical composition results, using an accelerating voltage of 4KV, for MgO film deposited with 0.093M solution at 600°C for a deposition time of 32 minutes.

Element	at %
O K	52.06
Mg K	47.94

The texture of MgO was stronger (Figure 8.2) compared to that obtained when using the nitrate precursor (Figure 7.22 and Figure 7.34). This was also confirmed

from the X-ray pole figure measurements for the samples deposited at 600°C and 650°C for 32 minutes from 0.093M solution (Figure 8.12 and Figure 8.13, respectively). It can be seen that there is a weak out-of-plane texture and no in-plane texture (no definite poles were obtained at the circumference but a ring was obtained instead) as was the case for the nitrate precursor. The out-of-plane texture of MgO (200) was quantitatively measured by the ω-scan for the sample deposited at 600°C (Figure 8.14) and 650°C (Figure 8.16) from 0.093M solution. The FWHM for MgO (200) was 18.7° and 17.67°, respectively.

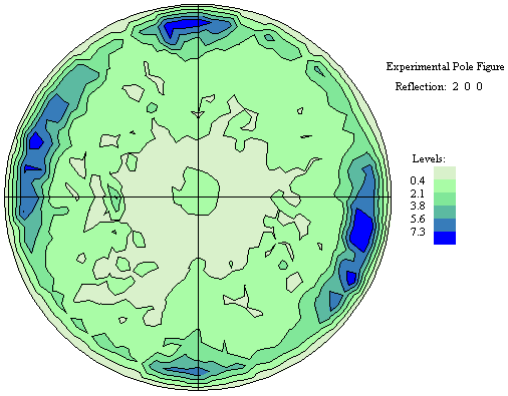

Figure 8.12: (200) X-ray pole figure, at 2θ of 43.12°, of the MgO film deposited at 600°C from a solution of 0.093M for 32 minutes.

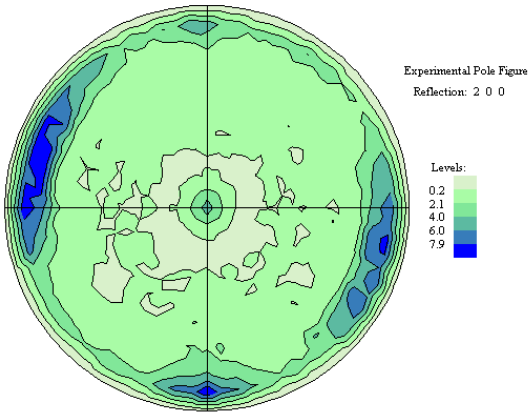

Figure 8.13: (200) X-ray pole figure, at 2θ of 43.12°, of the MgO film deposited at 650°C from a solution of 0.093M for 32 minutes.

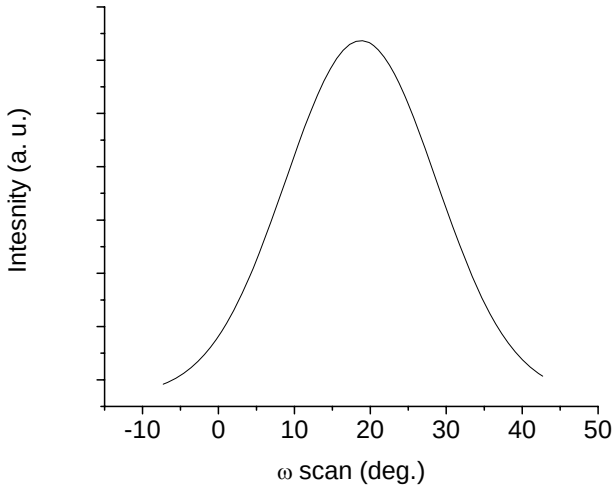

Figure 8.14: X-ray diffraction ω–scan for the film deposited at 600°C from 0.093M solution showing MgO (200) with a FWHM of 18.7°.

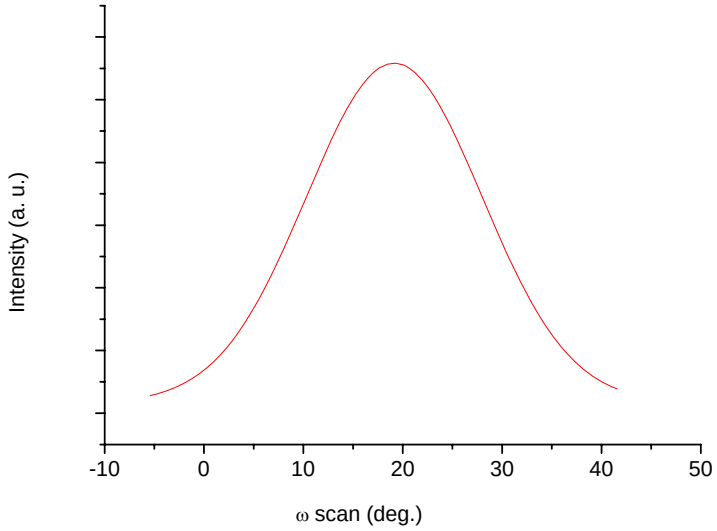

Figure 8.15: X-ray diffraction ω–scan for the film deposited at 650°C from 0.093M solution showing MgO (200) with a FWHM of 17.67°.

It was established in chapter 7 that MgO deposition on Hastelloy C276 using low concentrations of $Mg(NO_3)_2.6H_2O$ as a precursor resulted in no MgO XRD peaks. It was noticed that higher $Mg(NO_3)_2.6H_2O$ concentrations were needed to obtain a (200) oriented MgO film compared to that when using the $Mg(CH3COO)_2.4H_2O$ precursor. Amita Verma et al found that the crystallization and porosity behaviour of CeO_2-TiO_2 films coated on the transparent conducting oxide (SnO_2:F) coated on glass substrates were highly influenced by the precursor material [287]. Jin-Hyo Boo et al

found that the type of the precursor will affect the crystallinity, in terms of the preferred orientation, of MgO films deposited by metal-organic chemical vapour deposition (MOCVD) on c-plane sapphire substrates [288]. Soo Gil Kim et al found that the (100) preferred orientation of the MgO thin film deposited on Corning 7059 glass substrates was not affected by the type of the solvent used [289]. O. Renault and M. Labeau [146] deposited MgO on glass substrates using aerosol assisted-metalorganic chemical vapour deposition. They found that the deposition rate and the texture of MgO films changed by changing the nature of the solvent and that the deposition rate increased with increasing the deposition temperature. They concluded that the nature of the solvent and the aerosol flow rate both may play an important role on the obtained microstructure, as they control, in a way that is not fully understood yet, the deposition rate and processes at a given substrate temperature, and hence the direction of texture. So it can be seen that the solvent type and the precursor may or may not affect the preferred orientation of the produced film. In this study, it is still not clear why higher concentrations of the $Mg(NO_3)_2.6H_2O$ precursor was required for the deposition of MgO on Hastelloy C276 and more investigation is required in this field. However, it was believed that under the deposition conditions used during spray pyrolysis and the way the $Mg(NO_3)_2.6H_2O$ decomposes, a high vapour pressure of the Mg^{2+} cation was obtained when using low precursor concentration, hence, high number of collisions which in turn leads to its deficiency in the film. That is why higher concentrations were needed.

8.4 Effect of deposition time on MgO film properties

The effect of the deposition time on the deposited MgO films by spray pyrolysis was studied at different temperatures, using an Ar flow rate of 10 l/min, as can be seen from the XRD patterns in Figure 8.16. It can be seen that regardless of the deposition temperature, the intensity of MgO (200) increased by increasing the deposition time from 32 minutes to 64 minutes. However, the increase in intensity was accompanied by an increase in the roughness. This can be noticed by comparing the SEM images (Figure 8.17 and Figure 8.18) and the AFM images (Figure 8.19 and Figure 8.20) for the samples with a deposition time of 64 minutes with those with a deposition time of 32 minutes (Figure 8.5, Figure 8.6 and Figure 8.8).

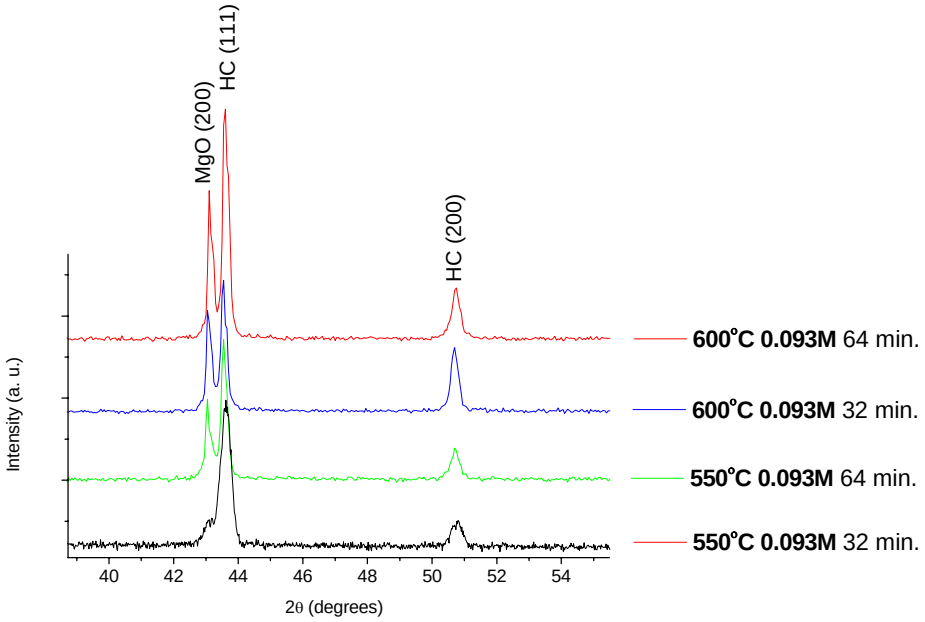

Figure 8.16: XRD patterns for MgO deposition on Hastelloy C276 using 0.093M of $Mg(CH3COO)_2.4H_2O$ at different temperatures and times.

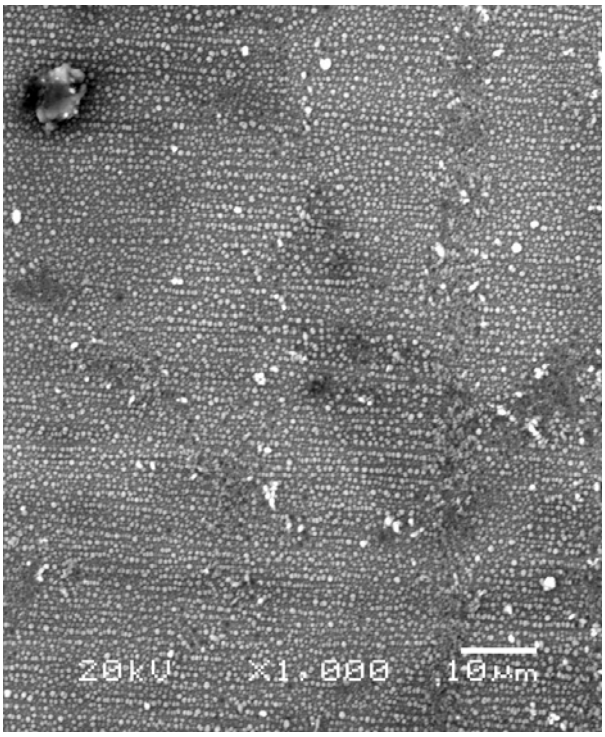

Figure 8.17: SEM image for the MgO film deposited on Hastelloy C276 using 0.093M of $Mg(CH3COO)_2.4H_2O$ at 550°C for 64 minutes.

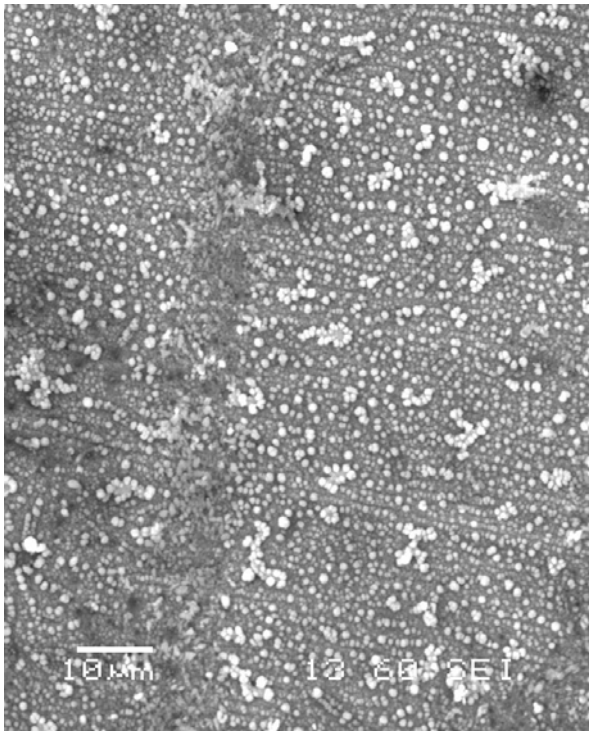

Figure 8.18: SEM image for the MgO film deposited on Hastelloy C276 using 0.093M of $Mg(CH3COO)_2.4H_2O$ at 600°C for 64 minutes.

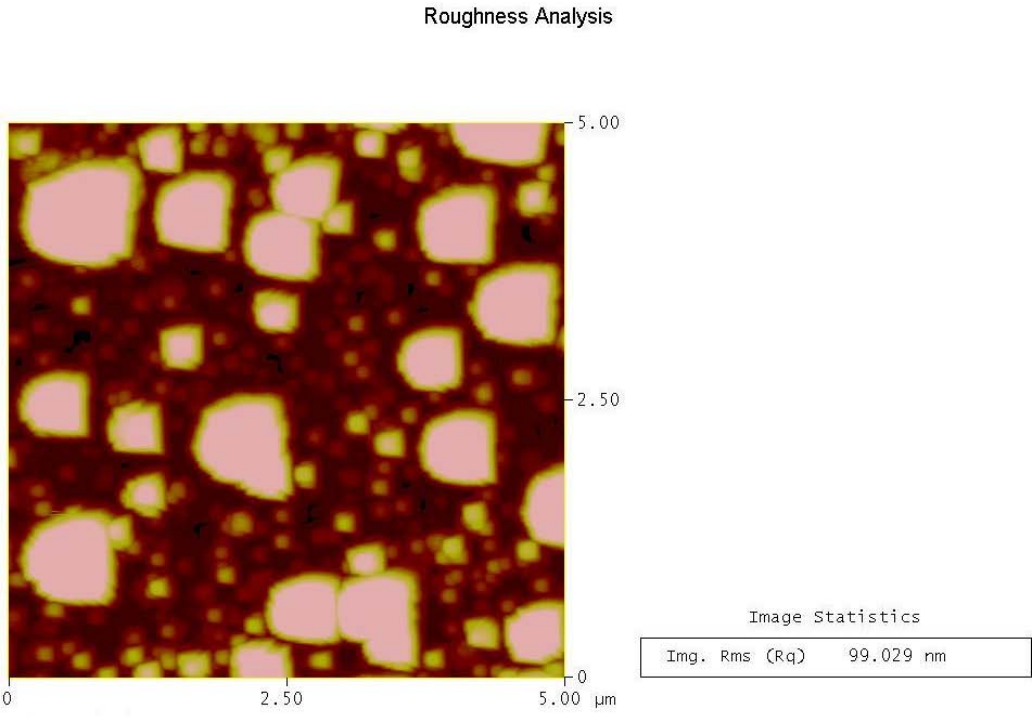

Figure 8.19: A 5x5µm^2 AFM image for the MgO film deposited on Hastelloy C276 using 0.093M of $Mg(CH3COO)_2.4H_2O$ at 550°C for 64 minutes.

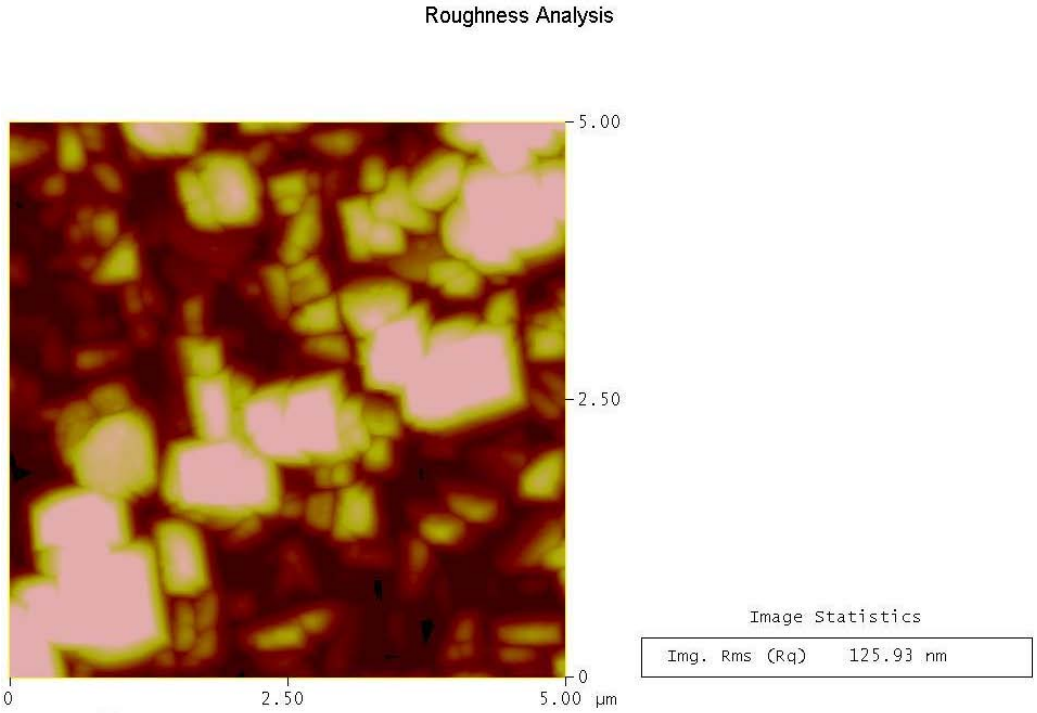

Figure 8.20: A 5x5µm^2 AFM image for the MgO film deposited on Hastelloy C276 using 0.093M of $Mg(CH3COO)_2.4H_2O$ at 600°C for 64 minutes.

The fourth mode of deposition leads to the formation of particles on the surface by increasing the temperature, where the full thermal decomposition takes place before the substrate and only finely divided solid product arrives at the substrate surface. It is also to be pointed out that the actual working mode depends not only on the substrate temperature, but also on the temperature of the working surrounding [83]. By increasing the deposition time from 32 minutes to 64 minutes, overgrown particles were formed suggesting that the growth of the particles is dominating the nucleation. However, no sound explanation was found to relate this behaviour with the type of the deposition mode that might be applied to this situation and further investigation is required.

In an attempt to improve the texture of the MgO (200) peak, without increasing the roughness, a double deposition was made. This means that the sample was deposited at certain conditions, left to be furnace cooled to room temperature, then deposited again at the same conditions. This was done at 600°C for 32 minutes each using 0.093M solution.

The XRD patterns in

Figure **8.21** show that the intensity of the MgO peak was not improved much. This slight improvement in intensity was accompanied by a slight increase in the

roughness as can be seen from the SEM images and AFM image in Figure 8.22 and Figure 8.23, respectively, when compared to the sample without the double deposition (Figure 8.6 and Figure 8.8). If it is assumed that the thickness of MgO film increases with increasing the deposition time, then it can be concluded that the texture improved slightly with thickness. Similar behaviour was found by other researchers [142, 146, 175]. More details on thickness dependence are found in section 8.7.

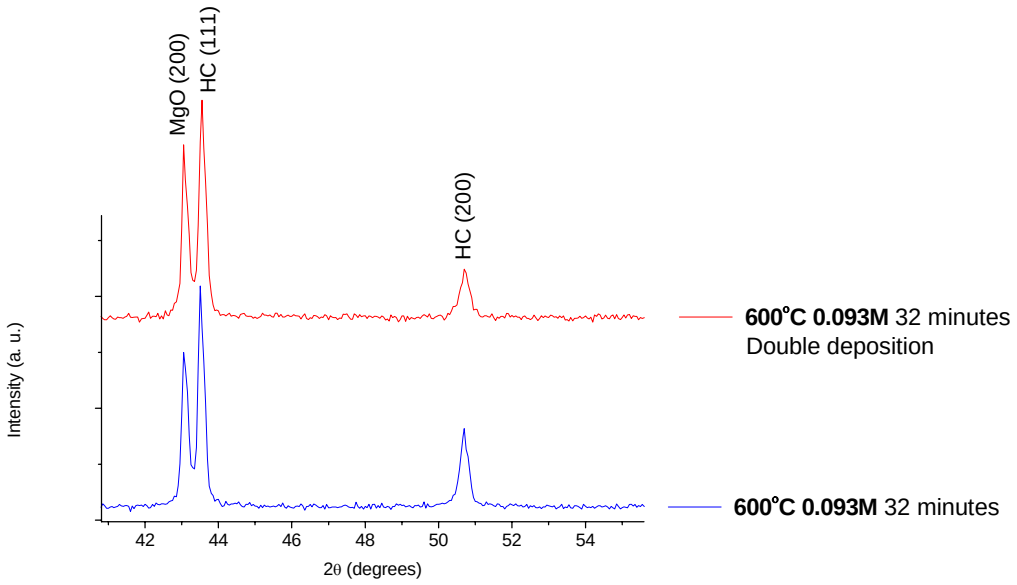

Figure 8.21: XRD patterns for MgO deposition on Hastelloy C276 showing the double deposition effect using 0.093M $Mg(CH3COO)_2.4H_2O$ at 600°C for 32 minutes.

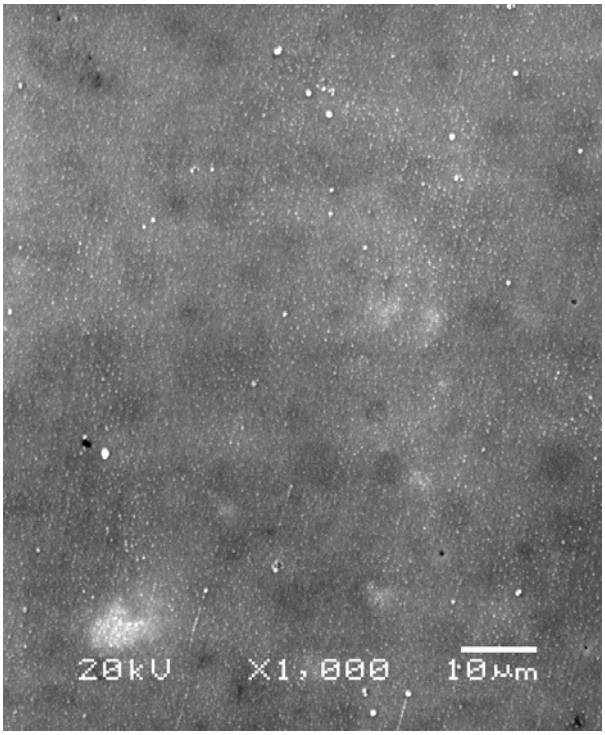

Figure 8.22: SEM image for MgO on Hastelloy C276 with the double deposition using 0.093M $Mg(CH3COO)_2.4H_2O$ at 600°C for 32 minutes.

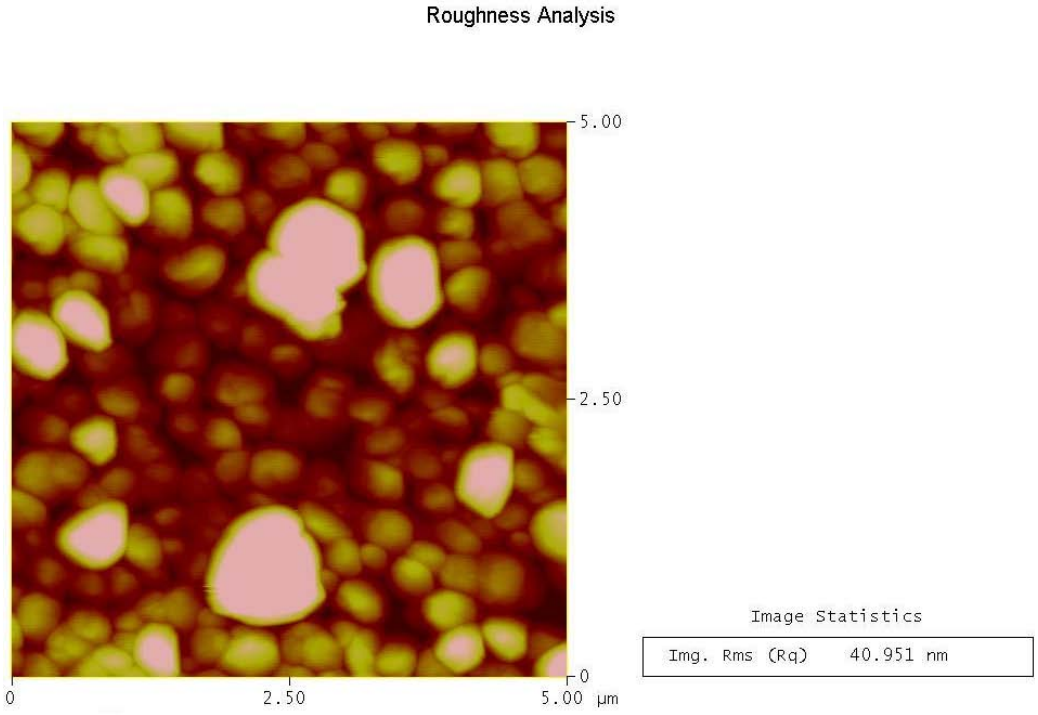

Figure 8.23: A 5x5µm^2 AFM image for MgO on Hastelloy C276 with the double deposition using 0.093M $Mg(CH3COO)_2.4H_2O$ at 600°C for 32 minutes.

8.5 Effect of precursor concentration on MgO film properties

MgO deposition on Hastelloy C276 was done at higher concentrations, using 0.14M and 0.279M solutions at 600°C, and using an Ar flow rate of 10 l/min. As can be seen from the XRD patterns in Figure 8.24, an MgO (200) peak, the only detected one, was normal to the substrate surface. It can also be seen that the peak intensity was not greatly affected by increasing the concentration. This can be attributed to the saturation effect; at concentrations higher than 0.093M, the growth rate will be low and hence the film thickness will not increase significantly, therefore almost no effect on texture was obtained. C. H. Lee and C. S. Huang [158] deposited In_2O_3 by spray pyrolysis on Si wafers using $InCl_3$-methanol solution as the source material, they found that at high flow rates, the growth rate is slow due to the reactant saturation effect. Other researchers [86] found that, for MgO films deposited on Si (100) substrates by electrostatic spray pyrolysis, the growth rate decreased with increasing the substrate temperature, others [114] found that, for ZnO films deposited on glass substrates by spray pyrolysis, at high temperatures the deposition rate was constant (saturated) where the growth rate is mass transport controlled; the reaction kinetics are so fast that the surface reaction finally becomes controlled by mass transfer of the reactants, and the concentration of the reactants on the surface is the limiting parameter.

When using the 0.14M solution, the roughness increased quite slightly as can be seen from the SEM image (Figure 8.25) and the AFM image (Figure 8.27) compared to that when using the 0.093M solution (Figure 8.6 and Figure 8.8); however, there was a further increase in the roughness when increasing the concentration to 0.279M as can be seen from the SEM image (Figure 8.26) and the AFM image (Figure 8.28), respectively. At 0.279M, overgrown particles were formed on the surface which led to an increase in the roughness. The lifetime required for evaporation increases by increasing the amount of solute in the droplet [110]; therefore, by increasing the concentration to 0.279M, the time was not enough to evaporate both the solvent and the solute, a situation similar to that encountered in the second mode of deposition [83]. A similar behaviour was encountered when depositing MgO from the nitrate precursor using 0.78M (Figure 7.27).

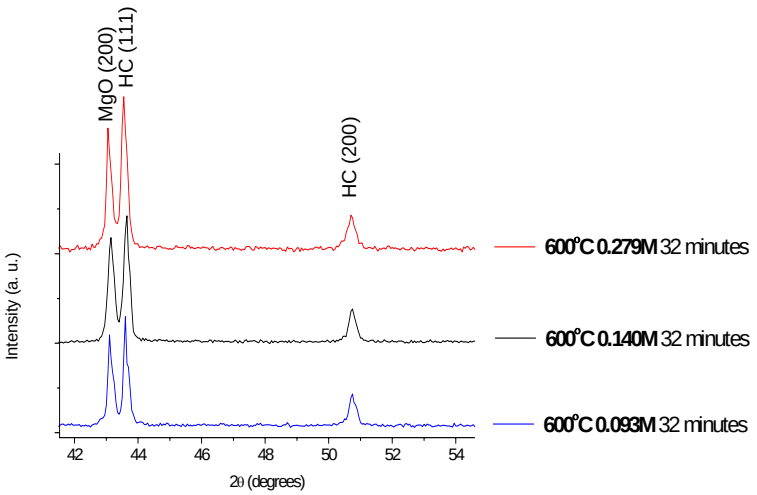

Figure 8.24: XRD patterns for MgO deposition on Hastelloy C276 at 600°C for 32 minutes using different concentrations of $Mg(CH3COO)_2.4H_2O$.

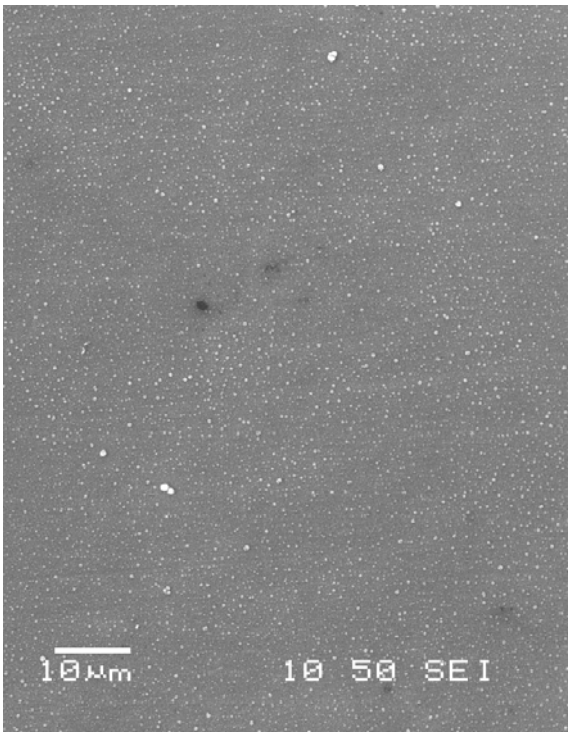

Figure 8.25: SEM image for MgO deposition on Hastelloy C276 at 600°C for 32 minutes using 0.14M $Mg(CH3COO)_2.4H_2O$.

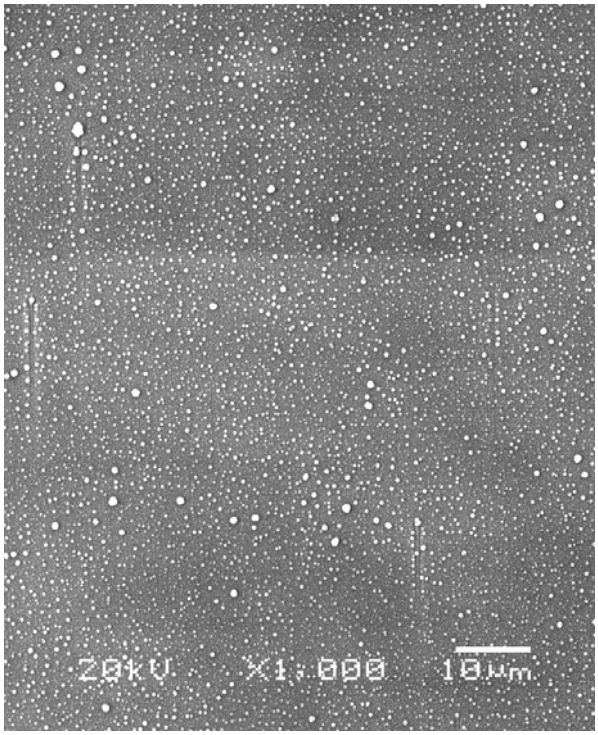

Figure 8.26: SEM image for MgO deposition on Hastelloy C276 at 600°C for 32 minutes using 0.279M $Mg(CH3COO)_2.4H_2O$.

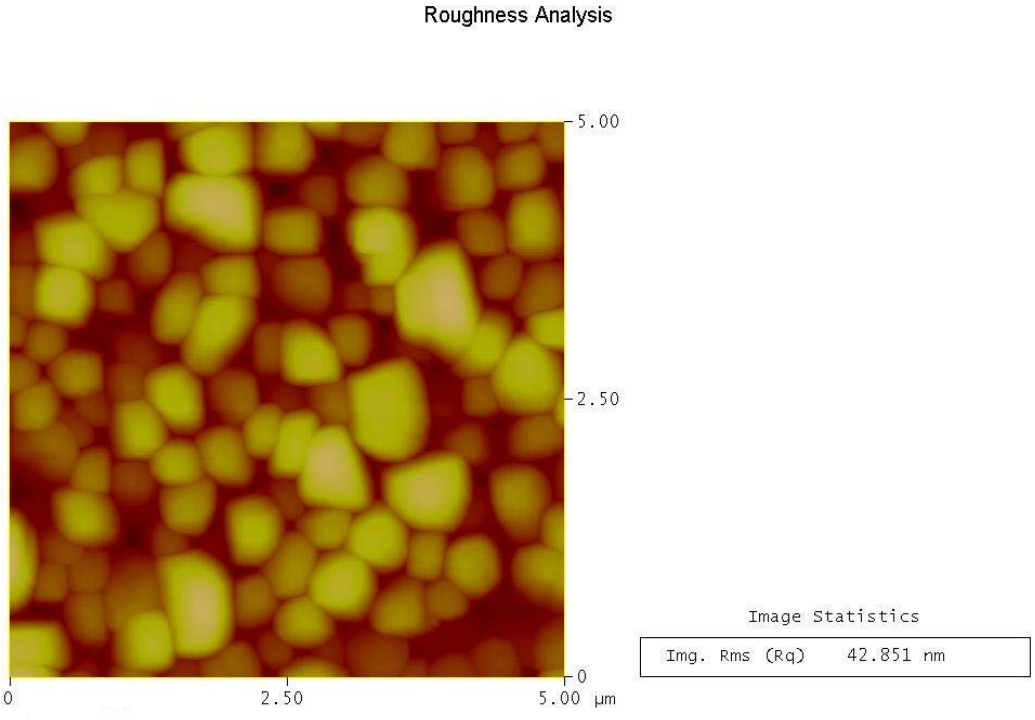

Figure 8.27: A 5x5µm^2 AFM image for MgO deposition on Hastelloy C276 at 600°C for 32 minutes using 0.14M $Mg(CH3COO)_2.4H_2O$.

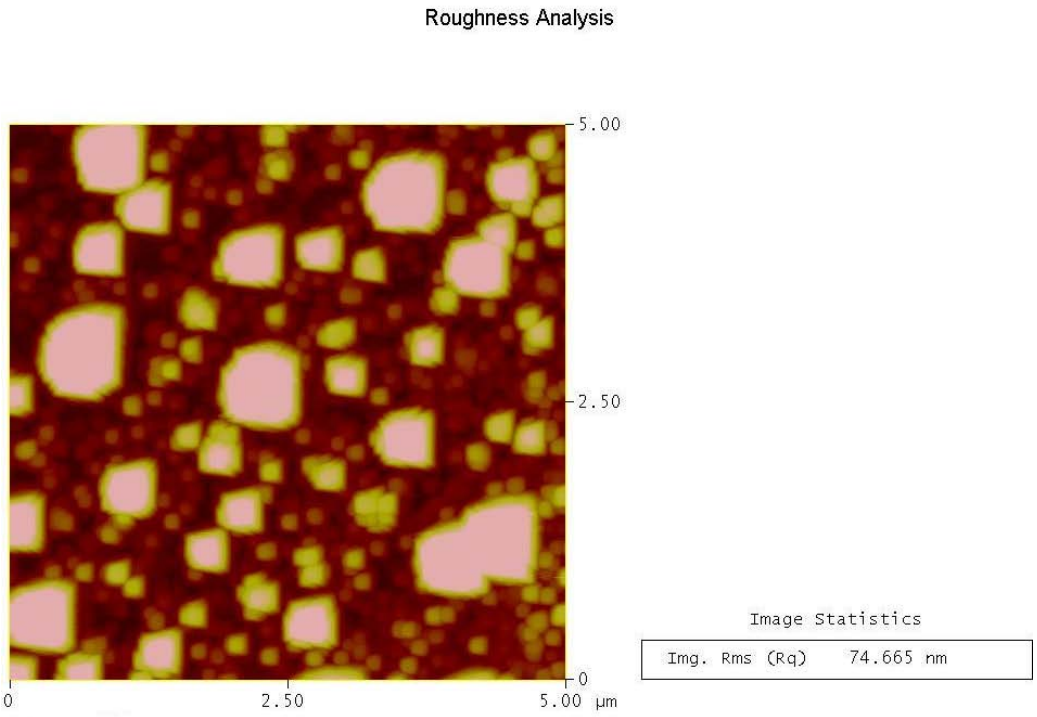

Figure 8.28: A 5x5µm^2 AFM image for MgO deposition on Hastelloy C276 at 600°C for 32 minutes using 0.279M $Mg(CH3COO)_2.4H_2O$.

When using the nitrate precursor, the low concentration (0.078M) resulted in amorphous MgO films. Higher concentrations were needed (0.468M and 0.78M) to get a weak MgO (200) peak. In contrast, the use of the acetate precursor resulted in textured MgO films even when using low concentrations (0.093M). This would be attributed to the nature of the used precursor, where it was established from the literature that the solvent type and the precursor may or may not affect the preferred orientation of the produced film (section 8.3). Therefore, in this study, the type of the precursor, and this time the type of the substrate as well, affects the concentration needed to get textured MgO films.

8.6 X-ray photoelectron spectroscopy (XPS) test

The samples deposited from 0.093M at 550°C and 600°C for 32 minutes using 10 l/min Ar flow rate were tested for surface contamination using the XPS. The XPS spectra were recorded with a standard Mg Kα source using 20 pass energy, 0.1 eV step, and 0.1 seconds per step for the detailed spectra. The Mg 2P scan was from 40-60eV and the O 1s scan was from 520-550eV. For the sample deposited at 550°C, the Mg 2P was found to be at 49.8eV (Figure 8.29). For the O 1s two peaks were obtained

at 529.8eV and at 531.5eV (Figure 8.30). For the sample deposited at 600°C, the Mg 2P was found to be at 50.5eV (Figure 8.31). For and the O 1s two peaks were also obtained at 531.3eV and at 532.9eV (Figure 8.32). The peak position for Mg 2P is due to the contribution of magnesium oxide/hydroxide (Figure 8.29 and Figure 8.31). In the O 1s spectra (Figure 8.30 and Figure 8.32), the two peak positions are for magnesium oxide and magnesium hydroxide. This indicates that the surface of MgO was contaminated with hydroxides as was expected as MgO is hygroscopic [194]. Similar result was found by others [201-208]. However, heating the contaminated layer briefly at a temperature of 450°C in air is sufficient to regenerate the MgO surface [116]; in our experiments this condition will be met during subsequent YBCO deposition. Although the sample analysis was carried out on fresh samples to minimise the effect of storage.

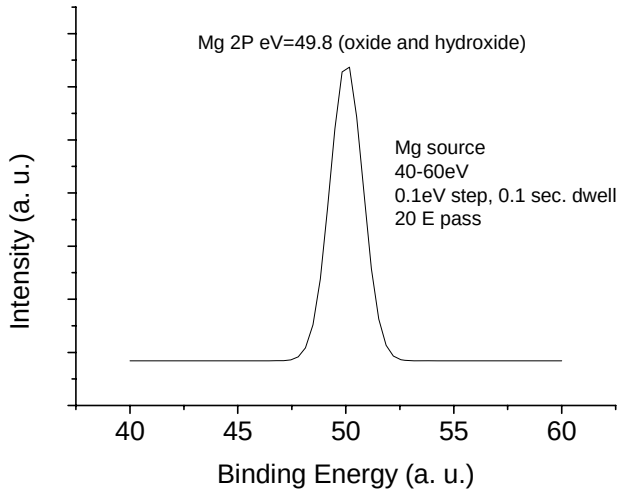

Figure 8.29: XPS spectrum for the MgO thin film deposited on Hastelloy C276 substrate using 0.093M $Mg(CH3COO)_2.4H_2O$ at 550^oC for 32 min. showing the Mg 2P.

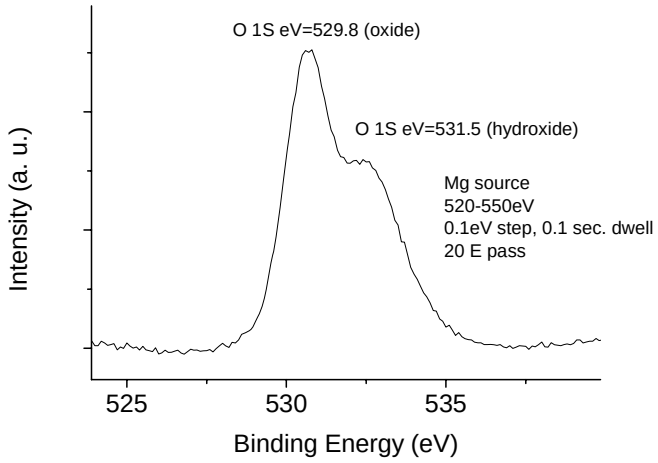

Figure 8.30: XPS spectrum for the MgO thin film deposited on Hastelloy C276 substrate using 0.093M $Mg(CH3COO)_2.4H_2O$ at 550^oC for 32 min. showing the O 1S.

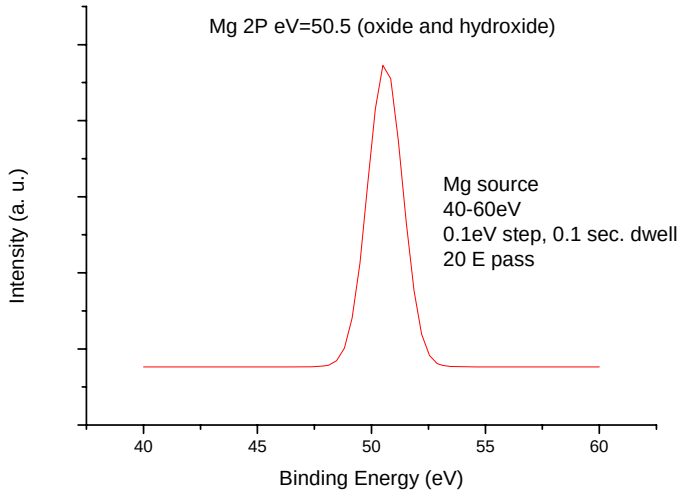

Figure 8.31: XPS spectrum for the MgO thin film deposited on Hastelloy C276 substrate using 0.093M $Mg(CH3COO)_2.4H_2O$ at 600^oC for 32 min. showing the Mg 2P**.**

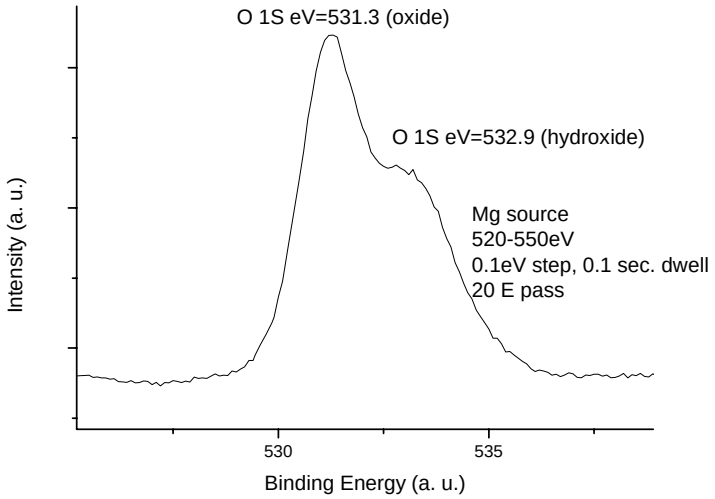

Figure 8.32: XPS spectrum for the MgO thin film deposited on Hastelloy C276 substrate using 0.093M $Mg(CH3COO)_2.4H_2O$ at 600°C for 32 min. showing the O 1S.

8.7 Effect of deposition parameters on MgO film thickness

As was mentioned in section 7.8, the thickness measurements for the MgO films deposited on metallic substrates, i.e. Hastelloy C276 was not straight forward. Therefore, not many thickness measurements were obtained. After many trials, a thickness measurement by mechanically polishing the sample deposited at 600°C from a solution of 0.093M for 32 minutes, using an Ar flow rate of 10 l/min, was achieved. However, that was done for the sample with YBCO deposition on top of that MgO as will be seen later in Figure 8.81. The thickness of MgO was 220nm. This gives a deposition rate of 9.25Å/sec (2200Å/240sec.)

8.8 Effect of inclination angle (ISD) on MgO film properties

As was mentioned before, the effect of inclination angle on the texture development of MgO thin films was studied by some researchers. They found that the shadowing effect is the mechanism which drives texture formation in MgO films by inclining the substrate, during pulsed laser deposition or e-beam evaporation relative to the flux direction (section 2.6). To our knowledge, no reports were found studying the effect of inclination angle on the texture development of MgO thin films using the spray pyrolysis technique. For this purpose, MgO deposition at 20°, 45°, and 60° using 0.093M solution at 600°C for 32 minutes was utilised for the investigation. The

used Ar flow rate was 10 l/min. The XRD patterns in Figure 8.33 show that the intensity of MgO (200) decreased by increasing the inclination angle from 0° to 45°. The peak was then disappeared when increasing the inclination angel to 60°, although, the EDX results showed the presence of Mg, and therefore the deposited MgO film was suggested to be amorphous. The same observation was noticed when depositing MgO from the nitrate precursor (Figure 7.41). This can be attributed to the low thickness of the deposited MgO at high inclination angle. The decrease of peak intensity with increasing the inclination angle was also observed when depositing MgO on Si single crystal and this was attributed to the lower thickness at higher inclination angles (section 4.3.4). It was found that the intensity of MgO (200) deposited on Si substrates at 650°C and 700°C from a 0.0078M and 0.078M $Mg(NO_3)_2.6H_2O$ decreased by increasing the inclination angle from 20° to 60°(Figure 4.17, Figure 4.18, Figure 4.29 and Figure 4.30) where the gas convection from the substrate pushes the droplets of the precursor away from it [65, 141] and this effect increased by increasing the inclination angle. Amorphous films of MgO, CeO_2, In_2O_3 deposited by spray pyrolysis on different substrates were obtained by others [140, 146, 154]. Others found that the texture of MgO developed with thickness [142, 242].

However, it is to be noted in this work that inclining the substrate again led to untilted MgO films with (200) direction parallel to the substrate normal and did not result in the shadowing effect which was observed for MgO and YSZ films deposited by ISD method using PLD and e-beam evaporation [39-41, 49, 50, 53, 167, 169, 173-175, 177-183]. One more point should be mentioned. As was said before, MgO can be deposited by inclined substrate deposition (ISD) using e-beam evaporation [173, 174]. By this method, the MgO film had the (200) with the c-axis being tilted from the substrate normal due to the shadowing effect [173-175]. The deposited YBCO film on top of that MgO also grows with the (00l) being tilted from the substrate normal, which has led to low J_c values. Higher J_c and T_c values are obtained by growing untilted YBCO films by depositing YSZ and CeO_2 buffers on top of the tilted MgO film [169, 176, 177]. We tried to deposit MgO from acetate precursor by inclining the substrate relative to the nozzle. This led to untilted MgO films with (200) direction parallel to the substrate normal; no shadowing effect was observed when using the ISD. However, this was at the expense of MgO (200) peak intensity. From one hand, spray pyrolysis gave MgO (200) peaks parallel to the substrate normal whether ISD was utilised or not. From the other hand, the ISD by spray pyrolysis was just affecting

the crystallinity (Figure 8.33), roughness (Figure 8.34) and thickness of the deposited MgO films. YBCO films grown on top of MgO deposited by spray pyrolysis (as will be seen later in this chapter) have the (006) of YBCO // (200) of MgO. Thus, spray pyrolysis offers an alternative method of depositing a single MgO buffer layer with no tilting for later YBCO deposition. The same behaviour was also observed for MgO deposition from the nitrate precursor.

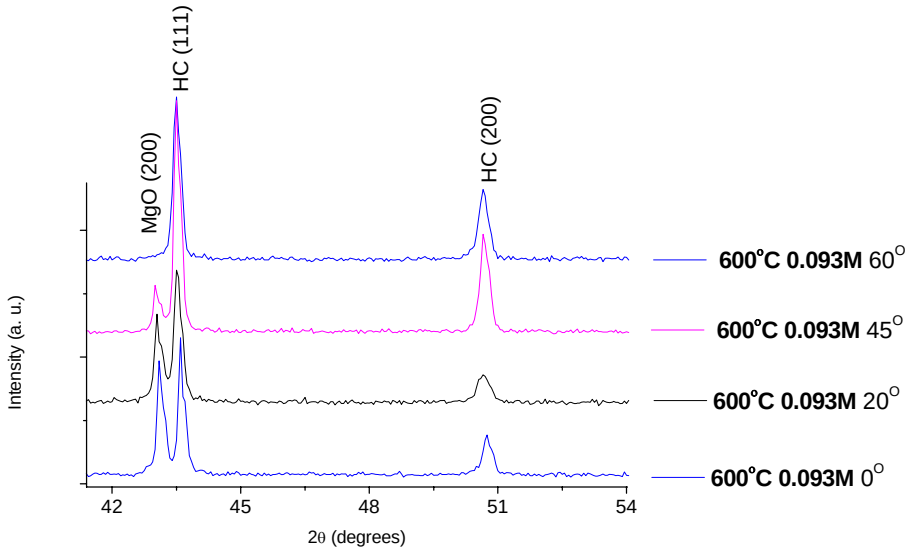

Figure 8.33: XRD patterns for MgO deposition on Hastelloy C276 using 0.093M $Mg(CH3COO)_2.4H_2O$ at 600°C for 32 minutes and at different inclination angles.

Figure 8.34-Figure 8.37 show that the roughness decreased with increasing the inclination angel from 20° to 60°, similar behaviour was found for MgO deposition on Si single crystals (Figure 4.31). This behaviour can be attributed to pushing of droplets of the precursor away from the substrates, and by increasing the inclination angle, smoother films were obtained. However, for MgO deposition on Si, the RMS of the film deposited with no inclination angle was rougher than the ones deposited with an inclination angle. A different situation was encountered when depositing MgO on Hastelloy C276. At zero inclination angle, the surface roughness was about 27 nm, and by increasing the inclination angle to 20°, the surface roughness increased to about 33 nm then decreased by increasing the inclination angle to 45° and 60°. This increase in the roughness at 20° may be attributed to a flow turbulence at the substrate surface leading to the formation of particles and hence to an increase in the roughness. This turbulence decreased by increasing the inclination angle, and therefore to a decrease in the roughness values. This behaviour was not really understood and

further investigation is required. The same behaviour was observed for MgO deposition from the nitrate precursor (Figure 7.42). Rachel E. Koritala et al [185] found that for the case of biaxially textured MgO films deposited by ISD using e-beam evaporation on Hastelloy C substrates that high roughness values were obtained at low and high inclination angles and the lowest roughness values were obtained for inclination angles of 20°-55° where the roughness was not affected by the inclination angle in this range.

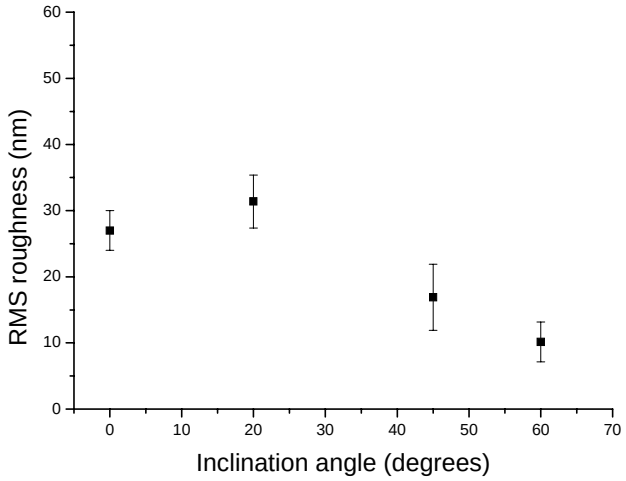

Figure 8.34: The effect of inclination angle on the film roughness of MgO film deposited from 0.093M solution at 600°C for 32 minutes.

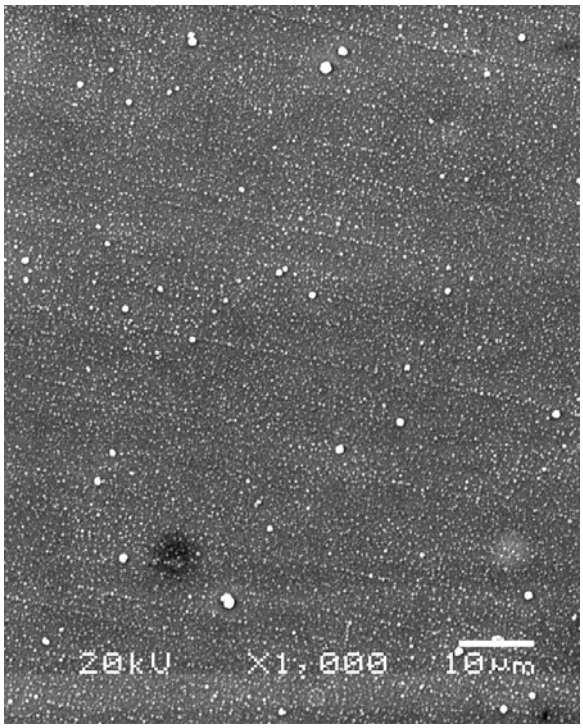

Figure 8.35: SEM image for MgO deposition on Hastelloy C276 using 0.093M $Mg(CH3COO)_2.4H_2O$ at 600°C for 32 minutes at 20°.

Figure 8.36: SEM image for MgO deposition on Hastelloy C276 using 0.093M $Mg(CH3COO)_2.4H_2O$ at 600°C for 32 minutes at 45°.

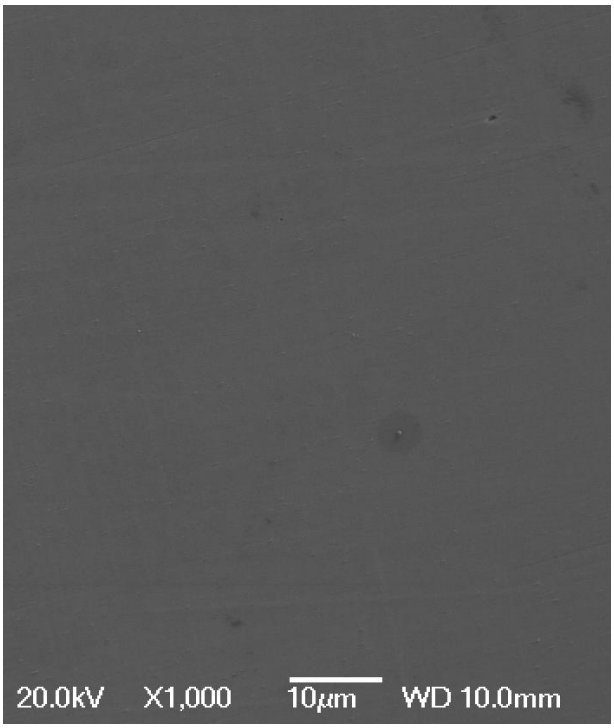

Figure 8.37: SEM image for MgO deposition on Hastelloy C276 using 0.093M $Mg(CH3COO)_2.4H_2O$ at 600°C for 32 minutes at 60°.

8.9 Effect of Ar flow rate on MgO film properties

The effect of Ar flow rate on the spray pyrolysis deposition of MgO was investigated using 5 l/min, 10 l/min, and 15 l/min. The depositions were made using 0.093M solution at 600°C for 32 minutes. The XRD patterns in Figure 8.38 show that low and high Ar flow rate (5 and 15 l/min) resulted in much lower intensity peaks for MgO compared to that when using an Ar flow rate of 10 l/min. This was assumed to be as a result of decreasing the thickness of the deposited MgO film when using low and high flow rates. The low flow rates decreased the amount of the precursor reaching the substrate and hence decreased the thickness. The high flow rates forces the particles to follow the gas flow away from the substrate, therefore decreasing the thickness of the deposited MgO which in turn affects its texture. Researchers found that the texture of MgO developed with thickness [142, 242]. The change in Ar flow rates also had an effect on the film smoothness. The low and high flow rates (5 and 15 l/min) had smooth surfaces (Figure 8.39-Figure 8.41) while the film deposited at 10 l/min, although had a strong MgO (200) peak, this was at the expense of it is surface smoothness. However, a flow rate of 10 l/min forms a relatively strong MgO (200) peak. Therefore, the flow rate affects the intensity or the strength of texture. This is in disagreement with what was found by Xiaorong Fu et al [72] and O. Renault and M. Labeau [146]. They found that the flow rate changed the preferred orientation. This was also found by others [144, 145]. Pavlopoulos D. also found a change of the preferred orientation by changing the flow rate in the case of depositing CeO_2 on borosilicate glass. Joseph Prince J et al [140] found that crystallinity changed with the flow rate in the case of depositing In_2O_3.

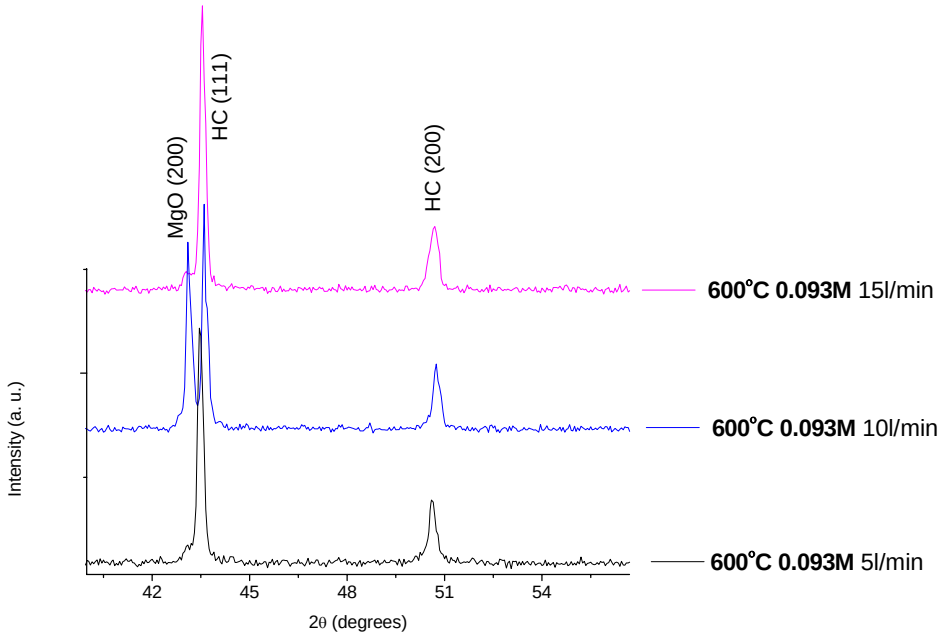

Figure 8.38: XRD patterns for MgO deposition on Hastelloy C276 using 0.093M $Mg(CH3COO)_2.4H_2O$ at 600°C for 32 minutes and at different Ar flow rates.

The situation encountered with the acetate precursor was slightly different to that found with the nitrate precursor. When using the nitrate precursor, the roughness increased, by increasing the flow rate from 10-15 l/min, due to the high concentration used. This gives large particles which will not follow the gas flow away from the substrate as was the case with the low acetate precursor concentration. Therefore, it was found that the optimum flow rate was 10 l/min which gives detectable MgO peaks and a relatively smooth MgO films.

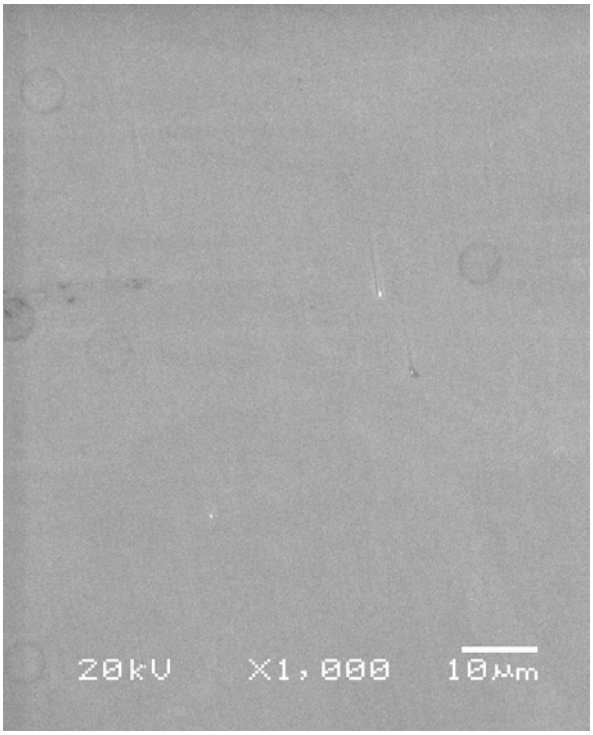

Figure 8.39: SEM image for the Hastelloy C276 deposited with MgO using 0.093M solution at 600°C for 32 minutes and using an Ar flow rate of 5 l/min.

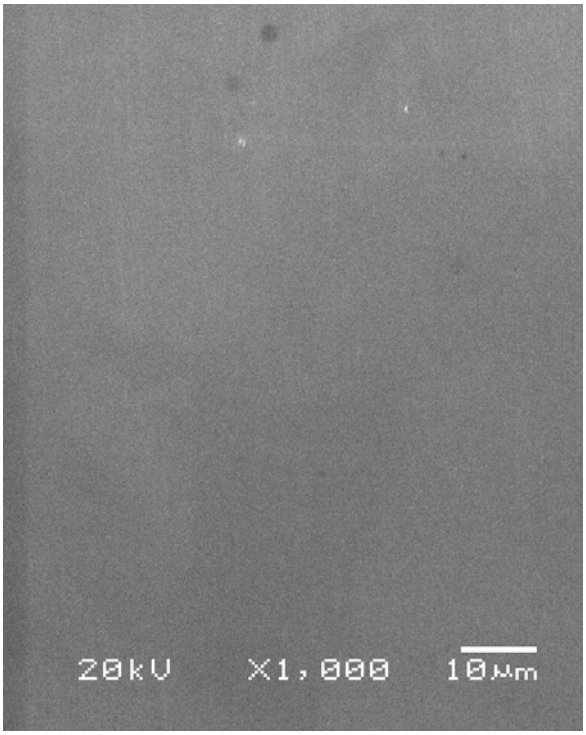

Figure 8.40: SEM image for the Hastelloy C276 deposited with MgO using 0.093M solution at 600°C for 32 minutes and using an Ar flow rate of 15 l/min.

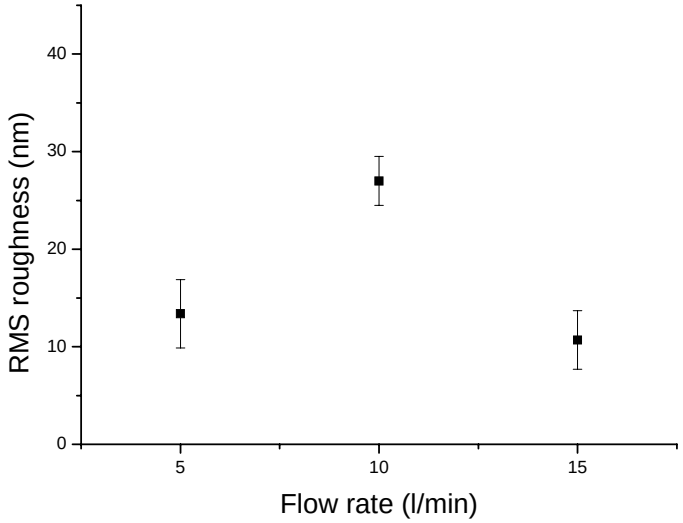

Figure 8.41: The effect of Ar flow rate on the roughness of MgO films deposited from 0.093M solution at 600°C for 32 minutes.

8.10 Effect of annealing on the texture of MgO films

YBCO films deposited on annealed MgO buffers had improved in-plane texture and superconducting properties [191-193]. As was the case when using the nitrate precursor, an attempt to improve the texture of MgO films deposited from the acetate precursors was investigated. This was done by applying annealing in different environments, using different temperatures and annealing times.

8.10.1 Annealing under O_2 atmosphere

The annealing experiments were carried out at the same conditions and following the same procedures and using the same system used for annealing MgO films deposited from the nitrates precursor (7.11.1). Figure 8.42 shows the XRD patterns for the sample deposited at 600°C for 32 minutes from a 0.093M solution after being annealed under O_2 atmosphere at different temperatures and times. A narrow XRD scan is given in Figure 8.43. It can be seen that annealing at temperatures of 400°C-650°C for three hours did not affect the texture of the MgO (200) peaks. The surface morphology and roughness were the same as that before the annealing (Figure 8.6 and Figure 8.8). This was expected as the annealing temperatures were very close to the deposition temperatures used during spray pyrolysis. This also confirms the stability of MgO film up to 650°C even under O_2 flow. However, when the annealing temperature was increased to 800°C and 1000°C

for a deposition time of three hours, other oxides started to appear (Figure 8.42), even a powder film of oxides formed on the surface, which is why the MgO (200) peak disappeared. The oxides were more pronounced by annealing at 1000°C for three hours. The oxide peaks could not be indexed and were referred to as complex oxides. It was believed that such oxides were composed of Ni and Cr in a complex chemistry which was why no JCPDS PDF files were found to index them.

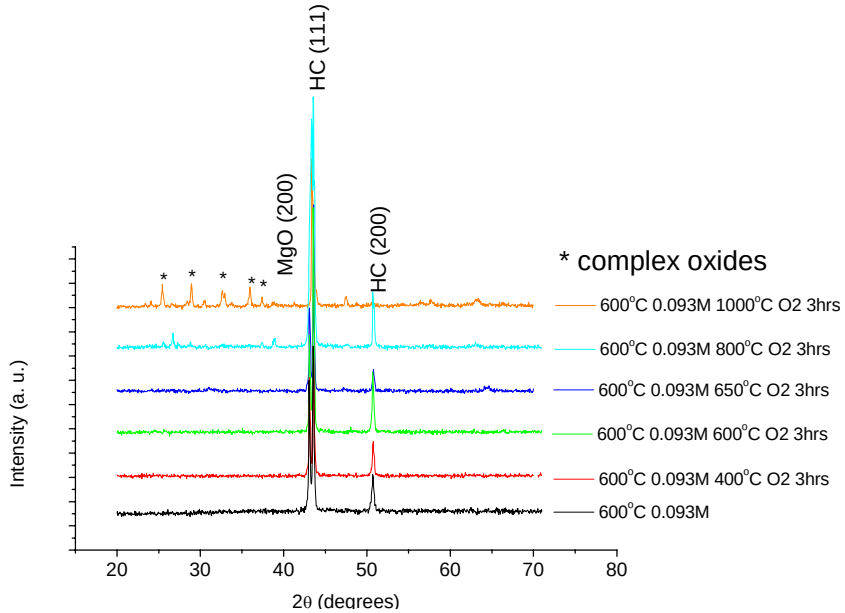

Figure 8.42: XRD patterns for the Hastelloy substrates deposited with MgO from 0.093M at 600°C for 32 minutes after O_2 anneal at different temperatures and times.

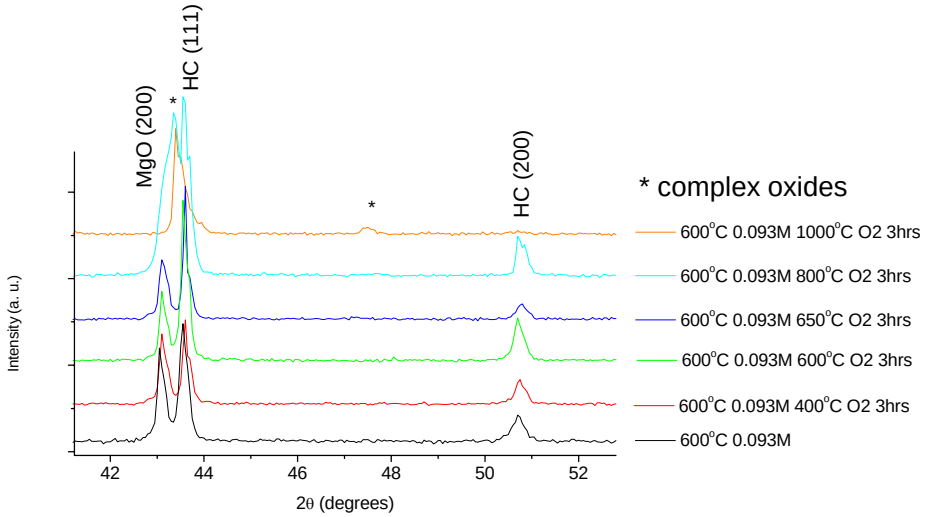

Figure 8.43: XRD patterns with a narrow scan for the Hastelloy substrates deposited with MgO from 0.093M at 600°C for 32 minutes after O_2 anneal at different temperatures and times.

The SEM and AFM images for the samples annealed at 800°C and 1000°C for three hours are shown in Figure 8.44-Figure 8.47. At 800°C, grain boundaries of the

substrate were revealed due to the thermal etching (Figure 8.44) and not due to any sensitisation effects. As from the boiling acid test it was found that the substrates were not susceptible to sensitisation. The revealing of the grain boundaries at high temperatures was even seen during pulsed laser deposition of YBCO on NiW RABiTS by Y L Cheung et al [259, 261]. The thermal etching effect on Ni RABiTS was also seen by others [32, 264, 265]. Therefore, grain boundaries were revealed as a result of thermal etching and this was also confirmed by heating a bare Hastelloy substrate at 800°C under O_2 atmosphere for three hours, where the same grain boundary structure was observed (Figure 8.48).

For MgO films, it can be seen that the surface roughness increased by annealing. It was 27 nm for the sample before annealing (Figure 8.8) and became 60 nm (as an average of three readings) for the sample annealed at 800°C for three hours and 240 nm (as an average of three readings) for the sample annealed at 1000°C for three hours. The EDX test showed an increase in the Cr and Ni content in addition to very low percentage of Mg, and this can be used to suggest the presence of complex oxides and the disappearance of the MgO (200) peak.

From this, it is clear that annealing up to 650°C was not improving the texture nor deteriorating the MgO film. However, annealing at 800°C-1000°C affected the surface stability by the oxidation of the substrate.

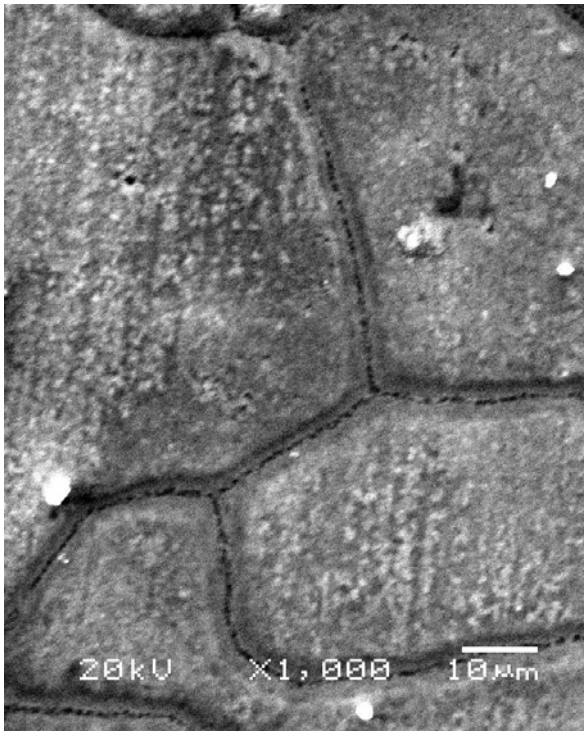

Figure 8.44: SEM image for the Hastelloy substrate deposited with MgO at 600°C for 32 minutes from 0.093M solution then annealed at 800°C under O_2 for three hours.

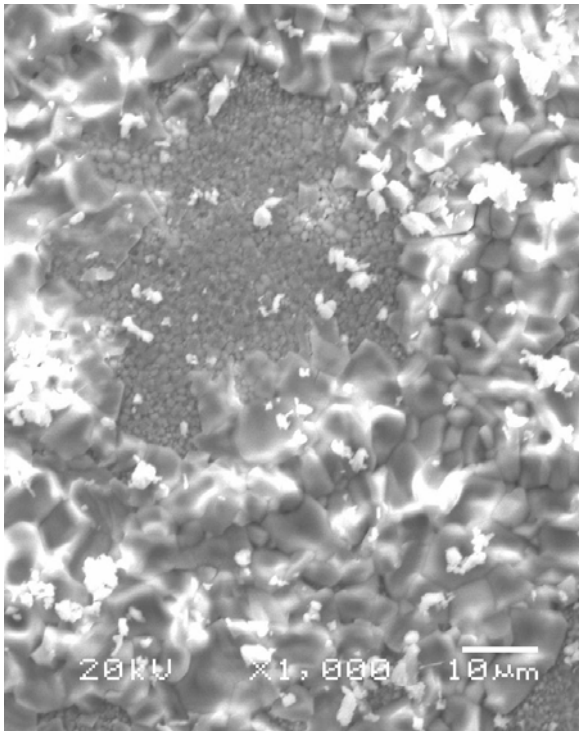

Figure 8.45: SEM image for the Hastelloy substrate deposited with MgO at 600°C for 32 minutes from 0.093M solution then annealed at 1000°C under O_2 for three hours.

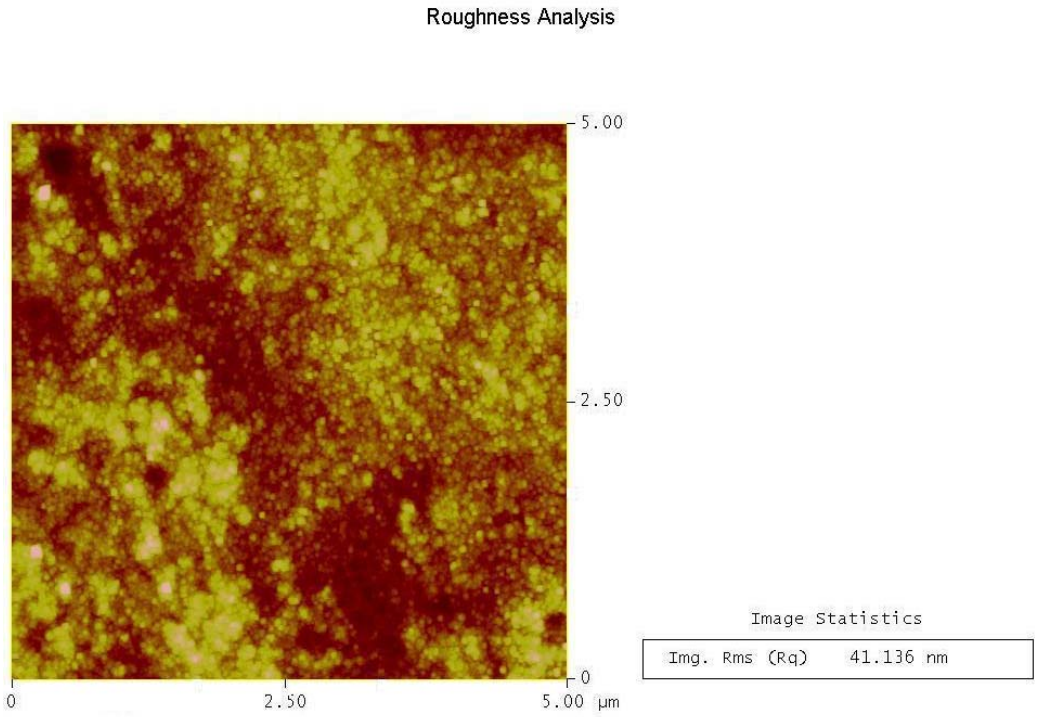

Figure 8.46: A 5x5µm^2 AFM image for the Hastelloy substrate deposited with MgO at 600°C for 32 minutes from 0.093M solution then annealed at 800°C under O_2 for three hours.

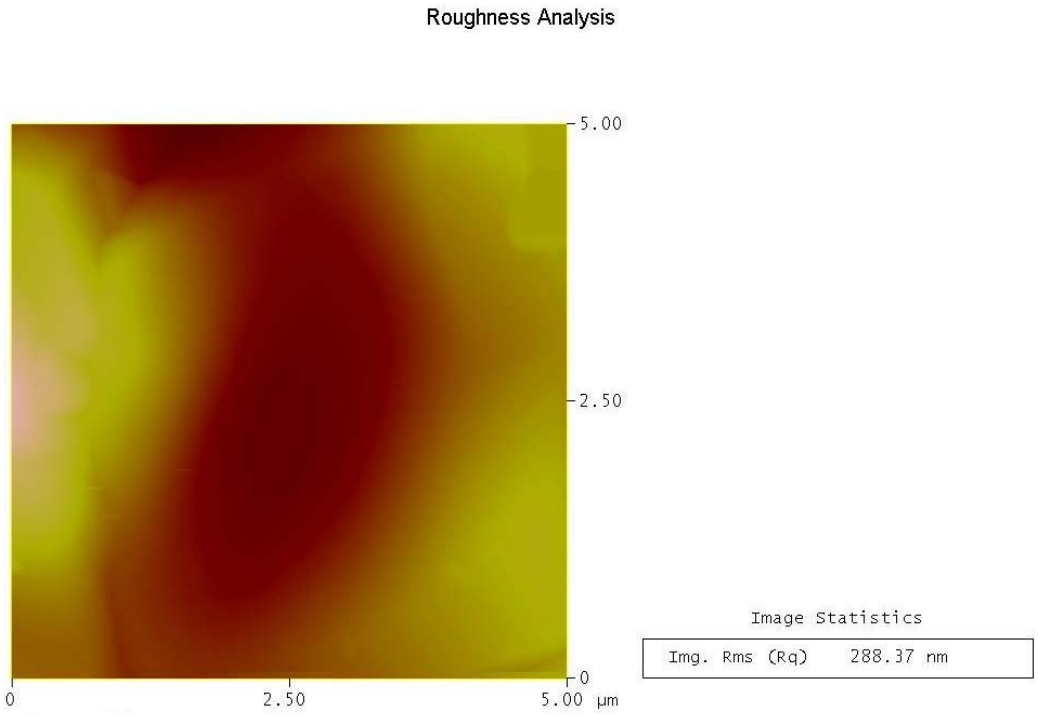

Figure 8.47: A 5x5µm^2 AFM image for the Hastelloy substrate deposited with MgO at 600°C for 32 minutes from 0.093M solution then annealed at 1000°C under O_2 for three hours.

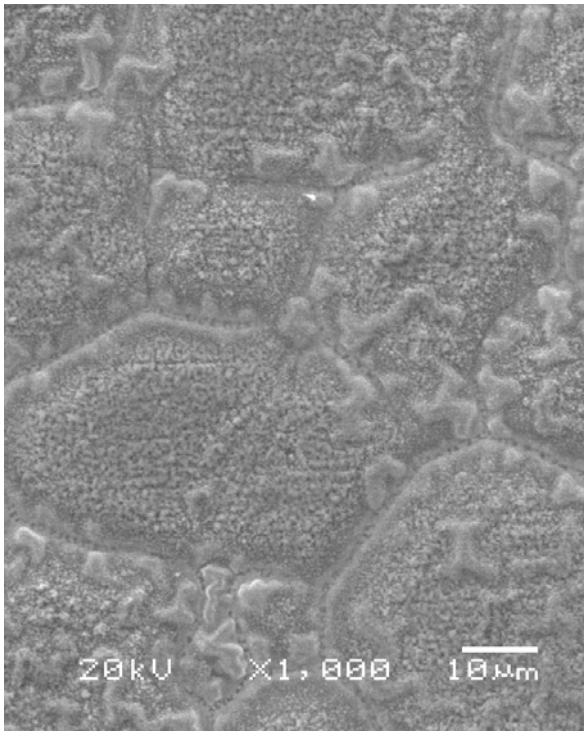

Figure 8.48: SEM image for a bare Hastelloy C276 substrate annealed at 800°C under O_2 for three hours.

8.10.2 Annealing under vacuum

The high temperature annealing under O_2 atmosphere resulted in substrate oxidation. Therefore, to protect the substrate from oxidation, high temperature annealing should be done in an O_2-free environment. This suggests doing the annealing under vacuum. The vacuum annealing experiments were carried out using the same system, the same conditions and following the same procedures as those done for the MgO films from the nitrate precursors (section 7.11.2).

Figure 8.49 shows the XRD pattern for the sample deposited at 600°C for 32 minutes from a 0.093M solution after being annealed under vacuum (~ $2x10^{-6}$ mbar) at different temperatures and times. A narrow XRD scan is given in Figure 8.50. It can be seen that up to 800°C with annealing time of three hours, no oxides were formed but at the same time, no improvement in the MgO (200) texture was obtained. The surface morphology and roughness were the same as that before annealing (Figure 8.6 and Figure 8.8). This confirms that the MgO film is stable under vacuum atmosphere up to 800°C which is good for later YBCO deposition as will be seen in section 8.11. By increasing the annealing temperature to 1000°C, the MgO (200) peak disappeared, besides that, the SEM image (Figure 8.51) show that the MgO film was

severely affected and grain boundaries were revealed on the substrate as a result of thermal etching. The EDX test showed Mg deficiency (Figure 8.52 and Table 8.3). This deficiency was due to Mg evaporation as was the case with the nitrate precursor (Figure 7.61) and confirmed when annealing MgO single crystals at the same conditions (Table 7.7 and Table 7.8). This behaviour was not mentioned by researchers who applied annealing treatments on MgO substrates [191-193]. However, some groups found that annealing MgB_2 resulted in Mg evaporation. K. A. Yates et al found that annealing MgB_2 (in vacuum) at 500°C resulted in significant Mg loss [277]. Z. Y. Fan et al [278] found that the onset of significant Mg evaporation under vacuum (10^{-9} torr) was observed near 425°C. The surface roughness of the sample increased from 27 nm before annealing (Figure 8.8) to about 50 nm after annealing (Figure 8.53). This increase in roughness was due to the high annealing temperature. This may enhance diffusion processes to occur in the MgO film leading to the formation of a rough surface.

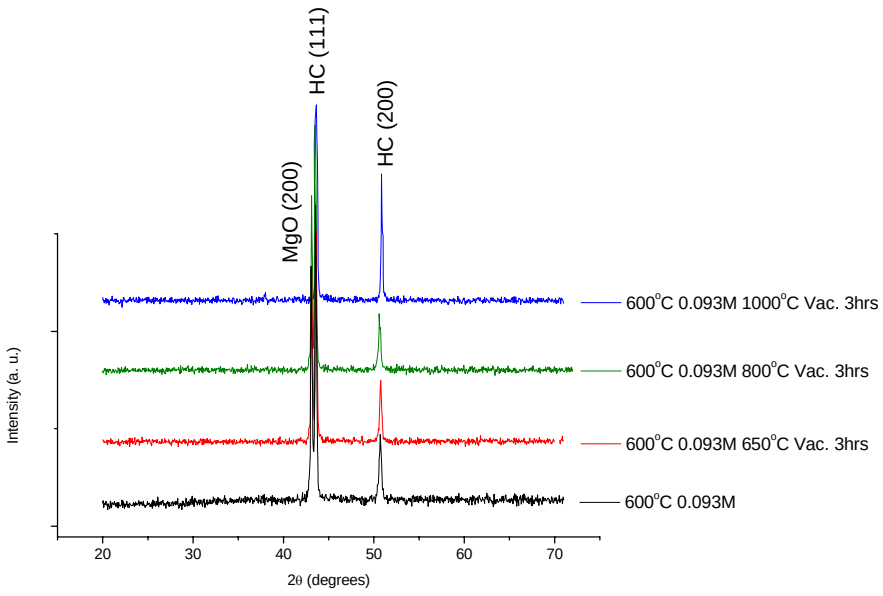

Figure 8.49: XRD patterns for the Hastelloy substrate deposited with MgO from 0.093M at 600°C for 32 minutes after vacuum anneal at different temperatures and times.

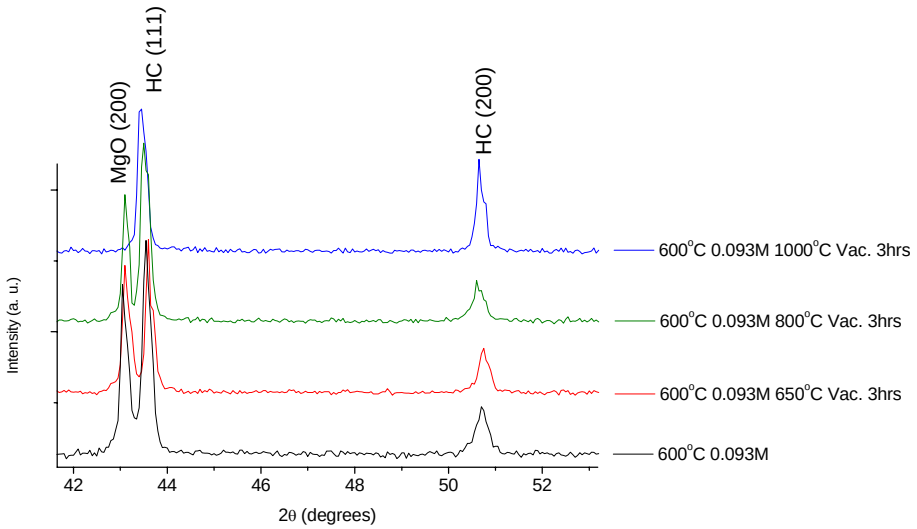

Figure 8.50: XRD patterns with a narrow scan for the Hastelloy substrate deposited with MgO from 0.093M at 600°C for 32 minutes after vacuum anneal at different temperatures and times.

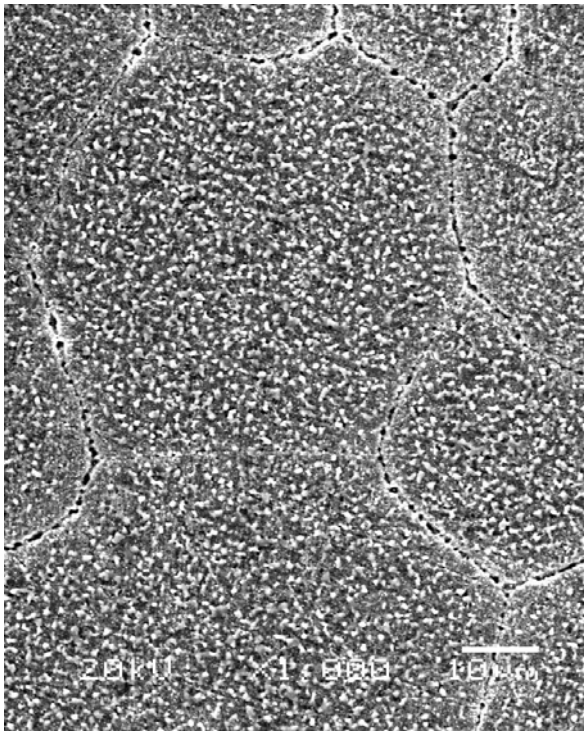

Figure 8.51: SEM image for the Hastelloy substrate deposited with MgO at 600°C for 32 minutes from 0.093M solution then annealed at 1000°C under vacuum for three hours.

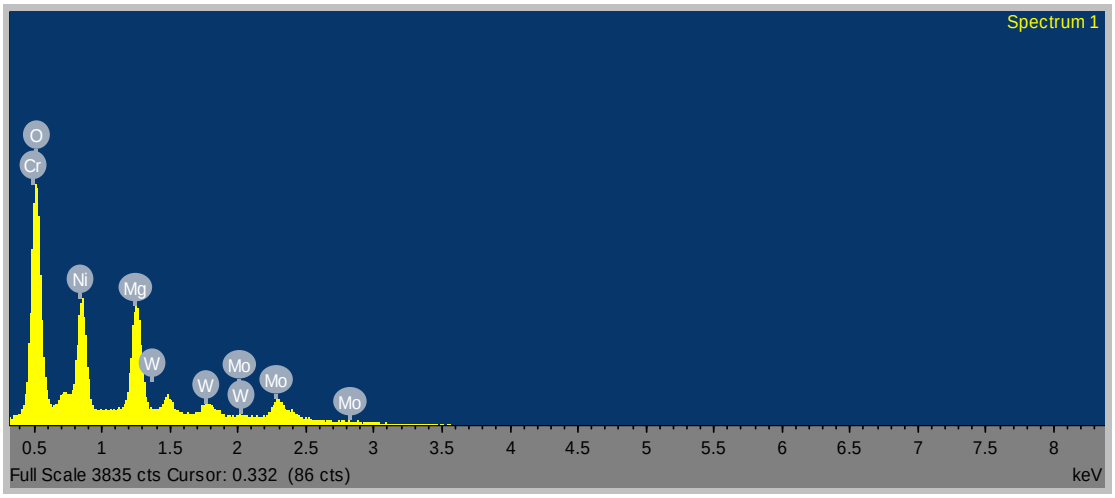

Figure 8.52: EDX spectrum, using an accelerating voltage of 4KV, for MgO film deposited on Hastelloy C276 using 0.093M at 600°C with a deposition time of 32 minutes after being annealed at 1000°C for 3 hours.

Table 8.3: Summary of the EDX chemical composition results, using an accelerating voltage of 4KV, for MgO film deposited on Hastelloy C276 using 0.093M at 600°C with a deposition time of 32 minutes after being annealed at 1000°C for 3 hours.

Element	at %
O K	42.87
Mg K	17.81
Cr L	11.79
Ni L	15.35
Mo L	10.71
W M	1.47

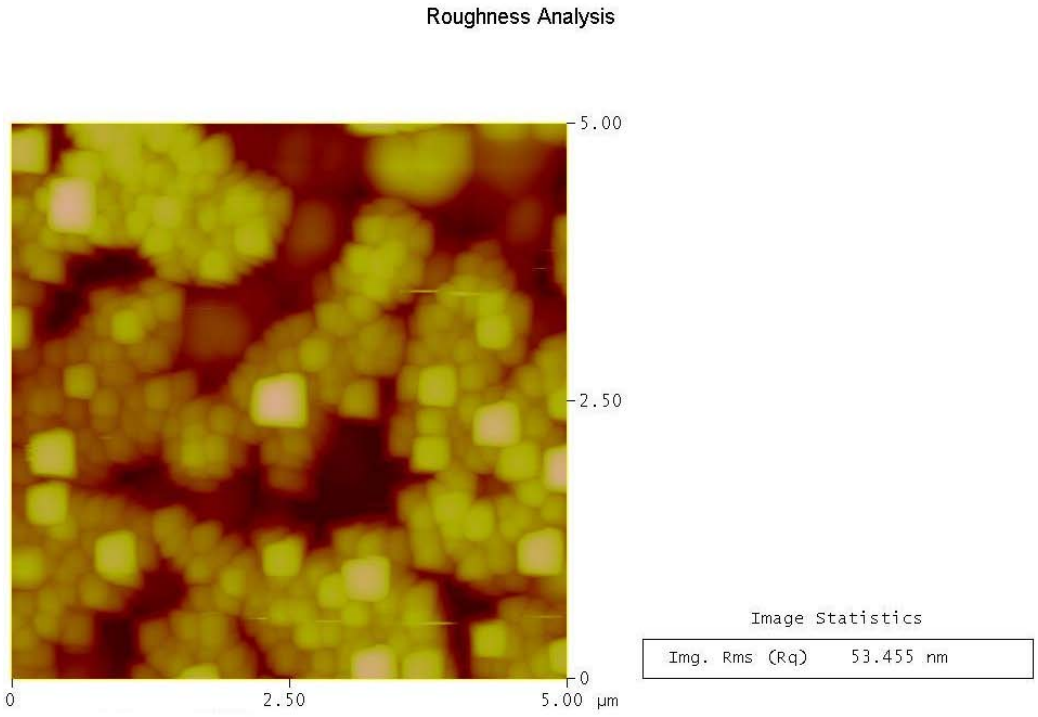

Figure 8.53: A 5x5µm^2 AFM image for the Hastelloy substrate deposited with MgO at 600°C for 32 minutes from 0.093M solution then annealed at 1000°C under vacuum for three hours**.**

In order to confirm that Mg evaporation needs high vacuum and high temperature to evaporate, we conducted a high temperature anneal using purified Ar. After pumping the system to 3.75x10^{-7} torr, 0.25 bar (0.246 atm.) of purified Ar was purged to the system. The purification was made to get rid of any traces of oxygen or moisture that may be present in Ar. After that, the sample was heated to 1000°C at a rate of 300°C/hr and held at that temperature for three hours then the sample was furnace cooled.

The XRD patterns in Figure 8.54 show that the annealing under purified Ar, for the sample deposited from 0.093M solution at 600C for 32 minutes, did not result in the elimination of the MgO (200) as a result of Mg evaporation as occurred during vacuum anneal (Figure 8.50), however, the peak intensity was slightly lower compared to that before Ar anneal. This confirms that the high temperature of annealing should be combined with high vacuum to lead to significant Mg evaporation. The SEM image for the sample after Ar annealing is shown in Figure 8.55. The AFM showed an RMS value of 45 nm compared to 27 nm for the sample before annealing (Figure 8.6 and Figure 8.8). This may be attributed to the high

temperature anneal which enhanced diffusion processes leading to the formation of tiny particles which in turn contribute to the deterioration of the surface smoothness.

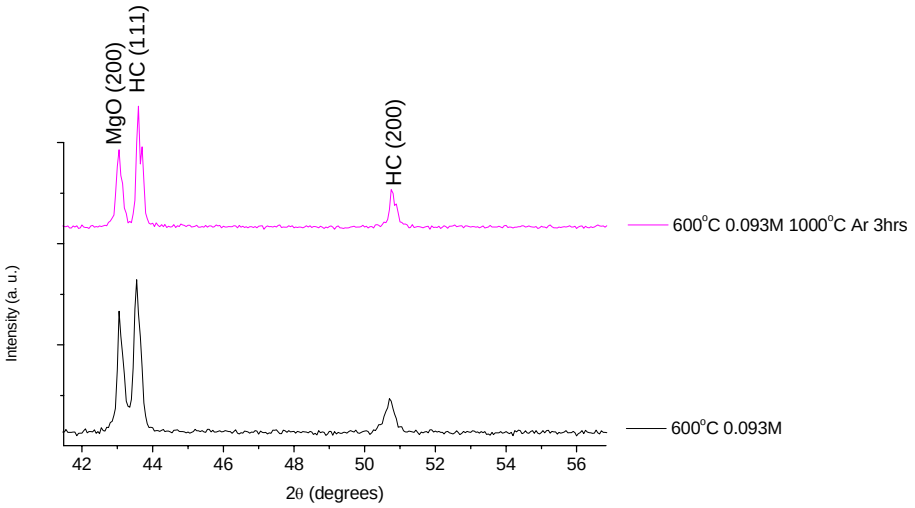

Figure 8.54: XRD patterns for the Hastelloy substrate deposited with MgO from 0.093M solution at 600°C for 32 minutes then annealed under 0.25 bar purified Ar at 1000°C for three hours.

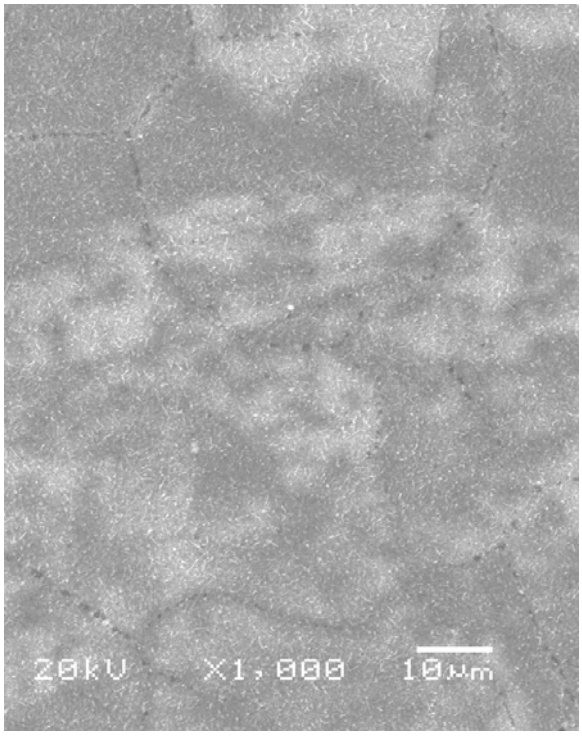

Figure 8.55: SEM image for the Hastelloy substrate deposited with MgO from 0.093M solution at 600°C for 32 minutes then annealed under 0.25 bar purified Ar at 1000C for three hours.

8.11 YBCO and ceria (CeO_2) deposition by PLD

8.11.1 Introduction

As in the previous chapters an objective of this work is to grow MgO as the only buffer layer before YBCO deposition in an attempt to make the process a cost-effective one by reducing the usual multi-layer buffer architecture to a single layer. To evaluate the performance of the MgO as a buffer the YBCO films have been deposited by PLD. This is a well established route to high quality films [244, 245], although spray pyrolysis of the YBCO layer should also be a possibility in the future [23, 24, 87, 93, 94]. YBCO deposition parameters were the same as those mentioned in section 7.12.1.

8.11.2 YBCO deposition on MgO spray pyrolysed at different temperatures, precursor concentrations and deposition times.

Before YBCO deposition, the MgO films deposited from 0.093M at 550°C and 600°C were heated in the YBCO deposition chamber at the same conditions used for YBCO deposition to see the stability of MgO film. It was found that the intensity of MgO (200) peak, surface morphology and surface smoothness were the same before and after the heating. This confirmed the stability of MgO film during YBCO deposition.

YBCO was deposited by PLD on MgO films spray pyrolysed at different conditions. The MgO and YBCO peaks were indexed according to the JCPDS PDF files 00-045-0946 and 00-038-1433, respectively. The XRD patterns in Figure 8.56 show that YBCO films deposited on MgO films deposited by spray pyrolysis from 0.093M solution at different deposition temperatures and times were polycrystalline. The film deposited from 0.279M solution at 600°C for a deposition time for 32 minutes was polycrystalline as well. The SEM images (Figure 8.57-Figure 8.60) of YBCO films deposited on MgO spray pyrolysed at the aforementioned conditions showed a granular structure. The roughness of the deposited YBCO films (Figure 8.61-Figure 8.64) was found to be higher than the corresponding values of the MgO buffers (Figure 8.19, Figure 8.20, Figure 8.8, and Figure 8.28, respectively).

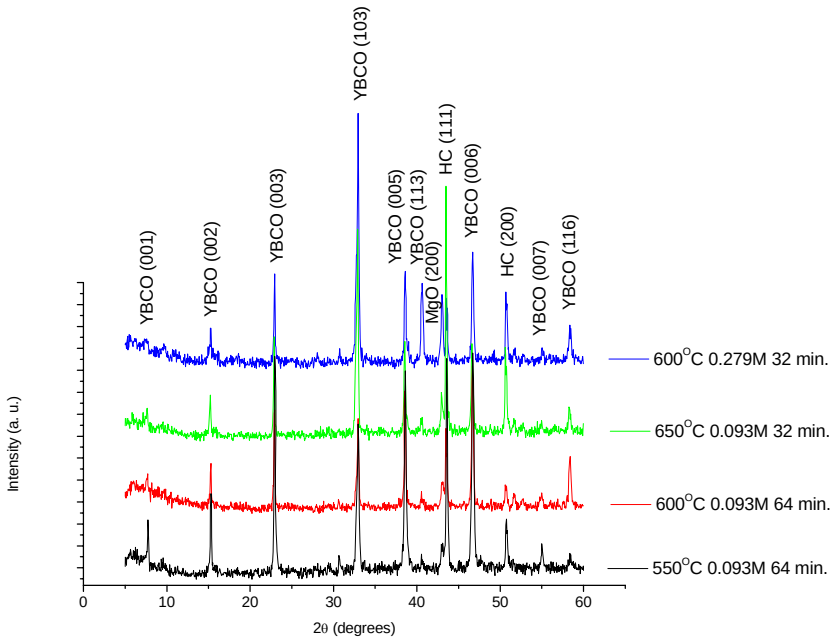

Figure 8.56: XRD patterns for YBCO films deposited by PLD on the MgO films spray pyrolysed at different conditions.

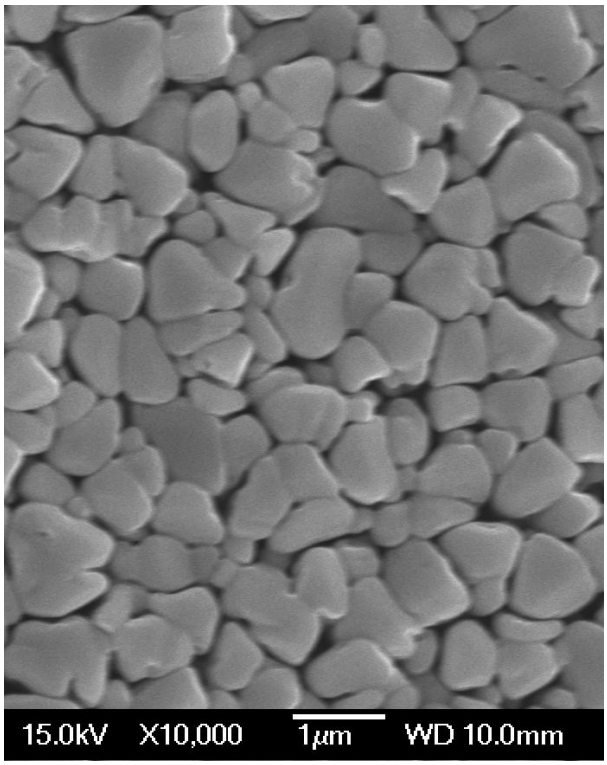

Figure 8.57: SEM image for YBCO film deposited on MgO film spray pyrolysed on Hastelloy C276 using 0.093M $Mg(CH3COO)_2.4H_2O$ at 550°C for 64 minutes.

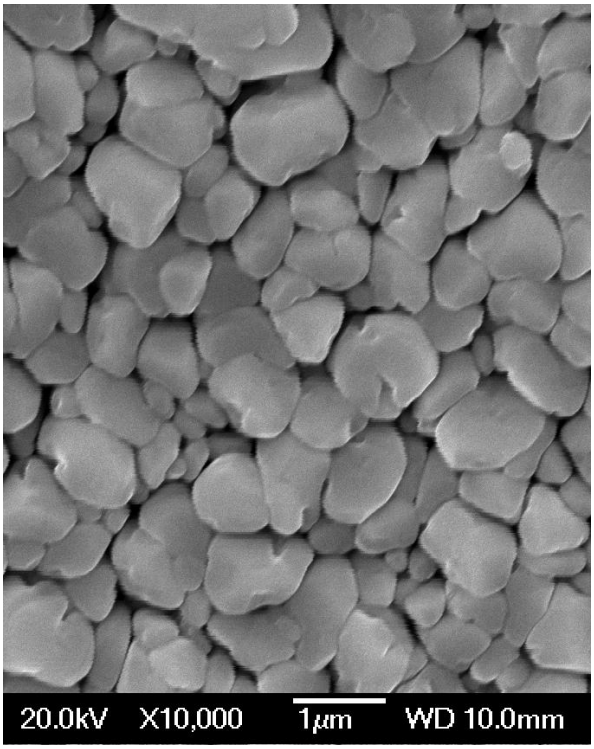

Figure 8.58: SEM image for YBCO film deposited on MgO film spray pyrolysed on Hastelloy C276 using 0.093M $Mg(CH3COO)_2.4H_2O$ at 600°C for 64 minutes.

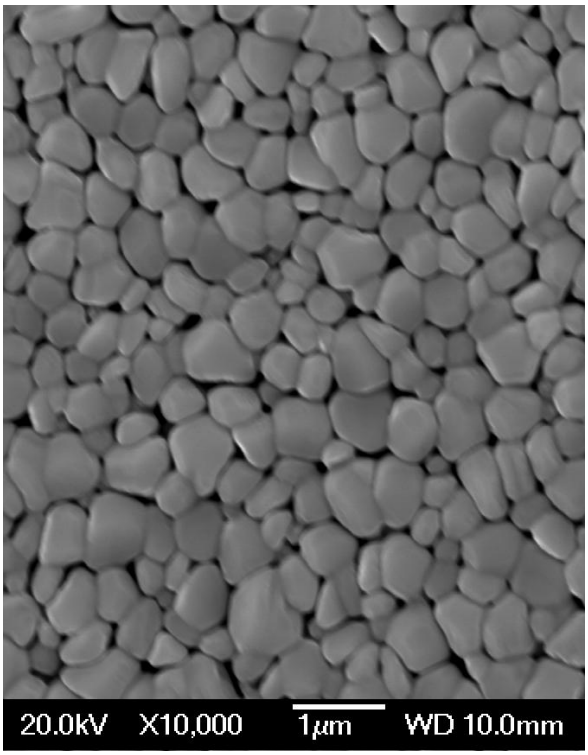

Figure 8.59: SEM image for YBCO film deposited on MgO film spray pyrolysed on Hastelloy C276 using 0.093M $Mg(CH3COO)_2.4H_2O$ at 650°C for 32 minutes.

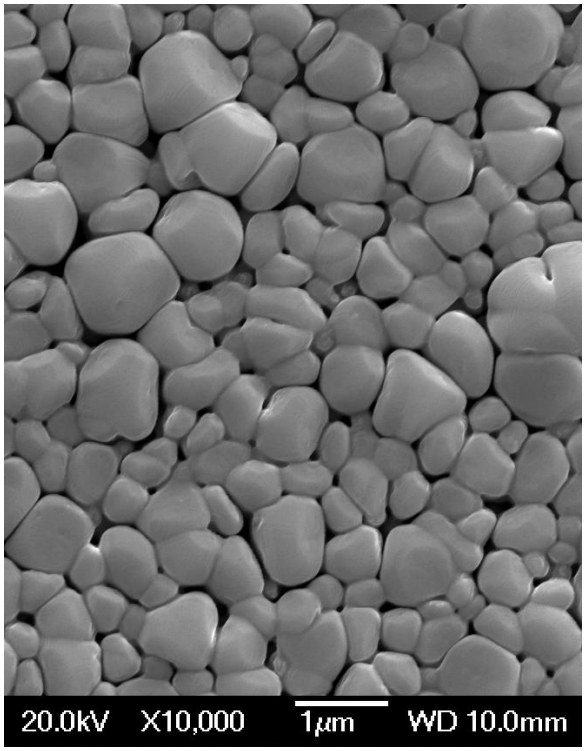

Figure 8.60: SEM image for YBCO film deposited on MgO film spray pyrolysed on Hastelloy C276 using 0.279M $Mg(CH3COO)_2.4H_2O$ at 600°C for 32 minutes.

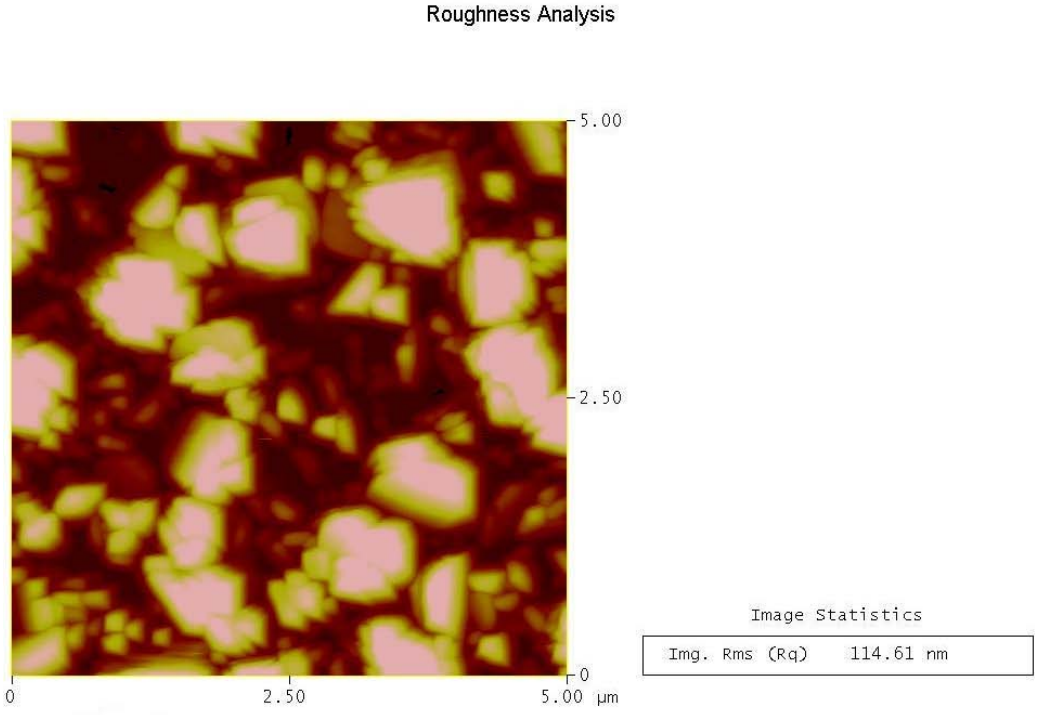

Figure 8.61: A 5x5μm^2 AFM image for YBCO film deposited on MgO film spray pyrolysed on Hastelloy C276 using 0.093M $Mg(CH3COO)_2.4H_2O$ at 550°C for 64 minutes.

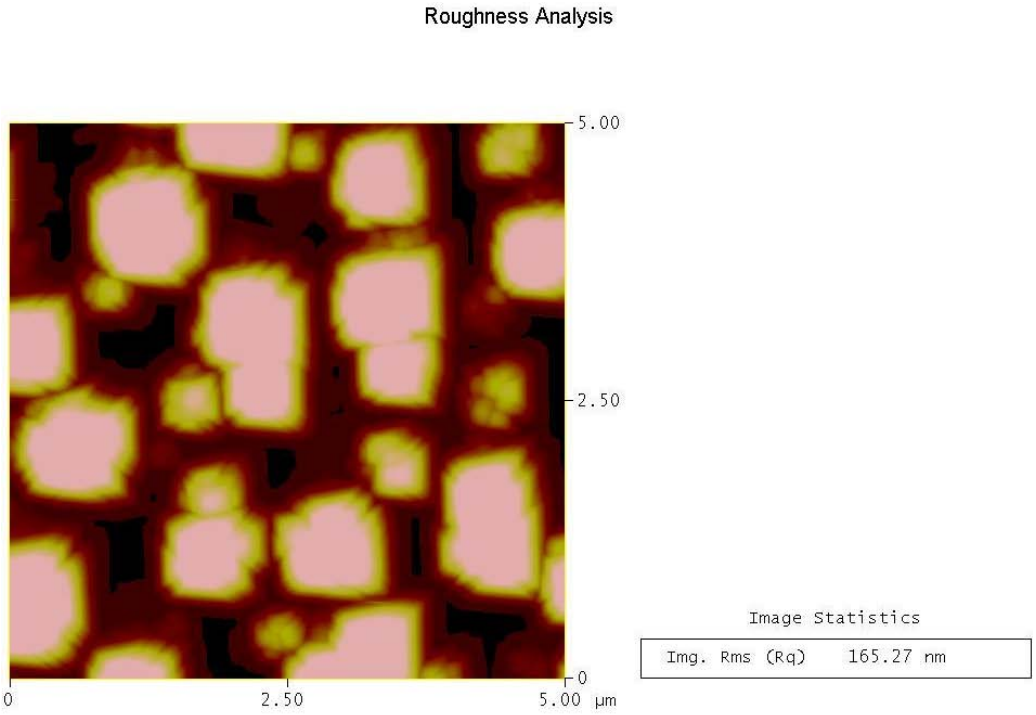

Figure 8.62: A 5x5µm^2 AFM image for YBCO film deposited on MgO film spray pyrolysed on Hastelloy C276 using 0.093M $Mg(CH3COO)_2.4H_2O$ at 600°C for 64 minutes.

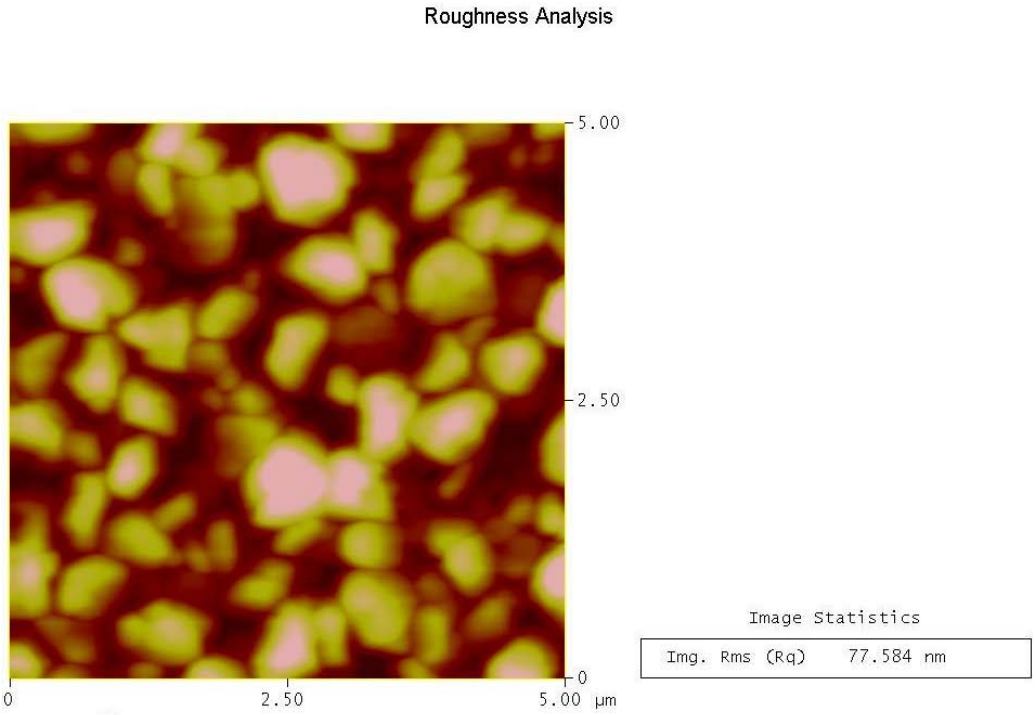

Figure 8.63: A 5x5µm^2 AFM image for YBCO film deposited on MgO film spray pyrolysed on Hastelloy C276 using 0.093M $Mg(CH3COO)_2.4H_2O$ at 650°C for 32 minutes.

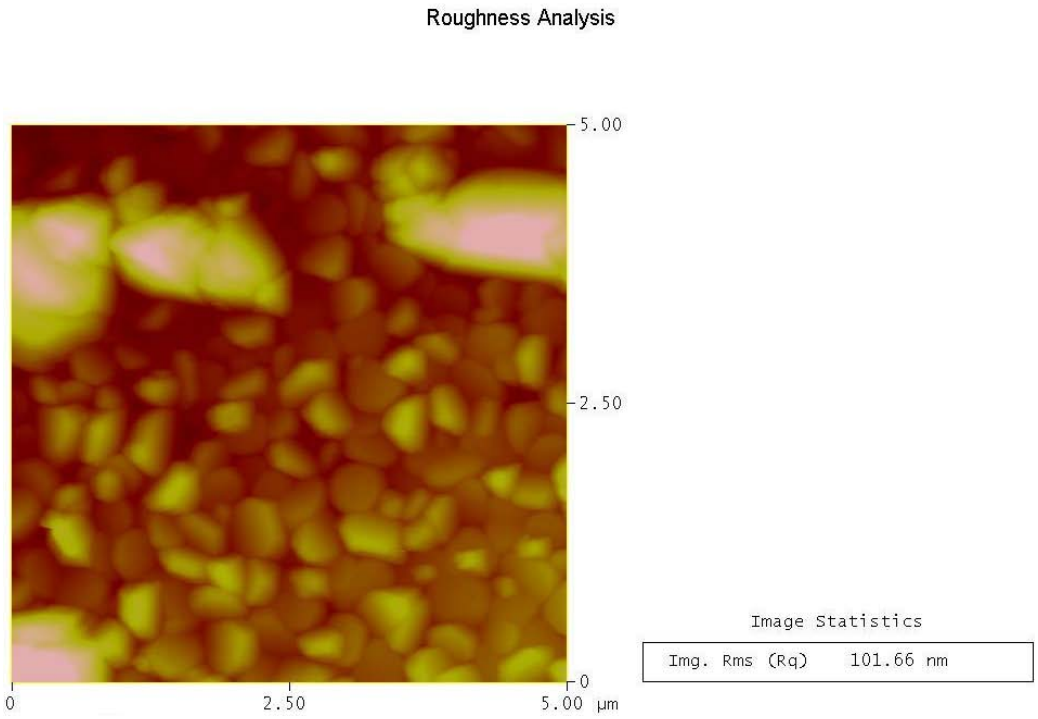

Figure 8.64: A 5x5µm^2 AFM image for YBCO film deposited on MgO film spray pyrolysed on Hastelloy C276 using 0.279M $Mg(CH3COO)_2.4H_2O$ at 600°C for 32 minutes.

From the above, it was clear that the MgO films with RMS roughness greater than about 42 nm (Figure 8.8, Figure 8.19, Figure 8.20, and Figure 8.28) resulted in polycrystalline YBCO films (Figure 8.56). Only the smoothest MgO films (Figure 8.8, Figure 8.23, and Figure 8.27), i.e. the ones deposited at 600°C and 550°C using 0.093M for 32 minutes, and the ones deposited at 600°C using 0.093M for 32 minutes with a double deposition, and at 600°C using 0.14M for 32 minutes, showed a well textured YBCO films (Figure 8.65). However, a weak 103 peak was obtained and was believed to be due to nucleation problems during the PLD deposition of YBCO. Such peak was even seen for YBCO films deposited on MgO single crystals (Figure 4.57). The (103) was lowest for the films deposited from 0.093M at 550°C and 600°C for 32 minutes. This demonstrates the critical role of the surface smoothness of MgO films, deposited by spray pyrolysis from the acetate precursor, on the subsequent growth of YBCO films as was the case for the nitrate precursor (section 7.12). The SEM images for YBCO films show that the films were more continuous (Figure 8.66-Figure 8.69) and smoother as can be seen from the AFM images in Figure 8.70-Figure 8.73, compared to YBCO films deposited on spray pyrolysed MgO films under different conditions (Figure 8.57-Figure 8.64). The film deposited at 550°C and 600°C from

0.093M solution for 32 minutes were found to be smoother (RMS 33 nm and 35nm, respectively) compared to the films deposited at 600°C for 32 minutes using 0.093M with a double deposition and 0.14M (RMS 60nm and 67, respectively). However, pores were formed in all of the YBCO films. Such porous films were noticed by others where it was attributed to the formation of Y_2O_3 or BaY_2O_4 [208, 209, 212]. The texture of MgO (200) was measured qualitatively using the X-ray pole figure scans (Figure 8.12) and quantitatively using the X-ray ω-scans (Figure 8.14) for the films deposited from 0.093M solution at 600°C for 32 minutes. From one hand, MgO films deposited at 550°C and 600°C show the same weak out-of-plane and in-plane texture. On the other hand, the YBCO films deposited on the MgO films spray pyrolysed from 0.093M at 550°C and 600°C for 32 minutes had a better out-of-plane texture (Figure 8.74 and Figure 8.75) with a FWHM of 12.5° and 11.6°, respectively (Figure 8.76 and Figure 8.77, respectively). The improvement of YBCO out-of-plane texture relative to the underlying buffers and substrate was observed by D. P. Norton et al [257] where they found that the out-of-plane texture of YBCO was narrower than the (100) Ni substrate and the CeO_2 and YSZ buffers. This improvement resulted from the low (001) surface energy and the anisotropic film growth nature commonly observed for YBCO [290]. The in-plane texture for the films deposited at 550°C and 600°C was weak, however the film deposited at 600°C, show a kind of good in-plane texture (Figure 8.75), although it was still weak and was confirmed by the phi scan in Figure 8.78 which shows a FWHM of 40°. This implied that the texture of the underlying MgO layer was copied by the growing YBCO film. It was also noticed that both films i.e. the one deposited at 550°C and 600°C, had a good number of low angle grain boundaries in addition to the presence of high angle grain boundaries (Figure 8.79 and Figure 8.80).

Figure 8.81 is a cross sectional SEM image for YBCO film deposited on MgO spray pyrolysed at 600°C from 0.093M solution for 32 minutes. It can be seen that YBCO, and MgO films had thicknesses of about 1.013 μm, 220 nm respectively. This means that the deposition rate of YBCO was 10013/5000 = 2 Å/pulse, and for MgO 2200Å / (240sec) = 9.16 Å/sec which were close to that obtained for MgO deposition from the nitrate precursor (section 7.8 and 7.12.4). The EDX scan suggested that the YBCO film was nearly stoichiometric i.e. a ratio of Y:Ba:Cu was 1:2.06:3.2. An EDX line scan across the substrate and the deposited MgO and YBCO films was performed to see if MgO was a good barrier to diffusion or not (Figure 8.82). The figure shows

(as a weight %) that there was neither a diffusion of elements from the substrate to YBCO film nor diffusion of YBCO elements to the substrate through the MgO buffer layer and this confirmed that MgO functioned as a good diffusion barrier.

AC susceptibility at zero field showed a broad superconducting transition temperature for all of the deposited YBCO films shown in Figure 8.65 with a T_c onset of about 84.8K (Figure 8.83). From the AC curves it can be seen that the YBCO film deposited on the spray pyrolysed MgO using 0.093M solution at 600°C for 32 minutes show a slightly better transition which can be attributed to a combination of continuous, smoother and better texture of YBCO films deposited on such MgO films compared to YBCO films deposited on the MgO films which were deposited under the other spray pyrolysis conditions. YBCO films shown in Figure 8.56 had no T_c.

The effect of inclination angle, flow rate, annealing under O_2, vacuum or Ar atmospheres resulted either in rough surfaces or in decreasing the intensity of MgO (200) peak. YBCO films deposited on such samples were polycrystalline and showed no T_c.

It is to be noted in this work that inclining the substrate led to untilted MgO films with (200) direction parallel to the substrate normal and did not result in the shadowing effect which was observed for MgO and YSZ films deposited by ISD method using PLD and e-beam evaporation [39-41, 49, 50, 53, 167, 169, 173-175, 177-183]. In this work, spray pyrolysis gave MgO (200) peaks parallel to the substrate normal whether ISD was utilised or not. It was found by researchers that YBCO deposition on c-axis tilted MgO resulted in c-axis tilted YBCO films. The tilt was found to affect the superconducting properties, i.e. J_c and T_c [169, 176, 177]. In this work YBCO films grown on top of the spray pyrolysed MgO films have the (006) of YBCO // (200) of MgO. Thus, spray pyrolysis offers an alternative method of depositing a single MgO buffer layer with no tilting for YBCO deposition.

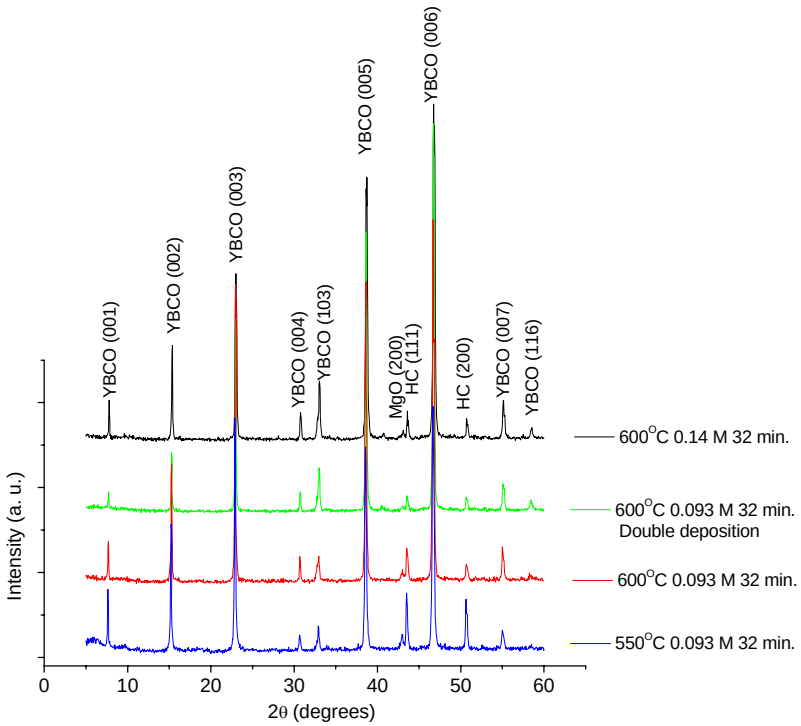

Figure 8.65: XRD patterns for YBCO films deposited by PLD on the MgO films spray pyrolysed at different conditions.

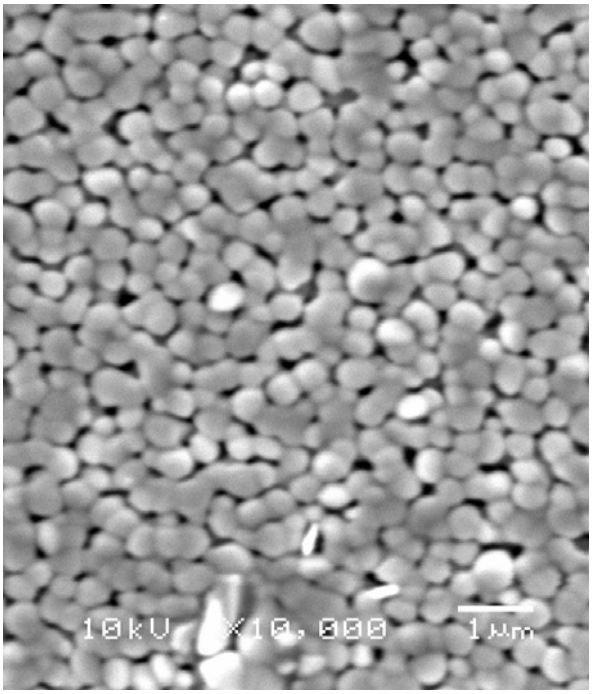

Figure 8.66: SEM image for YBCO film deposited on MgO film spray pyrolysed on Hastelloy C276 using 0.093M $Mg(CH3COO)_2.4H_2O$ at 550°C for 32 minutes.

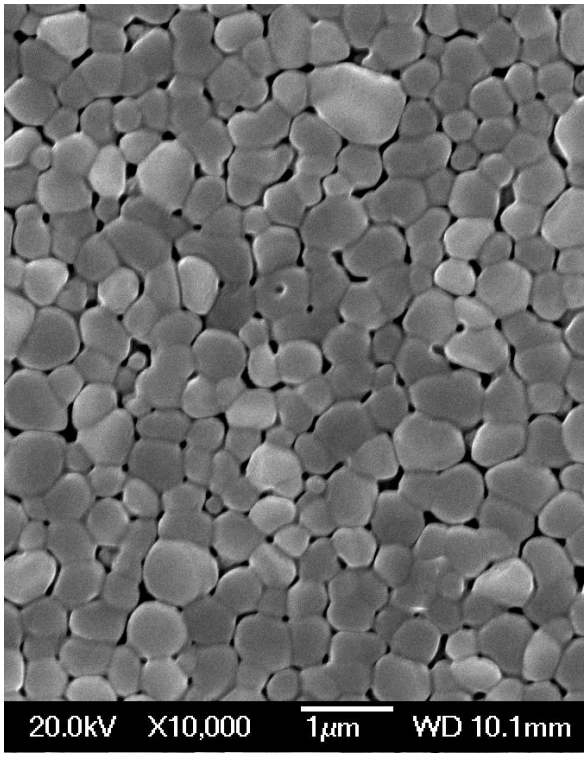

Figure 8.67: SEM image for YBCO film deposited on MgO film spray pyrolysed on Hastelloy C276 using 0.093M $Mg(CH3COO)_2.4H_2O$ at 600°C for 32 minutes.

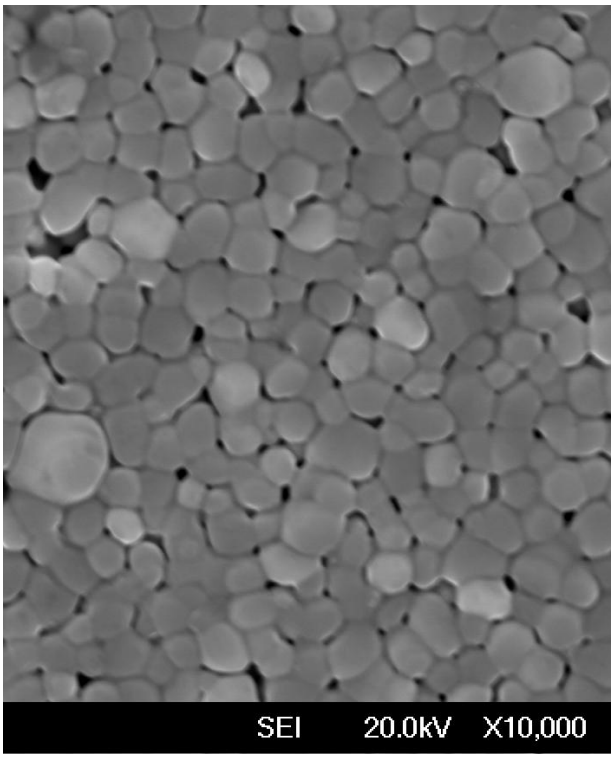

Figure 8.68: SEM image for YBCO film deposited on MgO film spray pyrolysed on Hastelloy C276 using 0.093M $Mg(CH3COO)_2.4H_2O$ at 600°C for 32 minutes, double deposition.

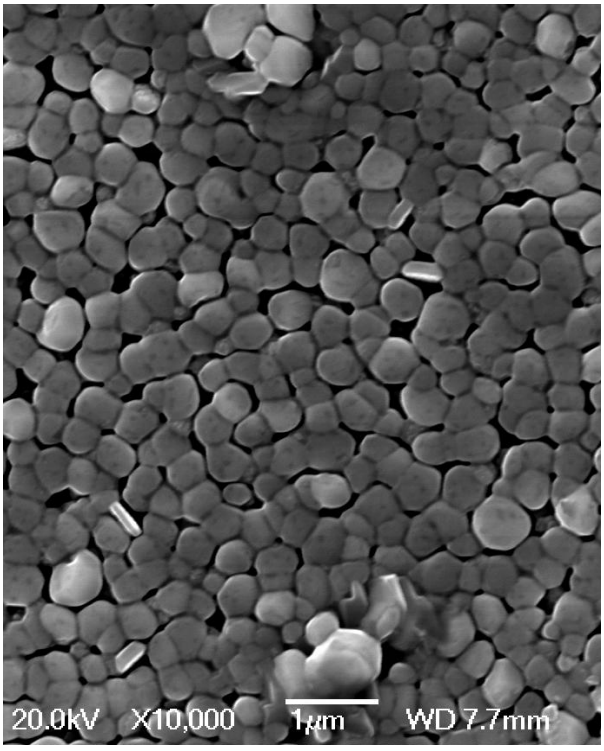

Figure 8.69: SEM image for YBCO film deposited on MgO film spray pyrolysed on Hastelloy C276 using 0.14M $Mg(CH3COO)_2.4H_2O$ at 600°C for 32 minutes.

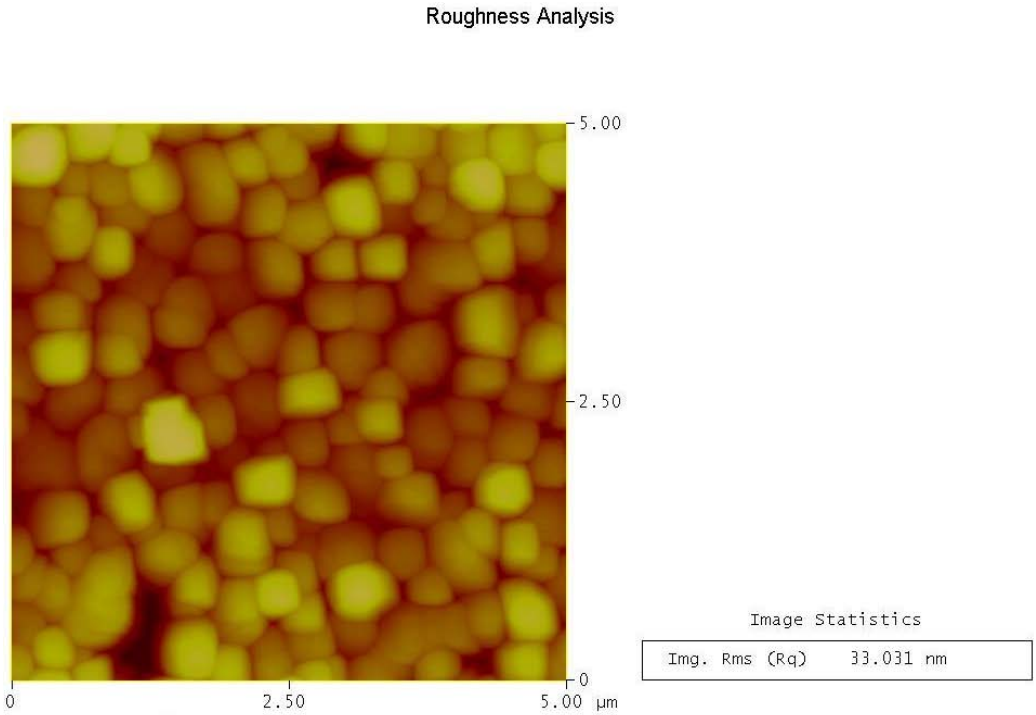

Figure 8.70: A 5x5μm^2 AFM image for YBCO film deposited on MgO film spray pyrolysed on Hastelloy C276 using 0.093M $Mg(CH3COO)_2.4H_2O$ at 550°C for 32 minutes.

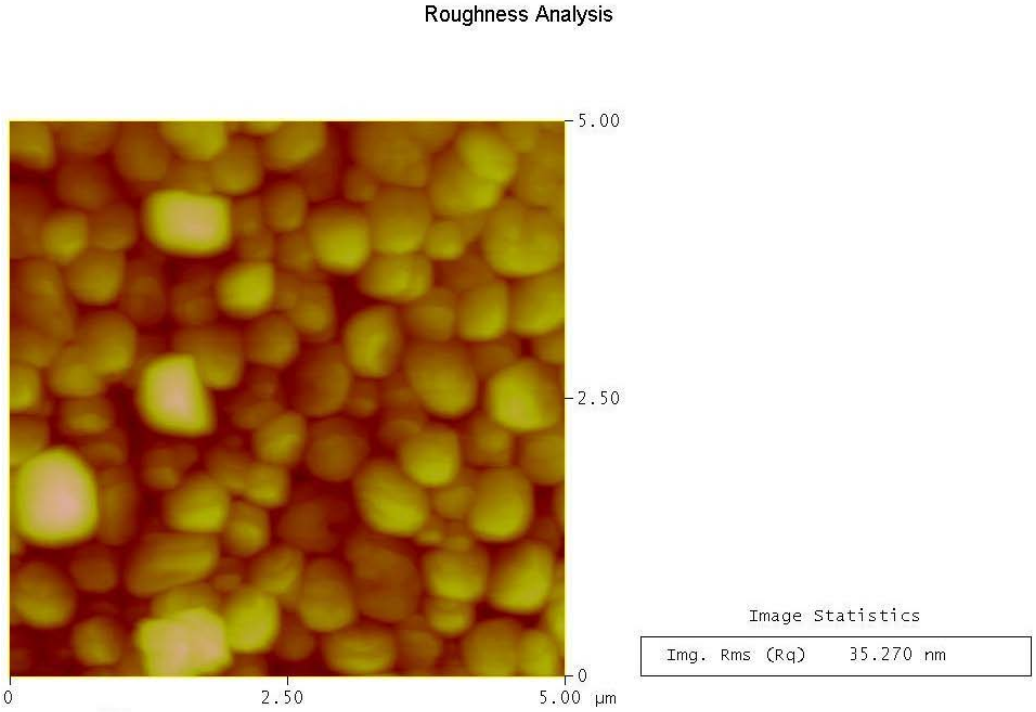

Figure 8.71: A 5x5µm^2 AFM image for YBCO film deposited on MgO film spray pyrolysed on Hastelloy C276 using 0.093M $Mg(CH3COO)_2.4H_2O$ at 600°C for 32 minutes.

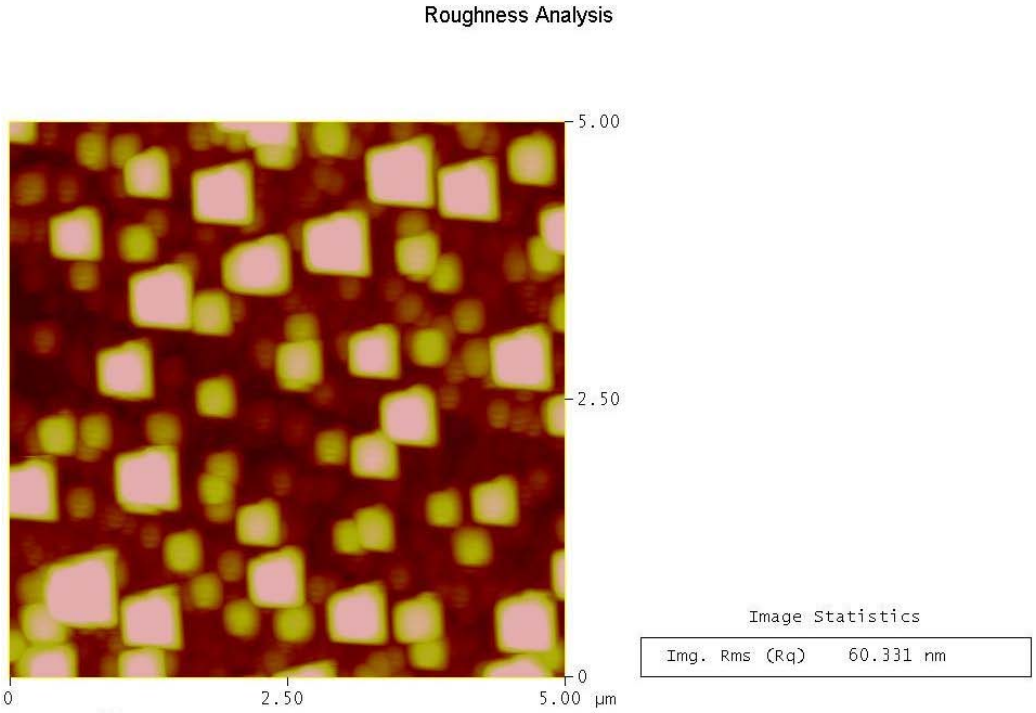

Figure 8.72: A 5x5µm^2 AFM image for YBCO film deposited on MgO film spray pyrolysed on Hastelloy C276 using 0.093M $Mg(CH3COO)_2.4H_2O$ at 600°C for 32 minutes, double deposition.

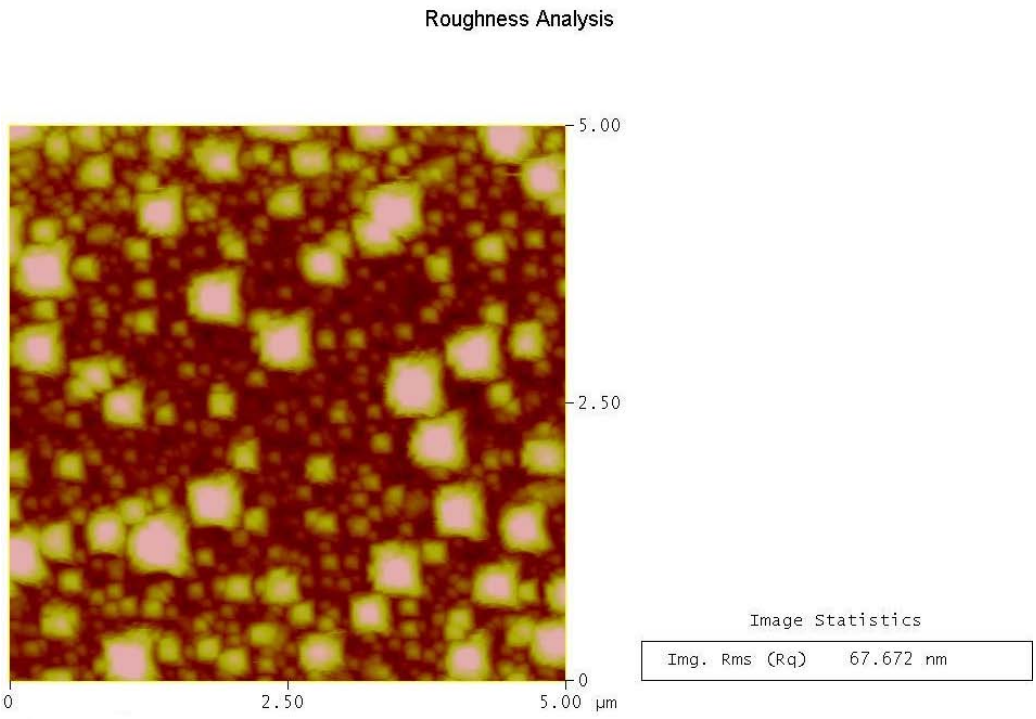

Figure 8.73: A 5x5µm^2 AFM image for YBCO film deposited on MgO film spray pyrolysed on Hastelloy C276 using 0.14M $Mg(CH3COO)_2.4H_2O$ at 600°C for 32 minutes.

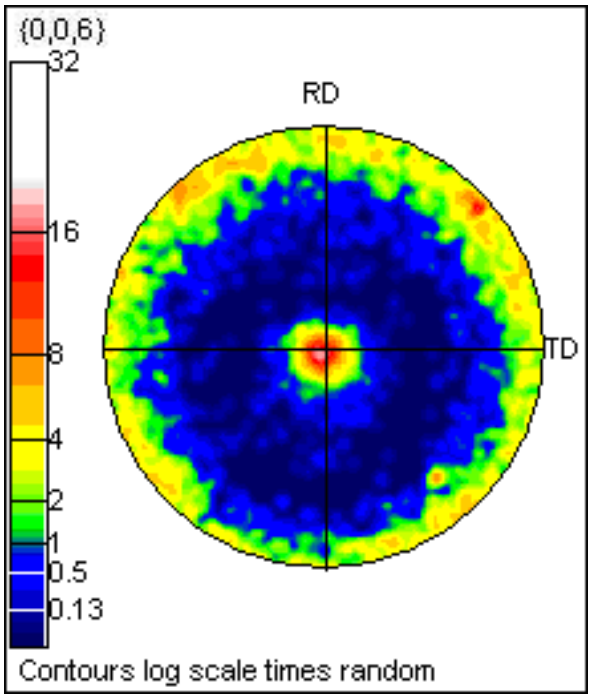

Figure 8.74: EBSD pole figure pattern showing the {006} planes for YBCO film deposited by PLD on Hastelloy substrate buffered with MgO deposited by spray pyrolysis at 550^{o}C for 32 min. from 0.093M $Mg(CH3COO)_2.4H_2O$.

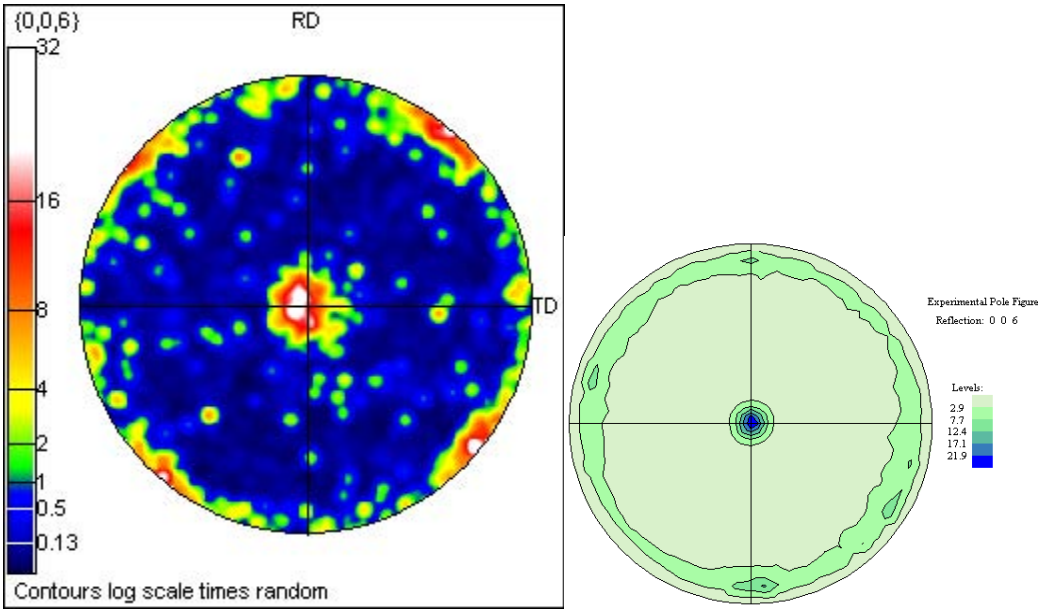

Figure 8.75: EBSD pole figure pattern (left) and (001) X-ray pole figure (right), at 2θ of 46.65°, showing the {006} planes for YBCO film deposited by PLD on Hastelloy substrate buffered with MgO deposited by spray pyrolysis at 600°C for 32 min. from 0.093M $Mg(CH3COO)_2.4H_2O$.

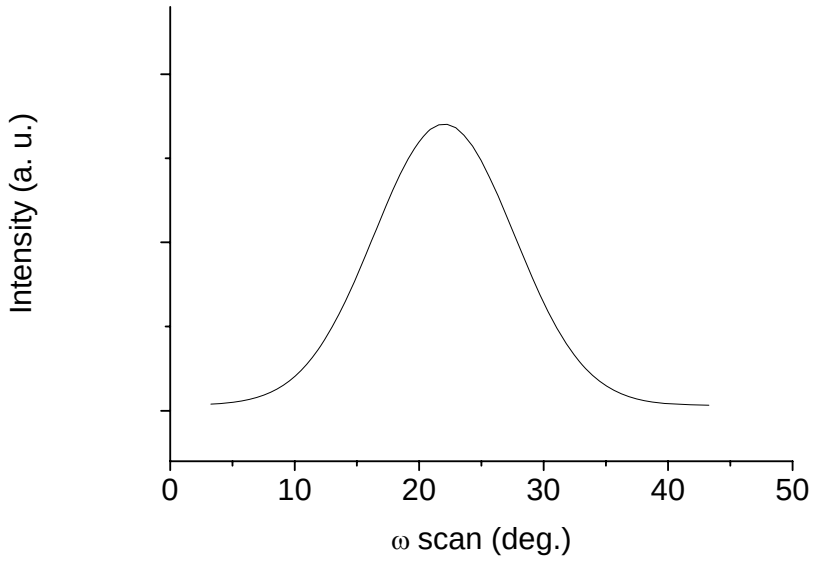

Figure 8.76: X-ray diffraction ω–scan for YBCO film deposited on MgO film spray pyrolysed at 550°C from 0.093M solution showing YBCO (006) with a FWHM of 12.5°.

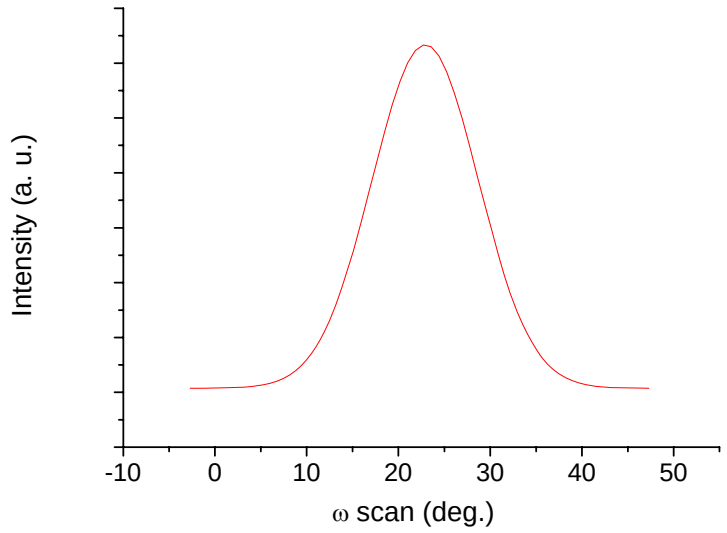

Figure 8.77: X-ray diffraction ω–scan for YBCO film deposited on MgO film spray pyrolysed at 600°C from 0.093M solution showing YBCO (006) with a FWHM of 11.6°.

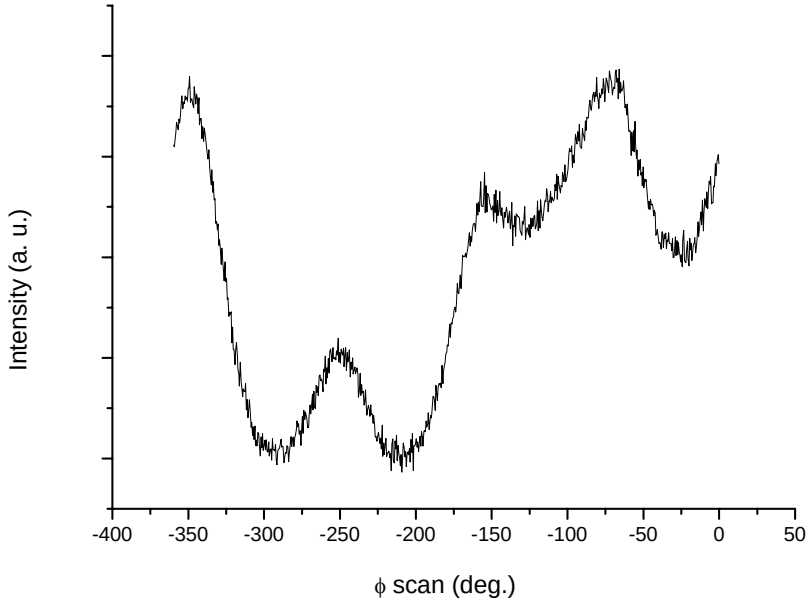

Figure 8.78: X-ray diffraction ϕ–scan for YBCO film deposited on MgO film spray pyrolysed at 600°C from 0.093M solution showing YBCO (013) with a FWHM of about 40°.

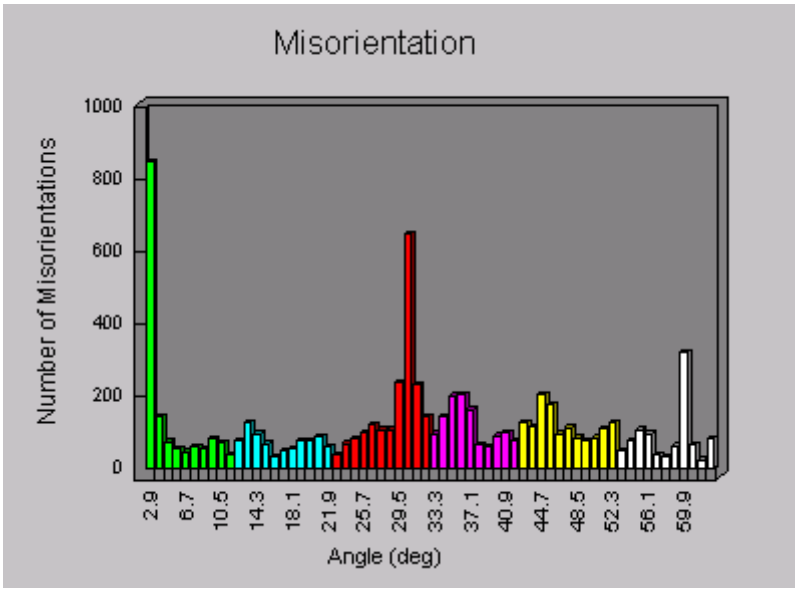

Figure 8.79: EBSD histogram showing grain misorientation angles for YBCO film deposited on MgO film spray pyrolysed on Hastelloy C276 using 0.093M $Mg(CH3COO)_2.4H_2O$ at 550°C for 32 minutes.

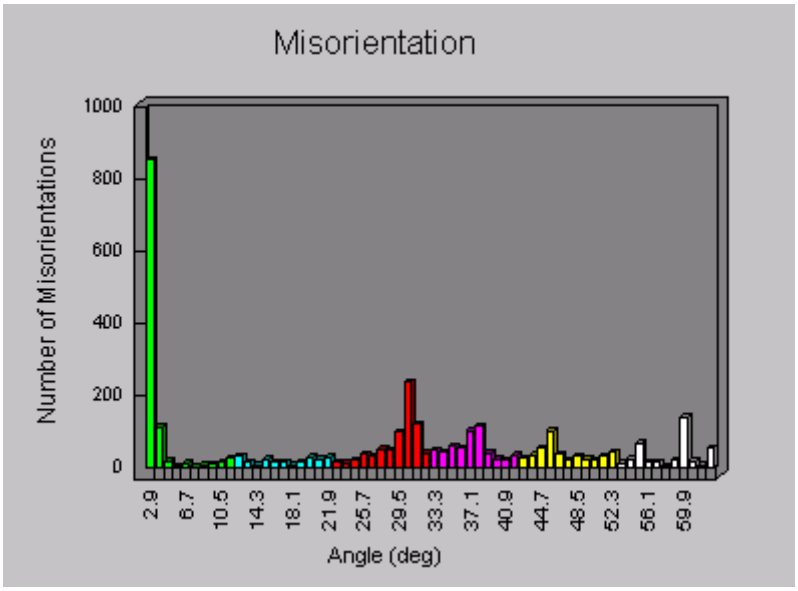

Figure 8.80: EBSD histogram showing grain misorientation angles for YBCO film deposited on MgO film spray pyrolysed on Hastelloy C276 using 0.093M $Mg(CH3COO)_2.4H_2O$ at 600°C for 32 minutes.

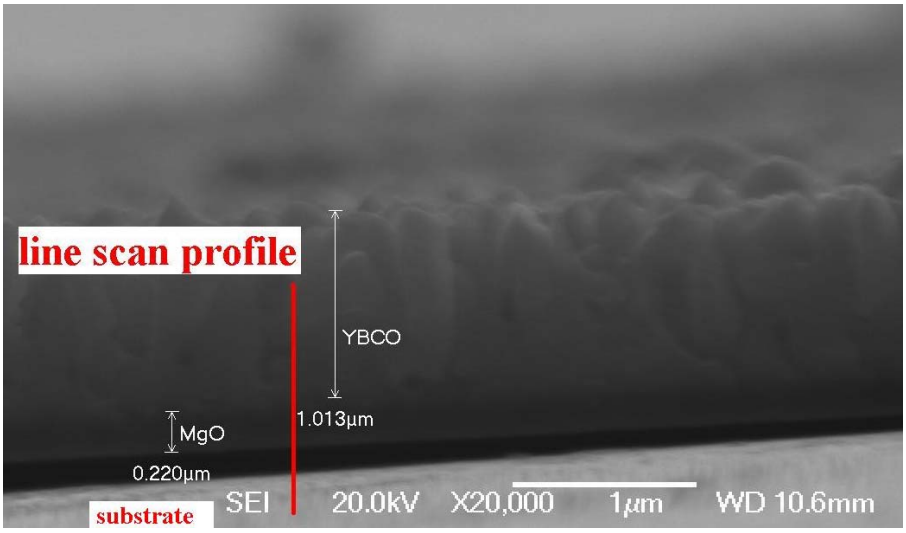

Figure 8.81: Cross sectional SEM image of YBCO film deposited on MgO film spray pyrolysed on Hastelloy C276 using 0.093M $Mg(CH3COO)_2.4H_2O$ at 600°C for 32 minutes.

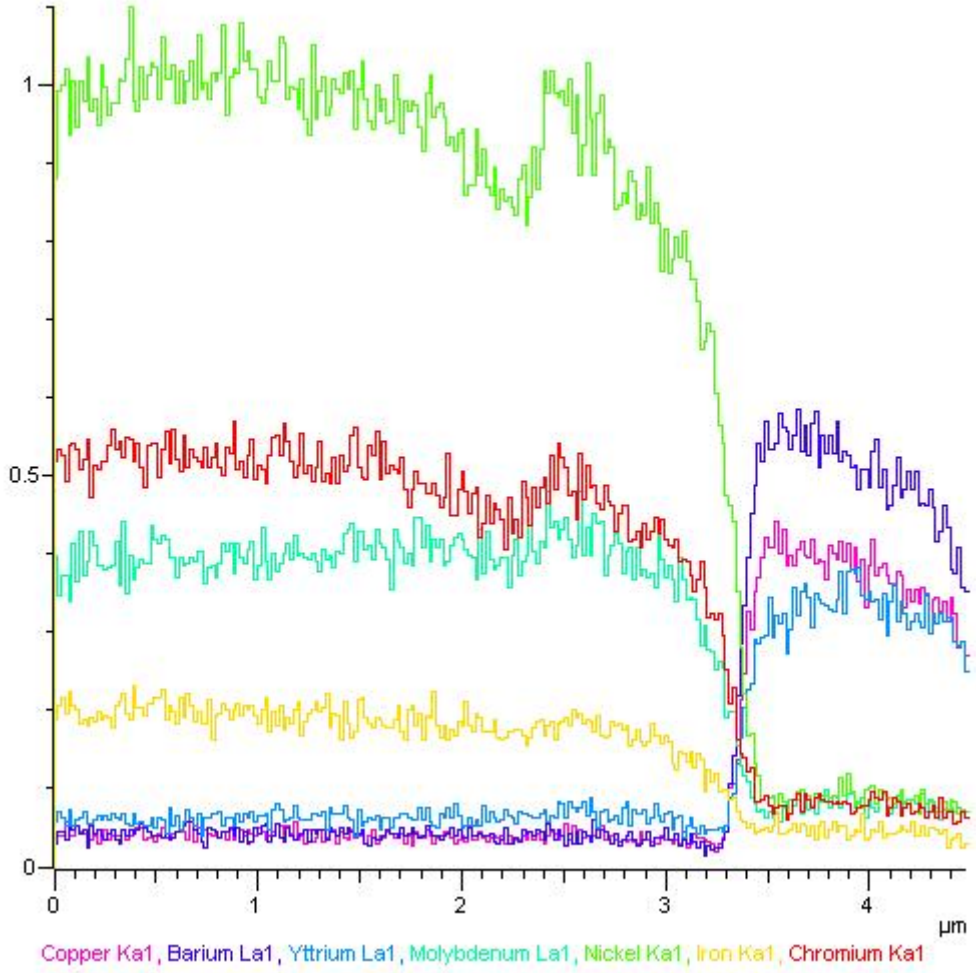

Figure 8.82: EDX line scan using 20KV of YBCO film deposited on MgO film spray pyrolysed on Hastelloy C276 using 0.093M $Mg(CH3COO)_2.4H_2O$ at 600°C for 32 minutes.

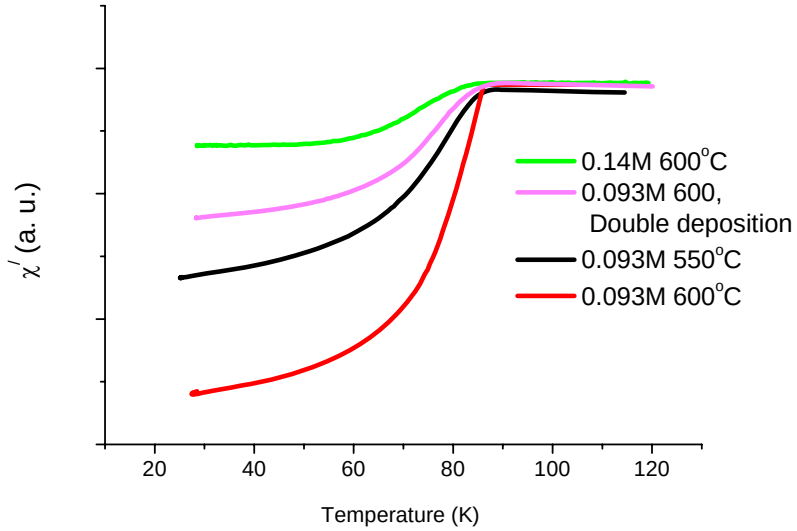

Figure 8.83: AC susceptibility measurement for YBCO deposited at 780°C on the MgO buffer layer spray pyrolysed at different conditions.

It is clear from the AC susceptibility measurements that the transition temperatures were almost the same as those obtained when using the nitrate precursor although the intensity of the MgO (200) peaks were much stronger when using the acetate precursor. It is known that MgO contaminants result from MgO reacting with water, carbon oxide, and solvents such as ethanol and acetone [197]. From the thermal decomposition of the acetate precursor, it was found that acetone and carbon dioxide were released during the decomposition process which can be a source of carbon contamination. It was found in the literature that in-plane 45° grain misorientation was frequently observed in YBCO films grown on degraded or contaminated MgO films with carbon compound such as bicarbonate, alcohols and carboxyl and this was found to affect the superconducting properties [197, 291]. The heating process while depositing thin films can improve the surface quality to a large degree with removal of some contaminants, but is not sufficient to recover the MgO surfaces completely [197]. In the case of MgB_2 it was found that a small amount of carbon contamination was not affecting the T_c onset, however the superconducting transition changed from sharp to a broad one due to the presence of carbon on the grain boundaries that isolates grains and prevents flow of supercurrents [292]. However, others found that carbon doping is an appropriate method of improving the critical fields and current densities of MgB_2 [293-295].

Because of this, an XPS test was performed on the sample deposited with MgO from 0.093M solution at 600°C for 32 minutes (Figure 8.84). The XPS spectrum was recorded with a standard Mg Kα source using 20 pass energy, 0.1 eV step, and 0.1

seconds per step for the detailed spectrum. The C 1S scan was from 270-300eV. A peak was found at 284.9eV which corresponds to C 1s. Similar peaks were found by others at 284.6 eV and 284.7 eV and was related to carbon based compounds or hydrocarbon contaminants [197, 198, 291]. Therefore, the broad superconducting transition temperatures can be related to carbon contamination from the thermal decomposition of the acetate precursor. It is to be noted that XPS test performed on the MgO film deposited from 0.468M solution of magnesium nitrate at 650°C for 48 minutes did not show any peaks corresponding to carbon contamination.

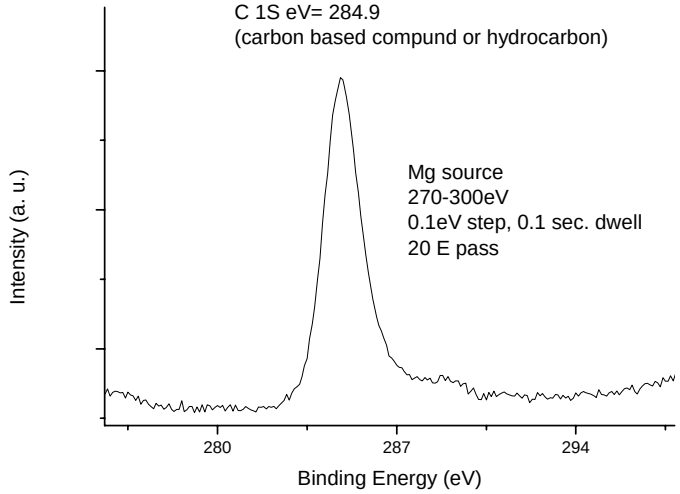

Figure 8.84: XPS spectrum for the MgO thin film deposited on Hastelloy C276 substrate using 0.093M $Mg(CH3COO)_2.4H_2O$ at 600°C for 32 min. showing the C 1s.

8.11.3 Pulsed laser deposition of Ceria (CeO_2) and YBCO on MgO deposited by spray pyrolysis

It was found (section 8.11.2) that YBCO deposition on MgO films deposited by spray pyrolysis resulted in YBCO films having very weak in-plane texture and with broad superconducting transition temperatures. In an attempt to establish a good in-plane texture, researchers found that the deposition of CeO_2, in the ISD approach using e-beam evaporation, will lead to a well defined and good in-plane textured YBCO films [39, 41, 50, 169, 171, 177, 182, 183]. For this reason and to improve the superconducting properties, and as was done with the nitrate precursor (7.12.4), CeO_2 was deposited by PLD on top of MgO films deposited by spray pyrolysis followed by YBCO deposition by PLD as well.

CeO_2 was deposited at two different conditions. The used energy fluence was $2J/cm^2$, the distance between the target and the substrate was fixed at 56mm, 500 and

1000 pulses were applied as it was found by researchers that cracks will form in 100-200 nm thick CeO_2 films [282-284]. The first deposition was made at 780°C using 0.6 mbar O_2 and the second one was made at 710°C using $2x10^{-4}$ mbar O_2. The YBCO deposition conditions were the same as those mentioned in section 7.12.1. The deposition was made on the samples spray pyrolysed with MgO from 0.093M solution at 600°C for 32 minutes.

The samples deposited with 500 pulses of CeO_2 show very weak CeO_2 peaks. Therefore, the deposition proceeded from now on with only 1000 pulses. Figure 8.85 shows the XRD patterns for CeO_2 films deposited on top of MgO deposited by spray pyrolysis. The CeO_2 peaks were indexed according to the JCPDS PDF file 00-004-0593. It can be seen that none of the CeO_2 deposition conditions resulted in a perfectly (200) oriented films. However, the deposition at 780°C using 0.6 mbar O_2 resulted in a dramatic change giving a much stronger CeO_2 (200) peak compared to the film deposited at 710°C using $2x10^{-4}$ mbar O_2. The surface roughness was increased after the CeO_2 deposition at 710°C using $2x10^{-4}$ mbar O_2 as was clear from the SEM and AFM images, in Figure 8.86 and Figure 8.88, respectively, compared to that before the deposition (Figure 8.6 and Figure 8.8). However, CeO_2 film deposited at 780°C using 0.6 mbar O_2 showed even a little smoother surface, as a result of the good texture of CeO_2, (Figure 8.87 and Figure 8.89) compared to that before deposition (Figure 8.6 and Figure 8.8). The same observation was seen for low thicknesses of CeO_2 films on YSZ buffer which were deposited by PLD on ISD MgO deposited by e-beam evaporation [169].

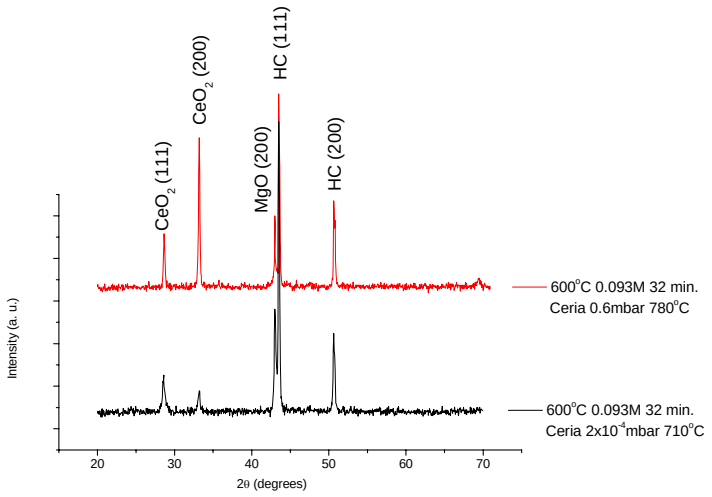

Figure 8.85: XRD patterns for CeO_2 films deposited by PLD at different conditions on the MgO films spray pyrolysed at 600°C from 0.093M for 32 minutes**.**

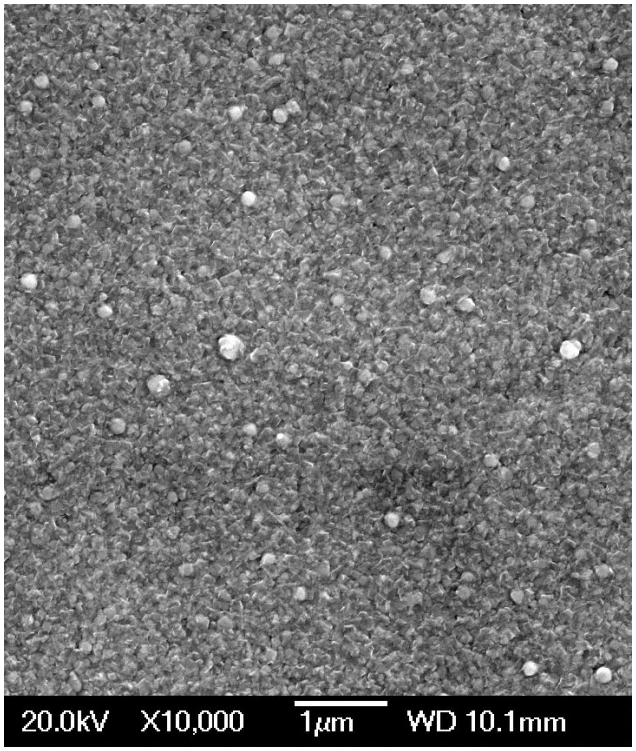

Figure 8.86: SEM image for CeO_2 film deposited by PLD at 710°C using $2x10^{-4}$ mbar O_2 on the MgO film deposited by spray pyrolysis at 600°C from 0.093M for 32 minutes**.**

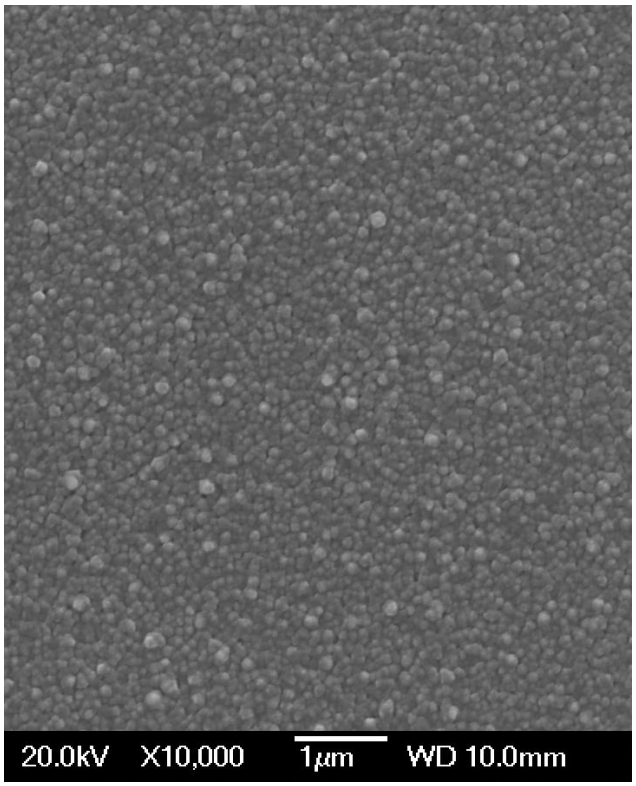

Figure 8.87: SEM image for CeO_2 film deposited by PLD at 780°C using 0.6 mbar O_2 on the MgO film deposited by spray pyrolysis at 600°C from 0.093M for 32 minutes**.**

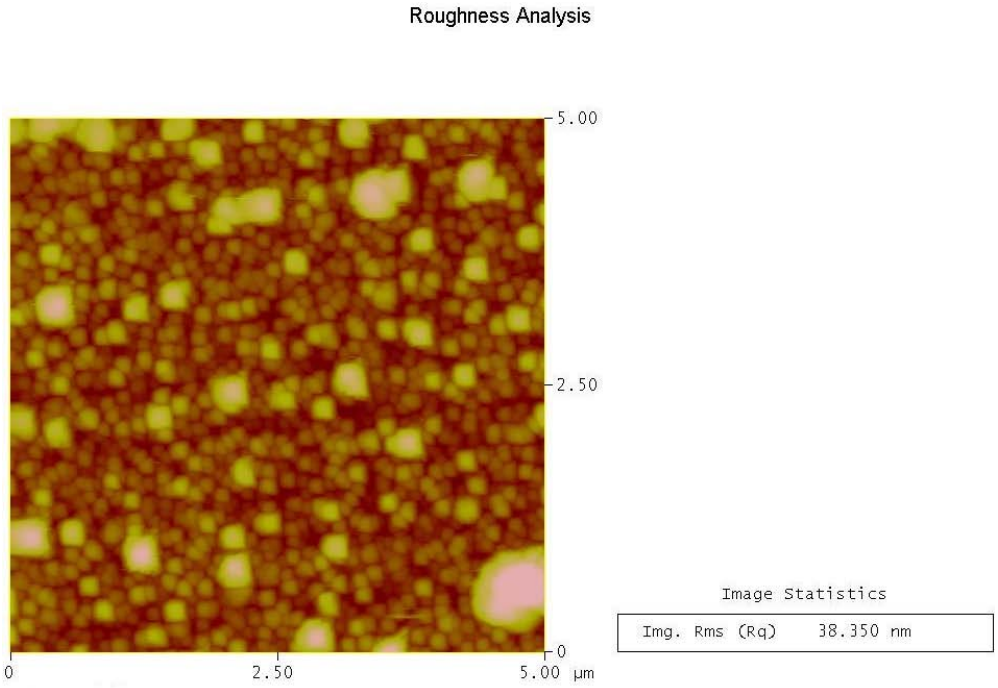

Figure 8.88: A 5x5µm^2 AFM image for CeO_2 film deposited by PLD at 710°C using 2x10^{-4} mbar O_2 on the MgO film deposited by spray pyrolysis at 600°C from 0.093M for 32 minutes**.**

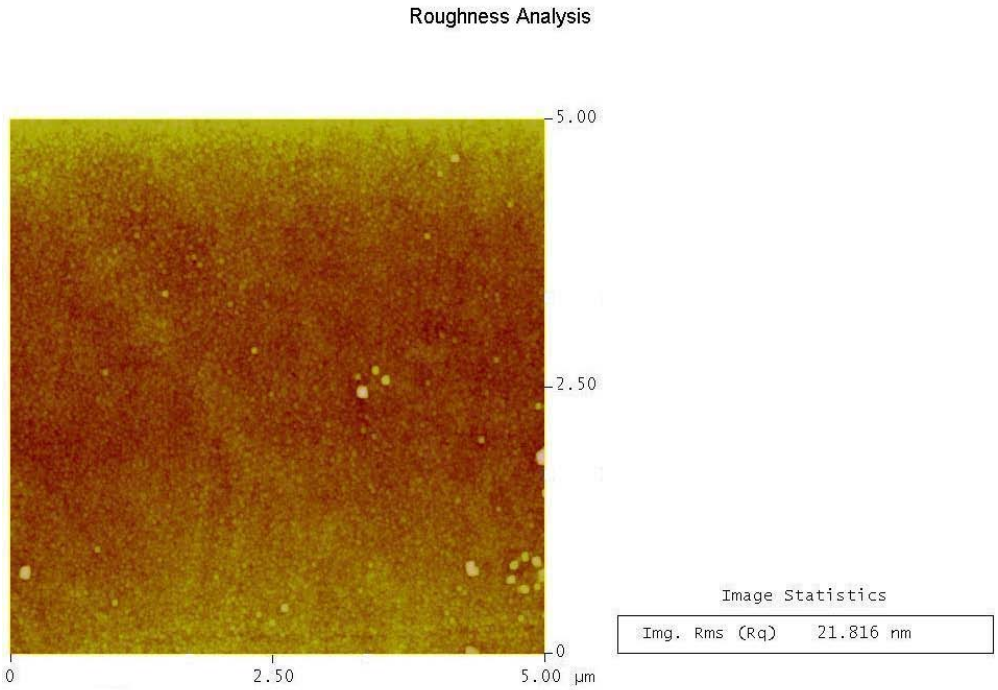

Figure 8.89: A 5x5µm^2 AFM image for CeO_2 film deposited by PLD at 780°C using 0.6 mbar O_2 on the MgO film deposited by spray pyrolysis at 600°C from 0.093M for 32 minutes**.**

To see the influence of the deposited CeO_2 film on the properties the superconducting layer, YBCO was deposited on each of the samples shown in Figure

8.85. Figure 8.90 shows the XRD patterns for YBCO films deposited on CeO_2, and Figure 8.91 and Figure 8.92 are the SEM images and the corresponding AFM images are shown in Figure 8.93 and Figure 8.94. It is clear that the YBCO film had a stronger (006) peak on the CeO_2 film deposited at 780°C using 0.6 mbar O_2. However, the YBCO films were rougher (Figure 8.92-Figure 8.94) compared to the YBCO film deposited directly on the MgO film deposited by spray pyrolysis (Figure 8.67 and Figure 8.71). CeO_2 film deposited at 780°C using 0.6 mbar resulted in a smoother YBCO film when compared to the CeO_2 film deposited at 710°C using $2x10^{-4}$ mbar. This can be attributed to the smoother CeO_2 film and stronger CeO_2 (200) peak deposited at 780°C using 0.6 mbar which gave stronger YBCO (006) peak and hence smoother film. The thickness of the CeO_2 should be in the range of 100nm as the deposition conditions were the same as those obtained when using the nitrate precursors (Figure 7.104).

The pole figure measurements show that YBCO had out-of-plane texture but still no in-plane texture. This means that CeO_2 deposition on the MgO deposited by spray pyrolysis had no effect in improving the in-plane texture of the subsequent YBCO layer which disagrees with what was found by other researchers [39, 41, 50, 169, 171, 177, 182, 183]. In addition to that, only the sample with CeO_2 deposited 780°C using 0.6 mbar had a T_c (Figure 8.95) which was even worse compared to that without CeO_2 deposition (Figure 8.83).

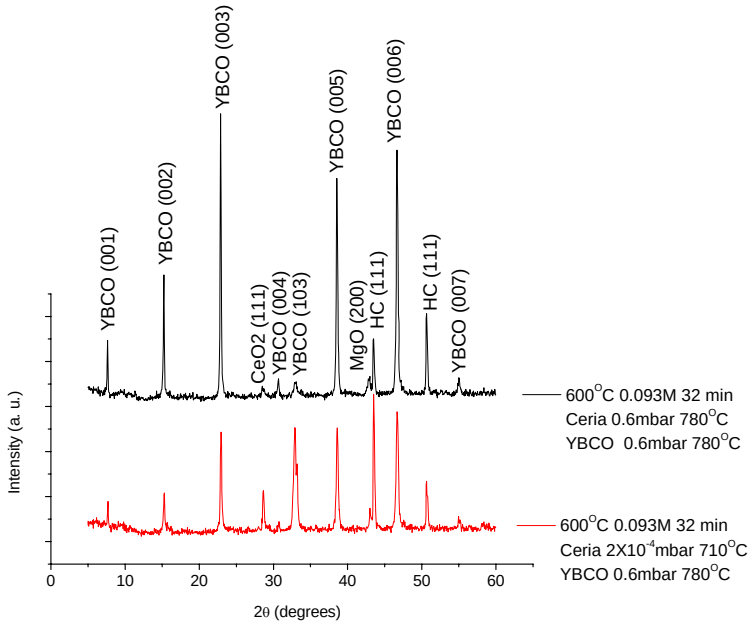

Figure 8.90: XRD patterns for YBCO and CeO_2 films deposited by PLD at different conditions on the MgO films deposited by spray pyrolysis at 600°C from 0.093M for 32 minutes**.**

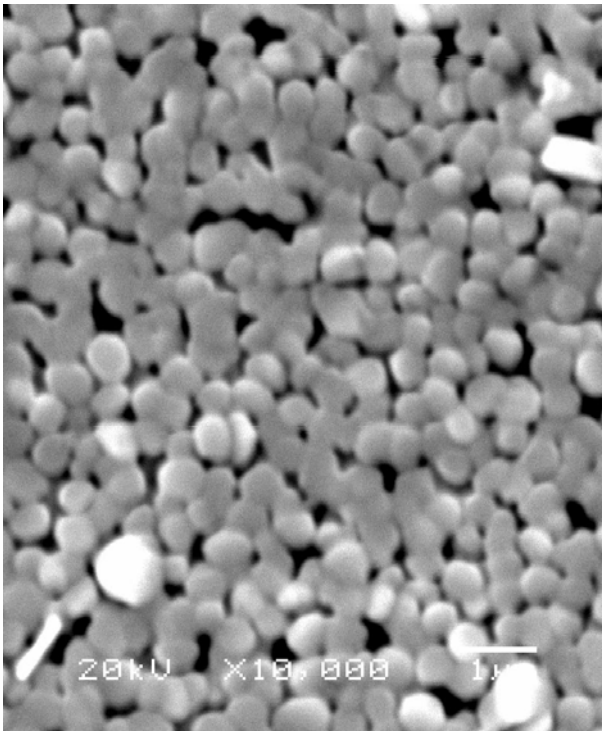

Figure 8.91: SEM image for YBCO on CeO_2 film deposited by PLD at 710°C using $2x10^{-4}$ mbar O_2 on the MgO film deposited by spray pyrolysis at 600°C from 0.093M for 32 minutes**.**

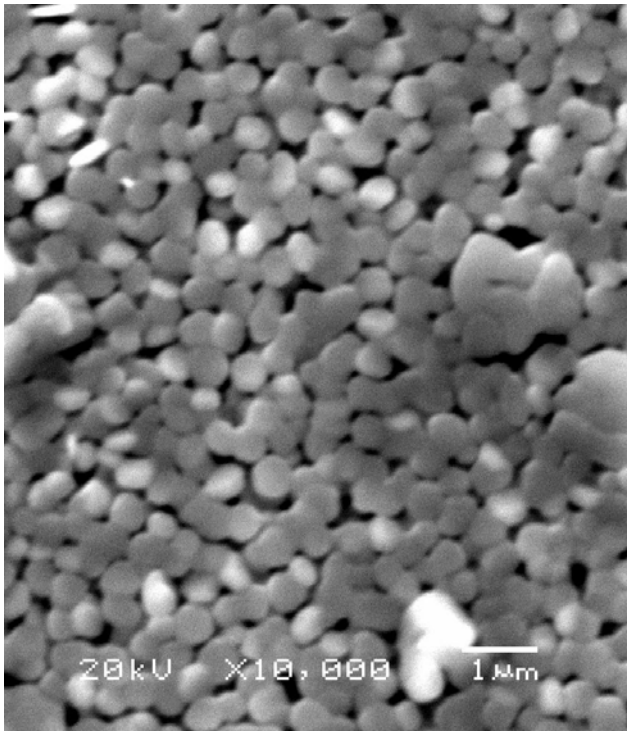

Figure 8.92: SEM image for YBCO on CeO_2 film deposited by PLD at 780°C using 0.6 mbar O_2 on the MgO film deposited by spray pyrolysis at 600°C from 0.093M for 32 minutes.

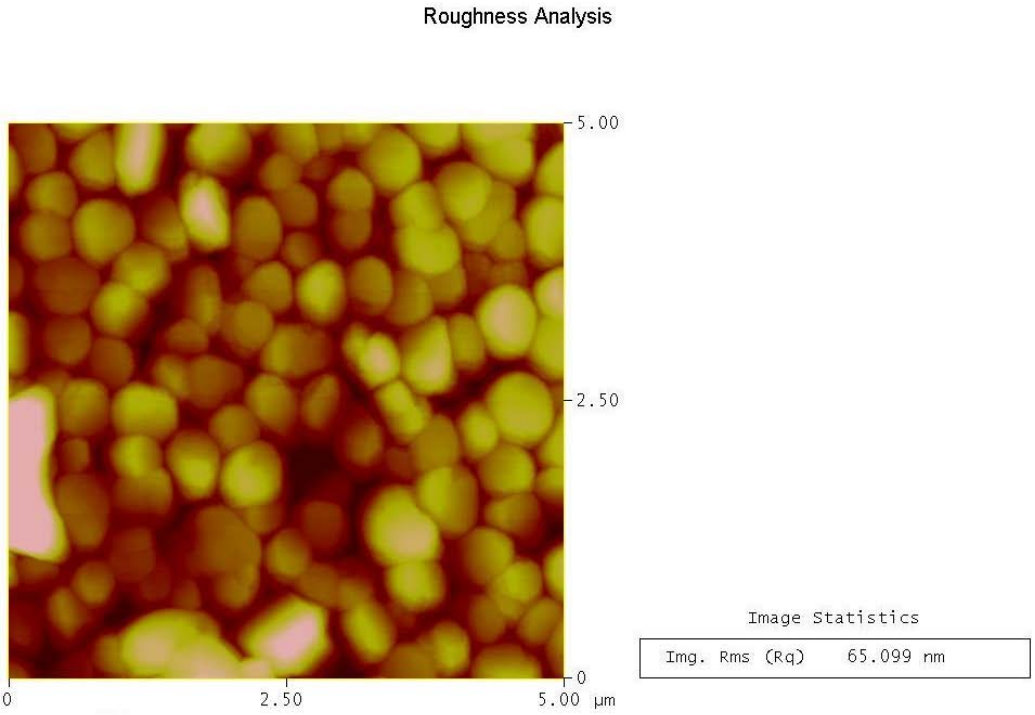

Figure 8.93: A 5x5µm^2 AFM image for YBCO on CeO_2 film deposited by PLD at 710°C using 2x10^{-4} mbar O_2 on the MgO film deposited by spray pyrolysis at 600°C from 0.093M for 32 minutes**.**

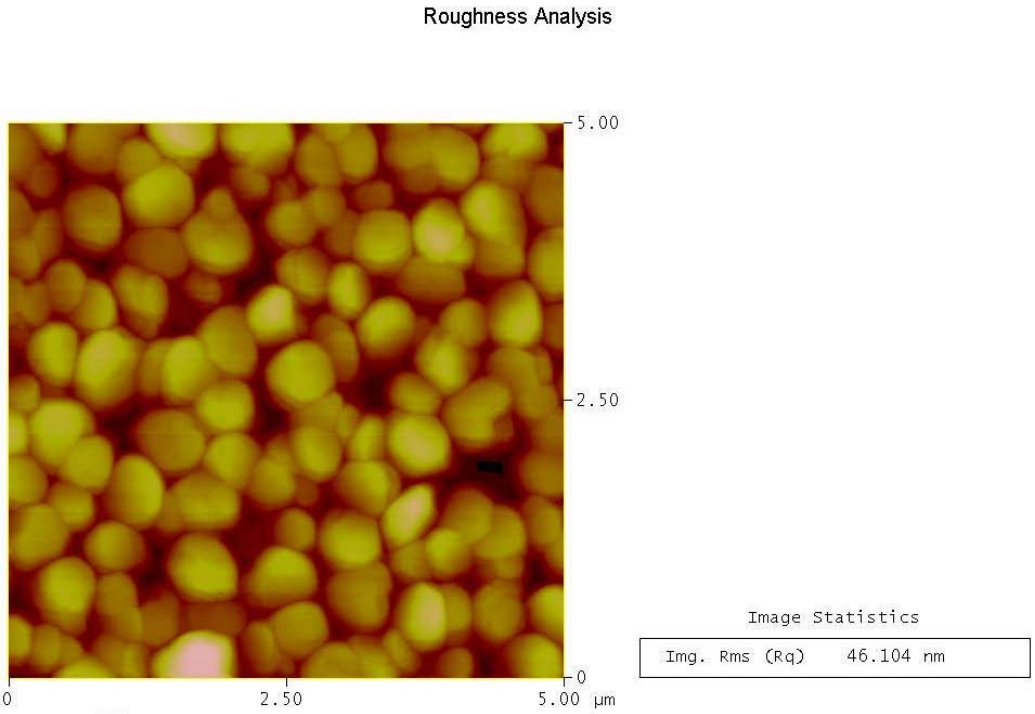

Figure 8.94: A 5x5µm^2 AFM image for YBCO on CeO_2 film deposited by PLD at 780°C using 0.6 mbar O_2 on the MgO film deposited by spray pyrolysis at 600°C from 0.093M for 32 minutes.

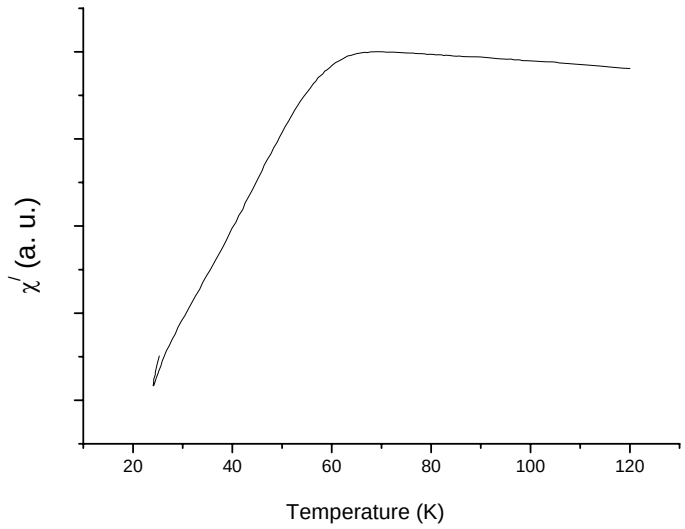

Figure 8.95: AC susceptibility measurement for YBCO deposited on CeO_2 film deposited by PLD at 780°C using 0.6 mbar O_2 on the MgO film deposited by spray pyrolysis at 600°C from 0.093M for 32 minutes.

9 Conclusions and future work

9.1 Introduction

MgO was deposited by spray pyrolysis on Si (100) single crystals, NiW tapes, polycrystalline 310-austenitic stainless steel and Hastelloy C276. The deposition was done at various conditions and different annealing treatments were performed on the deposited MgO films. CeO_2 was deposited by PLD on C276 buffered with MgO in an attempt to improve the in-plane texture of the subsequent YBCO which was also deposited by PLD.

9.1.1 Depositions on Si (100) single crystals using magnesium nitrate precursor

The substrate temperature was found to affect the crystallinity of the produced films, where at 600°C the films show very low intensity peaks with regard to MgO (200). However, the films produced at 650°C and at 700°C were (200) textured, irrespective of the precursor concentration. The MgO (200) peaks were strained due to the thermal expansion coefficient mismatch between the Si substrate and MgO. It was also found that the texture of MgO films improved with increasing the temperature and concentration and that the surface morphology of the produced film was affected by changing the substrate temperature from 650°C to 700°C.

At 650°C, the roughness increased by decreasing the concentration from 0.078M to 0.0078M. Conversely, at 700°C the roughness increased by increasing the concentration from 0.0078M to 0.078M. The roughness at 700°C was also higher than that at 650°C. The best film obtained was at 650°C from 0.078M solution and was deposited according to the third mode of deposition and was biaxially textured.

It was found that the ISD affects the crystallinity of the deposited MgO films. The intensity of MgO peaks and the thickness of MgO films decreased with increasing the inclination angle. The thickness was increased with increasing the concentration and the temperature. The deposition rate was found to depend on the substrate temperature and concentration in direct proportionality and that the texture improved with increasing thickness and temperature.

The roughness values, of the films produced at 650°C from 0.0078M, decreased by increasing the inclination angle from zero to 20°, and then became independent on the inclination angle from 20°-60°. At 0.078M, the roughness was almost independent

of the inclination angle. At 700°C the roughness decreased with increasing the inclination angle. In all cases, the roughness at zero inclination was the highest.

Biaxially textured and epitaxial MgO film ($MgO_{200}//Si_{200}$ and $MgO_{111}//Si_{111}$) was produced at 650°C from a 0.078M solution at zero degree inclination and by inclining the substrate at 20°. The biaxially textured and epitaxial film deposited at 700° from 0.078M solution was also obtained by inclining the substrate at 20°. However, the film had overgrown particles on the surface. From this it was concluded that the ISD deposition by spray pyrolysis on Si substrates was not giving the shadowing effect which produces c-axis tilted films.

MgO deposition by PLD was not as good as the films prepared by spray pyrolysis due to the low fluence used during PLD deposition.

YBCO deposition on MgO films deposited by spray pyrolysis, at 650°C using 0.078M solution of magnesium nitrate with zero inclination angle, resulted in a very weak superconducting transition temperature due to the thermal stresses developed in the MgO buffer. YBCO deposition on MgO films deposited by spray pyrolysis under other deposition conditions resulted in polycrystalline YBCO films with no T_c.

YBCO deposition on MgO films deposited by PLD resulted in no superconductivity due to the weak texture of the deposited MgO buffer layer.

9.1.2 Depositions on NiW tapes using magnesium nitrate and acetate precursors

The recrystallisation treatment of NiW tapes at 1100°C for 3 hours under Ar-5%H_2 atmosphere resulted in (200) textured tapes with a roughness of 14 nm and after polishing they had a roughness of about 4 nm compared to 50 nm for the as received substrates.

Deposition of MgO on recrystallised NiW tapes (i.e. (200) textured) resulted in the formation of an amorphous MgO film. This was due to the instability of the substrates during spray pyrolysis; where a polycrystalline NiO layer was formed.

Oxidation of recrystallised and unpolished NiW substrates at 1200°C under O_2 atmosphere resulted in (200) textured NiO film which was epitaxial with the NiW substrate, however, it was rotated 45° relative to the substrate. The texture was stable even by heating the substrate to 780°C under vacuum which resembles YBCO deposition conditions. The same texture relation was obtained after oxidising the

recrystallised and polished NiW substrates, however, the texture was disturbed when heating the substrate to 780°C under the same YBCO deposition conditions.

MgO deposition on NiO (200) did not result in any MgO XRD peaks irrespective of the used concentration or the used precursor (nitrate or acetate) and was attributed to the surface instability of the oxide during the spray pyrolysis deposition conditions.

9.1.3 Depositions on 310-austenitic stainless steel using magnesium nitrate precursor

Magnesium nitrate was used as a precursor, however, no MgO XRD peaks were observed (amorphous films were obtained) when using the 310-stainless steel as a substrate regardless of the deposition temperate, deposition time and precursor concentration. The oxalic acid test showed that the 310-austenitic stainless steels were not severely affected and a dual etch structure was obtained; however, some carbides were formed which disturbed the surface stability for MgO deposition. Therefore, it was concluded that 310-St. St. is not a good candidate as a substrate material for buffer layer deposition using the spray pyrolysis technique due to the thermal instability of the surface during deposition at relatively high temperature and wet environment.

9.1.4 Depositions on Hastelloy C276

This section is divided into two as the deposition of MgO was made on Hastelloy C276 using nitrate and acetate precursors.

The corrosion rates for Hastelloy C276 obtained after conducting the boiling iron (III) sulfate-sulfuric acid test was less than 1mm/month (the maximum allowable corrosion rate). Therefore, C276 was a good candidate as a substrate material for MgO deposition by spray pyrolysis. This was also confirmed by the SEM images where only pits formed as a result of the long contact with the acid.

9.1.4.1 MgO deposition from the nitrate precursor

MgO deposition on C276 from nitrate precursor using 0.078M solution resulted in the formation of amorphous MgO films irrespective of the deposition temperature or deposition time. However, when using 0.468M solution at 650°C for 32 minutes a weak MgO (200) peak was obtained. It was found that the peak intensity increased

with increasing the deposition time, deposition temperature, precursor concentration or applying the double deposition process. However, this was at the expense of the smoothness of the deposited MgO films.

The smooth MgO films deposited from 0.468M solution at 650°C for 32 and 48 minutes were deposited according to the third mode of deposition. The films deposited at other deposition conditions were deposited mainly according to the fourth mode of deposition except the ones deposited at 650°C for 64 minutes and 96 minutes from 0.468M which needs be further investigated to determine the mode of deposition. The films deposited from 0.78M solution were deposited according to the second mode of deposition.

XPS results show that the surface of MgO was contaminated with hydroxide; however, the MgO film was recovered during subsequent YBCO film deposition as found in the literature that heating the contaminated layer to 450°C in air is sufficient to regenerate the MgO surface [116].

Complete study on the effect of the thickness on the texture development was difficult to achieve due to the difficulty in preparing cross sectional samples for the thickness measurements. However, it was believed that the amorphous films obtained when using the 0.078M solution was due to the low thicknesses of the deposited MgO films. The MgO films deposited from 0.468M solution show a weak (200) texture. This suggests that the texture developed with thickness and thickness increased with increasing the concentration.

MgO deposition by inclining the substrate resulted in weaker MgO (200) peaks, smoother surfaces and lower thicknesses compared to the films deposited with no inclination.

Amorphous MgO films were obtained at low flow rates. The optimum Ar flow rate was found to be 10 l/min which gave detectable MgO peaks and the smoothest MgO films. Higher flow rate (15l/min) did not improve the texture of MgO films but increased the roughness.

In an attempt to improve the texture of the MgO peaks, different annealing treatments were performed. Annealing under O_2 atmosphere up to 650°C had no effect on the texture and roughness of the deposited MgO films. However, annealing at 800°C resulted in slight improvement in the intensity of MgO (200) peak but this was at the expense of substrate oxidation. Annealing at 1000°C resulted in severe substrate oxidation and no MgO peaks were detected. Annealing under vacuum up to 800°C

had no effect on the texture and smoothness of the MgO films. This confirmed the stability of MgO under such conditions which is required for later YBCO deposition. At 1000°C, the MgO peak disappeared due to Mg evaporation. Annealing under purified Ar at 1000°C did not result in Mg evaporation, but resulted in rough MgO films due to the high annealing temperature.

YBCO films deposited on MgO films, deposited by spray pyrolysis, with a roughness greater than 20nm were polycrystalline and had no T_c. The MgO films, deposited by spray pyrolysis, with a roughness of about 20nm had a weak in-plane and out-of-plane texture. The films grow with the (200) normal to substrate surface as distinct to MgO films grown by thermal evaporation which grow with the (200) tilted to the substrate normal. Subsequent YBCO deposition on such MgO films were textured with (006) being the strongest peak and have a slightly better out-of-plane texture compared to the MgO buffer and (006) of YBCO // (200) of MgO. Thus, spray pyrolysis offers an alternative method of depositing a single MgO buffer layer with no tilting for YBCO deposition. However, the deposited YBCO films had a broad superconducting transition temperature with a T_c onset of 84.5K. However, these results demonstrate the potential for this chemical route to the deposition of a single buffer layer of MgO with normal rather than tilted texture on a polycrystalline technical substrate which could have significant impact on coated conductor technology. YBCO films deposited on MgO films, deposited by spray pyrolysis at different inclination angles, or using Ar flow rate of 5 and 15l/min, were polycrystalline and had no T_c. The same result was found for YBCO films deposited on the annealed MgO films.

CeO_2 deposition on Hastelloy C276 buffered with MgO did not improve the texture of the subsequent YBCO film or the transition temperature. It even made the surface of MgO rougher and resulted in YBCO films with no T_c.

9.1.4.2 MgO deposition from the acetate precursor

MgO deposition from the acetate precursor resulted in stronger (200) oriented films, even by using much lower concentration, compared to the nitrate precursor. The intensity of MgO peak increased with increasing the deposition temperature, deposition time, but this was at the expense of surface roughness. Increasing the concentration did affect the intensity of MgO (200) peaks but increased the roughness of the deposited films.

The smooth MgO films deposited from 0.093M solution at 500°C-600°C for 32 minutes were deposited according to the third mode of deposition. The films deposited at 650°C were deposited according to the fourth mode of deposition. The films deposited at 600°C from 0.093M for 64 minutes needs to be further investigated to determine the mode of deposition and the films deposited at 600°C from 0.279M for 32 minutes deposited according to the second mode of deposition.

XPS results show that the surface of MgO was contaminated with hydroxide, however, the MgO film was recovered during subsequent YBCO film deposition as found in the literature that heating the contaminated layer to 450°C in air is sufficient to regenerate the MgO surface [116].

Complete study on the effect of the thickness on the texture development was difficult to achieve due to the difficulty in preparing cross sectional samples for the thickness measurements.

MgO deposition by inclining the substrate resulted in weaker MgO (200) peaks, smoother surfaces and lower thicknesses compared to the films deposited with no inclination.

The optimum Ar flow rate was found to be 10 l/min which gave detectable MgO peaks and the smooth MgO films. Higher (15 l/min) and lower (15 l/min) flow rates resulted in smooth films but with low intensity MgO peaks.

In an attempt to improve the texture of MgO peaks, different annealing treatments were performed. Annealing under O_2 atmosphere up to 650°C had no effect on the texture and roughness of the deposited MgO films. However, annealing at 800°C 1000°C resulted in substrate oxidation. Annealing under vacuum up to 800°C had no effect on the texture and smoothness of the MgO films. This confirmed the stability of MgO under such conditions which is required for later YBCO deposition. At 1000°C, the MgO peak disappeared due to Mg evaporation. Annealing under purified Ar at 1000°C resulted in partial Mg evaporation and led to the formation of rough films due to the high annealing temperature.

YBCO films deposited on MgO films, deposited by spray pyrolysis, with a roughness greater than about 42nm were polycrystalline and had no T_c. The MgO films, deposited by spray pyrolysis, with a roughness up to 42 nm had a weak in-plane and out-of-plane texture but better than those obtained when the magnesium nitrate precursor was used. The films grow with the (200) normal to substrate surface as distinct to MgO films grown by thermal evaporation which grow with the (200) tilted

to the substrate normal. Subsequent YBCO deposition on such MgO films were textured with (006) being the strongest peak and (006) of YBCO // (200) of MgO. Thus, spray pyrolysis offers an alternative method of depositing a single MgO buffer layer with no tilting for YBCO deposition. However, the deposited YBCO film had a broad superconducting transition temperature with a T_c onset of 84.8K. However, these results demonstrate the potential for this chemical route to the deposition of a single buffer layer of MgO with normal rather than tilted texture on a polycrystalline technical substrate which could have significant impact on coated conductor technology. The best texture, surface smoothness and T_c were obtained for the film deposited at 600°C using 0.093M for 32 minutes; besides that, an EDX line scan performed on such samples improved the effectiveness of MgO as a diffusion barrier layer. However, the superconducting transition temperatures were not improved compared to those when using the nitrate precursor although the acetate precursor gave stronger MgO (200) peaks and that was related to carbon contamination. YBCO films deposited on MgO films, deposited by spray pyrolysis at different inclination angles, or using Ar flow rate of 5 and 15 l/min, were polycrystalline and had no T_c. The same result was found for YBCO films deposited on the annealed MgO films.

CeO_2 deposition on Hastelloy C276 buffered with MgO did not improve the texture of the subsequent YBCO film or the transition temperature. The best YBCO films were those deposited on CeO_2 films deposited by PLD at 780°C using 0.6 mbar O_2 on the MgO films deposited by spray pyrolysis at 600°C from 0.093M for 32 minutes. However, the AC susceptibility measurement showed a bad superconducting transition temperature compared to that before CeO_2 deposition.

9.2 Suggestions for future work

Many parameters for the deposition of MgO by spray pyrolysis were investigated, however, due to the lack of time, some other parameters need to be investigated and some process modifications may need to be made.

9.2.1 Deposition of MgO thin films

It was noticed that higher $Mg(NO_3)_2.6H_2O$ concentrations were needed to obtain a (200) oriented MgO films compared to that when using the $Mg(CH3COO)_2.4H_2O$ precursor. This was believed to be due to a high vapour pressure of the Mg^{2+} when

using low concentrations of $Mg(NO_3)_2.6H_2O$; however this behaviour was not really understood and needs further investigation.

It was found that the broad superconducting transition temperatures can be attributed to carbon contamination from the acetate precursors. An Ar ion beam etch (IBE) cleaning process at low ion energy can be used to refresh the MgO surfaces [197, 198] and this may improve the transition temperatures.

CeO_2 deposition was found to improve the in-plane texture of the subsequent YBCO films; however, when deposited on MgO films deposited by spray pyrolysis, it did not; therefore, other buffer layers such as $SrTiO_3$ (STO) could be utilized for investigating this purpose.

Some of the parameters during the spray pyrolysis deposition were not investigated. These include: nozzle diameter, substrate-nozzle distance and the type of carrier gas which would be some suggestions for future work.

When depositing MgO films on metallic substrates, it was difficult to prepare cross sections to study the effect of thickness on the deposited MgO, CeO_2 and YBCO films. The use of focused ion beam (FIB) milling to prepare samples, where many problems associated with the mechanical preparation are eliminated, would be the solution.

The metallic substrates, especially NiW and 310-austenitic stainless steel substrates were not stable under the spray pyrolysis deposition conditions which provided wet environments that affected the stability of the substrates for thin film deposition. Therefore, ethanol or methanol solvents may be used to deposit MgO films on such substrates and its effect on substrate surface stability should be investigated.

To further investigate the deposited MgO films from the nitrate and acetate precursors, TEM samples would be of interest to study the growth behaviour and effect of thickness on the deposited thin films of MgO, CeO_2 and YBCO. In addition, performing an EDX profile scan across the substrate-MgO film interface could be made to confirm the effectives of MgO as a diffusion barrier layer.

The adhesion of MgO and YBCO films would be another issue that should be investigated on different substrates i.e. on Si single crystals and Hastelloy C276; as the MgO peaks were relatively strong on such substrates but the superconducting transition temperatures were broad.

9.2.2 System modification

To increase the amount of aerosol deposition, electrostatic spraying can be utilized by applying a DC voltage between the nozzle and the substrate; however, in this case the substrates are limited to conductive ones.

As mentioned earlier about the substrate instability under the spray pyrolysis conditions, a simple vacuum system may be incorporated in addition to the use of alcoholic solvents as an attempt to solve this problem.

It was found that the temperature of the substrate decreased during the spraying process which forced the use of pulse time to interval time of 1:7. To speed the process, the use of multi-zone tubular furnace may be beneficial to heat the aerosol stream in a more controlled manner before it reaches the substrate.

List of References

[1] Concise encyclopaedia of magnetic and superconducting materials First ed. J. E. Evetts, Frs, R.W.C, Bever, M. B., editor. OXFORD, NEW YORK, SEOUL, TOKYO: Pergammon Press; 1992.

[2] Lennard G,Richard E. Superconductivity: an overview Congressional Research Service. 1987: 1-11

[3] Superconductivity: the Meissner effect, Persistent currents, and the Josephson effects. MIT deptof physics. 2003: 1-16

[4] Handbook of applied superconductivity S. Berned, editor. Bristol and Philadelphia: IOP Publishing Ltd; 1998.

[5] Woods Halley J. Theories of high temperature superconductivity. Allan, M. Wyylde; 1988.

[6] Goyal A, Norton DP, Christen DK, Specht ED, Paranthaman M, Kroeger DM, et al. Epitaxial superconductors on rolling-assisted biaxially-textured substrates (RABiTS): A route towards high critical current density wire. Applied Superconductivity. 1996;4(10-11):403-427.

[7] Bednorz JG,Müller KA. Possible highTc superconductivity in the Ba−La−Cu−O system. Zeitschrift für Physik B Condensed Matter. 1986;64(2):189-193.

[8] Wu MK, Ashburn JR, Torng CJ, Hor PH, Meng RL, Gao L, et al. Superconductivity at 93 K in a new mixed-phase Y-Ba-Cu-O compound system at ambient pressure. Physical Review Letters. 1987;58(9):908.

[9] Superconductivity Harvard, University; [cited 2007 May 12th]; Available from: http://hoffman.physics.harvard.edu/research/SCintro.php

[10] Michael T. Introduction to Superconductivity. McGraw-Hill, Inc.; 1976.

[11] Parks RD. Superconductivity. Marcel Dekker INC.; 1969.

[12] Thompson DJ, Minhaj MSM, Wenger LE,Chen JT. Observation of Paramagnetic Meissner Effect in Niobium Disks. Physical Review Letters. 1995;75(3):529-532.

[13] Kuppusami P,Raghunathan VS. Processing and properties of thin films of high critical temperature superconductors. International Materials Reviews. 2003;48(1):1-43.

[14] Type II Superconductors. Mit,; [cited 2007 May 12th]; Available from: http://web.mit.edu/6.763/www/FT03/Lectures/Lecture17.pdf

[15] Amit G. Second Generatin HTS Conductors. Kluwer Academic Publishers; 2005.

[16] Goyal A, Paranthaman MP,Schoop U. The RABiTS approach: Using rolling-assisted biaxially textured substrates for high-performance YBCO superconductors. Mrs Bulletin. 2004;29(8):552-561.

[17] Kim K, Paranthaman M, Norton DP, Aytug T, Cantoni C, Gapud AA, et al. A perspective on conducting oxide buffers for Cu-based YBCO-coated conductors. Supercond Sci Technol. 2006;19(4):R23-R29.

[18] Riley GN, Li Q,Fritzemeier LG. High temperature superconducting composite wires. Current Opinion in Solid State and Materials Science. 1999;4(5):473-478.

[19] Heine K, Tenbrink J,Thoner M. High-field critical current densities in Bi2Sr2Ca1Cu2O8+x/Ag wires. Applied Physics Letters. 1989 Dec;55(23):2441-2443.

[20] Glowacki BA, editor. Texture development of HTS powder-in-tube conductors. International Symposium on Processing and Critical Current of High-Temperature Semiconductors; 1998 Feb 02-04; Wagga Wagga, Australia. Iop Publishing Ltd.

[21] Handbook of superconducting materials A. David Cardwell and S. David Ginley, editors. Brisyol and Philadelphia: IoP; 2003.

[22] Feldmann DM, Holesinger TG, Cantoni C, Feenstra R, Nelson NA, Larbalestier DC, et al. Grain orientations and grain boundary networks of YBa2Cu3O7-delta films deposited by metalorganic and pulsed laser deposition on biaxially textured Ni-W substrates. J Mater Res. 2006;21(4):923-934.

[23] Shields TC, Kawano K, Button TW,Abell JS. Spray pyrolysis of epitaxial YBCO films on (100) single crystal SrTiO3 substrates. Supercond Sci Technol. 2002;15(1):99-103.

[24] Shields TC, Abell JS, Button TW, Chakalov RA, Chakalova RI, Cai C, et al. Deposition of YBCO films by high temperature spray pyrolysis. Physica C-Superconductivity and Its Applications. 2002;372:747-750.

[25] Schieber M, Han SC, Ariel Y, Chokron S, Tsach T, Maharizi M, et al. Comparison of thin films of YBa2Cu3O7-x deposited by physical (laser ablation) and chemical (OMCVD) methods for device applications. Journal of Crystal Growth. 1991;115(1-4):31-42.

[26] Sheth A, Schmidt H,Lasrado V. Review and evaluation of methods for application of epitaxial buffer and superconductor layers. Applied Superconductivity. 1999;6(10-12):855-873.

[27] Cantoni C, Aytug T, Verebelyi DT, Paranthaman M, Specht ED, Norton DP, et al. Conductive buffer layers and overlayers for the thermal stability of coated conductors. Applied Superconductivity, IEEE Transactions on. 2001;11(1):3309-3312.

[28] Superconducting Coated Conductors University of Cambridge; [cited 2007 May 12th]; Available from: http://www-dmg.msm.cam.ac.uk/ResearchNew/Appl_Sup/CoatedConductors/calcium.html.

[29] Wordenweber R. Growth of high-Tc thin films. Superconductor Science and Technology. 1999;12(6):R86-R102.

[30] Dimos D, Chaudhari P, Mannhart J,Legoues FK. Orientation Dependence of Grain-Boundary Critical Currents in Yba2Cu3O7-Delta Bicrystals. Physical Review Letters. 1988;61(2):219-222.

[31] Huhne R, Beyer C, Holzapfel B, Oertel CG, Schultz L,Skrotzki W. Growth of biaxial textured MgO-Layers by ion-beam assisted pulsed laser deposition. Crystal Research and Technology. 2000;35(4):419-425.

[32] Bhattacharjee PP, Ray RK,Upadhyaya A. Nickel base substrate tapes for coated superconductor applications. Journal of Materials Science. 2007;42(6):1984-2001.

[33] MacManus-Driscoll JL. Recent developments in conductor processing of high irreversibility field superconductors. Annual Review of Materials Science. 1998;28:421-462.

[34] Paranthaman MP, Aytug T, Zhai HY, Heatherly L, Goyal A,Christen DK. Growth of YBCO films on MgO-based rolling-assisted biaxially textured substrates templates. Supercond Sci Technol. 2005;18(3):223-228.

[35] Mao Y, Ren C, Yuan J, Zhang F, Liu X, Zou S, et al. Ion beam assisted deposition of biaxially textured YSZ thin films as buffer layers for YBCO superconducting films. Physica C: Superconductivity. 1997;282-287(Part 2):611-612.

[36] Hirvonen JK. Ion-Beam Assisted Thin-Film Deposition. Materials Science Reports. 1991;6(6):215-274.

[37] Iijima Y, Kakimoto K, Sutoh Y, Ajimura S,Saitoh T. Development of long Y-123 coated conductors for coil-applications by IBAD/PLD method. Ieee Transactions on Applied Superconductivity. 2005;15(2):2590-2595.

[38] Brewer RT, Hartman JW, Groves JR, Arendt PN, Yashar PC,Atwater HA. Rheed in-plane rocking curve analysis of biaxially-textured polycrystalline MgO films on amorphous substrates grown by ion beam-assisted deposition. Applied Surface Science. 2001;175:691-696.

[39] Ma B, Koritala RE, Fisher BL, Uprety KK, Baurceanu R, Dorris SE, et al. High critical current density of YBCO coated conductors fabricated by inclined substrate deposition. Physica C: Superconductivity. 2004;403(3):183-190.

[40] Ma B, Li M, Fisher BL, Koritala RE,Balachandran U. Inclined-substrate deposition of biaxially aligned template films for YBCO-coated conductors. Physica C: Superconductivity. 2002;382(1):38-42.

[41] Li M, Ma B, Koritala RE, Fisher BL, Zhao X, Maroni VA, et al. c-Axis orientation control of YBa2Cu3O7-x films grown on inclined-substrate-deposited MgO-buffered metallic substrates. Solid State Communications. 2004;131(2):101-105.

[42] Wong-Ng W, Levin I, Feenstra R, Cook LP,Vaudin M. Phase evolution of Ba2YCu3O6+x films during the BaF2 process. Supercond Sci Technol. 2004;17(9):S548-S556.

[43] Goyal A, List FA, Mathis J, Paranthaman M, Specht ED, Norton DP, et al. High critical current density YBa2Cu3Ox tapes using the RABiTs approach. Journal of Superconductivity. 1998;11(5):481-487.

[44] Goyal A, Norton DP, Kroeger DM, Christen DK, Paranthaman M, Specht ED, et al. Conductors with controlled grain boundaries: An approach to the next generation, high temperature superconducting wire. J Mater Res. 1997;12(11):2924-2940.

[45] Vannozzi A, Rufoloni A, Celentano G, Augieri A, Ciontea L, Fabbri F, et al. Cube-textured substrates for YBCO-coated conductors: microstructure evolution and stability. Supercond Sci Technol. 2006;19(12):1240-1245.

[46] Goyal A, Ren SX, Specht ED, Kroeger DM, Feenstra R, Norton D, et al. Texture formation and grain boundary networks in rolling assisted biaxially textured substrates and in epitaxial YBCO films on such substrates. Micron. 1999;30(5):463-478.

[47] Vallejo RN,Wu JZ. Ion beam assisted deposition of textured magnesium oxide templates on un-buffered glass and silicon substrates. J Mater Res. 2006;21(1):194-198.

[48] Mohan S,Krishna MG. A review of ion beam assisted deposition of optical thin films. Vacuum. 1995;46(7):645-659.

[49] Hasegawa K, Fujino K, Mukai H, Konishi M, Hayashi K, Sato K, et al. Biaxially aligned YBCO film tapes fabricated by all pulsed laser deposition. Applied Superconductivity. 1996;4(10-11):487-493.

[50] Ma B, Li M, Jee YA, Koritala RE, Fisher BL,Balachandran U. Inclined-substrate deposition of biaxially textured magnesium oxide thin films for YBCO coated conductors. Physica C: Superconductivity. 2002;366(4):270-276.

[51] Ghekiere P, Mahieu S, De Winter G, De Gryse R,Depla D. Influence of the deposition parameters on the biaxial alignment of MgO grown by unbalanced magnetron sputtering. Journal of Crystal Growth. 2004;271(3-4):462-468.

[52] Balachandran U, Li M, Koritala RE, Fisher BF,Ma B. Development of YBCO-coated conductors for electric power applications. Physica C: Superconductivity. 2002;372-376(Part 2):869-872.

[53] Balachandran U, Ma B, Li A, Fisher BL, Koritala RE, Erck RA, et al. Inclined-substrate deposition of biaxially textured template for coated conductors. Physica C-Superconductivity and Its Applications. 2002;378:950-954.

[54] Wei M, Zhi D,Choy KL. Electrostatic spray assisted vapour deposition and structural characterisation of cerium oxide films on biaxially textured Ni tapes. Materials Letters. 2006;60(12):1519-1523.

[55] Xiong J, Chen Y, Qiu Y, Tao BW, Qin WF, Cui XM, et al. A novel process for CeO2 single buffer layer on biaxially textured metal substrates in YBCO coated conductors. Supercond Sci Technol. 2006;19(10):1068-1072.

[56] Rhee SH, Yang Y, Choi HS, Myoung JM,Kim K. Low-temperature deposition of highly [100]-oriented MgO films using charged liquid cluster beam. Thin Solid Films. 2001;396(1-2):23-28.

[57] Bhattacharya RN, Phok S, Xu YL,Bhattacharya R. Electrodeposited biaxially textured buffer layers for YBCO superconductors. Ieee Transactions on Applied Superconductivity. 2007;17(2):3321-3324.

[58] Carlson CM, Price JC, Parilla PA, Ginley DS, Niles D, Blaugher RD, et al. Laser-ablated epitaxial LaAlO3 buffer layers on biaxially textured Ni substrates for superconducting tapes. Physica C: Superconductivity. 1998;304(1-2):82-88.

[59] Chung JK, Ko RK, Shi DQ, Ha HS, Kim H, Song KK, et al. Use of SrTiO3 as a single buffer layer for RABiTS YBCO coated conductor. Ieee Transactions on Applied Superconductivity. 2005;15(2):3020-3023.

[60] Park C, Norton DP, Lee DF, Verebelyi DT, Goyal A, Christen DK, et al. Epitaxial yttria-stabilized zirconia on biaxially-textured (001) Ni for YBCO coated conductor. Physica C: Superconductivity. 2000;341-348(Part 4):2481-2482.

[61] He Q, Christen DK, Budai JD, Specht ED, Lee DF, Goyal A, et al. Deposition of biaxially-oriented metal and oxide buffer-layer films on textured Ni tapes: New substrates for high-current, high-temperature superconductors. Physica C. 1997;275(1-2):155-161.

[62] Konstantinov K, Stambolova I, Peshev P, Darriet B,Vassilev S. Preparation of ceria films by spray pyrolysis method. International Journal of Inorganic Materials. 2000;2(2-3):277-280.

[63] Petrova NL, Todorovska RV,Todorovsky DS. Spray-pyrolysis deposition of CeO2 thin films using citric or tartaric complexes as starting materials. Solid State Ionics. 2006;177(5-6):613-621.

[64] Kim HJ, Joo J, Ji BK, Jun BH, Jung CH, Park SD, et al. Deposition of CeO2 buffer layers for YBCO coated conductors on biaxially textured ni substrates by MOCVD technique. Ieee Transactions on Applied Superconductivity. 2003;13(2):2555-2558.

[65] Bian JM, Li XM, Chen TL, Gao XD,Yu WD. Preparation of high quality MgO thin films by ultrasonic spray pyrolysis. Applied Surface Science. 2004;228(1-4):297-301.

[66] Jergel M, Chromik S, Strbik V, Smatko V, Hanic F, Plesch G, et al. Thin YBCO films prepared by low-temperature spray pyrolysis. Supercond Sci Technol. 1992;5:225-230

[67] Stambolova I, Konstantinov K, Kovacheva D, Khristov M, Peshev P,Donchev T. Spray pyrolysis deposition of polycrystalline magnesia films and their use as buffer layers in Bi(Pb)-Sr-Ca-Cu-O/MgO/Al2O3 (or glass ceramics) structures. Materials Letters. 1997;30(5-6):333-337.

[68] Ghekiere P, Mahieu S, De Gryse R,Depla D. Structure evolution of the biaxial alignment in sputter-deposited MgO and Cr. Thin Solid Films. 2006;515(2):485-488.

[69] Kingery DD, Bowen HK,Uhlmann DR. Introduction to ceramics. John wiley & sons, 1976; 1960.

[70] William D. Callister J. Fundamentals of Materials Science and Engineering. John Wiley & Sons, Inc.; 2001.

[71] Lee SY, Lee SH, Nah EJ, Lee SS,Kim Y. Heteroepitaxial growth of MgO films on Si(0 0 1) substrates using cubic SiC as a buffer layer. Journal of Crystal Growth. 2002;236(4):635-639.

[72] Fu X, Wu G, Song S, Song Z, Duo X,Lin C. Preparation and characterization of MgO thin films by a simple nebulized spray pyrolysis technique. Applied Surface Science. 1999;148(3-4):223-228.

[73] Pradhan AK, Sahu DR, Roul BK,Feng Y. Lanthanum-based manganite films on MgO using SrTiO3 as a template layer. Journal of Applied Physics. 2004;96(2):1170-1173.

[74] Gila BP, Kim J, Luo B, Onstine A, Johnson W, Ren F, et al. Advantages and limitations of MgO as a dielectric for GaN. Solid-State Electronics. 2003;47(12):2139-2142.

[75] Caceres D, Vergara I,Gonzalez R. Microstructural characterization of MgO thin films grown by radio-frequency sputtering. Target and substrate-temperature effect. Journal of Applied Physics. 2003;93(7):4300-4305.

[76] Hellman ES,Hartford EH. Epitaxial Solid-Solution Films of Immiscible MgO and CaO. Applied Physics Letters. 1994;64(11):1341-1343.

[77] Niu F, Hoerman BH,Wessels BW. Epitaxial thin films of MgO on Si using metalorganic molecular beam epitaxy. Journal of Vacuum Science & Technology B. 2000;18(4):2146-2152.

[78] Yi X, Wenzhong W, Yitai Q, Li Y,Zhiwen C. Deposition and microstructural characterization of MgO thin films by a spray pyrolysis method. Surface and Coatings Technology. 1996;82(3):291-293.

[79] One-electron properties Crystal; [cited 2008 May, 12th]; Available from: http://www.crystal.unito.it/mssc2006_cd/tutorials/surfaces/surfaces_tut.html.

[80] Fork DK, Nashimoto K,Geballe TH. Epitaxial Yba2Cu3O7-Delta on GaAs(001) Using Buffer Layers. Applied Physics Letters. 1992;60(13):1621-1623.

[81] Tarsa EJ, De Graef M, Clarke DR, Gossard AC,Speck JS. Growth and characterization of (111) and (001) oriented MgO films on (001) GaAs. Journal of Applied Physics. 1993;73(7):3276-3283.

[82] Hung LS, Zheng LR,Blanton TN. Epitaxial growth of MgO on (100) GaAs using ultrahigh vacuum electron-beam evaporation. Applied Physics Letters. 1992;60(25):3129-3131.

[83] Milan J. Synthesis of high-Tc superconducting films by deposition from an aerosol. Supercond Sci Technol. 1995;8:67-78.

[84] Danius P,Ludwig J. Thin film deosition using spray pyrlolysis. Journal of electroceramics. 2005;14(2):103-111.

[85] Boo JH, Yu KS, Koh W,Kim Y. Preparation of MgO films on GaAs by metalorganic chemical vapor deposition. Materials Letters. 1996;26(4-5):233-236.

[86] Kim SG, Kim JY,Kim HJ. Deposition of MgO thin films by modified electrostatic spray pyrolysis method. Thin Solid Films. 2000;376(1-2):110-114.

[87] Liu M, Liu DM, Zhou ML, Zhao Y, Gao X,Liang JX. Fabrication of YBCO tapes on Ag substrates by the ultrasonic spray pyrolysis method. Supercond Sci Technol. 2004 Apr;17(4):676-680.

[88] Mateev E, Donchev T, Blagoev B, Nurgaliev T, Tsaneva V,Barber ZH. Deposition of YBa2Cu3O7-x superconducting films by magnetron sputtering and water vapour addition to the sputtering gas. Vacuum. 2004;76(2-3):241-244.

[89] Goyal A, Norton DP, Budai JD, Paranthaman M, Specht ED, Kroeger DM, et al. High critical current density superconducting tapes by epitaxial deposition of YBa2Cu3Ox thick films on biaxially textured metals. Applied Physics Letters. 1996;69(12):1795-1797.

[90] Takechi A, Matsumoto K,Osamura K. YBa2Cu3O7-x films on oxide buffer layer with perovskite structure prepared by metal-organic deposition method. Physica C: Superconductivity. 2003;392-396(Part 2):895-899.

[91] Marguillier D, Cloots R, Rulmont A, Fagnard JF, Vanderbemden P,Ausloos M. YBa2Cu3O7 tapes prepared by sol-gel deposition techniques: microstructure and

structural characterizations. Physica C: Superconductivity. 2002;372-376(Part 2):715-718.

[92] Wesolowski DE, Yoshizumi M,Cima MJ. Trajectory-property relationships in MOD-derived YBCO films. Physica C: Superconductivity. 2006;450(1-2):76-82.

[93] Vergnieres L, Donet S, Jimenez C, Odier P, Weiss F, Bruzek CE, et al. MOCVD and spray pyrolysis for coated conductor synthesis. Ieee Transactions on Applied Superconductivity. 2005;15(2):2759-2762.

[94] Vergnieres L, Odier P, Weiss F, Bruzek CE,Saugrain JM. Epitaxial thick films by spray pyrolysis for coated conductors. Journal of the European Ceramic Society. 2005;25(12):2951-2954.

[95] Méchin L, Villégier J-C, Rolland G,Laugier F. Double CeO2/YSZ buffer layer for the epitaxial growth of YBa2Cu3O7-delta films on Si (001) substrates. Physica C: Superconductivity. 1996;269(1-2):124-130.

[96] Qiao JM,Yang CY. High-Tc superconductors on buffered silicon - materials properties and device applications. Materials Science & Engineering R-Reports. 1995 Apr;14(4):157-201.

[97] High-Temperature Superconductivity Helsinki Univeristy of Technology; [cited 2008 May 19th]; Available from: http://www.tkk.fi/Units/AES/projects/prlaser/supercond.htm.

[98] Jorgensen JD, Veal BW, Paulikas AP, Nowicki LJ, Crabtree GW, Claus H, et al. Structural properties of oxygen-deficient YBa2Cu3O7- delta. Physical Review B. 1990;41(4):1863.

[99] Jeong YS, Park JH,Lee SY. Epitaxial growth of YBCO on Hastelloy with YSZ buffer layer by laser ablation. Thin Solid Films. 1998;318(1-2):262-264.

[100] Russo RE, Reade RP, McMillan JM,Olsen BL. Metal buffer layers and Y-Ba-Cu-O thin films on Pt and stainless steel using pulsed laser deposition. Journal of Applied Physics. 1990;68(3):1354-1356.

[101] Fukui S, Kojima R, Ogawa J, Yamaguchi M, Sato T,Tsukamoto O. Numerical analysis of AC loss characteristics of cable conductor assembled by HTS tapes in polygonal arrangement. Ieee Transactions on Applied Superconductivity. 2006;16(2):143-146.

[102] Donald LS. Thin-Film Deposition Principles and Practices. McGraw-ill; 1995.

[103] Woodcock TG. The crystallographic texture and morphology of nickel oxide layers grown on textured nickel and nickel alloy substrates [PhD Thesis]. Birmingham: University of Birmingham; July 2003.

[104] Narumi E, Song LW, Yang F, Patel S, Kao YH,Shaw DT. Critical current density enhancement in YBa2Cu3O6.8 films on buffered metallic substrates. Applied Physics Letters. 1991;58(11):1202-1204.

[105] Reade RP, Mao XL,Russo RE. Characterization of Y-Ba-Cu-O thin films and yttria-stabilized zirconia intermediate layers on metal alloys grown by pulsed laser deposition. Applied Physics Letters. 1991;59(6):739-741.

[106] Lewis JR. A dictionary of metallurgy. S. K. Jain 1997.

[107] Chopra KL. Thin film phenomena New York ; London McGraw-Hill; 1969.

[108] Herman MA, Richter, Wolfgang, Sitter, Helmut. Epitaxy : physical principles and technical implementation First ed. Berlin ; London Springer; 2004.

[109] Thompson CV, Floro J,Smith HI. Epitaxial grain growth in thin metal films. Journal of Applied Physics. 1990;67(9):4099-4104.

[110] Toivo TK,Mark JH. Aerosol processing of materials. New York: WILEY-VCH; 1999.

[111] Che S, Sakurai O, Shinozaki K,Mizutani N. Particle structure control through intraparticle reactions by spray pyrolysis. Journal of Aerosol Science. 1998;29(3):271-278.

[112] Chamberlin RR,Skarman JS. Chemical Spray Deposition Process for Inorganic Films. Journal of the Electrochemical Society. 1966;113(1):86-89.

[113] Patil PS. Versatility of chemical spray pyrolysis technique. Materials Chemistry and Physics. 1999;59(3):185-198.

[114] Paraguay F, Estrada W, Acosta DR, Andrade E,Miki-Yoshida M. Growth, structure and optical characterization of high quality ZnO thin films obtained by spray pyrolysis. Thin Solid Films. 1999;350(1-2):192-202.

[115] Ban E, Matsuoka Y, Ogawa H,Kurosawa K. High Jc Y-Ba-Cu-O thin films prepared by a spray pyrolysis method. Journal of Alloys and Compounds. 1992;187(1):193-205.

[116] Balkenende AR, Bogaerts AAMB, Scholtz JJ, Tijburg RRM,Willems HX. Thin MgO layers for effective hopping transport of electrons. Philips Journal of Research. 1996;50(3-4):365-373.

[117] Zaouk D, Zaatar Y, Khoury A, Llinares C, Charles JP,Bechara J. Fabrication of tin oxide (SnO2) thin film by electrostatic spray pyrolysis. Microelectronic Engineering. 2000;51-52:627-631.

[118] Arya SPS,Hintermann HE. Growth of Y---Ba---Cu---O superconducting thin films by ultrasonic spray pyrolysis. Thin Solid Films. 1990;193-194(Part 2):841-846.

[119] Langlet MJ, J.C. The pyrosol process or the pyrolysis of an ultrasonically generated aerosol. In: C. N. R. Rao, editor. Chemistry of advanced materials. Oxford, UK: Blackwell Scientific Publications; 1993. p. 55.

[120] Blandenet G, Court M,Lagarde Y. Thin layers deposited by the pyrosol process. Thin Solid Films. 1981;77(1-3):81-90.

[121] PLD. [cited 2008 March, 12th]; Available from: http://materials.web.psi.ch/Research/Thin_Films/Methods/PLD.htm?forprint.

[122] Pulsed laser deposition. Superconductivity center at Argonne Natinal Laboratory; [cited 2008 April, 20th]; Available from: http://superconductivity.et.anl.gov/Techniques/PLD.html.

[123] Hinds WC. Aerosol Technology. New York: Wiley interscience; 1982.

[124] The Chemistry of Metal CVD. T. T. Kodas, Hampden-Smith, M.J., editor. Weinheim, West GErmany: VCH Verlagsgesellschaft; 1994.

[125] Kodas TT, Sood A,Pratsinis SE. Submicron alumina powder production by a turbulent-flow aerosol process. Powder Technology. 1987 Mar;50(1):47-53.

[126] Pluym TC, Powell QH, Gurav AS, Ward TL, Kodas TT, Wang LM, et al. Solid silver particle-production by spray pyrolysis. Journal of Aerosol Science. 1993 May;24(3):383-392.

[127] Pluym TC, Lyons SW, Powell QH, Gurav AS, Kodas TT, Wang LM, et al. Palladium metal and palladium oxide particle production by spray pyrolysis. Materials Research Bulletin. 1993;28(4):369-376.

[128] German RM. Sintering theory and practice. New York: John Wiley and Sons; 1996.

[129] Roger C, Corbitt T, Xu C, Zeng D, Powell Q, Chandler CD, et al. Principles of molecular precursor selection for aerosol synthesis of materials. Nanostructured Materials. 1994;4(5):529-535.

[130] Malecki A, Gajerski R, Labus S, Prochowskaklisch B,Wojciechowski K. Thermal-decomposition of NI(NO3)2.2H2O. J Therm Anal. 1993 May;39(5):545-550.

[131] Kodas T.T. H-S, M.J. The chemistry of metal CVD. In: H.-S. Kodas T.T., M.J., editor. The chemistry of metal CVD. Weinheim, Germany: VCH; 1994.

[132] Parker C. Aerosol science and technology. Second ed.: McGraw-Hill, Inc.; 1993.

[133] Cabera N, Coleman, R. V. Theory of crystal growth from the vapor In: G. J.J., editor. The art and science of growing crystals. New York: John Wiley and Sons; 1963. p. 3-28.

[134] Bird R, Stewart, W.E., Lightfood, E.N. Transport phenomena. New York: John Wiley and Sons; 1960.

[135] Henry's law. Wikipedia; [cited 2009 Apr. 17]; Available from: http://en.wikipedia.org/wiki/Henry's_law.

[136] Chiang P-P,Donohue MD. A kinetic approach to crystallization from ionic solution : I. Crystal Growth. Journal of Colloid and Interface Science. 1988;122(1):230-250.

[137] Chiang P-P, Donohue MD,Katz JL. A kinetic approach to crystallization from ionic solution : II. Crystal Nucleation. Journal of Colloid and Interface Science. 1988;122(1):251-265.

[138] Katz JL,Donohue MD. Nucleation with simultaneous chemical reaction. Journal of Colloid and Interface Science. 1982;85(1):267-277.

[139] Reist PC. Introduction to aerosol science. New York: MacMillan Publishing Co.; 1984.

[140] Joseph Prince J, Ramamurthy S, Subramanian B, Sanjeeviraja C,Jayachandran M. Spray pyrolysis growth and material properties of In2O3 films. Journal of Crystal Growth. 2002;240(1-2):142-151.

[141] Krunks M,Mellikov E. Zinc oxide thin films by the spray pyrolysis method. Thin Solid Films. 1995;270(1-2):33-36.

[142] Stryckmans O, Segato T,Duvigneaud PH. Formation of MgO films by ultrasonic spray pyrolysis from [beta]-diketonate. Thin Solid Films. 1996;283(1-2):17-25.

[143] DeSisto WJ,Henry RL. Deposition of (100) oriented MgO thin films on sapphire by a spray pyrolysis method. Applied Physics Letters. 1990;56(25):2522-2523.

[144] Hill MR, Lee EYM, Russell JJ, Wang Y,Lamb RN. Growth Mechanism of Textured MgO Thin Films via SSCVD. Journal of Physical Chemistry B. 2006;110(18):9236-9240.

[145] Dong L,Srolovitz DJ. Mechanism of texture development in ion-beam-assisted deposition. Applied Physics Letters. 1999;75(4):584-586.

[146] Renault O,Labeau M. Strong < 200 > and < 111 > preferred orientations of MgO thin films synthesized on amorphous substrate by aerosol assisted-metallorganic

chemical vapor deposition. Journal of the Electrochemical Society. 1999;146(10):3731-3735.

[147] Pavlopoulos D. Spray pyrolysis for oxide buffer layers for second generation coated conductor applications [Ph.D. Thesis]: University of Birmingham 2008.

[148] D. Pavlopoulos , Shadi Al-Khatiab , T. W. Button,Abell JS. Spray Pyrolysis of Ceria (CeO2) Thin Films and the Effect of Deposition Parameters on the Textural and Structural Properties In press to be published.

[149] D. Pavlopoulos, Shadi Al-Khatiab, T. W. Button,J. S. Abell. Spray Pyrolysis of MgO Thin Films on Si Single Crystals and the Effect of Deposition Time and Inclination Angle on the Texture and Morphology of the Films In press to be published.

[150] Wang SY, Qiao ZP, Wang W,Qian YT. XPS studies of nanometer CeO2 thin films deposited by pulse ultrasonic spray pyrolysis. Journal of Alloys and Compounds. 2000;305(1-2):121-124.

[151] Wang S, Wang W, Zuo J,Qian Y. Study of the Raman spectrum of CeO2 nanometer thin films. Materials Chemistry and Physics. 2001;68(1-3):246-248.

[152] Wang S, Wang W, Liu Q, Zhang M,Qian Y. Preparation and characterization of cerium (IV) oxide thin films by spray prolysis method. Solid State Ionics. 2000;133(3-4):211-215.

[153] Pavlopoulos D, Shadi Al-Khatiab, Button TW,Abell JS. Effort to produce textured CeO2 and MgO films by the spray pyrolysis technique as buffer layers for coated conductors. Journal of Physics: Conference Series. 2008;97:012098.

[154] Elidrissi B, Addou M, Regragui M, Monty C, Bougrine A,Kachouane A. Structural and optical properties of CeO2 thin films prepared by spray pyrolysis. Thin Solid Films. 2000;379(1-2):23-27.

[155] Wei M,Choy KL. Deposition of cerium oxide films on Si(100) and glass substrates using the ESAVD method. Journal of Crystal Growth. 2005;284(3-4):464-469.

[156] Du J,Choy K-L. Electrostatic spray assisted vapour deposition of TiO2-based films. Solid State Ionics. 2004;173(1-4):119-124.

[157] Choy KL. Processing-structure-property of nanocrystalline materials produced using novel and cost-effective ESAVD-based methods. Materials Science and Engineering: C. 2001;16(1-2):139-145.

[158] Lee CH,Huang CS. Spray pyrolysis deposition for indium oxide doped with different impurities. Materials Science and Engineering B. 1994;22(2-3):233-240.

[159] Manoj PK, Gopchandran KG, Koshy P, Vaidyan VK,Joseph B. Growth and characterization of indium oxide thin films prepared by spray pyrolysis. Optical Materials. 2006;28(12):1405-1411.

[160] Elangovan E, Singh MP,Ramamurthi K. Studies on structural and electrical properties of spray deposited SnO2 : F thin films as a function of film thickness. Materials Science and Engineering B-Solid State Materials for Advanced Technology. 2004 Oct;113(2):143-148.

[161] Elangovan E,Ramamurthi K. A study on low cost-high conducting fluorine and antimony-doped tin oxide thin films. Applied Surface Science. 2005 Aug;249(1-4):183-196.

[162] Korotcenkov G, DiBattista M, Schwank J,Brinzari V. Structural characterization of SnO2 gas sensing films deposited by spray pyrolysis. Materials Science and Engineering B-Solid State Materials for Advanced Technology. 2000 Aug;77(1):33-39.

[163] Gurumurugan K, Mangalaraj D,Narayandass SK. Structural characterization of cadmium oxide thin films deposited by spray pyrolysis. Journal of Crystal Growth. 1995;147(3-4):355-360.

[164] Morales J, Sanchez L, Martin F, Ramos-Barrado J,Sanchez M. Use of low-temperature nanostructured CuO thin films deposited by spray-pyrolysis in lithium cells. Thin Solid Films. 2005 Mar;474(1-2):133-140.

[165] Develos KD, Kusunoki M, Mukaida M,Ohshima S. Effect of deposition rate on the surface morphology of CeO2 films deposited by pulsed laser deposition. Physica C: Superconductivity. 1999;320(1-2):21-30.

[166] Ohshima S, Develos KD, Ehata K, Ali MI,Mukaida M. Fabrication of low surface resistance YBCO films and its application to microwave devices. Physica C: Superconductivity. 2000;335(1-4):207-213.

[167] Yongli X,Donglu S. A review of coated conductor development. Tsinghua science and technology. 2003.

[168] Balachandran UB, Ma B, Li M, Fisher BL, Koritala RE,Miller DJ. Development of coated conductors by inclined substrate deposition. Advances in Cryogenic Engineering, Vols 50A and B. 2004;711:637-644.

[169] Li M, Zhao XZ, Ma B, Dorris SE, Balachandran U,Maroni VA. Effect of CeO2 buffer layer thickness on the structures and properties of YBCO coated conductors. Applied Surface Science. 2007;253(17):7172-7177.

[170] Uprety KK, Ma B, Koritala RE, Fisher BL, Dorris SE,Balachandran U. Growth and properties of YBCO-coated conductors on biaxially textured MgO films prepared by inclined substrate deposition. Supercond Sci Technol. 2005;18(3):294-298.

[171] Ma BH, Uprety KK, Koritala RE, Fisher BL, Dorris SF, Miller DJ, et al. Growth and properties of YBCO-coated conductors fabricated by inclined-substrate deposition. Ieee Transactions on Applied Superconductivity. 2005;15(2):2970-2973.

[172] Ma B, Li M, B.L.Fisher, E.Koritala, S.E.Dorris, V.A.Maroni, et al., editors. Inclined Substrate Deposition of Magnesium Oxide for YBCO Coated Conductors. American Ceramic Society; 2002 2002; Argonne. Proceedings of the American Ceramic Society, 104th annual meeting.

[173] Metzger R, Bauer M, Numssen K, Semerad R, Berberich P,Kinder H. Superconducting tapes using ISD buffer layers produced by evaporation of MgO or reactive evaporation of magnesium. Ieee Transactions on Applied Superconductivity. 2001;11(1):2826-2829.

[174] Xu Y, Lei CH, Ma B, Evans H, Efstathiadis H, Rane M, et al. Growth of textured MgO through e-beam evaporation and inclined substrate deposition. Supercond Sci Technol. 2006;19(8):835-843.

[175] Chudzik MP, Koritala RE, Luo LP, Miller DJ, Balachandran U,Kannewurf CR. Mechanism and processing dependence of biaxial texture development in magnesium oxide thin films grown by inclined-substrate deposition. Ieee Transactions on Applied Superconductivity. 2001;11(1):3469-3472.

[176] Li MY, Ma B, Koritala RE, Fisher BL, Zhao XZ, Maroni VA, et al. c-Axis orientation control of YBa2CU3O7-x films grown on inclined-substrate-deposited MgO-buffered metallic substrates. Solid State Communications. 2004;131(2):101-105.

[177] Ma B, Li M, Koritala RE, Fisher BL, Markowitz AR, Erck RA, et al. Pulsed laser deposition of YBCO films on ISD MgO buffered metal tapes. Supercond Sci Technol. 2003 Apr;16(4):464-472.

[178] Iijima Y,Matsumoto K. High-temperature-superconductor coated conductors: technical progress in Japan. Supercond Sci Technol. 2000 Jan;13(1):68-81.

[179] Bauer M, Semerad R,Kinder H. YBCO films on metal substrates with biaxially aligned MgO buffer layers. Ieee Transactions on Applied Superconductivity. 1999;9(2):1502-1505.

[180] Chudzik MP, Erck RA, Luo ZP, Miller DJ, Balachandran U,Kannewurf CR. High-rate reel-to-reel continuous coating of biaxially textured magnesium oxide thin films for coated conductors. Physica C: Superconductivity. 2000;341-348(Part 4):2483-2484.

[181] Koritala RE, Chudzik MP, Luo ZP, Miller DJ, Kannewurf CR,Balachandran U. Transmission electron microscopy investigation of texture development in magnesium oxide buffer layers. Ieee Transactions on Applied Superconductivity. 2001;11(1):3473-3476.

[182] Ma BH, Li MY, Koritala RE, Fisher BL, Markowitz AR, Erck RA, et al. Biaxially aligned template films fabricated by inclined-substrate deposition for YBCO-coated conductor applications. Ieee Transactions on Applied Superconductivity. 2003;13(2):2695-2698.

[183] Koritala RE, Ma BH, Miller DJ, Li MY, Fisher BL,Balachandran U. Texture development of MgO buffer layers grown by inclined substrate deposition. Ieee Transactions on Applied Superconductivity. 2003;13(2):2691-2694.

[184] Shi DQ, Ionescu M, Silver TM,Dou SX. Relationship between epitaxial deposition and growth modes of CeO2 films. Physica C: Superconductivity. 2003;384(4):475-481.

[185] Koritala RE, Ma BH, Miller DJ, Uprety KK, Fisher BL,Balachandran U. Surface roughness of magnesium oxide buffer layers grown by inclined substrate deposition. Ieee Transactions on Applied Superconductivity. 2005;15(2):3031-3033.

[186] Masuda A, Yamanaka Y, Tazoe M, Nakamura T, Morimoto A,Shimizu T. Preparation and crystallographic characterizations of highly oriented Pb(Zr0.52Ti0.48)O3 films and MgO buffer layers on (100)GaAs and (100)Si by pulsed laser ablation. Journal of Crystal Growth. 1996;158(1-2):84-88.

[187] Li X, Sakurai A, Shiratsuyu K, Tanaka K,Sakabe Y. Epitaxial growth of an MgO buffer layer and electrode layer on Si for Pb(Zr,Ti)O-3 by PLD. Proceedings of the 2001 12th Ieee International Symposium on Applications of Ferroelectrics, Vols I and Ii. 2001:909-912.

[188] Nashimoto K, Fork DK,Geballe TH. Epitaxial growth of MgO on GaAs(001) for growing epitaxial BaTiO3 thin films by pulsed laser deposition. Applied Physics Letters. 1992;60(10):1199-1201.

[189] Fork DK,Anderson GB. Epitaxial MgO on GaAs(111) as a buffer layer for z-cut epitaxial lithium niobate. Applied Physics Letters. 1993;63(8):1029-1031.

[190] Fork DK, Ponce FA, Tramontana JC,Geballe TH. Epitaxial MgO on Si(001) for Y-Ba-Cu-O thin-film growth by pulsed laser deposition. Applied Physics Letters. 1991;58(20):2294-2296.

[191] Degardin AF, Houze F,Kreisler AJ, editors. MgO substrate surface optimization for YBaCuO thin film growth. Applied Superconductivity Conference; 2002 Aug 04-09; Houston, Texas.

[192] Norton MG, Summerfelt SR,Carter CB. Surface preparation for the heteroepitactic growth of ceramic thin films. Applied Physics Letters. 1990;56(22):2246-2248.

[193] Moeckly BH, Russek SE, Lathrop DK, Buhrman RA, Li J,Mayer JW. Growth of YBa2Cu3O7 thin films on MgO: The effect of substrate preparation. Applied Physics Letters. 1990;57(16):1687-1689.

[194] Duriez C, Chapon C, Henry CR,Rickard JM. Structural characterization of MgO (100) surfaces. Surface Science. 1990;230(1-3):123-136.

[195] Langel W,Parrinello M. Hydrolysis at stepped MgO surfaces. Physical Review Letters. 1994;73(3):504.

[196] Kim BI, Hong JW, Jeong GT, Moon SH, Lee DH, Shim TU, et al., editors. Effect of Mg(OH)2 on YBa2Cu3O7 thin film on MgO substrate studied by atomic force microscope. The 1993 international conference on scanning tunneling microscopy; 1994; Beijing, China. AVS.

[197] Du J, Gnanarajan S,Bendavid A. Characterization of MgO substrates for growth of epitaxial YBCO thin films. Supercond Sci Technol. 2005;18(8):1035-1041.

[198] Du J, Gnanarajan S,Bendavid A. Influence of MgO surface conditions on the in-plane crystal orientation and critical current density of epitaxial YBCO films. Physica C-Superconductivity and Its Applications. 2004;400(3-4):143-152.

[199] Abriou D, Creuzet F,Jupille J. Characterization of cleaved MgO(100) surfaces. Surface Science. 1996;352-354:499-503.

[200] Abriou D,Jupille J. Self-inhibition of water dissociation on magnesium oxide surfaces. Surface Science. 1999;430(1-3):L527-L532.

[201] Altieri S, Contri SF, Agnoli S,Valeri S. Morphology of H2O dosed monolayer MgO(0 0 1)/Ag(0 0 1). Surface Science. 2004;566-568(Part 2):1071-1075.

[202] Khairallah F,Glisenti A. Synthesis, characterization and reactivity study of nanoscale magnesium oxide. Journal of Molecular Catalysis A-Chemical. 2007;274(1-2):137-147.

[203] Aswal DK, Muthe KP, Tawde S, Chodhury S, Bagkar N, Singh A, et al. XPS and AFM investigations of annealing induced surface modifications of MgO single crystals. Journal of Crystal Growth. 2002 Mar;236(4):661-666.

[204] Ardizzone S, Bianchi CL, Fadoni M,Vercelli B. Magnesium salts and oxide: an XPS overview. Applied Surface Science. 1997;119(3-4):253-259.

[205] Verebelyi DT, Christen DK, Feenstra R, Cantoni C, Goyal A, Lee DF, et al. Low angle grain boundary transport in YBa2Cu3O7-delta coated conductors. Applied Physics Letters. 2000;76(13):1755-1757.

[206] Ivanov ZG, Nilsson PA, Winkler D, Alarco JA, Claeson T, Stepantsov EA, et al. Weak links and dc SQUIDS on artificial nonsymmetric grain boundaries in YBa2Cu3O7-delta. Applied Physics Letters. 1991;59(23):3030-3032.

[207] Feldmann DM, Holesinger TG, Feenstra R,Larbalestier DC. A review of the influence of grain boundary geometry on the electromagnetic properties of polycrystalline YBa2Cu3O7-x films. Journal of the American Ceramic Society. 2008 Jun;91(6):1869-1882.

[208] Jackson TJ, Abell JS, Chakalov R, Colclough MS, Darlington CNW, Jones IP, et al. Holes in YBa2Cu3O7-x thin films on vicinal strontium titanate substrates. Thin Solid Films. 2004;468(1-2):332-337.

[209] Krupke R, Barkay Z,Deutscher G. On the origin of hole formation in YBCO films. Physica C: Superconductivity. 1997;289(1-2):146-150.

[210] Catana A, Broom RF, Bednorz JG, Mannhart J,Schlom DG. Identification of epitaxial Y2O3 inclusions in sputtered YBa2Cu3O7 films: Impact on film growth. Applied Physics Letters. 1992;60(8):1016-1018.

[211] Verbist K, Vasiliev AL,Van Tendeloo G. Y2O3 inclusions in YBa2Cu3O7-delta thin films. Applied Physics Letters. 1995;66(11):1424-1426.

[212] Develos-Bagarinao K, Yamasaki H, Nakagawa Y,Endo K. Pore formation in YBCO films deposited by a large-area pulsed laser deposition system. Supercond Sci Technol. 2004;17(11):1253-1260.

[213] Leonard KJ, Goyal A, Kroeger DM, Jones JW, Kang S, Rutter N, et al. Thickness dependence of microstructure and critical current density of YBa2Cu3O7-delta on rolling-assisted biaxially textured substrates. J Mater Res. 2003 May;18(5):1109-1122.

[214] OMRON ultrasonic nebuliser manual. 2000.

[215] Pulsed laser deposition. Argonne National Laboratory; [cited 2009 Mar. 17]; Available from: http://superconductivity.et.anl.gov/Techniques/PLD.html.

[216] Thermogravimetry (TG). NETZSCH; [cited 2009 Mar. 21]; Available from: http://www.e-thermal.com/methods.html#THERMOGRAVIMETRY.

[217] Brwon ME. Introduction to thermal analysis. second ed.: KluwersAcademic Publishers; 2001.

[218] Cullity BD,Stock SR. Elements of X-ray diffraction. third ed.: Prentice Hall; 2001.

[219] Pole figure measurement. Materials research laboratory-University of California; [cited 2009 Mar. 21]; Available from: http://www.mrl.ucsb.edu/mrl/centralfacilities/xray/xray-basics/index.html#x4.

[220] Electron_sample interaction. SERC; [cited 2009 Mar. 23]; Available from: http://serc.carleton.edu/index.html.

[221] Michael T P, Karens S H, Arthur H J,Kathlyn L M. Scanning electron microscopy. Ladd Research Industries, Inc.; 1980. p. 1, 7, 8, 26, 29, 33, 35, 37, 47, 52, 53, 69, 79, 81.

[222] Scanning electron microscopy. Materials Evaluation and Engineering, Inc.; [cited 2009 Mar. 24]; Available from: http://mee-inc.com/sem.html.

[223] Cullity BD. Elements of X-ray diffraction. Reading (Mass.) ; London : Addison-Wesley.; 1978.

[224] Electron backscattered diffraction. OXFORD instruments; [cited 2009 Mar. 24]; Available from: http://www.ebsd.com/ebsdbeginners1.htm.

[225] Valerie Randle OE. Texture Analysis: Macrostructure, Microstructure and Orientaion mapping. London: Taylor and Francis Ltd; 2000.

[226] Scanning probe microscopy training notebook. Digital instruments: Veeco Metrolgy group; [cited 2009 Mar. 25]; Available from: http://www.veeco.com/default.aspx.

[227] Christopher MY. Atomic force Microscopy: Probing Biomolecular interactions. University of Toronto. 2006.

[228] Nikolo M. Superconductivity - A guide to alternating-current susceptibility measurements and alternating-current susceptometer design. American Journal of Physics. 1995;63(1):57-65.

[229] Charles P P, Timir D,Horacio A F. Copper Oxide Superconductors. JOHN WILEY & SONS; 1988.

[230] Mehta SP, Aversa N,Walker MS. Transforming transformers [superconducting windings]. Spectrum, IEEE. 1997;34(7):43-49.

[231] Gomory F. Characterization of high-temperature superconductors by AC susceptibility measurements. Supercond Sci Technol. 1997;10(8):523-542.

[232] Goldfarb RB, Lelental M,Thompson CA. Alternating-field susceptometry and magnetic-susceptibility of superconductors. Magnetic Susceptibility of Superconductors and Other Spin Systems; 1991. p. 49-80.

[233] Schwenterly SW, Demko JA, Lue JW, Walker MS, Reis CT, Hazelton DW, et al. AC loss measurements with a cryocooled sample. IEEE Transactions on Applied Superconductivity. 2001;11(2):4027-4031.

[234] Magnetic susceptibility. Wikipedia; [cited 2009 Mar. 26]; Available from: http://en.wikipedia.org/wiki/Magnetic_susceptibility.

[235] Practical surface analysis second ed. D. Briggs, Seah, M. P. , editor.: JOHN WILLEY & SONS; 1996.

[236] Jarek Dabrowski H-JM. Silicon Surfaces and Formation of Interfaces: Basic Science in the Industrial World. World Scientific; 2000.

[237] XPS: Photoelectric effect. Wikipedia; [cited 2009 Mar. 18]; Available from: http://en.wikipedia.org/wiki/Photoelectric.

[238] Migdal-Mikuli A, Mikuli E, Dziembaj R, Majda D,Hetmanczyk L. Thermal decomposition of [Mg(NH3)(6)](NO3)(2), [Ni(NH3)(6)](NO3)(2) and [Ni(ND3)(6)](NO3)(2). Thermochimica Acta. 2004;419(1-2):223-229.

[239] Durand MA. The Coefficient of Thermal Expansion of Magnesium Oxide. Physics. 1936;7(8):297-298.

[240] Korotcenkov G, Brinzari V, Ivanov M, Cerneavschi A, Rodriguez J, Cirera A, et al. Structural stability of indium oxide films deposited by spray pyrolysis during thermal annealing. Thin Solid Films. 2005;479(1-2):38-51.

[241] Ratcheva TM, Nanova MD, Vasslev LV,Mikhailov MG. Properties of In2O3-Te Films Prepared by the Spraying Method. Thin Solid Films. 1986;139(2):189-199.

[242] Groves JR, Arendt PN, Kung H, Foltyn SR, DePaula RF, Emmert LA, et al., editors. Texture development in IBAD MgO films as a function of deposition thickness and rate. 2000 Applied Superconductivity Conference; 2000 Sep 17-22; Virginia Beach, Virginia.

[243] Dong L,Srolovitz DJ. Texture development mechanisms in ion beam assisted deposition. Journal of Applied Physics. 1998;84(9):5261-5269.

[244] Shi DQ, Ko RK, Song KJ, Chung JK, Choi SJ, Park YM, et al. Effects of deposition rate and thickness on the properties of YBCO films deposited by pulsed laser deposition. Supercond Sci Technol. 2004;17(2):S42-S45.

[245] Norton DP. pulsed laser deposition of complex materials: Progress towards applications. In: R. Eason, editor. pulsed laser deposition of thin films. New Jersey: WILEY-INTERSCIENCE; 2007. p. 3-31.

[246] Kawashima J, Yamada Y,Hirabayashi I. Critical thickness and effective thermal expansion coefficient of YBCO crystalline film. Physica C: Superconductivity. 1998;306(1-2):114-118.

[247] Tóth Z, Hopp B, Smausz T, Kántor Z, Ignácz F, Szörényi T, et al. Excimer laser ablation of molten metals as followed by ultrafast photography. Applied Surface Science. 1999;138-139:130-134.

[248] Transparent conductive zinc oxide: basics and applications in thin film solar cells. A. K. Klaus Ellmer, Bernd Rech, editor.: Springer; ; 2008.

[249] The effect of laser pulse length and the use of a tape target on the deposition of metallic films by pulsed laser deposition. CLF; [cited 2009 June, 23d,]; Available from: http://www.clf.rl.ac.uk/reports/1996-1997/pdf/75.pdf.

[250] Vale LR, Ono RH, McDonald DG,Phelan RJ. Large-area YBa2Cu3O7-x bolometers on Si substrates. Supercond Sci Technol. 1999;12(11):856-858.

[251] Matthee T, Wecker J, Behner H, Friedl G, Eibl O,Samwer K. Orientation relationships of epitaxial oxide buffer layers on silicon (100) for high-temperature superconducting YBa2Cu3O7-x films. Applied Physics Letters. 1992;61(10):1240-1242.

[252] Fork DK, Fenner DB, Barton RW, Phillips JM, Connell GAN, Boyce JB, et al. High critical currents in strained epitaxial YBa2Cu3O7-delta on Si. Applied Physics Letters. 1990;57(11):1161-1163.

[253] Matsumoto K, Seokbeom K, Jian-Guo W, Hirabayashi I, Watanabe T, Uno N, et al. Fabrication of in-plane aligned YBCO films on polycrystalline Ni tapes buffered with surface-oxidized NiO layers. Applied Superconductivity, IEEE Transactions on. 1999;9(2):1539-1542.

[254] Matsumoto K, Kim S, Yamagiwa K, Koike Y, Hirabayashi I, Watanabe T, et al. High critical current density YBa2Cu3O7-delta films on surface-oxidized metallic substrates. Physica C. 2000;335(1-4):39-43.

[255] Matsumoto K, Kim S, Hirabayashi I, Watanabe T, Uno N,Ikeda M. High critical current density YBa2Cu3O7-[delta] tapes prepared by the surface-oxidation epitaxy method. Physica C: Superconductivity. 2000;330(3-4):150-154.

[256] Khoi NN, Smeltzer WW,Embury JD. Growth and Structure of Nickel Oxide on Nickel Crystal Faces. Journal of the Electrochemical Society. 1975;122(11):1495-1503.

[257] Norton DP, Goyal A, Budai JD, Christen DK, Kroeger DM, Specht ED, et al. Epitaxial YBa2Cu3O7 on Biaxially Textured Nickel (001): An Approach to Superconducting Tapes with High Critical Current Density. Science. 1996 November 1, 1996;274(5288):755-757.

[258] Chakalova RI, Cai C, Woodcock T, Button TW, Abell JS,Maher E. Fabrication and characterisation of YBCO coated nickel-based tapes with various buffer layers. Physica C: Superconductivity. 2002;372-376(Part 2):846-850.

[259] Cheung YL, Jones IP, Abell JS, Button TW,Maher EF. Choice of insulating layer for YBCO in a multilayer architecture on buffered RABiTS. Supercond Sci Technol. 2007;20(3):216-221.

[260] Maher E, Abell JS, Chakalova RI, Cheung YL, Button TW,Tixador P. Multi-layer coated conductor cylinders—an alternative approach to superconducting coil fabrication. Superconductor Science and Technology. 2004;17(12):1440-1445.

[261] Cheung YL, Maher EF, Abell JS, Jones IP,Tse YY. Microstructural study of a YBCO multilayer coated conductor cylinder. Supercond Sci Technol. 2007;20(6):511-515.

[262] Woodcock TG, Abell JS,Hall MG. Characterization of textured NiO films for application as buffer layers in high temperature superconducting tapes. Journal of Microscopy-Oxford. 2002;205:231-237.

[263] Woodcock TG, Abell JS, Shields TC,Hall MG. The effect of different oxidation routines on the properties of surface oxidised epitaxial NiO layers on biaxially textured Ni tapes. Physica C-Superconductivity and Its Applications. 2002;372:863-865.

[264] Norton DP, Park C, Prouteau C, Christen DK, Chisholm MF, Budai JD, et al. Epitaxial YBa2Cu3O7 films on rolled-textured metals for high-temperature superconducting applications. Materials Science and Engineering B. 1998;56(2-3):87-94.

[265] Gladstone TA, Moore JC, Wilkinson AJ,Grovenor CRM. Grain boundary misorientation and thermal grooving in cube-textured Ni and Ni-Cr tape. Ieee Transactions on Applied Superconductivity. 2001;11(1):2923-2926.

[266] ASM handbook: Heat treating Metals Park, Ohio American Society for Metals (ASM) International; 1991.

[267] Hastelloy C276. Goodfellow; [cited 2008 May 10th]; Available from: www.goodfellow.com.

[268] Pat LM. The Principles of Materials Selection for Engineering Design. Prentice Hall; 1999.

[269] Philip A,P.E. Corrosion and Corrosion Protection Handbook. CRC press; 1989.

[270] T. Sourmail HKDHB. Stainless Steels. Unnversity of Cambridge; [cited 2009 May, 20th]; Available from: http://www.msm.cam.ac.uk/phasetrans/2005/Stainless_steels/stainless.html.

[271] Wu XQ, Xu S, Huang JB, Han EH, Ke W, Yang K, et al. Uniform corrosion and intergranular corrosion behavior of nickel-free and manganese alloyed high nitrogen stainless steels. Materials and Corrosion-Werkstoffe und Korrosion. 2008;59(8):676-684.

[272] Streicher MA. General and Intergranular Corrosion of Austenitic Stainless Steels in Acids - Effect of Cations in the Acids and the Influence of Heat Treatment

and Grain Size of the Steel. Journal of the Electrochemical Society. 1959;106(3):161-180.

[273] Streicher MA,Pickering FB. Stainless Steel: Past, Present and Future. The Metallurgical Evolution of Stainless Steel. Ohio, London: American Society for Metals (ASM) and The Metals Society; 1979. p. 442-475.

[274] Chia Hooi T. Sensitisation of Austenitic Stainless Steels [Master of Philosophy Dissertation]: University of Cambridge; 2002.

[275] ASM handbook, Corrosion: fundamentals, testing, and protection. Materials Park, Ohio American Society for Metals (ASM); 2003.

[276] Asm. Metals handbook. stainless steels, tool materials and special purpose metals / Vol.3, Properties and selection : prepared under the direction of the ASM Handbook Committee. 1980.

[277] Yates KA, Lockman Z, Kursumovic A, Burnell G, Stelmashenko NA, Driscoll JLM, et al. The effect of oxygenation on the superconducting properties of MgB2 thin films. Applied Physics Letters. 2005 Jan;86(2):3.

[278] Fan ZY, Hinks DG, Newman N,Rowell JM. Experimental study of MgB2 decomposition. Applied Physics Letters. 2001 Jul;79(1):87-89.

[279] Wu XD, Dye RC, Muenchausen RE, Foltyn SR, Maley M, Rollett AD, et al. Epitaxial CeO2 films as buffer layers for high-temperature superconducting thin-films. Applied Physics Letters. 1991 May;58(19):2165-2167.

[280] Cheung YL. Growth and characterisation of multilayer ybco coated conductors on curved surfaces University of Birmingham; 2005.

[281] Sørensen OT. Thermodynamic studies of the phase relationships of nonstoichiometric cerium oxides at higher temperatures. Journal of Solid State Chemistry. 1976;18(3):217-233.

[282] Leonard KJ, Kang S, Goyal A, Yarborough KA,Kroeger DM. Microstructural characterization of thick YBa2Cu3O7-delta films on improved rolling-assisted biaxially textured substrates. J Mater Res. 2003 Jul;18(7):1723-1732.

[283] Paranthaman M, Goyal A, List FA, Specht ED, Lee DF, Martin PM, et al. Growth of biaxially textured buffer layers on rolled-Ni substrates by electron beam evaporation. Physica C: Superconductivity. 1997;275(3-4):266-272.

[284] He Q, Christen DK, Budai JD, Specht ED, Lee DF, Goyal A, et al. Deposition of biaxially-oriented metal and oxide buffer-layer films on textured Ni tapes: new substrates for high-current, high-temperature superconductors. Physica C: Superconductivity. 1997;275(1-2):155-161.

[285] Raj AME, Nehru LC, Jayachandran M,Sanjeeviraja C. Spray pyrolysis deposition and characterization of highly (100) oriented magnesium oxide thin films. Crystal Research and Technology. 2007;42(9):867-875.

[286] McAdie HG,Jervis JM. The pyrolysis of metal acetates : Part I. Some group II acetates. Thermochimica Acta. 1970;1(1):19-28.

[287] Verma A, Bakhshi AK,Agnihotry SA. Effect of different precursor sols on the properties of CeO2-TiO2 films for electrochromic window applications. Electrochimica Acta. 2006;51(22):4639-4648.

[288] Boo JH, Lee SB, Yu KS, Koh W,Kim Y. Growth of magnesium oxide thin films using single molecular precursors by metal-organic chemical vapor deposition. Thin Solid Films. 1999;341(1-2):63-67.

[289] Gil Kim S, Hyun Choi K, Hwan Eun J, Joon Kim H,Seung Hwang C. Effects of additives on properties of MgO thin films by electrostatic spray deposition. Thin Solid Films. 2000;377-378:694-698.

[290] Norton DP, Lowndes DH, Budai JD, Christen DK, Jones EC, Lay KW, et al. High critical current densities in YBa2Cu3O-x films on polycrystalline zirconia. Applied Physics Letters. 1990;57(11):1164-1166.

[291] Su JH, Joshi PP, Chintamaneni V,Mukhopadhyay SM. Photoelectron spectroscopic investigation of transformation of trifluoroacetate precursors into superconducting YBa2Cu3O7-delta films. Applied Surface Science. 2007;253(10):4652-4658.

[292] Paranthaman M, Thompson JR,Christen DK. Effect of carbon-doping in bulk superconducting MgB2 samples. Physica C. 2001 Jun;355(1-2):1-5.

[293] Hassler W, Herrmann M, Rodig C, Schubert M, Nenkov K,Holzapfel B. Further increase of the critical current density of MgB2 tapes with nanocarbon-doped mechanically alloyed precursor. Supercond Sci Technol. 2008 Jun;21(6).

[294] Senkowicz BJ, Giencke JE, Patnaik S, Eom CB, Hellstrom EE,Larbalestier DC. Improved upper critical field in bulk-form magnesium diboride by mechanical alloying with carbon. Applied Physics Letters. 2005;86(20):202502-202503.

[295] Wilke RHT, Bud'ko SL, Canfield PC, Finnemore DK, Suplinskas RJ,Hannahs ST. Systematic Effects of Carbon Doping on the Superconducting Properties of Mg(B1-xCx)2. Physical Review Letters. 2004;92(21):217003.